



Universidade do Minho
Escola de Engenharia

Joaquim Bernardino dos Santos

Proof-of-concept of a Single-point Time-of-Flight LiDAR System and Guidelines towards Integrated High-accuracy Timing, Advanced Polarization Sensing and Scanning with a MEMS Micromirror

Dissertação de Mestrado

Mestrado Integrado em Engenharia Física

Ramo de Dispositivos, Microsistemas e Nanotecnologias

Trabalho efetuado sob a orientação de

Professor Doutor Eduardo Jorge Nunes Pereira

Dezembro de 2018

DECLARAÇÃO

NOME: Joaquim Bernardino dos Santos

ENDEREÇO ELETRÓNICO: joaquim.bsantos.1994@gmail.com CONTACTO TELEFÓNICO: 915402847

CARTÃO DE CIDADÃO: 14106067

TÍTULO DA DISSERTAÇÃO: *'Proof-of-concept of a Single-point Time-of-Flight LiDAR System and Guidelines towards Integrated High-accuracy Timing, Advanced Polarization Sensing and Scanning with a MEMS Micromirror'*

ORIENTADOR: Professor Doutor Eduardo Pereira (Departamento de Física, Universidade do Minho)

SUPERVISOR NA EMPRESA: Alexandre Correia (Bosch Car Multimedia S.A, CC-PS/ENG-Brg)

ANO DE CONCLUSÃO: 2018

Mestrado Integrado em Engenharia Física

É AUTORIZADA A REPRODUÇÃO PARCIAL DESTA DISSERTAÇÃO, APENAS PARA EFEITOS DE INVESTIGAÇÃO, MEDIANTE DECLARAÇÃO ESCRITA DO INTERESSADO, QUE A TAL SE COMPROMETE.

Universidade do Minho, ____ de _____ de _____

O Autor: _____

– This page is intentionally left blank –

Whereas the beautiful is limited, the sublime is limitless, so that the mind in the presence of the sublime, attempting to imagine what it cannot, has pain in the failure but pleasure in contemplating the immensity of the attempt.

Immanuel Kant in *Critique of Pure Reason*

– This page is intentionally left blank –

ACKNOWLEDGMENTS

Herein, and with no particular order, I would like to express my deeply sincere gratitude to everyone who somehow impacted me positively throughout these five years, contributing either directly or indirectly to my now-ceasing successful academic path and to my personal enhancement:

- . To my advisor, Professor Eduardo Jorge Nunes Pereira, for rescuing me after a slippery beginning, for offering me the opportunity to work on this project, for the vigorous words and advices, for the vote of confidence and for teaching me to never lose sight from the “bigger picture”.
- . To my supervisor at Bosch Car Multimedia, Alexandre Correia, not only for giving me the opportunity to integrate the LiDAR team, but also for the confidence deposited and for the chance to initiate my professional journey by remaining in this extremely impactful and promising project.
- . To my beloved life partner, Bárbara Peixoto, for sharing this harsh but rewarding path alongside me, for being an exquisitely determined, resilient and strong woman, for upholding me even in the murkiest and hopeless hours, for never letting me quit, for the experiences and for the most philosophical, constructive and meaningful debates.
- . To my parents, Rosa and Henrique, and grandma, Maria José, for being by my side from day one, for a truly peaceful and delightful childhood, for the open-minded and free education, for the culture, for the opportunities, for the values, for the rationality, for the sacrifices and for the inexhaustible support and encouragement.
- . To my adored sister Maria, for thriving with me, for the shared memorable adventures and enriching fights, for the unconditional love and for the safeguard in diverse occasions.
- . To my exceptional friend, Olivia Silva, for the emotional support, for the patience, for the kindness and for the impartiality.
- . To all my close family, for always backing me up and for consistently reminding me the meaningful and worthy aspects of life.
- . To my university colleagues and friends, from whom I would like to stand out Afonso, Fonseca, Moisés, Lomba, Nogueira, Ricardo, Rúben, Rui, Sanches and Zé Bruno, for the shared stressful hours, for the sleepless nights, for the amazing nights-out, for the shared ecstatic laughs and for making this tough and tiresome degree substantially more bearable.
- . To my team colleagues in Bosch Car Multimedia, for embracing me in this internship and for the constant availability to help me in whatever issue I have found.
- . To the most enthusiastic, empathetic, comprehensive and passionate professional I met in my entire academic path, Professor Salvatore Cosentino, for showing me the genuine value of doing what we love and for transmitting me his Physics and Mathematics devotion.

It has been an authentic privilege to share this odyssey with you and all my accomplishments would not have been conceivable without your influence. For everything, I will be forever thankful to you all and I dedicate a short excerpt from Haruki Murakami in *Kafka on the Shore*:

“Sometimes fate is like a small sandstorm that keeps changing directions. You change direction but the sandstorm chases you. You turn again, but the storm adjusts. Over and over you play this out, like some ominous dance with death just before dawn. Why? Because this storm isn't something that blew in from far away, something that has nothing to do with you. This storm is you. Something inside of you. So all you can do is give in to it, step right inside the storm, closing your eyes and plugging up your ears so the sand doesn't get in, and walk through it, step by step. There's no sun there, no moon, no direction, no sense of time. Just fine white sand swirling up into the sky like pulverized bones. That's the kind of sandstorm you need to imagine.

And you really will have to make it through that violent, metaphysical, symbolic storm. No matter how metaphysical or symbolic it might be, make no mistake about it: it will cut through flesh like a thousand razor blades. People will bleed there, and you will bleed too. Hot, red blood. You'll catch that blood in your hands, your own blood and the blood of others.

And once the storm is over you won't remember how you made it through, how you managed to survive. You won't even be sure, in fact, whether the storm is really over. But one thing is certain. When you come out of the storm you won't be the same person who walked in. That's what this storm's all about.”

ABSTRACT

The core focus of the work reported herein is the fulfillment of a functional Light Detection and Ranging (LiDAR) sensor to validate the direct Time-of-Flight (ToF) ranging concept and the acquisition of critical knowledge regarding pivotal aspects jeopardizing the sensor's performance, for forthcoming improvements aiming a realistic sensor targeted towards automotive applications. Hereupon, the ToF LiDAR system is implemented through an architecture encompassing both optical and electrical functions and is subsequently characterized under a sequence of test procedures usually applied in benchmarking of LiDAR sensors. The design employs a hybrid edge-emitting laser diode (pulsed at 6kHz, 46ns temporal FWHM, 7ns rise-time; 919nm wavelength with 5nm FWHM), a PIN photodiode to detect the back-reflected radiation, a transimpedance stage and two Time-to-Digital Converters (TDCs), with leading-edge discrimination electronics to mark the transit time between emission and detection events. Furthermore, a flexible modular design is adopted using two separate Printed Circuit Boards (PCBs), comprising the transmitter (TX) and the receiver (RX), i.e. detection and signal processing. The overall output beam divergence is $0.4^\circ \times 1^\circ$ and an optical peak power of 60W (87% overall throughput) is realized.

The sensor is tested indoors from 0.56 to 4.42 meters, and the distance is directly estimated from the pulses transit time. The precision within these working distances ranges from 4cm to 7cm, reflected in a Signal-to-Noise Ratio (SNR) between 12dB and 18dB. The design requires a calibration procedure to correct systematic errors in the range measurements, induced by two sources: the timing offset due to architecture-inherent differences in the optoelectronic paths and a supplementary bias resulting from the design, which renders an intensity dependence and is denoted time-walk. The calibrated system achieves a mean accuracy of 1cm. Two distinct target materials are used for characterization and performance evaluation: a metallic automotive paint and a diffuse material. This selection is representative of two extremes of actual LiDAR applications. The optical and electronic characterization is thoroughly detailed, including the recognition of a good agreement between empirical observations and simulations in *ZEMAX*, for optical design, and in a SPICE software, for the electrical subsystem.

The foremost meaningful limitation of the implemented design is identified as an outcome of the leading-edge discrimination. A proposal for a Constant Fraction Discriminator addressing sub-millimetric accuracy is provided to replace the previous signal processing element. This modification is mandatory to virtually eliminate the aforementioned systematic bias in range sensing due to the intensity dependency. A further crucial addition is a scanning mechanism to supply the required Field-of-View (FOV) for automotive usage. The opto-electromechanical guidelines to interface a MEMS micromirror scanner, achieving a $46^\circ \times 17^\circ$ FOV, with the LiDAR sensor are furnished. Ultimately, a proof-of-principle to the use of polarization in material classification for advanced processing is carried out, aiming to complement the ToF measurements. The original design is modified to include a variable wave retarder, allowing the simultaneous detection of orthogonal linear polarization states using a single detector. The material classification with polarization sensing is tested with the previously referred materials culminating in an 87% and 11% degree of linear polarization retention from the metallic paint and the diffuse material, respectively, computed by Stokes parameters calculus. The procedure was independently validated under the same conditions with a micro-polarizer camera (92% and 13% polarization retention).

KEYWORDS: LIDAR, RANGE SENSING, TIME-OF-FLIGHT, TIME-TO-DIGITAL CONVERTER, POLARIZATION SENSING, MATERIAL CLASSIFICATION, AUTONOMOUS DRIVING, AUTOMOTIVE SENSORS, CONSTANT FRACTION DISCRIMINATION, SCANNING, TIME-WALK

– This page is intentionally left blank –

RESUMO

O intuito primordial do trabalho reportado no presente documento é o desenvolvimento de um sensor LiDAR funcional, que permita validar o conceito de medição direta do tempo de voo de pulsos óticos para a estimativa de distância, e a aquisição de conhecimento crítico respeitante a aspetos fundamentais que prejudicam a performance do sensor, ambicionando melhorias futuras para um sensor endereçado para aplicações automóveis. Destarte, o sistema LiDAR é implementado através de uma arquitetura que engloba tanto funções óticas como eletrónicas, sendo posteriormente caracterizado através de uma sequência de testes experimentais comumente aplicáveis em *benchmarking* de sensores LiDAR. O design tira partido de um díodo de laser híbrido (pulsado a 6kHz, largura temporal de 46ns; comprimento de onda de pico de 919nm e largura espectral de 5nm), um fotodiodo PIN para detetar a radiação refletida, um andar de transamplificação e dois conversores tempo-digital, com discriminação temporal com *threshold* constante para marcar o tempo de trânsito entre emissão e receção. Ademais, um design modular flexível é adotado através de duas PCBs independentes, compondo o transmissor e o recetor (deteção e processamento de sinal). A divergência global do feixe emitido para o ambiente circundante é $0.4^\circ \times 1^\circ$, apresentando uma potência ótica de pico de 60W (eficiência de 87% na transmissão).

O sensor é testado em ambiente fechado, entre 0.56 e 4.42 metros. A precisão dentro das distâncias de trabalho varia entre 4cm e 7cm, o que se reflete numa razão sinal-ruído entre 12dB e 18dB. O design requer calibração para corrigir erros sistemáticos nas distâncias adquiridas devido a duas fontes: o desvio no ToF devido a diferenças nos percursos optoeletrónicos, inerentes à arquitetura, e uma dependência adicional da intensidade do sinal refletido, induzida pela técnica de discriminação implementada e denotada *time-walk*. A exatidão do sistema pós-calibração perfaz um valor médio de 1cm. Dois alvos distintos são utilizados durante a fase de caracterização e avaliação performativa: uma tinta metálica aplicada em revestimentos de automóveis e um material difusor. Esta seleção é representativa de dois cenários extremos em aplicações reais do LiDAR. A caracterização dos subsistemas ótico e eletrónico é minuciosamente detalhada, incluindo a constatação de uma boa concordância entre observações empíricas e simulações óticas em *ZEMAX* e elétricas num software SPICE.

O principal elemento limitante do design implementado é identificado como sendo a técnica de discriminação adotada. Por conseguinte, é proposta a substituição do anterior bloco por uma técnica de discriminação a uma fração constante do pulso de retorno, com exatidões da ordem sub-milimétrica. Esta modificação é imperativa para eliminar o *offset* sistemático nas medidas de distância, decorrente da dependência da intensidade do sinal. Uma outra inclusão de extrema relevância é um mecanismo de varrimento que assegura o cumprimento dos requisitos de campo de visão para aplicações automóveis. As diretrizes para a integração de um micro-espelho no sensor concebido são providenciadas, permitindo atingir um campo de visão de $46^\circ \times 17^\circ$. Conclusivamente, é feita uma prova de princípio para a utilização da polarização como complemento das medições do tempo de voo, de modo a suportar a classificação de materiais em processamento avançado. A arquitetura original é modificada para incluir uma lâmina de atraso variável, permitindo a deteção de estados de polarização ortogonais com um único fotodetector. A classificação de materiais através da aferição do estado de polarização da luz refletida é testada para os materiais supramencionados, culminando numa retenção de polarização de 87% (tinta metálica) e 11% (difusor), calculados através dos parâmetros de Stokes. O procedimento é independentemente validado com uma câmara polarimétrica nas mesmas condições (retenção de 92% e 13%).

– This page is intentionally left blank –

Table of Contents

List of Figures	xv
List of Tables	xxvii
List of Acronyms and Abbreviations	xxxi
1. INTRODUCTION	1
1.1. Context	1
1.1.1. Automated Driving Levels	2
1.1.2. Sensorial Perception	4
1.1.3. Sensor Fusion for Autonomous Vehicles	7
1.2. Motivation and Objectives	11
1.3. Bosch Group	13
1.4. Framework and Content	14
2. LIGHT DETECTION AND RANGING.....	17
2.1. Requirements for autonomous driving.....	19
2.1.1. Field of View (FOV) and Range.....	20
2.1.2. Frame Rate.....	22
2.1.3. Angular Resolution	22
2.1.4. Range Accuracy	24
2.1.5. Laser	24
2.1.6. Others	25
2.2. Techniques for Range Estimation.....	26
2.2.1. Triangulation.....	26
2.2.2. Interferometry	27
2.2.3. Direct Time-of-Flight	28
2.2.4. Random Pulse Modulation	29
2.2.5. Continuous Wave Modulation	30
2.3. Laser Sources	32
2.3.1. Laser Types	33
2.3.2. Wavelengths	34
2.3.3. Eye-safety and Limitations	35
2.3.4. Laser Driving	37
2.4. Scanning Mechanisms	39
2.4.1. Scanning LiDAR	40
2.4.2. Solid-State LiDAR	41
2.4.3. Hybrid LiDAR	42
2.4.4. Comparative Analysis.....	43
2.5. Photodetection	45

2.5.1.	Noise in Photodetection	47
2.5.2.	Avalanche Photodiodes	48
2.5.3.	Single-photon Avalanche Diodes	49
2.5.4.	PIN Photodiodes	50
2.5.5.	Detectors Array	52
2.5.6.	Photomultiplier Tubes	53
2.6.	Conditioning and Processing.....	53
2.7.	Hardware Timing Discriminator	57
2.8.	Optics	58
2.8.1.	Collimating Lens	58
2.8.2.	Focusing Lens	58
2.8.3.	Beam-shaping.....	59
2.8.4.	Optical Filters.....	60
2.9.	LiDAR Equation	61
3.	STATE-OF-THE-ART	63
3.1.	Automotive LiDAR Solutions.....	63
3.1.1.	Velodyne.....	64
3.1.2.	Quanergy Systems	68
3.1.3.	Innoviz.....	71
3.1.4.	LeeddarTech	72
3.1.5.	Valeo	74
3.1.6.	Continental AG.....	75
3.1.7.	Others	76
3.1.8.	Overview.....	79
3.2.	Out-of-the-box Concepts.....	81
3.2.1.	Luminar.....	81
3.2.2.	Interference Immunity and FMCW Technology	83
3.2.3.	LiDAR-on-a-chip.....	85
3.2.4.	Camera-LiDAR Fusion	86
3.2.5.	Polarization-modulated Flash LiDAR	87
4.	SYSTEM ARCHITECTURE.....	95
4.1.	Transmitter board (TX)	97
4.1.1.	Delay Block.....	98
4.1.2.	Laser Driver and Pulsed Laser.....	100
4.2.	Receiver board (RX).....	104
4.2.1.	Photodetection.....	104
4.2.1.1.	Return Photodetector	105
4.2.1.2.	Reference Photodetector.....	105
4.2.2.	Transimpedance Amplifier.....	106
4.2.3.	Leading-edge Discriminator	108
4.2.4.	Time-to-Digital Converters.....	111
4.2.4.1.	Operation and Integration	111
4.2.4.2.	Pulse Requirements.....	114
4.2.4.3.	Configuration.....	114

4.3.	Microcontroller Units	115
4.3.1.	MSP430FR5969 (RX MCU)	117
4.3.1.1.	Clock Sources	118
4.3.1.2.	TIA Configuration	118
4.3.1.3.	Pulse Width Modulation	118
4.3.1.4.	External Interrupt.....	119
4.3.1.5.	SPI.....	120
4.3.1.6.	UART	126
4.3.2.	MSP430F5529 (TX MCU)	127
4.4.	Architecture Diagram.....	129
4.4.1.	Boards Assembly	130
4.5.	Optical Setup	133
5.	RESULTS AND DISCUSSION.....	139
5.1.	Overall Sensor.....	139
5.1.1.	Precautions	139
5.1.2.	Targets Characterization	140
5.1.3.	Graphical User Interface.....	143
5.1.4.	Standard Test Conditions	144
5.1.4.1.	Reflection Component.....	145
5.1.4.2.	Transimpedance Gain.....	147
5.1.4.3.	Triggering/Timing Edge	149
5.1.4.4.	Return Threshold.....	150
5.1.5.	Calibration and Accuracy.....	151
5.1.5.1.	Amplitude Dependence and Time-walk.....	160
5.1.6.	LiDAR Performance.....	164
5.1.6.1.	Range	164
5.1.6.2.	Precision and Fluctuation Sources	166
5.1.6.3.	Signal-to-Noise Ratio (SNR)	170
5.1.6.4.	Dynamic Operation	171
5.2.	Optical Characterization	172
5.2.1.	Optical Simulation.....	172
5.2.2.	Optical Alignment and Optimization.....	181
5.2.3.	Stabilization Time and Laser Spectral Profile.....	182
5.2.4.	Laser Temporal Profile	185
5.2.5.	Optical Power and Eye-safety.....	187
5.2.6.	Beam Spatial Profile.....	191
5.2.7.	Reference and Return Paths.....	203
5.3.	Electrical Characterization	205
5.3.1.	Electrical simulation	205
5.3.2.	Transmitter Signals	207
5.3.3.	Reference Path	209
5.3.4.	Photodetection and Amplification	211
5.3.5.	Leading-edge Discriminator	214
5.3.5.1.	Thresholds' Configuration	214

5.3.5.2.	Timing.....	215
5.3.6.	Time-to-Digital Converters.....	218
5.3.6.1.	Configuration.....	218
5.3.6.2.	Jitter Analysis	221
5.4.	Adjustments to TIDA-00663 Design	224
6.	GUIDELINES TOWARDS ADVANCED FUNCTIONALITIES.....	229
6.1.	Scanning with Micromirror.....	229
6.1.1.	Optomechanical Guidelines.....	231
6.1.2.	Electrical Guidelines.....	233
6.1.3.	Projection Testing	235
6.2.	Polarization Sensing.....	240
6.2.1.	Advanced Polarimetric Imaging	241
6.2.2.	Stokes Parameters and Quantitative Analysis.....	243
6.2.3.	Experimental Setups and Results	248
6.3.	Advanced Timing Discrimination	253
7.	CONCLUSIONS AND FUTURE WORK.....	267
7.1.	Conclusions	267
7.2.	Future Work	278
	Bibliography.....	281
	Appendix I – Bill of Materials	293
	Appendix II – Final Codes.....	295
	RX MCU Code (C language)	295
	TX MCU Code (C language).....	299
	GUI Interface Code (Java)	300
	Cubic Spline and Peak Power Evaluation (MATLAB).....	304
	Polarimetric Images Processing (MATLAB)	306
	Appendix III – ZEMAX Object Data.....	311
	Before Optimization	311
	After Optimization	311

List of Figures

Figure 1. SAE international J3106 standard taxonomy for automated driving levels with several driver assistance systems discriminated for the corresponding levels (adapted from [4]).....	3
Figure 2. Remote sensing technologies taxonomy (adapted from [2] and [19])	4
Figure 3. Sensorial perception provided by cameras: (a) working principle of camera vision [20], (b) image produced by an infrared camera and detection of a pedestrian on the roadside [21] and (c) features extraction from a RGB image.	5
Figure 4. Basic principles of automotive sensors: (a) LiDAR [20]; (b) example of LiDAR resultant tridimensional frame where some obstacles are easily detected [24]; (c) Sonar and (d) Radar [20].	6
Figure 5. Elements of an highly-autonomous driving system [26].....	7
Figure 6. Diffraction-limited spatial resolution of an emitting system.	10
Figure 7. Panoply of sensing units and usage in the existing ADAS systems and respective coverage in the car surroundings [36].	11
Figure 8. General architecture of a LiDAR system, with scanning performed by beam steering though a rotating mirror. In this image the sensor is integrated in the car's front bumper (adapted from [40]).	18
Figure 9. Lateral view illustrating the point collection in LiDAR and the corresponding point cloud (the left vehicle, equipped with the sensor, is shown just for localization purposes). If there is not any target in the beam direction, no reflection occurs, and the point is not depicted in the point cloud.	18
Figure 10. Definition of the Cartesian and spherical coordinate systems, with origin located at the sensor's optical aperture, and angles' signal convention.....	19
Figure 11. Representation of the sensor's FOV, maximum and minimum range, measured radially from the LiDAR optical aperture (adapted from [40]).	20
Figure 12. System's FOV requisites.	22
Figure 13. Frame segmentation in pixels and geometrical representation of each pixel's relative position within it. Two perpendicular views are shown (top and lateral) for generic lines, $1 \leq i \leq m$, and columns $1 \leq j \leq n$	23
Figure 14. Geometrical schematic description of a 1D (a) passive and (b) active triangulation system [19].....	26
Figure 15. Working principle of Michelson Interferometer (adapted from [19]).	27
Figure 16. Illustrative representation of ToF principle (adapted from [50]).	29
Figure 17. Correlational ToF technique: (a) two different random bursts of pulses generated by the commercial LiDAR Garmin Lite [52]; (b) example of a correlation result between the transmitted signal and the echo, showing a peak corresponding to the correct ToF [51].	30

Figure 18. Accuracy vs. operating range for academically published and industrial LiDARs since 1990 [37].....	31
Figure 19. Pulsed laser parameters.	33
Figure 20. Solar irradiance spectrum at the top of the atmosphere (green) and transmitted to the Earth's surface (brown), at sea level [59].	35
Figure 21. Eye-safety considerations. (a) diagram of the human eye and (b) penetration of different wavelengths.	36
Figure 22. MPE vs. Wavelength for different pulse durations [62].	37
Figure 23. Laser diode typical response (output light power vs. forward electrical current) and temperature dependence.	38
Figure 24. Taxonomy of LiDAR classes based on the scene illumination mechanism.	39
Figure 25. Principle of a mechanical scanning LiDAR with 4 channels. The retroreflected light within each segment is detected by a dedicated photosensitive device. For simplicity, the receiving and transmitting optics were omitted.	40
Figure 26. Transmission system of a LiDAR based on micromirror scanning technique and illustration of the scene sweeping mechanism line by line.	41
Figure 27. Working principle of flash LiDAR with emphasis on the FOV segmentation and detection process at each pixel on the array. Also, a resulting point cloud of the scene is represented in 2D.	42
Figure 28. LeddarTech's automotive 3D hybrid LiDAR [66].	43
Figure 29. Integration of several automotive LiDAR sensors with FOV inferior to 360° in order to cover a 360° FOV [70].	44
Figure 30. Schematic diagram of the avalanche multiplication process within a p-n junction. The n+p junction is designated the avalanche layer [74].	48
Figure 31. i-V characteristic of a SPAD.	50
Figure 32. The p-i-n photodiode structure, energy-band diagram, and electric-field distribution (left). On the right, photodiode's electrical symbol and generic i-V characteristic. The device can be illuminated either perpendicularly or parallel to the junction (adapted from [72]).	51
Figure 33. Detection with (a) an SPAD FPA [37] and schematic illustration of a PMT [79].	53
Figure 34. Transimpedance Amplifier.	54
Figure 35. Architecture of a LiDAR with timing performed using a TDC.	55
Figure 36. Architecture of a LiDAR with timing performed using ADCs.	56
Figure 37. Light (a) collimation and (b) focusing processes.	59
Figure 38. Representation of a lens used to focus the incoming light from different angles in different pixels of a FPA.	59

Figure 39. Beam-shaping: (a) a pair of anamorphic prisms placed after a collimating lens to circularize the cross-sectional profile (adapted from [84]) and (b) beam-expander to shrink or expand the beam diameter.....	60
Figure 40. Lambertian reflection profile and receiver’s solid angle.	62
Figure 41. Geographical dispersion of the main presences in the automotive LiDAR market by April 2018 [87].....	64
Figure 42. <i>Velodyne’s</i> new products: (a) <i>VLS-128</i> and (b) <i>Velarray</i> . In (c), a comparison of a frame segment obtained with <i>VLS-128</i> (top) and <i>HDL-64E</i> (bottom) shows the huge difference in the point cloud density and resolution [98].	68
Figure 43. <i>Quanergy S3</i> LiDAR: (a) illustration of the working principle and (b) integration in automotive headlights [1].	69
Figure 44. <i>InnovizPro</i> LiDAR [104].....	71
Figure 45. Automotive-grade <i>InnovizOne</i> . Due to the compact housing, this stand-alone unit can be readily integrated in several strategic points in the car’s structure [105].	72
Figure 46. Signal travelling through the main components of Leddar sensing module [108].....	74
Figure 47. <i>Valeo’s SCALA</i> laser scanner [110].	74
Figure 48. <i>Continental’s Flash</i> LiDAR [112].	75
Figure 49. (a) Peregrine Series 3D Flash LiDAR [120] and (b) Integration of three <i>LUX</i> units in the <i>HAVEit</i> project.....	78
Figure 50. FOV segmentation in <i>Hesai PANDAR</i> . [123]	79
Figure 51. Main automotive LiDAR players segmented according to the technological implementation [87].....	80
Figure 52. (a) <i>Luminar</i> LiDAR and (b) generated high resolution point cloud [135].....	81
Figure 53. Patented <i>Luminar</i> LiDAR’s block diagram [138].	82
Figure 54. (a) <i>Blackmore</i> automotive LiDAR, example of a generated high-resolution point cloud and (c) velocity measurement through the FMCW Doppler-shift [142]......	84
Figure 55. (a) <i>Oryx</i> LiDAR [141] and (b) <i>Garmin Lite v3</i> [143].	84
Figure 56. (a) Intensity profile (array factors) for different antennas spacing, (b) 3D rendering of the OPA and SEM images: (c) phase shifter architecture, (d) thermal phase shifters and (e) silicon grating based antennas with waveguide width of 400nm and a pitch of 2µm [145].	86
Figure 57. (a) <i>TetraVue</i> 4D camera and (b) example of a generated frame, in which the color scale indicates the depth [148].....	87
Figure 58. <i>TetraVue’s</i> patented LiDAR technology employing a electro-optical modulator (524), to modulate the returning light polarization state, and a PBS (527) that posteriorly splits two orthogonal states to two distinct FPAs (528 and 529) [151].	88
Figure 59. <i>TetraVue’s</i> patented conceptual diagram of a 3D camera sensor employing a modulator and a polarizing grid array. The returning light is collected by an optical element (12) and then passed	

through a Pockels cell (14) and then is detected by a camera sensor (20) interfaced by a polarizer grid (18) [149].	90
Figure 60. Schematic diagram of the micropolarizer Flash LiDAR [152].	91
Figure 61. Block Diagram of the implemented LiDAR system. The polarity of the digital signals is evidenced.	95
Figure 62. TIDA-00663 PCB layout: (a) top view with components in Altium as provided in the Gerber files and (b) top view of the printed PCB.	97
Figure 63. Electrical schematic of the system's transmitter (adapted from [156]).	97
Figure 64. Schematic representation of the delay block.	98
Figure 65. (a) Transfer curve of an inverter Schmitt-trigger and (b) working principle of the delay block.	99
Figure 66. Schematic representation of the laser emitter and respective driver.	100
Figure 67. <i>UCC27321DR</i> MOSFET Driver: (a) block diagram and (b) switching characteristic [159].	101
Figure 68. Equivalent circuit when the gate signal, $GATE_DRV=V_G$ is in (a) low-state and (b) high-state.	102
Figure 69. <i>SPL LL90_3</i> characteristics: (a) optical pulse's form for different trigger pulse widths [161] and (b) optical output power response as a function of the temperature and charge voltage (triggering pulse with 30ns and 1kHz PRR) [160].	103
Figure 70. Schematic representation of the photodetection process.	105
Figure 71. Simplified representation of the process for generating the reference voltage pulse.	106
Figure 72. Simplified current-to-voltage conversion process.	106
Figure 73. <i>OPA857's</i> functional block diagram [165].	107
Figure 74. Electrical schematic of the system's amplifier stage (adapted from [156]).	108
Figure 75. Leading-edge discriminator architecture.	108
Figure 76. Electrical schematic of the leading-edge discriminator (adapted from [156]).	109
Figure 77. Leading-edge discrimination.	110
Figure 78. TDC7200 functioning principle: (a) schematic integration on the system where two TDCs are used operating in a similar manner; (b) measurement mode 2 (adapted from [168]).	111
Figure 79. Electrical diagram (adapted from [156]).	112
Figure 80. Configured registers summary and bits nomenclature (adapted from [168]).	115
Figure 81. Flowchart of the RX MCU program.	116
Figure 82. MSP-EXP430FR5969 connectors pinout (top) [169] and RX PCB headers pinout (bottom) [156].	117
Figure 83. Serial Peripheral Interface: (a) detailed connection between a master and a single slave and (b) connection of three slaves to the master with separate CS lines (adapted from [170]).	121

Figure 84. Digital Interface Write Sequence [166].	123
Figure 85. SPI protocol and frames for TDC transactions [168].	124
Figure 86. Interface between the MSP-EXP430FR5969 and PC for ToF data transmission.	126
Figure 87. (a) Right-side 20×2 header and pins' functions [172] and (b) respective TX board headers [156]. In (c) the flowchart for the TX MCU program.	127
Figure 88. Boards' intra and inter-connections and exchanged signals between components. In blue is represented the emitted light from the transmitter and the incoming light on both detectors. The SPI signals are represented through net labels for visual simplicity. The components' and, consequently, the signals relative positions are merely indicative and do not correspond necessarily to their positions in the actual assembly.	128
Figure 89. Representation of the vital signals involved in the sequential process of single-point acquisition.	129
Figure 90. LiDAR final boards. On the left, the TX PCB mounted on the TX MCU. On the center, the backsides of both PCBs. On the right, the RX PCB mounted directly on the RX MCU. The headers to connect the external power source are highlighted by the orangish rectangles.	130
Figure 91. Photography of the MSP-EXP430F5529 attached to the acrylic slab.	131
Figure 92. Front-view of the hardware setup on the optical breadboards. It is noticeable that the TX-end is mounted on a smaller breadboard.	131
Figure 93. Hardware supports: (a) 3DOF stage for the RX hardware and (b) screws holding the acrylic plate.	132
Figure 94. Electrical wiring: (a) jumper to transfer <i>BP_TRIG</i> from the RX to the TX side and (b) external power supply cable with a fuse in series.	132
Figure 95. Connection between the reference photodetector and the receiver PCB.	133
Figure 96. (a) Diffraction angles in a semiconductor laser diode and (b) resulting astigmatism [156].	134
Figure 97. Diagram of the complete optical system.	135
Figure 98. Spherical aberration phenomenon (left) and correction using aspherical lenses (right)....	136
Figure 99. Mounted lens layout and respective parameters.	136
Figure 100. B-coating reflectance spectrum [177].	137
Figure 101. Photos of the optical system interfaced with the hardware. On the left, the reference path, on top, the TX path and, on the right, the RX path.	138
Figure 102. Oscilloscope probe: (a) short ground lead and (b) equivalent circuit connected to the DUT.	140
Figure 103. Characterization of the targets' reflective characteristics: (a) illustration of specular and diffuse reflection on a surface; (c) measurement setup with sample and detector angle definitions. [180].....	141

Figure 104. Vauxhall Green Lemon Grass Metallic target: (a) sample used in the experimental tests with 10.5cm×15cm; (b) metallic flakes made visible when the plate is struck by an He-Ne laser; (c) specular reflection peaks for several AOI. In the last image, the width of each peak depends purely on the detection optics in the measurement device (f-number). 142

Figure 105. (a) K-line White target sample used in the experimental tests with 50cm×70cm. (b) In-plane BRDF for several target materials as a function of the detection angle. The angle of incidence is fixed at 0° and the angles between -20° and 20° are unavailable due to occlusion. 143

Figure 106. Developed GUI for the LiDAR prototype. 144

Figure 107. Setup for establishing the standard test conditions of the 1D LiDAR sensor. On the left, the lateral view with the prototype (westside) and the *Vauxhall Green Metallic* target (east), with the light path marked from the transmission to the reflection back to the receiver. On the right, the front view of the mounted target with the rotating direction highlighted (to alternate between specular and diffuse components). 146

Figure 108. Top view schematic to illustrate the required adjustments to the LiDAR system to measure the diffuse (a) and specular (a and b) components at distinct distances: (a) rotation or (b) translation of the TX whenever the target distance is modified. 147

Figure 109. Return pulse acquired with gain 20k for diffuse reflection on *Vauxhall* at 671mm: (a) zoom-out of the pulse to show the oscillations on the baseline, (b) overlaid thresholds and return pulse and (c) zoom-in of the baseline and respective limits and mean value. The back-reflected pulse is detected at t=0. 151

Figure 110. Simplified schematic of the setup for range measurements and characterization of the 1D LiDAR prototype. On the top right, it is shown how the actual distance is measured with the rangemeter: the device is softly landed on top of the RX optics, to ensure a stable and correct measurement without compromising the delicate optical alignment. 153

Figure 111. Shift in the calibration distance as a function of the (actual) distance to the *K-line* target. Simultaneously with the experimental points, the error bars are also depicted alongside the three established calibration constants. 155

Figure 112. Experimental mean values vs. actual distance measured with the rangemeter. In blue, the calibration line that linearly fits to the experimental points. Simultaneously, the best relative and absolute calibration curves are also traced, with some regions zoomed-in to highlight the misfit from the real response..... 156

Figure 113. Absolute and relative residues of the ideal linear calibration. On the left, using the “best relative calibration”, applied by summing a constant range of 1.528m to each measured value. On the right, after implementation of the “best absolute calibration” by applying a positive offset of 1.480m to each result. 158

Figure 114. Measured distance vs. actual distance after applying a range-dependent calibration. On top, it is shown the nearly-ideal linear fit with unitary slope and null y intersect. On the bottom, the residues in mm as a function of this distance. The latter are the calculated deviations from the linear regression and represent the inaccuracy at each marked distance..... 159

Figure 115. Back-reflected pulses (<i>return_analog</i>) on <i>K-line white</i> for 5 distinct distances and after transamplification. Inside the highlighted rectangle, a zoom-in on the threshold crossing region.	160
Figure 116. Pulses acquired for the back-reflection on the <i>Vauxhall</i> target at $d_{\text{actual}}=1.204\text{m}$ for different alignments. Zoomed-in, the $V_{\text{th,A}}=1.7\text{V}$ crossing instant showing that, the greater the amplitude, the faster the crossing instant and, therefore, the shorter the effective ToF.	162
Figure 117. Time-walk vs amplitude of the transamplified return pulse after reflection on the <i>Vauxhall</i> target at $d_{\text{actual}}=1.204\text{m}$. The ToF for the specularly reflected component is used as reference and, hence, the time-walk for the respective amplitude (1.56V) is zero. Overlapped with each experimental point are the error bars referent to the standard deviation.	163
Figure 118. Schematic of the benchmarking experiment [34].	164
Figure 119. Analog return pulse (<i>return_analog</i>) after transamplification and reflected at the K-line white target placed at $d=4.420\text{m}$. It is visible that the return optical intensity still triggers a detectable STOP signal do TDC2.	165
Figure 120. Overlap between laser beam and detector FOV and minimum sensing distance [156]. .	166
Figure 121. Gaussian probability density distribution and illustration of the difference between accuracy and precision. The accuracy is the deviation between d_{actual} and the mean value $\langle d \rangle$. The precision is linked to the dispersion of the measurements around the mean value, i.e. to the width of the normal distribution in this example.	166
Figure 122. Standard deviation in the range measurements, σ_d , as a function of the calibrated distance to the target. Additionally, for the initial, final and an intermediate distance, the histograms are detailed with the Gaussian fits according to the determined mean and standard deviation.	167
Figure 123. Periodic oscillations in the $\text{BP}_{3.3} \equiv V_{\text{cc}} \equiv V_{\text{S}}$ signal arising from the RX MCU board around the mean value of 3.58V. The oscillations are periodic with approximately 100kHz frequency. .	168
Figure 124. Standard deviation of commercial LiDAR sensors for a 95% diffusely reflective target. The vertical axis is in a logarithmic scale [34].	170
Figure 125. SNR vs. distance for reflection on K-line white with 95% overall reflectivity: (a) LiDAR prototype and (b) commercial sensors [156].	171
Figure 126. Dynamic response recorded on the GUI for a movement of the K-line white target between 4.4m and 2.8m during a total time of less than 5s. The clear fluctuations on the graphical trace are a consequence of the imprecision sources studied.	172
Figure 127. (a) Layout for obtaining the reference conditions and (b) False colormap of the Incoherent Irradiance on the detector plane.	173
Figure 128. Cross-sectional Incoherent Irradiance profiles along the central detector's (a) row at $y=0\text{mm}$ (slow-axis) and (b) column at $x=0\text{mm}$ (fast-axis).	174
Figure 129. Merit Function defined in <i>ZEMAX</i> 's Optimization Wizard.	174
Figure 130. NSC Shaded Model of the LiDAR optics with the most relevant points zoomed-in. The reference number for each optical element are identified.	176

Figure 131. Beam cross-section after optimization along (a) the x-axis for the central pixels' row ($y=0\text{mm}$) and (b) the y-axis for the central pixels' column ($x=0\text{mm}$), both passing through the point of maximum Incoherence Irradiance (central pixel).....	178
Figure 132. Incoherent irradiance data on the $1\times 1\text{mm}^2$ reference detector (a) before and (b) after optimization.....	180
Figure 133. Optical alignment and optimization procedure: (a) beam spot made visible by the NIR-visible converter card and (b) setup for visualizing the beam projection (spot) on the <i>K-line White</i> target plane.....	181
Figure 134. Experimental setup to determine the approximate warm-up time of the LiDAR sensor properly labeled.	182
Figure 135. (a) Spectral center and average power variation during warm-up time for the developed LiDAR prototype and (b) peak wavelength for commercial sensors during the stabilization period [34].	183
Figure 136. Spectral profile of the developed LiDAR sensor as measured after warm-up with a repetition rate of $f_p=6\text{kHz}$ and for three different duty cycles for the BP_TRIG triggering signal: 5%, 30% and 65%.....	184
Figure 137. Laser zoomed-out temporal profile for a repetition rate of $f_p=6\text{kHz}$ and 65% duty cycle. In red, the laser driving signal and, in blue, the emitted light pulses detected in the reference path.	185
Figure 138. Zoomed-in profile in a rising-edge transition of the driving signal. The overshoot at the abrupt transitions in the driving signal (red) is induced by the long ground wire of the oscilloscope scope used to measure the signals.	186
Figure 139. Setup for measuring the transmitted optical power (a) at the laser emitter output and (b) after the TX optics. In the second image, the focusing on the powermeter photosensitive area is verified using the NIR-visible converter card.....	187
Figure 140. Graphical superposition of the experimental pulsed signal after normalization, the cubically interpolated waveform, $f_0(t)$, and the integral estimation at each point.	189
Figure 141. EASY HAZ TM laser hazard analysis calculator to evaluate the system eye-safety and ascertain the suitable eyewear protection.	191
Figure 142. Scale calibration in ImageJ and measurement of the central circular feature.....	193
Figure 143. Estimation of the diameter of the central circular feature in the calibration target. As visible, the acquired monochromatic images reflect the underlying projection pattern. On the bottom left corner, the coordinate referential used in the image processing procedures.....	194
Figure 144. Linear fit to the spatial widths in the horizontal, x, and vertical, y, directions experimentally measured as a function of the distance to the target, d. In dashed lines, the 95% confidence interval is represented ($\pm 2\sigma$).....	198
Figure 145. Raw photos of the beam projected in K-line at distances below 489mm. It is visible the granularity of the beam spot.	199

Figure 146. (a) Acquired beam spot image at $d=3890\text{mm}$ and respective intensity profiles over the vertical and horizontal lines passing through the centroid. (b) Beam cross-sectional profiles and appearance at 930mm for the Garmin lite v3 commercial sensor projected on K-line White. In both images, the centroid coordinates are generically marked.	200
Figure 147. Photography of the beam spot after reflection on the microscope slide. The actual beam spot is imperceptible due to a glare in the surrounding area.....	204
Figure 148. Schematic process showing the process implemented by the additional LA1074-B-ML lens in the return path. In the first situation, when the photodetector is translated axially by 2cm , the intensity detected decreases since the received power is dispersed over a larger area. In the second case, the additional lens collimates the beam to yield a more constant intensity on the $1\times 1\text{mm}^2$ photosensitive area. Yet, the residual divergence still induces a small variation in intensity.	204
Figure 149. Rising-edge of the laser driving signal: (a) acquired with the short ground lead and with (b) the standard ground probe.	205
Figure 150. Transmitter schematic as simulated in <i>TINA</i>	206
Figure 151. Electrical signals achieved in the simulation.	206
Figure 152. Electrical signals throughout the electronics for the pulsed LD emission. The <i>BP_TRIG</i> shown herein is directly measured on the TX board, after the jumper wire. On the right, the zoom-in evidencing the dephasings between the falling-edges of <i>BP_TRIG</i> , <i>delayed_trigger</i> and the rising edge of <i>GATE_DRV</i>	207
Figure 153. <i>BP_TRIG</i> signal as generated in the RX board (top) and after the jumper wire, on the TX board (bottom). Although the baseline presents more noise, the falling-edge does not suffer visible changes.	208
Figure 154. (a) Measurements with the oscilloscope probe directly in the test point TP2 and (b) example of measurement with the tip contacting the measurement point.	209
Figure 155. <i>laser_on</i> signal without the BNC 50Ω terminator to match the coaxial cable's characteristic impedance to the <i>DET10A/M</i> impedance.....	211
Figure 156. Measurement of the SPI signals for the DPOT configuration: (a) sampled signals (SPI CLK, CS and MOSI, from the top to the bottom), (b) oscilloscope probes contacting the SPI CLK, MOSI and CS pins and (c) real-time decode of the data line.	214
Figure 157. Fluctuations in $V_{th,A}$ around the mean value of 1.733V	215
Figure 158. Signals involved in the measure of a single point at 3.560m , from the reception to the STOP events. At alternative distances, the signals appearance is the same unless for the return pulse (as verified in Table 38). Moreover, the timing instants regarding ToF2 also change in accordance with the distance.	217
Figure 159. STOP pulses width in the reference and return paths at $d_{actual}=3.560\text{m}$	218
Figure 160. Authentication of the configuration registers in both TDCs. These registers are read and then directly printed on a Serial Monitor.....	219

Figure 161. Monitoring of the INTB signals of both TDCs whenever so STOP pulse is detected. In yellow, the falling-edge of the <i>BP_TRIG</i> signal marking the START event. In pink and blue, respectively, the interruption on TDC1 (after 750µs) and TDC2 (after 1µs), triggered in the falling-edge.	219
Figure 162. Some signals involved in the ToF acquisitions in each TDC for $f_p=6\text{kHz}$. From the top: <i>SPI_CLK</i> , <i>BP_TRIG</i> , <i>TDC_TX_CS</i> , <i>TDC_RX_CS</i> , <i>TDC_TX_INT</i> and <i>TDC_RX_INT</i> . The horizontal time-scale is 50µs/div and the vertical 1V/div. Since the TDCs reading time is inferior to the time between consecutive falling-edges in <i>BP_TRIG</i> , the point acquisition frequency replicates the laser pulses frequency f_p , as seen in the last two signals.	220
Figure 163. Some signals involved in the ToF acquisitions in each TDC for $f_p=9\text{kHz}$. From the top: <i>SPI_CLK</i> , <i>BP_TRIG</i> , <i>TDC_TX_CS</i> , <i>TDC_RX_CS</i> , <i>TDC_TX_INT</i> and <i>TDC_RX_INT</i> . The horizontal time-scale is 50µs/div and the vertical 1V/div. The frequency of the two interrupt signals on the bottom is exactly 4.5kHz because the TDCs reading-times cannot trail the laser pulses frequency and one in two START/laser pulses are ignored by the sensor.	221
Figure 164. TDCs' external clock signal with 16MHz nominal frequency and cycle-to-cycle jitter quantification as directly provided in the <i>HD04034</i> oscilloscope.	222
Figure 165. Histograms and respective gaussian fits showing the LSB distributions for the internal time-base in (a) TDC1 (reference) and (b) TDC2 (return). Directly printed on each graph, the average and standard deviation results of the descriptive statistical analysis.	224
Figure 166. First iteration of the LiDAR prototype: (a) laser connected through jumper wires to the PCB; (b) <i>laser_on</i> (yellow) and <i>laser_on_threshold</i> (red) signals.	225
Figure 167. Effect of the ground-loop. In yellow, the laser driver signal, and, below, the direct output of the external power supply $V_{cc,laser}$. Whenever the driver switches, a strong voltage peak is noticed in the latter, with polarity depending on the edge.	226
Figure 168. $V_{cc,laser}$ signals supplied to each board. On top, the signal generated by the <i>Agilent 3630A</i> to the RX board. On the bottom, the signal generated by the <i>Agilent 3631A</i> to the RX board. The voltage peaks in the latter board do not propagate to the former.	226
Figure 169. MAR1100 MEMS micromirror. The mirror is electrostatically and electromagnetically actuated in normal axis and is covered by a package with a transparent optical cover. The module has a total size of $12\times 6.5\times 5.9\text{ mm}^3$ (L×W×H) [197].	230
Figure 170. Gilboa control board. The FPGA and the MAR2100 ASIC are indicated, as well as all the connectors to the MEMS micromirror, power supply, external laser circuit, among others (adapted from [199]).	231
Figure 171. FPC connector to attach the MEMS micromirror to the control board and proper assembly. The trimming is essential due to the symmetry of the electrical connector that theoretically accepts two assembly configurations with a 180° rotation (adapted from [198]).	232
Figure 172. Top view of the mechanical assembly for the proposed LiDAR scanning system, highlighting the angular orientation of the elements. The laser is focused on a fixed mirror at a 22° angle in relation to the axis normal to the micromirror surfaced. The light is directly reflected to the MEMS reflective region that oscillates to scan the beam over a maximum 45° HFOV [198].	232
Figure 173. Maradin projection sequence [200].	233

Figure 174. Maradin timing diagram and outputted signals [200].	234
Figure 175. Simplified block diagram of the scanning system integration in the developed sensor. The receiver side remains unaltered.	235
Figure 176. Tested patterns, both with a total used resolution of 900×480 pixels. On top, pattern A, on the bottom, pattern B.	236
Figure 177. Experimental setup to test the Maradin scanning system: (a) emitter of the INNOVCAR prototype, designed according to the optomechanical guidelines aforementioned; (b) connection between the Gilboa control board and the oscilloscope to measure the Pixel Out pin.	237
Figure 178. Pixel Out signal during 3 complete scanning cycles. Each segment corresponds to a complete field and, therefore, each pair to a complete frame.	237
Figure 179. Pixel activation pulse (yellow) versus the MCU external interruption (red). A time delay of 136.2ns is verified between the rising-edge of the first and the falling-edge of the latter.	238
Figure 180. Projected patterns on a wall at 108cm. On the left, pattern A. On the right, pattern B with the width and height marked to calculate the FOV.	239
Figure 181. The three states of polarization.	240
Figure 182. Genie Nano M2450 polarimetric camera: (a) stack of arrays comprising the sensor, (b) micropolarizers disposal and identification of a super-pixel and (c) setup for polarimetric measurements of the Vauxhall target [155].	241
Figure 183. False Color intensity images of the laser polarization states in the region of interest for four angles after reflection on the Vauxhall Green Lemon Grass Metallic target.	242
Figure 184. False color intensity images of the laser polarization states in the region of interest for four angles after reflection on the K-line White target.	243
Figure 185. Degree of Linear Polarization in percentage after reflection on the (a) Vauxhall Green Metallic and (b) K-line White targets.	246
Figure 186. False color image of the calculated Angle of Linear Polarization, Ψ , after reflection on the Vauxhall Green Metallic target. Note that the black background region does not represent an AoLP of 0° but the absence of polarization since it corresponds merely to background noise and not an actually illuminated region.	246
Figure 187. Polarimetric measurements of the DoLP for an optical setup with no internal reflections and no artefacts in the beam spatial profile. On top, for projection on the Vauxhall target and on the bottom for the K-line. The average results are also presented on the right-side.	247
Figure 188. Proposed polarization measurement setup with a single photodetector.	249
Figure 189. Operation of a Liquid Crystal: (a) when no electric field is applied, the molecules create an optical anisotropy in the media; (b) if an electric field is applied, the molecules tilt according to its intensity, creating birefringence [203]; (c) modulated signal to be applied to allow alternation between horizontal and vertical polarization measurements.	251
Figure 190. Setup for detection of the vertical polarization component and polarization states on each step of the way for reflection on the Vauxhall Green Metallic target. For simplicity, the lenses are not	

represented because they do not interfere directly in the process. The optical axis of the LC is oriented at 45° to allow the interconversion between linear vertical and horizontal polarization components.252

Figure 191. Process for measuring the vertical polarization component for reflection on the K-line white target. Since the reflected light is mostly unpolarized, there is always a substantial intensity detected, independently on the LC configuration.253

Figure 192. CFD block diagram with a leading-edge arming discriminator. Illustrative pulse shapes are shown on each stage.254

Figure 193. CFD circuit implemented and tested in *TINA-TI*.255

Figure 194. Study of the impact of the shaping parameters on the timing point and triggering ratio: (a) varying p with $t_d=11ns$ and (b) varying t_d with $p=0.5$258

Figure 195. Transient signals for $p=0.5$ and $t_d=11ns$. The input pulse has a 1.2V peak and the graphs are divided in analog (above) and digital (below) signals. The transition points are marked to demonstrate the time delay.258

Figure 196. Graphical representation of the time-walk for $p=0.5$ and $t_d=11ns$. On top, the input sinusoidal pulses with amplitudes from 0.5V to 2V. On the bottom, the corresponding STOP signals, with emphasis on the zoomed-in leading-edge transition. Complementary, the time-walk between the limit amplitudes for a leading-edge discriminator with $V_{th}=0.15V$ is also pictured.259

Figure 197. *TZA3036* ACG integrated circuit. In (a) the block diagram. The photodetector is connected directly to the *IPHOTO* (2) pin and is reversely biased by V_{cc} . The output is at the pin *OUT* (8 or 14). In (b), the transimpedance response in $k\Omega$ as a function of the PIN photogenerated current in μA . [208].....261

Figure 198. Possible block diagram for the LiDAR system with all the identified improvements. The models for the new hardware components are evidenced, while the remaining do not suffer any changes comparing with the initial prototype. The polarization sensing is not included due to the unavailability of compatible LC retarders. For simplicity the ferrite beads are represented outside the LiDAR PCB although in practice they must be integrated on-board as close as possible from the DC supply inputs.280

List of Tables

Table 1. Advantages and disadvantages of each automotive sensor.....	8
Table 2. Comparative analysis of automotive technologies in some performance parameters (adapted from [27]).	12
Table 3. Imposed requirements for L4/L5-suitable LiDAR sensor.	25
Table 4. Comparison between the semiconductors most commonly used in photodetectors (adapted from [71]).	45
Table 5. Comparison between APDs, SPADs and PIN photodiodes in several key parameters (adapted from [80]).	52
Table 6. Comparison between MCUs and FPGAs in some relevant aspects.	57
Table 7. Technical specifications of Velodyne's LiDAR systems. For the fields marked with (-), no information from the manufacturer is available.....	66
Table 8. Specifications of Quanergy's first and second-generation products.	70
Table 9. Key technical specifications of Leddar Vu8 [109]......	73
Table 10. Key technical specifications of Ouster's products [114] [115].	76
Table 11. Main performance specifications for RoboSense's products [117][118][119].	77
Table 12. Comparison between the main performance metrics of several commercial LiDAR sensors and the requirements for Level 4 and Level 5 autonomous vehicles. The "X" indicates that the device does not meet the requirements, the "✓" marker indicates the opposite and the (?) indicates that the lack of information does not allow any conclusion.	80
Table 13. <i>SPL LL90_3</i> most relevant characteristics and specifications [160].	101
Table 14. TDCs configuration registers and defined values in binary.	114
Table 15. SPI modes description.	121
Table 16. <i>ThorLabs</i> lenses' characteristics [173]–[176]......	137
Table 17. Standard test conditions to be used throughout the system characterization phases, imposed either experimentally or by hardware restrictions.	145
Table 18. Acquired pulses in the <i>Teledyne Lecroy HDO4034</i> oscilloscope for the two gain settings and the <i>Vauxhall</i> target at 671mm superimposed with the 1.7V threshold. Below, the distributions of the 2400 raw data points sensed under the same conditions. From the pulses, it is visible that the threshold crossing at the falling-edge occurs at a point with larger absolute derivate comparing with the rising-edge and, thus, less conspicuous to jitter.	148
Table 19. Histogram (frequency distributions) for the raw gToF data (2400 points) acquired for diffuse and specular reflection on the <i>Vauxhall</i> target at 671mm. In parallel, the results for a STOP trigger	

in the fall and rise edges of the respective digital pulses. Overlaid with the histograms are the respective gaussian fits.....	149
Table 20. LiDAR range and ToF measurements after statistical treatment to determine the average and standard deviations. The results are compared with the actual reference values and, on the rightmost column, the calibration constants for each distance are computed. The actual ToF, $t_{D,actual}$, is calculated directly via equation (5.8) using the actual distance, d_{actual}	154
Table 21. Accuracy analysis for the three distinct global calibrations studied for the LiDAR prototype. In red and green are highlighted respectively, the best and worst overall results. The values in parenthesis in the last four lines are the actual target distances.....	157
Table 22. Numerical evaluation of the time-walk due to the intensity dependence and comparison between the shift in the calibration constants and the shift in the threshold crossing time of <i>return_analog</i> pulses. The calibration data is retrieved from Table 20.....	161
Table 23. Global <i>ZEMAX</i> simulation parameters.....	173
Table 24. Distances between optical elements before and after optimization in <i>ZEMAX</i>	175
Table 25. False color incoherent irradiance at several critical points of the TX optical setup. The size of each detector is not the same and is represented on the 4th column.....	177
Table 26. Calculations of the output beam divergence before and after optimization.....	178
Table 27. Peak powers measured by $12.7 \times 12.7 \text{ mm}^2$ detectors.....	179
Table 28. Comparison between the nominal and experimentally estimated spectral characteristics of the <i>SPL LL90_3</i> laser in the standard test conditions of $f_p=6\text{kHz}$ and $dc=65\%$ on <i>BP_TRIG</i>	184
Table 29. Temporal parameters characterizing the laser pulsed emission: experimental vs. nominal. $\langle X \rangle$ is the arithmetic average and σ_x the respective standard deviation of the experimental values, presented as histograms acquired directly from the <i>Teledyne HDO4034</i>	186
Table 30. Average optical power measurements and numerically computed peak-powers directly at the laser emitter output and after the transmitting optical system. The power loss is calculated using the average powers since the peak powers provide a less accurate estimate due to the numerical approximation induced by the employed computational methods.....	190
Table 31. Beam spatial profiles acquired at $d=489\text{mm}$ and $d=632\text{mm}$ from the output iris, for the projection in the <i>K-line White</i> target.....	196
Table 32. Beam spatial profiles acquired at $d=1103\text{mm}$ and $d=1514\text{mm}$ from the output iris, for the projection in the <i>K-line White</i> target.....	197
Table 33. Estimations of the parallel (θ'_{\parallel}) and perpendicular (θ'_{\perp}) divergence angles and the spot size at the TX output aperture.....	198
Table 34. Comparison between the simulated results and the empirically acquired results.	201
Table 35. Comparison of three different approaches for beam circularization: cylindrical lens pair, anamorphic prism pair and spatial filtering. [193]	203
Table 36. Comparison of the computed, simulated and experimentally measured delays and laser charge voltage.....	208

Table 37. Comparison of the reference pulse parameters: directly in the <i>DET10A/M</i> photodetector, on the left, and at TP4 on the RX board (<i>laser_on</i>), on the right. The threshold crossing points are marked by the intersection between the pulses (blue) and the threshold value (green). The statistical quantities are directly retrieved from the <i>HDO4034</i> oscilloscope. $\langle X \rangle$ is the arithmetic average and σ_x the respective standard deviation.	210
Table 38. Comparison of the return pulses for reflection on the <i>K-line</i> target at two distinct ranges: 0.560m and 3.560m. The statistical quantities are directly retrieved from the <i>HDO4034</i> oscilloscope. $\langle X \rangle$ is the arithmetic average and σ_x the respective standard deviation.	212
Table 39. Summary of the empirical values concerning the configuration of the discriminator thresholds.	215
Table 40. Summarized results of the jitter analysis on the external clock source for the TDCs.	223
Table 41. <i>MAR1100</i> optical and mechanical characteristics (typical values). [196]	230
Table 42. Estimated FOV and angular resolutions.	239
Table 43. False color normalized S_1 and S_2 parameters for both analyzed targets in the region of interest.	245
Table 44. Average values estimated after segmentation. The Stokes parameters are normalized to S_0	247
Table 45. Peak voltage of the back-reflected laser pulses for each target and each selected polarization component. Additionally, the DoLP is also provided. For each material, the pulses are represented at the same scale.	250
Table 46. CFD results for three distinct attenuation factors. Highlighted in green, the condition that minimizes the time-walk.	256
Table 47. CFD results for increasing time delays. Highlighted in green, the condition that minimizes the time-walk.	257
Table 48. Examples of Transimpedance Amplifier ICs with integrated AGC and respective specifications. The electrical current values are peak-to-peak (N/S-Not Specified).	260
Table 49. Summary of the specifications of the developed LiDAR prototype.	271

– This page is intentionally left blank –

List of Acronyms and Abbreviations

ADAS	Advanced Driver Assistance Systems
ADC	Analog-to-Digital Converter
AGC	Automatic Gain Control
AOI	Angle of Incidence
 AoLP	Angle of Linear Polarization
APD	Avalanche Photodiode
AR	Anti-reflective
BFL	Back Focal Length
BOM	Bill of Materials
BPF	Bandpass Filter
CAGR	Compound Annual Growth Rate
CFD	Constant Fraction Discrimination
CW	Continuous Wave
DOF	Degrees-of-freedom
DoLP	Degree of Linear Polarization
DPOT	Digital Potentiometer
EFL	Effective Focal Length
ESD	Electrostatic Discharge
FOM	Figure of Merit
FOV	Field of View
FMCW	Frequency Modulated Continuous Wave
FWHM	Full Width at Half Maximum
FPA	Focal-plane Array
FPGA	Field-programmable Gate Array
FPS	Frames per Second
GUI	Graphical User Interface
HFOV	Horizontal Field of View
IC	Integrated Circuit
IEC	International Electrotechnical Commission
IP	International Protection or Ingress Protection
Laser	Light Amplification by Stimulated Emission of Radiation
LC	Liquid Crystal

LD	Laser Diode
LED	Light-emitting Diode
LHP	Linear Horizontally Polarized
LiDAR	Light Detection and Ranging
LPF	Low-pass Filter
LSB	Least Significant Bit/Byte (depending on the context)
LVP	Linear Vertically Polarized
MCU	Microcontroller Unit
MEMS	Microelectromechanical System
MOSFET	Metal-Oxide-Semiconductor Field-Effect Transistor
MPE	Maximum Permissible Exposure
MSB	Most Significant Bit/Byte (depending on the context)
NIR	Near-Infrared
OD	Optical Density
OEM	Original Equipment Manufacturer
OPA	Optical Phased Array
PBS	Polarizing Beam Splitter
PC	Pockels Cell
PCB	Printed Circuit Board
PD	Photodiode
PRR	Pulse Repetition Rate
PWM	Pulse Width Modulation
Rpm	Rotations per minute
RX	Receiver
SMD	Surface Mount Device
SNR	Signal-to-Noise Ratio
SPAD	Single Photon Avalanche Diode
SPI	Serial Peripheral Interface
TIA	Transimpedance Amplifier
ToF	Time-of-Flight
TDC	Time to Digital Converter
TX	Transmitter/Sending Unit
UART	Universal Asynchronous Receiver-Transmitter
USB	Universal Serial Bus
VCSEL	Vertical-Cavity Surface-Emitting Laser
VFOV	Vertical Field of View

1

INTRODUCTION

*Never forget your humanity,
and respect human dignity in your dealings with others.*

Robert Bosch, 1931

In this first chapter, the bigger picture is initially drawn by presenting a succinct context on the thematic underlying the present dissertation project. Afterwards, the objectives are defined, followed by a brief description of the company in which the project was executed and the framework presentation.

1.1. Context

Nowadays, the ability to meticulously sense and image the environment in real-time is crucial in a broad range of fields, particularly in robotics, automotive, security, military and mapping [1]. More specifically and within these, countless applications rely on environmental sensing, from which driving assistance systems [1], autonomous driving [1], drone and robot collision avoidance and navigation [2], traffic management [1], surveying and surface mapping [3], can be highlighted. Among these fields, there is a common need to accurately detect and define the position, dimension or movement of surrounding objects (or targets) relative to the sensing unit, in the absence of physical contact.

Focusing on the automotive sector, in recent decades the contemporary society has been assisting to an exponential growth in mobility driven by global development trends, a large part of which has been absorbed by road transportation. As a result, the referred sector has followed the same tendency to a point where it can currently be considered one of the most evolved and valuable industries.

On the other side of the coin, alongside with the technological progress and the rising number of vehicles in circulation, assorted severe problematics have arisen, from which road accidents (and subsequent fatalities) and atmospheric pollution stand out.

In order to reliably solve the aforementioned challenges, autonomous driving has been pointed out as the fresher revolution in the automotive industry. The increase in vehicle's automation through the gradual introduction of Advanced Driver Assistance Systems (ADAS) and, eventually, fully autonomous driving is expected to expand the driver's comfort and passenger's security, by minimizing the human intervention in the driving process, while potentiating a better sustainability and mitigating the number of accidents and fatalities (mainly associated with human errors [4]). Furthermore, optimized traffic flow and lower congestion will ultimately lead to a reduction in CO₂ emissions, a major issue for the environment and people's health, and to time saving. Finally, self-driving vehicles will also accompany the demographically-imposed needs, resulting from tendencies such as population ageing and increase in life expectancy, broadening the accessibility for people who are unable to drive by themselves. [5]

On another front, truck platooning is also expected to create a huge impact in road transportation of goods. With increased autonomy and inter-vehicle communication, the plurality of truck traffic can potentially be transferred from day to night platooning with a minimum number of human drivers enrolled in the task. This scenario will have a particularly powerful impact in central Europe, where a large percentage of traffic during normal working hours is generated by lorries and trucks. [6]–[8]

Hereby, and supported by the referred strategic pillars, the debate and competition for autonomous driving technology is tremendously fierce and has progressed day-by-day to a point where, presently, a fully automated vehicle is no longer a futuristic idealization but a likely event in the near-future. Simultaneously, some companies have been working on car-sharing (e.g. *Uber*) and connected mobility solutions (e.g. *Bosch*) to also support in reducing the impact of road transportation. For instance, *Bosch* is developing innovative solutions to make parking more efficient by using real-time parking lot data from a cloud to reduce the parking search times by up to 60 hours per year [9]. Hereupon, the trend is for the market to evolve towards a joint paradigm between car-sharing and autonomous driving.

According to *Grand View Research, Inc.*, the global demand for ADAS is expected to witness a swift growth, with a market reaching approximately 67 billion USD by 2025, spreading at a Compound Annual Growth Rate (CAGR) of 19% [10]. Regarding fully-autonomous driving, the most desired milestone in automotive industry at the moment, huge progresses are anticipated for the next years and the segment is projected to grow at a CAGR of 41.26% from 2025 to 2030 [11].

1.1.1. Automated Driving Levels

With the intuit of handling and adjusting the development of technical and regulatory aspects, the Society of Automotive Engineers (SAE) conceived in 2014 the standard J3016 that stratifies and classifies autonomous driving in six levels based on the amount of driver intervention and attentiveness required [12]. This categorization, ranging from no automation (level 0) to a fully autonomous vehicle (level 5), is schematically represented in Figure 1. These levels are descriptive rather than normative and technical rather than legal.

According to the mentioned standard, in a level 0 vehicle the system issues warnings and may momentarily intervene but the sustained vehicle control is always in charge of the human driver, responsible for performing all the aspects of the dynamic driving task [12]. In level 1 vehicles (“hands on”), the majority of functions are still controlled by the human driver, responsible for steering,

accelerating/decelerating and keeping full situational awareness, although the vehicle can automatically execute specific driving assistance functions through some ADAS [12]. For e.g., Adaptive Cruise Control, where the driver controls steering and the automated system dynamically controls speed (accelerating or braking) to regulate the spacing to the vehicle ahead, falls into this category [13]. At this level, the driver must be constantly ready to retake full control at any time, including when automation fails. At level 2 vehicles (“hands off”), the automated system takes full control of the vehicle (accelerating, braking and steering) under certain conditions, with a permanent monitoring by the driver that must be prepared to intervene immediately whenever the automated system fails to respond properly [12]. To serve as an example for an ADAS system integrated in this automation category, Automated Parking allows the vehicle to park itself with minimal driver input [14].

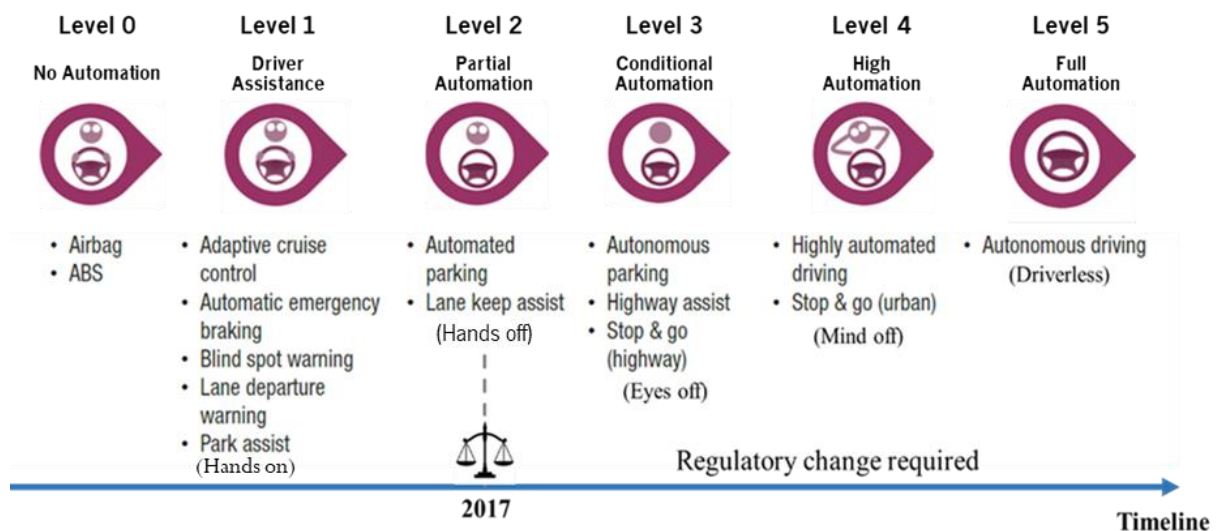


Figure 1. SAE international J3106 standard taxonomy for automated driving levels with several driver assistance systems discriminated for the corresponding levels (adapted from [4]).

A significant leap in automation occurs between level 2 and level 3, not only because the vehicle takes the leading role in the driving process through a constant and automated monitoring of the surrounding environment, but also because a regulatory change is required to provide legal coverage to the latter. At this level (“eyes off”), the driver can safely turn the attention away from the driving task and the vehicle handles situations that call for immediate responses. Whatsoever, the driver must still be prepared to intervene when necessary and cannot be completely alienated from the driving task. The biggest gap occurs at the transition to level 4 (“mind off”), since the driver attention is no longer required for safety and self-driving is supported in limited spatial areas and under special circumstances, i.e., it does not cover every driving scenario (vehicles still include pedals and steering wheel). At last, level 5 contemplates a full-time performance by the automated driving system of all aspects of the dynamic driving task under all roadway and environmental conditions, with full alienation of the driver. [12]

Presently, several level 1 and 2 ADAS are being implemented by multiple car manufacturers and are gradually gaining autonomy and facilitating partially automated driving, for e.g. on highways, and will ultimately lead to fully driverless solutions [15]. As examples, one can highlight the *Tesla Autopilot*, the *Volvo Pilot Assist*, the *Mercedes-Benz Drive Pilot* and the *Cadillac Super Cruise*, all level 2 systems [16]. More recently, in 2018, *Audi* launched the *A8* model claiming to be capable of level 3 self-driving, with a

Traffic Jam Pilot that can take full control of all driving labor in slow-moving traffic at up to 60km/h [16], and *Renault* demonstrated a Level 4 autonomous vehicle, the *SYMBIOZ* Demo car [17].

As for self-driving vehicles, there is still no consensus about when it will become a reality, but some manufacturers are currently making predictions. For example, autonomous systems specialist *NVIDIA* announced that a level 5 vehicle will be on the road by 2025, while *Audi* and *Ford* expect to reach level 4 autonomy by 2020 and *Bosch* by 2025 [18].

1.1.2. Sensorial Perception

To progress to higher automation levels and gradually remove the onus from the driver, a panoply of remote sensing technologies (often referred to as detection and ranging techniques) ought to be combined to provide an uninterrupted perception of the car surroundings in diverse scenarios. To fulfil this purpose and generate a timely and trustworthy map of the circumambient to support correct and safe driving decisions towards collision avoidance, sensors as cameras, Sonar (Sound Navigation and Ranging), Radar (Radio Detection and Ranging) and LiDAR (Light Detection and Ranging) must be incorporated in the vehicle's structure [15].

These sensors may be divided in two main categories: passive and active. While passive devices (cameras) receive direct information from the objects, active technologies (Radar, Sonar and LiDAR) involve projecting energy onto the neighboring, collecting the reflected signals and analyzing it to position various objects within the sensor's Field of View (FOV) [2]. The diagram of Figure 2 visually represents and classifies the referred automotive sensors according to this criterion.

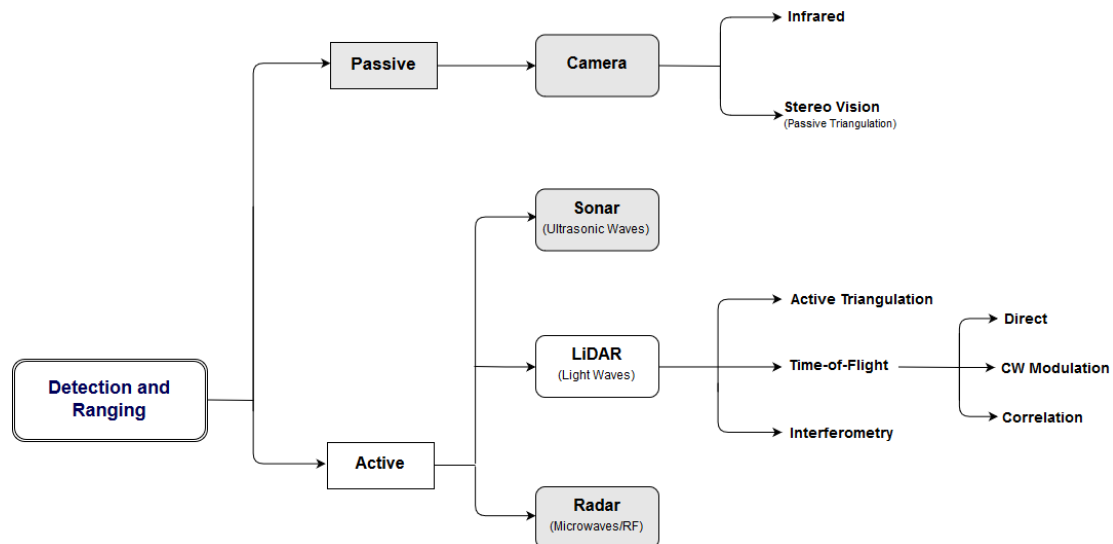


Figure 2. Remote sensing technologies taxonomy (adapted from [2] and [19]).

Being a passive technology, cameras are implemented onboard either to capture real-time images for computer stereo vision or to directly provide video streaming to the driver. In the former situation, the acquired pictures are, *à posteriori*, handled by complex deep-learning algorithms to process the images and extract objects from the background (segmentation), mostly pedestrians, other vehicles and traffic signs, being possible to classify them (Figure 3c). Moreover, and although still very constrained in capability, stereo cameras allow 3D reconstruction by evaluating relative distances through a technique

called passive triangulation [2]. In low light conditions, infrared (IR) thermographic cameras can detect animals and human beings based on the emitted thermal radiation (night vision - Figure 3b).

Since the three remaining sensors actively send a signal to the targets, they are more suitable for distance measurement. Even though the physical principle of all is similar, their applicability differs considerably due to the proprietary differences in the signal employed.

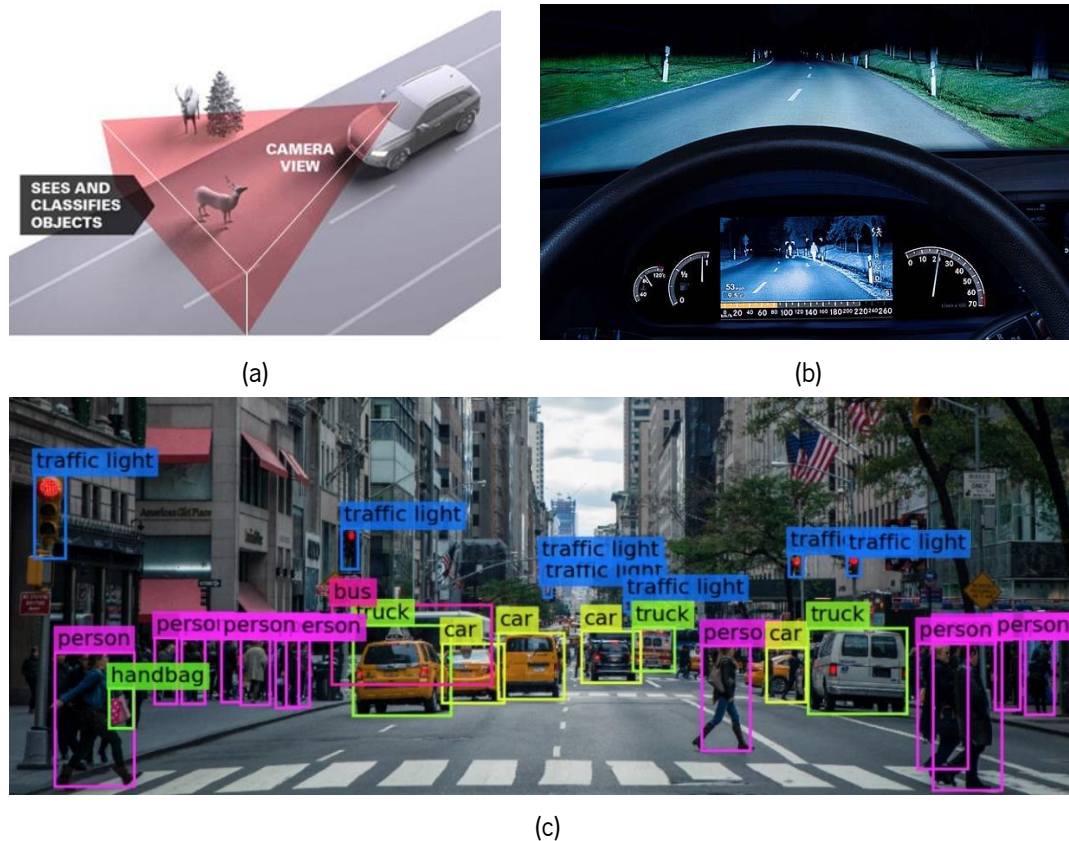


Figure 3. Sensorial perception provided by cameras: (a) working principle of camera vision [20], (b) image produced by an infrared camera and detection of a pedestrian on the roadside [21] and (c) features extraction from a RGB image.

The physical principle of LiDAR (also denoted laser rangefinding) consists on a laser source that emitting optical waves over a certain distance and within a FOV. The light emitted by the laser is transmitted to the target, interacting with it. A portion of this light is reflected/scattered at its surface and returns back towards the receiver, depending on the target's reflectivity and, thus, geometry and composition. Based on the detected changes in the echoed signal, some properties of the object can be acquired in real-time, namely the relative position (x,y,z) , and thus the distance and angle to the sensing unit, the speed and the reflectivity (Figure 4a). This technique can be implemented with beam scanning mechanisms to allow a 360° view using a single device, being possible to obtain an accurate topographic (3D) image in the shape of a point cloud (Figure 4b). Herein, each point (or pixel) corresponds to a position of the scanning system, i.e., to a beam direction, and it is possible to identify and distinguish objects. Similar to cameras, machine learning algorithms can also be used for segmentation and classification. [22]

Sonar performs measurements acoustically using ultrasonic waves and is already integrated in most of the commercial vehicles for parking assistance (Figure 4c). The principle, again, is the same and the distance is determined based on the Time-of-Flight (ToF), i.e., based on the measured time elapsed between the emission and reception of an acoustic pulse, t_D . By knowing the speed of sound in the medium, v_s , the distance to the target, d , is calculated by:

$$d = \frac{t_D \cdot v_s}{2} \quad (1.1)$$

where the factor 2 accounts the roundtrip since the signal travels twice the distance between the sensor and the obstacle. The frequencies used are typically in the 0.3 – 3 MHz range [19]. Since this technique is highly affected by noise provenient from external sources (e.g. other vehicles and traffic) and atmospheric attenuation [23], the range is very limited (up to 2m approximately). Thus, in the ADAS and autonomous driving context, Sonar is simply used in proximity sound sensors, mainly motivated by the reduced cost and ease of implementation.

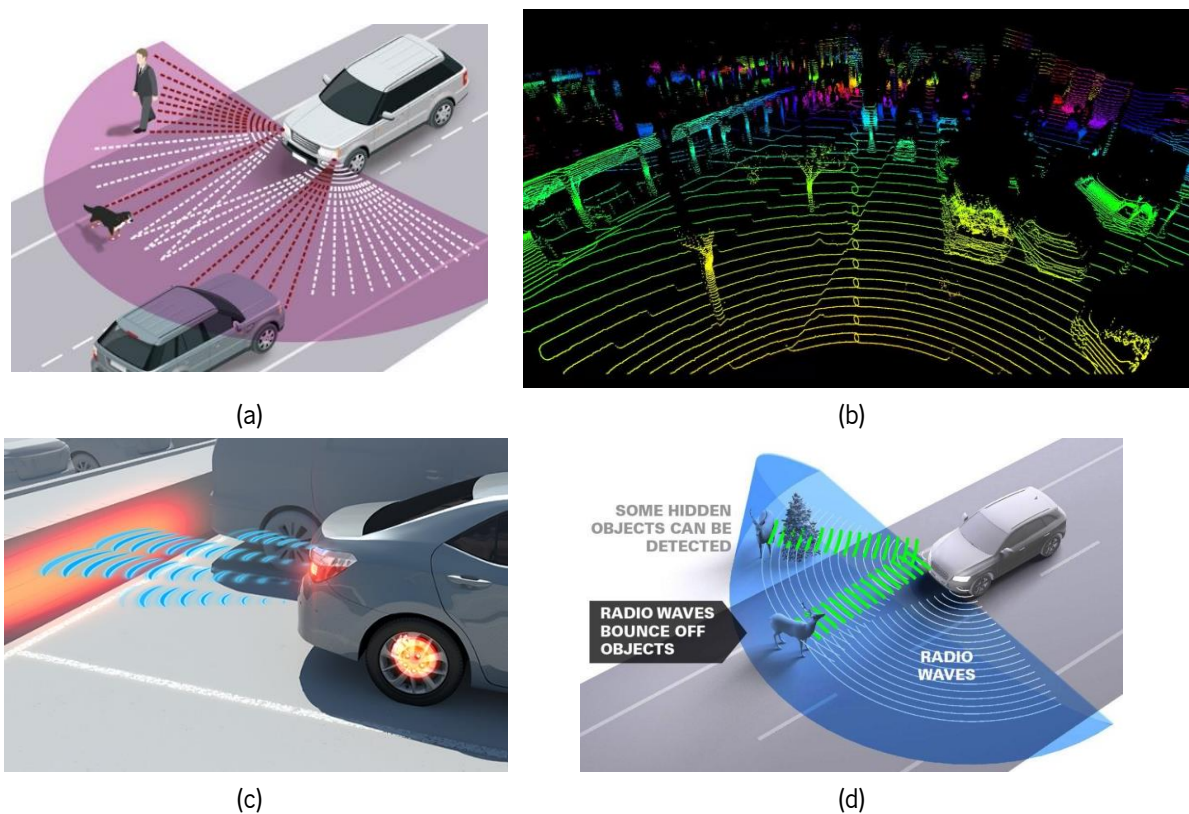


Figure 4. Basic principles of automotive sensors: (a) LiDAR [20]; (b) example of LiDAR resultant tridimensional frame where some obstacles are easily detected [24]; (c) Sonar and (d) Radar [20].

Lastly, in Radar an invisible electromagnetic wave in the radio-frequency (RF) spectrum is transmitted to the surroundings (alike LiDAR, covering 360° horizontally) and, after reflection due to differences in the electromagnetic properties of materials, the returned fraction is detected and processed to determine the distance (Figure 4d). Normally, the distance is also determined through the ToF, knowing the speed of light in the medium. Alternatively, frequency modulation can be adopted, in which the range is estimated through frequency shift between the emitted and received signal. Typically, Radar systems use

frequencies from 10GHz to 100GHz ($\lambda=3-30\text{mm}$) and can be divided according to the maximum measurable range: Short-Range Radar, ranging from 0.2 to 30m and using 24GHz Ultra-Wide Band (UWB), spanning 5GHz from 21.65GHz to 26.65GHz; Mid-Range Radar, ranging from 30m to 80m and Long-Range Radar, measuring distances up to 200m generally using 77GHz due to high-allowed equivalent radiated power in this spectral region [25].

To conclude, while the sensing units provide the vehicle with the needed situational awareness, the interpretation of the data from all sensors is performed by advanced processing units (central computer), responsible for identifying and recognizing obstacles (relative position, movement or/and dimensions) and combining all the information from these and other units to make real-time decisions based on the judgments (steering, accelerator and brakes actuation and/or warning the driver). The main constituent elements that must be connected to underlie self-driving vehicles are exposed in Figure 5.

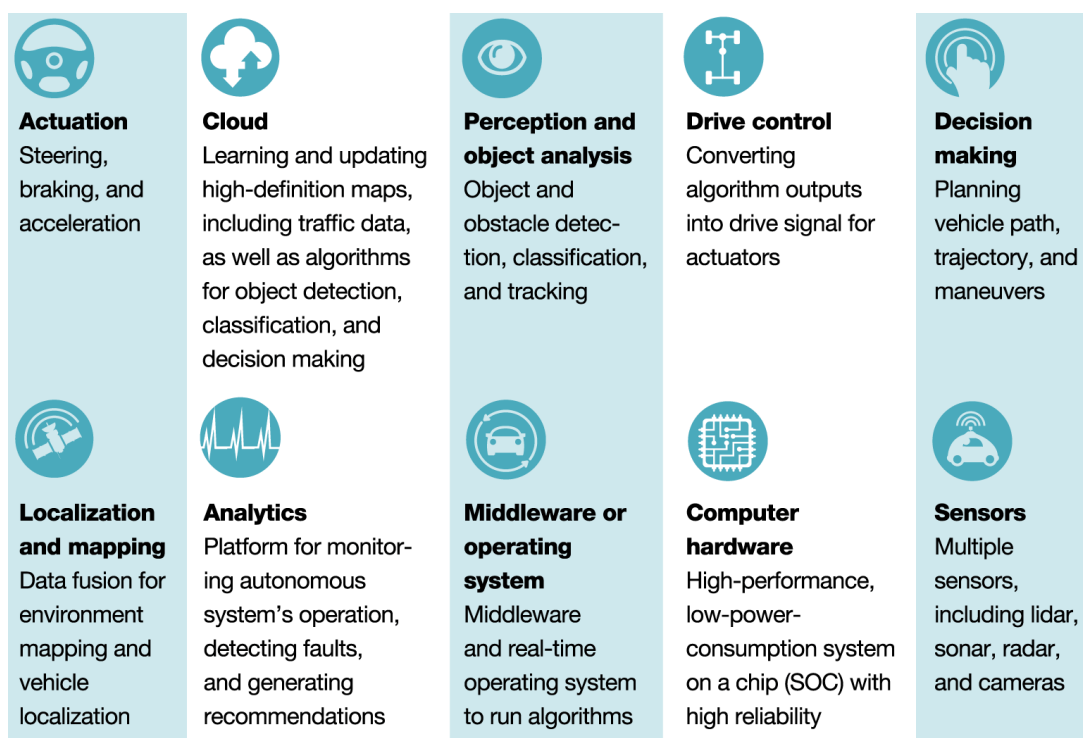


Figure 5. Elements of a highly-autonomous driving system [26].

1.1.3. Sensor Fusion for Autonomous Vehicles

At this point, one may ask why the integration of several distinct sensors is essential in self-driving vehicles. Because autonomous driving is a high-responsibility task, the diverse driving situations and scenarios, i.e., different roads topologies, conditions, speed limits and different illumination and climacteric conditions, must be contemplated and verified. Naturally, since cameras, Radar, Sonar and LiDAR differ in operating principles, their characteristics will also contrast and, therefore, each one will have a different applicability. To substantiate this matter, the weaknesses and strengths of each sensor are gathered in Table 1.

Table 1. Advantages and disadvantages of each automotive sensor.

	Strengths	Weaknesses
Camera (Stereo)	<ul style="list-style-type: none"> ✓ Most available and cheapest sensor ✓ Master of classification and scene interpretation (obstacles, textures, colors) and distinction (ability to read traffic signs and lane markings), crucial for autonomous navigation [27] 	<ul style="list-style-type: none"> ✗ Poor in 3rd dimension (distance) ✗ Great dependence on environmental lighting and weather conditions [27] ✗ Bad at speed measurements ✗ High processing power and complex algorithms to analyze the massive amount of data generate [27]
LiDAR	<ul style="list-style-type: none"> ✓ Master of 3D mapping (topography) [28] ✓ Highest spatial and angular resolution (able to identify, differentiate and classify objects in the surroundings) ✓ Highly accurate and fast measurements ✓ No lighting dependency due to use of own light source (operates equally during day and night) [27] ✓ Content-rich data (x, y, z and reflectivity) for better and more reliable intelligent decisions [27] ✓ Not impacted by light interference (unless on the same wavelength as the laser) 	<ul style="list-style-type: none"> ✗ Extremely expensive solutions on market, lacking reliability and specifications for level 4-5 vehicles ✗ Performance deteriorates under bad weather conditions (fog, rain, blizzard) [29] ✗ In some systems, the minimum discernable distance is limited to 1.5-2m due to hardware restraints
Radar	<ul style="list-style-type: none"> ✓ Master of motion measurement (Doppler shift) [25] ✓ Operates successfully in poor weather conditions ✓ Does not depend on environmental lighting ✓ Longest range from all sensors and good performance at short range ✓ Computationally lighter than cameras and less data to process than LiDAR [28] ✓ Relatively cheap sensor ✓ Poorly affected by pollution and blockage [27] 	<ul style="list-style-type: none"> ✗ Much less angularly accurate than LiDAR ✗ Uses frequencies susceptible to interference [30] ✗ Does not provide object recognition and it is unable to differentiate physical shapes due to small resolution [27]
Sonar	<ul style="list-style-type: none"> ✓ Excellent performance at short ranges (up to 2m) ✓ Cheap sensor ✓ Barely affected by blockage 	<ul style="list-style-type: none"> ✗ Highly affected by noise and atmospheric attenuation [27] ✗ Poor angular resolution ✗ Short-range

Starting with stereo vision, cameras provide 2D images with incomparable resolution, being the only sensor sensitive to color, indispensable for classification and interpretation. Nevertheless, they lack in tridimensionality and are strongly affected by lighting conditions. Moreover, and not properly a downside, cameras have limited FOV and multiple devices ought to be integrated in several strategic points (e.g., front grilles, side mirrors, rear door, rear windshield) in the car to accomplish 360° coverage. Referring to Sonar, the strong attenuation of ultrasonic waves limits the applicability of these units to short-ranged parking assistance systems and, thus, this sensor plays a minor role in autonomous driving. In Radar and LiDAR, the employed waves propagate across long distances, making both technologies very

appropriate for distance measurements with lighting independency. Besides being the sensor with longer range, Radar operates successfully in harsh weather conditions (fog, rain, blizzard, snow), with negligible degradation and is the master of motion measurement. Whatsoever, it lacks in reliability and resolution and does not allow to differentiate physical shapes. This resolution is imposed by the wave diffraction limit. Notwithstanding, the shorter wavelength and superior beam properties of light waves used in LiDAR offer a more suitable choice for accurate 3D imaging and point cloud generation. Although LiDAR bridges the resolution gap between Radar and cameras, its performance strongly deteriorates under bad weather conditions and blockage. Further, some systems cannot perform measures at short ranges (1.5 to 2m) due to hardware limitations.

To further understand the fundamental reasoning beyond the superior resolution in LiDAR technology, one may recall the diffraction limit that establishes the minimum feasible divergence, θ_{min} , of an emitting element for a circular aperture or, equivalently, the lowest angular resolution [31]:

$$\theta_{min} \approx 1.22 \frac{\lambda}{D} [rad] \quad (1.2)$$

where λ is the wavelength of the emitted signal and D the output aperture diameter. By increasing the size of the output aperture, the system's resolution is increased at an expense of an increased footprint. Considering this limit, and referring to the illustrative schematic of Figure 6, the minimum achievable spatial resolution in a given direction in the target plane, Δ_{min} , positioned at a distance d can be computed by:

$$\Delta_{min} = D + 2d \tan\left(\frac{\theta_{min}}{2}\right) \quad (1.3)$$

Typically, LiDAR employs wavelengths of either 905nm or 1550nm, while Long-range Radar uses microwaves with 77GHz frequency ($\lambda \approx 3.896\text{mm}$) and Short-range Radar of 24GHz ($\lambda \approx 12.5\text{mm}$). Considering, for instance, an emitting element with an aperture of $D=10\text{mm}$, then the lower limits for the spatial and angular resolutions in each system are, at a distance $d=10\text{m}$.

<u>LiDAR</u>	<u>Radar</u>
<u>$\lambda=1550\text{nm}$:</u>	<u>$\lambda=3.896\text{mm}$ (Long-range):</u>
$\theta_{min} \approx 0.189\text{mrad} \approx 0.0108^\circ$	$\theta_{min} \approx 0.475\text{rad} \approx 27.215^\circ$
$\Delta_{min} \approx 11.88\text{mm}$	$\Delta_{min} \approx 4.851\text{m}$
<u>$\lambda=905\text{nm}$:</u>	<u>$\lambda=12.5\text{mm}$ (Short-range):</u>
$\theta_{min} \approx 0.110\text{mrad} \approx 0.00633^\circ$	$\theta_{min} \approx 1.525\text{rad} \approx 87.376^\circ$
$\Delta_{min} \approx 11.10\text{mm}$	$\Delta_{min} \approx 19.114\text{m}$

Hence, the previous numerical estimates show the notorious superiority and the potential of LiDAR technology regarding both spatial and angular resolution (smaller attainable values), due to the employment of frequencies on a higher spectral region.

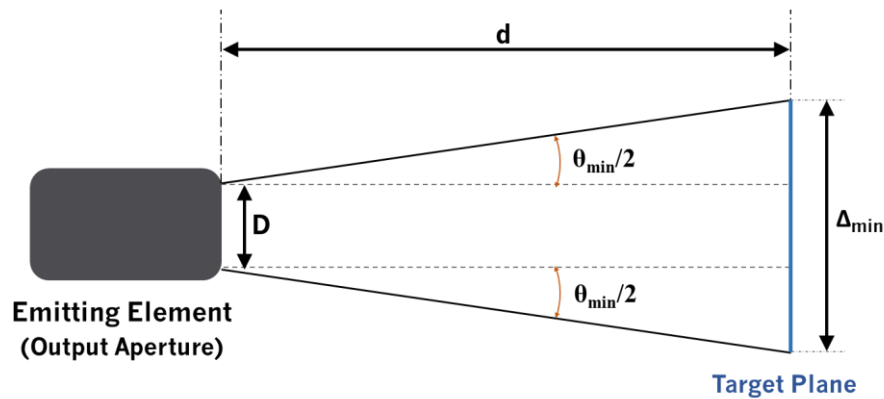


Figure 6. Diffraction-limited spatial resolution of an emitting system.

The impact of weather conditions on LiDAR is a consequence of the light scattering phenomena in which the light is forced to deviate from its straight trajectory due to non-uniformities in the medium. Based on the relation between wavelength and particles' size, two phenomena can occur: Rayleigh scattering (particles with dimensions much smaller than the wavelength of the radiation, up to about a tenth) and Mie scattering (particles with size approaching or surpassing the optical wavelength). [32]

As LiDAR typically uses Near-Infrared (NIR) light (from 700nm to 2000nm) and since the particle size of fog and rain droplets ranges from a few dozen micrometers to a few millimeters, then the light undergoes Mie Scattering and is dispersed in every direction following an antenna lobe like pattern. As the particle radius increases with respect to the wavelength, the distribution becomes more pointed in the forward direction. Every time this process occurs, only a fraction of light is transmitted to the target and, therefore, only a tiny portion of the initially emitted light returns to the detector, vastly reducing the effectiveness of LiDAR. [33]

From this analysis, one deduces that none of the sensors completely fits to every occasion by itself and each one has an indispensable role in different occasions within advanced driving assisting functions. Hence, they must be synchronized, complemented and synergistically fused to obtain, in conjunction, all the required information to achieve a complete unambiguous coverage and perception of the vehicle's environment, in real-time and in any circumstances [34]. For example, while LiDAR is the master of 3D mapping in favorable atmospheric conditions, Radar takes the leading role as ranging unit, whatever with inferior accuracy and detail (object identification can be achieved by complementing the results with IR camera images). Moreover, there is also an economically-driven motivation for sensor fusion. It is estimated that a death costs \$200 000 in average. At some point in the gradual introduction of autonomous vehicles, the liability will be transferred from the driver to the car Original Equipment Manufacturer (OEM). With the previous responsibility relocation, the costs will also be transferred to the OEM and increased by a factor of at least 10 times. Thereby, there is an urge to reduce the death contingency in vehicles by a similar or larger factor [35].

Figure 7 summarizes the role and applicability of each the above-discussed sensors in several ADAS and the coverage each one furnishes to allow appropriate decision-making in each situation. One important aspect to consider, evidenced in the image, is that redundant data sources are deliberately required for security reasons, in case of failure or bad functioning of some sensor. [15]

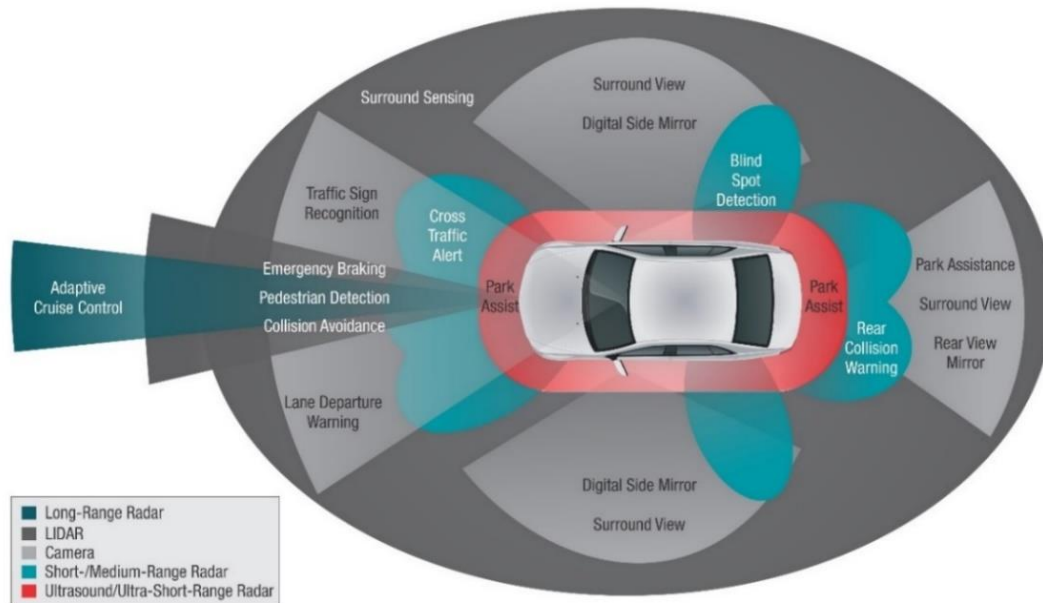


Figure 7. Panoply of sensing units and usage in the existing ADAS systems and respective coverage in the car surroundings [36].

1.2. Motivation and Objectives

As discussed, LiDAR is a key-enabling technology in the road map for level 4 and 5 autonomy and is supposed to play a major role as an imperative sensor (heart of 3D mapping), working in tandem with Radar and cameras. To enhance the essentiality of LiDAR, its performance is qualitatively evaluated and compared with the remaining sensors in several key parameters using a five-level discrete scale (Bad, Barely Satisfactory, Good, Very Good and Ideal Solution). The results are summarized in Table 2.

Whilst cameras and Radar are well-established and matured tools, having been widely adopted for many years in several fields including, more recently, in level 1 and level 2 vehicles, in LiDAR there are still many technical issues to be solved before the steering wheel can be completely abandoned. Although currently there are already commercialized LiDAR systems, the majority are still intended for industrial applications, airborne scanning and mapping. Yet, assorted companies are specifically focusing on developing automotive solutions and, inclusive, some of them have already come out with concrete products. From these, one can highlight *Velodyne*, a pioneer company in the area offering mechanical sensors with multi-laser technology. Unfortunately, apart from being pricey, bulky and power-hungry, the state-of-the-art for automotive LiDAR sensors still cannot entirely fulfill the requirements to cover all driving ambiances (highway, urban roads, country roads, etc.), lacking on the maximum range and angular resolution [37].

Hence, the deficiency for a suitable LiDAR is, undoubtedly delaying and compromising the roll out of driverless vehicles and, at the moment, multiple companies are strongly motivated and focused to debut an inexpensive solution with extended range and refined 3D imaging and mapping that offers the required performance.

Table 2. Comparative analysis of automotive technologies in some performance parameters (adapted from [27]).

	Radar		Sonar	Camera		LiDAR
	Short Range (24 GHz)	Long Range (77 GHz)		Stereo Vision	Infrared	
Short Range (0 to 2m)	Very Good	Barely Satisfactory	Ideal Solution	Good	Good	Bad (exceptions)
Medium Range (2 to 30m)	Very Good	Very Good	Bad	Good	Good	Ideal Solution
Long Range (30 to 200m)	Bad	Ideal Solution	Bad	Barely Satisfactory	Barely Satisfactory	Ideal Solution
Narrow Vertical FOV (<10°)	Good	Good	Bad	Ideal Solution	Ideal Solution	Ideal Solution
Wide Vertical FOV (>10°)	Barely Satisfactory	Barely Satisfactory	Good	Very Good	Very Good	Ideal Solution
Angular resolution	Bad	Bad	Bad	Ideal Solution	Very Good	Very Good
Speed measurement	Ideal Solution	Ideal Solution	Very Good (Low speeds)	Bad	Bad	Very Good
Object Differentiation	Bad	Bad	Bad	Ideal Solution	Good	Very Good
Robustness to weather	Ideal Solution	Ideal Solution	Good	Barely Satisfactory	Good	Bad
Night Operation	Ideal Solution	Ideal Solution	Very Good	Bad	Ideal Solution	Ideal Solution
Cost	Very Good	Very Good	Ideal Solution	Very Good	Good	Bad
Blockage (pollution)	Very Good	Very Good	Ideal Solution	Good	Barely Satisfactory	Bad

In the present work, the central goal is to implement a LiDAR system as a proof-of-concept for the ToF technology. To accomplish this, a design proposed by *Texas Instruments*, the TIDA-00663, will serve as basis and starting point to the development of this sensor. The goal is to reuse the hardware, since the components were previously chosen and the Printed Circuit Boards (PCBs) designed, select and mount a lens system with off-the-shelf components to optimize the optical performance and program a microcontroller unit to come out with an automated laser ranging system.

Afterwards, and based on the functional and characterized prototype, the proposal is to provide some guidelines for implementing advanced functionalities and perform some tests to support it. Firstly, and since the sensor only performs single-point measurements (1D) through a single 905nm laser, the idea is to study and suggest a way to interface the prototype with a 2D scanning system using a Maradin micromirror to steer the beam in a $45^\circ \times 14^\circ$ FOV (horizontal \times vertical) and accomplish tridimensional measurements. Secondly, a setup for measuring the state of polarization of the backscattered light is proposed using a single detector and a full-wave liquid crystal variable retarder. The motivation is that the initial polarization properties may vary when interacting with matter and, thus, the polarization state

of the returning light can provide information on the type of material of the target and can be used to support object recognition. At last, a timing technique is proposed to trigger a digital signal at a constant amplitude of the echo and hereby to increase the ToF accuracy and reduce the time-walk due to amplitude variations. Complementary, a hardware implementation of the latter is projected and simulated to prove the concept and suitability.

The greatest advantage of the implemented system is the low-cost, since it adopts a single laser and detector, and the ability to measure even in short-ranges. Hereby, and comparing with the state-of-the-art mechanical scanners using multiple lasers, the data processing can be done using a microcontroller instead of substantially more complex Field-Programmable Gate Arrays (FPGAs) needed for massive parallel processing. Furthermore, temperature is a less critical factor since the heating is smaller. Thus, and in case of needing a hypothetical housing (not in the scope of this project), the heat dissipation mechanisms can be simpler and more compact. Otherwise, and since temperature variation induces optical misalignments and shifts in the laser wavelength of around $0.33\text{nm}/^{\circ}\text{C}$, a complex temperature control and cooling system would be necessary.

Since the project was carried out in the LiDAR team at *Bosch Car Multimedia Portugal S.A.*, a company in the frontline of autonomous vehicle technology development, the emphasis of the carried-out research was on the automotive LiDAR segment. It is noteworthy that, naturally, the objective of this dissertation project is not to implement a fully working and apt sensor to support autonomous driving but to acquire know-how and critical knowledge in the area for the future. The LiDAR system is an exceedingly complex system involving several technical areas that can only be addressed by a large and multidisciplinary professional team.

1.3. Bosch Group

Bosch is a German multinational engineering and electronics company headquartered in Stuttgart and founded in 1886 by Robert Bosch (1861-1942), initially as a “workshop for precision mechanics and electrical engineering”. Today, the *Bosch* group is a leading global supplier of technology and services, offering the most innovative solutions for smart homes, smart cities, connected mobility and connected manufacturing. Furthermore, *Bosch* is internationally recognized as a main Tier 1 in the automotive supply chain, supplying directly automotive-grade hardware to OEMs in this market [38]

With engineering locations in 150 countries (including sales and services partners) and a sales revenue of 78.1 billion euros in 2017, Bosch counts with roughly 402 000 associates worldwide, divided into four distinct sectors: mobility solutions, consumer goods and energy, industrial technology and building technology. [38]

Established in Portugal since 1911, *Bosch* is currently represented in this country by *Bosch Termotecnologia* in Aveiro, *Bosch Car Multimedia Portugal S.A.* in Braga and *Bosch Security Systems* in Ovar. The group’s headquarters in the country is in Lisbon, where the sales, marketing, accounting and communication activities are carried out. [39]

Focusing in *Bosch Car Multimedia*, the bulk presence in Portugal, around 3280 employees are divided between Manufacturing, Logistics and R&D areas. In terms of production, the product portfolio includes instrumentation clusters for vehicles and motorcycles, steering angle sensors, head-up displays and navigations systems for leading automotive customers such as *BMW*, *Audi*, *Ford* and *Citroën*. As for product development, the R&D center comprises two main divisions: Car Multimedia (CM), dealing with infotainment, display and human machine interaction, and Chassis System control (CC-PS), developing solutions in the field of vehicle safety, dynamics and driving assistance. The dissertation activities were performed in the latter department. [39]

1.4. Framework and Content

This dissertation is composed of 7 chapters, each one centered around a section of the developed work, divided into three main parts: *Prologue*, *Experimental Work* and *Epilogue*.

The first chapter, which is not included in any of the three parts, is an introduction to the thematic to be tackled in this project. A brief background for autonomous vehicles and the sensors required to accomplish a reliable perception is conducted to contextualize and support the motivation and objectives proposed for this dissertation. Furthermore, the *Bosch* group is shortly presented.

In the first part encompassing chapters 2 and 3, a biographic research is carried-out to acquire critical knowledge about the subject and to provide a deep understanding on the foundations of LiDAR sensors. In Chapter 2, a theoretical background is given, comprising the requirements for a sensor to support level 4 and 5 autonomies and the detailed operating principle of LiDAR, including the different physical principles for range estimation and the fundamental constituent blocks of a generic system. In Chapter 3, the state-of-the-art for automotive LiDAR sensors is presented as several sensors are explored to give an insight on the current panorama, understand common characteristics and verify if the market offer fulfils the requisites for level 4 and 5 automation. Furthermore, emerging and innovative concepts are also studied.

The second part, *Experimental work*, incorporates all the work autonomously developed. In chapter 4, the system architecture is exposed, namely the hardware components and working principle, the optical system and the microcontroller unit and corresponding programming. Subsequently, chapter 5 includes both the characterization of each system block and of the overall system, as well as the description of the measurement processes and results discussion. To close this part, chapter 6 contains the guidelines to implement the suggested advanced functionalities.

Finally, the third part, the *Epilogue*, contains the 7th chapter where the conclusions of this project are drawn and some propositions for future work are disclosed.

Part I

Prologue

– This page is intentionally left blank –

2

LIGHT DETECTION AND RANGING

In Section 1.1.2 the broader LiDAR working principle was explained. Going into more detail on laser rangefinding, the fundamental setup is shown in Figure 8. The LiDAR system consists of a laser source, usually with wavelength in the NIR region, capable of transmitting pulsed or continuous light over the required FOV, a low-noise high-speed receiver capable of detecting and processing the reflected light beam and a low power controlling unit [40].

The laser is controlled using specific electronics, namely the output power, pulses' frequency and duration (in case of a pulsed usage), among others. The laser rangefinder only detects the distance to one point in its line of sight. To overcome this and acquire information over the required two-dimensional FOV, an optical scanning system (for e.g., beam steering using rotating mirrors) is used to control the horizontal and vertical direction of the transmitted beam, giving the system a tridimensional perspective. Additionally, a complex optical lens system is internally mounted at the transmitter and receiver ends, allowing a notable improvement on the overall sensor performance. This system is responsible for collimating and shaping the output laser beam, filtering the received echo to eliminate external spurious wavelengths, as sunlight, that tend to add noise and degrade the Signal-to-noise Ratio (SNR) and sensor's sensitivity [41], and focusing the latter into the photodetector. The fraction of light that returns to the sensor is converted into an electrical signal proportional to the light intensity via the photodetector and the resulting signal is conditioned, i.e. amplified and filtered, to finally be processed and extract the desired information. The information gathered in this signal, in conjunction with the known angle, is stored in a controlling unit that processes the data to construct the topographic frame. Consecutively, the collected data is represented as a 3D intensity cloud of the car's external environment, where each point corresponds to a beam orientation within the FOV (Figure 9). *Á posteriori*, based on the LiDAR image, conclusions about the vehicle's surroundings can be drawn, as objects' presence, location and classification (using recognition algorithms).

The LiDAR system is enclosed by a housing responsible for withstanding exterior temperature variations, protect the system hardware and optics against water splashes (for e.g. rain) and pressurized steam, and provide immunity to vibrations and shock resistance with impact on misalignments in the optical system [40]. This way, the housing must be hermetically sealed to prevent degradation of the internal assembly. To create this, it is necessary to include an optical aperture (glass cover) for light

exchange with the exterior. Besides, the data collected must be somehow transferred to the central processing unit of the car to be conjugated with the information provided by other sensors. For this purpose, several protocols are available, for e.g., Ethernet, CAN and Wi-fi (advantageous since does not require wired connections, allowing a fully sealed packaging).

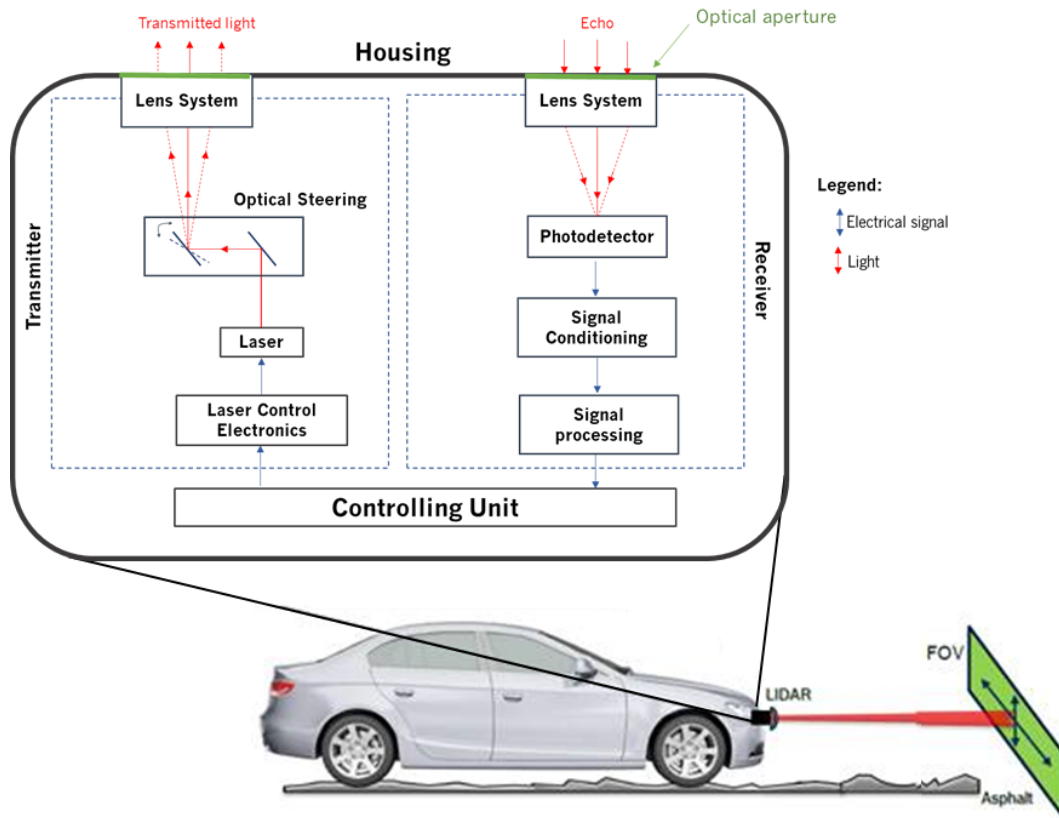


Figure 8. General architecture of a LiDAR system, with scanning performed by beam steering through a rotating mirror. In this image the sensor is integrated in the car’s front bumper (adapted from [40]).

Now, each of the identified individual parts is going to be explored, after setting the requirements with emphasis in driverless vehicles and presenting several techniques to evaluate distances by means of light. The objective is to provide a deep understanding on the physical foundations of LiDAR.

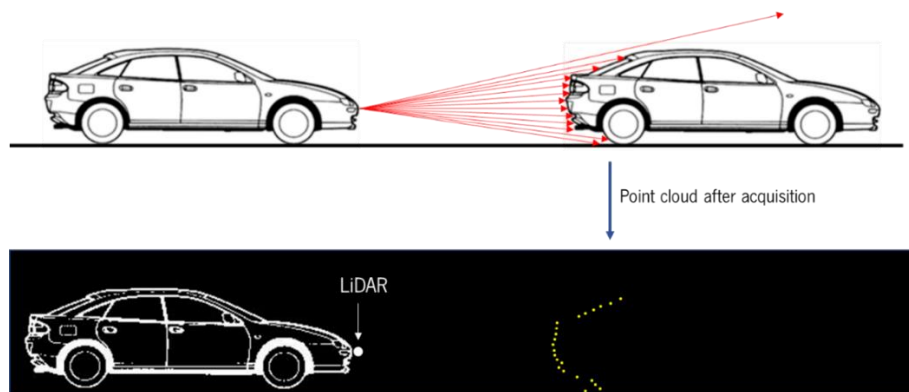


Figure 9. Lateral view illustrating the point collection in LiDAR and the corresponding point cloud (the left vehicle, equipped with the sensor, is shown just for localization purposes). If there is not any target in the beam direction, no reflection occurs, and the point is not depicted in the point cloud.

2.1. Requirements for autonomous driving

Concerning the application in highly-autonomous vehicles (Level 4/5), the device must have the ability to sense relevant objects from far enough to prevent any kind of danger and avoid or reduce the consequences of an accident. Hence, the sensor must mandatorily fulfill a set of strictly imposed requirements regarding measurement, operation and usage. The critical performance metrics are the FOV, the maximum operating range, the frame rate, the angular resolution, the axial range accuracy and the laser transmit power concerning to eye-safety.

As in any detection system, a coordinate system must be defined to locate and position a subject in relation to the reference. Here the reference is the LiDAR sensor and, for the purpose, a Cartesian xyz coordinate system is defined as depicted in Figure 10, centered at the device's optical aperture. The x axis is defined parallel to the aperture plane; the z axis is set upwards and perpendicularly to the ground plane; the y axis is determined using the right-hand rule and perpendicularly to the aperture plane.

Given the context, it is physically more intuitive to use spherical coordinates to represent positions in the point cloud. This way, the distance, d , in each pixel is measured radially and the horizontal/azimuthal, φ , and vertical/polar, θ , angles are given by the laser beam angle direction. This is the system to be used throughout this chapter, with the angle's signal convention as represented. The conversion between Cartesian coordinates (x,y,z) and spherical coordinates can be easily done using the relations below. [42]

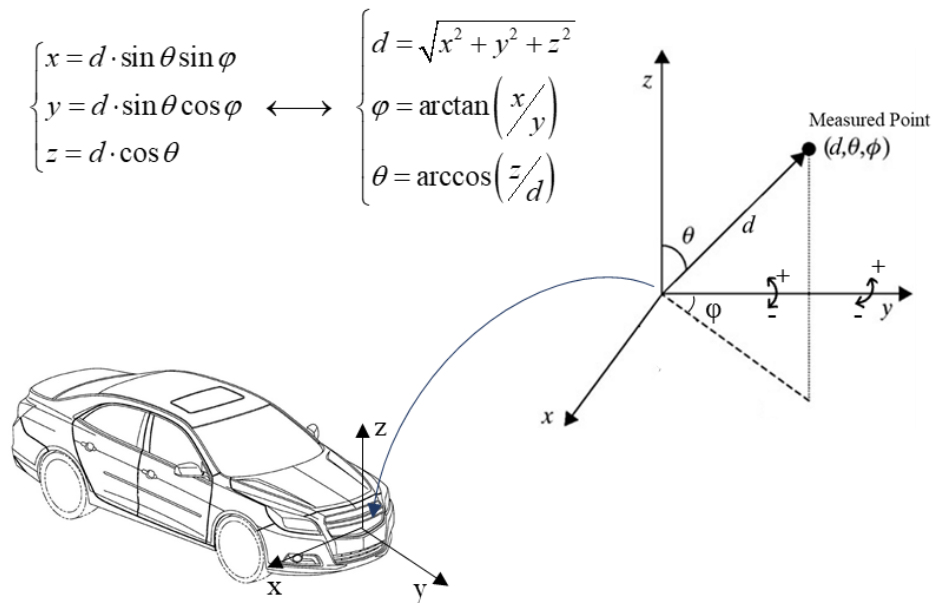


Figure 10. Definition of the Cartesian and spherical coordinate systems, with origin located at the sensor's optical aperture, and angles' signal convention.

Since this dissertation project was performed at *Bosch Car Multimedia*, the focus is directed towards units with potential for autonomous driving applications. Whatsoever, it is important to keep in mind that LiDAR is present in a wide variety of other application fields. Naturally, the requirements are not universal and must be adapted to each circumstance.

2.1.1. Field of View (FOV) and Range

The FOV is defined as the spatial window inside which the sensor can perform range measurements. Since the sensor must detect and track obstacles in some tridimensional extent of the vehicle's external environment, this FOV must be defined both horizontally and vertically. This specification is represented through a maximum total azimuthal (Horizontal FOV – HFOV) and vertical (Vertical FOV – VFOV) angle, corresponding to a window with size dependent on the radial distance to the aperture, d (Figure 11). The FOV can be expressed in terms of φ and θ :

$$\begin{aligned} HFOV &= \varphi_{\max} - \varphi_{\min} \\ VFOV &= \theta_{\max} - \theta_{\min} \end{aligned} \quad (2.1)$$

Alongside with the FOV, the maximum and minimum range (d_{\max} and d_{\min}) are other key specifications that restrict the sensor's operation. These are, respectively, the superior and inferior distance limits measurable by the device, radially to its aperture. In conjunction, the FOV and the range limits define the volume inside which the LiDAR system can detect and, thus, the spatial dimensions of each frame.

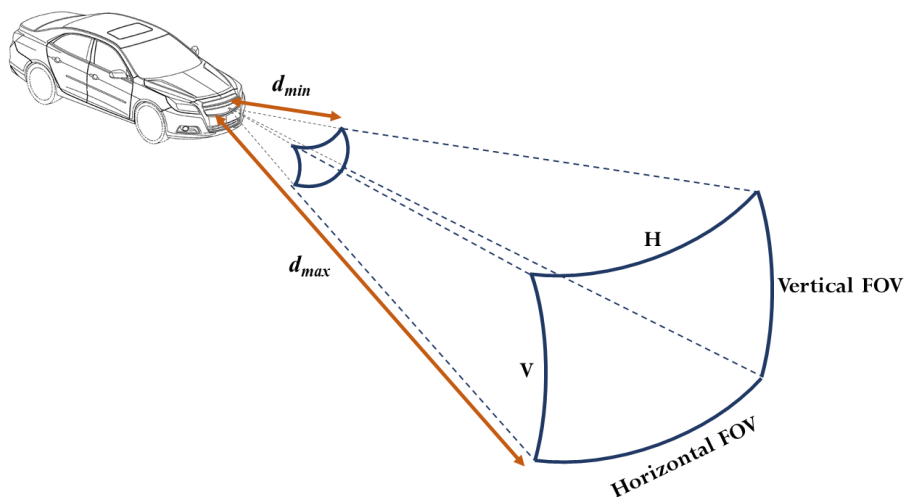


Figure 11. Representation of the sensor's FOV, maximum and minimum range, measured radially from the LiDAR optical aperture (adapted from [40]).

The sensor must present the versatility to provide reliable data in every environment. To set the requirements, one considers two different driving ambiances: highway and urban. The former is characterized by higher and more constant speeds while the latter is characterized by lower speed limits but more variations (due to fluctuations in traffic flow, traffic signals, headlights, etc.), more complex road layouts and more information to process, like other steady or moving vehicles, pedestrians, cyclists, and alternative obstacles.

Ideally, the minimum measurable range should be 0m for the LiDAR to perceive obstacles in front of it, no matter how close. However, this inferior limit is usually set by the system receiver, namely by its components' response time and speed, to an interval up to 1.5-2m. This factor it is not critical since there are other sensing technologies capable of detecting in the previous range. In terms of point cloud, a circular dark region centered on the sensor is seen as consequence.

To determine the maximum range, one considers the extreme scenario: emergency braking. Considering a steady object in the path of a vehicle travelling at the speed limit, the control unit timely react and immobilize the system before collision. The braking distance, i.e., the distance travelled between the point where the brakes are fully applied until the point where the vehicle is immobilized, can be determine through the work performed by the frictional force to dissipate the vehicle's kinetic energy. The total stopping distance can be obtained by summing the braking distance, d_{break} , and the distance travelled during the perception-reaction time of the decision-making unit, t_{reac} :

$$d_{\max} = d_{break} + v_i \cdot t_{reac} = \frac{v_i^2}{2g\mu_k} + v_i \cdot t_{reac} \quad (2.2)$$

where μ_k is the coefficient of kinetic friction, $g = 9.82 \text{ m/s}^2$ is the Earth's gravitational acceleration and v_i the vehicle's initial speed.

To project the maximum range, the maximum speeds allowed by law must be examined (worst-case scenario). These limits are not universal and are set independently for each country. After a survey, the most common speed limit is found to be 130km/h on highways [43]. As for the kinetic friction coefficient between the vehicle's tires and the road, it depends on the road material and its conditions. For an asphalt road, a broadly used material in highway pavements, this coefficient is estimated to be 0.7 when wet (identical for concrete) [44]. Though for human-caused accident reconstruction a reaction time of 1.5s is frequently used, in autonomous vehicle the latency of the decision-maker unit is much smaller and an overestimated 0.5s delay is considered. In these conditions, the total stop distance is:

$$d_{\max} = \frac{(130000/3600 [m/s])^2}{2 \cdot 0.4 \cdot 9.8 [m/s^2]} + 0.5 \cdot \frac{130000 [m]}{3600 [s]} \approx 184m \quad (2.3)$$

Naturally, the maximum range measured depends on the target's properties, as the reflectivity, and other environmental aspects. Furthermore, in another driving contexts, either on urban environments or even following on highways, the range requirements are less demanding. For instance, in [45] a guideline for adaptive cruise control defines a 70m following distance at 130km/h and with a 2s timed headway. Yet, by designing the device for the superior demand, these diverse situations are automatically fulfilled. Hereupon, the LiDAR system must be able to detect obstacles up to approximately 180m, at least, to allow comfortable following and navigation, as long as the legal speed requisites are guaranteed.

Regarding the minimum FOV necessary for safe navigation, it is determined based on the road layout and morphology. The minimum azimuthal FOV required is calculated based on the LiDAR operation through road curves, i.e., the roadway curvature, whilst the minimum VFOV is derived from the road slope and pitch [45]

To settle this requisite, urban or alternative itineraries other than highways are considered, due to the existence of more obstacles and more curvy and inclined roads. Ideally, the HFOV should be 360° to provide a full visualization of the circumambient. However, this is not a strict requisite for single devices as several LiDAR sensors can be integrated to cover the HFOV totality, for e.g. in each corner of the car. Attending the previous factors, the required HFOV has been shown to be, at least, 50° . Naturally, the VFOV demand is considerably milder because the potentially threatening obstacles are located near the ground plane, where the vehicle circulates. Hereby, it has been shown that a 9° VFOV is adequate. [40]



Figure 12. System's FOV requisites.

2.1.2. Frame Rate

Another vital parameter is the frame or scanning rate, i.e., the inverse of the time spent to acquire a single frame or, equivalently, the number of frames collected per second. Each frame is a single complete image of the entire FOV where each pixel is a measured point. Regularly, this metric is also referred to as the refresh rate because it matches the speed at which each point in the cloud is replenished.

In practice, a minimum frame rate of 10Hz (or frames per second, FPS) is sufficient for the system to keep a comfortable track of objects and handle unexpected situations (like a sudden appearance) without any major threats [40]. In between the frame update time ($1/10\text{Hz} = 0.1\text{s}$) and at a speed limit of 130km/h, the vehicle moves 3.6m. This distance becomes substantially more insignificant for smaller velocities, such as those of a pedestrian (5km/h average, implying a walked distance of 14cm in 0.1s), a cyclist (20km/h average, resulting in a travelled of 56cm in the same amount of time), or even a vehicle in an urban context.

2.1.3. Angular Resolution

The angular resolution is the minimum increment in the laser beam angle in each one of the two possible degrees of freedom (vertical, z , and horizontal, x), i.e., the angular spacing between consecutive points in the considered direction. This resolution is a measure of the LiDAR ability to distinguish two adjacent points in the FOV and is of extreme significance because it defines the frame resolution and the point density of the topographic point cloud.

In Figure 13 is illustrated the angular resolution and the frame division in pixels, denoted as $P(i,j)$ with integer indexes referring to a general position within the matrix. The number of rows in a frame, m , is related to the polar angular resolution, $\Delta\theta$, and the VFOV, while the number of columns is related to the azimuthal resolution, $\Delta\varphi$, and the HFOV:

$$m = \frac{VFOV}{\Delta\theta} \quad n = \frac{HFOV}{\Delta\varphi} \quad (2.4)$$

Besides the frame resolution, the angular resolution also sets the lateral spatial resolution, meaning the minimum discernable distance, in both horizontal and vertical directions, between consecutive points in a transversal plane: Δx_i and Δy_i , respectively. By using the nomenclature expressed in Figure 13, these quantities can be determined using the distance, $d_{i,j}$, and the angular resolutions:

$$\begin{aligned} \Delta x_i &= \left| d_{i,j} \cdot \sin(\varphi_{i,j}) - d_{i,j+1} \cdot \sin(\varphi_{i,j} - \Delta\varphi) \right|, \quad \Delta\varphi = \varphi_{i,j} - \varphi_{i,j+1} \\ \Delta z_i &= \left| d_{i,j} \cdot \sin(\theta_{i,j}) - d_{i,j+1} \cdot \sin(\theta_{i,j} - \Delta\theta) \right|, \quad \Delta\theta = \theta_{i,j} - \theta_{i,j+1} \end{aligned} \quad (2.5)$$

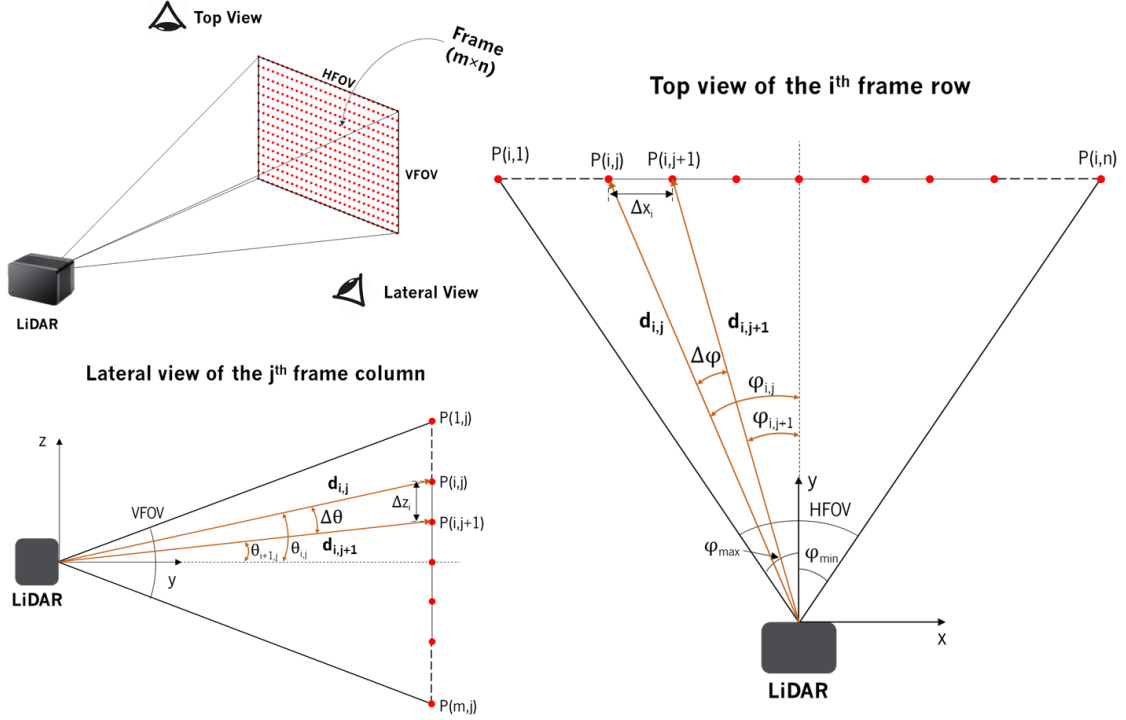


Figure 13. Frame segmentation in pixels and geometrical representation of each pixel's relative position within it. Two perpendicular views are shown (top and lateral) for generic lines, $1 \leq i \leq m$, and columns $1 \leq j \leq n$.

The resolution specifications are set based on the detection of pedestrians at 180m, considering a waist width of 50cm and a height of 150cm. To perform the calculations, the angular resolution is, in an acceptable approximation, considered extremely small: $\Delta\theta, \Delta\varphi \ll 1$ [rad]. Moreover, at a radial distance of 180m from the sensor and in the small-angle approximation ($\cos \theta \approx 1$, $\sin \theta \approx \theta$), the distances $d_{i,j}$ and $d_{i,j+1}$ are similar: $d_{i,j} \approx d_{i,j+1}$. Under these conjectures, equation (2.5) can be rewritten as:

$$\begin{aligned} \Delta x_i &\approx d_{i,j} \cdot \Delta\varphi \\ \Delta y_i &\approx d_{i,j} \cdot \Delta\theta \end{aligned} \quad (2.6)$$

where the angular resolutions are expressed in radians and take positive values. Introducing the restrictions into the previous equation ($d_{i,j}=180m$, $\Delta x_i=0.5m$, $\Delta y_i=1.5m$) holds:

$$\Delta\varphi = \frac{0.5}{180} \approx 2.78mrad \approx 0.15^\circ \quad \Delta\theta = \frac{1.5}{180} \approx 8.33mrad \approx 0.5^\circ \quad (2.7)$$

To finalize, the frame resolution ($m \times n$) is strictly related to the frame rate and the point acquisition rate through:

$$Point\ rate = m \times n \times frame\ rate \quad (2.8)$$

The point acquisition rate is set by the laser shooting frequency. If the latter is fixed, then the point acquisition rate is constant. Hence, for scanning systems, when the frame rate is increased the angular resolution also increases at an expense of a less resolved frame. Thus, in scanning systems, the angular resolution is typically defined for different frame rate configurations.

2.1.4. Range Accuracy

The range accuracy is the system's degree of conformance between the measured range and its true value, i.e., the uncertainty in the obtained result. Practically, various factors limit this quantity, as it will be discussed when appropriate, and a numeric estimation can be provided through the difference between the actual range, d_{actual} , and the mean result of N measurements performed per individual point, $\langle d \rangle$:

$$\delta d = |d_{actual} - \langle d \rangle| = \left| d_{actual} - \frac{1}{N} \sum_{i=0}^{N-1} d_i \right| \quad (2.9)$$

where d_i is the i^{th} range measurement.

At this point, it is relevant to make the distinction between the latter performance metric and another characterizing parameter often used in metrology, the precision. Although the accuracy and precision can be synonymous in colloquial use, they are deliberately contrasted in the scientific context. This concept is related to the system's reproducibility and repeatability and represents the degree at which repeated measurements under unchanged conditions show the same results. The system's precision is estimated by a statistical measure of the system error for multiple consistent range measurements, the standard deviation σ_d [37]:

$$\sigma_d = \sqrt{\frac{\sum_{i=0}^{N-1} (d_i - \langle d \rangle)^2}{N}} \quad (2.10)$$

Inasmuch as in automotive applications extraordinarily high-accuracies are not required since the system aims to detect obstacles predominantly from mid-to-long ranges, depth precisions of a few centimeters are still desired, in opposition to close-range sensors requiring sub-millimetric certainties. Thereby, a reasonable accuracy level can reach up to 10cm [40]. As for the system precision, despite the fact that reproducibility is desired, no numerical restriction is appointed. A legitimate approach to improve precision is averaging multiple samples.

2.1.5. Laser

Concerning the light source, a non-visible laser must be adopted, and, above all, it must be unarmful to the human eye. Therefore, the wavelength must be in the NIR region of the spectrum (since ultraviolet radiation, in the lower wavelength range of the spectrum, is harmful to biological systems) and the radiant power must be so that allows to achieve the imposed range without compromising safety. To guarantee eye-safety, the system must classify as Class 1 according to a certified international standard (EN/IEC 60825) and shall not exceed the Maximum Permissible Exposure (MPE). To complete, the operation principle is not restricted, meaning that either pulsed lasers or Continuous Wave (CW) lasers can be employed.

2.1.6. Others

Besides the previous critical requirements, there are other more general and secondary requisites that the system must accomplish, namely a hermitically sealed housing with electromagnetic compatibility (EMC), to prevent noise and interference in the photodetection and withstand severe environmental conditions, and an optical aperture protected against external pollution (insects, dust, blizzard) with a self-cleaning mechanism. To classify the degree of protection provided by electrical enclosures against intrusions, such as dust and water, the IP (International Protection or Ingress Protection) rating, defined in the international standard IEC 60529, is used. To support the variety of working environments the enclosure must have, at least, an IP68 rating level, meaning the sealing must totally prevent the intrusion of dust (dust tight) and support protection against the effects of long term immersion in water under 1m [40]. The device must also be resistant to vibrations due to, for e.g., road irregularities.

Moreover, the device must be able to operate under a wide range of temperatures to support different climactic conditions and the storage temperature must be regulated to diminish mirrors and lens distortion, avoid thermal gradients within optical elements that might provoke misalignments and shifts in the laser beam, as well as to guarantee that the components operate inside the respective limit ratings. Additionally, the system must recognize objects with varying reflectivity. There are several sources that give boundaries for the reflection as the ISO16331 that sets a maximum and minimum reflectivity of 80% and 10% [22]. Withal, some studies identify asphalt as the material with lowest reflectivity ($\approx 10\%$ at 905nm) and snow ($\approx 90\%$ at 905nm) as the material with highest relative reflectance in the NIR region of the spectrum [46].

Regarding the physical dimensions, the device must present a compact design, with reduced dimensions to facilitate integration directly in the vehicle's structure or on top of it, and lightweight to avoid damaging the chassis or any other part. One last important factor is the product industrialization. To achieve mass production, the device must have a design compatible with manufacturing and assembling in a production line and it must be price-wise affordable.

Table 3. Imposed requirements for L4/L5-suitable LiDAR sensor.

Parameter	Specification
Minimum range, d_{min}	1.5-2m (max.)
Maximum range, d_{max}	180m (min.)
Range Accuracy, δd	10cm (max.)
FOV (H×V)	50° × 9° (min.)
Angular Resolution, $\Delta\theta \times \Delta\varphi$ (H×V)	0.15° × 0.5° (max.)
Laser Class / Wavelength	Class 1 eye-safe / NIR
Frame Rate	10Hz (min.)

2.2. Techniques for Range Estimation

The optical distance measurements using lasers may be divided into three main approaches (Figure 2), all of them based on the same basic active principle already explained. The necessary components for the LiDAR sensor differ between techniques but, however and in sequence, a generic description of each will be given.

2.2.1. Triangulation

Triangulation is a geometrical technique in which the target is one point of a triangle whose two remaining points are known parts of a measuring system. By measuring the triangle's angles or its base, the distance to the target can be determined through geometrical relations. This method can be subdivided into active and passive triangulation.

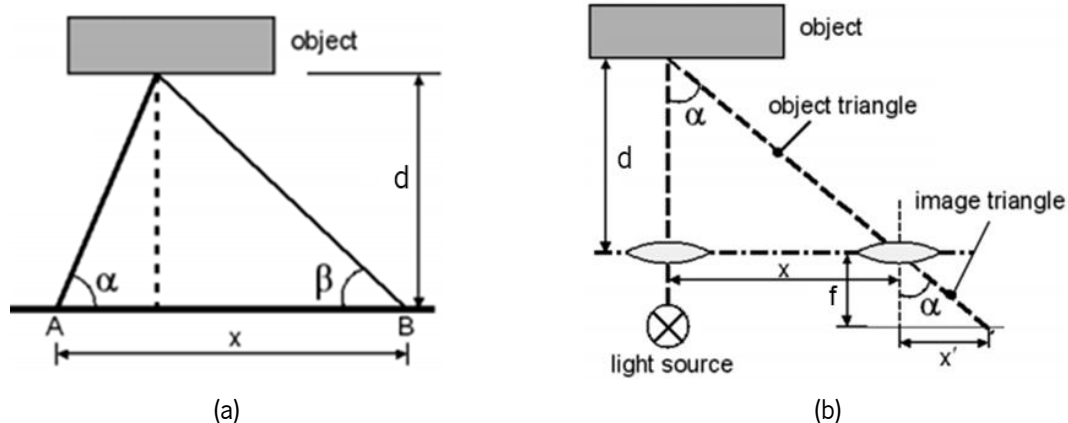


Figure 14. Geometrical schematic description of a 1D (a) passive and (b) active triangulation system [19].

Passive triangulation (Figure 14a) relies on observing the same point from two distinct positions, A and B, with a known spacing, x . By measuring the viewing angles α and β in respect to the base AB, the distance to the subject, d , can be calculated [19]:

$$\tan \alpha = \frac{d}{x - \frac{d}{\tan \beta}} \Leftrightarrow x \cdot \tan \alpha - \frac{d \cdot \tan \alpha}{\tan \beta} = d \Leftrightarrow d = \frac{x}{\frac{1}{\tan \alpha} + \frac{1}{\tan \beta}} \quad (2.11)$$

Since two different perspectives are needed, passive triangulation requires at least two detectors and, using 2D correlation, typical object features are found and compared in both images. From the position of each feature's centroid in both separate images, the angles α and β can be determined. As each point to measure must be identified from both viewing positions unambiguously, passive triangulation requires a scene with high contrast and depends largely on illumination, contrary to active triangulation that uses its own light source. Additionally, the computational complexity and the shadowing effects are other major drawbacks among these systems. Stereo-vision is based on passive triangulation, using a set of two mono-vision cameras to perceive the scene alike human eyesight. [19]

Regarding active triangulation, a laser is projected into the scene and the reflection is observed by a detector array. Rather than measuring angles directly, active triangulation is based on the similarity of triangles (object and image triangles). In the simplest case of a single illuminated point and a single line detector array (Figure 14b), the similarity of triangles is fully defined by the optical axis of the imaging device, the focal length of the system, f , and the position of the point projection on the detector, x' . Knowing the distance between the light source and the imaging device, x , the distance to the target can be determined [19]:

$$\frac{d}{x} = \frac{f}{x'} \Leftrightarrow d = f \frac{x}{x'} \quad (2.12)$$

In case multiple points are illuminated, the position sensitive line sensor needs to be replaced by a multiple-line array. This system is available for applications ranging from millimetric scales to several hundred meters. Nevertheless, the main drawback is that, with higher range interval comes larger dimensions, since a wide triangulation base is required for the objects to be detected. This affects the usability of this technique in LiDAR sensors to integrate in self-driving vehicles. [19]

2.2.2. Interferometry

Interferometry is described by the superposition of two monochromatic waves of wavelength λ , resulting in another monochromatic wave with same frequency but with a different phase and amplitude. There are several possible setups but the simplest is the Michelson interferometer (Figure 15). In this setup a monochromatic and coherent laser beam is split into two rays through a beam-splitter. One ray is projected to a mirror at a constant displacement (reference path), d_1 , whereas the other ray is targeted to the object at a variable distance d_2 (measurement path). Both beams are reflected to the beam-splitter where they combine to be projected onto an integrating detector. The light intensity at the detector is given by [19]:

$$I = I_1 + I_2 + 2\sqrt{I_1 \cdot I_2} \cos \left\{ \frac{4\pi \cdot (d_1 - d_2)}{\lambda} \right\} \quad (2.13)$$

where I_1 and I_2 are the respective optical intensities.

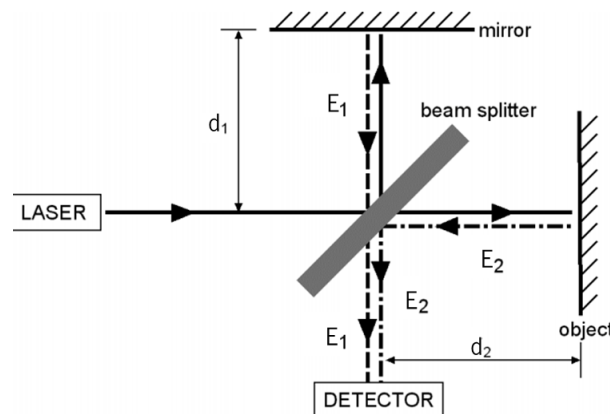


Figure 15. Working principle of Michelson Interferometer (adapted from [19]).

If the paths' length difference is a multiple of the laser's half wavelength, $d_1 - d_2 = k \lambda/2$, $k \in Z$, the intensity at the detector reaches a maximum (constructive interference). For a path difference of a fourth of the wavelength $d_1 - d_2 = \lambda \cdot (k/2 + 1/4)$, $k \in Z$, the intensity reaches a minimum (destructive interference). A movement of the object away or towards the system results in intensity peaks. By recording and counting the number of minimum-maximum transitions in the interference pattern while the object moves, the distance can be incrementally determined with high accuracy. [19]

Although interferometry has the big advantage of providing highly accurate range measurements (down to $\lambda/1000$ accuracy), it has many drawbacks that make this method unfeasible for autonomous vehicles, namely the short range (up to a few centimeters, restricted by the limited laser coherency and the unambiguous range of half wavelength), impossibility to perform direct absolute range measures and high sensitivity to misalignments [19].

2.2.3. Direct Time-of-Flight

In direct ToF LiDARs, a laser emits uniform light pulses (same waveform, duration, amplitude and temporal sending spacing) with lengths in the nanoseconds order. The elapsed time between the sending and receiving events, t_D , also denoted by delay or, akin to the technique's name, ToF, is determined electronically and is proportional to the distance to the reflection point. Since the laser and the detector are practically at the same location, the distance can be directly determined through [47]:

$$d = \frac{c \cdot t_D}{2n} = \frac{c \cdot t_D}{2} = 0.15m \cdot t_D [ns] \quad (2.14)$$

where n is the refraction index of the transmitting medium ($n \approx 1$ for air) and $c \approx 3 \cdot 10^8$ m/s is the speed of light in vacuum. The previous equation takes into consideration the fact that the measured ToF corresponds to the whole roundtrip (to the target and back to the receiver), hence the factor 2. This equation is analog to Equation (1.1) but using the speed of light instead of the speed of sound.

Figure 16 illustrates the ToF principle. After reflection, both the pulse shape and width are conserved but the intensity is reduced thanks to reflection and propagation losses. If there is not any object in the light path or if the pulses are reflected with such an angle that they do not reach the detector, a black point is generated in the point cloud, corresponding to a missing measurement. Based on the points acquired in the FOV, the point cloud can be constructed in real-time.

There are multiple reasons that justify the common usage of direct ToF in most of today's LiDAR systems: measurements accuracy is distance independent and depends only on the timing accuracy [48]; proximity of the light source and receiver allows compact systems; high measurement rates; short-to-large range measurements by using short pulses with great peak power, making the return signal stronger and enlarging the SNR, while keeping eye-safety [49]; most straight-forward method, requiring simple signal-processing techniques to extract ranges. All these reasons make this method appropriate for the intended application and, hence, this is the underlying principle chosen for this work and is the focus of the next sections.

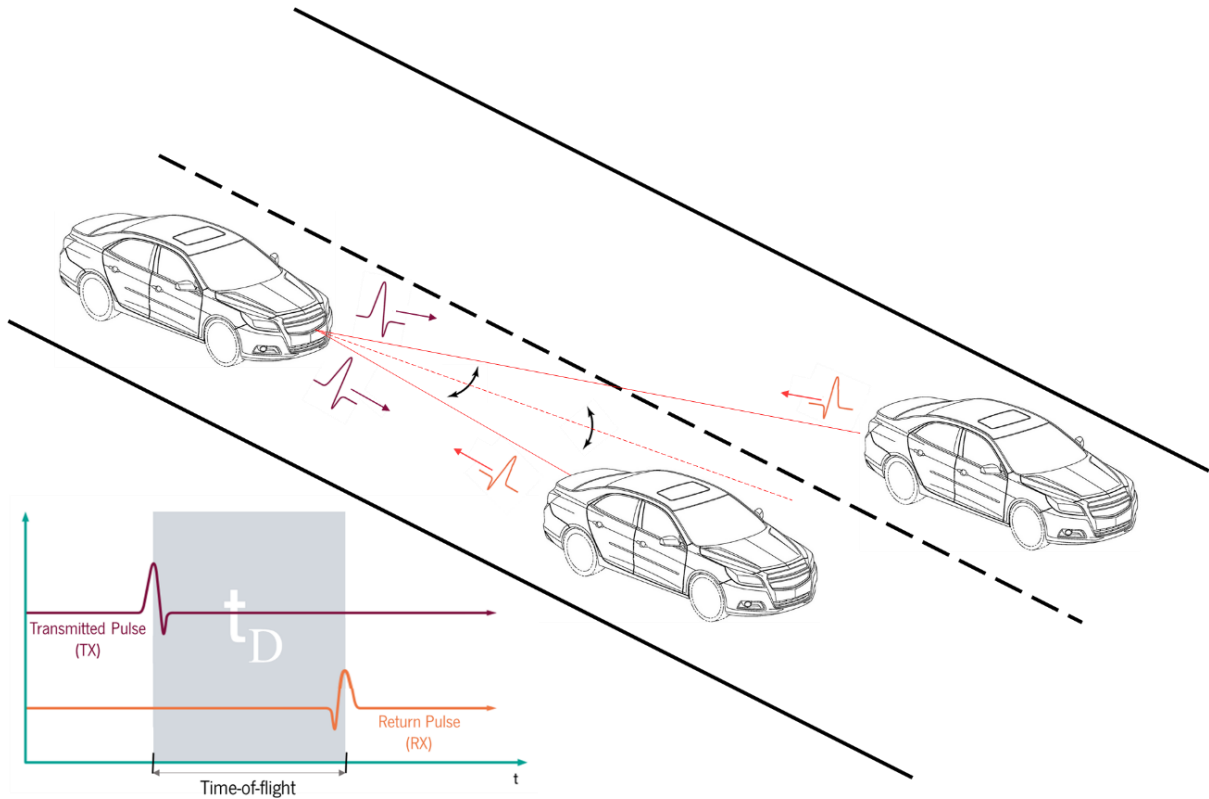


Figure 16. Illustrative representation of ToF principle (adapted from [50]).

Despite the benefits, there are also some drawbacks to this technique. One of the most relevant is the susceptibility to interference from other LiDAR sensors and light sources using the same wavelength. This interference can either be direct, if the sensors are aligned and within each other's FOV, or indirectly through reflections, resulting in erroneous results. Besides, the accuracy is also inferior comparing with other techniques like interferometry.

2.2.4. Random Pulse Modulation

Instead of using single or multiple uniform pulses to measure the ToF, a random burst/sequence of pulses with different amplitudes and width is emitted - Figure 17a. After the reflected signal is received, it is digitalized and then cross-correlated with the reference before performing the range calculations - Figure 17b [51]. When and if a correlation maximum is recorded above a defined threshold, the corresponding ToF is translated into distance using equation (2.14).

This LiDAR technique is extremely resilient to interference and external noise due to the singular nature of the pulse sequence [52]. If a spurious signal is detected by the sensor, it will be discarded. In spite of overcoming the main downside of direct ToF, this approach is not as straightforward, being associated with larger complexity both on the sensor's transmitter and emitter.

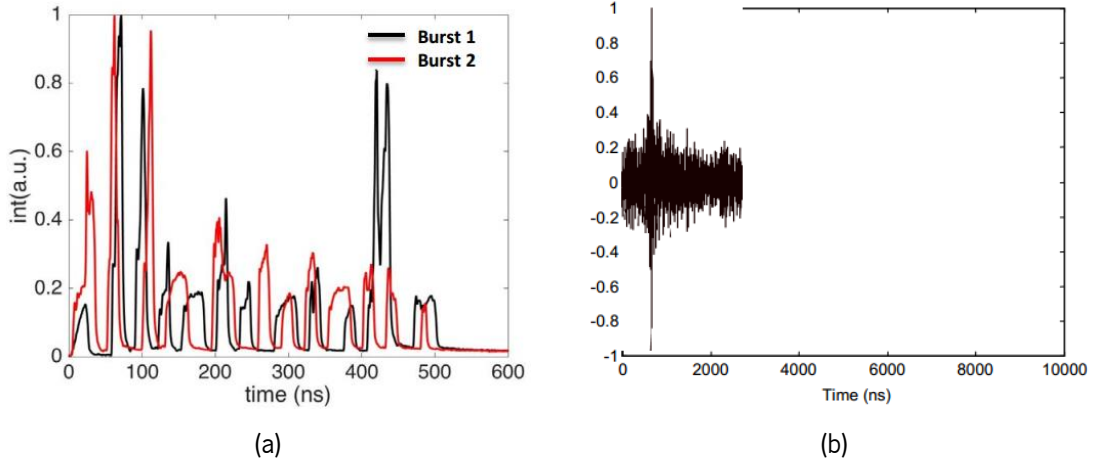


Figure 17. Correlational ToF technique: (a) two different random bursts of pulses generated by the commercial LiDAR *Garmin Lite v3* [52]; (b) example of a correlation result between the transmitted signal and the echo, showing a peak corresponding to the correct ToF [51].

2.2.5. Continuous Wave Modulation

The previous techniques relied on a direct range estimation based on the time-delay between sending and receiving events. Whatsoever, some techniques infer range information indirectly from dephasing and frequency. These systems are most commonly referred to as CW modulated LiDARs. The light source can either be modulated in amplitude or in frequency by different shapes of signals. Compared to pulsed modulation, a larger variety of light sources is available for these operation modes because extremely fast rise and fall times are not required.

When the CW source is modulated in amplitude, the system is called AMCW (Amplitude Modulated CW) LiDAR. These systems employ laser diodes on the transmitter whose intensity is modulated by varying the bias current in the electrical domain and the phase shift, $\Delta\varphi$, is measured [37]. Posteriorly, the ToF can be calculated as [19]:

$$\Delta\varphi = 2\pi f_0 \cdot t_D \quad (2.15)$$

where f_0 is the modulation frequency, and, subsequently, the range calculated using equation (2.14).

Frequency Modulated CW (FMCW) LiDARs are fundamentally different from pulsed and AMCW schemes as the photons are not treated as particles with range information encoded in their arrival times. In contrast, FMCW techniques rely on the wave properties of light. In these systems, the frequency of the light field is swept across a determined range and an interferometric detection scheme is employed at the receiver to estimate the frequency shift between the transmitted and received fields, proportional to the distance. Therefore, the large frequency bandwidth in the optical domain becomes accessible and can be exploited to improve the performance, eliminating the need for wideband electrical circuits. [37]

Unlike any other technique where the detection is incoherent (only the received signal power is measured as a function of time), FMCW involves coherent detection and has the capacity to measure not only range but also the speed of a target through the Doppler shift (frequency shift in the signal due to reflection on a moving target) because the phase information is preserved in the receiver. [48]

Figure 18 illustrates the radial accuracy as a function of the range for the different ToF techniques. AMCW LiDARs can achieve accuracies similar to that of the pulsed ToF, reaching less than a centimeter but only at moderate ranges. This technique is not popular for long-range measurements because it transmits continuous optical power that has to remain eye-safe, therefore the echo signal is not as strong as in pulsed LiDARs [37]. Furthermore, it yields a reduced unambiguous distance, limited by the modulation wave frequency. This range is limited to half-wavelength, corresponding to a 2π phase-shift in the roundtrip of light, after which the periodic signal repeats. By using high modulation frequencies, enhanced resolutions can be achieved with a trade-off of shorter measurement range. For e.g., if $f_0 = 1\text{MHz}$, the unambiguous range is:

$$t_D = \frac{1}{f_0} \rightarrow d = \frac{c}{2 \cdot f_0} = 150\text{m} \quad (2.16)$$

Since dephasing introduces ambiguity, this indirect technique is usually restricted to short-range LiDAR applications, as in the so-called ToF cameras that use LED flash illumination to illuminate and image the scene at once [53] [54]. This is an interesting concept and so important within automotive applications that dedicated sensors with integrated processing are currently available and under R&D phase, such as Driver Monitoring Cameras (DMCs) or Occupant Monitoring Cameras (OMCs).

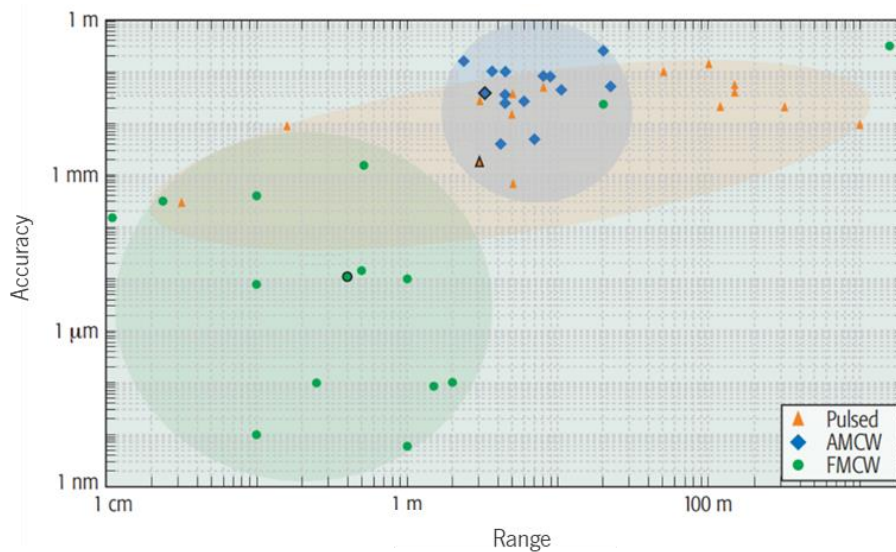


Figure 18. Accuracy vs. operating range for academically published and industrial LiDARs since 1990 [37].

FMCW is the only rangefinding technique achieving sub-micrometer accuracies besides interferometry, enabled by the direct modulation and demodulation of the signals in the optical domain. The accuracy depends on the measurement accuracy of the frequency shift. In addition to finer accuracies, FMCW offers better sensitivity and robustness against environmental disturbances and cross-talk from other light sources because spurious light incoherent with the local oscillator are rejected [37]. For these reasons, FMCW LiDARs are increasingly gaining popularity within the automotive context.

The maximum range measurable through FMCW is also limited by the unambiguous range, that depends on the modulation pattern, and the coherence length of the laser, i.e. the propagation distance inside which the laser conserves a constant phase relation, frequency and waveform. The finite value of the latter is typically in the order of tens of meters. Moreover, compared to direct ToF LiDAR, more

computational power and more complex transceivers are required, resulting in a slower 3D view generation. [55]

While the intensity modulation is easily achieved by current modulation in laser diodes, in frequency modulation the response of the laser is, in general, nonuniform against the modulation signal, so that a linear optical frequency swept cannot be fully realized by a linear modulation of the control current since deviations from linearity usually occur.

2.3. Laser Sources

The light source is one of the core components of the LiDAR as it is the basis for all the measurements. The transmitted beam is generated using lasers (acronym for light amplification by stimulated emission of radiation), justified by various factors. Firstly, lasers produce highly focused and directional beams, with little beam divergence, making it possible to use a narrow beam for point measurements up to long ranges with high spatial resolution. Furthermore, a laser has the advantage of having a very narrow bandwidth, making it possible to use a narrow bandwidth receiver with less sensitivity to ambient noise and simpler signal processing architectures [49]. In addition, there are several existent lasers suitable for the context with low power consumption, compact size and light weight, at low costs [56]. Lastly, lasers produce highly-coherent beams, maintaining a fixed phase relationship for several meters, allowing coherent detections.

The most important parameters of a laser source are the emitted power and the beam optical intensity (or irradiance). The power, P , is defined as the output energy per time unit while the intensity, I , is defined as the emitted power per unit area and, thus, the energy per time and area units. Since the energy of each stimulated photon is related to its wavelength through the Planck's constant, $h \approx 6.625 \times 10^{-34} \text{ J}\cdot\text{s}$:

$$E_{ph} = \frac{h \cdot c}{\lambda} \text{ [J]} \quad (2.17)$$

and considering an output photon flux Φ_{ph} [photons/sec], the power can be calculated as:

$$P = \frac{\text{Beam Energy}}{\text{time}} = \frac{\# \text{ photons} \cdot E_{ph}}{\text{time}} = \Phi_{ph} \cdot E_{ph} \text{ [W = J} \cdot \text{s}^{-1}] \quad (2.18)$$

On the other hand, the beam intensity is related to the optical power and the area of the irradiated region, A , through:

$$P = \int I \cdot d\vec{A} \rightarrow I = \frac{P}{A} \text{ [W} \cdot \text{m}^{-2} = \text{J} \cdot \text{s}^{-1} \cdot \text{m}^{-2}] \quad (2.19)$$

As aforementioned, the laser output can either be continuous or a train of pulses. In the first, the laser power is approximately constant over time, in opposition to pulsed operation, where the energy is transmitted over short periods of time and, thus, the output power varies with time (Figure 19). In this situation, two different types of power are defined: peak power, corresponding to the maximum

instantaneous output power, and average power, corresponding to the energy transmitted over one full period.

The peak power, P_{peak} , is determined from the pulse energy and temporal distribution. It can be roughly estimated by the ratio between the pulse energy, E_{pulse} , and the pulse temporal width measured at FWHM (Full Wave Half Maximum), t_{pulse} :

$$P_{peak} = \frac{E_{pulse}}{t_{pulse}} \quad (2.20)$$

The average power, P_{avg} , is calculated by averaging the energy over one full period of the laser pulses' sequence. Inasmuch as the pulses frequency, usually referred as Pulse Repetition Rate (PRR), corresponds to the number of pulses emitted per second, then the average power is determined through:

$$P_{avg} = P_{peak} \cdot PRR \cdot t_{pulse} = P_{peak} \cdot dc_{opt} \quad (2.21)$$

where dc_{opt} is the optical duty cycle, i.e., the fractional amount of time the laser is transmitting per period with duration T_p :

$$dc_{opt} = \frac{t_{pulse}}{T_p} = t_{pulse} \cdot PRR \quad (2.22)$$

The maximum optical duty cycle of a certain laser is always specified in the datasheet (typically 0.001 \Leftrightarrow 0.1%) and its value restricts the maximum PRR and, thus, the maximum point rate and measurement speed.

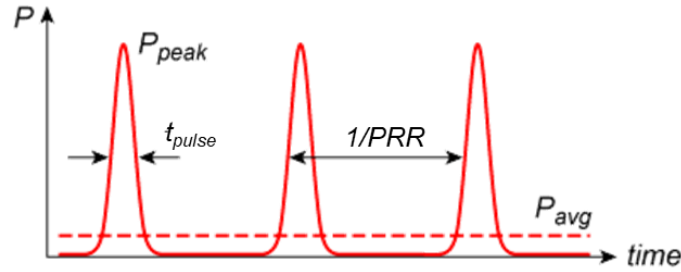


Figure 19. Pulsed laser parameters.

2.3.1. Laser Types

To minimize the costs, a common type of laser shall be used. As the intended application is a direct ToF LiDAR, it must be capable of supplying high power in short pulses to give the receiver a stronger return signal to work with, while meeting the safety requirements. Although there is a vast number of laser sources available that can fulfil the requirements for the application, only two types can reasonably be employed based on the number of alternatives and their usual size: solid-state lasers and laser diodes (LDs) or semiconductor lasers. [49]

Solid-state lasers, as the name indicates, are based on a solid-state active gain medium such as crystals or glasses doped with rare earth or transition metal ions. The pump is achieved optically via flash-lamps or laser diodes. The latter pumping method brings many advantages, in particular compact

setups, long lifetimes and often very good beam quality [57]. However, unless pre-assembled modules can be found, they are likely to be very expensive, especially if a specific wavelength is required.

Laser diodes are electrically pumped lasers in which the gain is generated by an electrical current flowing through a p-n or a p-i-n structure [58]. The characteristics that make these lasers preferable for the application are the compact size, the reduced cost and the power supply and control easiness since an output pulsed modulation can be achieved by a modulated electrical current. Nonetheless, they deliver a beam quality inferior to solid-state lasers and require lenses to function as a laser beams. [49]

In this project, a laser diode is going to be used due to the yielded benefits. Inside this category, there are several subtypes of LDs, with the most significant being edge-emitting LDs and Vertical-cavity surface-emitting laser (VCSEL) diodes.

Most LDs are built as edge-emitting lasers, often based on double heterostructure with an active region stacked between two confining materials with larger bandgap. The photons are generated within the active medium and the adjacent layers serve as a waveguide for the optical field, conducting the photons to the edge of the active region to be outputted. The active region is so thin that it acts as a quantum well [58]. These lasers are cheap, easy to manufacture and common, giving a larger freedom of choice. Notwithstanding, they produce an elliptical beam rather than a round one [49].

The second type of lasers are surface-emitting diodes, where the emission is perpendicular to the surface and the gain is provided by multiple quantum wells, producing round beams. These lasers are a relatively new concept of semiconductor lasers particularly highlighted for the higher reliability compared to the formers. Since it is a rather recent technology, this kind of lasers is not very widely available making them more expensive and at smaller peak powers. [58]

The emission wavelength of a LD is essentially determined by the bandgap of the laser-active semiconductor material and, if applicable, by the quantum well thickness. A variety of semiconductor materials make it possible to cover wide spectral regions. Most LDs emit in the NIR spectral region, but others can emit visible or mid-infrared light.

2.3.2. Wavelengths

One of the most critical choices for automotive LiDAR systems is the light wavelength. Several factors constrain this choice: safety to human vision, interaction with the atmosphere, availability of lasers and photodetectors and solar background irradiance. [47]

As the system must discriminate weak echoes from the background radiation, the first factor to consider when selecting the optimum laser wavelength for automotive LiDARs is the solar spectral irradiance at the earth's surface, whose profile is given by the ASTM G173 standard (Figure 20).

Formerly, it was stated that one of the requirements for the laser is its invisible nature. Despite being useful a visible light source during development for optical alignment, this is not an advantage for the end user because the sensor must not interfere with its normal life. Besides, in this spectral range, the solar irradiance is considerably high, which generates appreciable noise in the detection.

In this sequence and considering the major absorption bands in the atmosphere due to several elements like water vapor, oxygen and carbon dioxide, apparent in Figure 20, the two most popular

wavelengths for automotive LiDAR are 905nm and 1550nm, both corresponding to local minimums in the spectra.

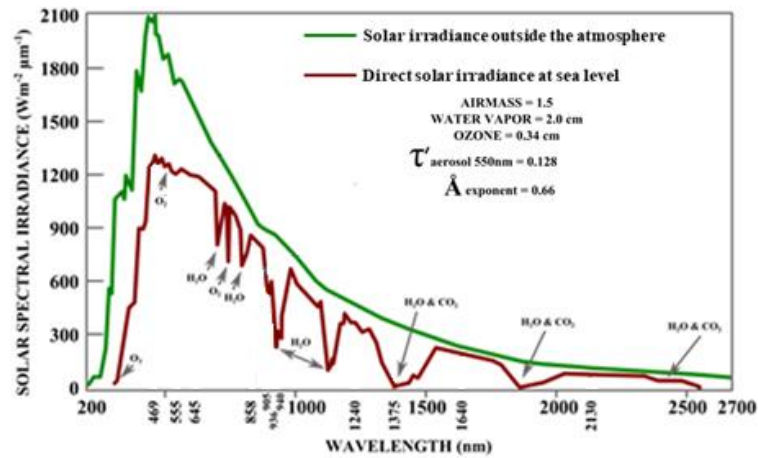


Figure 20. Solar irradiance spectrum at the top of the atmosphere (green) and transmitted to the Earth's surface (brown), at sea level [59].

The prime advantage of 905nm is that silicon absorbs this wavelength and thus, silicon-based photodetectors can be used, which are generally rather common and less expensive than InGaAs IR detectors needed for 1550nm, since the nanofabrication technology is optimized for silicon, while for GaAs based semiconductors is not as mature [47]. Moreover, the offer of LDs is vast in this spectral range.

On the other hand, the higher human-vision safety of 1550nm allows the use of lasers with much more radiant energy per pulse, theoretically allowing larger detection ranges [47]. Notwithstanding, the offer of high-power pulsed LDs is inferior, justified by difficulty to achieve this wavelength using standard semiconductor fabrication techniques. [49]

At last, atmospheric attenuation under all weather conditions, scattering from aerosols (e.g. fog) and reflectance from target surfaces are wavelength-dependent. This is a complex issue for automotive LiDAR because of the myriad of possible weather conditions and types of reflecting surfaces. Under most realistic scenarios, loss of light at 905nm is less because water absorption is stronger at 1550nm [47]. Considering the argumentation and overall, the most reasonable wavelength to use is 905nm.

2.3.3. Eye-safety and Limitations

One of the biggest issues concerning lasers usage is safety. As laser radiation has the potential to be harmful to biological systems, various precautions and limitations must be considered when designing a LiDAR system. For LiDAR applications where a longer operating range is important, a larger transmit power is desired to obtain a stronger return signal and, thus, to ease detection. Whatsoever, the maximum transmit power is often limited by eye-safe regulations. [37]

The primary concern in laser safety is the possibility of eye injury, either by burning the retina or the eye's surface. Biological effects of laser light depend on manifold factors, including the light wavelength, its power, whether it possesses a continuous or pulsed nature, or whether it is the result of a direct exposure rather than reflection.

Important components of the eye, such as the cornea, crystalline lens, retina and fovea are susceptible to damage by laser light (Figure 21a). Light enters through the transparent layers of the cornea and then is focused by the lens to the retina, being intensified. The retina is the light-sensitive inner coat of the eye, responsible for receiving the light and convert it into a neural signal to be send to the brain for image formation. The fovea is a small area located on the retina ($\approx 4\%$ of its total area) responsible for sharp central and color vision. [60]

The human evolved to capture light very efficiently around the peak of solar irradiance (400-700nm) and is more sensitive in this spectral region. Hence, lasers with wavelength with visible wavelengths extending up to 1400nm are focused onto the retina (Figure 21b) with significant magnification (as high as 100 000 times in some particular cases [60]). Once and if a certain threshold is achieved, the retina and the fovea can be damaged resulting in a significant and permanent loss of sight or even blindness.

Lasers with a wavelength beyond $1.4\mu\text{m}$ or below $0.4\mu\text{m}$ are safer than lasers between these range because the water present in the cornea and anterior chamber strongly absorbs light in these regions, preventing it from penetrating the eye and focusing on the retina (Figure 21b). Nonetheless, they can still burn the cornea (with a much higher damage threshold) but do not create the large increase in irradiance resulting from focusing the light in the retina. To complete, invisible NIR lasers are particularly hazardous because natural protection mechanisms of the eye, such as the blink reflex do not work.

Owed to the previous reasons, some standards were defined to set constraints to the output average and peak power, exposure duration, pulse repetition rate and safety procedures and measures, as a function of the wavelength. These restrictions are dictated by the international IEC (International Electrotechnical Commission) 60825-1 standard.

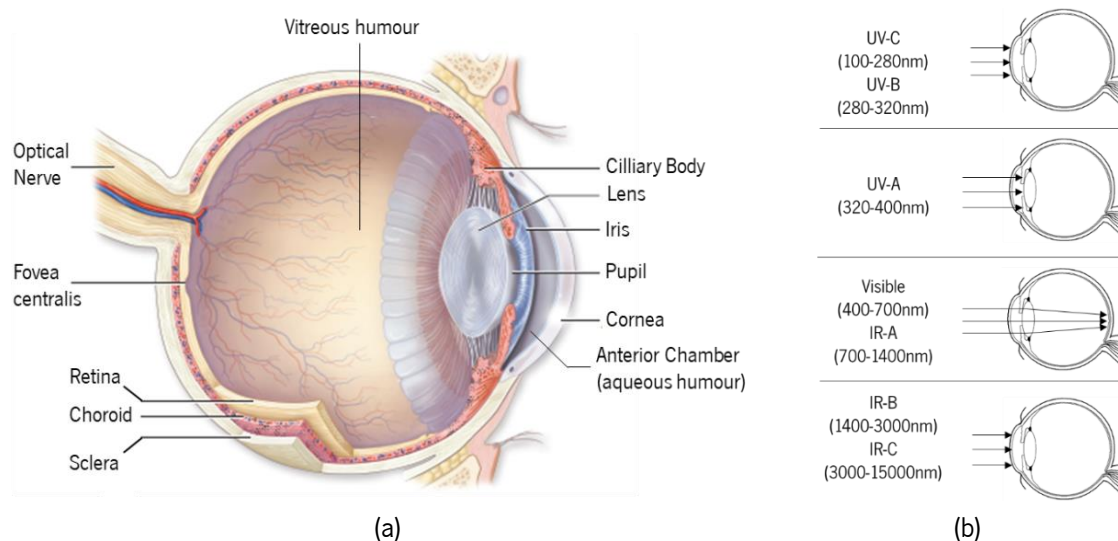


Figure 21. Eye-safety considerations. (a) diagram of the human eye and (b) penetration of different wavelengths.

Because of the wide ranges possible for the wavelength, energy content and pulse characteristics of a laser beam, the hazards arising in its use vary widely. It is impossible to regard lasers as a single group to which common safety limits can apply. For this reason, lasers are divided in classes: Class 1, Class 1M, Class 2, Class 2M, Class 3R, Class 3B and Class 4. [61]

As only Class 1 lasers can be used in automotive LiDAR (lasers that are safe under reasonably foreseeable conditions of operation, including the use of optical instruments for intrabeam viewing), some very restricting criteria must be fulfilled. The objective is to maximize the output power while keeping the system eye-safe. Naturally, as the signal to be used in direct ToF is pulsed, the power is concentrated in small intervals of time, which permits to achieve higher peak powers comparing to CW. [49]

The parameter that reflects the maximum level of radiation to which, under normal circumstances, persons may be exposed to without suffering adverse effects is denoted the Maximum Permissible Exposure (MPE) and cannot, in any circumstance, be exceeded. The MPE is set for lasers' users and represents the maximum level to which the human eye can be exposed without consequential injury.

The MPE must be always determined considering the worst-case scenario, which means that for this application, a direct exposure of the cornea to laser radiation, right in front of the laser's aperture, and considering that all the outputted light strikes the cornea, without losses. The MPE is lower in the visible range slowing increasing up to 1400nm. Above 1400nm the increase is significant. This situation is graphically illustrated in Figure 22 for several pulses' width.

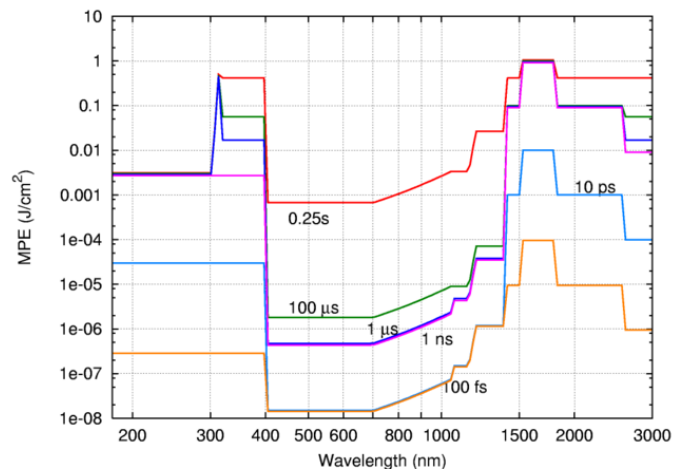


Figure 22. MPE vs. Wavelength for different pulse durations [62].

2.3.4. Laser Driving

As previously stated, the laser diode is current controlled, which means that the output power is controlled by an electrical current, rather than voltage. By applying a pulsed modulated input current, the output light is similarly modulated, that is, the optical gain is modulated by switching the pump current (gain switching). Although for automotive ToF LiDAR short pulses with lengths in the order of nanoseconds are required, mainly limited by the detector bandwidth, the fundamental minimum pulse width is set by the current switching speed. To ensure peak output powers in the order of watts, the current pulses need to vary from a few amperes to tens of amperes in a few nanoseconds. The FWHM and amplitude of the optical output pulse are defined by the amplitude and rise/fall time of the current pulse. [48]

A typical response curve of a LD is portrayed in Figure 23. LDs only emit light when forward biased, i.e., when its anode (p-region) is at a higher potential than its cathode (n-region), allowing a current flow

in the same sense. Below the current threshold, I_{th} , the device emits radiation spontaneously since no population inversion can be reached. Once the current exceeds the threshold, the diode starts to predominantly emit stimulated light in a quasi-linear fashion (output power varies linearly in relation to the current). In this region, spontaneous emissions persist but in more reduced number comparative to stimulated emission, contributing to intensity noise (mitigated by operating high enough above the threshold) [48].

Most LDs emit a beam with an optical bandwidth typically in the order of 10nm with a temperature sensitive peak wavelength resulting from the temperature-dependence of the gain medium (influences the thermal population distributions in the valence and conduction band) and, also, of the bandgap (bandgap decreases with temperature). With an increase in temperature, a shift towards higher wavelengths occurs, commonly in the order of 0.3nm/°C. Besides, the threshold current and the laser efficiency are also temperature dependent, with the first increasing and the second decreasing with a temperature increase. Since in direct ToF the pulse is short, the output power does not change significantly over time since the laser has time to cool off between pulses. [49]

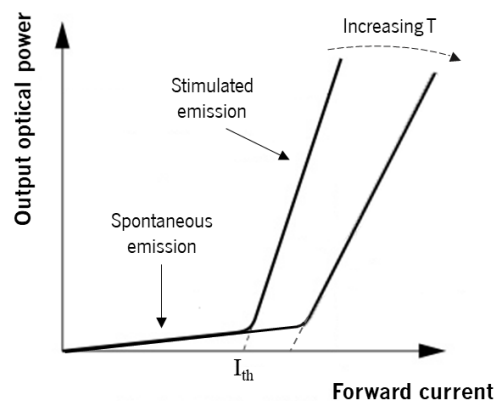


Figure 23. Laser diode typical response (output light power vs. forward electrical current) and temperature dependence.

The triggering instants of the laser are instructed by the control unit to the laser electronics in the form of a digital signal. Since the laser output is controlled via electrical current, the PWM (Pulse Width Modulation) voltage outputted at the controller cannot be directly used to feed the LD. Additionally, to achieve fast rise and fall times and short pulses width, increased current drive is necessary as well as fast switching techniques. For this purpose, the current through the laser is frequently controlled using regular MOSFETs (Metal-Oxide-Semiconductor Field-effect Transistors) or power MOSFETs, depending on the power involved, justified by the low gate drive power and high-efficiency (low power losses since once turned-on, the driving current is practically reduced to zero), fast switching speed and high-frequency operation. Alternatively, programmable resistors (drawback that the commercial solutions are both slow and have high resistance values) [49], insulated-gated bipolar transistors (slower and lower switching frequencies), avalanche transistors (bipolar transistors) and thyristors can also be adopted [48].

The main drawback of avalanche transistors is that these bipolar transistors function in the avalanche breakdown region, above the breakdown voltage, which typically requires high voltages (200-300V), making it unfeasible for laser driving in automotive LiDARs. Furthermore, the control is easier and power

losses for driving a MOSFET are inferior compared with bipolar transistors, since the control electrode is isolated from the current conducting silicon, the switching time is shorter and are less affected by temperature. More information can be found in [48] and [63].

Gain switching is not the only way to generate short laser pulses in LDs. An alternative is using Q-switching [48]. This technique involves pumping the upper level for a time comparable to its lifetime (time until spontaneous recombination) while holding off the cavity feedback via a Q-switch located inside the laser resonator between the lasing medium and the output mirror. When population inversion reaches a high value, the feedback is turned on to produce a sudden burst of photons [32]. Active Q-switching is usually implemented through an active shutter that can be either an acousto-optical modulator or an electro-optical modulator (Pockels cells combined with a linear polarizer). When a voltage is applied, the active Q-switch alters the polarization of the beam so that this is no longer transmitted by the polarizer and the gain is held [32]. Overall, this technique is either more complex and leads to bigger laser setups. Alternatively, passive Q-switching is performed by replacing one of the cavity mirrors with a Semiconductor Saturable Absorber Mirror (SESAM). This absorber is a distributed Bragg reflector in which a set of quantum wells are located within the surface layer, with an energy gap chosen to match exactly the energy of the lasing transition. The quantum wells initially absorb the incident radiation arriving from within the cavity and this action holds the gain below unity. During this stage, the population inversion builds up steadily within the laser cavity. Eventually, the quantum wells in the SESAM become saturated and, at this point, its reflectance climbs to unity. Correspondingly, feedback is provided, resulting in a sharp increase in the roundtrip gain and a high-power pulse is produced by the laser. This quickly depletes the population inversion in the active material and the quantum wells empty rapidly [32].

2.4. Scanning Mechanisms

One indispensable element in a LiDAR system for autonomous vehicles is a mechanism to illuminate several points within the scene and responsible for providing a tridimensional awareness over the required FOV in the shape of a 3D point cloud of distance and intensity information. Hereupon, LiDAR sensors may be divided into three categories based on how they illuminate and sense the 3D scene, as depicted in Figure 24.

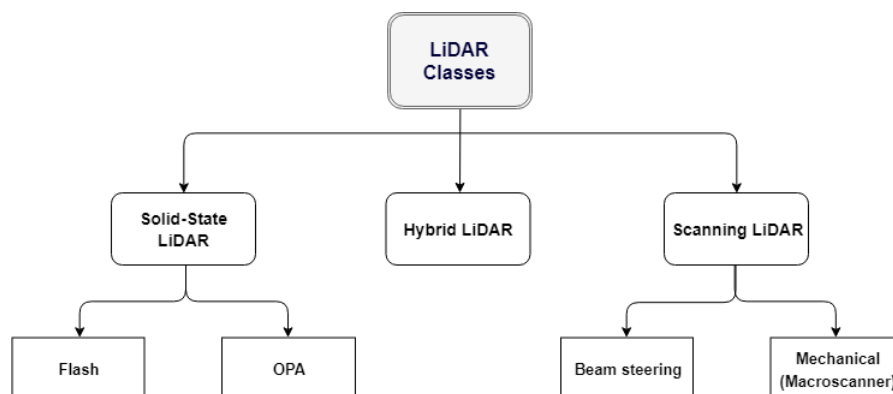


Figure 24. Taxonomy of LiDAR classes based on the scene illumination mechanism.

2.4.1. Scanning LiDAR

In scanning LiDAR systems (laser scanners), the scene is illuminated by sweeping a single or multiple narrow laser beams within the FOV and sensing the return light with the same number of photodetectors. In between this category, diverse techniques can be used, from which one highlights the mechanical macro-scanners and beam steering systems.

Mechanical macro-scanners are, perhaps, the most known and more commonly scanning methodologies used in current automotive LiDARs. By using multiple fixed laser-receiver channels (each laser with a dedicated detector) aligned to cover different angular sections in the desired VFOV and combining with a mechanically rotating system, the whole assembly is rotated around the vertical axis to provide a 360° HFOV. This way, each frame is obtained via a complete rotation of the system. While the horizontal resolution and point density is a function of the rotational speed, in the vertical direction these parameters are established by the lasers number and angular spacing between them.

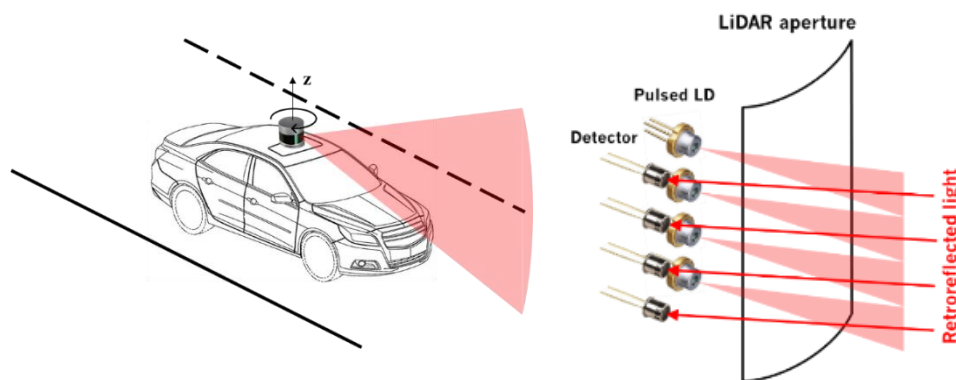


Figure 25. Principle of a mechanical scanning LiDAR with 4 channels. The retroreflected light within each segment is detected by a dedicated photosensitive device. For simplicity, the receiving and transmitting optics were omitted.

In steering beam scanners, as the name indicates, the horizontal and/or vertical direction of the laser beam is controlled through an optical system constituted by a set of mirrors and lenses, with the housing remaining stationary. This is performed by firing a single laser onto a rotating or oscillating mirror, that, according to its positioning, deflects the pulses and outputs them in a specific direction. The echo is measured by a single fixed detector and, by addressing the ToF measurement to the mirror deflection correspondent to a certain laser direction, one yields the respective point in the cloud. To endow a tridimensional FOV, the rotations/oscillations must have 2 orthogonal degrees-of-freedom.

The beam can be steered using multi-faceted rotating mirrors with each facet at a slightly different tilt angle to steer the single beam of pulses into different azimuthal and polar angles. However, the number of points is limited to the number of faces of the polygonal mirror, making it unfeasible for the context.

A more compact approach to beam steering scanning LiDAR is the use of a microelectromechanical system (MEMS) based on microscopically small mirrors (micromirrors) to electrically deflect the beam. These devices are electromagnetically and/or electrostatically driven, which means that, according to the actuation signal intensity and the device's morphology, the mirror is tilted by a determined angle and, consequently, a corresponding optical beam direction is defined [64]. The single beam is focused on the

micromirror and is reflected according to the reflection law (angle of reflection is equal to the angle of incidence), without dispersion and polarization modification [62]. To avoid unintended energy losses, the beam cross-section must completely fit in the micromirror area. This is accomplished by collimating the laser output using lenses.

Micromirrors are controlled using Application-specific ICs (ASIC) and can be programmed to scan the scene according to a specific pattern, assigned by a specific sequence of actuation signals, which is often done line-by-line as depicted in Figure 26. The FOV is limited by the mirror's maximum deflection angle while the angular resolution (horizontal and vertical) is set by the minimum increment in the mirror position in the respective direction.

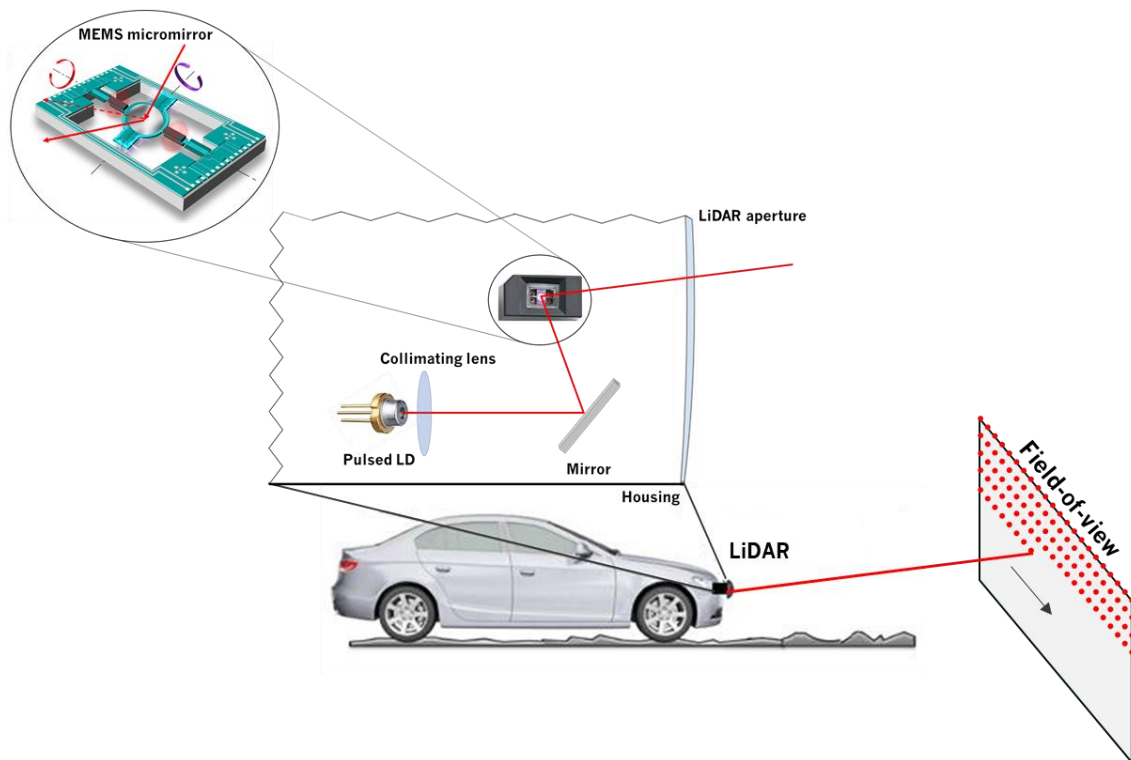


Figure 26. Transmission system of a LiDAR based on micromirror scanning technique and illustration of the scene sweeping mechanism line by line.

2.4.2. Solid-State LiDAR

In solid-state LiDARs, the laser beam is spanned into the scene and the return signals are measured with a photodetector array accordingly to the line-of-sight direction, without any moving parts either at macro or micro scale. Each pixel on the array measures independently the echo in a specific region of the scene and, knowing the respective location in the matrix, the frame is generated by combining the results provided by the totality of segments. In general, in solid-state LiDARs the characteristics of the detector array set the image resolution and size. The point density is defined by the array density and fill factor, while the angular resolution is set by the pitch between consecutive pixels and the FOV by the total area.

In Flash LiDARs, a single beam is diffused onto the entire FOV, illuminating all the field of interest simultaneously, and the ToF is measured directly for each pixel. The name arises from the fact that each

frame is captured at once by sending single or multiple laser pulses (“flash”) to the scene. Thus, the laser PRR in this system equals the frame rate scaled by the number of pulses used to obtain it. This system is portrayed in Figure 27, being evidenced the FOV segmentation and the photodetector array at the receiver.

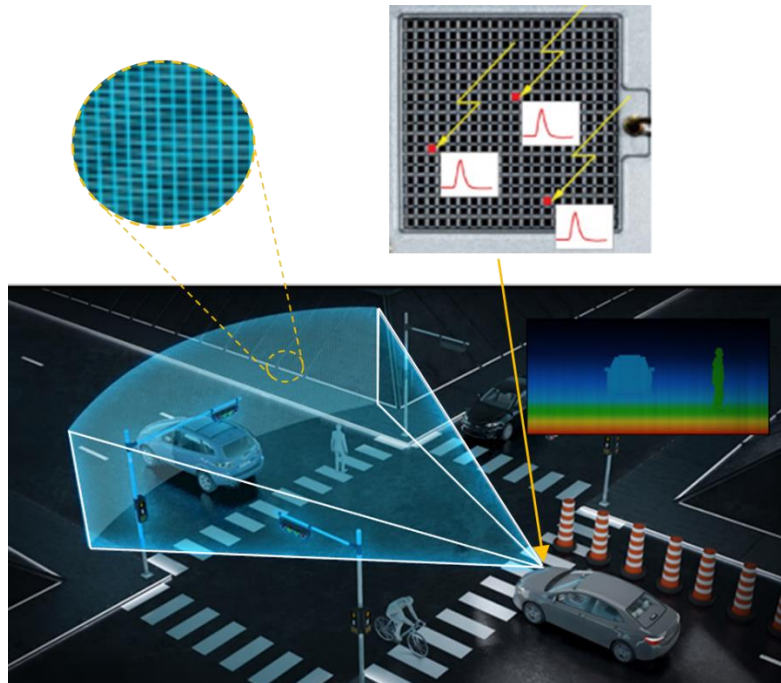


Figure 27. Working principle of flash LiDAR with emphasis on the FOV segmentation and detection process at each pixel on the array. Also, a resulting point cloud of the scene is represented in 2D.

An emerging alternative to Flash LiDAR in the same category is designated Optical Phased Arrays (OPA). These phased arrays can broadcast light waves in any direction, by using a microscopic array with several individual optical antenna elements synced in a specific way. A coherent laser beam is split into multiple channels and, by electronically controlling the phase between each re-emitter, one coherent and cohesive beam is achieved by constructive interference and is transmitted in a certain direction. By changing the phase, the beam can be steered into different directions without any mechanical movement. [65]

Although this technique does not illuminate the entire scene simultaneously and involves beam scanning, it is still included in the solid-state class because the control is all performed electronically without moving parts. The array of optical antennas can be fabricated using liquid crystals (Spatial Light Modulators) or silicon-photonics tunable phase elements (Photonic Integrated Circuits), and the detection is fulfilled in the same way with an array. Silicon-photonics phased arrays are more popular because of their compatibility with fully-integrated chip-scale LiDARs. [37]

2.4.3. Hybrid LiDAR

Hybrid LiDAR systems employ a combination of distinct techniques onto a single device. Assorted combinations are possible as the solution proposed by *LeddarTech*, depicted in Figure 28. This proposal combines horizontal beam scanning using a single-axis oscillating MEMS micromirror with solid-state

detection [66]. The micromirror is synchronized with the lasers pulses that, before being outputted, are directed through a diffuser lens to vertically expand the beam. After the light is reflected by a target, it is focused on a linear array of detectors where every individual pixel senses the light coming from a small vertical segment of each slice. This way, for any position of the micromirror a full line of the scene is acquired, and the total point cloud is given by horizontally scanning the beam and merging the collected slices [66].

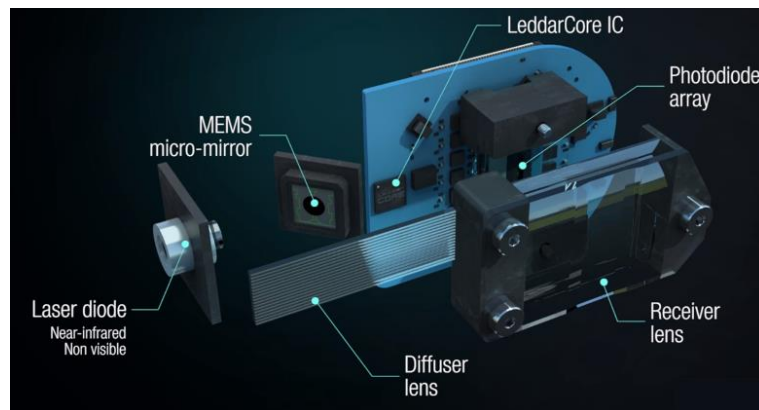


Figure 28. *LedaarTech's* automotive 3D hybrid LiDAR [66].

2.4.4. Comparative Analysis

Nowadays, the aforementioned techniques are being applied by different manufacturers in automotive LiDARs as each one is appealing in different parameters. Anyhow, all of them still reveal some downsides.

Starting by each class in general. In scanning LiDARs, because each laser performs only a single point measurement at a time, the beam can be narrowed and collimated very precisely to create extremely highly-resolved point clouds that facilitate the discrimination of small features in the scene, simplifying the processing.

The main problem associated with scanning LiDARs are the moving parts that can wear out over time and potentially be a source of failure. If the mechanical system gets stuck, an eye-safety problem arises [65]. To compensate this problem, the scanning assemblies require a lot more adjustment and calibration, making high-volume manufacturing a costly proposition [30].

Solid-state LiDARs are more robust since no moving parts are present either at macro or microscales, removing one of the most failure-prone components of the previous class [67]. This assures a highest level of performance, reliability and reproducibility, robustness and stability, longevity and cost efficiency while enabling increasingly smaller footprints that require less power [68]. Everything (except the lenses) is made up of electronic components and the assembly can easily be automated for high-volume production, demanding simpler calibration and reflecting in lower assemblage and maintenance costs [30]. Notwithstanding, since they are built with no mechanical components, they have some restrictions in the FOV coverage (usually not exceeding 120° horizontally) [69].

Specifying in the discussed scanning LiDARs approaches, the superiority factors of mechanical scanners are the total coverage of the vehicle's environment with a single device (360° HFOV) and the

high point rates and densities, made possible by the simultaneous acquisition of data through several channels in conjunction with high spinning rates.

Whatsoever, the complete HFOV does not only bring positive aspects. Firstly, to take benefit of the full 360° HFOV, the device must be mounted on top of the car where it is more susceptible and exposed to external hazards. Besides, mechanical scanning LiDARs are usually bulkier and pricier. Thus, even though the other classes cannot afford full HFOV in single devices, the more diminished costs and sizes allow the seamless and strategic integration of multiple of these devices directly in the car's structure (e.g. headlights, bumpers, fender, grill, side panel, spoiler, headlights, hood or trunk) to cover larger FOVs and also provide additional protection (Figure 29). Moreover, the power consumption is considerably larger, as it is going to be demonstrated for the state-of-the-art automotive sensors [69].

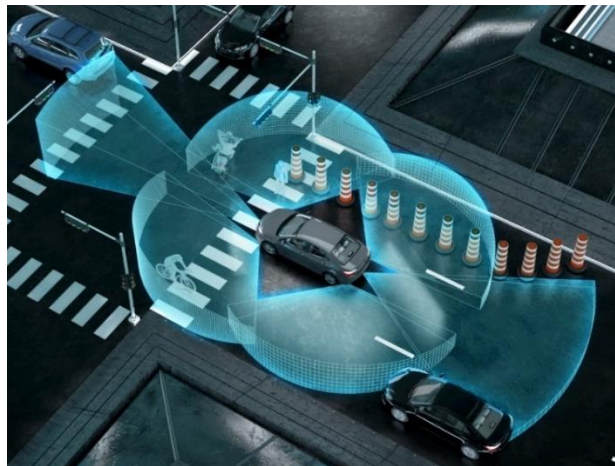


Figure 29. Integration of several automotive LiDAR sensors with FOV inferior to 360° in order to cover a 360° FOV [70].

Although technically there are still moving parts in micromirror scanning, the amplitude of the oscillation is small, and the frequency is high enough to prevent mechanical resonances between the MEMS and the car. However, the confined geometry of the mirror constrains its oscillation amplitude, which translates into a limited FOV. Nevertheless, this method is attractive because of the low cost, proven technology and extremely compact size for easy integration in the housing with low power consumption. In addition, the programmability of this devices is another attraction since, besides the scanning pattern (that can be defined randomly to work around eye-safety), one can define the resolution and the frame rate, to adapt these parameters to the driving context. One challenge is to align the beam correctly with all the optics. Micromirrors rotating in both axis can be susceptible to shock/vibrations and MEMS can drift out of alignment, deviating from calibration. Also, the system is temperature dependent and, to mandatorily fulfill a correct alignment, it needs to be recalibrated during the its lifetime. [65]

At last, in Flash LiDAR, since the scene is illuminated at once, each frame is also generated at once and very high frame rates are possible, allowing faster analysis for safer decision-making. Yet, the system achieves this advantage by employing a detector array, abundantly more expensive and harder to calibrate, and more complex detection circuitry. Additionally, the fabrication technologies are still not sufficiently evolved to achieve the required resolutions, with current arrays reaching resolutions of about 1-2 hundred by several tens of pixels.

The major downside of Flash LiDAR is the intensity of the returning light. Since the system illuminates the same scene repeatedly, the maximum laser output power must be smaller, affecting the sensor's maximum range. One workaround is to use SPAD (single-photon avalanche diode) arrays with sensitivities down to single-photon level combined with multiple optical cycles averaging to reduce the various sources of noise. Other way is to use an OPA. Although in this alternative the laser is scanned across the scene at inferior frame rates, there still are not any moving parts and the power can be increased since the beam is swept across the FOV without repeatedly illuminating the same area [65].

To conclude, hybrid LiDARs merge the advantages and some of the disadvantages of the implemented techniques onto a single device.

2.5. Photodetection

The returning photons cannot directly induce an electrical current in the receiver. Instead, a photodetector is used to convert the light intensity into an readable electrical signal to be transferred to other subsystems within the receiver [62]. Currently, there are several available types of photodetectors, from which one can highlight solid-state detectors, as PIN photodiodes (PDs), Avalanche Photodiodes (APDs) and Single Photon Avalanche Diodes (SPADs). Some of these devices can be used individually or combined to form arrays.

Solid-state photodetectors rely on the generation of charged carriers (electrons/holes) within semiconductors through absorption of light (photogeneration or internal photoelectric effect). When a photon with wavelength λ strikes the semiconductor, it can generate free electrons and holes through intrabands optical transitions, only if its energy is equal or superior to the gap energy, E_{gap} :

$$E_{ph} = \frac{hc}{\lambda} \geq E_{gap} \Leftrightarrow \lambda[\mu m] \leq \frac{1.24}{E_{gap}[eV]} \quad (2.23)$$

A comparison of different materials typically used in photodetectors is presented in Table 4. For compound semiconductors, the bandgap depends on the relative compositions. Since silicon has a bandgap of approximately 1.12eV, the maximum absorbable is around 1.1 μ m and, thus, it cannot be used alongside 1550nm lasers.

Table 4. Comparison between the semiconductors most commonly used in photodetectors (adapted from [71]).

Material	Dark Current	Speed	Sensitivity (nm)	Cost
Si	Low	High	400 - 1100	Low
Ge	High	Low	900 - 1600	Low
GaP	Low	High	150 - 550	Medium
InGaAs	Low	High	800 - 1800	Medium
Extended Range InGaAs	High	High	1200 - 2600	High

Certain features are conceptually common to all detectors, such as the quantum efficiency, the responsivity and the rise time. The quantum efficiency of the detector, η ($\eta \in [0,1]$), is the probability that a single photon incident on the device will generate a photocarrier pair that contributes to the detector current [72]:

$$\eta = \frac{\# \text{collected photocarriers pairs}}{\# \text{incident photons}} = \zeta(1 - \rho_D) [1 - e^{-\alpha d}] \quad (2.24)$$

where ρ_D is the optical power reflectance at the surface, ζ the fraction of electron-hole pairs that successfully contribute to the detector current (avoiding recombination), α the absorption coefficient of the material and d the photodetector depth. The second factor represents the portion of light transmitted at the detector's surface, while the third represent the fraction of photon flux that is absorbed in the bulk material. The quantum efficiency is wavelength-dependent, through the absorption coefficient (the depth at which carriers are generated depends on the wavelength of the incident light).

The detector's responsivity (or spectral sensitivity or photosensitivity) is one of the most important parameters and it relates the generated electric current, I_p , to the incident optical power, P_s . A photon flux produces an electron flux $\eta \cdot \Phi_{ph}$ corresponding to an electric current:

$$I_p = \eta \cdot e \cdot \Phi_{ph} = \frac{\eta \cdot e \cdot \lambda \cdot P_s}{h \cdot c} = \mathfrak{R} \cdot P_s \quad [A] \quad (2.25)$$

where $e = 1.6 \times 10^{-19} C$ is the elementary charge. The proportionality factor between the electric current and the optical power is the wavelength-dependent responsivity:

$$\mathfrak{R} = \frac{\eta \cdot \lambda \cdot e}{h \cdot c} = \eta \frac{\lambda[\mu m]}{1.24} \quad [A/W] \quad (2.26)$$

In principle, each photon can potentially generate a maximum of one electron. However, some photodetectors incorporate internal gain mechanisms so that the photocurrent can be amplified by carrier multiplication within the detector and whereby make the signal more easily detectable. Thus, each photocarrier pair can generate more than one circuit electron and the gain, G , is given by the ratio between the circuit charge produced by each photocarrier, q , and the electron elementary charge: [72]

$$G \equiv \frac{q}{e} \quad (2.27)$$

In the presence of gain, the responsivity as given by equation (2.26) must be modified to:

$$\mathfrak{R} = \frac{\eta \cdot G \cdot e \cdot \lambda}{h \cdot c} = \eta \cdot G \frac{\lambda[\mu m]}{1.24} \quad (2.28)$$

Finally, the rise time is the time required for the detector to increase its output from 10% to 90% of the pulse's final amplitude in its leading edge. This quantity is directly related to the device's bandwidth, B , via:

$$B = \frac{0.35}{t_r} \quad (2.29)$$

Photodetectors are the prime component in the definition of the receiver's sensitivity. The main properties required are a good responsivity, good linearity, small noise, high dynamic range (ratio between the maximum and minimum measurable intensities) and high-enough bandwidth. Two noteworthy aspects when choosing the photodetector is that its peak responsivity must be near the laser's peak, to maximize its performance, and the bandwidth must be balanced. As the laser pulses are in the order of nanoseconds, the response time must match the laser pulse width or else the receiver will not be able to react with full amplitude and the channel sensitivity is reduced. In contrast, the excess bandwidth contributes to the production of noise, deteriorating the measurements precision [73].

2.5.1. Noise in Photodetection

Inherent to the photodetection process, there is always noise manifesting in fluctuations on the resulting electrical current around an average value. There are various noise additive sources inherent to the photodetection process that limit the precision and dynamic range of the sensor. In these conditions, while the upper limit of the latest is limited by the largest output of the detector, the minimum distinguishable return signal is limited by the noise amplitude. This lower limit affects both the sensor's range. [72]

Among the noise sources, the ones playing a more restrictive role in photodetection are the following [72]:

- Photocurrent noise: quantum noise effect related to the discreteness of photons and electrons. The randomness of photon stream transforms into a fluctuating electric current. This is called shot noise and the discreteness of photons and charge carriers makes the fluctuations Poisson distributed.
- Background noise: associated with light from extraneous optical sources that reach the detector (e.g. sunlight).
- Dark-current noise: resulting from random electron-hole pairs generated thermally and by tunneling in the absence of light (usually inferior to 1nA [48]). At the same temperature, photodetectors based on shorter-gap semiconductors generate larger dark currents.

Besides, there is also noise inserted in the electrical circuitry of the optical receiver, introduced in the succeeding amplification stages by components such as resistors and amplifiers. These components introduce noise resulting from the thermal motion of charged carriers in dissipative elements causing fluctuations in the resistance value (thermal noise or Johnson noise), and from fluctuations of charge carriers in the receiver amplifier. [72]

The introduction of gain mechanism increases the system sensitivity as the signal is amplified. Whatsoever, the gain sources are also amplified alongside with the effective signal. Furthermore, in most solid-state detectors, the internal gain is usually a stochastic factor that induces additional fluctuations, denoted Gain noise [72]. Thereby, the introduction of gain it is not always favorable as it can result in smaller SNRs.

With good quality photodetectors, the dark current noise is small and shot noise dominates together with the thermal noise. For small-signal levels, the thermal noise dominates over all the other sources. [48]

2.5.2. Avalanche Photodiodes

The APD is a high-speed and high-linearity photodiode that internally multiplies photocurrent when a high reverse voltage is applied, below the breakdown. The internal multiplication function, referred to as avalanche multiplication, features high photosensitivity that enables measurements of low-level light signals.

Structurally, an APD is a p-n junction with an internal gain mechanism illustrated in Figure 30. When electron-hole pairs are generated in the depletion layer of an APD with a reverse voltage applied (n-region at a higher potential), the electric field created across it causes the electrons to accelerate toward the n+ region and the holes to the p+ region. The higher the intensity of the electric field, the higher the drift speed of these carriers but, when the electric field reaches a certain level, the acceleration process is constantly interrupted by random collisions with the semiconductor's crystal lattice, causing the carriers to reach an average saturation drift velocity [72]. Under these conditions, carriers that do not collide with the lattice will acquire a great amount of energy and, when colliding with the crystal lattice, new electron-hole pairs are generated by impact ionization. These electron-hole pairs then create additional electron-hole pairs, which generate a chain reaction of ionization (avalanche multiplication). A single photon can then be sufficient to generate a measurable electric current. [74]

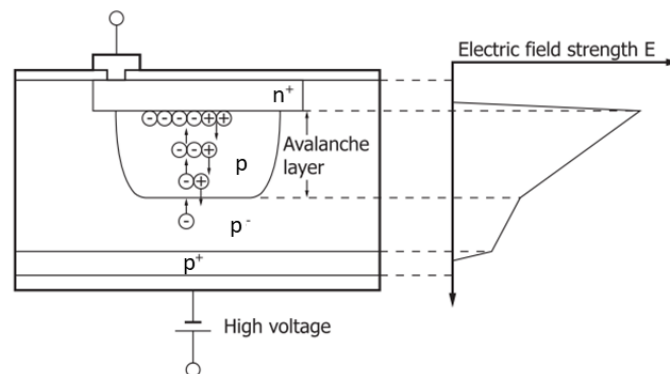


Figure 30. Schematic diagram of the avalanche multiplication process within a p-n junction. The n+-p junction is designated the avalanche layer [74].

The APD gain, G , is determined by the ionization rate, i.e. the number of electron-hole pairs generated during the time that a carrier moves a unit distance and is strongly dependent on the electric field across the depletion layer. When an appropriate reverse voltage is applied to the junction, the electric field in the depletion layer increases so avalanche multiplication occurs. As the reverse voltage is increased, the gain increases and the APD will eventually reach the breakdown voltage. The gain is also temperature-dependent, decreasing as the temperature rises due to an increase in the crystal lattice vibrations and consequent increase in the collision probability. To keep a constant output, the reverse voltage must be adjusted to match changes in temperature. Typically, the gain achieves a factor 100 with reverse voltages up to 100V [75], but in certain devices the amplification can be as high as 1000.

The factors that determine the response speed of photodiodes are the RC time constant, the carrier transit time within the semiconductor, the multiplication time and the time delay caused by the diffusion

current of carriers from outside the depletion zone. The APD, and all the other solid-state detectors, have a low-pass frequency response profile characterized by a cut-off frequency, f_c (and bandwidth, B):

$$B = f_c = \frac{1}{2\pi R_L C_t} \quad (2.30)$$

where C_t is the APD terminal capacitance (order of a few pF [48]). To improve the rise time, the terminal capacitance must be reduced, for e.g., by making the photosensitive area smaller and the depletion layer thicker. The response frequency of an APD is typically in the order of several hundreds of MHz or even GHz, for a 50Ω load. [75]

In most NIR compact laser rangefinders, APDs are applied as detectors due to their internal signal multiplication, which results in overall high sensitivity [76].

2.5.3. Single-photon Avalanche Diodes

SPADs, also known as Photon Counters or Geiger-mode APDs, are the most sensitive solid-state detectors possessing the ability to count individual photons and detect the arrival times with jitters of a few tens of picoseconds, mitigating against gain noise and circuit noise due to a binarized response of the detector. [72]

The principle of charged-carriers' generation is the same as within APDs, with an avalanche being created by impact ionization. However, the fundamental difference between both is that SPADs are specifically designed to operate with a reverse-bias voltage well above the breakdown voltage, in the non-linear Geiger-mode. At this bias, the electric field is so high (above 3×10^5 V/cm) that a single charge carrier injected into the avalanche layer can trigger a self-sustaining avalanche. The current rises swiftly to a macroscopic steady level, generating a pulse in the mA range. If the primary carrier is photo-generated, the leading edge of the avalanche pulse marks the arrival time of the detected photon.

Comparing with APDs, SPADs can achieve higher gains, from 10^5 to 10^6 . Unfortunately, this superiority results in instability: after the avalanche is generated, it becomes self-sustained and the current keeps increasing, eventually destroying the diode. To avoid this, a suitable external circuit is needed, referred as quenching circuit. This circuit senses the leading edge of the avalanche current, posteriorly generating a standard output pulse synchronous with the avalanche build-up. Then, the avalanche is quenched by lowering the reverse-bias below the breakdown voltage, where the lower electric field is no longer able to accelerate carriers to impact-ionize lattice atoms, ceasing the current. Ultimately, the photodiode is restored to the operative level to detect further photons without destroying the detector. The i-V characteristic of SPADs is shown in Figure 31. [77]

SPADs are susceptible to erroneous pulses due to either thermally-generated carriers (dark pulses, analog to dark current) or photons from the background light that happen to be at the detectable wavelength window. Therefore, SPAD receivers are often employed in a statistical architecture where the arrival times of multiple repetitive pulses are accumulated. [37]

Silicon SPADs offer high efficiency ($\eta \approx 75\%$), low dark-count rates (≈ 75 counts/s) and sub-nanosecond timing resolution (≈ 100 ps). For higher wavelength bands, InGaAs/InP heterostructures are

the devices of choice but the performance is far less impressive (typically $\eta \approx 20\%$, timing resolution $\approx 500\text{ps}$ and dark count rate ≈ 5000 counts/s). [72]

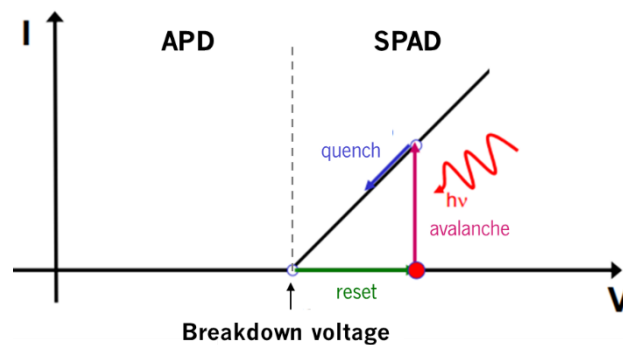


Figure 31. i-V characteristic of a SPAD.

The difference in the reverse-bias level used in APDs and in SPADs origins several operational contrasts. An APD operates as linear amplifier, producing an analog output corresponding to a proportional amplification of the received photons by a certain gain. The SPAD is a trigger device where a single photon generates a digital current pulse with an amplitude of mA. In this device, the gain concept is, then, meaningless.

For the previous reasons, SPADs are very relevant for long-range automotive LiDARs based on direct ToF, since the detection of extremely low-level echoes is possible, requiring almost no additional post processing [78]. However, the response speed in a SPAD, represented by the photon-count rates, can only achieve frequencies up to around 10MHz [79], which is inferior when comparing with the other solid-state detectors. Additionally, the power consumption is larger due to the superior reverse-bias.

2.5.4. PIN Photodiodes

PIN photodiodes consist on two doped regions (p and n) separated by an intrinsic layer (i) to whom a reverse voltage is applied to induce a photogenerated reverse current (from n to p) whenever the semiconductor absorbs photons.

Considering a reverse-biased p-i-n junction under illumination, the photons are absorbed everywhere with absorption coefficient α . Whenever a photon is absorbed, an electron-hole pair is generated but only when an electric field is present the charge carriers can be transported in a particular direction. In a p-n junction, the electric field can only be supported in the depletion layer, hence this is the region in which it is desirable to generate photocarriers. The depletion region is generated when opposite doped semiconductors are contacted. Through diffusion, the electrons will move to the p region and the holes to the n region, due to concentration gradients. When this occurs, the corresponding ions are “left behind”, generating a region with low concentration of electron and holes in the contact’s vicinity, constituted by the ionic cores (positive in the n-side and negative in the p-side). These cores act as a parallel plate capacitor, generating an electric field in the depletion region in the n→p direction. By adding an intrinsic layer, the region supporting the electric field is extended, in effect widening the depletion layer and the area available for capturing light. [72]

This way, the electron-hole pairs generated [72] in the depletion region quickly drift in opposite directions under the influence of the electric field (electrons move to the n-side and holes to p-side). As a result, the photocurrent induced in the external circuit is always in the reverse direction (n to p). Each carrier pair generates an electric current pulse of area $e(G=I)$ since recombination does not take place in the depleted region. Besides these carriers, the electron-hole pairs generated in the depletion layer vicinity have a chance of entering it by random diffusion and identically contribute with a charge e .

As an electronic device, the photodiode has the typical i - V characteristic of an p-n junction with an added photocurrent, $-i_p$, proportional to the photon flow (Figure 32) [48]:

$$i = i_s \left[\exp\left(\frac{eV}{k_B T} - 1\right) \right] - i_p \quad (2.31)$$

Photodiodes are usually operated in strongly reverse-biased mode, well below the breakdown voltage, since this bias creates a strong electric field in the junction that increases the drift velocity of the carriers in the direction of the generated photocurrent, reducing the transit time. Additionally, a strong reverse bias increases the width of the depletion layer, thereby enlarging the photosensitive area, reducing the junction capacitance and improving the response time (equation (2.30)). On the other hand, it increases the dark current noise. This analysis is enhanced by the addition of the intrinsic region.

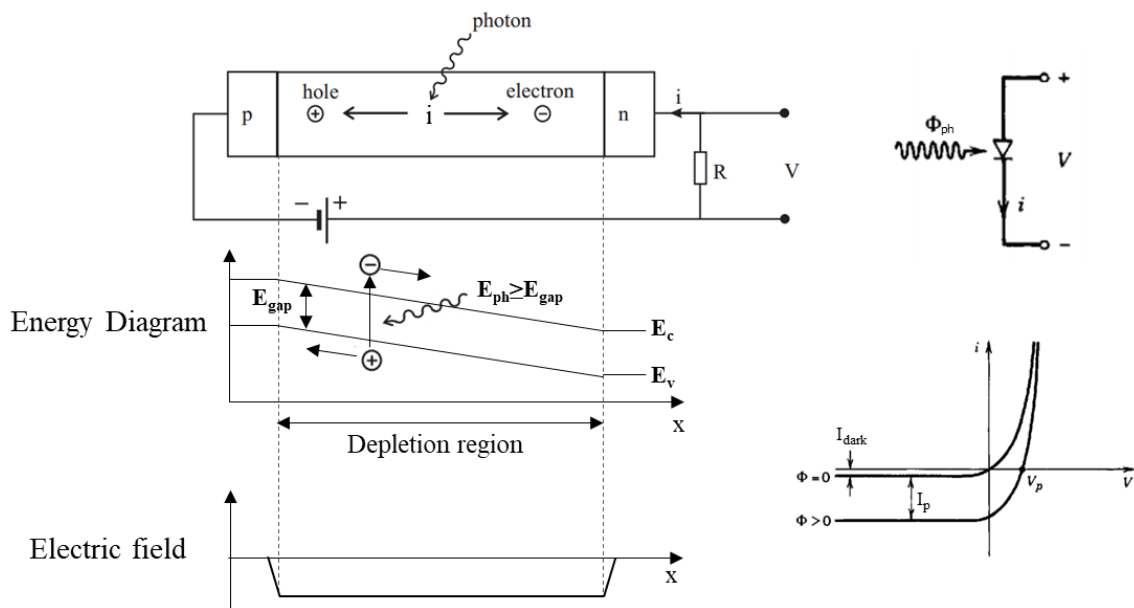


Figure 32. The p-i-n photodiode structure, energy-band diagram, and electric-field distribution (left). On the right, photodiode's electrical symbol and generic i - V characteristic. The device can be illuminated either perpendicularly or parallel to the junction (adapted from [72]).

PIN photodiodes are advantageous for rangefinders thanks to their fast response, with cut-off frequencies that can exceed 10GHz [19] and rise times under 10ns, to their commonness, making them the cheaper detector solution in the market, to their stability, providing a wide dynamic and linear range, and to the low power consumption (reverse bias significantly smaller than APDs and SPADs) [2]. Withal, these photodetectors do not exhibit gain, which, in one hand reflects in a smaller temperature sensitivity since the detection noise does not undergo amplification but, on the other, in a smaller SNR and

photosensitivity comparing with APDs and SPADs, restricting the measurements to short-to-mid ranges. Table 7 summarizes and compares the three referred solid-state photodetectors.

Table 5. Comparison between APDs, SPADs and PIN photodiodes in several key parameters (adapted from [80]).

Detector Parameter	SPAD	APD	PIN photodiode
Range	Long	Long	Short-to-Mid
Accuracy	High	High	High
Operation voltage (typ.)	>100V	Up to 100V	Few dozen Volts (around 20V-30V)
Gain	10^5 to 10^6	<100 (typical)	1
Response time	Medium	Fast	Fast
Ambient light immunity	Medium	Medium	High
Temperature sensitivity	High	High	Low
Integration in array	Suitable	Suitable	Suitable

2.5.5. Detectors Array

An individual photodetector registers the photon flux striking it as a function of time. Whatsoever, in solid-state LiDARs linear arrays or 2D arrays of individual detectors are required to measure the returned signals from several directions, alike the lens-set of a photographic camera (Figure 33a). In this context, the image is generated on the focal plane of the detecting optical system and the photodetector array can also be referred as Focal-plane Array (FPA) [72].

Modern microelectronics technology, namely CMOS, allows the fabrication and integration of large numbers of similar photodetecting elements (pixels) into a single device. These uniform light-sensitive elements are disposed in a single matrixial package at an equal spacing (pitch). Each pixel can be made of PIN photodiodes, APDs or SPADs, and has its own readout and timing circuitry that reads, amplifies and processes the measured signal to convert it into a ToF measurement. By these means, each frame is generated by assembling the results provided by each segment. Naturally, as several detectors and timing circuitries are employed, the complexity associated with this receivers' type is usually appreciable.

The most important parameter that describes a photodetector array is designated the fill-factor and describes the ratio of light sensitive area versus the total area of a single pixel, since a part of its area is occupied by the timing circuitry and only the light sensitive part might contribute to the current signal. The larger the fill-factor, the larger the light sensitive area and, thus, the larger the resulting signal. In case the fill factor is too small, the performance can be improved by adding microlenses to each pixel to focus the light into the sensitive area. [81]

A major issue when considering optical detectors arrays for these sensors is the optical cross-talk between pixels. This can occur due to spontaneous recombination with photon emission of some carriers

after light absorption. The secondarily emitted photons can be detected by adjacent detectors, corrupting the data acquired. The cross-talk intensity increases by reducing the distance between pixels, setting a limit to the array density.

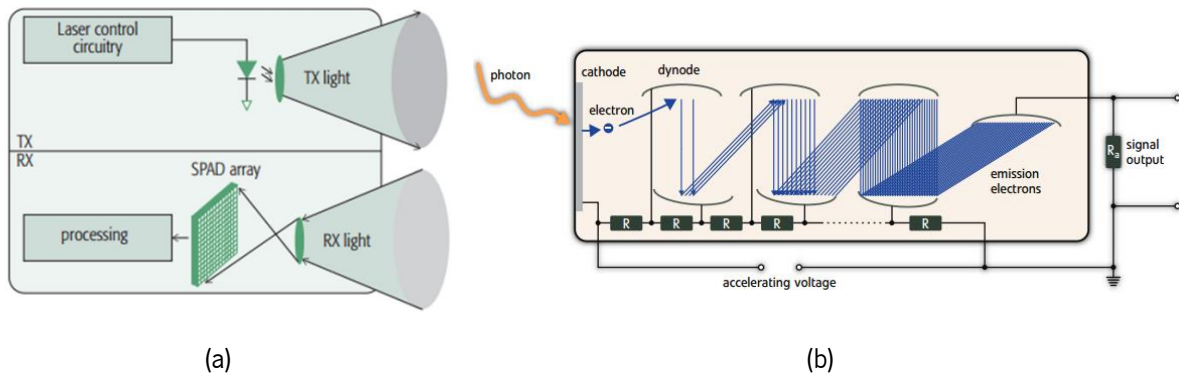


Figure 33. Detection with (a) an SPAD FPA [37] and schematic illustration of a PMT [79].

2.5.6. Photomultiplier Tubes

Besides the previous solid-state detectors, Photomultiplier Tubes (PMTs) are also a possible solution. A PMT (Figure 33b) is a vacuum tube consisting of an input window, a photocathode, electron multipliers (dynodes) and an anode. When the light passes through the input window, it strikes the photocathode, a photoemissive material, emitting free electrons into vacuum through the external photoelectric effect (while in internal photoelectric effect the carriers remain within the semiconductor, in this process the electrons are completely removed from the material). The generated photons are then accelerated via an applied electric field and focused onto the first dynode (electrode) where they are multiplied by means of secondary electron emission. This secondary emission is repeated through several dynodes at increasing electric potentials until the generated electrons reach the anode to be collected to an external circuitry. This results in a current proportional to the photon flux with an amplification as high as 10^8 [72]. The pressure inside the tube must be kept low to minimize the collisions between the generated electrons and other particles.

PMTs can be used to detect and count individual photons while offering a large dynamic range. However, they are bulky and expensive, and require high-voltage supplies (1 to 3 kV [79]) compared to small-sized and low-cost solid-state detectors, making them unlikely for automotive LiDAR. [48]

2.6. Conditioning and Processing

Posterior to light detection, and since the Integrated Circuits (ICs) used in subsequent stages only accept voltages as input, the low-level signal must be translated into a usable and acceptable voltage to be analyzed and processed in the readout circuitry. This way, the first stage of the receiver is a Transimpedance Amplifier (TIA), whose most straightforward implementation is depicted in Figure 34. This amplifier quickly converts the detected current pulse, I_p , into a proportional voltage pulse, V_{out} :

$$V_{out} = -R_F \cdot I_p \quad (2.32)$$

where R_F is the feedback resistor that sets the gain and the minus indicates an inversion in the signal. To prevent oscillations in the output due to the detector's capacitance and stabilize the system, a compensation capacitor, C_F , must be mounted in parallel with the resistor. This capacitor must be warily dimensioned since if it is too small, oscillations still occur, but if its capacitance is too large, it will reduce the usable bandwidth.

A simple structure as this is recommended for current-to-voltage amplifiers in a LiDAR receiver because the bandwidth shall be wide and the delay small. Usually one amplifier is enough but, in some occasions where the bandwidth is a critical requirement, the best approach is to opt for a moderate transimpedance gain stage followed by a broadband voltage gain stage, because the bandwidth is inversely proportional to the gain set by the resistor.

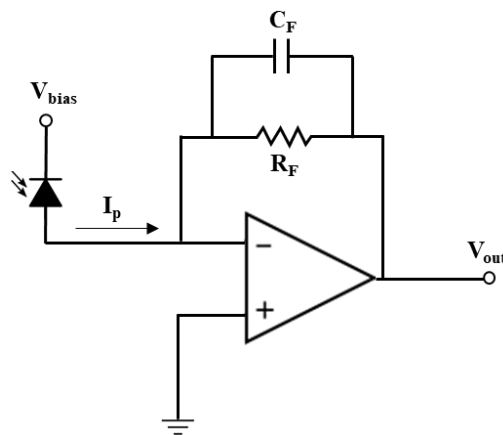


Figure 34. Transimpedance Amplifier.

Inherent to the amplification process, there is always noise addition. In most cases, the dominant source of noise in a transimpedance amplifier is the feedback resistor that produces thermal noise. The rms amplitude is calculated as [49]:

$$v_{noise,or} = \sqrt{4k_B \cdot T \cdot R_F \cdot B_{TIA}} \quad (2.33)$$

where B_{TIA} is the amplifier's bandwidth. This value of noise adds up to the detector noise and contributes to the limitation on the minimum discernible signal. For an improved noise performance, a high feedback resistance shall be used, with a drawback of decreasing the bandwidth as aforementioned. Therefore, the feedback resistance and, thus, the sensitivity are limited by the required operating frequency.

The following stages of the receiver depend on the technique used to sample the returned signal and obtain the direct ToF. At this point, two preminent timing options arise. The first one is to use a Time-to-Digital Converter (TDC) while the second is to apply Analog-to-Digital Converters (ADC). A possible block diagram for the global LiDAR system with both approaches is exposed in Figure 35 and Figure 36.

Regarding the TDC, this is a device that operates like a high-speed, high-accuracy and high-stability stopwatch directly counting the time elapsed between START and STOP events. The control unit establishes the instants where each measurement must be started, usually coinciding with the transmission of a digital pulse to the laser driver. After the return pulse is photodetected and

transamplified, it is inputted at a timing discriminator block that converts the measured pulse into an output digital pulse. This signal triggers the STOP event that indicates the end of this measurement. The time interval between START and STOP is digitally recorded by the TDC and corresponds to the ToF. The result is transferred to the control unit to be converted into distance and addressed to the scanning angle, completing a point measurement. One can intuitively perceive that it is extremely important to use a high-speed photodetector and amplifier. Because both stages precede the TDC, the response time of both adds up to the measured ToF, influencing the measured range.

TDCs can be a timer in a microcontroller unit (MCU), dedicated logic on a field-programmable gate array (FPGA) or, more simply, a dedicated IC [82]. Since the light speed is very high, small amounts of time equate to substantial distances. The range estimation performance is therefore directly proportional to the ability of the system to measure small amounts of time. To achieve high-accuracies inferior to 10cm, the TDC must provide a resolution in the sub-nanosecond order. When the TDC is implemented directly in the control unit, time resolutions are limited by the core/processor speed. These speeds are ordinarily inferior to 500MHz (CPU clock frequency), reflecting a time resolution superior to 2ns, manifestly insufficient for automotive LiDARs. Consequently, the best and most common solution are TDC ICs.

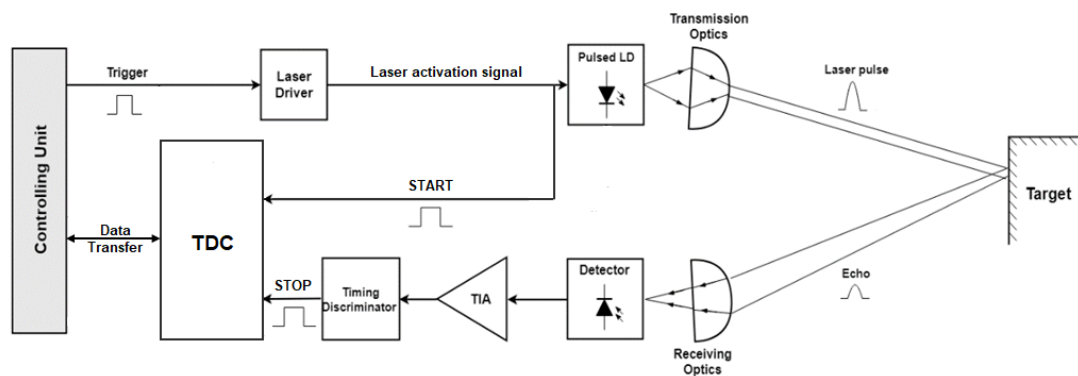


Figure 35. Architecture of a LiDAR with timing performed using a TDC.

In ADC-based architectures, the sending procedure is the same. Nonetheless, while in TDC-sampling the detected signal is only required to generate a digital signal indicating whether an echo was received, in ADC-sampling the pulse shape and analog level are relevant. Therefore, as post-amplifying stage is implemented to raise the signal to levels easily distinguished by the ADC. Posteriorly, a Low-pass filter (LPF) to remove high-frequency noise from the analog signal and to guarantee that the Nyquist-Shannon sampling theorem (sampling frequency must be at least the double of the highest frequency component of the analog signal) is verified, hereby, preventing aliasing. The resulting analog signal is then converted to a bits' sequence representing its magnitude at each sampling instant, and the digital image of the pulse is transmitted to the control unit.

In this architecture, the timing is performed via software, based on the digital reconstruction of the received signal. However, to estimate the ToF, it is also required a digital image of the signal transmitted to the target. To fulfill this, a reference photodetector is mounted on the transmitter, next to the laser, to detect the instant when the pulse is sent. This detector is connected to a readout circuitry like the abovementioned. By this means, and by synchronizing both ADCs using the same clock (CLK) signal,

whose frequency sets the sampling rate, each ADC measures the emitted or the return signal at regular time intervals.

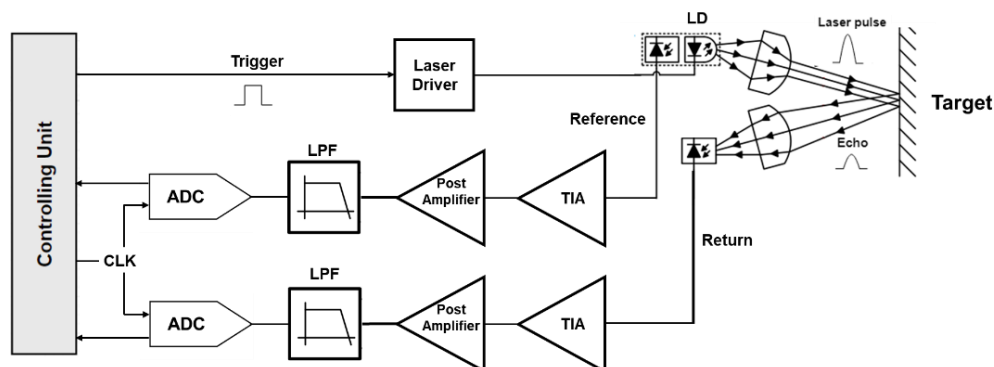


Figure 36. Architecture of a LiDAR with timing performed using ADCs.

ADCs are a frequent hardware component of microcontrollers but, similarly to TDCs, are often implemented as separate integrated circuits, justified by the larger freedom of choice in terms of key-parameters. The critical ADC parameters are the resolution and the sampling rate. The first is normally specified as the number of bits an ADC handles and determines the number of distinct output sequences the converter can produce, in other words, the minimum input voltage the device can resolve. The sampling rate is the number of analog points sampled per second and is also referred to as the ADC speed. As the optical pulses' width is in the nanosecond order and to be able to reconstruct them reliably, several points must be sampled in this time interval and high-speeds are required.

The main advantage of ADC-based LiDARs when comparing with TDC-sampling is the higher accuracy in the ToF measurements due to two factors. Firstly, the detector's and amplifiers' response time is removed from the equation since both the reference and the return signals are sampled in an identical circuit. Secondly, and more relevant, while in TDC-sampling the timing is done via hardware, in ADC-sampling the ToF estimation is performed digitally in the control unit, allowing a better control over the timing instants. In this situation, the accuracy is mainly set by the converter's resolution and sampling rate, and the noise, which is also sampled but can be mitigated through digital filtering. As downsides, the complexity of the circuitry and computational processing, as well as the price of context-proper ADC ICs, are extensively superior. TDC-sampling allows simpler and straightforward architectures, with lower costs.

The control unit is the most vital component, acting as the system's "brain". It is responsible for configuring and controlling the ICs, triggering the laser emitter, which includes setting both the pulse width and PRR, and registering the ToF from each point, addressed to the scanning angle. Besides, it also serves as an interface to external units connected to LiDAR.

The two preeminent options for this unit are FPGAs and MCUs. FPGAs are integrated circuits designed to be configured after manufacturing (hence "field-programmable"). They contain an array of configurable logic blocks and a hierarchy of reconfigurable interconnects that allow to program how the blocks are inter-connected using hardware description languages like VHDL or Verilog. Furthermore, I/O pads are also integrated. Each logic cell, which include memory elements, consist of logic components such as multiplexers, flip-flops, lookup tables and adders, and can be configured to perform complex

digital computations or merely simple logic operations. FPGAs are especially useful when there is an immense amount of data to process in parallel, for e.g., in multi-beam macro-scanners.

A microcontroller is an IC containing one or more dedicated microprocessor cores along with memory, timers and programmable I/O peripherals. However, the big difference to FPGAs are the fixed interconnections that cannot be configured. MCUs are based on software programming to execute a pre-defined instruction set and, for this reason, are easier to use since there are compilers that can convert the high-level (C, C++, Java) or Assembly code into machine code for the microprocessor to use. After the software is written, it is loaded into the microcontroller's Flash memory and stored until it is erased or replaced. Table 6 schematizes the up and downsides of MCUs and FPGAs.

Table 6. Comparison between MCUs and FPGAs in some relevant aspects.

MCU	FPGA
<ul style="list-style-type: none"> ✓ Easier to program (high-level or assembly software programming) ✓ Low cost due to large offer and mass production ✓ Available units with low power consumption ✓ All necessary support components embedded 	<ul style="list-style-type: none"> ✗ Complex and time-consuming programming (hardware programming) ✗ Higher costs, consequence of lower demand ✗ High power consumption ✗ Requires external peripherals
<ul style="list-style-type: none"> ✗ Fixed circuitry and instruction set creates some restrictions ✗ Sequential execution (microprocessor handles every instruction) → time-limited (execution dependent of the processor cycling power) 	<ul style="list-style-type: none"> ✓ High flexibility due to complete programmability ✓ Instructions are processed concurrently, enabling massive parallelism and lower latencies → space-limited (more work requires more logic blocks)

2.7. Hardware Timing Discriminator

As in any measurement system, accuracy is a crucial parameter since it indicates the total uncertainty in the obtained value. In automotive ToF LiDARs, the accuracy with which range information can be determined depends on the system capability to precisely attain the echo arrival time. The timing accuracy meaningfully depends on both the photodetector properties, such as the response time, and the electronics employed to detect the signal [83]. In a measurement range from 1.5m to 180m, the ToF fluctuates from 10ns to 1.2 μ s. For every uncertainty of one nanosecond in the ToF estimation, there is a potential error of 15cm in the range determination.

Marking the exact arrival time of detected events with precision and consistency is the primary function of the timing discriminator. This block sets the condition the incoming pulse must verify to be considered and converts it into a logic-level STOP pulse for the TDC, with defined positions in the time scale at a defined point of the return pulse. The initial transition of the logic pulse is used to mark the arrival time of the analog pulse [83]. Another task for the timing discriminator is to separate the timing pulses from noise.

The timing event can be generated either from the edge of the pulse which is allowed to saturate in the receiver channel, or by linear signal processing, in which gain control structures are usually needed, due to the wide dynamics of the input signal and the limited dynamic range of the receiver [48].

2.8. Optics

The optical system plays a huge part in the definition of the sensor's performance. In automotive LiDARs, due to the high optical powers involved, the transmitter-end is optically isolated from the receiver by using separate apertures (differentiated in Figure 8), in a configuration called bistatic LiDAR. This way, the high-power radiation backscattered at the output lens does not reach the photodetector, preventing blindness or even damages to the latter. The basic and main optical components used are collimating lens at the transmitter, focusing lens at the receiver and optical filters. Supplementary, secondary components can be utilized, for example, to shape the beam as desired.

2.8.1. Collimating Lens

The beam originally emitted by the laser is not perfectly collimated and it diverges with an angle dependent on the chip morphology and the cavity structure. Most of the times, the outputted beam is not very useful in LiDAR technology since the interest is to perform quasi-punctual measures, with narrow laser footprints to maximize accuracy, resolution and power delivery. To address this problem, the beam must be collimated using adequate lenses.

The collimation process takes the fan of light rays from the laser and straightens them out into a narrow beam with small divergence (Figure 37a). To numerically evaluate and optimize the system, a parameter designated spot diameter (or spot size) is consistently used. This parameter evaluates the transversal laser footprint as a function of the distance to the source. Because the laser has an emitter with a finite aperture size (not a perfect point source), some residual divergence remains after collimation. This way, the beam will inevitably continue to diverge and increase in spot size, yet at a much lower rate. The emerging beam divergence and spot size immediately after collimation shall be balanced through proper selection of the focal length.

2.8.2. Focusing Lens

On receiver side, the light returning from the target must be focused into the detector's photosensitive area to maximize the transduced signal, regardless of the angle. This is the inverse process of collimation since the rays are converged into a small area (Figure 37b). The light-collecting capability is determined by the focusing lens' diameter, D_{lens} , while the FOV is set by its focal length. If the lens' front profile is circular, the area is given by:

$$A_{lens} = \pi \left(\frac{D_{lens}}{2} \right)^2 \quad (2.34)$$

The greater the lens area, the greater the captured light, both wanted and unwanted. Hereby, to maximize the SNR at the receiver of a single point LiDAR, the focal length must be chosen to match the collimated beam divergence and the lens size ought to balance effective light versus background noise collection.

As the focusing and collimation processes are inverse, the same lenses' morphologies can be employed to both, differing only in the light propagation sense across the lens. In either case, the optical element must be placed, respectively, at a distance from the photodetector and laser aperture equal to its focal length, f , measured along the optical axis. A positive lens must be applied otherwise it will lead to beam divergence. These lenses have positive focal lengths and are thicker at the center, on the optical axis, and thinner toward the outer portions.

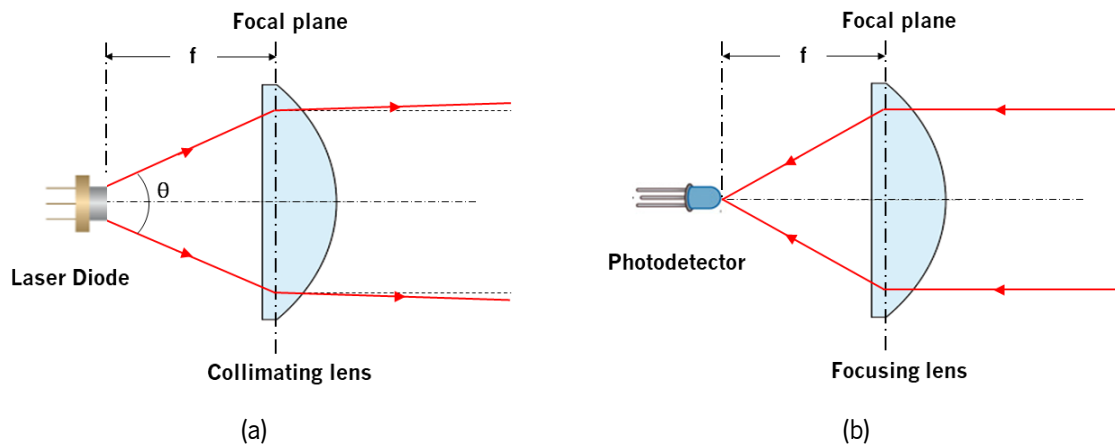


Figure 37. Light (a) collimation and (b) focusing processes.

In solid-state LiDAR, the conditions are different. While in macro-scanners a single detector is needed per laser source, in solid-state LiDARs the beam direction must also be recorded. The interest stops being to focus the echo in any region of the photosensitive area, as explained formerly, but to focus the light beams with different angles of incidence into different pixels of the FPA. This way, it is possible to associate each pixel with a segment of the scene (Figure 38).

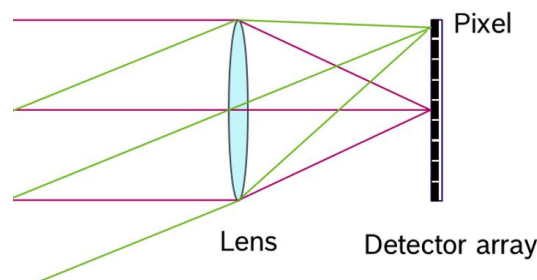


Figure 38. Representation of a lens used to focus the incoming light from different angles in different pixels of a FPA.

2.8.3. Beam-shaping

In most situations, the laser beam has an elliptical cross-sectional profile with a faster diverging-axis, i.e., with different horizontal and vertical divergence angle. Usually, a circular cross-section is more

desirable than the elliptically-shaped beam transmitted across the collimating lenses. To perform this conversion, additional components must be added, such as an anamorphic prisms pair (Figure 39a). Through this, the collimated beam is circularized by expanding it in the slow axis of the ellipsis. After propagation across them, a minor lateral beam displacement occurs. The advantage of using anamorphic prisms is that this setup is easily found on the market already mounted and properly aligned at reasonable prices. Alternatively, other solutions can be employed, as for example, a pair of perpendicular cylindrical lenses.

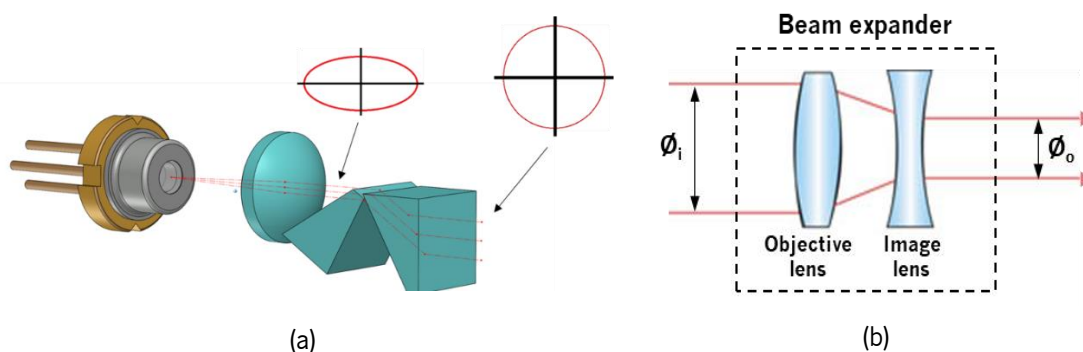


Figure 39. Beam-shaping: (a) a pair of anamorphic prisms placed after a collimating lens to circularize the cross-sectional profile (adapted from [84]) and (b) beam-expander to shrink or expand the beam diameter.

In some occasions, due to physical constraints of the previous beam-shaping systems and spot size requirements (e.g. in micromirrors), additional modules are required to decrease the beam diameter. The most remarkable solution is a beam expander and, depending on its configuration, it can be used for either expanding or shrinking the beam. Several configurations can be adopted, regularly composed by a convex-concave lens pair (Figure 39b). The beam-expander is characterized by a magnifying factor, M , given by the modulus of the ratio between the focal lengths of the objective, $f_{objective}$, and image, f_{image} , lenses. This parameter also expresses the relation between the output and input beam divergences and diameters:

$$M = \left| \frac{f_{objective}}{f_{image}} \right| = \frac{\phi_o}{\phi_i} = \frac{\alpha_i}{\alpha_o} \quad (2.35)$$

where ϕ_i and ϕ_o , α_i and α_o are, respectively, the input and output beam diameters and divergences. The price to pay for a smaller beam spot is a larger divergence angle: for $M < 1$, the divergence of the output beam is increased by a factor $1/M > 1$.

2.8.4. Optical Filters

A huge challenge faced in the development of a LiDAR system for outdoor applications, like autonomous driving, is the glare caused by the background ambient light that corrupts the measurements and helps in setting the lower bound for the minimum discernible effective signal. During the day and depending on the atmospheric conditions, the intensity of the solar radiation may vary by several orders of magnitude.

The noisy photocurrent induced by the background light is particularly critical when detecting low-level signals with APDs and SPADs due to the amplification mechanism. Besides, one must consider that the detector is sensitive to a broad range of wavelengths (above 100nm FWHM) that add-up to the background noise.

To minimize the effect of the light component caused by solar radiation and increase the SNR, optical filters are applied on the glass cover to selectively transfer spectrum band where the laser wavelength is included to the detector and to reject further radiation. This is the reason why, if one analyzes the glass cover of the automotive LiDAR state-of-the-art, it is noticeable that it is not transparent to visible light. Ideally, this filter shall be bandpass to eliminate spurious wavelengths (highly-reflective, HR) either above or below the interest. A not-so-good alternative but still viable is using high-pass filters, since LiDAR uses NIR light and most of the solar irradiance is concentrated in the visible spectrum. Background noise on the same wavelength will still be detected and cannot be dissociated from the effective signal.

Another mechanism to improve the device's optical performance is to coat the transmitting and receiving lenses with anti-reflective (AR) coatings tuned for the laser wavelength. This way the power transmitted to the target and the light-collecting capability of the receiver are maximized.

The physical principle behind optical filtering is the enhancement or reduction in the reflectance of an optical element through, respectively, multi-path constructive or destructive interference between light partially reflected and transmitted within thin film coatings.

As the laser peak wavelength shifts with the temperature, one challenge when developing a suitable narrow bandpass filter (BPF) is the dynamic adjustment of its central wavelength to the shift. This is extremely important because the receiver must maintain its performance in every situation within the specified temperature ratings. In case the filter is not tuned to the laser and to the incident angle, a significant decrease in the received power will affect the range limitations.

2.9. LiDAR Equation

In principle, the maximum detectable distance depends on several parameters: laser transmitted power, beam divergence and optics employed, characteristics of the transmission medium (atmospheric conditions), target characteristics (reflectivity, dispersion and size) and the sensitivity of the detector. Some of them are hardware-related and can be modified during design process and others are imposed by local time-dependent environmental conditions, which cannot be controlled in any way [76]. These dependences can be combined into the so-called LiDAR equation that estimates the peak power of the signal returning to the photodetector, P_s [76]:

$$P_s(d) = P_{peak} \cdot \eta_{atm}^2 \cdot \frac{A_{lens}}{\pi d^2} \rho_T \cdot \cos \theta_i \quad (2.36)$$

This equation estimates the laser power returning to the receiver as a non-linear function of the distance to the target, d , the atmospheric transmission efficiency, η_{atm} , the laser pulse peak power, P_{peak} , the receiving lens area, A_{lens} , the target's reflectivity, ρ_T , and the incidence angle, θ_i . The optical peak power is then converted into a current pulse with a peak proportional to its responsivity:

$$I_p = \mathcal{R}P_s \quad (2.37)$$

The presented expression is a simplified result valid under several assumptions. Firstly, the laser peak power is efficiently outputted at the system, with no losses between the emitter and the output lens. Secondly, the atmospheric transmission efficiency, a parameter estimating the portion of light that avoids scattering and absorption by gaseous elements and aerosols, is estimated by Beer's law [76]:

$$\eta_{att} = e^{-\gamma \cdot d} \quad (2.38)$$

with an atmospheric extinction factor, γ , considered constant through all roundtrip. In fact, this is an extremely complex coefficient that depends on several parameters such as the wavelength and air density and composition. Followingly, the reflection is diffuse and is roughly modulated by the Lambertian model. In this model, the backscattered power has a cosine dependency on the incident angle (maximum for normal incidence, as seen in Figure 40, and is uniformly dispersed over a solid-angle of π steradians. Finally, the entire laser spot is reflected on the same surface, the detector's FOV matches the beam divergence angle and all the light collected by the receiver's lens is focused on the photosensitive area.

When the target's surface area is smaller than the laser's footprint, only a portion of the laser peak power can be potentially reflected, while the other is lost. In this case the analysis is far more complex and is outside the scope of this project.

Although the equation does not indicate any explicit wavelength dependency, environmental factors as the background noise, the atmospheric extinction coefficient and the target reflectivity (through the refractive index), all depend on the optical frequency. For this reason, the LiDAR equation has an implicit wavelength dependency. Furthermore, the deduced equation takes only into consideration the resulting signal induced by the LiDAR laser source, assumed nearly monochromatic. Nonetheless, in practice the effect of noisy background illumination on the employed central wavelength must be added. For the effective signal to be differentiated from the background noise, the return power level must surpass the threshold imposed by the latter. [76]

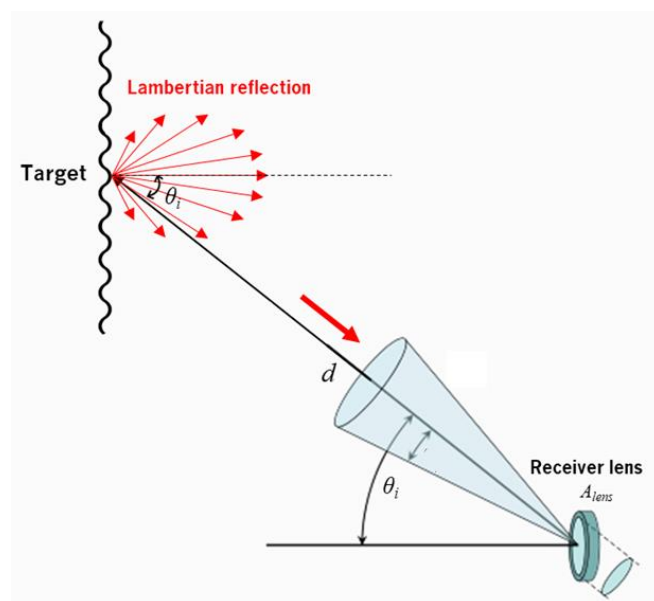


Figure 40. Lambertian reflection profile and receiver's solid angle.

3

STATE-OF-THE-ART

In this chapter, several existing and proposed solutions for laser detection and ranging are surveyed, examined and compared, aiming to understand and assimilate common characteristics and typical specifications and to give an insight on the current panorama. Moreover, this analysis seeks to verify if the state-of-the-art for automotive LiDAR sensors fulfills the requirements for highly autonomous driving levels (4 and 5) established previously, to address the points that need to be rectified among them and to evaluate the market tendencies regarding the technology.

In a first stage, a brief market analysis is performed, culminating in the identification of the main manufacturers for the automotive industry. Subsequently, and based on the information directly provided by these companies, the more relevant products are presented and separately studied in terms of technological implementation and performance metrics. Later, a comparative evaluation is executed, and the fundamental conclusions are stated on whether the sensors are appropriate or not for the context. Lastly, innovative solutions emerging in this market and new concepts proposed in the literature are studied.

One must have in consideration that this research was performed by May 2018 and, as the market is continuously evolving, new products are constantly being introduced as well as improvements in the existing ones.

3.1. Automotive LiDAR Solutions

Most of the automotive LiDAR sensors market is located in the North American Continent, with countries like the United States and Canada playing the main role, and in Europe, namely in Germany and United Kingdom [85]. Moreover, nations like India, China and Japan are continuously blooming in this sector, being expected a prosperous contribution to the segment growth in the Asia Pacific region. The key industry participants include *Velodyne*, *Quanergy Systems*, *Innoviz*, *LeddarTech*, *Valeo* and *Continental AG*, which already commercialize LiDAR sensors [86]. Besides these manufacturers, several

others preeminent companies, like *Luminar*, are yielding meaningful progresses. The geographical distribution of the major automotive LiDAR competitors can be seen in Figure 41.

In April 2018, *Woodside Capital Partners (WCP)* and *Yole Développement* published a very insightful automotive market report detailing the active and dominant players in the LiDAR segment. This study not only specifies the geographical presence and a technological overview of the current solutions, but it also recognizes the main OEMs and manufacturers of the individual components, such as photodetectors, ICs, laser sources and optical elements. [87]



Figure 41. Geographical dispersion of the main presences in the automotive LiDAR market by April 2018 [87].

Following this research, and in between the identified manufacturers, a selection of the products with potential for autonomous driving was carried out and the result is reviewed herein. The main excluding criteria comprised: maximum range, FOV, tridimensionality, frame rate and form factor. An effort was made to cover all the implementations and technologies stated in the theoretical background.

3.1.1. Velodyne

When one refers to LiDAR sensors for automated driving assistance systems, *Velodyne LiDAR* can be easily highlighted as one of the pioneers and main competitors in this sector, since 2005. This company, settled in Silicon Valley, was seminal to the current awareness of the automotive industry on LiDAR technology and their products are still a strong reference any candidate must be gauged against with. [34]

Velodyne has set a canonical patented rotating scanning mechanism (US7969558B2, US8767190B2, US20100020306A1) in which the housing is rotated through a rotary motor to cover a complete 360° HFOV, while the vertical FOV is covered by several discrete and fixed laser-detector channels vertically aligned with co-linear directions [34]. By using several channels, each vertical slice is acquired at once for each angle of the rotating head, resulting in high frame rates and point densities. Each pixel is measured through a single laser pulse and, to overcome losses associated with bad weather conditions, two measuring modes are available. In single mode, the strongest (default) or the last return

is reported while in dual mode, both returns are recorded (beneficial when the same pulse is reflected at different points) [88].

The detection in each channel is performed via an APD and, posterior to amplification, the signal is digitalized via a high-speed ADC. The ToF is then extracted using digital signal processing algorithms. The laser and APD are precisely aligned to provide maximum sensitivity while minimizing the signal crosstalk. Moreover, the sensors are equipped with a glass cover coated with optical filters and a rotary encoder is integrated to convert the rotation angle into a digital signal, which is then addressed to each measurement point, to precisely position each measure in the real-time point cloud. The system is also incorporated with automatic power control to vary the amplitude of the laser based on the return signal strength and, thus, decrease the heating inside the unit, keep the detectors out of saturation and raise the power in the signal when it is close to the noise floor. [41]





The products developed and, some of them, already made commercial, are divided in two families: *Puck* and *HDL* (acronym for High-Definition LiDAR). The former is characterized by smaller and more compact designs, making it suitable for applications where miniaturization mandatory [89]. The second family of sensors was designed to satisfy the demands of autonomous vehicle navigation, providing extremely accurate and dense point clouds [90]. The most relevant technical information on the current products is exposed in Table 7. It is noteworthy that *HDL-64E* was the first developed product, in 2005, although posteriorly, several improvements were applied.

By looking at the specs, all devices provide adequate FOV, accuracies and frame rates required for highly autonomous vehicles. In terms of angular resolution, the *HDL64E* and *VLP-32C* are, by far, superior and, hereby, generate higher density point clouds. The vertical resolution of the remaining products is insufficient for the context since there is a possibility of missing some relevant objects altogether. Notwithstanding, both *HDL* devices and the *VLP-16* lack in the maximum attainable range, which limits its application to ADAS. Moreover, *HDL-64E*'s form factor reflects in greater driving powers and may restrain its direct integration in the vehicle's structure (rooftop). All the other models are sufficiently miniaturized to be integrated directly in the vehicle's structure.

Velodyne's products, particularly the *HDL* models, share the most common obstacles for the technological development in the field of self-driving vehicles, the high costs. Since each channel has a dedicated transmitter and APD detector, the price of this devices sums up to several thousand dollars. The *VLP-16* is, currently, the most economical model, mainly due to the reduced number of channels. These prices make it unfeasible for large-scale integration in vehicles. Though, *Velodyne*'s has been putting efforts in price reduction and, including, the prices are expected to drop with mass-production.

Besides the previously presented products, *Velodyne* has been developing two new products expected to be launched still in 2018. The first is the *VLS-128* model (Figure 42a), also a mechanical macro-scanner, with 128 laser beams for improved resolution. This device is specifically made for high-level autonomous driving and advanced vehicle safety at highway speeds where fast decision-making is essential. It provides 360° HFOV and 40° VFOV, down to 0.11° horizontal and 0.3° vertical angular resolution, a range up to 300m and a data rate achieving 9.6M px/sec [91]. Comparing with the predecessor *HDL-64*, the *VLS-128* is 70% more compact and supplies point clouds with four times the resolution (and, thus point density), allowing it to see objects more clearly (Figure 42c).

Table 7. Technical specifications of *Velodyne's* LiDAR systems. For the fields marked with (-), no information from the manufacturer is available.

Model					
	HDL-64E S3	HDL-32E	Puck VLP-16	VLP-32C (Ultra Puck)	
References	[41] [90] [92]	[92] [93]	[88] [92] [94]	[95] [96]	
Overall	Class	3D Macro-scanner (patented mechanical rotating head)			
	#Lasers / #Detectors	64 / 64	32 / 32	16 / 16	32 / 32
	Max. Range (Reflectivity)	40 m (10%) 120 m (80%)	100 m	100 m	200 m
	Range Accuracy	± 2 cm (typical)	± 2 cm (typical)	± 3 cm (typical)	± 3 cm (typical)
	Data per point	ToF distance measurement Intensity Angle	ToF distance measurement Calibrated Reflectivity Angle	ToF distance measurement Calibrated Reflectivity Angle	ToF distance measurement Calibrated Reflectivity Angle
	Data Acquisition Rate (Sampling Rate)	1.3M px/sec (Single Return) 2.2M px/sec (Dual Return)	695k px/sec (Single Return) 1.39M /sec (Dual Return)	300k px/sec (Single Return) 600k px/sec (Double Return)	600k px/sec (Single Return) 1.2M px/sec (Double Return)
	FOV (H×V)	360° × 26.9° (+2° to -24.9°)	360° × 41.33° (+10.57° to -30.67°)	360° × 30° (-15° to +15°)	360° × 40° (-25° to +15°)
	Scanning/Frame Rate	5 - 20 Hz (300 - 1200 rpm)			
	Angular Resolution (H×V)	0.08° × 0.4° @ 5Hz 0.17° × 0.4° @ 10Hz 0.35° × 0.4° @ 20Hz	0.1° × 1.33° @ 5Hz 0.4° × 1.33° @ 20Hz	0.1° × 2.0° @ 5 Hz 0.2° × 2.0° @ 10 Hz 0.4° × 2.0° @ 20 Hz	0.1° × 0.33° @ 5 Hz 0.4° × 0.33° @ 20 Hz

Laser	Operation mode	Pulsed			
	Laser Class / Wavelength	Class 1 eye-safe per IEC 60825-1:2014 / 903nm			
	Power / Pulse width / PRR	60 W / 5ns / ≈20kHz	- / - / ≈21kHz	- / 6ns / ≈21kHz	- / - / ≈18kHz
	Beam divergence (H×V)	-	0.18° x 0.07°	0.18° x 0.07°	-
Mechanical and Electrical	Input Voltage / Power Consumption	12-32 VDC / 60 W	9-18 VDC / 12 W	9-18 VDC / 8 W	10.5-18 VDC / 10 W
	Enclosure Rating	IP67			
	Operating Temp.	-10°C ... +60°C	-10°C ... +60°C	-10°C ... +60°C	-20°C ... +60°C
	Storage Temp.	-40°C ... +85°C	-40°C ... +105°C	-40°C ... +105°C	-40°C ... +85°C
	Interfaces	100 Mbps Ethernet RS-232 (Serial)			
	Weight	12.7 kg (w/o cabling)	1.0 kg (+0.3kg for cabling)	830 g (w/o cabling)	925 g (w/o cabling)
	Size	Ø215mm × 282mm	Ø85mm × 144mm	Ø103mm × 72mm	Ø100mm × 87mm
Estimated Price (March 2018)	\$75 000	\$29 900	\$4 000	-	

The second product, the *Velarray* (Figure 42b), has started to be developed with the ambition to deliver a low-cost product (target price in the hundreds of dollars, when produced in mass volumes), compatible with the integration and industrialization in common vehicles, yet with the high-performance required for the context. In terms of technology, it comes completely out-of-the-box comparing with all the other devices. Instead of a multi-beam rotating head, the *Velarray* is a fixed-beam solid-state LiDAR with a miniaturized form factor ($125\text{mm} \times 50\text{mm} \times 55\text{mm}$) to be seamlessly embedded into the front, side and corners of vehicles. It provides 120° HFOV and 35° VFOV, with a 200 meter range even for low-reflectivity objects [97]. In addition, this product also accommodates all the already referred advantages of solid-state sensing.

While it is likely for both devices to first show up enabling ADAS such as adaptive cruise control, they also gather the range, resolution and accuracy requirements critical to ensure safe operation in Level 4 and Level 5 autonomous vehicles.

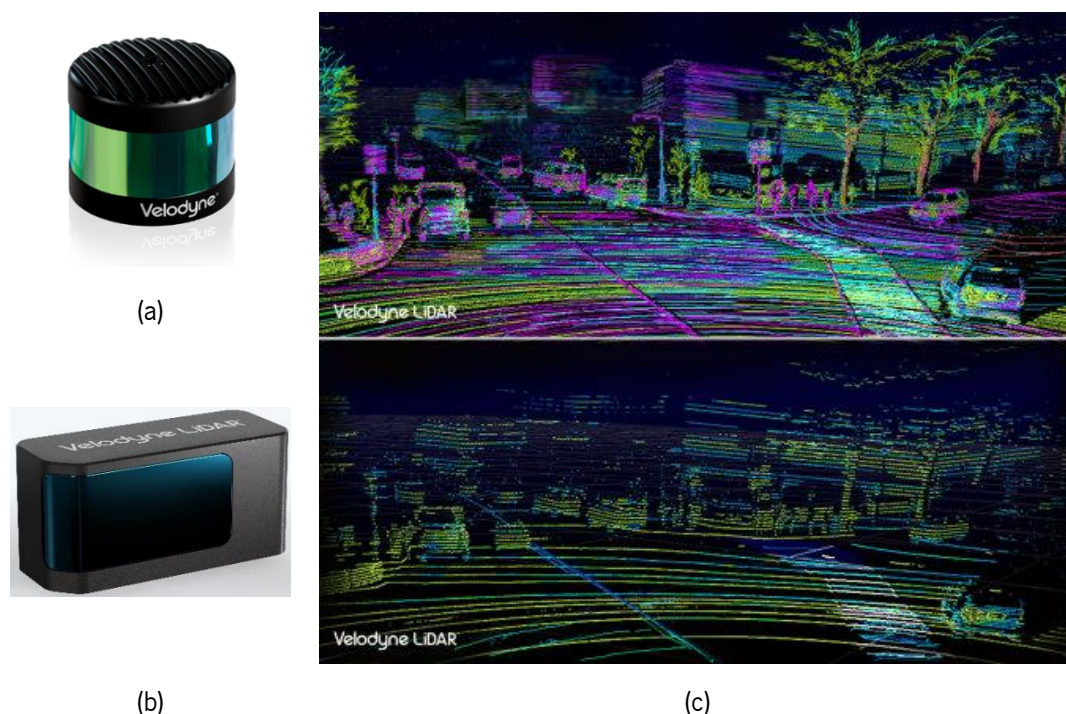


Figure 42. *Velodyne's* new products: (a) *VLS-128* and (b) *Velarray*. In (c), a comparison of a frame segment obtained with *VLS-128* (top) and *HDL-64E* (bottom) shows the huge difference in the point cloud density and resolution [98].

3.1.2. Quanergy Systems

Founded in 2012 and headquartered in Sunnyvale, a city located in the heart of Silicon Valley, *Quanergy* is a provider of 3D ToF LiDAR sensors and perception software for real-time capture and processing. *Quanergy's* innovations, covered by 11 patents, address the needs in various markets for 3D LiDAR sensors and LiDAR-based sensing systems, including unmanned driving and ADAS [99].

At the moment, *Quanergy* counts with two distinct product generations with disparate technologies. The first generation, *Gen 1*, encompasses the model *M8*, a mechanical scanner LiDAR. For the second

generation, *Gen 2*, a solid-state approach was taken, with the *S3* model. The relevant technical specifications for both products are exposed in Table 8, according to manufacturer's documentation.

Starting with *Quanergy's M8* LiDAR, the working principle is very alike *Velodyne*. The housing integrates 8 emitter-receiver channels fixedly disposed to cover a 20° VFOV and, through a mechanical rotary mechanism, the whole system rotates to cover a 360° HFOV. Although there is no direct information on signal processing mechanism, some documentation indicates that it is presumedly via TDCs [1]. The laser PRR is indirectly estimated at roughly 52.5kHz, knowing that a single pulse is emitted per pixel and dividing the point rate by number of lasers.

Analyzing in terms of suitability for autonomous navigation, even though the frame rate and the horizontal resolution are enough, the 150m maximum range is slightly below the requirements and the vertical resolution is considerably large and strongly affects the point cloud density, limiting the applicability. Furthermore, this product presents the same price-related issues abovementioned.

To work around the main downsides of mechanical LiDARs and in a tentative to extensively reduce manufacturing costs, *Quanergy's* LiDAR smart sensing technology has evolved into solid-state implementations with the model *S3*. Architecturally-wise, the *S3* is composed of 3 main Si CMOS ICs (Figure 43a). The first is the transmitter, which is an OPA photonic IC, conjugated with the control ASIC for beam forming and steering. The second is the receiver, an SPAD array IC with 8 layers to detect the returning light and a read-out IC with TDC circuitry to measure the pulse ToF. At last, the processing unit, is a FPGA that parallelly processes raw data to form the point cloud, and an ARM-based processor for data fusion, object recognition and classification. [1]

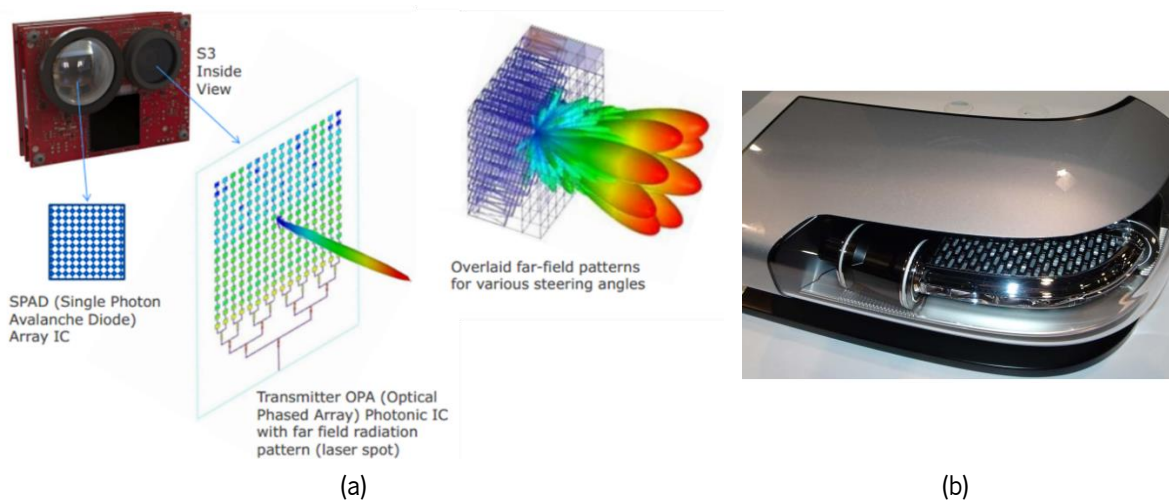




Figure 43. *Quanergy S3* LiDAR: (a) illustration of the working principle and (b) integration in automotive headlights [1].

As announced by *Quanergy*, the *S3* is expected to come out at about \$250 once full-scale manufacturing begins [100], being one of the cheapest sensors in this market. This factor, allied with small dimensions, will allow the seamless integration of several packages in the vehicle's design to cover a larger FOV. As a matter of fact, in a partnership with *Koito*, the larger global marker of automotive headlights, the first automotive headlight with built-in LiDAR sensors was developed (Figure 43b). Each

headlight, to be located on every corner, incorporates two *S3* sensors to sense forward and to the sides, and provides protection from dust, dirt and water [1].

Table 8. Specifications of *Quanergy's* first and second-generation products.

Product Name			
	M8	S3	
References	[101]	[1] [102]	
Overall	Class	3D Macro-scanner	3D Solid-State w/ OPA
	#Lasers / #Detectors	8 / 8	1 / 8
	Max. Range (Reflectivity)	1m ... 150m (80%)	5cm ... 150m (80%)
	Range Accuracy	± 3 cm (typical)	± 5 cm (typical)
	Data per point	ToF distance measurement, Intensity, Angle	
	Data Acquisition Rate (Sampling Rate)	420k px/sec (Single Return) 1.26M px/sec (Dual Return)	320k px/sec
	FOV (H×V)	360° × 20°	120° × 10°
	Frame Rate	5-20 Hz	10-25 Hz
	Angular Resolution (H×V)	0.03° × 2.5° @ 5Hz 0.20 × 2.5° @ 20Hz	0.1° × 0.8° @ 10Hz 0.5° × 0.8° @ 25Hz
Laser	Operation Mode	Pulsed	
	Laser Class / Wavelength	Class 1 eye-safe per IEC 60825-1 / 905nm	
	Beam spot size	-	< Ø5cm @100m
Mechanical and Electrical	Input Voltage / Power Consumption	24 VDC / 18 W	9-14 VDC / 12-15 W
	Enclosure Rating	IP69K	
	Operating Temperature	-20°C ... +60°C	-40°C ... +85°C
	Storage Temperature	-40°C ... +105°C	-40°C ... +105°C
	Interfaces	100 Mbps Ethernet	1 Gbps Ethernet
	Weight	900g	500g
	Size	Ø103mm × 87 mm	100mm × 60mm × 120mm (W×H×D)
Estimated Price (March 2018)	\$4 000	-	

3.1.3. Innoviz

Headquartered in Israel and founded in January 2016, *Innoviz* is a leading provider of cutting-edge LiDAR remote sensing solutions mainly directed to enable mass commercialization of autonomous vehicles. The company is backed by strategic partners and top-tier investors from which *Aptiv* and *Magna* can be highlighted. As both previous companies, *Innoviz* also counts with several patents among the automotive LiDAR sector [103].

Innoviz is currently working on *InnovizPro*, a single-laser solid-state MEMS-based scanning LiDAR. The most relevant key performance metrics regarding the applicability of this product in the concerning context are explicit below [104].



Figure 44. *InnovizPro* LiDAR [104].

Class: 3D MEMS micromirror scanning LiDAR

Optical performance:

- Maximum range of 150m @ 80% reflectivity, 130m @ 50% reflectivity and 70m @ 10% reflectivity
- 3cm range accuracy with up to 3 returns per pixel
- $73^\circ \times 20^\circ$ FOV (H×V) with respective $0.15^\circ \times 0.3^\circ$ angular resolution
- Frame rate up to 20Hz
- Class 1 905nm eye-safe laser (IEC 60825-1)

Output:

- Distance and reflectivity information per pixel
- Point rates of 711k px/sec, 1422k px/sec and 2133k px/sec for, respectively, single, dual and triple return

Mechanical, electrical and operational:

- 42W power consumption with an operating voltage from 9 to 32 VDC
- $83 \times 90 \times 175 \text{ mm}^3$ (H×W×D) and 800gr
- IP67 environmental protection
- Operating temperature from -10°C to $+50^\circ\text{C}$
- Storage temperature from -40°C to $+85^\circ\text{C}$

This sensor is designed as a stand-alone unit that can be added to existing vehicles. It primarily aims for automated driving applications and, in terms of specs, it meets almost all the requirements for high-level automation, lacking only in the maximum attainable range (plus substantial power consumption). The biggest impact of this product relies in the fact that it is currently going to mass production, enabling the industry to move towards mass commercialization at an accelerated pace.

Further, the company claims that, by 2019, a new product with the same operation principle but with improved performance will be introduced in the market, the *InnovizOne*, a seamless and easy-to-integrate automotive-grade LiDAR (Figure 45). Considering the official information on the website, this product will detect obstacles up to 250m and within a FOV of $120^\circ \times 25^\circ$. With an accuracy inferior to 3cm and an unrivaled angular resolution of $0.1^\circ \times 0.1^\circ$, the device will be able to acquire 7.5M points per

second, at a frame rate of 25Hz. As a result, the device will output highly-precise and dense real-time point clouds, enabling the provision of a superior algorithmic layer that uses deep learning to turn 3D vision into critical driving insights (recognition, classification and tracking). Moreover, the compact housing and the expected low costs, well below \$1000, will open new horizons for the integration of several units in strategic locations in the vehicle's layout [105]. Hereby, this new product has a tremendous potential for fully-autonomous vehicles (level 3-5), meeting all the requirements, and is prone to turn out as a preeminent reference in terms of performance, reinforcing *Innoviz's* position on the verge of the competitive panorama. Indeed, the *InnovizOne* has been announced in advance as the winner of the "Best of Innovation" award to be showcased at the Consumer Electronics Show (CES) 2019, given to the highest-rated product in each category, and is to be deployed as part of BMW's autonomous vehicle program to start in 2021 [106].

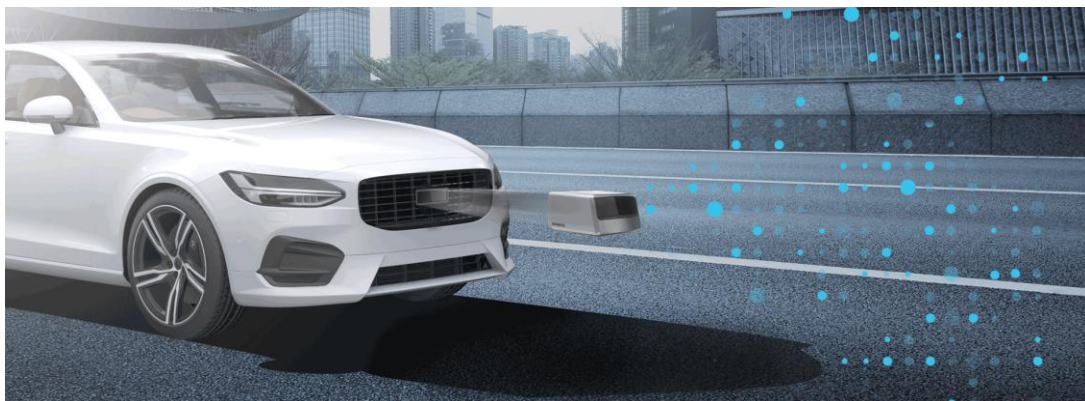


Figure 45. Automotive-grade *InnovizOne*. Due to the compact housing, this stand-alone unit can be readily integrated in several strategic points in the car's structure [105].

3.1.4. LeddarTech

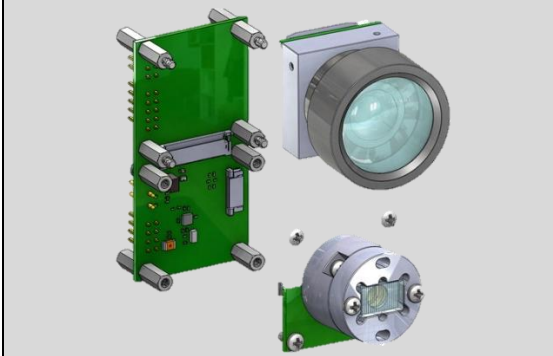
Founded in 2007, *LeddarTech* is a Quebec City-based company proposing to bridge the cost-performance gap in existing LiDAR sensors, offering affordable high-performance solutions. [107]

LeddarTech is the developer and owner of *Leddar*, a proprietary solid-state LiDAR sensing technology, covered by 58 patents, that combines advanced light wave digital signal processing and software algorithms. Figure 46 illustrates the main components of a *Leddar* sensing module. Rather than working directly on the analog signal, Leddar samples the received echo and the resulting signal is inputted at the *LeddarCore*, a system-on-chip that, besides synchronizing and driving the emitter and receiver functions, digitalizes (around 1.3 billion samples per second) and filters the signal via software, providing patented signal processing to increase the system SNR and the resolution. Utilizing sophisticated software-based algorithms, the discrete-time signal is analyzed and the ToF is directly recovered for every object in the FOV. The timing is performed through advanced thresholding techniques and, since the generated return signal is cleaner, lower detection thresholds are enabled, which significantly increases the range, sensitivity and timing accuracy. [108]

In-between *LeddarTech* products, the most interesting within the context, and the most recent, is the *Leddar Vu8*, a 2D solid-state flash LiDAR. In this device, the fixed-beam is dispersed by a diffusing lens

to cover a determined FOV and the detection is achieved by a 1D array of 8 independent detector units, each one probing a different region in space after imaging through a single objective. The technical specifications for this unit are exposed in Table 9. [34]

Table 9. Key technical specifications of *Leddar Vu8* [109].

 Leddar Vu8	
LiDAR Class	2D Solid-state Flash
#Lasers / #Detectors	1 / 1D array of 8 independent detectors
FOV (H×V)	Narrow FOV: 20°×0.3° / 20°×3° Medium FOV: 48°×0.3° / 48°×3° Wide FOV: 100°×0.3° / 100°×3°
Max. Range (Reflectivity)	Narrow FOV: 185m (retro-reflector) / 60m (90%) Medium FOV: 118m (retro-reflector) / 31m (90%) Wide FOV: 61m (retro-reflector) / 12m (90%)
Range accuracy/resolution	± 5 cm / 10mm
Frame Rate	Up to 100Hz
Laser Class / Wavelength	Class 1 Eye-safe per IEC 60825-1:2014 / 905nm
Pulse width / PRR	10ns / 10 kHz
Supply Voltage / Power consumption	12±0.6 VDC / 2W
Data per point	ToF distance measurement Intensity/Amplitude
Operating temperature	-40°C ... +85°C
Interfaces	SPI, USB-CAN-Serial
Dimensions (H×W×D)/ Weight	Narrow FOV: 70×35.2×67.5 mm ³ / 110.3g Medium FOV: 70×35.2×45.8 mm ³ / 107.6g Wide FOV: 73×50×65 mm ³ / 128.5g
Price	From \$450 (depends on the modules)

The most appellative feature of this design is the intended modular architecture, achieved through the division into three different boards: source, receiver and carrier board. This allows for multiple configurations and specifications that can be adopted by simply swapping the building blocks to afford versatility, adaptability and flexibility. Hence, the device is customizable to a certain degree of extent and several combinations of FOVs (Narrow, Wide, Medium) and ranges can be selected to best fit each

scenario. Moreover, the modules are available in horizontal and vertical configurations, to adapt to different mechanical design requirements.

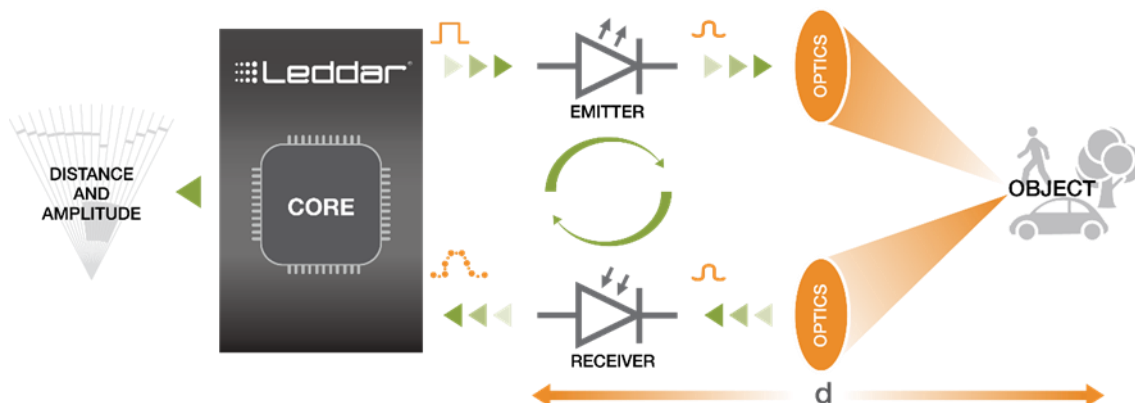


Figure 46. Signal travelling through the main components of Leddar sensing module [108].

Conclusively, since the output point cloud is two-dimensional, the *Leddar Vu8* cannot provide a whole profile of the surrounding environment and the usability in high-level autonomous vehicles is circumscribed. On the other hand, the highly competitive price, the compact lightweight and the exceedingly low power consumption, meet the requirements of mass-market automotive deployments supporting low levels of driving automation.

3.1.5. Valeo

Valeo is a multinational automotive supplier based in France and founded in 1923. In 2014, this company introduced its first laser scanner in the market, the *SCALA*, a 3D pulsed ToF scanning LiDAR with a rotating macro-mirror that simultaneously scans 4 horizontal layers with a patented technology (WO2013079331A1) [110]. According to *Valeo's* allegations back in 2016, this was the first ever LiDAR device prepared for the automotive volume production, with an estimated price around \$600 [87]. The relevant performance metrics are as follows.

Class: 3D macro-mirror scanning LiDAR

Optical performance:

- Four class 1 eye-safe lasers @ 905nm
- Range from 0.3m to 327m (retro-reflector), detecting vehicles from >150m and pedestrians from >50m.
- 4cm range resolution and accuracy <10cm
- 12.5 to 25 FPS
- Single shot per pixel and up to 3 returns per pixel to overcome bad weather conditions
- HFOV of 145° with 0.25° angular resolution @ 12.5Hz
- VFOV of 3.2° with 4 parallel scanning layers spaced by 0.8° (vertical angular resolution)

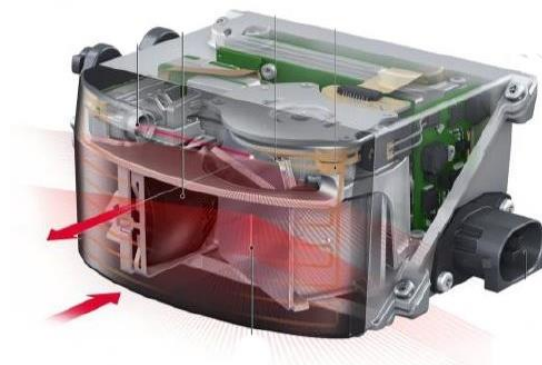


Figure 47. *Valeo's SCALA* laser scanner [110].

Output:

- ToF distance measurement and angle (longitudinal and lateral position)
- Frame with 580×4 pixels @ 12.5Hz (145°/0.25° per horizontal layer)
- Relative velocity with an accuracy of 0.25m/s

Mechanical, electrical and operational:

- 6W average power consumption with an operating voltage from 9 to 16 VDC
- 108 × 102 × 60 mm³ (H×W×D) and 600gr
- IP67 environmental protection
- Operating temperature from -40°C to +85°C

Although, the VFOV is narrower than any of the previous presented sensors, which may restrict the applicability in L4/L5 automated vehicles, the sensor has already been applied into a highly-automated solution, the *Drive4U*, shown during a demonstration in real traffic conditions at the 2015 CES, being a proven technology. In automated mode, the system takes full control of the vehicle's steering, acceleration and brakes [111]. Moreover, this sensor is already being integrated in the new *Audi A8 L3* car.

3.1.6. Continental AG

Continental AG is a leading German automotive manufacturing company founded in 1871 that specializes in tires, brake systems, automotive safety, chassis components, among others. More recently, this organization entered the LiDAR market and is currently developing a long-range solution for high-level vehicle automation.

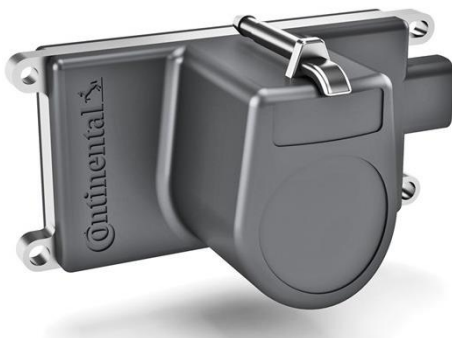


Figure 48. *Continental's* Flash LiDAR [112].

The proposed technological solution is a High-Resolution 3D Flash LiDAR intended to replace the current mechanical scanners mainly due to the superior price-wise affordability and image quality, through excellent vertical and horizontal angular resolutions, with contiguous pixels and without gaps. The stationary laser modules are to be placed at each corner of the car to construct a real-time 360° view around it and support the information provided by cameras and mid-to-long range radar sensors. [112]

Regarding technical specifications, the more meaningful parameters were not yet revealed. However, following *Continental's* predictions, the production is to begin aiming to integrate vehicles by 2020.

As a matter of fact, *Continental* already has some of the required know-how in LiDAR development, that arises from a successfully commercialized sensor. The SRL 1X (Short Range LiDAR) is an infrared sensor with 3 distinct channels that cover a total FOV of 27°×11° using 33ns pulses at 905nm and with an 80W peak power to estimate directly the ToF. The measurable range climbs up to 10m for natural non-reflector targets, with an accuracy of 10cm and a repetition rate of 100Hz. It is needless to refer that these characteristics are not proper for the final application, limiting this sensor to industrial appliances and simple close-range automated tasks. [113]

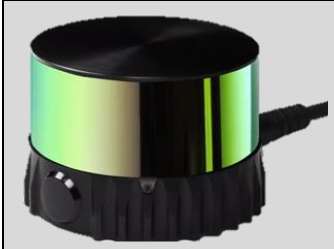
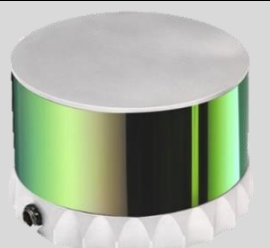
3.1.7. Others

Last but not least, besides the most preeminent references and competitors in the state-of-the-art for automotive LiDAR sensors, there are many other small companies and startups, some of them financed by key vehicles' manufacturers, introducing compelling products in the market and trying to make their way to the frontline in the race for a fully capable LiDAR sensor. In this subsection, the most alluring selections among a vast panoply of solutions are enumerated and briefly presented.

Ouster

Ouster is a privately held small company, based in San Francisco, focused on hardware and software development and computer vision. Their offer comprises two LiDAR product lines: *OS-1* and *OS-2* (still to be launched). Both products, whose specs are exposed in Table 10, are mechanical macro-scanners with a working principle and channels' disposition identical to *Velodyne's* LiDARs.

Table 10. Key technical specifications of *Ouster's* products [114] [115].

		
	OS-1	OS-2
LiDAR Class	3D mechanical macro-scanner	
Channels	16 or 64	64
Frame Resolution	64 vertical layers × 2048 points per line (@ 10Hz)	
Max. Range	120m	>200m
Accuracy	± 3 cm	
Frame Rate	10–20 Hz	
FOV (H×V)	360° × 31.6° (vertically symmetrical)	360° × 15.8° (vertically symmetrical)
Angular Resolution (H×V)	0.09° × 0.52° (@10Hz and 64 channels)	0.18° × 0.26° (@10 Hz)
Laser Class	Class 1 Eye-safe	
Beam divergence	0.13° full angle	
Sampling rate	1 310 720 px/sec	
Data per point	Range, Ambient NIR, Reflectivity, Angle	
Dimensions	Ø80mm × 63 mm	Ø85mm × 110 mm
Price	\$3 500 (16 channels) \$12 000 (64 channels)	\$24 000

RoboSense

RoboSense is a recently-founded (2014) Chinese business focusing on high-end LiDAR technology for autonomous driving [116]. Besides two mechanical scanners, the *RS-LiDAR-16* and *RS-LiDAR-32*, this company presented at CES 2018 a new MEMS solid-state LiDAR, the *RS-LiDAR-M1 Pre*, and an OPA solid-state Lidar, the *RS-LiDAR-M1*. The first will begin mass-production at the end of 2018 as the second is going to be released next year and is estimated to be massively produced by 2020. Regarding the key performance metrics, exposed in Table 11, the *M1* is unequivocally the most capable sensor.

Table 11. Main performance specifications for *RoboSense*'s products [117][118][119].

	 RS-LiDAR-16	 RS-LiDAR-32	 RS-LiDAR-M1
LiDAR Class	3D mechanical macro-scanner		3D Solid-State OPA
Channels	16	32	1
Sampling Rate	320k px/sec	640k px/sec	-
Range (Reflectivity)	20cm..150m (20%)	20cm...200m	Up to 200m
Accuracy	± 2 cm (typical)		-
Frame Rate	5–20 Hz		25Hz
FOV (H×V)	360° × 30°	360° × 30° (v.32A) 360° × 40° (v.32B)	120° × 25°
Angular Resolution (H×V)	0.09° × 2° (5Hz) 0.36° × 2° (20Hz)	0.09° × 0.33° (5Hz) 0.36° × 0.33° (20Hz)	0.1° × 0.1°
Laser Class	Class 1 Eye-safe @ 905nm		
Data	3D Spatial Coordinates / Intensity		
Dimensions	Ø109mm × 82.7 mm	Ø115mm × 95.7 mm (v.32A) Ø115mm × 110.5 mm (v.32B)	-
Weight	0.84 kg (w/o cabling)	1 kg	-

ASCar

In 2012 the Californian company *ASCar Inc* developed the *Peregrine* family of 3D solid-state Flash LiDAR cameras that are immune to sun interference and can image through dust, smoke and fog or at night. [120]

Peregrine (Figure 49a) illuminates an area of interest with a single 5ns 80W peak-power Class 1 eye-safe laser pulse at 1570nm wavelength, and simultaneously acquires ToF and intensity information within a full frame through a FPA to create a point cloud with 128×32 pixels at a rate of 20Hz (with optional 30Hz). The FOV is configurable with the wider option of bayonet mount lens of (HFOV×VFOV) 60°×15°, holding a measurable range from 20.3cm up to a maximum of 200m and an angular resolution of

$0.47^\circ \times 0.47^\circ$, calculated through equation (2.4). With no moving parts other than a fan for active temperature stabilization, a compact form factor of $5\text{cm} \times 7.6\text{cm} \times 14.95\text{cm}$ (W×H×D), weighing less than 680g and consuming 13W on stable operation, this device is proper to be applied on safe driving assistance systems. [120]

Ibeo

Ibeo Automotive Systems GmbH is a German specialist in automotive LiDAR sensor technology located in Hamburg and founded in 1998. In addition to the state-of-the-art *LUX* family of LiDAR sensors, presented subsequently, this company develops software for environmental detection and referencing tools for autonomous driving systems. Since December 2000, *Ibeo* operates as a subsidiary of *SICK AG* and both offer analogous products, with spec, operational and appearance-wise similarities. [121]

Among the aforementioned family of laser scanners, the standard *LUX* model (2010) and *LUX 8* layers can be highlighted as the most auspicious. They both rely on direct ToF measurements and a macro-mirror scanning technique to simultaneously scan each horizontal slice, akin to *Valeo SCALA*. The elected units are spec-wise very identical, differing only in the number of horizontally-scanned layers (4 in the standard model versus 8 layers in the alternative) and, consequently, in the VFOV (3.2° vs. 6.4°), and in the frame rate configurations (12.5/25/50Hz vs. 6.25/12.5/25 Hz) [122]. The shared technical parameters are: distance measurements ranging from 0.3 to 200m for a 90% remission and 50m for 10% with a distance-independent accuracy of $\pm 10\text{cm}$ and a 4cm resolution; HFOV of 110° with down to 0.125° resolution and fixed vertical resolution of 0.8° ; up to consecutive 3 returns per point for higher reliability in poor weather conditions; class 1 eye-safe laser with 905nm wavelength; IP69K enclosure rating; 9 to 27 VDC supply voltage and 8W average power consumption; dimensions $164.5 \times 93.2 \times 88\text{ mm}^3$ with a weight of approximately 1kg [122]. The two output dynamic properties in real-time (vector speed and position) to predict the relative movement of obstacles and grant safer decisions. Price-wise, the estimation is ranged between \$10 000 and \$20 000 [87].

In terms of proof-of-concept, the *Ibeo LUX* laser scanner has already been tested in *HAVEit* project, which presented a typical LiDAR fusion system with three single sensors integrated in the vehicles front bumper (Figure 49b). A sensor fusion algorithm created a complete 180° view of the vehicle's front.

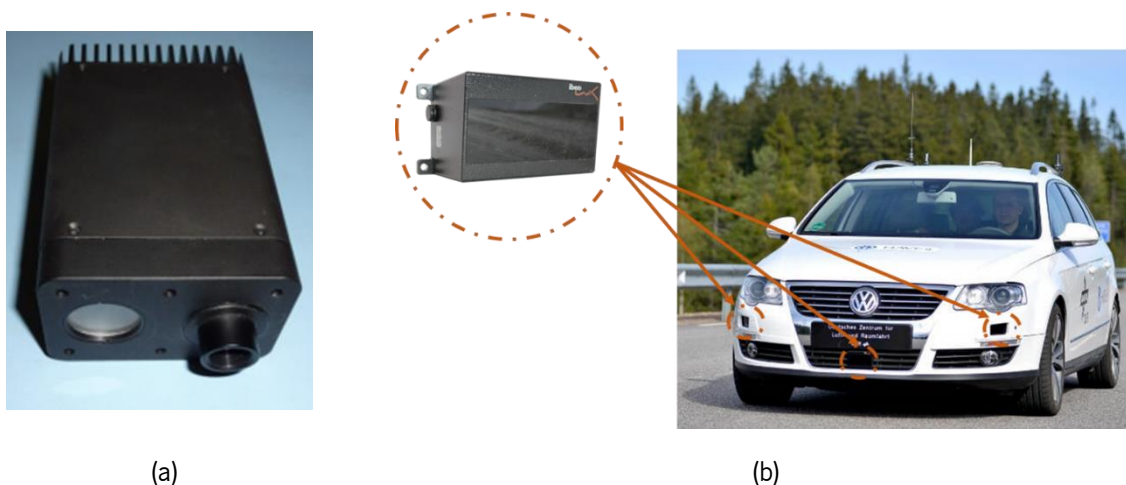


Figure 49. (a) Peregrine Series 3D Flash LiDAR [120] and (b) Integration of three *LUX* units in the *HAVEit* project.

Hesai

In 2017, *Hesai*, a Shanghai-based company founded in 2013, launched its first LiDAR sensor, the *Pandar40*, a 40-channel hybrid, with a solid-state and mechanical rotating technology. The distance measurement is performed via pulsed ToF simultaneously through 40 vertically aligned lasers in a range from 0.3 to 200m (at 20% reflectivity). The whole system rotates at a rate of 10 or 20Hz and the points are sampled at 720kHz. The class 1 eye-safe (IEC 60825-1:2014) lasers cover an VFOV from -16° to $+7^\circ$ with an angular resolution of 0.33° from -6° to $+2^\circ$, 1° from -16° to -6° and $+2^\circ$ to $+7^\circ$ (Figure 50). The device covers a 360° HFOV with a resolution of 0.2° at 10Hz and 0.4° at 20Hz. The unit consumes 15W. [123]

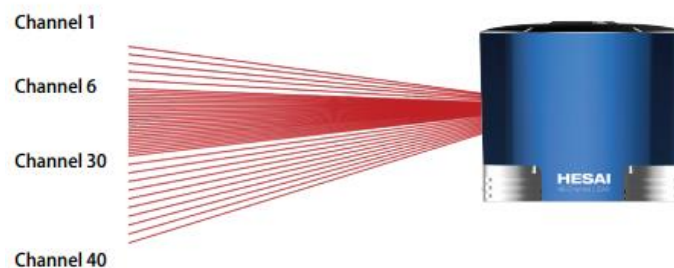


Figure 50. FOV segmentation in *Hesai PANDAR*. [123]

3.1.8. Overview

Among the surveyed sensors, it is intelligible that up until this moment mechanical macro-scanners have dominated the market due to the superior FOV and resolution. However, the high costs are needlessly delaying the roll out of autonomous vehicles and strongly contributing to a trend reversion. With the evolution of solid-state technologies and due to the advantages stated in Section 2.4.3, most manufacturers are opting for these approaches to potentiate mass-production and massive cost-reduction, while maintaining or even improving the performance. In the next 1-2 years it is expected for this technology to replace mechanical scanners in the lead of automotive LiDAR sensors. This analysis is supported by several market studies reporting that solid-state is the LiDAR technology to have a most noticeable growth in automotive applications until 2023 [124]. Regarding the employed rangefinding technique, direct Time-of-flight (pulsed) is outstandingly dominant essentially because it is the most straightforward methodology, commonly adopting 905nm eye-safe lasers. A schematic summary of the technological implementations of several manufacturers is portrayed in Figure 51.

To ascertain if any of the studied sensors is spec-wise appropriate for autonomous driving, the main performance metrics from five of the principal units of each class allegedly on market are compared with requirements settled for highly-automated driving (Level 4 to Level 5). Table 12 resumes this comparative analysis. Despite being an acutely important factor, the cost is not encompassed.

It is possible to conclude that neither one of the five sensors fit completely the requirements. Clearly, the products that are closer to meeting the requirements are the *InnovizPro* and the *Velodyne HDL-64E*. However, in general, the sensors lack mostly either in the maximum range and/or the angular resolution, two of the most critical parameters. Whatsoever, the sensors' do still fit in partially automated vehicles

(up to Level 3) as monitoring systems to support a broad diversity of ADAS such as blind spot detection, lane keeping and collision avoidance.



Figure 51. Main automotive LiDAR players segmented according to the technological implementation [87].

The need for improvement has already been identified by the manufacturers and, inclusively, the majority have already proposed and are working on future products that overcome the failures of the preceding generations.

Table 12. Comparison between the main performance metrics of several commercial LiDAR sensors and the requirements for Level 4 and Level 5 autonomous vehicles. The “X” indicates that the device does not meet the requirements, the “✓” marker indicates the opposite and the (?) indicates that the lack of information does not allow any conclusion.

	Requisites	Velodyne HDL-64E S3	Quanergy S3	InnovizPro	Valeo SCALA	ASCar Peregrine
LiDAR class	3D LiDAR	✓ 3D Macro-scanner	✓ 3D Solid-state OPA	✓ 3D MEMS-based	✓ 3D Macro-mirror	✓ 3D Flash
Maximum Range	180m	X 120m	X 150m (80% remission)	X 150m (80% remission)	(?) >150m (vehicles)	✓ 200m
Accuracy	10cm	✓ 2cm	✓ 5cm	✓ 3cm	✓ 10cm	(?)
FOV (H×V)	50°×9°	✓ 360°×26.9°	✓ 120°×10°	✓ 73°×20°	X 145°×3.2°	✓ 60°×15°
Angular resolution (H×V)	0.15°×0.5°	✓ 0.17°×0.4° (@10Hz) X 0.35°×0.4° (@20Hz)	X 0.1°×0.8° (@10Hz) X 0.5°×0.8° (@25Hz)	✓ 0.15°×0.3°	X 0.25°×0.8° (@12.5Hz)	X 0.47°×0.47°
Frame Rate	10FPS	✓ 5-20FPS	✓ 10-25FPS	✓ 20FPS	✓ 12.5-25FPS	✓ 20/30FPS
Laser class /Wavelength	Class 1 / -	✓ Class 1 eye-safe / 905nm	✓ Class 1 eye-safe / 905nm	✓ Class 1 eye-safe / 905nm	✓ Class 1 eye-safe / 905nm	✓ Class 1 eye-safe / 1570nm

Aside from the preceding manufacturers list, there are plenty other companies, for instance *Benewake* [125], *Bosch*, *Cepton* [126][127], *DENSO* [128], *Hella* [129], *Neptec Technologies* [130], *Ocular Robotics* [131], *Phantom Intelligence* [132], *Pioneer*, *Strobe*, *Toyota R&D* [133] and *TriLumina* [134], who have joined the race for a fully adequate and reliable automotive LiDAR and are bringing notable contributions to the sector.

Presently, the competition is utterly fierce with the referred companies offering interesting value propositions and state-of-the-art solutions which encompass the implementations discussed in the latter chapter. Whatsoever, at this point and as expected, there is a tremendous secrecy and intellectual protection around the operating principles and some technical specifications. Furthermore, the carried out aggressive marketing campaigns make it hard to figure out what products have effectively passed the idealization stage and are already concluded and ready for commercialization.

3.2. Out-of-the-box Concepts

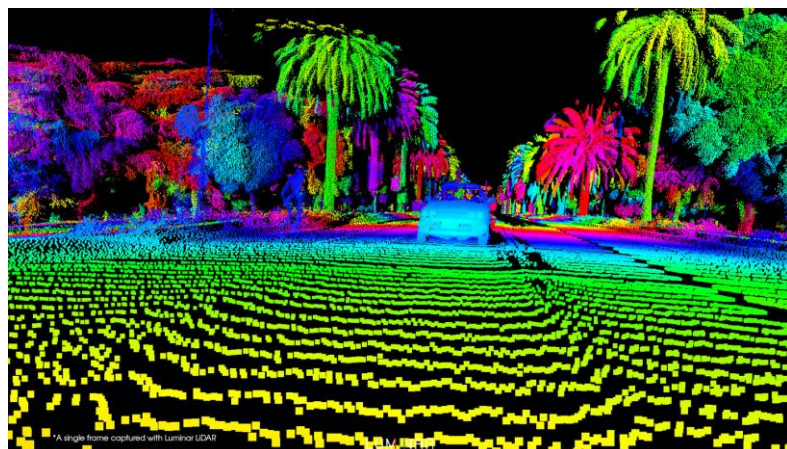
Recently, a number of stimulating and innovative concepts have arisen within the automotive LiDAR research field and industry in an attempt to overcome the main obstacles of conventional systems. Furthermore, other already existing sensors employ distinctive detection techniques that are noteworthy. In this sequence, a selection of these concretizations is discussed herein.

3.2.1. Luminar

Luminar is a Californian breakout company created in 2012 and, recently, announced to have built an unparalleled LiDAR sensor, either regarding the operating principle and performance. The key is the shift from the conventionally used 905nm lasers to an eye-safe wavelength around 1550nm to support a pulses' power increase by a factor of 40 times. Comparing with 905nm eye-safe limited LiDAR systems, this superiority holds a stretching in the maximum range beyond 200m at only 10% remission and an increasing in the resolution by 50 times [135].



(a)



(b)

Figure 52. (a) *Luminar* LiDAR and (b) generated high resolution point cloud [135].

In Figure 52b it is shown an example of generated point count, evidencing the difference-making resolution, particularly at highway speeds. Concerning the performance metrics, the sensor can perceive targets up to 250m with an angular resolution as little as 0.05° . The default frame rate is 10Hz, but it can be lowered to 1Hz for extremely resolute images or increased up to 20Hz at a cost of resolution. [136]

To overcome the costly proposition of InGaAs sensors required to absorb this wavelength and overperform either the conventional 905nm-systems and other devices as *ASCar Peregrine* that use nearby wavelengths, *Luminar* opted to design and manufacture its own components and specific ICs from the ground-up, instead of using off-the-shelf parts. This does not only enable a huge cost reduction but also high-scale production. In particular in photodetection, by using just a small amount of InGaAs, about the width of a human hair, the company asserts that the receivers' cost has been brought down to just \$3 per unit. [137]

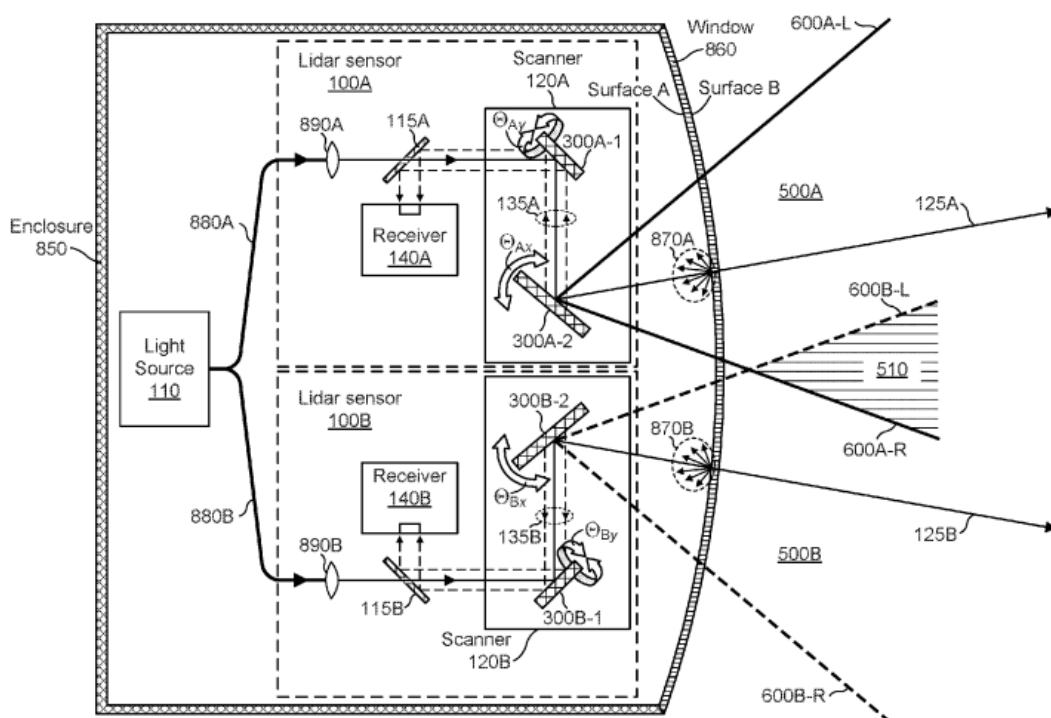


Figure 53. Patented *Luminar* LiDAR's block diagram [138].

Naturally, since every block was created from scratch, the whole system is intellectually protected through patents. In Figure 53 is exposed the device's block diagram as presented in one of *Luminar's* patents. The LiDAR module includes two distinct sensors (100A and 100B) placed side-by-side, each one including a scanner (120) and a receiver (140). Both sensors are contained in the same housing (850) and share a single pulsed laser source (110) that is optically coupled to both sensors through a Silica optical-fiber (880), with minimum losses around 1550nm [139], terminated by a collimating lens (890) to produce a free-space beam directed to the scanner. The scanner comprises two micromirrors (300-1 and 300-2) rotating in orthogonal directions to steer the beam over the FOV (500). It is not clear the type of mechanical driving mechanism for the micromirrors but, presumably, a galvanometer (electrical current is supplied to a coil that generates a rotational force in a magnet, causing the mirror attached to it to rotate) or a MEMS device seem to be the most plausible. The two FOVs are partially overlapped in

the central angular/spatial region (510) to allow for the data to be combined and stitched together to form a single continuous 120° point-cloud. An overlap mirror (115) located between the scanner, the collimating lens and the receiver, allows the emitted pulses to be transmitted to the scanner through an aperture (hole), while the return light is partially reflected and focused towards the receiver. Thus, the emitted and returned pulses overlap in a substantially coaxial manner. Each receiver comprises an InGaAs APD detector reversely biased by a voltage superior to 50V to absorb 1550nm photons. An optical BPF is located in front of APD, with an attenuation up to 40dB for wavelengths outside the passing band [139]. The APD is electrically coupled to a pulse-detection system comprising a TIA, a gain stage with additional low-pass filtering capability to remove high-frequency electrical noise, a threshold comparator and a TDC [139]. The whole enclosure includes a window (860) to allow light exchanges with the environment. [138]

3.2.2. Interference Immunity and FMCW Technology

With the development of LiDAR sensors and its introduction in the market, it is expected for more and more cars to integrate this technology. In this scenario, an inevitable source of error arises: interference between sensors. As the state-of-the-art of automotive LiDAR sensors includes mainly pulsed systems at around 905nm wavelength, interference can turn out to be a serious problem these systems will have to deal with. Although this problem was already discussed in the previous chapter and some solutions to avoid it were presented, here concrete companies and products addressing this problem are explored.

The first identified solution is to replace incoherent pulsed ToF techniques by coherent detection. This is exactly what *Aeva* [140] and *Oryx* [141] implement. By working with FMCW Flash LiDARs, potential interference sources are eliminated as the receiver is only responsive to signals coherent with a local oscillator.

However, the current most remarkable FMCW LiDAR is beginning commercialization and is the *Blackmore LiDAR* (Figure 54a). This sensor adopts beam steering with an OPA and is highlighted because it is the first automotive solution to target mass production and takes advantage of the FMCW Doppler technology to furnish a unique competitive advantage [142].

Blackmore implements a CW eye-safer laser at a nominal wavelength of 1550nm. A portion of the laser beam is split off to a local receiver and the frequency of the received signal is compared with the local reference signal by means of an optical mixer integrated in a heterodyne receiver with a well-determined local oscillator frequency [142]. This coherent detection mechanism leverages the single-photon sensitivity limitation to the quantum noise level and nullifies the interference and cross-talk from another sensors (signals incoherent with the local oscillator).

As a complement to the range measurements above 200m and up to 1.2Mpx/sec rates, the system can also evaluate radial velocities by measuring the Doppler-shift in frequency (Figure 54c). A target moving towards or away from the sensor induces an upwards or downwards frequency shift, respectively. The speed's dynamic range is between $\pm 150\text{m/s}$ with 0.2m/s resolution [142].

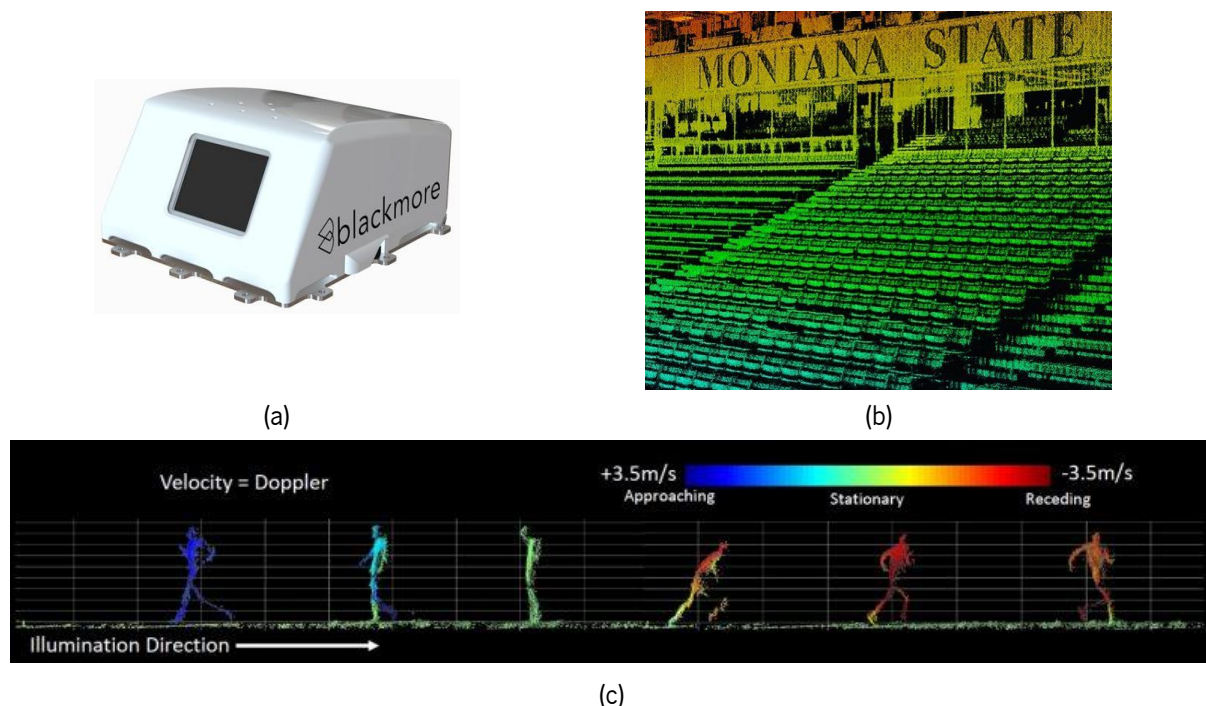


Figure 54. (a) *Blackmore* automotive LiDAR, example of a generated high-resolution point cloud and (c) velocity measurement through the FMCW Doppler-shift [142].

An alternative solution is implemented in the *Garmin Lite v3*. With up to 40m range, an accuracy of 10cm, a class 1 eye-safe laser at 905nm emitting pulses with 1.3W peak power from 10kHz to 20kHz PRR and angular divergence of $4\text{mrad} \times 2\text{mrad}$ (H×V), and a compact form factor of 22g and $20 \times 48 \times 40\text{mm}^3$, this single-point LiDAR sensor stands out essentially due to the unorthodox ToF technique. Instead of using single pulses, it emits trains of 500ns bursts each one with a unique signature, randomly generated (Figure 17a). The detection is done by a PIN photodiode followed by a 40kΩ-gain TIA and an ADC that samples the signal at 500MHz. The subsequent detection process is identical to the description in Section 2.2.4. The back-reflected signal is digitalized and then cross-correlated with the outgoing reference burst. Whenever a peak surpasses a resemblance threshold calculated from the noise floor, the respective ToF is attained. Hereby, the resilience to interference is ensured due to the unique signature of each burst that prevents. If a spurious signal is detected by the sensor, it will be discarded because only a signal with a shape similar to the reference is able to trigger a valid ToF measurement.



Figure 55. (a) *Oryx* LiDAR [141] and (b) *Garmin Lite v3* [143].

3.2.3. LiDAR-on-a-chip

A group of researchers at MIT's Photonic Microsystems Group started, in 2016, a project to develop a potentially far cheaper and miniaturized LiDAR system, the *Lidar-on-a-chip*. The silicon photonic chip, with no moving parts and measuring only $0.5 \times 6 \text{mm}^2$, features nanophotonic optical phased arrays (OPA) at the transmitter (TX), to steer the laser beam, and at the receiver (RX), as well as on-chip germanium photodetectors. [144]

It is demonstrated that for an 1D OPA consisting of N uniformly spaced antennas placed along a line, with spherical coordinates $\{r, \theta, \varphi\}$, the electric far-field can be expressed as [145]:

$$E_{tot}(\theta, \varphi) = E(\theta, \varphi) \cdot \exp\left[\frac{i(N-1)(kd \cos \theta + \alpha)}{2}\right] \frac{\sin(N(kd \cos \theta + \alpha)/2)}{\sin((kd \cos \theta + \alpha)/2)} \quad (3.1)$$

where $E(\theta, \varphi)$ is the individual emission pattern of each antenna, $k=2\pi/\lambda$ the wavenumber, d the spatial spacing between antennas and α the linearly progressing phase of each antenna. The previous equation is only a function of θ and not φ since the 1D array acts as an 1D aperture confining light in a single direction. To add an additional scanning dimension, the array should be made 2D [145].

The previous equation represents a *sinc()-like* function with a maximums occurring at such angles that the beam is created in the far field due to constructive interference of radiation, i.e. [145]:

$$\theta = \arccos\left(\frac{\lambda}{2\pi d}(-\alpha \pm 2\pi m)\right), \quad m \in \mathbb{N}_0 \quad (3.2)$$

At another angles light interferes destructively, and no beam is observed. Thus, by controlling the phase α , the maximum intensity angle is changed, and the beam is physically steered across a single direction, with small side lobes.

Finally, the previous relationship has multiple solutions, causing higher-order beams to be emitted from the array. These beams can be suppressed if the antenna spacing is equal or less than half of the laser wavelength: $d \leq 0.5\lambda$. In this situation, a single solution exists for $m=0$ (Figure 56a) [145].

In terms of structural layout, Figure 56b shows some portions of the device. The phased-array consists of 50 grating-based antennas with a $2\mu\text{m}$ pitch. This holds a highly-focused beam with an FWHM intensity spot size of 0.8° , dispensing the need for lenses. The antennas length is $500\mu\text{m}$ and they are designed to have a uniform emission pattern. The main beam is centered at 0° and can be steered in a single direction over a 51° FOV. The OPA is fabricated using a 193nm immersion lithography on a 300mm silicon-on-insulator wafer. [145]

Operationally, the laser beam is conducted to the phased-array through nanometric silicon waveguides. Phase modulation is primarily done using thermo-optic effect in these waveguides, directly heated by thermal phase shifters. As the index of refraction of silicon is heavily dependent on temperature, the speed and phase of the light passing through changes [145]. To emit the light out of the chip plane, antennas are created by a notch fabricated in the silicon substrate, scattering the light out of the waveguide into free space to create the interference pattern [144]. The device relies on a coherent method (FMCW) to estimate the range with an 1550nm laser and a germanium detector [145].

The laser is not integrated directly on-chip and it must be inputted via an optical fiber. Similarly, the TIA stage is also off-chip.

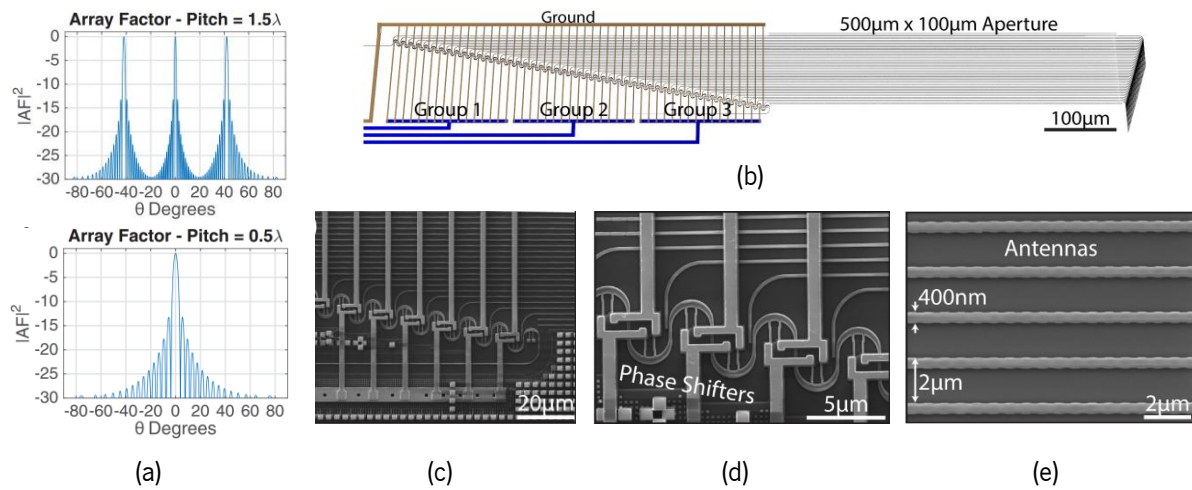


Figure 56. (a) Intensity profile (array factors) for different antennas spacing, (b) 3D rendering of the OPA and SEM images: (c) phase shifter architecture, (d) thermal phase shifters and (e) silicon grating based antennas with waveguide width of 400nm and a pitch of 2 μ m [145].

This chip aims mainly to bring a small, inexpensive and robust microchip that can be mass produced using conventional CMOS techniques for highly-autonomous applications. Since the micro and nanofabrication processes for silicon have been extensively used for many years, fundamental issues such as waveguide losses and optical isolation were already addressed, and the technology is already at a state where complex photonic systems can be created. Effectively, the chips have been successfully produced on 300mm wafers, which confirms the potential for mass production, with costs reaching as low as \$10. [144]

Although the initially developed device detects objects from 5cm up to 2-meter ranges with 3cm lateral resolution, a clear development path towards a maximum range 100m is reported. The FOV is limited by the space between antennas. Reducing the spacing is challenging as there is a limitation to how small silicon waveguides can be while still confining light adequately, although previsions point to 100° steering. [144]

To complete, silicon thermal phase shifters require a lot of power because of free-carrier and two-photon absorption. To achieve a 2π phase shift, electrical power of 10mW per antenna is needed. Hence, the 50-antenna OPA needs roughly 0.5W of power to fully steer the beam [145]. The alternative is to use silicon nitride waveguides, also a CMOS compatible material. This material has a higher bandgap than silicon and can handle power on the order of watts at 1550nm with much lower losses, allowing to significantly increase the laser power at the output [145].

3.2.4. Camera-LiDAR Fusion

To utterly increase resolution without major consequences in price, some manufacturers opted to directly fuse a camera with a LiDAR sensor by integrating both into a single device, overlaying and co-locating the immense spatial-resolute 2D color-video of cameras with pixel-level depth information in real-

time of LiDAR. This unification allows for increased compactivity and for decreased delay and computational drain, minimizing the post-processing and granting faster data interpretation.

Currently, this concept is being scrutinized in, at least, three different technologies: the *LASiris VR* by *NCTech* [146], the *AEye iDAR* (Intelligent Detection and Ranging) [147] and *TetraVue*'s 4D camera (three dimensions of space plus the one dimension of time) [148]. The former system consists in a vivid 120 Megapixels camera combined with a 100m range mechanically rotating LiDAR covering a FOV of $360^{\circ} \times 300^{\circ}$ (H×V) with 30mm accuracy [146]. It uses 16 precision lasers to acquire ToF range data over at 10FPS with an angular resolution as low as $0.02^{\circ} \times 0.1^{\circ}$ [146].

The second device is a fusion of a Micro-opto-electro-mechanical LiDAR (MEMS combined with micro-optics) with a low-light camera embedded with artificial intelligence. Thanks to the latter, this technology can identify and track objects with minimal computational latency, and revisit them even within the same captured frame, giving the perception and path planning layers of the software the ability to make more sophisticated calculations simultaneously, such as multi-directional velocity and acceleration vectors. Regarding the LiDAR, it acquires frame at a rate from 30Hz to 50Hz, synchronously with the camera, using an 1550nm laser that ranges farther than 230m with a 70° FOV. [147]

Finally, *TetraVue* associates high-resolution video, through a multi-megapixel CMOS sensor, with a non-visible ToF Flash LiDAR. This camera, contrary to the previous, outputs a grayscale image with depth information for each pixel represented through an intensity scale (Figure 57b). Instead of imaging the intensity image, each CMOS pixel in the *TetraVue* images a distance to then construct the latter image (imaging LiDAR). The FOV is illuminated at once at up to 30FPS and ranges until 100m with 2mm depth resolution. [148]



Figure 57. (a) *TetraVue* 4D camera and (b) example of a generated frame, in which the color scale indicates the depth [148].

3.2.5. Polarization-modulated Flash LiDAR

More recently, significant amounts of development efforts have concentrated on time-sensitive Flash LiDARs measuring the ToF to scene objects. Currently, there are various flash techniques to measure the ToF, but all involve individual complex circuitry for each pixel in the array that records the time of arrival of the returning light in that pixel (either by amplitude or phase). However, the complexity of such circuitry, as well as the extensive data recorded, has stymied development of such sensors. Moreover, the most advanced time-sensitive sensors are limited to around 200 pixels on a side due to challenges

of chip scaling, which extensively limits the resolution of the acquired 3D point cloud, and are extremely costly. [149]

In 1992, the patent *US005157551A* was registered by *J. Taboada* and *Louis A. Tamburino* describing a completely innovative technique to encode the distance to the target in a flash Laser Imaging and Ranging System (LIMARS) by means of electro-optical modulation using a Pockels Cell (PC) and reading the signals with conventional camera sensors [150]. Furthermore, in 2010, *TetraVue* also patented a polarization-sensing Flash LiDAR with a similar technology, which is believed to be the basis of the range measurement in its current product, presented in the latter section [151].

This polarization concept is particularly pertinent in the Flash LiDAR framework since the use of a modulator to encode the range information eliminates the need for expensive and complex circuitry as the time-dependent element is placed in front of the photosensitive array [149]. Therefore, instead of using electronic means to affect the charge signals at each pixel, the technique uses electro-optic means of affecting the light field in front of each pixel [149]. Consequently, the effect of timing jitter caused by electronics and shot noise is smaller because the echo's intensity is measured rather than the direct ToF [152]. Ultimately, and more importantly, high resolution CMOS or CCD sensors (several Megapixels → several million of points per frame) can be adopted to yield highly-resolute images, at a cost of less light sensitivity comparing with APD and SPAD arrays.

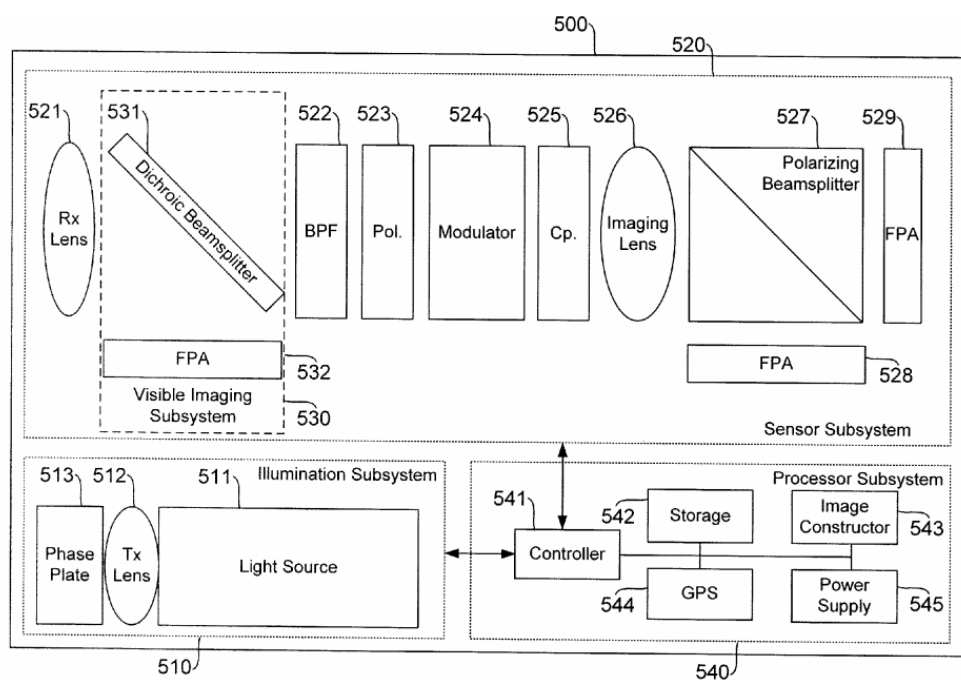


Figure 58. *TetraVue*'s patented LiDAR technology employing a electro-optical modulator (524), to modulate the returning light polarization state, and a PBS (527) that posteriorly splits two orthogonal states to two distinct FPAs (528 and 529) [151].

Both the former systems take advantage of the polarized radiation emitted by the laser source and the returning light is captured by the electro-optic element (PC) and then split by a Polarizing Beam Splitter (PBS) into two separate and complementary partial images, each corresponding to orthogonal polarization states (Figure 58) [151]. These images are transduced to electrical signals at two Focal Plane Arrays (FPAs) that can either be an off-shelf CCD or CMOS sensor placed at the focal plane of the

imaging lens [151]. The PC modulates the returning using a time-dependent voltage that indicates the range signal and enables decoding of the pixel intensity by combining the images of the two cameras [151]. The light emerging from the modulator will be in accordance with the modulation signal at the pulse reception instants and its polarization is sensed on each FPA [150]. Thus, the range signals are preserved in the form of intensity ratio modulation without reliance on the absolute intensity values. The imaged data is then transferred to a microprocessor that uses the intensities of corresponding pixels to determine the distance to the target on that point [150].

Usually, electro-optical modulators are employed as amplitude modulators. In these, the electric field can be applied to the Pockels cell either longitudinally or transversally to the light beam propagation direction. The phase shift across the Pockels cell, $\phi(t)$, is proportional to the applied voltage (modulation signal), $V(t)$, and, hence, to the applied electric field, as is described through [153]:

$$\phi(t) = \frac{\pi V(t)}{2 V_{\pi}} \quad (3.3)$$

where V_{π} is the half-wave voltage, yielding a phase retardation of π . This voltage depends on the crystal properties and on the direction of the electric field. For longitudinal and transversal KDP amplitude modulators it is shown to be [153]:

Longitudinal Modulator

$$V_{\pi} = \frac{\lambda}{2n_o^3 r_{63}} \quad (3.4)$$

Transversal Modulator

$$V_{\pi} = \frac{\lambda}{n_o^3 r_{63}} \left(\frac{d}{l} \right) \quad (3.5)$$

where l is the crystal length in the propagation direction, d is the crystal thickness, λ is the light wavelength, $n_o=1.5115$ the ordinary refraction index of KDP (polarization perpendicular to the optic axis) and $r_{63}=10.3$ the electro-optical coefficient. Thus, by varying the applied voltage, the output light is modulated.

The duration of the voltage signal applied to the Pockels cell defines the time-window for range measurement and the precision. The intensity on each FPA pixel (i,j) is a function of the applied voltage and can be described for each orthogonal state as [151]:

$$I_{528}(i, j) = I_{total} \cos^2 \phi(t = t_D) \quad (3.6)$$

$$I_{529}(i, j) = I_{total} \sin^2 \phi(t = t_D) \quad (3.7)$$

where I_{total} is the non-modulated returning intensity, given by the sum of both pixels' intensity, ϕ is the phase retardance introduced in the Pockels cell and I_{528} and I_{529} the intensities in each FPA, marked as 528 and 529 in Figure 58. The ToF corresponding to each pixel, $t_D(i,j)$, is then determined using equation (3.6) and doing the correspondence with equation (3.3):

$$\phi(t = t_D) = \frac{\pi}{2} \cdot \frac{V(t = t_D)}{V_{\pi}} = \arccos \left(\sqrt{\frac{I_{528}}{I_{total}}} \right) \quad (3.8)$$

Conclusively, rewriting the previous equation yields a ToF:

$$t_D(i, j) = t_0 + V^{-1} \left[\frac{2V\pi}{\pi} \arccos \left(\sqrt{\frac{I_{528}(i, j)}{I_{total}(i, j)}}} \right) \right] \quad (3.9)$$

where t_0 is the time delay between the laser firing instants and the instant the Pockels cell begins to modulate the polarization of the returning light, i.e., the instant the voltage $V(t)$ starts to be applied. This time represents a distance offset between the device and the object in the scene [151]. At last, the ToF in each pixel can be translated to a distance using equation (2.14). The function $V(t)$ is a monotonic function of time and the calculation may require the knowledge of the inverse of the time-varying voltage.

Regarding the hardware proof-of-concept, the presented system was firstly reported also in 1992 in the reference [154]. The first prototype used a frequency doubled Q-switched Nd:YAG laser ($\lambda=532\text{nm}$) with 35ps pulses. The Pockels cell was a KDP crystal longitudinally actuated by a 60ns monotonically decreasing voltage profile, between 3.5kV and 0V, corresponding to a 18m range gate. The system was validated for a target at 16.5m using two CCD FPAs.

In the last year, *TetraVue* patented an alternative Flash system for measuring the ToF using the same fundamental polarization-sensing principle but, instead of a PBS and a pair of camera sensors, it employs a single CMOS or CCD FPA and a polarizer grid array (Figure 59) [149]. The polarized grid can either be placed on front of the camera sensor or even a layer directly on its surface, with the later having the advantage of a much easier and precise alignment. The returning light is collected by a receiver lens and modulated through a Pockels cell. Then the polarizer grid filters a certain polarization state and transmits it to be detected on a CCD/CMOS pixel. The proposed grid alternates between horizontal and vertical orthogonal states and is aligned such the center of each polarizing element is positioned approximately at coincident with the respective pixel center. This highly integrated configuration can be constructed using standard lithographic, etching and deposition techniques. [149]

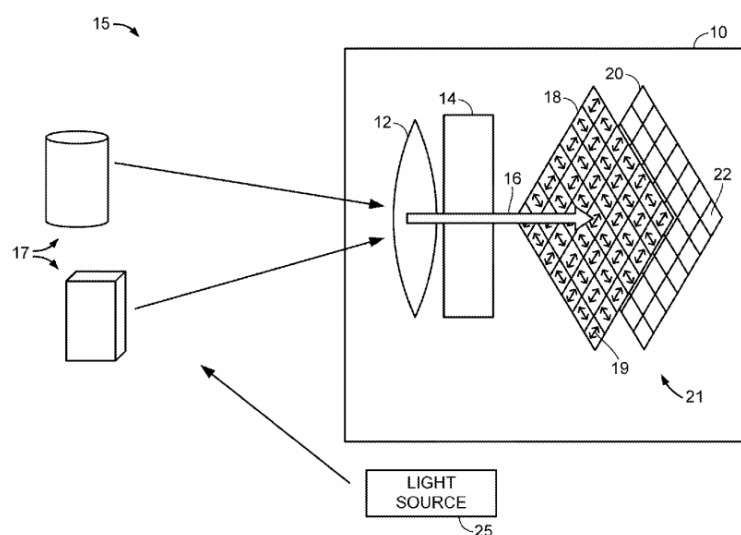


Figure 59. *TetraVue*'s patented conceptual diagram of a 3D camera sensor employing a modulator and a polarizing grid array. The returning light is collected by an optical element (12) and then passed through a Pockels cell (14) and then is detected by a camera sensor (20) interfaced by a polarizer grid (18) [149].

The reasoning and procedure to compute the ToF in each pixel is exactly the same as previously and the only innovative aspect is that the orthogonal states are measured in adjacent pixels instead of in different camera sensors. Each pair of pixels forms a super-pixel that yields a single ToF in the resulting point cloud. Therefore, the evident drawback relatively to the first hardware solution is the loss of resolution by a factor equal to the number of distinct polarization elements in the grid. Whatsoever, several improvements reflect the beneficial impact of this modification [149]:

- Eliminated the need to have two separate sensor arrays and a bulky PBS, thus the setup can be severely miniaturized.
- Simpler data streams to the microprocessor since there is only one FPA.
- Utterly reduction in the manufacturing and calibration complexity as the alignment of the 2 FPAs with the PBS to ensure a correct pixel-to-pixel match is an arduous task. With a single sensor, the location of each polarization pixel is automatically known relatively to the orthogonal and there is an automatic alignment between the “two virtual arrays”.

In an article published in 2016, the validation of a Flash LiDAR system with a micro-polarizer array had already been reported [152]. The setup is schematically represented in Figure 60. Before being transmitted to the external environment, each laser pulse passes through a collimation lens (CL), triggering a delay pulse generator (DPG). Subsequently, the DPG triggers a Pockels cell (PC) at a certain time delay t_0 , and a time-varying voltage increasing from 0 to V_π starts to be applied to the PC during a modulation time T_m . This time sets the length of the range gate that represents the measurable range section in one measurement, and it can be adjusted by simply changing the value of a resistor or a capacitor in the PC electric circuit. The PC is placed between a linear polarizer (P) and a quarter-wave plate (QWP) whose function is to introduce an extra phase delay $\pi/2$ and bias the electro-optic modulator in the linear transmission region. The assembly of these three optical elements composes the polarization modulator (PM). The pulse reflected on the target is detected by a micro-polarizer Charge-coupled Device (MCCD), after being transmitted across the PM, where it experiences a phase retardation $\phi(t)$ and its polarization is rotated by an angle according to the pulse ToF.

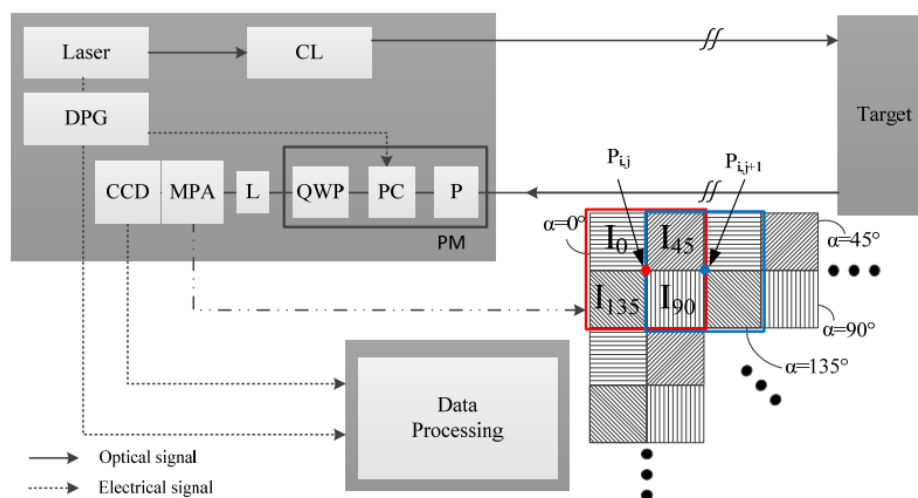


Figure 60. Schematic diagram of the micropolarizer Flash LiDAR [152].

As MCCD, the *Polarcam 4D* was used in the work, with a 1024×1024 CCD array. The micro-polarizer array (MPA) is composed by sets of four linear polarizers with polarization axis of 0°, 45°, 90° and 135°, as shown in Figure 60. The MCCD measures the intensity of the laser through the polarizer array and, using the values for the four intensities, the phase retardation can be determined via:

$$\phi(t = t_D) = \arctan\left(\frac{I_{45} - I_{135}}{I_{90} - I_0}\right) \quad (3.10)$$

where I_0 , I_{45} , I_{90} and I_{135} are the intensities measured in the CCD after the polarizers whose axis are oriented at an angle indicated by the subscript. Since the relationship between the phase retardation and time is defined the ToF can be obtained directly from the polarization rotation angle of the laser return pulse:

$$t_D(i, j) = t_0 + V^{-1} \left[\frac{2V_\pi}{\pi} \arccos\left(\phi|_{t=t_D}\right) \right] \quad (3.11)$$

The performed tests also used a doubled-frequency Nd:YAG laser and 900ps pulses and were mainly directed towards range precision evaluation and not range extension. A flat object was located at 16m and an average standard deviation of 5.2mm (≈ 35 ps) was obtained for 200 measurements, mainly limited by the timing jitter in the DPG output signal that triggers the PC. The single shot rms (root mean square) accuracy was determined to be 4.8mm and it is dependent on the accuracy at which the phase retardations are distinguished. More, an angular resolution of 0.12mrad (roughly 0.007°) was demonstrated.

The biggest disadvantage of this implementation is that the *PolarCam 4D* is an extremely costly proposition. Notwithstanding, at the present *Sony* already manufactures and distributes integrated sensors with micro-polarizer arrays correctly aligned at reasonable prices, such as the *Sony Pregius IMX250MZRCMOS* sensor with 5.1 Megapixels.

To complete, overall the Pockels cells are expensive components and commonly require high-voltage modulation signals on the order of magnitude of a few kV for a considerable effect to be observable. This drawback is more evident in longitudinal amplitude modulators since the half-wave voltage, V_π , is independent on the crystal dimensions [153]. On the other hand, in transversal modulators the latter voltage can be controlled through the crystal medium dimensions, as reflected by the d/l factor in equation (3.5) that can be chosen to be small to lessen V_π . Another effect to be accounted is the cross-talk between pixels, which can be resolved by adding a micro-lens array on top of the polarizer grid [155].

Part II

Experimental Work

– This page is intentionally left blank –

4

SYSTEM ARCHITECTURE

The starting and central point of this project is the implementation of a pulsed ToF LiDAR system with a single laser for single point measurements (1D). In this chapter, the system's architecture is presented alongside the hardware components employed and the respective operating principle and role within the system.

The system, whose block diagram is shown in Figure 61, is divided in two PCBs: the transmitter (TX) and the receiver (RX) boards. The former encompasses the laser control electronics, responsible for triggering the laser and emitting short light pulses to the target. As for the latter, it comprises a photodetector to convert the returning pulse into a manipulable electric current, a transimpedance amplifier (TIA) to perform the current-to-voltage conversion, a leading-edge discriminator to convert the analog pulse into a STOP pulse and two Time-to-digital Converters (TDCs) to estimate the ToF. The proposed system uses an additional off-board reference photodetector placed close to the laser output to time the instant when a light pulse is transmitted and, consequently, a supplementary on-board leading-edge discriminator to carry-out the conversion analogously to the return pulse. Both boards are connected to a microcontroller unit (MCU) belonging to *Texas Instruments'* MSP430 family. The RX MCU is a MSP430FR5969 and the TX MCU is a MSP430F5529.

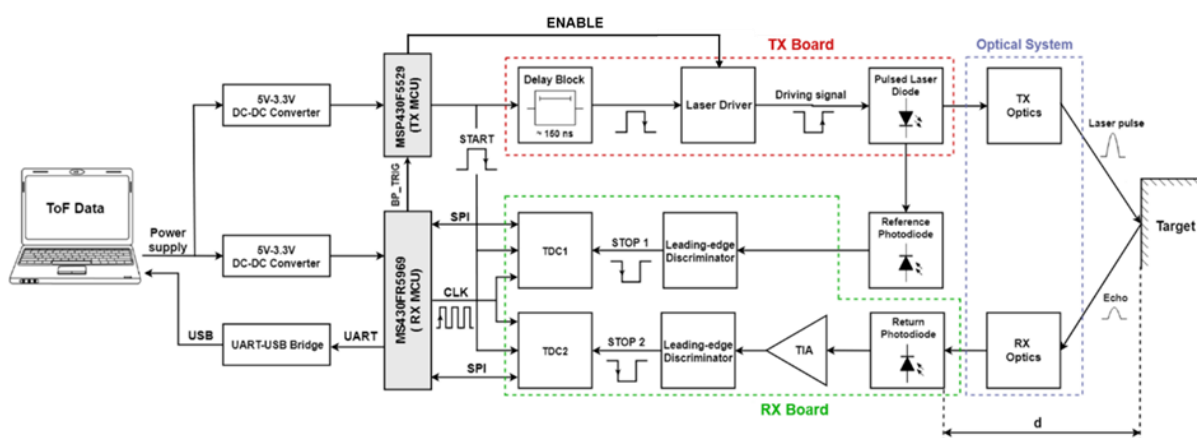


Figure 61. Block Diagram of the implemented LiDAR system. The polarity of the digital signals is evidenced.

The RX MCU acts as the system brain, controlling the laser activation instants that coincide with the START event to both TDCs, through the *BP_TRIG* signal. To ensure a complete tuning between the transmitting and receiving ends, the pulses' sequence generated by the RX MCU is directly connected to the TX board, avoiding the need for complex synchronization techniques. Hereby, the TX MCU does only control the respective PCB through the enabling signal to the laser driver. Besides, each MCU acts as a powering interface between the 5VDC from a computer's USB (Universal Asynchronous Receiver-Transmitter) port and the corresponding board, accomplishing the 5VDC-to-3.3VDC down-conversion required to supply most of the hardware components.

Since the TDCs adopted in this design have a non-zero blank interval immediately after a START event, inside which no STOPS may be detected, the previous pulses undergo a certain delay before activating the laser. When a laser pulse is emitted, the reference photodiode detects it and a STOP signal is generated to TDC1, declaring the beginning of the effective ToF counting. At the end of each measurement, by subtracting the time accumulated on the previous TDC to the time counted by TDC2 after a return pulse is detected, one obtains the total ToF. This approach allows to virtually eliminate the blank time, a limiting factor in the minimum measurable distance. The TDCs' data is transferred to the RX MCU via SPI (Serial-Peripheral Interface) and, after the ToF calculation and conversion to distance, d , the results are sent via UART to the USB (Universal Serial Bus) port of a computer to be displayed. This port is the same supplying the electric energy to the boards.

Lastly, an optical setup is mounted at both ends with off-shelf components selected to improve the system performance. This system collimates the laser beam, to reduce its divergence and the spot size at the target, and focuses the returning light in the photodetector.

The developed and implemented LiDAR is based on the TIDA-00663 reference design proposed by *Texas Instruments* [156]. Besides establishing and providing a complete electric schematic of both front-end (optical side) and back-end (timing side), *Texas* also furnishes the *Gerber* files necessary to print the respective pre-designed PCB (Figure 62a) and the components list. The referred design is integrated into a single $50 \times 50 \text{mm}^2$ PCB that was printed with no alterations to serve as a basis for the implementation (Figure 62b). Whatsoever, *Texas* does not supply the firmware nor a proposal for the optical system, whereby the programming and lens selection has to be done independently.

Nevertheless, as one could ascertain, the TIDA-00663 has never been tested or proven and several problems were detected, either at the beginning and throughout the first iteration. These issues, explored in the next chapter, forced several practical adjustments and architectural modifications to achieve a functioning prototype. Therefore, the single PCB had to be divided in the two aforementioned boards, both with the same layout but in each of which only the necessary components have been soldered to fulfil the respective functionalities. Furthermore, an external PD had to be added that, in an upcoming evolution, shall be substituted by an on-board detector adjacent to the laser. The complete Bill-of-Materials (BOM) required to implement the system are disposed in '*Appendix I – Bill of Materials*' and encompasses both the hardware and the optical components.

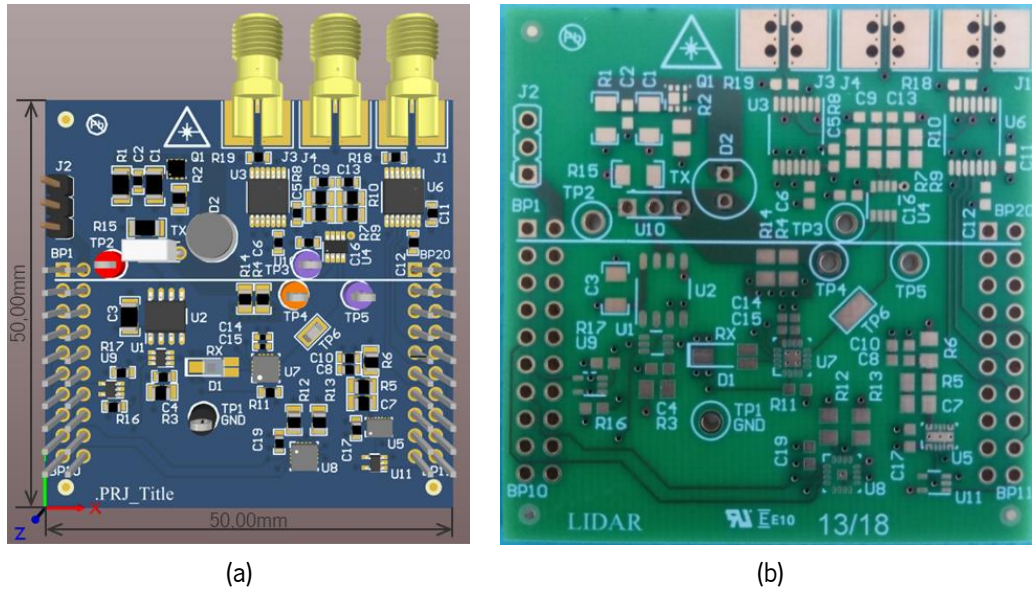


Figure 62. TIDA-00663 PCB layout: (a) top view with components in *Altium* as provided in the *Gerber* files and (b) top view of the printed PCB.

4.1. Transmitter board (TX)

The transmitter board is responsible for sending short light pulses to the environment and comprises a delay block, a laser driver and a laser diode. The respective electrical schematic is shown in Figure 63.

As already stated, the *BP_TRIG* is generated in the RX MCU to initialize a ToF measurement, i.e., to start the TDCs and trigger the laser. This digital signal is inputted to the TX board through a jumper wire and since is the system's driving signal, naturally, its frequency and duty cycle control both the point acquisition rate and the light output.

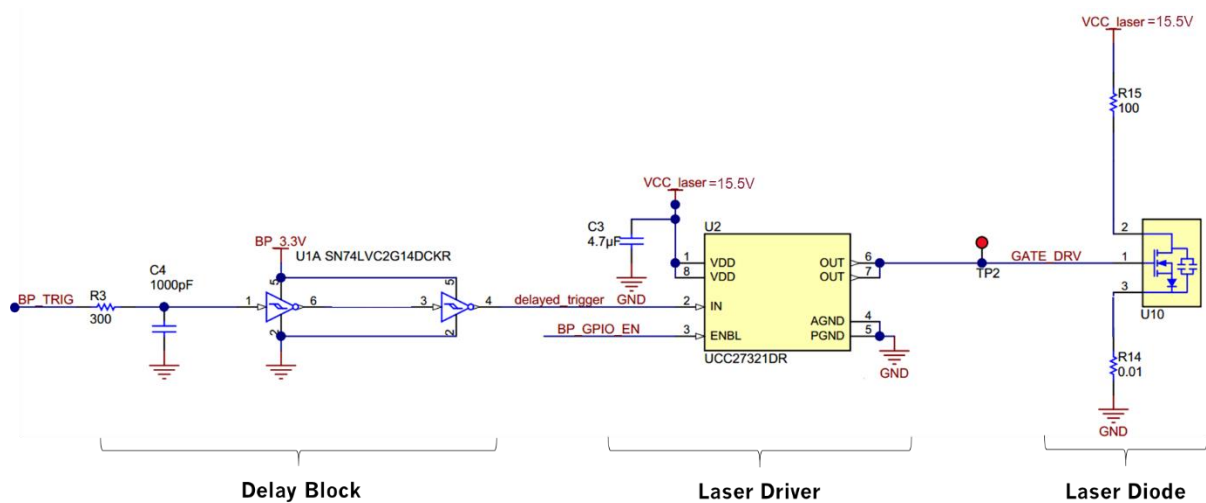


Figure 63. Electrical schematic of the system's transmitter (adapted from [156]).

4.1.1. Delay Block

Since the TDCs have a non-null blank time, a delay is added between the START event unleashed by *BP_TRIG* and the laser activation instant. As this blank time depends on the TDC operating mode, to be explained ahead, one opts to play it safe by introducing an overcompensated delay to guarantee any STOP pulse is recognized and ceases the time count, regardless of the mode and the effective ToF. Overall, this time will not be accounted in the final ToF because the latter is held by subtracting the results of the TDCs and both will measure this delay.

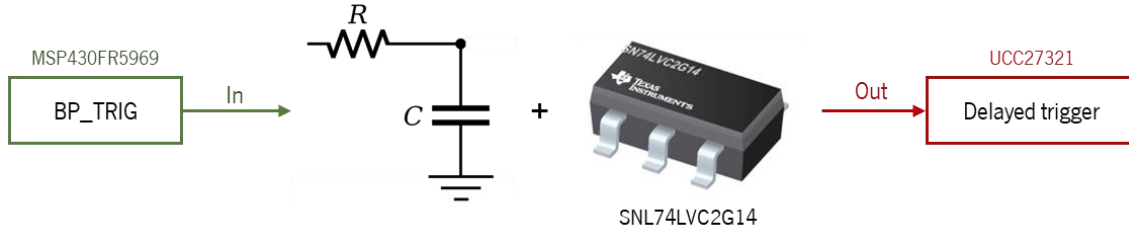


Figure 64. Schematic representation of the delay block.

The delay is accomplished electrically through a series of a RC circuit with a time constant $\tau = R_3 \times C_4 = 300ns$ and a *SN74LVC2G14DCKR* dual Schmitt-trigger inverter IC (U1) supplied at $+V_S = 3.3V$ to preserve the signal amplitude. When *BP_TRIG* is in a high-state (3.3V), the capacitor charges through the resistor as:

$$V_{C_4}(t) = 3.3 \cdot \left[1 - \exp\left(-\frac{t}{R_3 C_4}\right) \right] \quad (4.1)$$

When the input signal commutes to a low-state (0V) after the on-time, t_{on} , the capacitor discharges through the same resistor. Assuming the previous time is large enough for the capacitor to completely charge and achieve $V_{C_4}(t=t_{on}) \approx 3.3V$ (after approximately 5τ the capacitor is over 99% charged), then the discharging can be described via:

$$V_{C_4}(t) = 3.3 \cdot \left[1 - \exp\left(-\frac{t_{on}}{R_3 C_4}\right) \right] \cdot \exp\left(-\frac{t}{R_3 C_4}\right) \approx 3.3 \cdot \exp\left(-\frac{t}{R_3 C_4}\right) \quad (4.2)$$

Consequently, the digital pulses are translated into logarithmic-shaped analog pulses. To re-convert them into digital sequence with a certain delay relatively to the original signal, two Schmitt-trigger inverters are connected in series to the RC output. Each Schmitt-trigger inverter, whose response is characterized in Figure 65a, is a comparator with hysteresis that performs the Boolean function $Y = \bar{A}$. These devices compare an input signal with two different threshold voltages depending on the signal monotony: when the input signal exceeds the upper threshold, V_{T+} , the output transits to a low-state; when the input signal falls below the lower threshold, V_{T-} , the output commutes to a high-state. Consulting the datasheet, for $V_{cc} = 3V$ (closer value to 3.3V), the hysteresis, ΔV_T , and the thresholds are [157]:

$$V_{T+} = 1.3 - 2.2V, \quad V_{T-} = 0.6 - 1.3V, \quad \Delta V_T = V_{T+} - V_{T-} = 0.4 - 1.1V$$

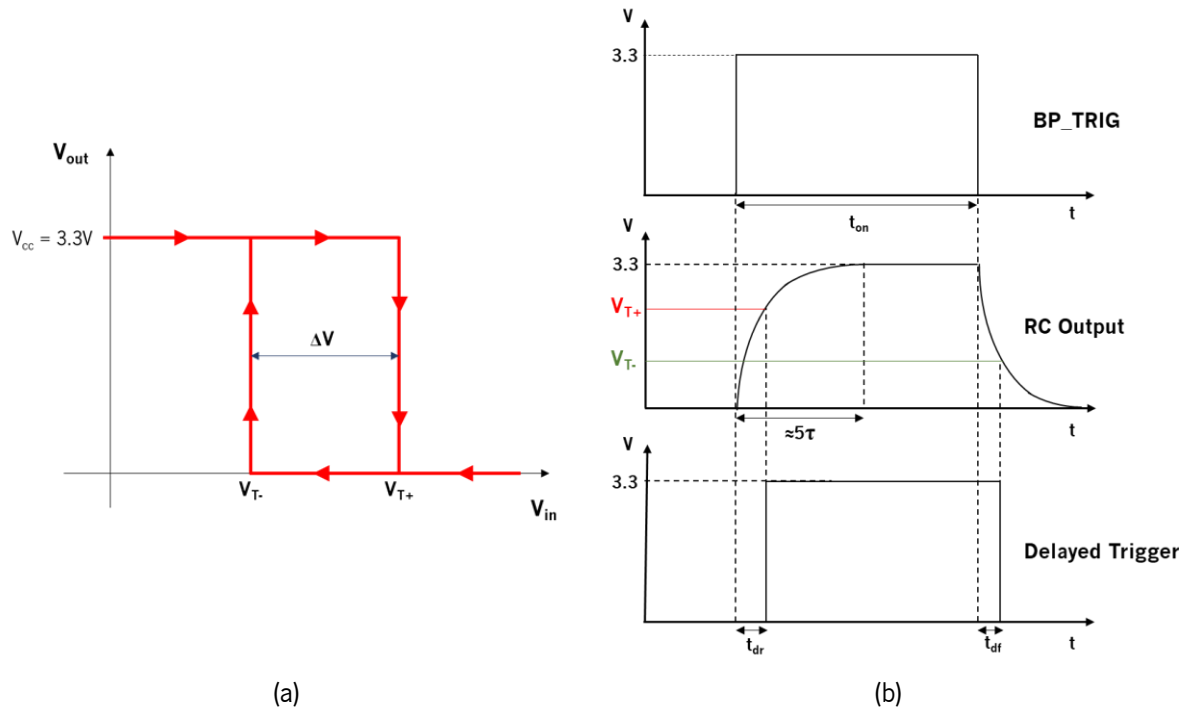


Figure 65. (a) Transfer curve of an inverter Schmitt-trigger and (b) working principle of the delay block.

Using equation (4.1), the voltage across the capacitor rises above V_{T+} after a time, t_{dr} :

$$V_{C4}(t = t_{dr}) = V_{T+} \Rightarrow t_{dr} = -R_3 C_4 \cdot \ln\left(1 - \frac{V_{T+}}{3.3}\right) \quad (4.3)$$

and, therefore, the trigger output switches to a low-level after the same temporal amount. Similarly, after a high-to-low commutation in BP_TRIG , the capacitor falls below V_{T-} after an off-time, t_{df} , deduced through equation (4.2):

$$V_{C4}(t = t_{df}) = V_{T-} \Rightarrow t_{df} = -R_3 C_4 \cdot \ln\left(\frac{V_{T-}}{3.3}\right) \quad (4.4)$$

and the output switches to a high-level. Replacing the nominal values in the previous equations yields:

$$\begin{aligned} t_{dr} &\approx 150 - 330ns \\ t_{df} &\approx 280 - 511ns \end{aligned} \quad (4.5)$$

Hereby, t_{dr} matches the time delay introduced by this block in the rising edge of BP_TRIG pulses. Furthermore, it also corresponds to the minimum pulse width required, otherwise the capacitor will not charge enough to trigger the IC. This value is independent on the pulses duration and is constant. Likewise, t_{df} corresponds to the delay instigated in the falling edges under the assumption that the capacitor charges almost completely during t_{on} . Besides these delays in a time-scale comparable with the RC time constant, the *SN74LVC2G14DCKR* inherently introduces a maximum delay of 5.4ns [157]. Because of the hysteresis, and although the pulses' frequency remains unchanged, the output width is altered to $t_{on} - t_{dr} + t_{df}$ (neglecting the IC delay) and, thus, so does the duty cycle.

As one desires to recover the same polarity as BP_TRIG , the two Schmitt-triggers ought to be connected in series to invert the signal twice. Since after the first comparison a digital signal is obtained

with nominal rise and fall times of 2.5ns [157], the second Schmitt-trigger behaves as a straightforward inverter. The whole delay process is portrayed in Figure 65b through the waveforms in three stages.

Lastly, as recommended in the datasheet, the power supply pin is bypassed to ground via a decoupling 0.1 μ F ceramic capacitor to prevent power disturbance and the propagation of any AC component to the IC, as high-frequency noise, while delivering the DC component directly to the supply pin [157].

4.1.2. Laser Driver and Pulsed Laser

The following system components are the laser emitter and the respective driving electronics. As discussed in the theoretical background, there are many advantages in using laser diodes for laser ranging. Since these emitters are current controlled, they can be readily modulated by gain switching through a similarly modulated electrical current.

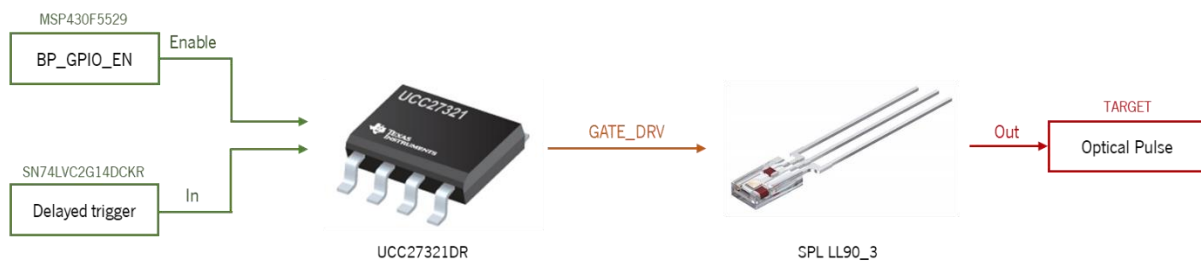


Figure 66. Schematic representation of the laser emitter and respective driver.

Because the signal arising from the previous delay block (*delayed_trigger*) is a PWM voltage signal, it cannot be directly applied to activate the light output. Then, and aiming to achieve optical pulses with fast rise and fall times and high peak power, the current across the laser is chosen to be controlled using a MOSFET repeatedly switching between OFF (cut-off) and ON (triode) states. The MOSFET is a voltage-controlled device as the gate terminal is insulated from both the source and drain by a thin layer of SiO₂. By controlling the voltage applied to the former terminal, the characteristics of the conductive channel between the drain and the source can be varied to hold either a very large or negligible resistance.

The MOSFET cannot be simply driven using the 3.3V-logic signal, since high current peaks are required. Hereby, a high-power buffer stage must be used to interface the latter PWM signal and the MOSFET gate. This circuit, called MOSFET driver (or also laser driver, because the MOSFET, in turn, drives the laser), is responsible for providing the adequate current signal to the LD by boosting the PWM signal to higher voltage levels and, in sharp time periods, dump a lot of power into the gate and during the Miller plateau. This way, the device spends a minimum amount of time in the transition state, minimizing the power losses through heating. More technical information on the underlying principle of fast MOSFET switching can be consulted in reference [158].

Currently, there are assorted commercially available solutions directed and optimized to perform MOSFET driving. In this work and motivated by the compactness (replaces multiple components by a single unit) and reduced power losses, the *UCC27321DR* IC manufactured by *Texas Instruments* is elected. This integrated device (U2 in the electrical schematic), for which the block diagram is shown in

Figure 67a, is supplied at a voltage $V_{DD}=V_{cc,laser}$ up to 16VDC and consumes a maximum of 650mW. The supply pins (1 and 8) are interconnected and a 4.7 μ F ceramic capacitor bypasses them to AGND and PGND. The driver includes a 3.3V-logic enable input (pin 3) internally pulled up to V_{DD} for active high operation. To disable the IC and force a low-level output regardless of the input state, $ENBL$ must be kept low. This input is controlled by the TX MCU (MSP430F5529). [159]

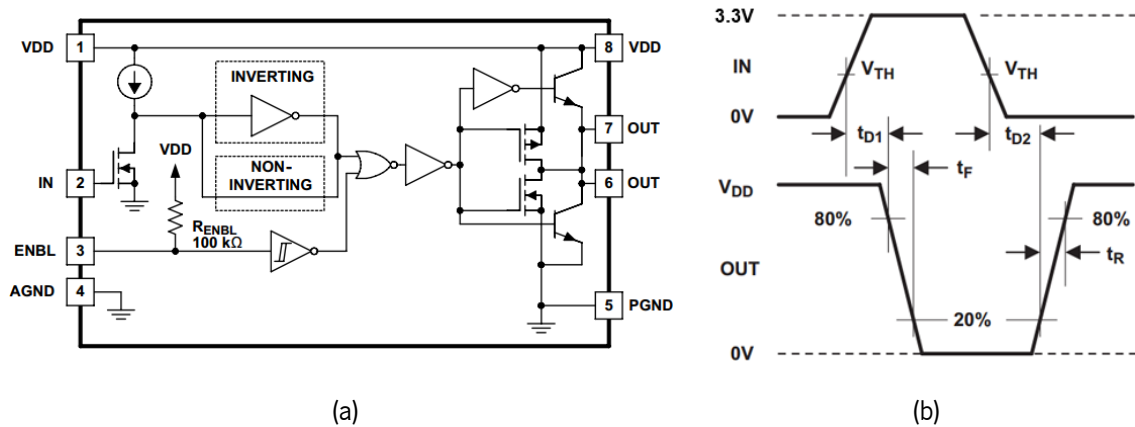


Figure 67. *UCC27321DR* MOSFET Driver: (a) block diagram and (b) switching characteristic [159].

The switching characteristic and, thus, the underlying principle, is displayed in the waveforms of Figure 67b. The input stage is driven by the direct output of the Schmitt-trigger IC since it has full sensitivity to the 3.3V-logic with short rise and fall times (<200ns). At the output, this signal is translated into an inverted signal, similarly shaped but with amplitude $V_{CC,laser}$ ($GATE_DRV$). Besides raising PWM signal amplitude, the driver introduces a maximum propagation delay of 70ns in both the rising (t_{D1}) and falling (t_{D2}) edges of the input signal that adds up to the delay induced in the previous block. As for the rise and fall times of the output signal, their typical nominal value is around 20ns. During the switching, this device can supply up to 9A peak currents at the Miller plateau.

Table 13. *SPL LL90_3* most relevant characteristics and specifications [160].

Peak wavelength, λ	895 ... 915 nm	Peak Power, $P_{peak,max}$	60 ... 80 W
Spectral FWHM, $\Delta\lambda$	7 nm	Max. Optical duty cycle	0.1%
FWHM parallel divergence, $\theta_{ }$	12° ... 18°	FWHM perpendicular divergence, θ_{\perp}	27° ... 33°
Pulse FWHM, t_{pulse}	37 ... 43 ns	Maximum pulse width	80 ns
Rise/Fall times (t_r / t_f)	7 ... 13 ns / 40 ... 50 ns	Aperture size ($w \times h$)	200 \times 100 μ m ²
Maximum charge voltage, $V_{cc,laser,max}$	20 V	Maximum Gate voltage, $V_{G,max}$	20 V
Charge voltage threshold, $U_{c,th}$	4.5 V	Switch-on gate voltage, $V_{G,on}$	5V
Operating Temperature, T_{op}	40 ... 100 °C	Temperature coefficient, TC_{λ}	0.3 ... 0.33 nm/°C

Regarding the LD module, the *OSRAM SPL LL90_3* is adopted in this design. This is a hybrid edge-emitting laser module with a nominal 905nm peak wavelength. The laser chip comprises 3 epitaxially stacked emitters and each resonant cavity is built with strained InAlGaAs/GaAs quantum-well structures. The greatest upside of this device is that, besides the low-price, it comes directly integrated with a NMOS (*Infineon's BSP318S*) driving stage and two 47nF capacitors connected in parallel between the drain and the source for pulse control [161]. The nominal characteristics and specifications of this laser are exposed in Table 13.

As evidenced in Figure 63, the gate terminal of the LD module (U10) is connected directly to the driver's output, while the charge voltage pin (drain) is connected through a 100Ω (R15) (R14) resistor to $V_{cc,laser}$. The laser emitter anode is connected to the MOSFET source terminal and the cathode to ground through a 10mΩ resistor.

The underlying principle for short light pulses generation is the charging and discharging of the capacitors. When the *GATE_DRV* signal is in a low-state (corresponding to *BP_TRIG* high), the NMOS is in cut-off and the drain-to-source resistance, R_{DS} , is extremely large, acting as an open-switch (Figure 68a). In this scenario, the capacitors, whose capacitance adds up, are charged by $V_{cc,laser}$ through R15 and R14 and the current across the laser is theoretically null. When the gate is triggered, i.e., when *GATE_DRV* rises to $V_{cc,laser}$, the NMOS is switched-on. In this region, the NMOS has an insignificant drain-to-source resistance, $R_{DS(on)} \approx 0.09\Omega$ (Figure 68b) [162]. Then, the capacitors are uncharged via the laser chip (low-ohmic load in forward direction), leading to a short current pulse in the Ampere order that induces a high-power optical pulse. Since the driver is an inverter, the emission is triggered by a falling-edge in *BP_TRIG*. This 2-step process repeats cyclically.

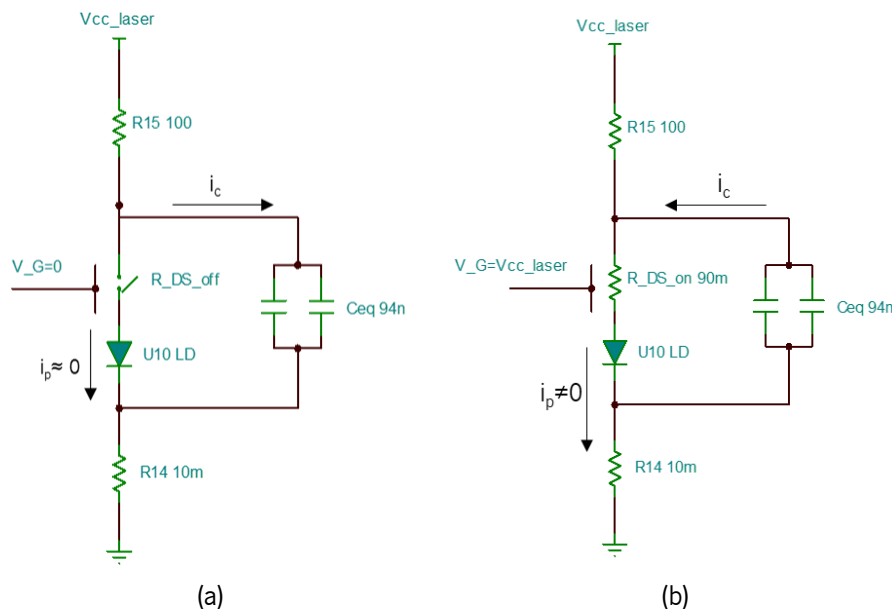


Figure 68. Equivalent circuit when the gate signal, $GATE_DRV = V_G$ is in (a) low-state and (b) high-state.

The charging resistors (R14 and R15) determine the charging current and, therefore, the time necessary to charge the capacitors, i.e., the maximum laser PRR. The FWHM of the laser pulses is determined by the value of the capacitors and limited to 40ns as shown in Figure 69a. Even though an additional tuning can be achieved from 5 to 40ns FWHM by adjusting the pulse width of *GATE_DRV*, the

peak output power decreases for pulses shorter than 20ns and, in addition and as already concluded, the minimum trigger width is limited to 150-330ns by the Schmitt-Trigger. Beyond an 80ns trigger pulse, the output shape remains unchanged but with increased fall-times comparatively to 40ns. [161]

The PRR of the laser is established by the frequency of the triggering signal and, ultimately, by the frequency of BP_TRIG . In this design, due to the restrictions in the BP_TRIG width, the output pulses will always have an 80ns width. Since the maximum duty cycle of the light output is limited to 0.1% due to heat dissipation within the laser chip, the maximum frequency for BP_TRIG is limited to 12.5kHz, through equation (2.22).

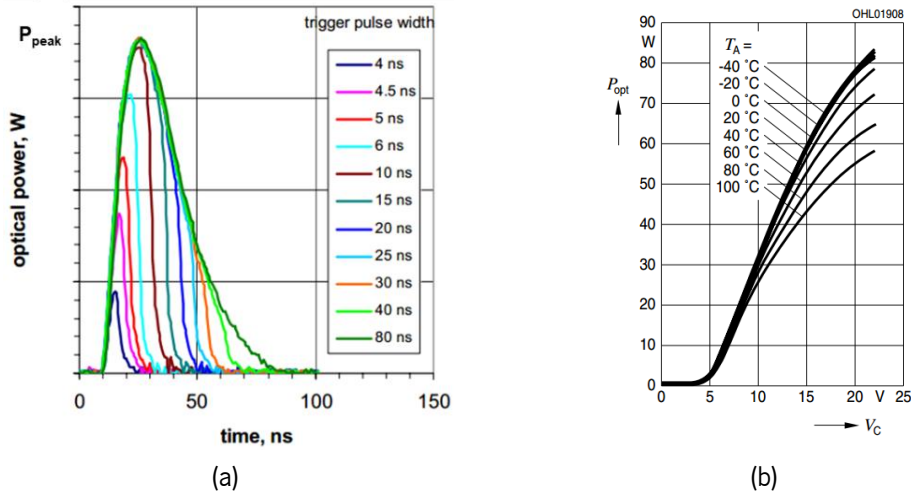


Figure 69. *SPL LL90_3* characteristics: (a) optical pulse's form for different trigger pulse widths [161] and (b) optical output power response as a function of the temperature and charge voltage (triggering pulse with 30ns and 1kHz PRR) [160].

To reinforce the qualitative explanation, a mathematical analysis can be given to better understand the system. Considering a steady operation, when the NMOS is switched-on the capacitors discharge through the LD. Nevertheless, this discharge is not complete because the LD is forward biased and maintains a constant voltage across the p-n junction of $U_{c,th}=4.5V$. Hence, this is the starting point for the charging process when the NMOS alternates to OFF. The time required for the capacitors to completely charge and reach $V_{cc,laser}$ is:

$$t_{charge} \approx (R_{14} + R_{15})C_{eq} \left[5 + \ln \left(1 - \frac{U_{c,th}}{V_{cc,laser}} \right) \right] \quad (4.6)$$

where $C_{eq}=94nF$ is the equivalent capacitance of the parallel capacitors and five time-constants are considered as setpoint for completed charging. As aforementioned, the charging velocity is defined for the most part by R_{15} , since R_{14} is negligible by comparison (10 000 times smaller), also depending on the laser charge voltage. When the previous $GATE_DRV$ off-time is guaranteed, the charge accumulated is maximized and, consequently, so does the peak power. If the NMOS is switched-on before this is accomplished, the optical power will deteriorate.

During the discharging process, the circuit time-constant differs as evident in Figure 68b, since R_{15} is no longer involved. In this situation its value is considerably smaller, $\tau=C_{eq} \cdot (R_{14}+R_{DS(on)})$, justifying

the fastest discharging and the nanosecond-order current pulse. In [73] a rough approximation for the peak current, I_p , is presented as a function of the total storage capacitance, the optical pulse width and the charge voltage:

$$C_{eq} \cdot (V_{cc,laser} - U_{c,th}) = I_p \cdot t_{pulse} \quad (4.7)$$

the left-hand term corresponds to the charge accumulated in the capacitor (complete charge), which is discharged during a time corresponding to the pulse width. This relation assumes the charge is uniformly unloaded over the whole pulse duration (squared pulse).

To operate the *SPL LL90_3*, two DC voltages are needed, namely the supply voltage for the MOSFET driver IC and the charge voltage for charging the capacitors. Since in this design, both devices are powered by the same voltage source ($V_{cc,laser}$), then one must decide its setting. First, the threshold charge voltage for the laser, $U_{c,th}$, is 4.5V and the switch-on gate voltage is specified at 5V. Furthermore, the larger the supply voltage, the larger the peak current across the laser because the charge accumulated in the capacitors is superior. Consequently, the amount of free-carriers injected in the quantum-wells is superior and the population inversion is more accentuated leading to more stimulated photons and larger output peak power (Figure 69b). Finally, looking at the maximum ratings, the highest supply voltage for the driver is found to be 16V and 20V for the laser. Hereupon, to ensure the system operates inside the specifications one decides to use $V_{cc,laser} = 15.5V$, externally supplied to the board through a separate source. For this voltage, equation (4.6) results in approximately 44 μ s while equation (4.7) holds an estimated peak current of around 13A.

As a final remark, to minimize the parasitic inductances the pins' length was minimized before soldering in the TX PCB (each centimeter of pin length introduces approximately 8nH [163]). This is an unwanted and unavoidable effect consequence of the time varying electric field induced by the pulsed current through the metallic pins. Due to the high peak-currents involved, these inductances may have a strong effect on the shape of the current pulse, namely on the rise/fall-times and ringing.

4.2. Receiver board (RX)

In what concerns with the receiver board, it is responsible for detecting the back-reflected pulses, condition and process them to extract the ToF necessary for distance estimation. This PCB is considerably more complex than the previous and incorporates a photodetector, a transimpedance amplifier, two leading-edge discriminators and two TDCs for timing.

4.2.1. Photodetection

For the returning light portion to be processed, it must be firstly converted into an electrical signal at the sensor's receiving-end. This conversion is realized by the return photodetector. Furthermore, in this architecture the reference photodetector, needed for timing purposes, similarly detects a tiny amount of the transmitted light. Although this detector is off-board, it is going to be presented herein.

4.2.1.1. Return Photodetector

As first component of the detection module in this design, the *OSRAM SFH 2400 FA* is employed as illustrated in the schematic diagram of Figure 70. This photodetector is a silicon PIN photodiode without any gain mechanism, as explained in section 2.5.4, and with a spectral sensitivity (or responsivity) of $\mathfrak{R} = 0.65\text{A/W}$ and a quantum efficiency of $\eta=0.93$ electrons/photon, at 870nm. In terms of range of spectral sensitivity, the $1\times 1\text{mm}^2$ sensitive chip is protected with a dark package to filter visible radiation and avoid the need for additional optical filters in this spectrum range, leading to an overall 750nm to 1100nm sensitive interval with a nominal peak at 900nm. Regarding the power supply, this device operates under a maximum reverse bias of 20V to generate an electric current proportional to the flux of incident photons with a typical power dissipation of 120mW. To keep coherency with the transmitter, the reverse voltage is chosen to be $V_{cc,laser}=15.5\text{V}$, also supplied by an external voltage source. Concerning the response time, this photodetector has 5ns rise and fall times to completely match the laser pulses, allowing a full amplitude response. Finally, the dark current noise reaches a maximum of 5nA at 20V reverse voltage and 25°C. This noise source is temperature-dependent and increases with an increase in the previous due to a rise in the number of thermally-generated carriers. [164]

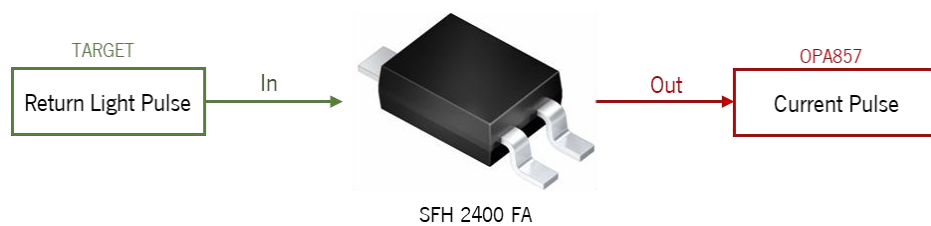


Figure 70. Schematic representation of the photodetection process.

4.2.1.2. Reference Photodetector

To measure a minor portion of the transmitted light, a *ThorLab's DET10A/M* silicon PIN photodetector is adopted. This photodetector has a circular sensitive area with diameter $\varnothing 1.0\text{mm}$, a sensitivity ranging from 200 to 1100nm with a peak of $\mathfrak{R}=0.44\text{A/W}$ at 730nm and $\mathfrak{R}\approx 0.2\text{A/W}$ at 905nm. The detector is reversely biased at 10V by an integrated 12VDC battery and the 1 nanosecond rise time is sufficient to completely respond to the 80ns laser pulses. To convert the generated photocurrent pulse into a voltage pulse, a load resistor is used (Ohm's Law). As recommended to maximize the bandwidth while minimizing parasitic oscillations and amplitude losses, a 50Ω low-inductance coaxial cable is picked to conduct the signal from the detector's 50Ω-BNC output terminal to the RX PCB, selecting a 50Ω BNC terminator (*FT500* by *ThorLabs*) to match the cable to its characteristic impedance and maximize the signal delivered to the board. Further, since the termination is matched, the length of the coaxial cable does not have a remarkable impact on the response. The simplified process is shown in Figure 71. The resulting analog pulse (*laser_on*) is then conducted to the input of a leading-edge discriminator to generate a STOP event for TDC1 and indicate the beginning of an effective measurement cycle. The electrical connection to the board is evidenced in Figure 76. [71]



Figure 71. Simplified representation of the process for generating the reference voltage pulse.

4.2.2. Transimpedance Amplifier

Since the TDC only accepts voltage signals as input, the return current pulse must be converted into an analog voltage pulse (I-to-V conversion). Moreover, due to absence of an internal gain mechanism in the photodetector, a low-level current signal is expected and it must be amplified to hold useful voltage values. In principle, a simple resistor would be enough to perform this conversion according to the Ohm's law and the gain could be adjusted through its resistance. Whatsoever, by increasing the resistance, the response time would be greatly affected because the latter would pair up with the photodiode's output capacitance to attain a larger time-constant. To avoid poor gain and/or slow response, the photodiode's output current is directly applied to the input of an *OPA857IRGTR* transimpedance amplifier (U7). This IC isolates the photodiode from the output and decreases the impedance seen by it allowing for enhanced response time while simultaneously admitting a larger resistor and improved SNR.

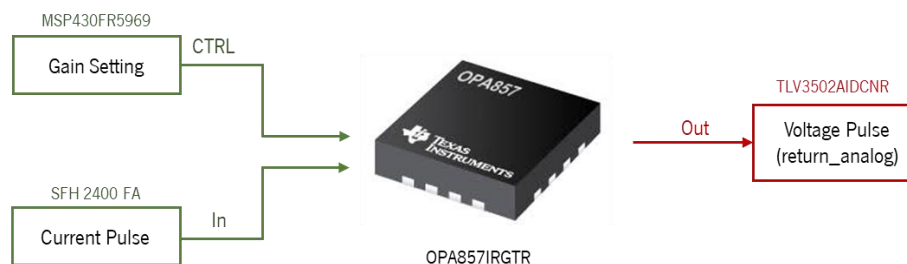


Figure 72. Simplified current-to-voltage conversion process.

The block diagram of the TIA adopted in this design is displayed in Figure 73 and it consists of a selectable feedback resistor that sets the gain of the AmpOp according to equation (2.32) and a feedback capacitor to maintain stability and prevent undesired oscillations. The device has two distinct gain configurations, controlled via the CTRL pin, to dynamically adjust the output to the input current levels: setting the pin high (logic '1' = 3.3V) results in a transimpedance gain of $R_F=20\text{k}\Omega$; setting this pin to low results in a gain of $R_F=5\text{k}\Omega$. Naturally, each resistor has a distinct feedback capacitor to keep a constant adjustment. [165]

Besides the TIA itself, the IC integrates three more blocks: a reference voltage (REF) block, a test structure (TEST) block and an internal clamping (CLAMP) block. The REF block provides an adequate DC reference voltage for both the input and output. This reference, V_{ICR} , is set to 5/9 of the power supply and is directly connected to the common-mode voltage output (OUTN) through a 25 Ω resistor and to the non-inverting input of the TIA AmpOp through a RC filter to reduce the noise contribution. The TEST block

allows the characterization of this IC without the PD and using standard lab equipment. The clamping circuit is implemented through two ESD diodes connected to the power rails ($+V_S$ and GND) to assure a quick recovery after saturation and provide a moderate protection to input overdrive. [165]

Since the TIA has a class-A output stage, the usable output swing is limited between V_{ICR} , expressed as an offset in the output, and the negative rail. Because of the internal clamping diodes, the negative swing cannot go closer than 0.6V to the rail. It is noteworthy that the internal 25Ω resistors reduce the overall gain. For e.g., for a 500Ω differential load, the gain is reduced by 0.83dB to $18.2k\Omega$ and $4.5k\Omega$ in each configuration. [165]

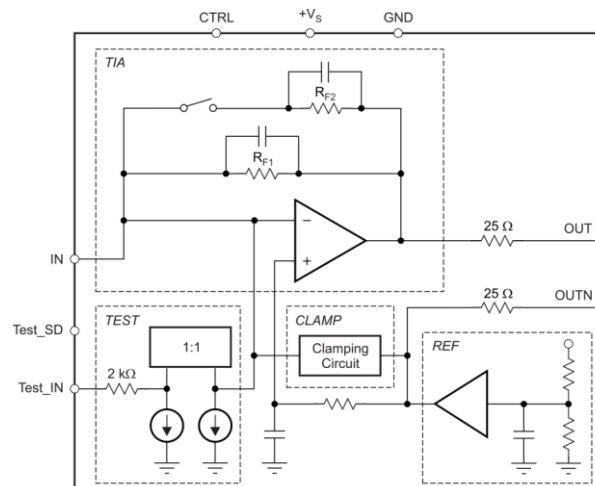


Figure 73. *OPA857*'s functional block diagram [165].

In Figure 74, the electric diagram of the amplifying block is presented to evidence how the TIA is integrated in this LiDAR design, in conjunction with the return photodetector (D1). The photodiode is directly connected to the TIA input (IN pin) and the reverse voltage, $V_{cc,laser}$, is bypassed by a $4.7\mu\text{F}$ capacitor to avoid spurious oscillations from propagating to the TIA output pin, OUT (*return_analog*). The gain is controlled by the RX MCU via the CTRL pin that is pulled-up to the power supply ($+V_S$) for a default gain of $20k\Omega$. This microcontroller also controls the TEST inputs, always disabled for normal operation with the photodiode as current source (Test_SD to GND and Test_IN to $+V_S$). The IC power supply is bypassed to GND by a parallel of two $0.1\mu\text{F}$ ceramic capacitors.

Although nominally the RX MCU supplies the board with 3.3VDC, in practice this value is found to be around $+V_S = BP_{3.3} \approx 3.5\text{V}$. In these conditions, the output common-mode voltage is about 1.94V ($5 \times V_S / 9$) and the maximum output amplitude about 1.34V (dynamic range of $\approx 3:1$). Additionally, as already discussed, this amplifier is an inverter and thus the positive current peaks are translated into a *return_analog* negative pulses, i.e. with a falling-edge as leading-edge and a 1.94V baseline. The entire 1.34V swing corresponds to a maximum nominal current input of $67\mu\text{A}$ for maximum gain and $268\mu\text{A}$ for the minimum gain, above which the output saturates (non-linear effect).

To conclude, alongside with the photodetectors, the *OPA857* shall also offer a large-enough bandwidth to ensure a sufficiently fast response to detect the short current pulses. As the nominal bandwidth, B , is superior to 100MHz [165], the response time is inferior to 3.5ns as calculated through equation (2.29). Hence, the TIA can indeed timely respond to the current pulses, preserving its shape.

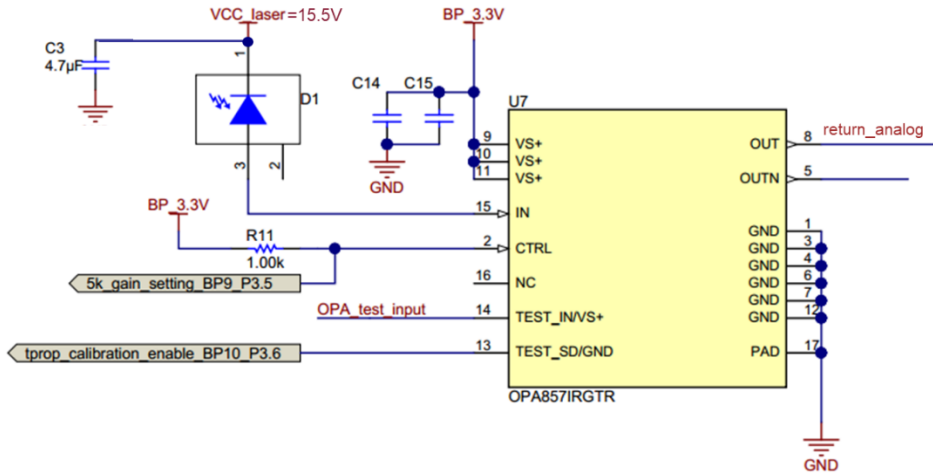


Figure 74. Electrical schematic of the system’s amplifier stage (adapted from [156]).

4.2.3. Leading-edge Discriminator

The following stage is the conversion of the analog pulses coming from the TIA (*return_analog*) and from the reference detector (*laser_on*) to voltage pulses with the required characteristics to induce well-defined and discernible STOP events on both TDCs. To execute this conversion, a leading-edge discrimination technique is implemented via hardware. The leading-edge discriminator is the most straightforward technique and consists on a comparator that triggers a digital pulse whenever the input pulse crosses a fixed voltage threshold. Since two TDCs are used in this architecture, this discrimination must be applied both to the return pulse and the reference pulse. Whatsoever, because in principle the transmitted laser pulses are uniform either in amplitude and shape (rise and fall times), the timing is simpler for the reference path.

This receiver’s block can be divided in two phases. In a first phase, the constant threshold values are set independently for both discriminators. In the subsequent phase, the analog pulses are compared with the previously defined levels to yield the final STOP pulses. This process is represented in Figure 75.

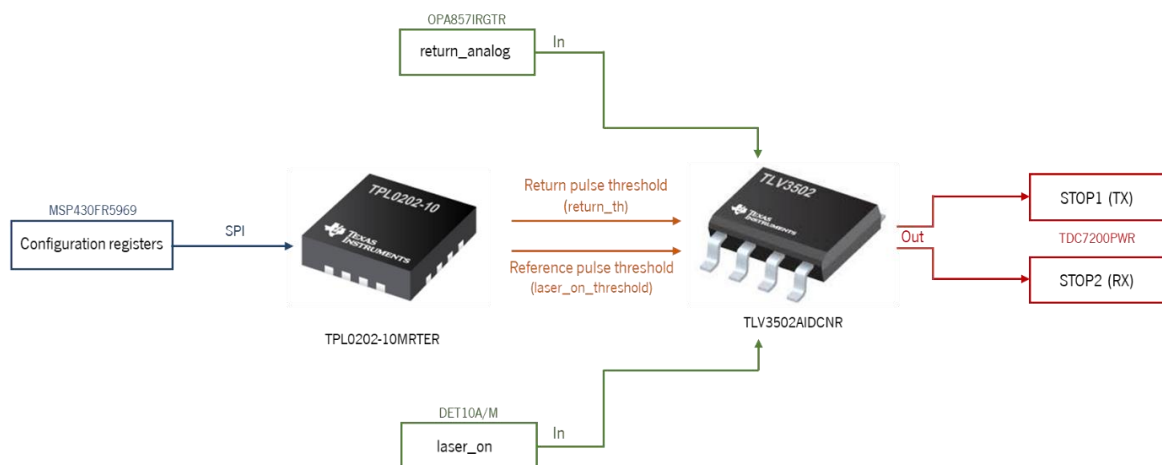


Figure 75. Leading-edge discriminator architecture.

Beginning with the first phase, the fixed thresholds are generated by a digital potentiometer (DPOT), the *TPL0202-10MRTER* manufactured by *Texas Instruments*. This IC includes two independent potentiometers (A and B) with a 256-position resolution and a 10kΩ end-to-end resistance each. Both devices are used as three-terminal potentiometers to function as voltage-dividers, with the high (H) and low (L) terminals resembling the fixed terminals of a mechanical potentiometer. The wiper (W) position is digitally controlled independently via SPI by writing a 1-byte sequence to the wiper register (WR). The *TPL0202* has a non-volatile memory (EEPROM) used to store the wiper position and automatically recall it upon power-up. [166]

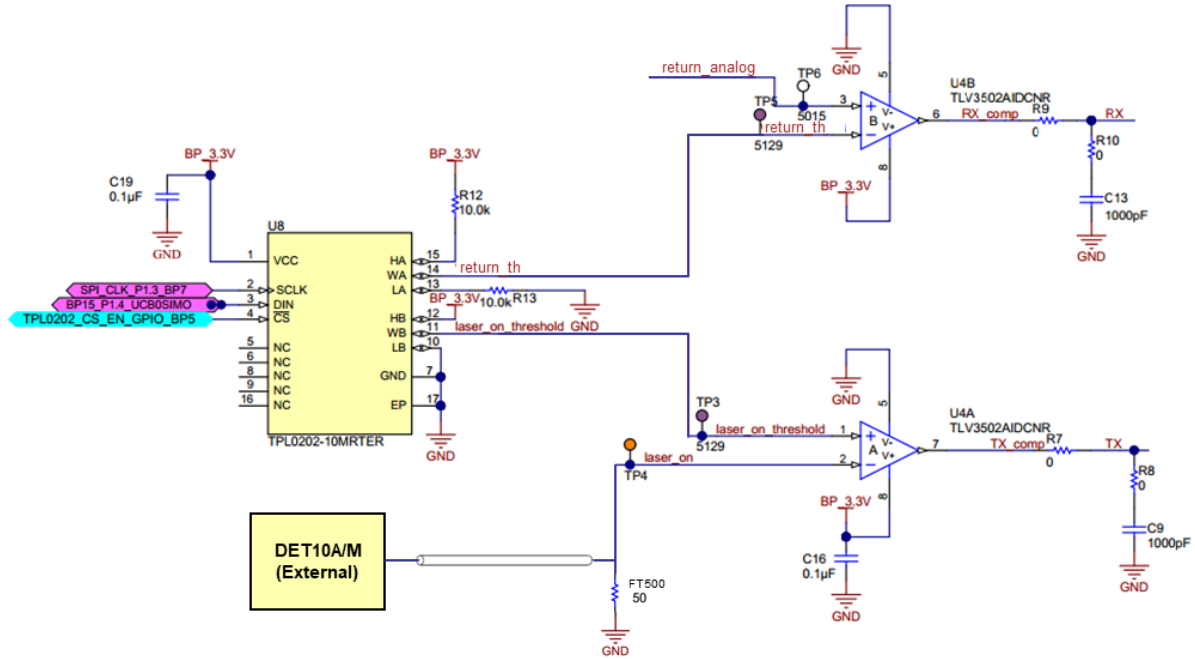


Figure 76. Electrical schematic of the leading-edge discriminator (adapted from [156]).

To better understand how the threshold is defined in this particular system, one will refer to the electrical diagram in Figure 76. The DPOT is supplied at $+V_s \approx 3.5\text{V}$ and is configured through the SCLK, DIN and CS SPI inputs as it is going to be explained ahead. The pins HA, WA, LA and HB, WB, LB are the terminals of each potentiometer. In this configuration, the outputs on the respective wiper terminals can be expressed by the voltage-dividers:

$$V_{th,A} = \text{return_th} = +V_s \cdot \frac{R_{WL,A} + R_{13}}{R_{12} + R_{13} + R_{HL,A}} = +V_s \cdot \frac{R_{WL,A} + 10}{30} \quad (4.8)$$

$$V_{th,B} = \text{laser_on_threshold} = +V_s \cdot \frac{R_{WL,B}}{R_{HL,B}} = +V_s \cdot \frac{R_{WL,B}}{10}$$

where all the resistances are in kΩ and the variables $R_{WL,x}$ ($X=A, B$) are set by the corresponding wiper register, W_x . Since the previous register has one byte, it can take decimal values between 0, indicating a W terminal closer to L, and 255. Hence, the variable resistances can be written as:

$$R_{WL,x} = 10 \cdot \frac{W_x}{256} \text{ [k}\Omega\text{]} \quad (4.9)$$

Hence, replacing $+V_S$ in equation (4.8) and taking the maximum and minimum values for the wiper registers, yields the following thresholds' limits:

$$\begin{aligned} V_{th,A} &= return_th \approx 1.17V - 2.33V \\ V_{th,B} &= laser_on_threshold \approx 0V - 3.49V \end{aligned} \quad (4.10)$$

As one can deduce, the fact that potentiometer A has two additional 10kΩ resistors in series shortens the configurable interval but, whatsoever, increases the resolution. In practice, the threshold is usually set just above the noise level to detect exclusively real events and avoid false triggering. For this reason, it is more useful to rewrite the equations above to directly calculate the wiper registers' value depending on the intended threshold:

$$\begin{aligned} W_A &= nint \left[\frac{256}{10} \cdot \left(\frac{V_{th,A}}{V_S} \cdot 30 - 10 \right) \right] \\ W_B &= nint \left[\frac{256}{10} \cdot \frac{V_{th,B}}{V_S} \cdot 10 \right] \end{aligned} \quad (4.11)$$

where $nint[x]$ is the nearest integer function towards $-\infty$ (floor rounding).

Advancing to the second phase, the voltage pulses are compared with the established threshold. This comparison is performed in the *TLV3502AIDCNR* IC. This integrated circuit includes two rail-to-rail comparators with a nominal 4.5ns propagation delay and is supplied at $V_+ = +V_S = 3.5V$ and $V_- = GND$. The output digital signals are CMOS and TTL compatible with rise and fall times of 1.5ns, achieving a maximum toggle frequency of 80MHz, manifestly enough considering the laser maximum PRR of 12.5kHz. [167]

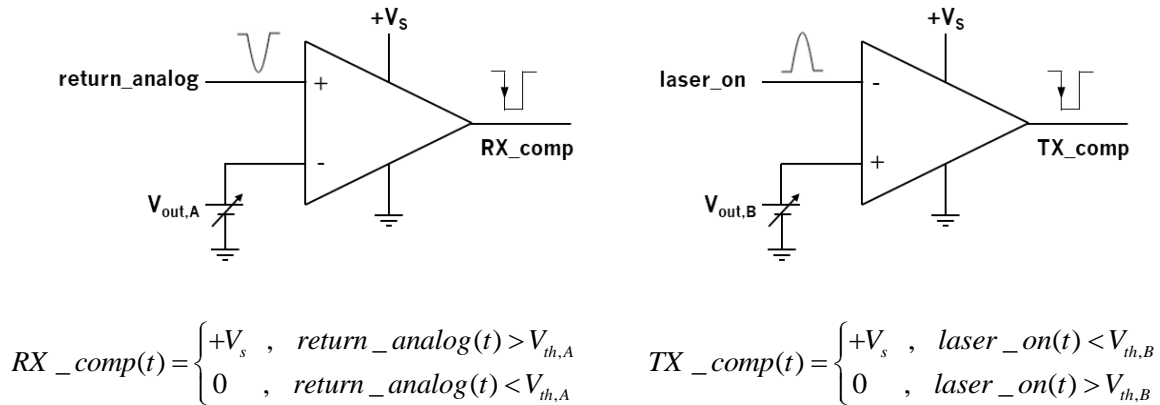


Figure 77. Leading-edge discrimination.

As aforementioned, *return_analog* is a pulsed signal with a falling-edge as leading-edge, while *laser_on* is a voltage signal with a rising-edge as leading-edge. Moreover, the former signal is inputted at the non-inverting terminal of one comparator and the latter to the inverting terminal of the other. Therefore, whenever *return_analog* falls below *return_th*, the output (*RX_comp*) commutes from $+V_S$ to 0V and restores the initial value when *return_analog* rises again above *return_th*. For *laser_on*, the situation is similar and the output (*TX_comp*) switches from $+V_S$ to 0V when the latter rises above *laser_on_threshold* and commutes again to a high-level when *laser_on* falls below the threshold, i.e.,

when the laser pulse is completely transmitted. Both cases are portrayed in Figure 77. As a result, both RX and TX pulsed signals, to be applied directly to the TDCs, have a falling-edge as leading-edge, which is going to be used to STOP the time counting.

To finalize, the outputs of the comparators are not directly connected to the TDCs. Instead, a 1000pF (C_{13} and C_9) capacitor is connected between each one of the previous and GND to prevent ringing in the STOP signals RX and TX . These capacitors oppose to abrupt changes in voltage by charging and discharging. However, as a major side-effect, the fall and rise-times of the signals is substantially increased. The 0Ω resistors serve only as wire links between traces on the PCB.

4.2.4. Time-to-Digital Converters

To determine the distance between the target and the sensor, the Time-of-Flight of a laser pulse is estimated. As light travels at around 0.3 meters per each nanosecond, the requirement on resolution for the time-measuring unit is very strict, since the range accuracy, δd , is directly affected by the uncertainty in measuring the time delay, δt [56]:

$$\delta d = \frac{1}{2} c \cdot \delta t \quad (4.12)$$

In addition, to identify times and pulses in the nanosecond order with a reasonable accuracy, a device working with picosecond resolutions is necessary. Accordingly, in this design the ToF is estimated using two $TDC7200$ ICs with a nominal accuracy 28ps [168]. This is the hardware component that ultimately limits the precision, if all the remaining possible artefacts can be eliminated.

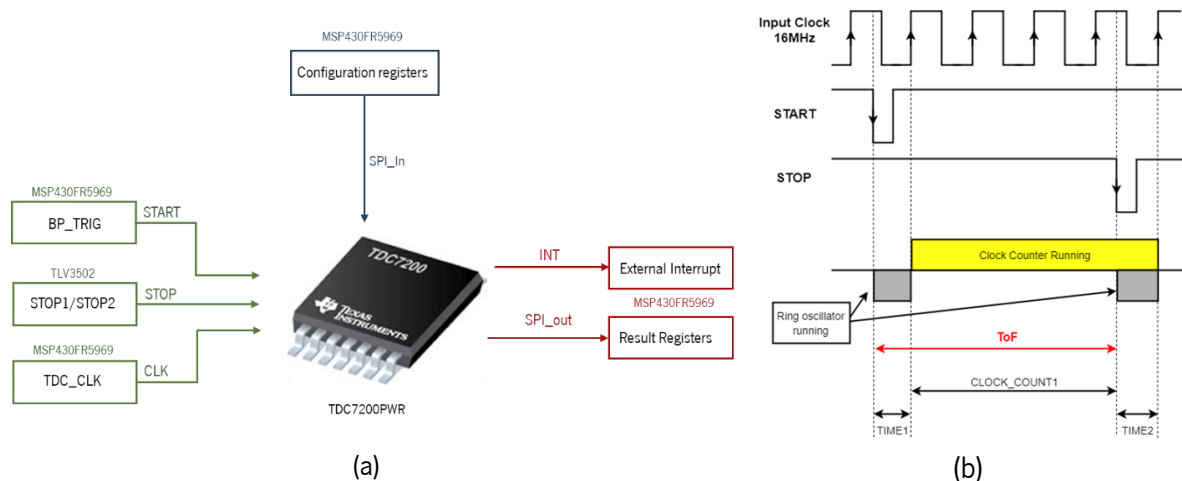


Figure 78. TDC7200 functioning principle: (a) schematic integration on the system where two TDCs are used operating in a similar manner; (b) measurement mode 2 (adapted from [168]).

4.2.4.1. Operation and Integration

In this context, the TDCs are used as stopwatches to measure the time between a single START event unleashed by an edge in the START pin and a single subsequent edge on the STOP pin. The START signal for both TDCs is, as already referred, the falling-edge on BP_TRIG , the same transition triggering the laser pulses. As for the measurement end, the TDC1 (U3) is stopped by the falling-edge of the TX pulse and the TDC2 (U6) by the analogous edge on the RX pulse, both arising from the timing discrimination

of, respectively, the reference pulse and the return pulse. The electrical schematic of Figure 79 shows the TDCs integration in the system. The ceramic capacitors C_{11} , C_{12} , C_5 , C_6 are applied for external decoupling and are chosen accordingly to the indications explicit in the datasheet [168].

Each device has two measurement modes: Mode 1, to perform measures from 12ns to 500ns, and Mode 2 to perform measures from 125ns to 8ms. As recommended in the TIDA-00663 guide [156] and because in this design there is a deliberately introduced delay with a 150ns minimum to add to several other physical and uncontrollable delay sources, such as cabling, the Mode 2 is adopted for both TDCs. In this mode, the TDCs use an external clock source to support the time counting. Besides, this clock is used by all the digital circuits integrated in this device. Following the recommendations for optimal performance and a minimized standard deviation (around 35ps), a 16MHz clock is supplied by the MSP430FR5969 through the CLOCK pin (*TDC_CLK*). [168]

The time measurements rely on two counters with distinct underlying time-bases, as suggested in Figure 78b. First, the internal ring oscillator of the TDCs counts fractional parts of the total measured time, starting from when it receives the START signal until the first rising edge of *TDC_CLK*. The count result is stored in the TIME1 register. Posteriorly, the internal ring oscillator switches off and the clock counter counts the number of integer *TDC_CLK* cycles until the STOP is received. The total count is stored in the CLOCK_COUNT1 register. Finally, the internal ring oscillator starts counting again from the STOP until the next rising edge of the *TDC_CLK*. This last result is stored in the TIME2 register. The TDCs support several consecutive STOPS for a single START but this feature has no interest in these circumstances. [168]

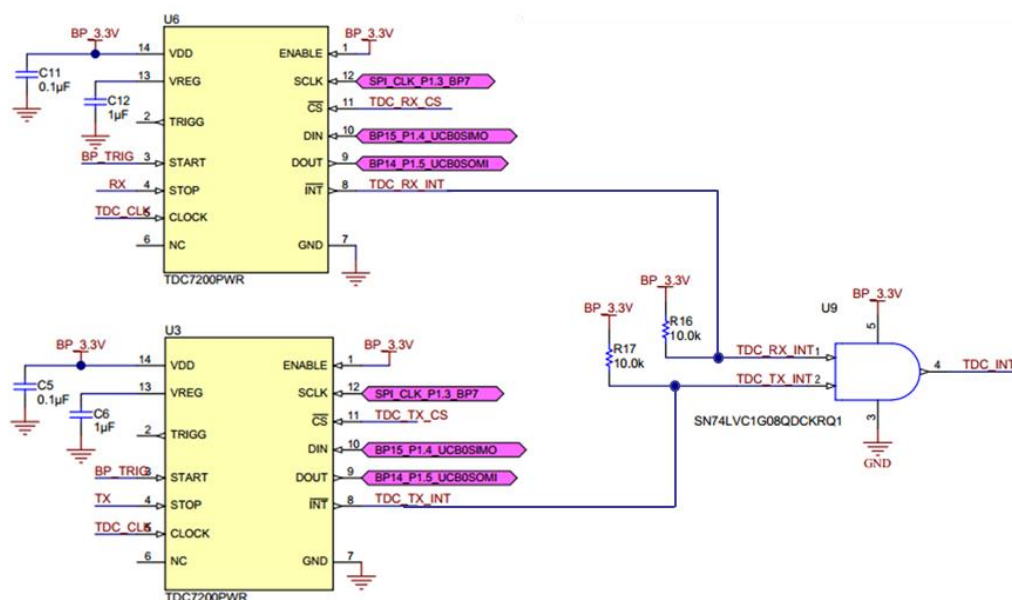


Figure 79. Electrical diagram (adapted from [156]).

The internal time-base is represented through the LSB value of the TIME1 and TIME2 registers and has a nominal value of 55ps (corresponding to 1.65cm). However, its actual value varies depending on environmental variables such as temperature and systematic noise. Since this variation can introduce a significant error in the measurement result, a calibration is performed to continuously calculate the actual Least Significant Bit (LSB) value and compensate for these errors. The calibration is always carried out

in real-time at the end of each measurement cycle and consists of two stages. In the first, a single TDC_CLK period is measured using the internal time, while the second consists on the measurement of 2 TDC_CLK periods as set in the $CALIBRATION2_PERIODS$ bits in the $CONFIG2$ register. The results are stored, respectively, in the $CALIBRATION1$ and $CALIBRATION2$ registers. [168]

As seen in the electric schematic, the $ENABLE$ pin of both TDCs is connected to $+V_S=3.5V$ to allow an uninterrupted operation. When the device is turned-on, a 1.9ms wait time is required for the TDC to fully settle. After this time has passed, the TDC is ready to start a measurement as soon as the $START_MEAS$ bit is set in the $CONFIG1$ register. Posteriorly, the $START$ pin is enabled and the TDC waits for the $START$ pulse edge. After the blank time has passed, the $STOP$ pin waits to receive a single pulse. The measurement is terminated once the $STOP$ signal is received or when the clock counter has reached a pre-defined overflow value. In either case, the $INTB$ pin of the respective TDC reacts by transitioning from high-to-low to indicate the measurement cycle has terminated. [168]

The overflow condition is set in the 1-byte $CLOCK_CNTR_OVF_H$ (Most Significant Byte, MSB) and $CLOCK_CNTR_OVF_L$ (Least Significant Byte, LSB) registers for the clock counter and in the 1-byte $COARSE_CNTR_OVF_H$ and $COARSE_CNTR_OVF_L$ for the coarse counter [168]. The final condition for each is given by multiplying the MSB by 2^8 and summing the result to the LSB to hold a 2-byte word. By default, these registers are set to $0xFF$, holding a decimal count of 65536 in the respective time base.

Since the result registers ($TIME1$, $TIME2$, $CLOCK_COUNT1$, $CALIBRATION1$, $CALIBRATION2$) can only be read after the measurement cycle has been completed, the $INTB$ transition is used to activate an external interrupt in the RX MCU to trigger the transmission. Hereby, the $INTB$ pin of each TDC (TDC_RX_INT and TDC_TX_INT) is inputted at an AND-Gate IC ($SN74LVC1G08QDCKRQ1$). These inputs are pulled up to $+V_S$ and, whenever the $INTB$ in either one of the TDCs transitions to low, the output (TDC_INT) interrupts the MCU. After the results are retrieved, the MCU can then start a new measurement by setting the $START_MEAS$ bit again. This will clear all the result registers and reset the interrupts. The ToF between the $START$ and the $STOP$ in each TDC can be calculated using the succeeding equation [168]:

$$ToF_n = normLSB(TIME1 - TIME2) + (CLOCK_COUNT1) \times 62.5 \quad [ns]$$

$$normLSB = \frac{62.5}{calCount} \quad [ns] \quad (4.13)$$

$$calCount = \frac{CALIBRATION2 - CALIBRATION1}{CALIBRATION2_PERIODS - 1}$$

where the index $n=1,2$ indicates to which TDC the calculation is referred and 62.5ns is the TDC_CLK period. Finally, to obtain the effective ToF, the time measured by TDC1 must be subtracted to the time measured by TDC2. Additionally, an offset, ToF_{cal} , is added or subtracted to the total ToF for calibration because there are delays exclusive of each path (reference and return) that must be corrected. This adjustment process is explained in the next chapter.

$$t_D \equiv \Delta ToF = ToF_2 - ToF_1 \pm ToF_{cal} \quad (4.14)$$

where $t_D \equiv \Delta ToF$ is the effective Time-of-flight.

4.2.4.2. Pulse Requirements

The *TDC7200* has some restrictions to be considered. The prime is that, in Mode 2, the minimum time between the START and STOP signals must be, at least: [168]

$$T_{2_{STARTSTOP_Min}} = 2 \times T_{TDC_CLK} = 125ns \quad (4.15)$$

where T_{TDC_CLK} is the external clock period. In practice, this time manifests as a blank time in the ToF measurement. Whatsoever, this design overcomes this restraint by adding the initial delay. The second requirement for the START and STOP pulses is they must both have a minimum width of 10ns to be recognized. Since the voltage input high-level goes from $0.7 \times V_S \approx 2.45V$ to $V_S = 3.5V$ and the low-level from 0 to $0.3 \times V_S \approx 1.05V$, the direct pulses from the TIA output and the reference photodetector could not be directly used as STOPS owed to the insufficient amplitude.

4.2.4.3. Configuration

Both TDCs are configured at power-up and read at the end of each measurement cycle via SPI. Although each device has 10 read/write configuration registers with 1-byte capacity, only half of them are handled, while the others are left at their default setting due to the unimportant role in the system functioning. The configured registers are exposed in Table 14 and the nomenclature of each bit is illustrated in Figure 80.

Table 14. TDCs configuration registers and defined values in binary.

Register	Configuration	Description
CONFIG1	0b10111011	Calibration always performed at the end, parity bit disabled, measurement stopped and started on the falling-edge of the respective signal, mode 2, start new measurement set (after a measure cycle, this bit is reset to 0 and it must be rewritten)
CONFIG2	0b00000000	2 periods for Calibration 2, 1 measurement cycle only (no multi-cycle averaging), single STOP
INT_MASK	0b00000101	Enable clock counter overflow and new measurement interrupts, disable coarse counter overflow interrupt
CLOCK_CNTR_OVF_H	0b00000000	Set the CLOCK_CNTR_OVF condition to 12 for TDC1 and 16 to TDC2 corresponding to, respectively, 750ns and 1000ns
CLOCK_CNTR_OVF_L	0b00001100 (TDC1) 0b00010000 (TDC2)	

Both TDCs are configured in a similar manner except for the overflow condition. The coarse counter overflow condition is left at default because TIME1 and TIME2 only serve to measure fractional parts of TDC_CLK and must not interfere with the measurement process by activating the respective overflow interrupt. On the other hand, the clock counter overflow condition is used to limit the temporal window in which the STOPS are expected and optimize the time management. In a default configuration, if no STOP is detected, the clock counter will count up to 65536 until the interrupt is activated to indicate the end of the cycle, corresponding to a time of approximately 4ms and a range above 1000km. By limiting

this time interval, the time unnecessarily wasted waiting for the interrupt can be minimized in the latter scenario. Furthermore, since both TDCs are configured for a single STOP with no averaging, the laser PRR and, thus, the point rate, can be maximized. For TDC1, the overflow condition is set to 750ns determined experimentally by the delay between *BP_TRIG*'s falling-edge and the discrimination of the reference pulse with an added safety margin. As for TDC2, the overflow condition is set to 1000ns leaving a 250ns margin between STOP1 and STOP2 for the effective ToF. This margin translates into a 75m travelled distance and a 37.5m separation between sensor and the target.

7	6	5	4	3	2	1	0
CONFIG1: Configuration Register 1 (Address=0x00)							
FORCE_CAL	PARITY_EN	TRIGG_EDGE	STOP_EDGE	START_EDGE	MEAS_MODE		START_MEAS
R/W-0h	R/W-0h	R/W-0h	R/W-0h	R/W-0h	R/W-0h	R/W-0h	R/W-0h
CONFIG2: Configuration Register 2 (Address=0x01)							
CALIBRATION2_PERIODS		AVG_CYCLES			NUM_STOP		
R/W-0h	R/W-1h	R/W-0h	R/W-0h	R/W-0h	R/W-0h	R/W-0h	R/W-0h
INT_MASK: Interrupt Mask Register (Address=0x03)							
Reserve	Reserve	Reserve	Reserve	Reserve	CLOCK_CNTR_OVF_MASK	COARSE_CNTR_OVF_MASK	NEW_MEAS_MASK
R/W-0h	R/W-0h	R/W-0h	R/W-0h	R/W-0h	R/W-1h	R/W-1h	R/W-1h
CLOCK_CNTR_OVF_H: Clock Counter Overflow Value High (Address=0x06)							
CLOCK_CNTR_OVF_H							
R/W-1h	R/W-1h	R/W-1h	R/W-1h	R/W-1h	R/W-1h	R/W-1h	R/W-1h
CLOCK_CNTR_OVF_L: Clock Counter Overflow Value Low (Address=0x07)							
CLOCK_CNTR_OVF_L							
R/W-1h	R/W-1h	R/W-1h	R/W-1h	R/W-1h	R/W-1h	R/W-1h	R/W-1h

Figure 80. Configured registers summary and bits nomenclature (adapted from [168]).

4.3. Microcontroller Units

To control the system, two microcontroller units from *Texas'* MSP430 family are adopted: the MSP430FR5969 controls the RX board and the MSP430F5529 controls the TX board. Due to restrictions in the TIDA-00663 design, the referred microcontrollers are used as an integral part of the respective MSP430 LaunchPad™ Evaluation Modules with respective part-numbers MSP-EXP430FR5969 and MSP-EXP430F5529, instead of standalone chips. Both the RX and TX PCBs have two 10×2 receptacles to directly plug-in on the headers incorporated on the launchpad boards.

Besides the previous design-imposed restriction, the use of these Development Kits is an advantageous option because it offers an easy-to-use environment by integrating an on-board eZ-FET emulator to enable programming, debugging and communication with the computer via USB, and to provide power to the target MCU through the earlier mentioned DC-DC Converters. Additionally, the boards feature LEDs and buttons for simpler and intuitive user interfaces. Both boards are connected to a dedicated USB-port via a micro-USB connector. [169]

The MCUs were programmed in C++ language through the open-source prototyping platform *Energia*. This software resulted from the expansion of the Arduino/Wiring framework to the *Texas Instruments* MSP430-based launchpads and includes a user-friendly IDE (Integrated Development Environment) backed by the *mspgcc* compiler.

The complete final code developed for each board is in 'Appendix II – Final Codes' properly commented. It consists, basically, on two main functions: *void setup()* executed at the beginning to configure the system; *void loop()* executed continuously in loop. Herein, one will only introduce the essential code excerpts and the flowcharts.

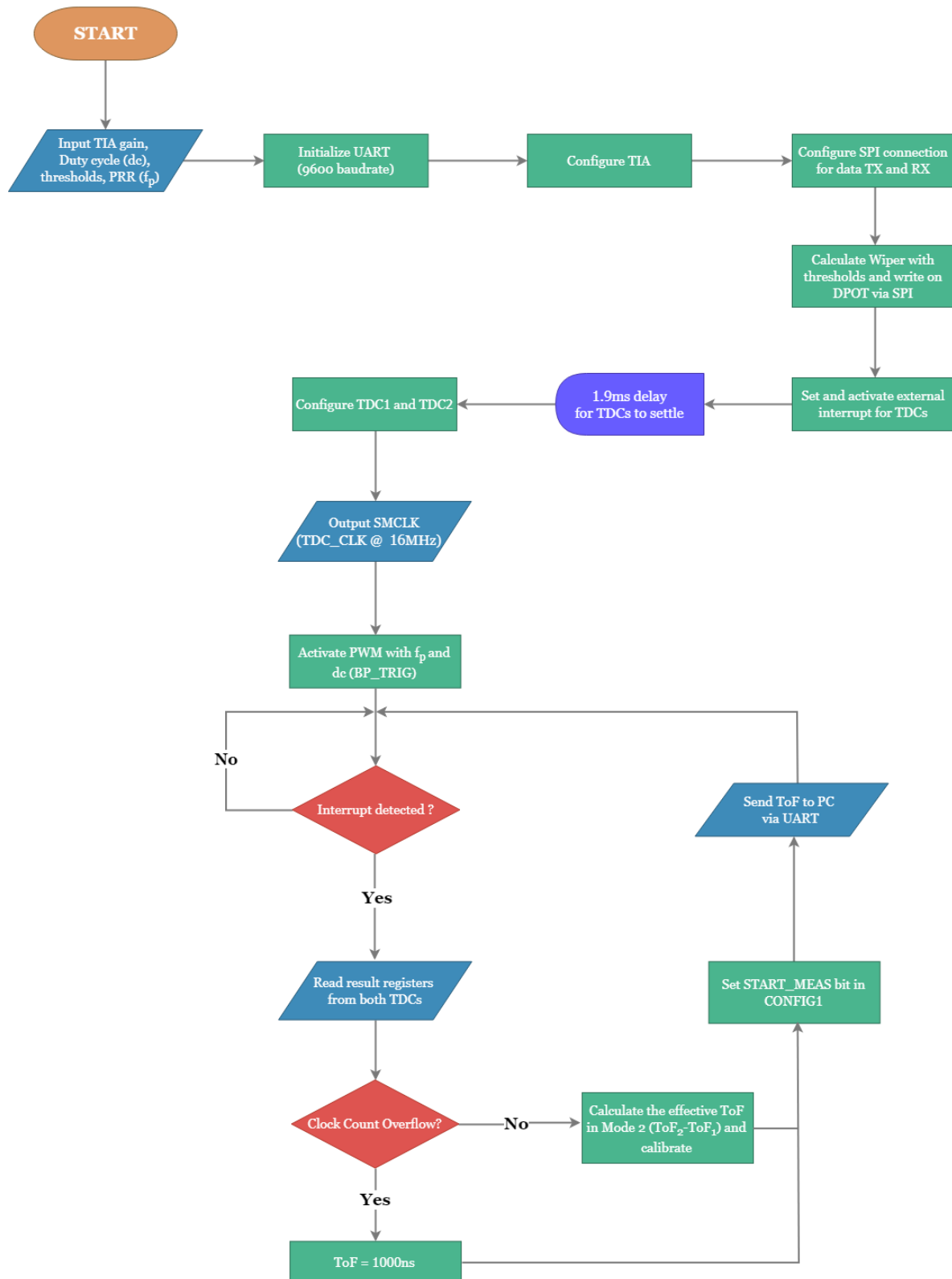


Figure 81. Flowchart of the RX MCU program.

4.3.1. MSP430FR5969 (RX MCU)

The RX MCU is essentially the system’s brain and it both controls the emission and detection modules and processes the data. The whole sequential procedure starting from the components’ configuration to the periodical acquisition of ToF of measurements and subsequent processing is illustrated in the self-explanatory flowchart of Figure 81. This diagram represents concisely the microcontroller’s program flow. It is important to note that, after configuration, the device cyclically performs the measurements until the MCU is disconnected from the power-source (in this case, the computer). The main and more relevant aspects of the code are to be discussed next.

Regarding the CPU core characteristic, the MSP430FR5969 features an embedded 64KB FRAM (Ferroelectric Random-Access Memory), a non-volatile memory with ultra-low power consumption, high endurance and high-speed write access. The device supports speeds up to 16MHz and has integrated peripherals for SPI, UART and I2C communication, five 16-bits timers and a 12-bits ADC. [169]

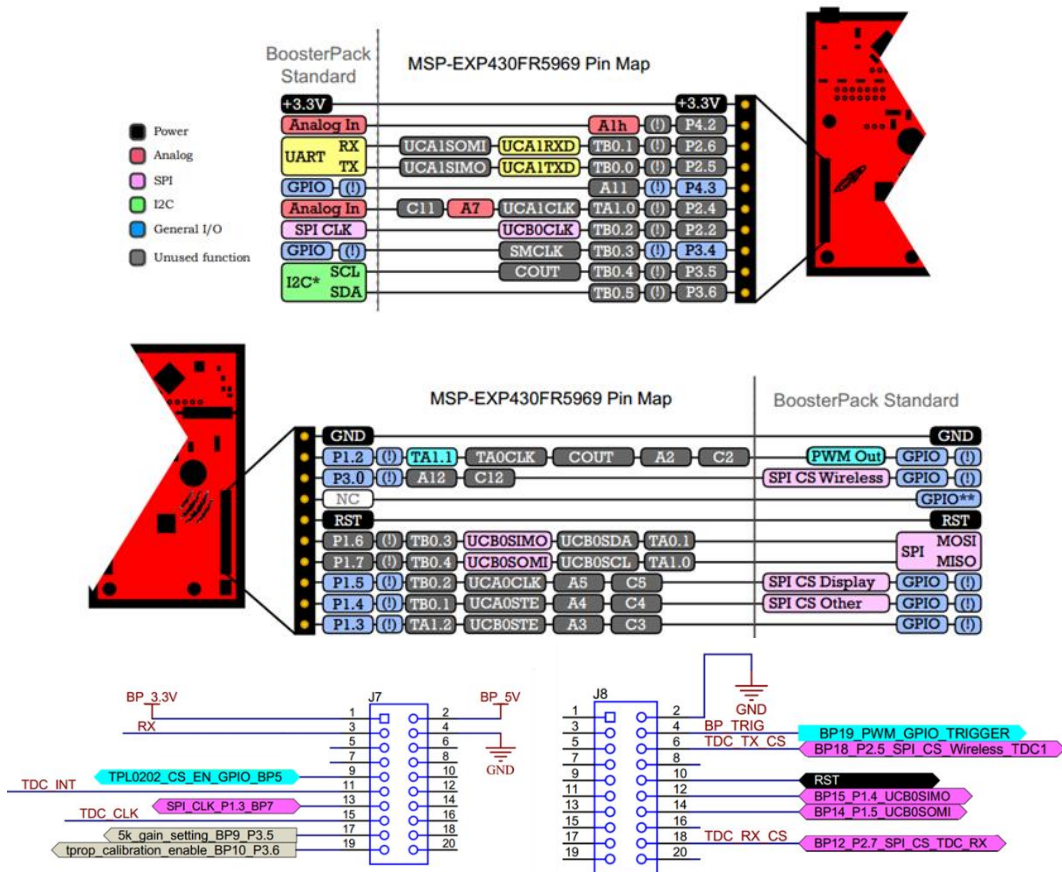


Figure 82. MSP-EXP430FR5969 connectors pinout (top) [169] and RX PCB headers pinout (bottom) [156].

Since this launchpad controls the RX board, it must be directly connected to it. To fulfill this linkage, the MCU includes a pair of 10x1 headers in which each pin has the nomenclature identified in Figure 82. As one can notice, several of these pins have dedicated and exclusive functions that must be matched when connected directly to the PCB to control. In this case, the headers are connected directly onto the outermost column of the 10x2 receptacles pair (J7 and J8) incorporated in the RX PCB, also shown in Figure 82. It is, then, possible to notice the RX PCB has complete compatibility with this MCU and each

pin in either board pairs with the respective on the other. This condition is satisfied because the TIDA-00663 design was specifically designed to be controlled by the MSP-EXP430FR5969. For this reason, and since the pinout differs intra-MSP430 family, the referred board has to be imperatively adopted.

As already mentioned, the *BP_3.3V* supply pin deviates slightly from the nominal value and, in practice, a voltage around 3.5V is measured in this pin. Notwithstanding, this fluctuation does not represent a threat since all the ICs support supply voltages above with this value.

4.3.1.1. Clock Sources

The MSP430FR5969 accommodates three internal clocks: the master clock (MCLK) drives the CPU, the subsystem master clock (SMCLK) is distributed to peripherals, and the auxiliary clock (ACLK), also assigned to peripherals. The SMCLK runs at the same frequency as MCLK, i.e., at a maximum of 16MHz while ACLK runs at 32kHz. [170]

The system operation requires three clock sources: one to drive the SPI communication with the TDCs and the DPOT (*SPI_CLK*), another to externally supply the TDCs for time-counting and time-base calibration (*TDC_CLK*), the last to support the *BP_TRIG* generation. Inasmuch as high-measurement rates are desirable, the time spent on data transactions must be minimized. Hence, the SMCLK is used to carry the latter tasks. Nonetheless, in some occasions the peripherals may not always need to run as fast and a slower clock as ACLK is often more precise and induces inferior power-consumption.

The MCLK frequency is fixed to the ceiling frequency of 16MHz and the SMCLK is outputted in the reserved pin P3.4 (*TDC_CLK*) with the same speed. This is done by simply setting to '1' the corresponding bit (BIT4 \leftrightarrow 0b00010000 \leftrightarrow 0x10) in the port selection, *P1SEL1*, and port direction registers, *P3DIR*, as specified in 'Table 6.57. Port P3 (P3.4 to P3.7) Pin Functions' on the microcontroller's datasheet: [171]

```
P3DIR |= 0x10;
P3SEL1 |= 0x10;
```

4.3.1.2. TIA Configuration

The TIA configuration consists uniquely on defining the gain and disabling the test mode for a steady operation using the photodiode as current source. As regards the implementation, the General Purpose I/O (GPIO) pins P3.5 and P3.6 are defined as outputs to match the CTRL (*5k_gain_setting_BP9_P3.5*) and Test_SD (*t_prop_calibration_enable_BP10_P3.6*) inputs of the *OPA857*. Subsequently, P3.6 is cleared and P3.5 is set up according to the specified gain ('1' for 20k Ω and '0' for 5k Ω gains).

```
P3DIR |= 0b01100000;
(TIA_gain == 20 ? P3OUT |= 0x20 : P3OUT &= ~0x20);
P3OUT &=~ 0x40;
```

4.3.1.3. Pulse Width Modulation

The signal triggering each measurement cycle is *BP_TRIG*. This is a 3.3V–logic signal generated by a technique called Pulse Width Modulation (PWM), the most unequivocal and straightforward approach to control the frequency, f_p , and duty cycle, dc , of digital signals. The indicated signal is outputted at P1.2, a pin reserved for this purpose.

The basis of the PWM process is the use of timers to measure time intervals and set the output pin to a high or low state accordingly. In this specific situation, the timer *TA1.1* is used. The first step is, then, to establish the port as output by setting the respective bit in the *P1DIR* register and, posteriorly, select the destined functionality by configuring the selection registers *P1SELO* and *P1SEL1*. In the former register, the BIT2 is written to '1' while in the latter is left to the default value '0', in conformation with 'Table 6.49. Port P1 (P1.0 to P1.2) Pin Functions' in [171]:

```
P1DIR  |= 0x04;
P1SELO |= 0x04;
```

Posteriorly, the control, *TAICTL*, and the capture and compare control, *TACCTL1*, registers are configured as follows:

```
TAICTL  |= TASSEL_2 | ID__1 | MC_1 | TACLR;
TACCTL1 = OUTMOD_7;
```

to, respectively, hold SMCLK as the clock source without any pre-scaler, i.e., at 16MHz, count exclusively upwards from 0 to the value set in *TA1CCR0*, clear the count direction after a complete cycle/period and reset the timer whenever *TA1CCR0* is achieved. In this arrangement, each SMCLK period corresponds to one increment in timer *TA1*. When it reaches the value set on the control and compare register *TA1CCR1* the pin is commuted to a low-level and when it reaches the count limit in *TA1CCR0*, the timer is reset and the pin rewritten to '1'. Hereby, the value written to the previous registers set, respectively, the period and duty cycle (percentage of on-time per period) of *BP_TRIG*:

```
int T_0 = int(16000/f_pwm);
int T_1 = int(dc_pwm*T_0);
TA1CCR0 = T_0;
TA1CCR1 = T_1;
```

To complete, the output signal operates uninterruptedly to guarantee a constant and stable *BP_TRIG* and is only activated after configuring the TDCs since it immediately starts the measurements. The parameters f_p and dc are partially defined experimentally, backed by a theoretical grounding.

4.3.1.4. External Interrupt

After the initial configuration, the microcontroller enters an endless loop and, whenever the TDCs complete a measurement the processing unit must be notified to retrieve the result registers and reconfigure CONFIG1 to proceed to the next cycle.

To activate these specific microcontroller actions and because the time instant at which each measurement stops is unpredictable, the signal *TDC_INT* is used as an external hardware interrupt. Every time the TDCs complete a measurement, the previous signal switches from a high to a low level (active-low). This transition is detected in pin P2.4 and is then used to force the processor to immediately stop its current activity and execute a specific function called Interrupt Service Routine (ISR). In this function, all the registers needed to calculate the ToF are read and the START_MEAS bit is set in CONFIG1. After this, the processor resumes the activity in execution prior to the interruption.

Concerning the code implementation, the external interrupt is firstly configured for P2.4 in the *void setup()* function. It is noteworthy that this is not an exclusive function and every pin is interruptible. The first step is to define the pin as input by clearing the bit in *P2DIR*. Posteriorly, and as *TDC_INT* is pulled-up by two resistors connected to the AND-GATE inputs, the respective bit in the resistor enable register,

P2REN, is set to '1'. After, the interrupt is set on the falling-edges of *TDC_CLK* with a write to '1' in the interrupt edge select register, *P2IES*. Finally, the interrupt flag register, *P2IFG*, is cleared and the interrupt is enabled by setting the corresponding bit in *P2IE*.

```
P2DIR  &= ~0x10;
P2REN  |= 0x10;
P2IES  |= 0x10;
P2IFG  &= ~0x10;
P2IE   |= 0x10;
```

When the selected transition is detected on P2.4, the ISR, *void PORT2_ISR_HOOK*, is executed to read the TDCs registers and reset CONFIG1. At the end, the interrupt flag is cleared and the interrupt re-enabled.

```
#pragma vector=PORT2_VECTOR
__interrupt void PORT2_ISR_HOOK(void) {
    ToF_read();
    P2IFG &= ~0x10;
    P2IE  |= 0x10;
}
```

4.3.1.5. SPI

The central underlying communication protocol for data transaction between the RX MCU and the respective board is the Serial Peripheral Interface (SPI). The latter is employed in this context at the beginning to configure both TDCs and the DPOT, and during steady operation to read and restart the time-counting units.

In a nutshell, SPI is a synchronous protocol in which a master device communicates with one or several slaves. In its full form, the physical interface requires four wires/lines, plus the essential ground reference that is not counted (Figure 83a) [170]:

- Two data lines called Master In Slave Out (MISO or SOMI) and Master Out Slave In (MOSI or SIMO) to support a full-duplex communication, meaning that data can be transferred simultaneously in both directions. These are also frequently referred to as DIN and DOUT for serial data in and out respectively and, naturally, the slave input is connected to the output of every slaves and vice-versa.
- A clock line most popularly called SCLK or SPI_CLK common to all slaves and fed through a single clock provided by the master to ensure full synchronization in data transfers. The frequency of the clock sets the bit rate (bps).
- A line for slave selection called Chip Select (CS). The multiplexing in selecting the different slaves is accomplished by using distinct CS lines. Each slave CS pin is connected to a distinct pin in the master (Figure 83b). This line is active low, thus the \overline{CS} representation, and the master selects the desired slave by writing '0' on the corresponding pin during the duration of the transaction. When CS is idle/inactive, the output of the particular slave, DOUT, goes to a high-impedance state and data on DIN is ignored despite the activity on SCLK.

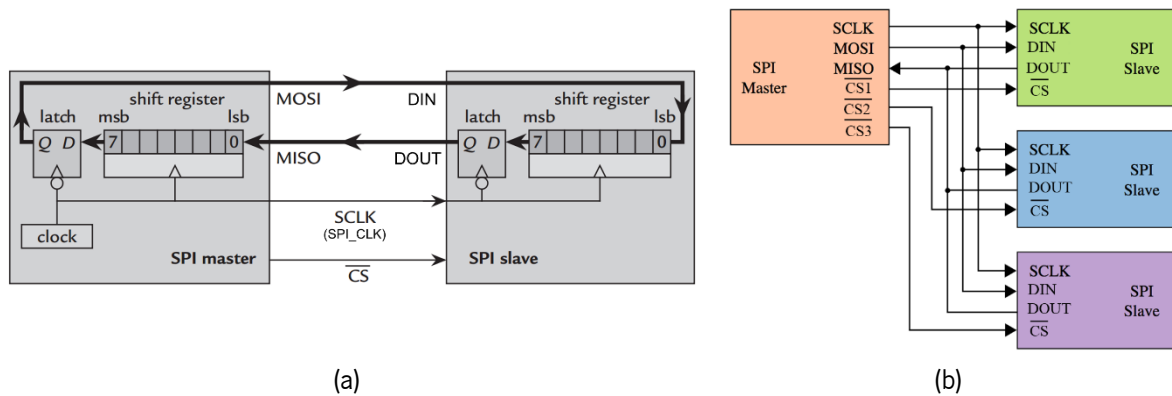


Figure 83. Serial Peripheral Interface: (a) detailed connection between a master and a single slave and (b) connection of three slaves to the master with separate CS lines (adapted from [170]).

The concept of SPI is based on two 1-byte shift registers, one on each slave and another on the master, connected to form a loop. Each device places a new bit on its output whenever a pre-defined clock edge is detected, either from the LSB to the MSB or vice-versa depending on the configuration. SPI supports 4 conventional operation modes to yield different combinations of clock polarity (CPOL) and phase (CPHA) required by contrasting devices. The latter controls whether the writing takes place on the leading and trailing edges of the clock pulses or vice-versa. These modes are explicit in Table 15. [170]

Table 15. SPI modes description.

Mode	CPOL/ CKPL	CPHA/ CKPH	Description
0	0	0	Clock idles low between transfers (when inactive); data read on leading edge and written on trailing edge of clock pulses
1	0	1	Clock idles low between transfers; data written on leading edge and read on trailing edge of clock pulses
2	1	0	Clock idles high between transfers; data read on leading edge and written on trailing edge of clock pulses
3	1	1	Clock idles high between transfers; data written on leading edge and read on trailing edge of clock pulses

SPI has as main upsides its straightforwardness and easiness to use once configured, the high transfer rates, because it runs at frequencies up to the CPU limit, and the robustness to clock jitter, since the data transfer is triggered by edges. Theoretically, it can use any frequency, but the slaves and the master usually set the maximum limit.

The first step is to initially set up the SPI interface to yield data transactions. On-board, the SPI is physically implemented through the synchronous Universal Serial Communication Interface (USCI_B0) peripheral and the architecture encompasses the RX MCU as master and TDC1, TDC2 and DPOT as slaves. Each device has a specific CS line, initially defined as output and set to '1' for deactivation: *P4.3 (TPL020_CS_EN_GPIO_BP5)* for the DPOT, *P1.4 (TDC_RX_CS)* for TDC1 and *P3.0 (TDC_TX_CS)* for TDC1.

```
P4DIR |= 0x08;
```

```

P4OUT  |= 0x08;
P3DIR  |= 0x01;
P3OUT  |= 0x01;
P1DIR  |= 0x10;
P1OUT  |= 0x10;

```

The next step on the process is to route the main pins to the USCI_B0 module by setting the bits in the respective port selection registers, *PnSEL*. The master provides the clock to all the slaves through the common dedicated pin P2.2 (*UCB0CLK*) and all slaves' DIN and DOUT pins share the same lines and are connected respectively to the single microcontroller's reserved pins P1.6 (*UCB0SOMI*) and P1.7 (*UCB0SOMI*). According to the microcontroller's datasheet [171], *PnSEL1* and *PnSEL0* shall be written to '1' and '0'.

```

P1DIR  &= ~0b10000000;
P1DIR  |= 0b01000000;
P1SEL1 |= 0b11000000;
P1SEL0 &= ~0b11000000;
P2DIR  |= 0b00000100;
P2SEL1 |= 0b0000100;
P2SEL0 &= ~0b00000100;

```

After, the SPI parameters are established for operation. In first place, the module is put and kept in reset mode throughout the whole configuration by setting the *UCSWRST* bit in *UCB0CTLW0* and SMCLK is chosen as source for SCLK (*UCSSEL_2*). Subsequently, several bits are set in the same register: *UCMSB* to fix the bit order from MSB (first) to LSB (last); *UCSYNC* to select SPI since the USCI_B0 also supports asynchronous communication protocols; *UCMST* to specify the RX MCU as master board. The SPI Mode 0 is settled (*CPHA= ~UCCKPH=0* and *CPOL=UCCKPL=0*) in accordance to the slaves' datasheets [166][168]. The clock frequency is then divided by the value in *UCB0BR1:UCB0BR0* registers, considered a 2-byte word, to hold the SCLK frequency. Here, two distinct configurations arise. For the DPOT, the maximum SPI frequency is limited to 5MHz [166] and the SCLK frequency is set to 4MHz using a clock divider of 4 to SMCLK. After the initial configuration of the DPOT, the frequency is changed to 16MHz (divider of 1) as the *TDC7200* supports up to a 20MHz SPI_CLK and the transfer rate is to be maximized for a faster point acquisition. Finally, USCBI_0 is taken out from the reset mode and activated by clearing *UCSWRST*.

```

UCB0CTLW0 = UCSWRST | UCSSEL_2;
UCB0CTLW0 |= UCCKPH | UCMSB | UCSYNC | UCMST;
UCB0CTLW0 &= ~UCCKPL;
// DPOT
UCB0BR0 = 4;
UCB0BR1 = 0;
UCB0CTLW0 &= ~UCSWRST;
// TDCs
UCB0BR0 = 1;
UCB0BR1 = 0;

```

The TDCs and the DPOT (slaves) are configured initially in the *void setup()* and this arrangement remains constant through the whole operation. The procedure consists on sending 2-byte data packets with a first address byte, specifying the register to be written, followed by the byte to be inscribed. Both bytes are represented in an unsigned integer format (*uint8_t*).

To use the same sending function for all the slaves, an integer parameter (*sel*) is defined to select the CS pin accordingly. After selecting the device by pulling-down the respective CS line, the first byte is written to the transmitting buffer, *UCB0TXBUF*, and remains there until the previous byte has been sent, at which point it is moved to the transmit shift register. The shift register is then unloaded on the MOSI

accompanied by the SCLK activation to drive the transmission. Before transferring the next byte to the buffer, the transmit interrupt flag, *UCTXIFG*, is tested. This flag is raised when *UCBOTXBUF* is ready to accept another byte. After sending the pair of bytes, the flag *UCBUSY* must be checked to guarantee the shift register has been completely sent and avoid data corruption before idling CS. When finalized, *UCBUSY* is cleared and it is essential that CS goes idle between transfers because the first output is stimulated by the activation of CS.

```
void SPI_send(uint8_t *data, int len, int sel) {
    while (len){
        (sel==1 ? P4OUT &=~0x08 : (sel==2 ? P3OUT &=~0x01 : P1OUT &=~0x10));
        while(!(UCB0IFG & UCTXIFG));
        UCB0TXBUF = *(data++);
        while(!(UCB0IFG & UCTXIFG));
        UCB0TXBUF = *(data++);
        while(UCB0STAT & UCBUSY);
        (sel==1 ? P4OUT |= 0x08 : (sel==2 ? P3OUT |= 0x01 : P1OUT |= 0x10));
        len-=2;
    }
}
```

DPOT Configuring

Specifying on the *TPL020-10MRTER*, it uses a 3-wire SPI-compatible write-only interface, i.e., the registers can only be configured and not read (there is no DOUT pin). The SPI signals are qualitatively illustrated in Figure 84. The sequence includes two command bits, C1 and C0, two address bits, A0 and A1, to specify which potentiometer the command affects (01 for A, 10 for B), and 8 data bits with the wiper position. Since the thresholds are introduced independently and the expression for the wiper value differs in equation (4.11), the wipers are also written independently using the command bits C1,C0=00. Posteriorly, the wiper registers are both copied to non-volatile registers (C1,C0=10) to restore the same conditions upon power-up. [166]

```
uint8_t stream_DPOT[] = {0b00000001, W_A,
                        0b00000010, W_B,
                        0b00100011, 0b00000000};
SPI_send(stream_DPOT, sizeof(stream_DPOT)/sizeof(stream_DPOT[0]), 1);
```

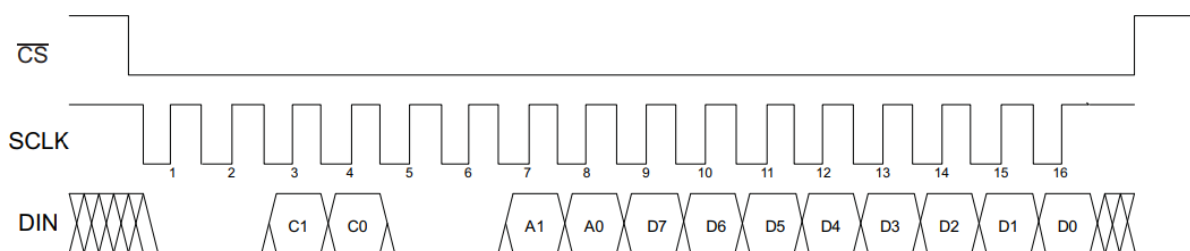


Figure 84. Digital Interface Write Sequence [166].

TDC Transactions

Regarding the TDCs, the communication on the SPI bus supports write and read transactions. A write transaction consists of a single write command byte, followed by a single data byte. A read transaction of any of the measurement registers consists of a single read byte followed by 24 SCLK cycles, since each one of these registers has a 3-byte capacity. Each command consists of a 1 auto-increment bit (0 for

OFF and 1 for ON), a 1-bit read or write instruction (0 for reading, 1 for writing), and a 6-bit register address. Figure 85 shows the protocol for a transaction involving one byte of data. [168]

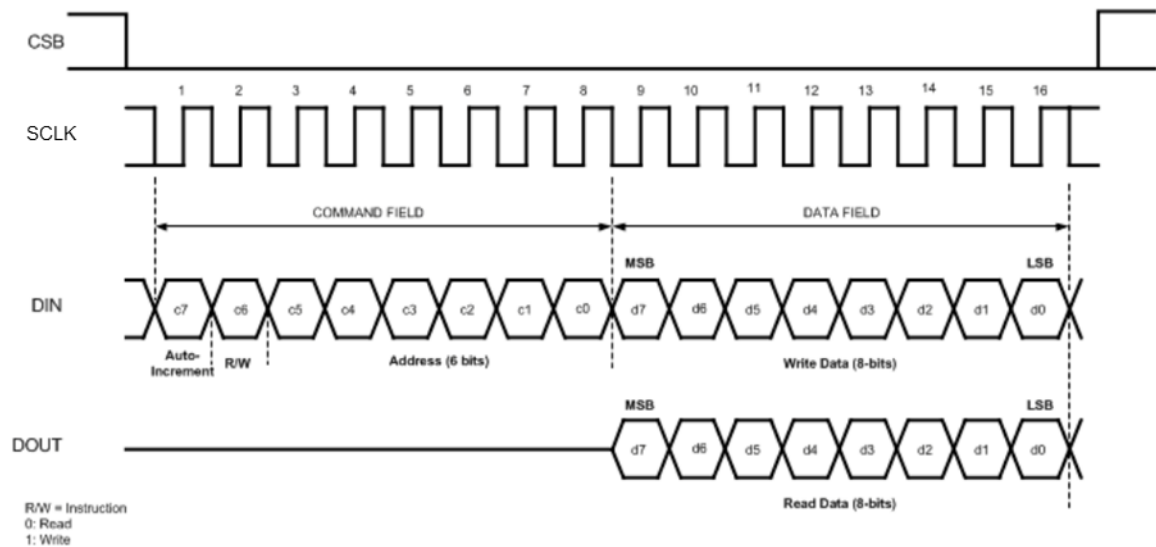


Figure 85. SPI protocol and frames for TDC transactions [168].

The TDCs are configured according to Table 14. Since the writing and reading processes do not refer to registers in contiguous memory addresses, the auto-increment bit is always cleared. The sending sequences is as follows:

```
uint8_t CONFIG1[] = {0b01000000, 0b10111011};
uint8_t CONFIG2[] = {0b01000001, 0b00000000};
uint8_t INT_MASK[] = {0b01000011, 0b00000101};
uint8_t CLOCK_CNTR_OVF_H[] = {0b01000110, 0b00000000};
uint8_t CLOCK_CNTR_OVF_L_1[] = {0b01000111, 0b00001100};
uint8_t CLOCK_CNTR_OVF_L_2[] = {0b01000111, 0b00010000};
int config_len = sizeof(CONFIG1)/sizeof(CONFIG1[0]);

SPI_send(CONFIG2,config_len,2);
SPI_send(INT_MASK,config_len,2);
SPI_send(CLOCK_CNTR_OVF_H,config_len,2);
SPI_send(CLOCK_CNTR_OVF_L_1,config_len,2);
SPI_send(CONFIG2,config_len,3);
SPI_send(INT_MASK,config_len,3);
SPI_send(CLOCK_CNTR_OVF_H,config_len,3);
SPI_send(CLOCK_CNTR_OVF_L_2,config_len,3);
SPI_send(CONFIG1,config_len,2);
SPI_send(CONFIG1,config_len,3);
```

After the interrupt is detected, the result registers are read sequentially and individually. The reading process is identical to sending. After selecting the TDC, the register address is sent via MOSI. Posteriorly, the MCU waits for the *UCTXIFG* flag to set and then a dummy byte (0x00 for e.g.) is sent to the *UCBOTXBUF*. This is necessary because to keep the clock line active a byte must be sent by the master even if it is not read. Simultaneously, as there are separate shift registers for transmitting and receiving, a byte is read to the receive shift register. Next, the read value is transferred to the receiver buffer, *UCBORXBUF*, and the master waits for the byte to be completely moved (*UCBOSTAT* flag test), leaving the shift register ready to accept a new transfer. When completed, *UCBORXBUF* is copied to a data buffer and the process is repeated three times to acquire 24 bytes.


```

SPI_receive(TIME1_1,0x10,2);
SPI_receive(TIME1_2,0x10,3);
SPI_receive(CLOCK_COUNT_1_1,0x11,2);
SPI_receive(CLOCK_COUNT_1_2,0x11,3);
SPI_receive(TIME2_1,0x12,2);
SPI_receive(TIME2_2,0x12,3);
SPI_receive(CALIBRATION1_1,0x1B,2);
SPI_receive(CALIBRATION1_2,0x1B,3);
SPI_receive(CALIBRATION2_1,0x1C,2);
SPI_receive(CALIBRATION2_2,0x1C,3);

void SPI_receive(uint8_t *buffer, uint8_t addr, int sel){
    (sel==2 ? P3OUT &= ~0x01 : P1OUT &= ~0x10);
    while(!(UCB0IFG & UCTXIFG));
    UCB0TXBUF = addr;
    for(int w=0;w<3;w++){
        while(!(UCB0IFG & UCTXIFG));
        UCB0TXBUF = 0x00;
        while (UCB0STAT & UCBUSY);
        buffer[w] = UCB0RXBUF;
    }
    while (UCB0STAT & UCBUSY);
    (sel==2 ? P3OUT |= 0x01 : P1OUT |= 0x10);
}

```

The time needed to read all the variables can be estimated. Considering that each variable requires 32 SCLK cycles to be transferred to the master (1 byte for address + 3 bytes for data, each bit on a clock edge), and 10 registers must be read at a 16Mbps rate to calculate the ToF in Mode 2, then the total time sums up to:

$$32 \times 10 \times 62.5ns = 20\mu s \quad (4.16)$$

To add up to this time, one must also enter with the function calls, the chip selection, the TDCs restart and the flags advancing conditions.

After reading the registers, one verifies if the STOP was detected or not by checking the CLOCK_COUNT result. When no STOP is detected, the clock counter overflows and the CLOCK_COUNT register remains 0 at the end of the cycle. Hereby, and since there is a minimum guaranteed delay of 150ns introduced by hardware (> 2 clock cycles), one can directly deduce that an overflow occurred if the last byte read either on TDC1 or TDC2 is null. In this scenario, the ToF is written to 1000ns (150m range) to indicate a missed point:

```

if(CLOCK_COUNT_1_1[2] == 0 || CLOCK_COUNT_1_2[2] == 0) ToF = 1000;

```

If no overflow is detected, then the total ToF is calculated as per equations (4.13) and (4.14). The first byte on CLOCK_COUNT1 (MSB) is not encompassed in the calculation as specified in [168]. The normLSB values are first computed separately in picoseconds and only converted in nanoseconds in the ToF calculation to ensure superior precision in the final ToF calculation. At the end of this cycle, the TDCs START_MEAS bit is reset in CONFIG1.

```

uint8_t restart[2] = {0b01000000, 0b10111011};

SPI_send(restart,restart_len,2);
SPI_send(restart,restart_len,3);

```

4.3.1.6. UART

At the end of each measurement cycle, the obtained ToF is sent to the computer. The transmission is carried-out using the embedded Universal Asynchronous Receiver/Transmitter (UART). The latter is a physical peripheral implemented to support the RS-232 serial communication protocol for transmission and reception of serial data.

In this protocol, two devices with a common ground reference communicate directly with each other using two data lines: a reading line for one device, corresponding to a writing line in the other, and vice-versa. Unlike SPI, the devices can communicate without any previous authorization, i.e. asynchronously, and no clock is required, making this a more dynamic protocol. Instead of a clock signal, the transmitting UART adds a start and stop bits to the data package to define the beginning and end of each transmission. The data is exchanged serially, bit by bit in messages contain from 5 to 9 data bits. Both devices must be configured to the same baud rate, a measure of the speed of data transfer expressed in bits per second (bps) in this context, otherwise the data is not interpreted correctly. [170]

The data is transferred to one of the PC's USB port. Since this peripheral is not compatible with UART's package structure, the data sequence must be converted to an appropriate form and then re-transmitted. This conversion is implemented automatically in hardware through the back-channel UART via an UART-to-USB bridge integrated in the RX MCU board (Figure 86). It is noteworthy that this protocol is not used herein to communicate with the RX board. Hereby, neither of the pin headers is used.

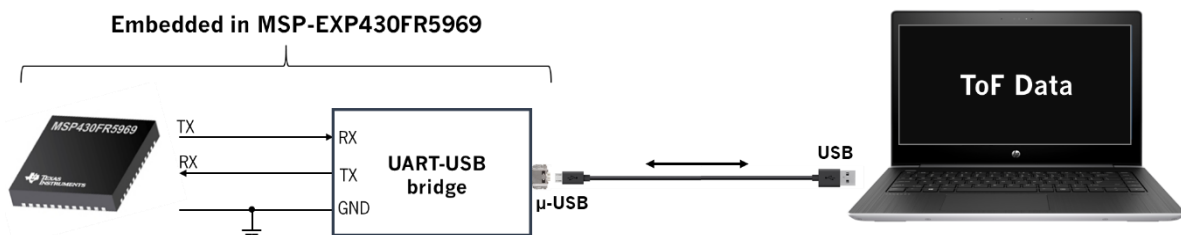


Figure 86. Interface between the MSP-EXP430FR5969 and PC for ToF data transmission.

Application-wise, the communication is implemented using high-level pre-defined functions. First, the UART is initialized with a standard baud rate of 9600 in the *void setup()* function:

```
Serial.begin(9600);
```

This baud rate is chosen to minimize the transmission and reception errors. For this rate and a 16MHz clock, the maximum error is 0.05% for transmission and 0.1% for reception [171]. Subsequently, the ToF data is printed/sent in to the serial port in the *void loop* as a float (4 bytes) in nanoseconds:

```
Serial.println(ToF);
```

As the data is transmitted while the CPU is idled and waiting for an interruption, time-minimization is not a major concern. Herupon, one opted to use these non-optimized functions for simplicity and automation reasons. Otherwise, the implementation would be far more extensive as it would have to include the individual configuration of all UART registers, the addition of start and stop bits and the manual dissection of each 4-byte float in four data packages, with a maximum of 9 data bits each, to send separately.

After the data is sent to the PC, it can be visualized in a Serial Port configured for the correct COM port and baud rate. However, as it will be elucidated in the next chapter, a Graphic User Interface (GUI)

can be conceived to directly retrieve the values from the serial port and graphically display or save them into a file for further processing.

4.3.2. MSP430F5529 (TX MCU)

Since *BP_TRIG* is generated in the RX MCU and connected to the TX board through a jumper wire, the TX MCU plays a secondary role in the system and, in fact, its usage is not indispensable. The prime function is to directly support and power the TX board and control the laser enabler (*BP_GPIO_EN*) through the headers. Both activities could potentially be executed by the RX MCU but a larger number of jumper wires would be required to connect the *BP_3.3V*, *GND* and *BP_GPIO_EN* pins to the TX PCB, and by powering two PCBs with the same master board could lead to potential disturbances in the supplying performance.

Regarding the architecture and performance, this MSP430F5529 has an internal 128KB flash memory, 8KB of RAM, up to 25MHz CPU clock frequency and also integrates three serial interfaces (SPI, UART, I2C). The launchpad includes a pair of 10×2 headers and outputs approximately 3.3V on the *BP_3.3V* power pins. [172]

Even though this board is clearly superior to the RX MCU in performance, the pinout is not compatible with the RX PCB. For example, the SMCLK (Figure 87a) necessary to deliver the external *TDC_CLK* signal to both TDCs is outputted at P2.2 in the TX MCU, corresponding to the TDC1 CS input on the RX PCB (Figure 82). This board was adopted uniquely because it had already been acquired for other uses.

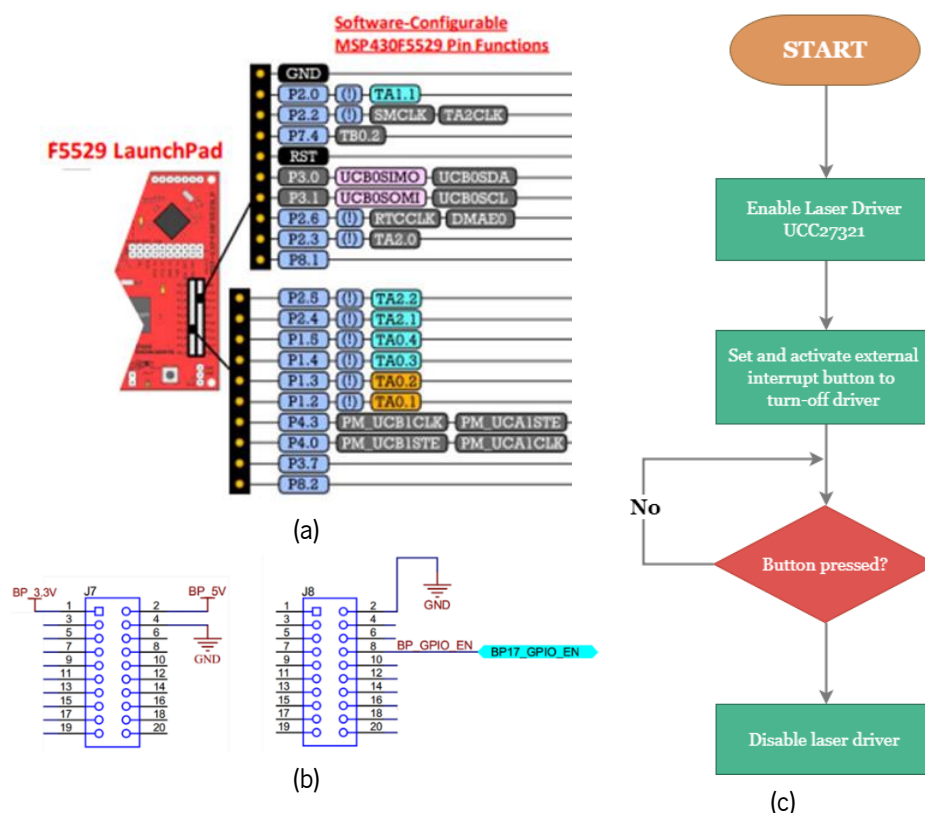


Figure 87. (a) Right-side 20×2 header and pins' functions [172] and (b) respective TX board headers [156]. In (c) the flowchart for the TX MCU program.

Programming-wise, the flowchart is very elementary and is shown in Figure 87c. The program starts by setting pin General Purpose I/O P7.4 to a high-state to enable the laser driver. Posteriorly, an external interrupt is activated for pull-up and on a low-to-high transition in the on-board button P1.1. When this button is pressed, the respective ISR is executed to disable the driver (P7.4 to a low-state) and the red LED (P1.0) is turned-on to announce the laser is OFF. To re-enable, the board must be reset in the S3 button. This implementation allows to swiftly shut down the laser in an emergency scenario.

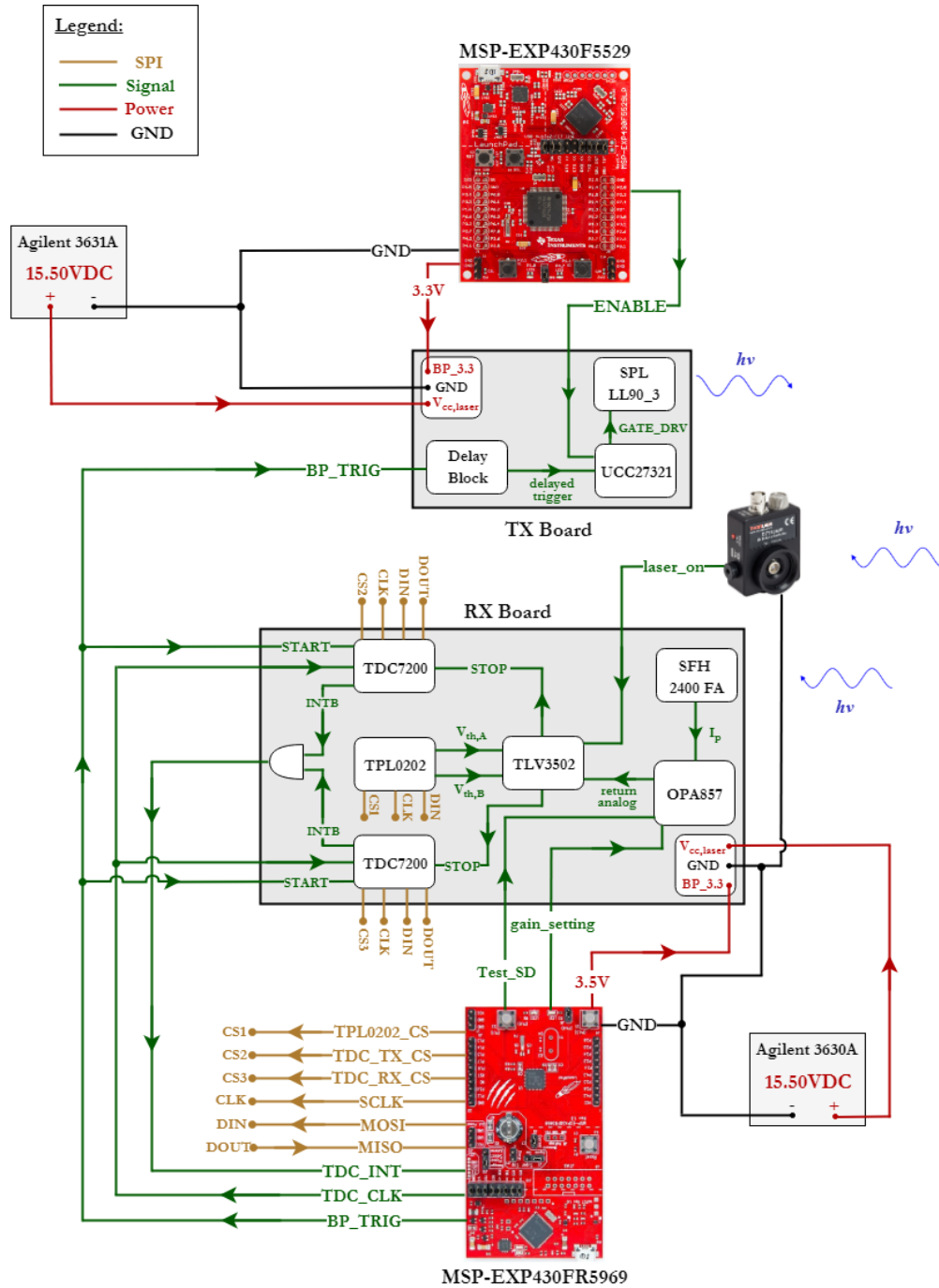


Figure 88. Boards' intra and inter-connections and exchanged signals between components. In blue is represented the emitted light from the transmitter and the incoming light on both detectors. The SPI signals are represented through net labels for visual simplicity. The components' and, consequently, the signals relative positions are merely indicative and do not correspond necessarily to their positions in the actual assembly.

4.4. Architecture Diagram

To consolidate the architectural discussion, a diagram with all the system components and their connections is portrayed in Figure 88, including exchanged analog and digital signals and powering. The external voltage sources for $V_{cc,laser}$ are discriminated. The TX and RX boards are supplied independently to avoid propagation of power disturbance since at the lasing instants the laser pulls high-current peaks translated to voltage peaks on the supply.

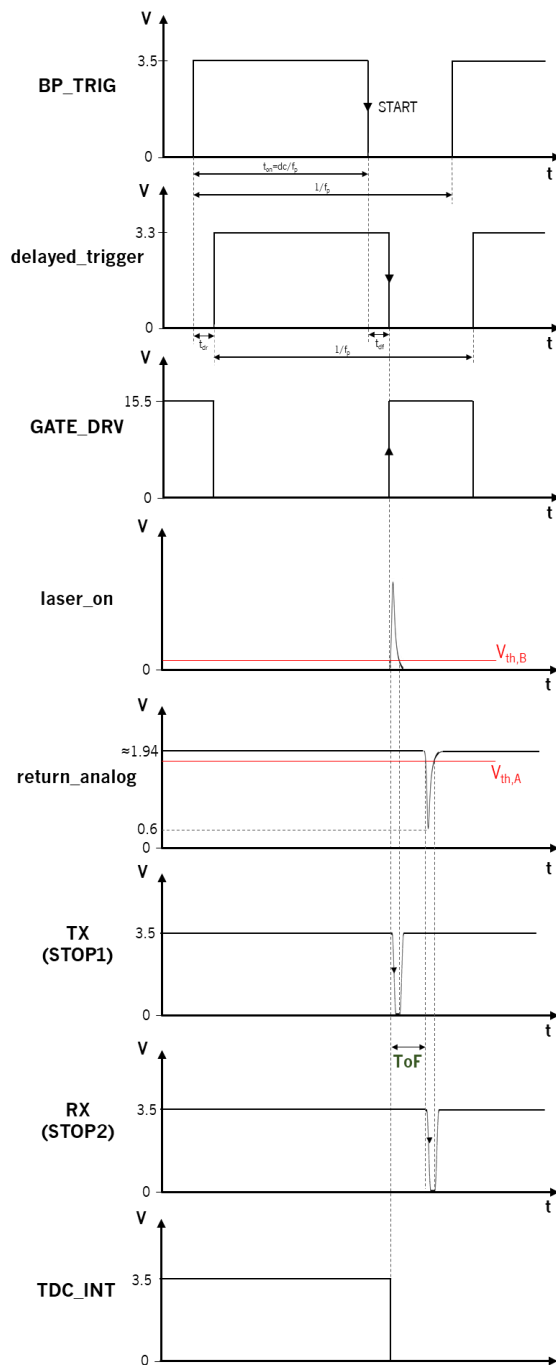


Figure 89. Representation of the vital signals involved in the sequential process of single-point acquisition.

Moreover, the sequence of signals used to acquire a single point using the LiDAR technology is generically shown in Figure 89 which excludes the SPI, UART and CLK signals. After the initial configuration, these steps are as follows:

- 1) Generation of a trigger pulse BP_TRIG – MSP430FR5969;
- 2) Start time-counting on the falling-edge – TDC7200;
- 3) Add a >150 ns delay to the digital pulse – Delay block;
- 4) Invert and boost the digital pulse to higher voltage levels and apply to the MOSFET gate in the laser driving stage – UCC27321;
- 5) Laser activation and emission of an optical pulse – SPL LL90_3;
- 6) Detection of a portion of the sent pulse and conversion to a voltage pulse – DET10A/M;
- 7) Detection of the back-reflected light pulse – SFH 2400 FA;
- 8) Conversion and amplification of the induced current pulse to a voltage pulse – OPA857;
- 9) Leading-edge discrimination of both analog voltage pulses with fixed thresholds to yield the STOP signals – TLV3502;
- 10) Stop the time counting and activate interrupt on INTB – TDC7200;
- 11) Acquisition of the measurement registers from TDCs – MSP430FR5969;
- 12) ToF calculation and transmission to PC – MSP430FR5969;

4.4.1. Boards Assembly

The final constituent boards of the LiDAR prototype are pictured in Figure 90 mounted on the respective controller boards. On the left-side picture, the TX PCB is depicted with just the indispensable components applied. On the opposite end, the RX PCB is shown directly mounted on the respective master board. Some of the components visible on the upper board, namely on the bottom-right corner (U11, U5, C17, C7, C8, C10, R5, R6) and the SMA connectors, are not contemplated in the conclusive system. Yet, they were deployed in a first iteration subsequently discarded and, to avoid damages during the unsoldering process, they were left on-board and disconnected to eliminate any possible interference. Finally, on the middle images, the PCBs' backside is displayed to evidence the pair of 10×2 headers. All the capacitors and resistors adopted are SMDs (Surface Mount Device).

Each board encompasses a 3×1 header (J2) to connect the external power supply $V_{cc,laser}$ in the central pin. In the RX board, J2 is placed on the top surface to grant an easier access. Whatsoever, and since the pins' height surpasses the laser height, this header is soldered on the rear-end off the TX board to permit an optical application adjacently to the emitter.

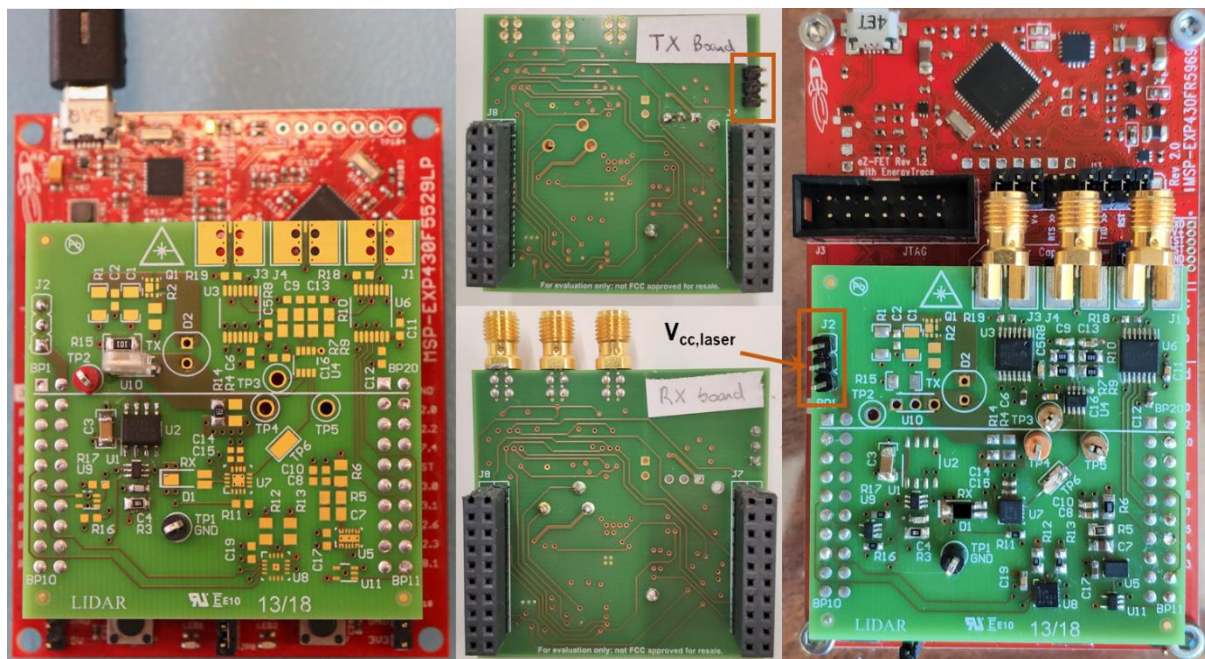


Figure 90. LiDAR final boards. On the left, the TX PCB mounted on the TX MCU. On the center, the backsides of both PCBs. On the right, the RX PCB mounted directly on the RX MCU. The headers to connect the external power source are highlighted by the orangish rectangles.

In turn, the launchpads are mounted on two perforated acrylic plates with $12.5 \times 11 \text{cm}^2$ (TX) and $14.5 \times 11 \text{cm}^2$ (RX). To immobilize the boards, four M3 screws are firmly fixed on each corner-hole of the MCUs and passed through four 20mm metallic spacers to ensure physical separation (Figure 91). On the opposite end, M3 nuts are applied to inhibit any screws rotation. This assembly garnishes stability and robustness to the system, making it less propitious to misalignments induced by external disturbances (e.g. vibrations), and avoids conductive contacts with the metallic parts that may cause short-circuits with irreversible consequences.



Figure 91. Photography of the MSP-EXP430F5529 attached to the acrylic slab.

The boards are mounted on top of and optical breadboard firmed on an optical table. Additionally, the transmitting side is installed over a smaller breadboard to fine-tune the ensemble direction and position during testing and system alignment. As exhibited in Figure 92, the TX hardware on the left is fixed by an optical post and its vertical position can be adjusted in order to match the emitter height to that of both photodetectors. The RX acrylic slab on the right is supported by a translation stage with 3DOF (degrees of freedom). On the background, it is seeable the connection of each board to a computer's USB port.

This setup refers only to the hardware and is yet to be interfaced with the optical system. The fact that TX is mounted farther from the target, i.e. farther from the photo's point of view, does not have any implication because the system will invariably have to be calibrated to disregard differences in the optical and electrical path lengths between transmission and reception.

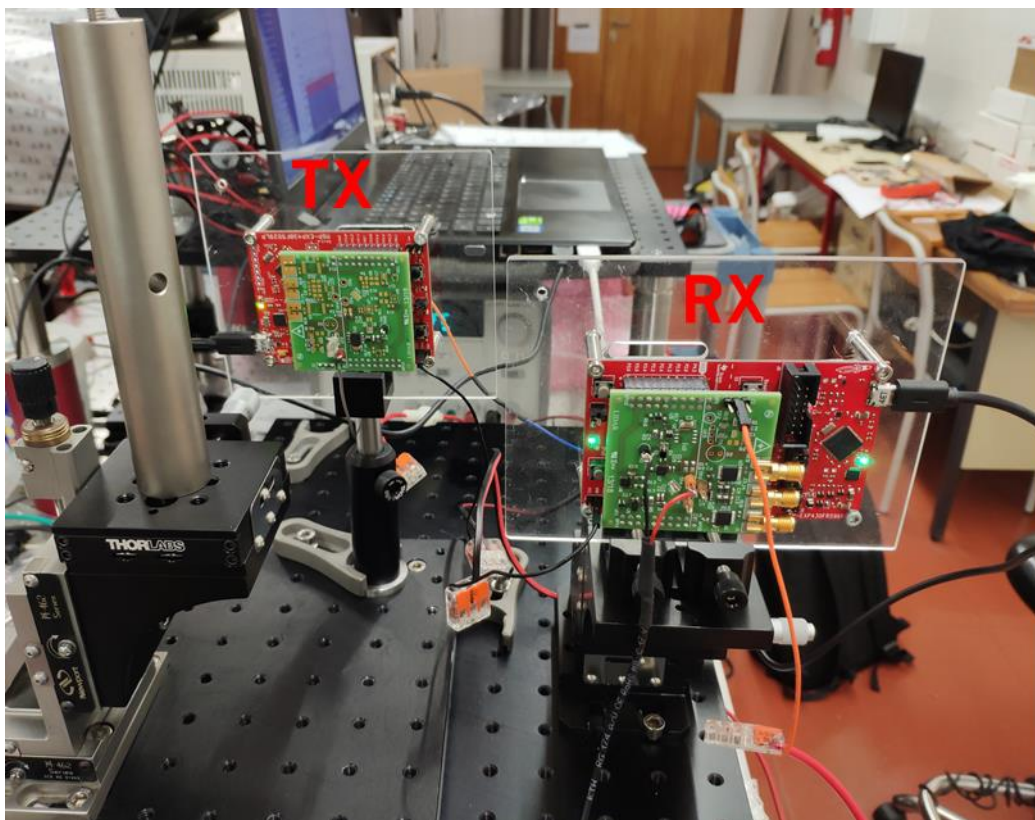


Figure 92. Front-view of the hardware setup on the optical breadboards. It is noticeable that the TX-end is mounted on a smaller breadboard on the left-side.

In Figure 93a, the translation platform is shown in more detail. While the TX support has only 1DOF, with this stage the (x,y,z) position of the RX boards can be adjusted inside specific range limits through three screwdrivers (3DOF). In Figure 93b, the mechanism to immobilize the acrylic is zoomed in. It consists of two screws pressing the plate against a flat surface.

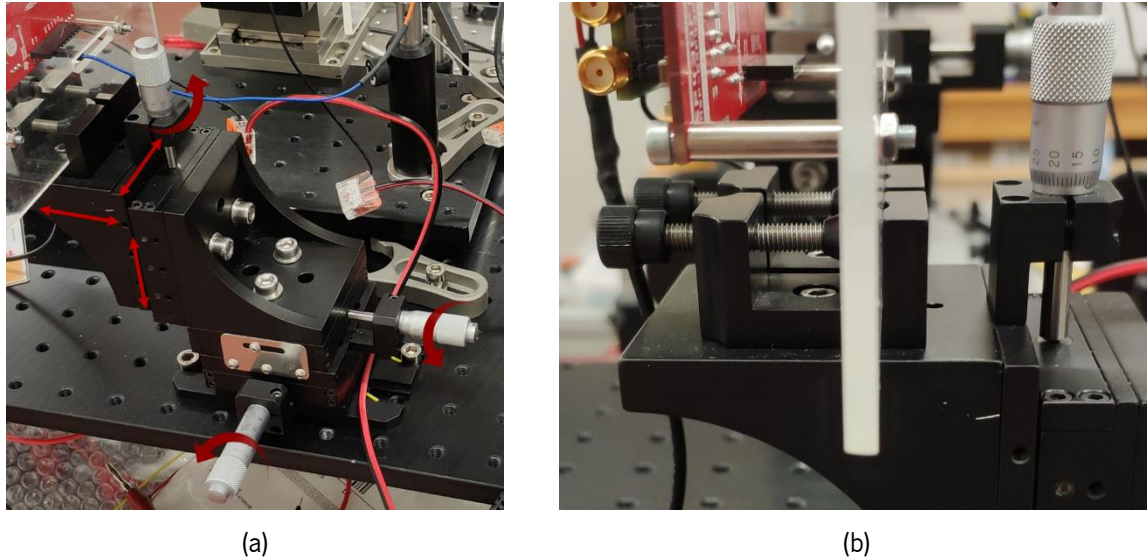


Figure 93. Hardware supports: (a) 3DOF stage for the RX hardware and (b) screws holding the acrylic plate.

The triggering signal generated in the RX MCU is conducted to the TX board to instruct the laser activation and accomplish a complete synchronization between both system's ends. Hereby, the *BP_TRIG* signal is transferred directly between boards through a jumper wire as evidenced in Figure 94a. The male-male wire connects *P1.2* on the MSP-EXP430FR5969 to *P2.0* on the MSP-EXP430F5529 both, in turn, connected to *BP_TRIG* of the PCBs. The acrylic plates were perforated to allow a connection between the back receptacles of the launchpads, with correspondence with the front-face headers.

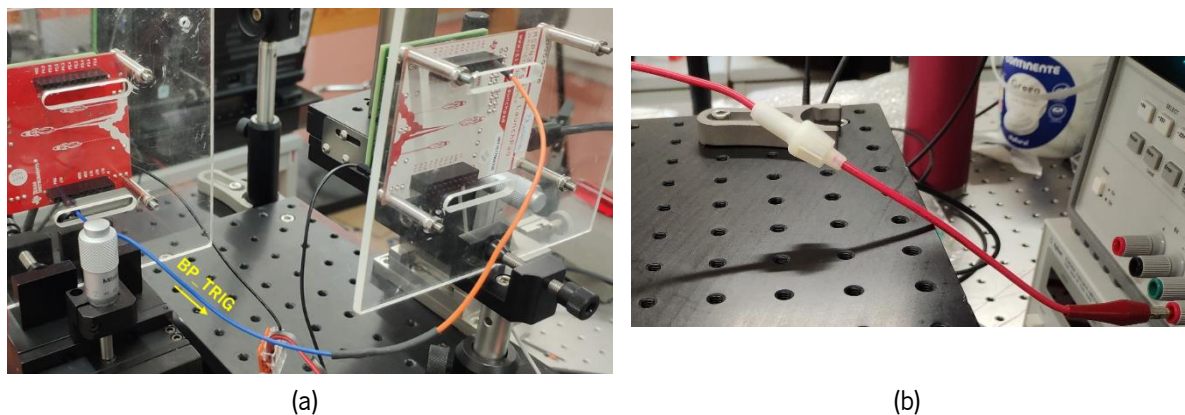


Figure 94. Electrical wiring: (a) jumper to transfer *BP_TRIG* from the RX to the TX side and (b) external power supply cable with a fuse in series.

The boards are supplied by two *Agilent 3630A* ($\pm 20V/0.5A$ DC) and *3631A* ($\pm 25V/1A$ DC) sources, from which the positive terminal is coupled to the $V_{cc,laser}$ pin header and the ground reference to a GND header in the MSP430 boards. The power cables are terminated in a banana connector at the supplier and a female receptacle at the PCBs. As the laser driver is a sensitive IC, very susceptible to overcurrent,

a fuse is applied in series to prevent the latter from burning. This element limits the consumed current to 200mA in a steady regime. Because fulfilling the pulsed emission are charged by a 100Ω resistor (R15), the peak current during charging is $V_{cc,laser}/100=155mA$, and the fuse does not interfere in this process. Furthermore, since the Ampere-order current to generate the light pulses is provided by the capacitors, it will not limit the optical output power. To play it safe, a fuse was also applied on the supply cable for the RX board, although the photodetector does not consume any electrical current.

To conclude, a missing aspect is the connection of the reference photodetector to the RX PCB (Figure 95). The DET10A/M is, similarly to the transmitter, fixed to the breadboard by a 1DOF post (vertical translation). Through and BNC “T” adaptor, the photodetector output is connected to a 50Ω impedance on one side and to a coaxial cable on the opposite. The 91-cm long coaxial cable is terminated on the opposite end by two 5cm wires. One of these is linked to the central conductive line of the coaxial cable (core) to retrieve the signal, the other to the outer shielding mesh (GND). The photogenerated voltage pulse (*laser_on*) is applied to the PCB by connecting the signal wire directly to the test point TP4, while the GND is attached to the test point TP1 (PCB GND) to attain a common reference for the whole circuit. The test points, identified in the electrical schematics as TPn, n=1...6, are simply small metallic hooks serving multiple purposes such as connecting external signals or oscilloscope probes for signal visualization on specific points of the circuit.

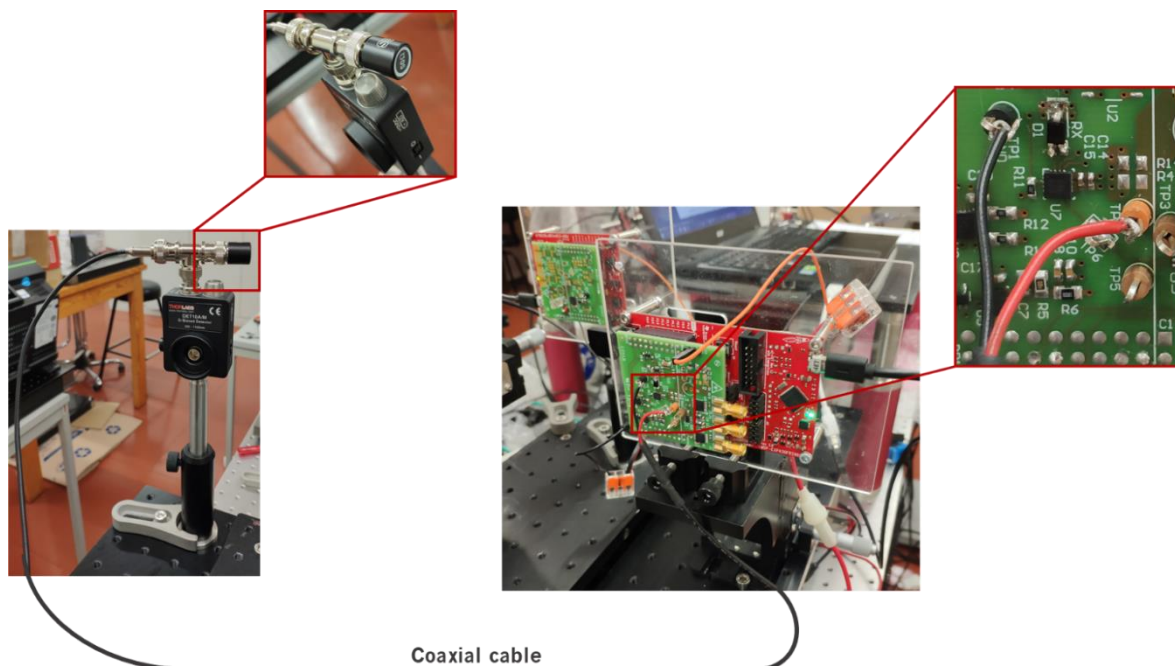


Figure 95. Connection between the reference photodetector and the receiver PCB.

4.5. Optical Setup

As the *SPL LL90_3* is a vertically stacked edge-emitting LD, the horizontal slit creates a highly-divergent light beam in an elliptical cone (Figure 96a) that has a wider perpendicular angle to the p-n junction, θ_{\perp} (30° typical), than the parallel angle, θ_{\parallel} (15° typical) [156]. Hereby, this beam cannot be

favorably employed in range measurements because the optical power disperses very fast, leading to an inefficient power-delivery to the target. To improve the transmitted beam, i.e., to minimize its divergence and spot size and, consequently, optimize the power transfer to the target, a collimation setup is dimensioned. Furthermore, due to the difference in the vertical and horizontal diffraction angles, an astigmatism problem arises. Astigmatism is an optical aberration occurring when the focal point of the perpendicular axis is not the same as the focal point of the parallel axis (Figure 96b).

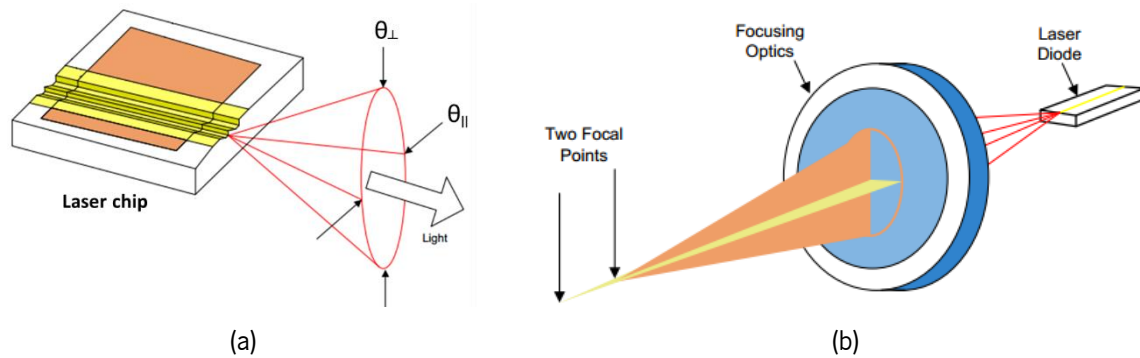


Figure 96. (a) Diffraction angles in a semiconductor laser diode and (b) resulting astigmatism [156].

On the receiving end, the reflected light needs to be collected and focused on the photodetector with a dedicated set of lenses. Otherwise, and due to the exceedingly small active area of the detectors, the detection process becomes inefficient and the sensor's sensibility worsens.

Accordingly, it is relevant to define a Figure of Merit (FOM) for the optical system. The FOM is a numerical quantity that characterizes the system performance. Naturally, this physical quantity is not universal and differs between the collimation and focusing setup. For collimation, the FOM is a compromise between divergence angle and spot size because, generally, the improvement in one comes at an expense of a degradation in the other. For focusing, the FOM is the lens FOV and the spot size on the detector, jointly translated in the light-collecting capacity.

The full optical diagram of the prototype is shown in Figure 97 as a 2D view from a plane parallel to the fast-diverging direction. The beam-shaping process is also illustrated, as well as the lenses relative placement and distances (not at scale). In practice, the distances may suffer slight modifications to optimize the system, supported by optical simulations in *ZEMAX*, but the qualitative process is not altered. All the elements are aligned through their optical axis and the TX and RX have independent optics (bistatic LiDAR).

Transmission-wise, the laser beam is firstly collimated by an aspheric lens placed at its focal length to collect as much as possible of the laser emission. Since this lens has an extremely small focal length, a non-negligible divergence remains at its output. Thereby, a set of four biconvex lenses is applied to re-focus the laser and collimate it subsequently to hold a much smaller residual divergence. Because all the previous lenses do not correct the elliptical laser beam, an iris diaphragm with an aperture adjustable between 0.8mm and 12mm is used to circularize the beam. The upside of this element is the simplicity when comparing to the anamorphic prisms pair. Whatsoever, a portion of the light is blocked (beam clipping) leading to a loss in optical power.

To reflect a portion of the transmitted light to the reference path, a microscope glass slide with $18 \times 18 \text{mm}^2$ is positioned at a 45° angle with the beam and its extremity is aligned with the optical axis. Since the glass reflectivity is small, the deflected power is insignificant and just enough to detect the sending events and generate the STOP1 pulse. Hereby, the reference light is focused on the photosensitive area of the *DET10A/M* by a biconvex lens to maximize the signal.

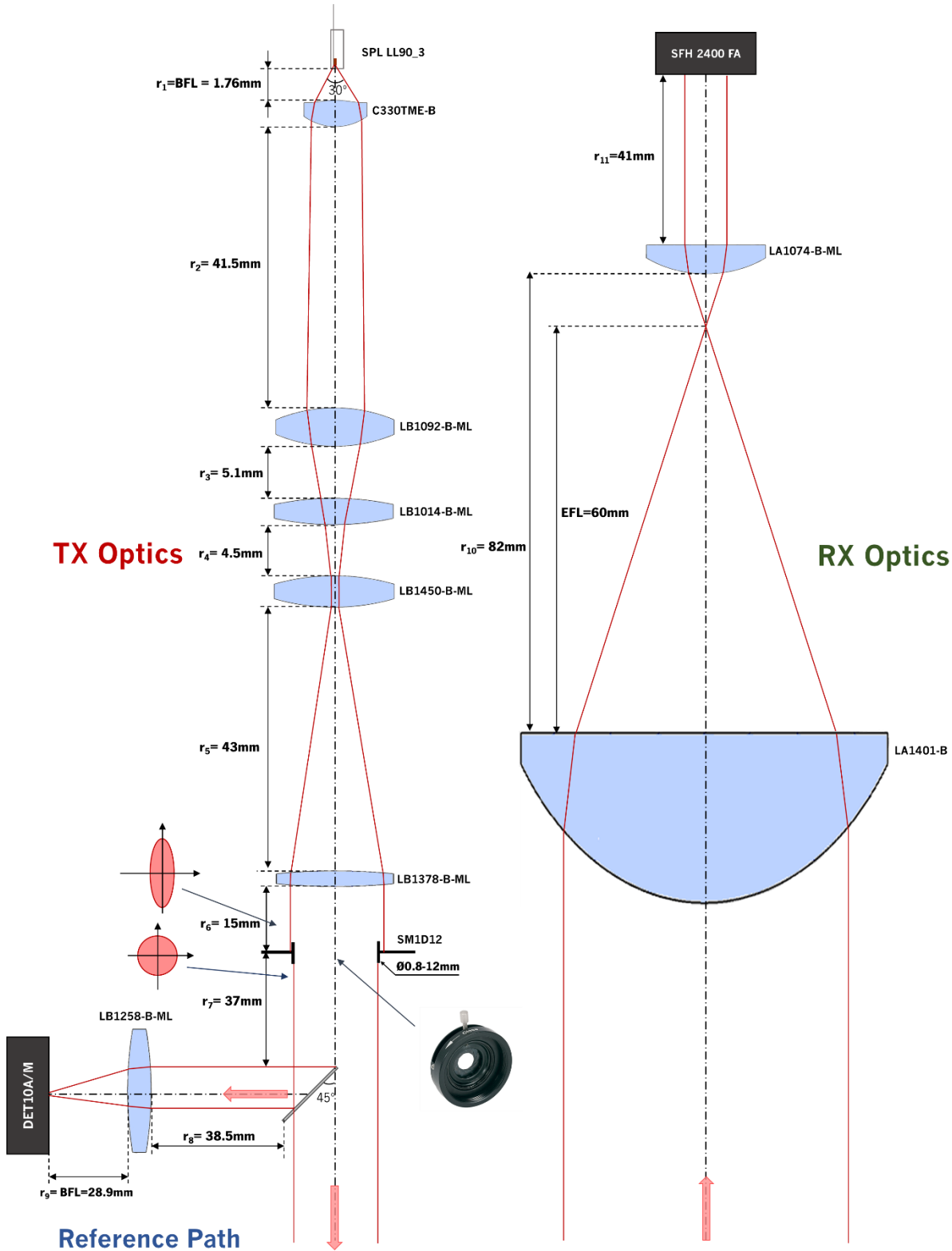


Figure 97. Diagram of the complete optical system.

In the receiver path, the returning light is collected and focused through a plano-convex lens. The additional lens (*LA1074-B*) is added to minimize the change of the beam spot size in the detector, when changing the target distance. Although the additional lens does not always ensure a collimated beam in the detector, it greatly reduces the variation of the beam size due to changes in the distance to the backreflecting target. This is important for the distances tested in the laboratorial environment but, naturally, is much less important for realistic working distances in actual LiDAR sensors of, say, from 10 to 100m.

Assorted lens morphologies are adequate for the occasion: plano-convex, biconvex, positive meniscus, doublet, best form and aspheric. The first five lens are spherical and are the most common lenses due to the easier manufacturing process, simpler profile and lower costs. However, they all induce spherical aberration, a phenomenon independent of alignment and in which the collimated rays are focused in different points of the optical axis according to their radial distances (Figure 98). Aspherical lenses are a proper option since they correct the previous aberration and are specifically designed for collimation and focusing. As a counterpart, they are more sensitive to tilts and misalignments.

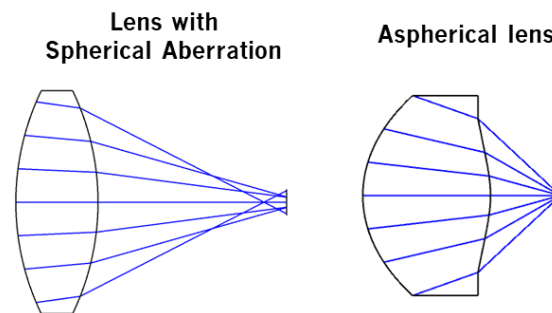


Figure 98. Spherical aberration phenomenon (left) and correction using aspherical lenses (right).

The employed lenses' models are described in Table 16. The most relevant parameters are defined in accordance to the schemes in Figure 99. The effective focal length, *EFL* or *f*, is measured in relation to the lens back principal plane *H''*, the back focal length, *BFL* or *f_b*, is measured in relation to the lens' back vertex, while the working distance, *WD*, is the distance between the back of the mount/housing and the focal point. It is essential to bear in mind that these are not the unique choices and the principal aspect is the process each lens implements and not the model itself.

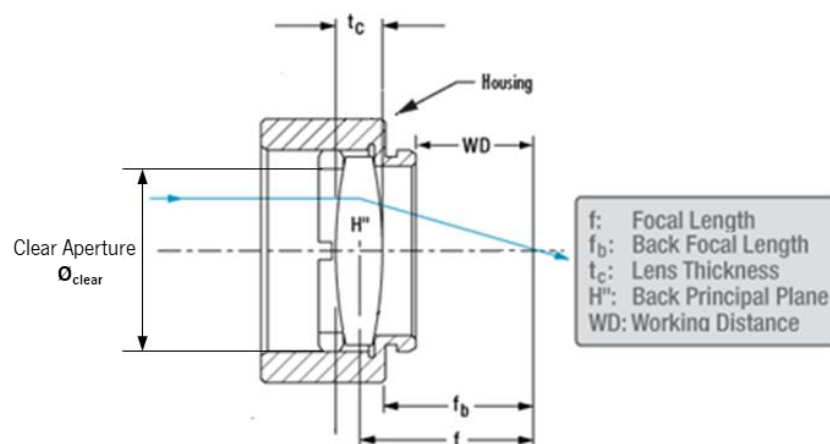


Figure 99. Mounted lens layout and respective parameters.

The process of lens selection follows a compromise between availability and performance. The aspheric lens is chosen with the intuit of collecting a major portion of the laser output while yielding a favorable first-collimation step. Ideally, the reception lens should be an aspheric lens to eliminate spherical aberration and maximize the power collected from an extended source as the LD with several epitaxial emitting layers. However, all the accessible aspheric lenses were small in size, compromising the light collecting capacity. Hence, the *LA1401-B* lens is used following the proposition in [59]. All the other lenses were selected in between the kits available at the laboratory. Since the lens are designed for a different wavelength rather than 905nm, some deviations may occur from the expected operation because the refractive index is wavelength-dependent.

Table 16. *ThorLabs* lenses' characteristics [173]–[176].

Model	Shape	EFL [mm]	WD [mm]	BFL [mm]	t_c [mm]	\varnothing_{clear} [mm]	Glass / refractive index	Coating
C330TME-B	Aspheric	3.1	1.68	1.76	3.18	5	ECO-550 / 1.597 @ 830nm	
LB1092-B-ML	Biconvex	15.0	11.8	13.4	4.7			
LB1014-B-ML	Biconvex	25.0	21.7	23.8	3.4	11.4		
LB1450-B-ML	Biconvex	20.0	16.7	18.7	3.9			
LB1378-B-ML	Biconvex	40.0	36.7	39.1	2.8			
LB1258-B-ML	Biconvex	30.0	26.6	28.9	3.1			
LA1401-B	Plano-convex	60.0	N/A	49.1	16.3	45.7		
LA1074-B-ML	Plano-convex	20.0	17.3	14.5	4.0	11.4 (SM05)	N-BK7 / 1.515 @ 633nm	AR 650- 1050nm (B-coat)

To complete, all the lenses are AR-coated for the wavelength interval between 650nm and 1050nm, to minimize light reflection on the surfaces and power losses. In this bandpass range, the average reflectance is less than 0.5% per surface for angles between 0° (normal incidence) and 30°.

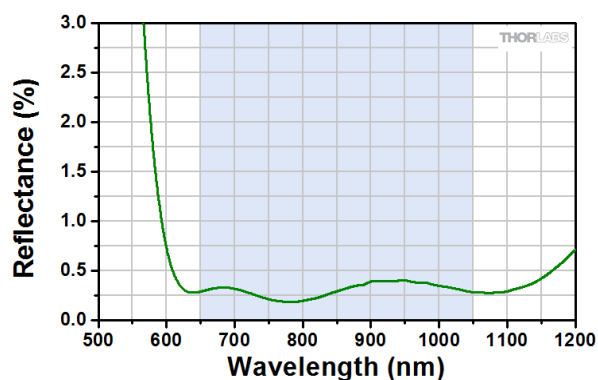


Figure 100. B-coating reflectance spectrum [177].

Due to the bulky nature of the setup, the LiDAR is only characterized indoor. For this reason, no additional filtering is required, besides the intrinsic band-pass filter on the detector.

In Figure 101 it is pictured the total system with emphasis on the interface between the optical system and the hardware. The optical elements are mounted on the same breadboard as the corresponding electronics. On the TX side, the lenses are mounted on a *ThorLabs* 30mm Cage System

to ensure an automatic alignment along a common optical axis. As the TX boards are fixed, the cage is supported by a 3DOF stage similar to that holding the RX boards, to allow a relative adjustment between laser and optics. In addition, the small aspheric lens is mounted on an appropriate adapter (*E06RMS* manufactured by *ThorLabs*) which is fixed in a *KC1-T* support with tilt regulation in three directions, adding 3 more DOF to this lens, since it is the component with most sensitivity to misalignments. The set of 3 pre-mounted convex lenses are screwed together. The glass slide and the detector are mounted on fixed posts with one vertical DOF. Regarding the RX optics, it is mounted on a fixed post with vertical adjustment since the hardware supporting the RX PCB already has 3DOF for alignment.

In addition, the post supporting the TX acrylic plate is replaced by a 1DOF rotation stage to maximize the coupling laser-collimating lens since the aspheric lens is extremely sensitive to tilts and misalignments.

Finally, an *AFB0712HHB* CPU fan supplied at 6V is fixed above the laser and directed towards it to provide temperature stabilization. This is critical to prevent wavelength shifts and deterioration of the optical output power, and, thereby, to assure a stable operation.

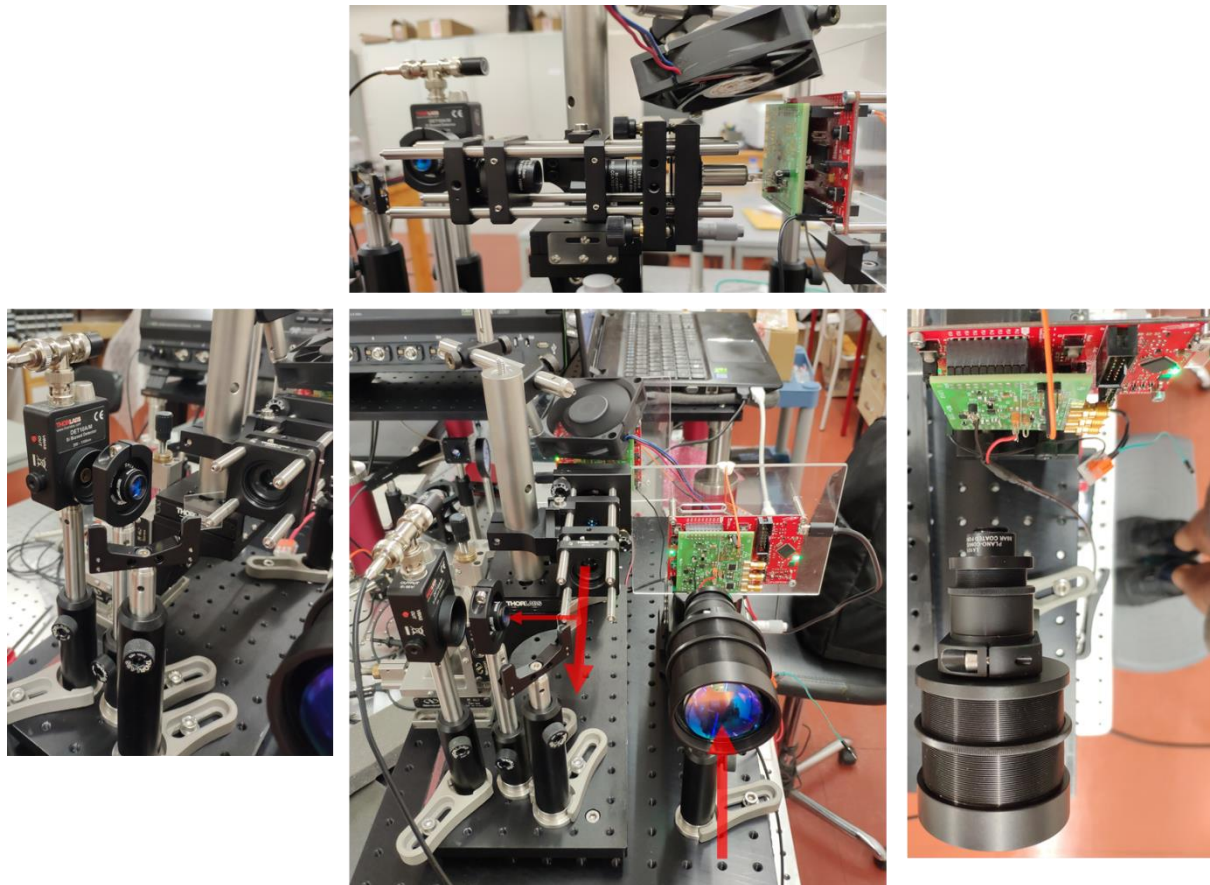


Figure 101. Photos of the optical system interfaced with the hardware. On the left, the reference path, on top, the TX path and, on the right, the RX path.

5

RESULTS AND DISCUSSION

This chapter aims to expose and dissect the experimental procedures to extract the system characteristics, alongside with the main results and a critical discussion of the respective. Furthermore, it also intends to identify the foremost factors limiting the performance of the current design as well the points with most potential for improvement.

In a first stage, the 1D LiDAR prototype is characterized as a whole in relevant performance metrics to validate its operating principle and prove the ToF concept as proposed in the initial goals. Posteriorly, and after drawing the *big picture*, the individual elements are characterized to give a more profound insight on its role within the system and impact on the overall results. This phase is split in electrical and optical characterization and some simulations are presented to support the tests. The objective is not to exhaustively study each component but rather to analyze them in the scope of this work. At last, the weaknesses of the TIDA-00663 reference design are described to motivate the preferences and modifications implemented.

5.1. Overall Sensor

Before evaluating the LiDAR performance as a whole, it is necessary to establish and define the test conditions. This definition process involves a previous addressing of the dangers, auxiliary testing of the sensor to find the optimum parameters configuration and calibration. All the testing is performed indoors.

5.1.1. Precautions

During testing at the laboratory, several precautions must be taken to either avoid biological damages by laser radiation and Electrostatic Discharge (ESD) to the electronic components. To prevent the first hazard, whenever the laser is turned-on, one must use safety eyewear because there are high optical powers involved and in the NIR region the natural blink-reflex does not work. The glasses used throughout the experiments are the *ThorLabs LG12* with an *ANSI Z136*-compliant Optical Density (OD) factor above

7 at 905nm, translated in a transmittance below 0.00001% [178]. Even with the protective glasses, one must avoid leaning to the laser to prevent direct or indirect (through reflection on metallic parts) incidence of the beam on the lenses.

When handling the PCBs, an antistatic wrist strap shall be worn to safely ground the person and prevent the buildup of static electricity on the body, which can result in an ESD to the electrical components. This is extremely important since most of the components are SMD and very sensitive to ESD, that may burn them without one noticing.

To add up to the previous precautions, when measuring the electrical signals on the oscilloscope directly from the PCB, a short ground lead (Figure 102a) is used, when possible, instead of the standard 3-inch long ground wire supplied with the probe. The passive *Teledyne LeCroy PPO22-1* probes employed have a 10pF capacitance, 10M Ω inductance and a parasitic ground lead inductance. To measure the signal at a specific point and produce a voltage waveform on the oscilloscope, these impedances are connected in parallel with the Device Under Test (DUT) - Figure 102b. Consequently, the tip draws some current and, thus, interferes with the circuit. The larger the ground wire, the larger the parasitic inductance introduced and, therefore, the larger the unrealistic ringing induced by the measuring device. This effect is particularly impactful because of the fast rise and fall times of the signals involved.

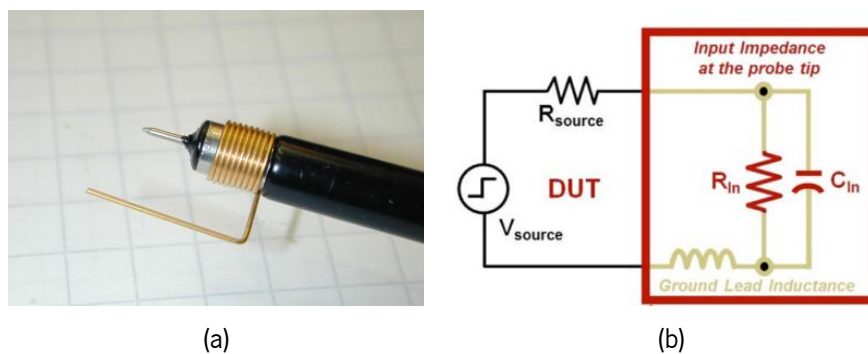


Figure 102. Oscilloscope probe: (a) short ground lead and (b) equivalent circuit connected to the DUT.

5.1.2. Targets Characterization

The LiDAR system performance is evaluated with two distinct targets named *Vauxhall Green Lemon Grass Metallic* and *K-line White*. Before characterizing both, it is important to briefly introduce some concepts. Firstly, the reflective properties are indicated by the target's reflectivity, relating the incident luminous power, P_i , to the reflected power, P_R , as:

$$\rho_T = \frac{P_R}{P_i} \quad (5.1)$$

In this context, two types of reflections arise as relevant [179], depending on the target physical composition and characteristics, such as geometry, composition and surface finishing. First, in diffuse reflection (red in Figure 103a), also denoted as Lambertian scattering, the reflected light disperses uniformly in every direction with a relatively predictable percentage finding its way back to the sensor. This type of reflection tends to be easily measured. The second type is specular reflection, in which the energy is reflected according to the law of reflection (blue in Figure 103a). When light undergoes this

type of reflection, the energy is reflected almost perfectly to the detector, with minor dispersion. Nevertheless, when the beam is not reflected directly to the detector, it misses the receiver altogether and a range loss is incurred. In most objects, a mix of diffuse and specular reflection is verified, and, in these cases, the total reflectivity, ρ_T , is given by the sum of the two components:

$$\rho_T = \rho_{diffuse} + \rho_{specular} \quad (5.2)$$

Additionally, in specific targets, a hybrid between the two antecedent reflection extremes can emerge and is denoted glossy scattering. This scattering phenomena, illustrated in Figure 103b, is particularly importante for back reflection on car paints.

The selection of both targets is motivated by the portrayal of the two most representative examples of actual realistic scenarios: an almost ideal Lambertian back-reflection and an actual of an actual sample of a car finishing. Also, the choice is also dictated by the goal to evaluate the possibilities for the use of the polarization signature in LiDAR, for advanced signal processing, more specifically, target material identification. In this respect, these two targets represent the extreme conditions of almost full depolarization and almost complete polarization retention in back-reflection, as it will be shown latter in section 6.2.

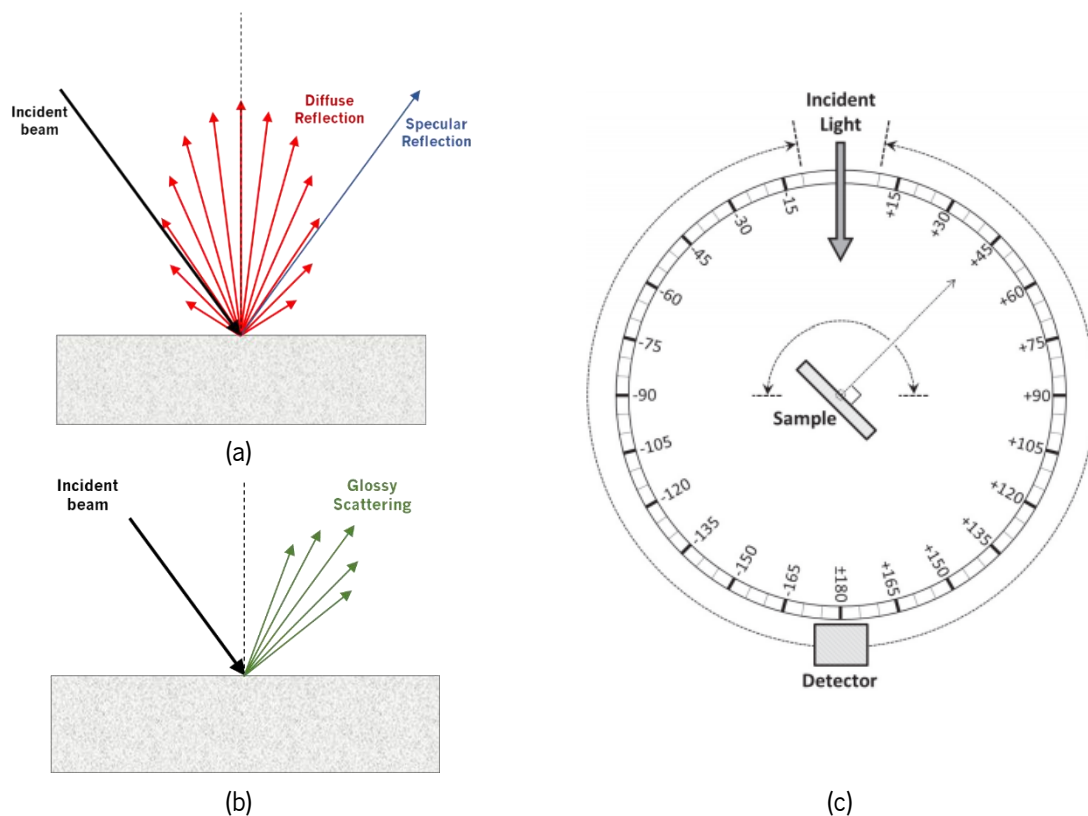


Figure 103. Characterization of the targets' reflective characteristics: (a) illustration of specular and diffuse reflection on a surface; (c) measurement setup with sample and detector angle definitions. [180]

Both targets are characterized at 905nm (5nm spectral width) using an *Agilent Cary Series 7000 UV-Vis-NIR Spectrometer* complemented with the *UMA (Universal Measurement Accessory)*. The setup consists on an incident beam at 0° plus a detector and a sample-holder with independent angular coordinates that can separately rotate 360° (Figure 103c). Thereby, the sample can be positioned at a

fixed angle and the detector can scan an angular section. The measuring device has a blind range between -10° and $+10^\circ$, where it cannot detect the reflected light.

The *Vauxhall Green Lemon Grass Metallic* (Figure 104a) target is a sample from a real car paint yielding both specular and diffuse reflective properties. Structurally, this target is composed of a stack of several layers. The uppermost is a clearcoat layer of a resin with thickness in the order of tens of micrometers. Underneath this layer is a basecoat (tens of μm thick), with the same refractive index as the former, and where the light is reflected. The latter consists of a binder with metallic flakes, prominently visible when struck by visible light (Figure 104b), and color pigments that cause scattering and absorption [181]. The diffuse reflectivity component, $\rho_{diffuse}$, is approximately 0.8% at 905nm, while the specular component is depicted in Figure 104c for s-polarized light and for several Angles of Incidence (AOI), θ_i . For each AOI, a peak is observed at $2\theta_i$ corresponding to the specular component at the detector. At normal incidence (AOI= 0°), the specular reflection coefficient, $\rho_{specular}$, is approximately 5%. At the same angle, the results for p-polarized light are similar. Whatsoever, with increasing AOI, the reflectivity decreases up to the Brewster's angle of incidence (increasing posteriorly).

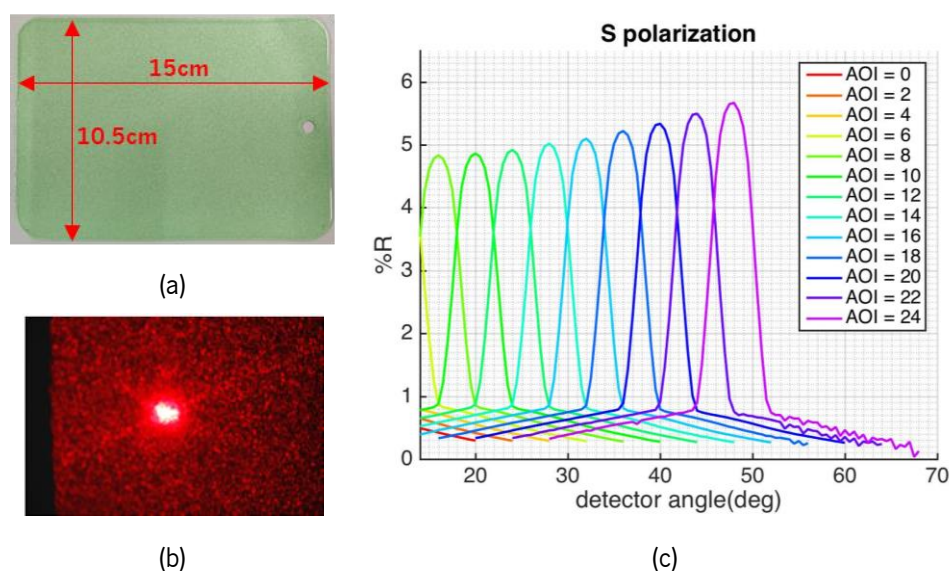


Figure 104. *Vauxhall Green Lemon Grass Metallic* target: (a) sample used in the experimental tests with $10.5\text{cm} \times 15\text{cm}$; (b) metallic flakes made visible when the plate is struck by an He-Ne laser; (c) specular reflection peaks for several AOI. In the last image, the width of each peak depends purely on the detection optics in the measurement device (f-number).

The other target is a *K-line White* paperboard plaque (Figure 105a) with a purely diffuse behavior. Empirically, the reflective properties are measured on the abovementioned spectrometer by fixing the angle of incidence to 0° while the detector measures the reflected intensity in an angular section between -90° and $+90^\circ$, restricted to the plane of incidence. The obtained data is displayed in Figure 105b and represents the in-plane Bidirectional Reflectance Distribution Function (BRDF) [179]. The results are determined by dividing the actual measurements by a geometrical cosine factor of the detection angle.

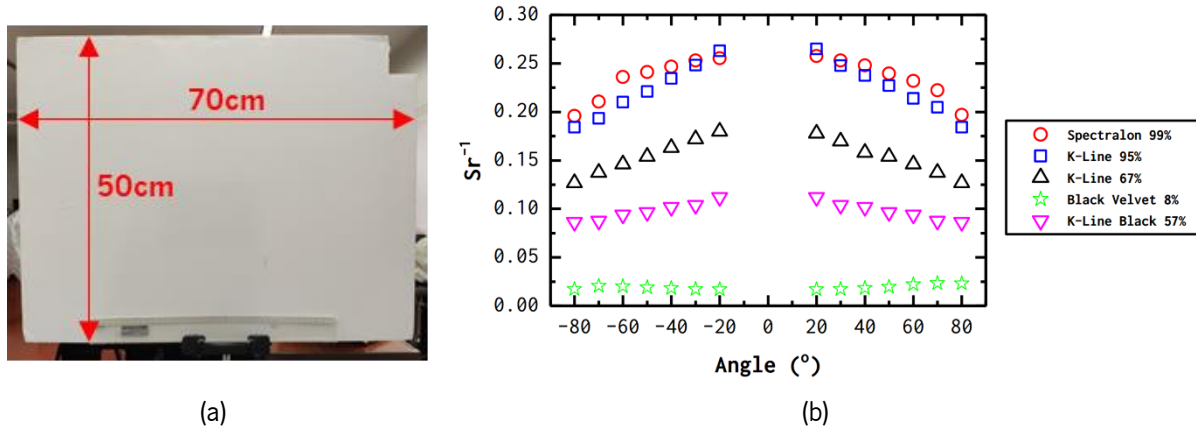


Figure 105. (a) *K-line White* target sample used in the experimental tests with 50cm×70cm. (b) In-plane BRDF for several target materials as a function of the detection angle. The angle of incidence is fixed at 0° and the angles between -20° and 20° are unavailable due to occlusion.

The BRDF is defined as the ratio of the radiance of a sample to the irradiance upon that sample, for a given direction of incidence and direction of scatter. It can be calculated using [182]:

$$BRDF = \frac{P_s}{P_i \cdot \Omega \cdot \cos \theta_s} [sr^{-1}] \quad (5.3)$$

where P_s is the scattered power sensed by the detector, P_i is the incident power on the sample, Ω the detector's solid angle and θ_s the detector's angle relative to the sample's surface. This quantity is given in inverse of steradians, a fairly abstract unit manifesting the intensity distribution of the scattered beam. Ideally, a perfect Lambertian material should have a flat BRDF, constant with the detection angle. However, such materials do not exist and the BRDF results are compared with a diffuse reflectance standard, the *Labsphere Spectralon SRS-99-010* (calibrated reflectance of 99%) [182]. By comparison, the *K-line White* target is at least as Lambertian as the reference standard material, stated as being highly Lambertian [182].

To conclude, the total diffuse reflectance of this target is estimated through the integral of the measured intensity values over the collected range, knowing the initial incidence intensity. Overall, the reflection coefficient is evaluated 95% at 905nm ($\rho_T = \rho_{diffuse}$).

5.1.3. Graphical User Interface

To access the LiDAR range data in real-time and display it directly and intuitively in a user-friendly channel, a Graphical User Interface (GUI) is developed in *Java*. This programming language is well-suited since it is object-oriented, allowing an efficient and straightforward manipulation of the elements in the graphic window. The complete code is provided in '*Appendix II – Final Codes*'.

The program reads the ToF data from the serial port at a 9600 baud rate. As these results are sent as floats via the RX MCU UART to the PC, then they are read in the same numerical format and continuously stored in an array. Posteriorly, the ToF is converted *in-loc*o to range and the instantaneous data displayed. At the same time, the standard-deviation and average are calculated for the accumulated data and also outputted to the GUI window. Finally, a range graph is traced and refreshed every 10

seconds to show the evolution. Additionally, three action buttons are available to control the acquisition: the START begins the acquisition that runs until the STOP is pressed; the RESET clears all the variables, including the data arrays, to restart a new acquisition segment. The GUI main window is shown in Figure 106 with all the referred elements identified.

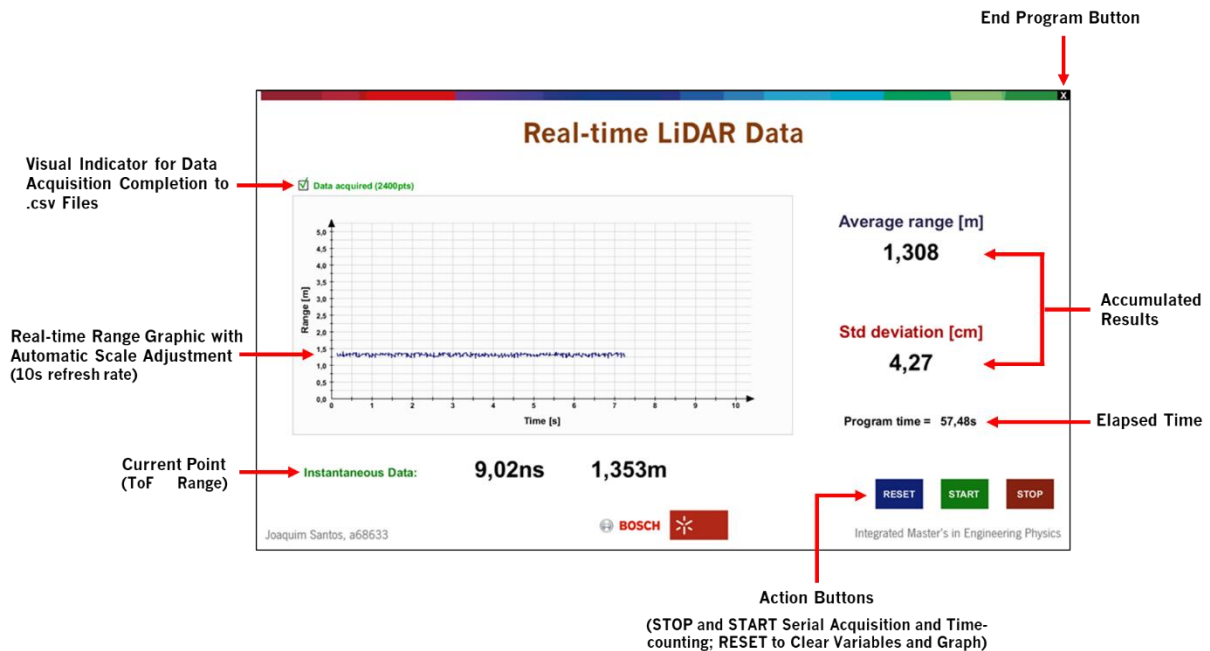


Figure 106. Developed GUI for the LiDAR prototype.

Besides the visual functionality, the program has another major task: to automatically save a set of 2400 range and ToF points in separate *.csv* files for posterior processing in *MATLAB*. The stored points are the initially acquired, with the nuance of rejecting the first hundred due to instability when establishing the connection to the serial port and a higher susceptibility to communication errors.

5.1.4. Standard Test Conditions

First and foremost, before the functional characterization of the 1D LiDAR prototype, it is utterly vital to establish the sensor operating conditions to use throughout the stage of results' extraction in order to preserve consistency during the process, yield a stable response and assess the impact of each operational setting on the overall quality/performance of the sensor. Thence, the initial step is the definition of the standard test conditions either from ground truth, i.e. from direct empirical evidences, or argumentation based on hardware restrictions. The settled parameters are listed in Table 17. Unless explicitly stated otherwise, all the results and data analysis in the document correspond to the test conditions defined in the latter table.

The repetition rate, $PRR \equiv f_p$, i.e. the point acquisition speed, is entrenched through the *BP_TRIG* PWM signal and a restrictive limitation to 6kHz is fundamentally imposed by the TDCs reading times, explored in sub-section 5.3.6. The *BP_TRIG* duty cycle, *dc*, is set to 65% since the lasing capacitors (C_{eq}) require a minimum time of 44 μ s to fully charge. Moreover, the latter definition is supported by experimental observations. These two parameters are restraint by hardware. Followingly, the threshold

for the reference pulse (*laser_on_threshold*) is established assuming that the pulses amplitude in the reference path is constant, true for a stabilized laser, and to ensure no false triggerings. The remaining parameters must be selected and correspond to either operational values (threshold for level crossing timing, amplifier gain and triggering edge) or test conditions (back reflection component from diffuse target). These parameters are studied individually in the following sub-sections and are delimited by factual observations to provide the best overall performance for this LiDAR.

In the present settlement tests, only the system precision is analyzed and not its accuracy. This means that average ToF measurement is not compared to the real distance to the target neither between different parametrical configurations since the shifts in the ToFs are not critical and can be corrected through calibration. Instead, only the fluctuations around the mean value (imprecision) are considered, numerically implicit in the standard deviation, σ , computed using equation (2.10).

Table 17. Standard test conditions to be used throughout the system characterization phases, imposed either experimentally or by hardware restrictions.

$f_p \equiv$ PRR (point rate) [kHz]	6
dc (BP_TRIG) [%]	65
$V_{th,B}$ (laser_on_threshold) [V]	0.15
Reflection Component	Diffuse
Transimpedance Gain [kΩ]	20
Triggering/Timing Edge	Falling
Return Threshold, $V_{th,A}$ [V] (return_th)	1.7

5.1.4.1. Reflection Component

To enable the study of both reflection components, the *Vauxhall Green Metallic* target is used (representative of an actual car paint). The setup consists on mounting the target on a rotational support that, in turn, is fixed on a movable table in front of the prototype at a given distance. Posteriorly, the target is aligned with the sensor in order to directly reflect the specular component to the RX optics. This is performed by simultaneously monitoring the return pulse until a maximum amplitude is attained. In these conditions, a complete set of 2400 points is acquired with the GUI. Posteriorly, the target is slightly rotated around the vertical axis, through a screw in the support, to remove the specular component from the detector. When the return signal amplitude reaches a point at which it turns almost invariant with the target rotation, one can acknowledge that the diffuse component is being detected. This way, it is possible to alternate between the diffuse and specular reflection components. This procedure and setup are explicit in Figure 107. This is the same setup employed for setting the other system operating conditions and parameters.

The acquisitions for both components are performed at a range of $d_{actual}=671\text{mm}$ for a 20k Ω transimpedance gain and the thresholds listed in Table 17. The raw results are displayed in Table 19 both for a triggering in the falling and rising edge of the digital STOP pulses (STOP1 and STOP2), accompanied by the standard deviation in the measure ToFs, σ_t , and the corresponding standard

deviation in range, σ_d . In short, the standard deviation between both components is in the same order of magnitude when the STOP triggering for the TDCs occurs at the falling-edge (around 5cm), a behavior that is verified even for farther distances. A slight difference is noticed for triggerings in the rising-edge. Regarding the statistical distributions, the fluctuations in the ToF are stochastic and induced by several factors such as jitter and photodetection noise (to be explored) and the histogram for specular reflection and rising-edge appears to fit into a more gaussian-like distribution. Yet, this is only a portrayal artefact arising from the combination of a larger standard deviation and the constant number of bins (50) in each representation.

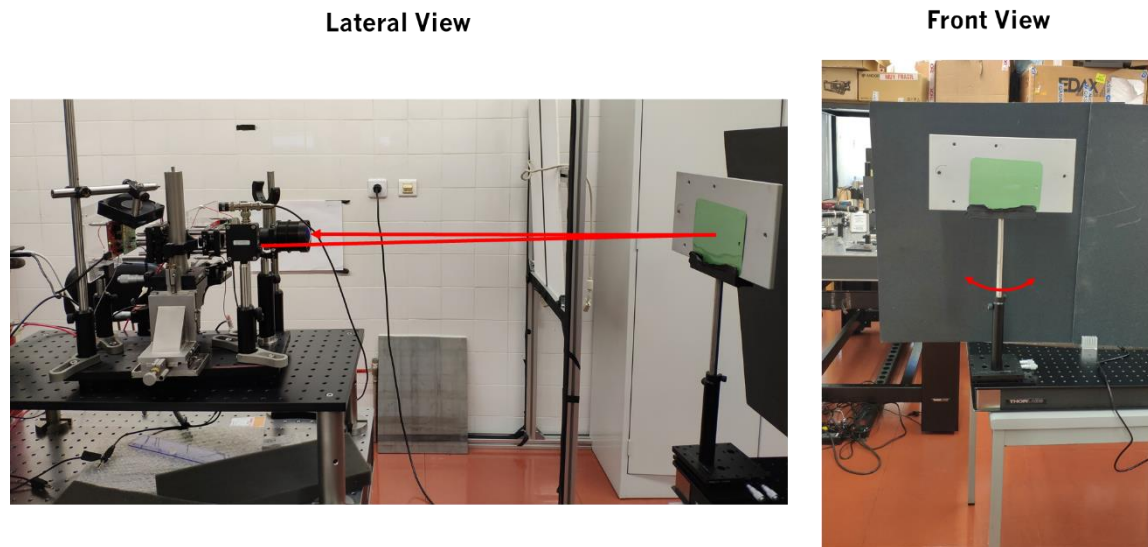


Figure 107. Setup for establishing the standard test conditions of the 1D LiDAR sensor. On the left, the lateral view with the prototype (left) and the *Vauxhall Green Metallic* target (right), with the light path marked from the transmission to the reflection back to the receiver. On the right, the front view of the mounted target with the rotating direction highlighted (to alternate between specular and diffuse components).

Withal, the critical aspect to infer herein is another. Since the LiDAR prototype is bistatic (separate optical apertures for TX and RX) and does not have scanning, whenever the target is moved further from the sensor it is useful to re-align the sending unit to ensure that the receiving unit is aligned with the back-reflection. Recalling that the TX side is mounted as a whole on a smaller and movable breadboard and the RX is fixed, this procedure is done by rotating the sending unit, as perceived through the schematic in Figure 108a, and does not depend whether one intends to measure the specular or diffuse components. Whatsoever, when measuring the specular component, it is also necessary to posteriorly align the target (through rotation) to collect the specular component. Alternatively, the TX may also be translated parallelly to the target plane (Figure 108b).

Even though the specular component is significantly more intense, allowing measurements up to longer ranges, it requires a more precise and less likely alignment between the transmitter, receiver and target, otherwise this component is missed altogether. The previous procedure is impracticable for a final product as the components are fixed to a hermetically sealed housing and cannot be adjusted on-the-fly (in scanning systems, the equivalent of “rotating the sending unit” is achieved by the scanning itself).

Hence, in a realistic scenario targeting automotive applications, the diffuse component, present in the bulk of materials, is then ordinarily detected and measured. This component is the most representative of the practical LIDAR usage and commercial LiDAR specs, generally specified for diffuse targets, because it is less sensitive to angles since the diffusely reflected light is dispersed over a hemispherical volume in a near-Lambertian distribution. Hereupon, the functional tests are carried out using the *K-line White* target, which is assumed at first level to only have a diffuse reflection component as characterized in section 5.1.2.

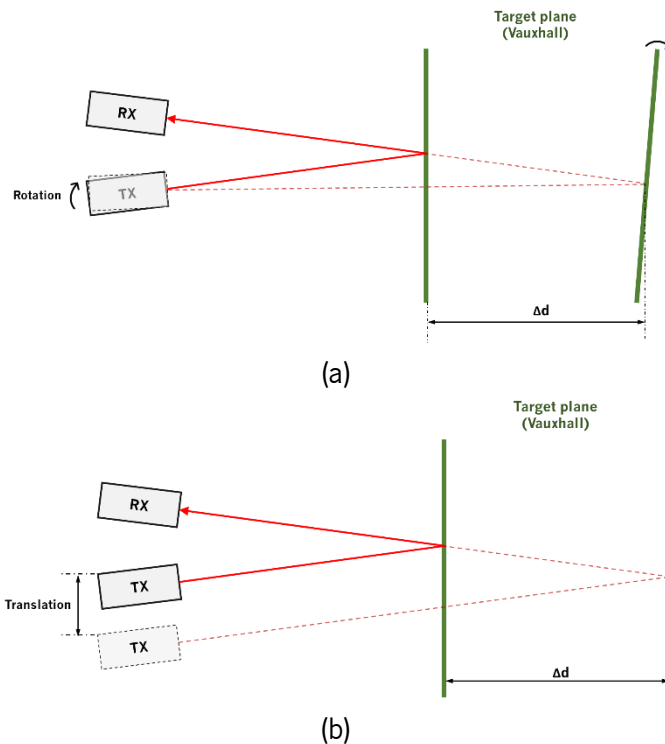
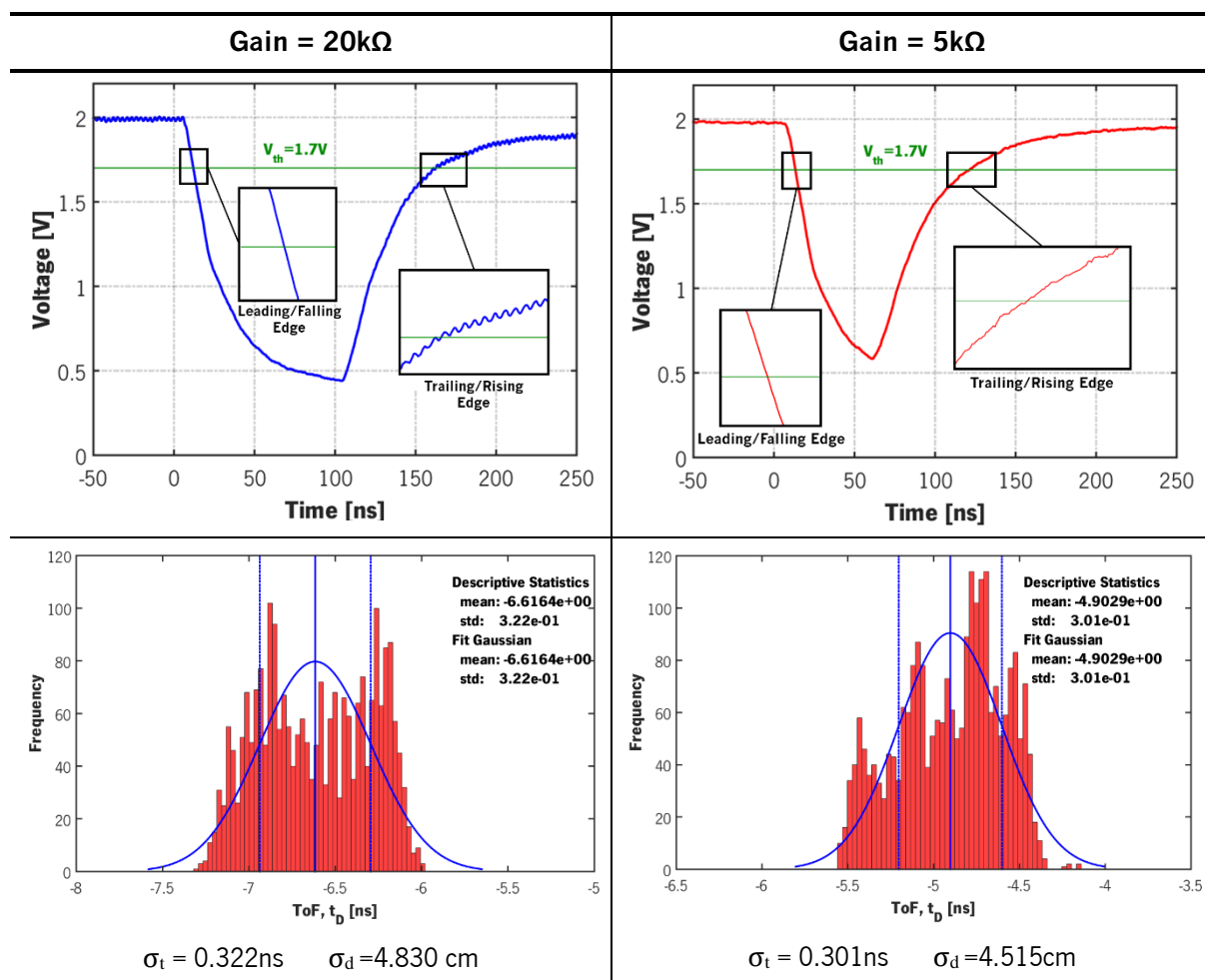


Figure 108. Top view schematic to illustrate the required adjustments to the LiDAR system to measure the diffuse (a) and specular (a and b) components at distinct distances: (a) rotation or (b) translation of the TX whenever the target distance is modified.

5.1.4.2. Transimpedance Gain

Concerning the transimpedance gain, the discussion is clear and straightforward. The sensor or, more concretely, the TIA, has two possible gain configurations: $5\text{k}\Omega$ and $20\text{k}\Omega$. To alternate between both, the pin P3.5 of the MSP430FR5969 shall be written, respectively, to '0' or '1'. The LiDAR prototype, and automotive LiDAR systems in general, aims to maximize the measurable range. Therefore, a maximum sensitivity is desired and the gain must be set to $20\text{k}\Omega$, which translates into a larger dynamic range because the receiver will discern less intense returning light pulses. However, in general, larger amplification gains also means larger fluctuations induced and less precision (larger standard deviation), since the photodetection noise is amplified alongside the effective detected signal. Hereby, one must evaluate the better balance. Note that, contrary to the gain mechanism in APDs, the TIA gain is not generated through a stochastic phenomenon and is defined by a feedback resistor. Hereupon, there is no gain noise.

Table 18. Acquired pulses in the *Teledyne Lecroy HDO4034* oscilloscope for the two gain settings and the *Vauxhall* target at 671mm superimposed with the 1.7V threshold. Below, the distributions of the 2400 raw data points sensed under the same conditions. From the pulses, it is visible that the threshold crossing at the falling-edge occurs at a point with larger absolute derivate comparing with the rising-edge and, thus, less conspicuous to jitter.



Then, the analog pulses at the TIA output must be analyzed in the two gain settings conditions. In Table 18, the return pulses are shown as acquired for diffuse reflection on the *Vauxhall* target at $d_{actual}=671mm$ and the other parameters in agreement with the standard values. From the experimental observables, it is possible to apprehend that the meaningful differences arise in the noise levels (origin on photodetection and amplification) of the baseline and trailing-edges between both gains. Nonetheless, the noise difference at the critical level, i.e. in the threshold crossing level for the leading-edge, is imperceptible. The previous statement is confirmed by the histogram data also shown: for triggering in the leading-edge, the standard deviation increases from around 4.515cm to around 4.830cm with the rise in gain. Hereafter, one can conclude that the inconsequential increase in the system imprecision does not justify the loss of 1/4 in gain and the maximum setting shall be used to maximize the sensitivity. This clear response may be attributed in part to the optical filtering in the *SFH 2400 FA* PIN photodetector's packaging, that greatly reduces the background noise by blocking radiation below 750nm.

This conduct remains when the range is raised. However, as the return intensity decreases, there will be a point at which the imprecision for 5kΩ gain will rise above the standard deviation for 20kΩ

because the timing point at the fixed threshold of $V_{th,A}=1.7V$ will occur nearer the pulse peak, where the voltage rate of change is smaller and where the jitter has a larger effect. Further, all this discussion is only referent to the return path. In the reference path, the photocurrent pulses are transampled with a constant gain because the *DET10A/MPD* is not configurable.

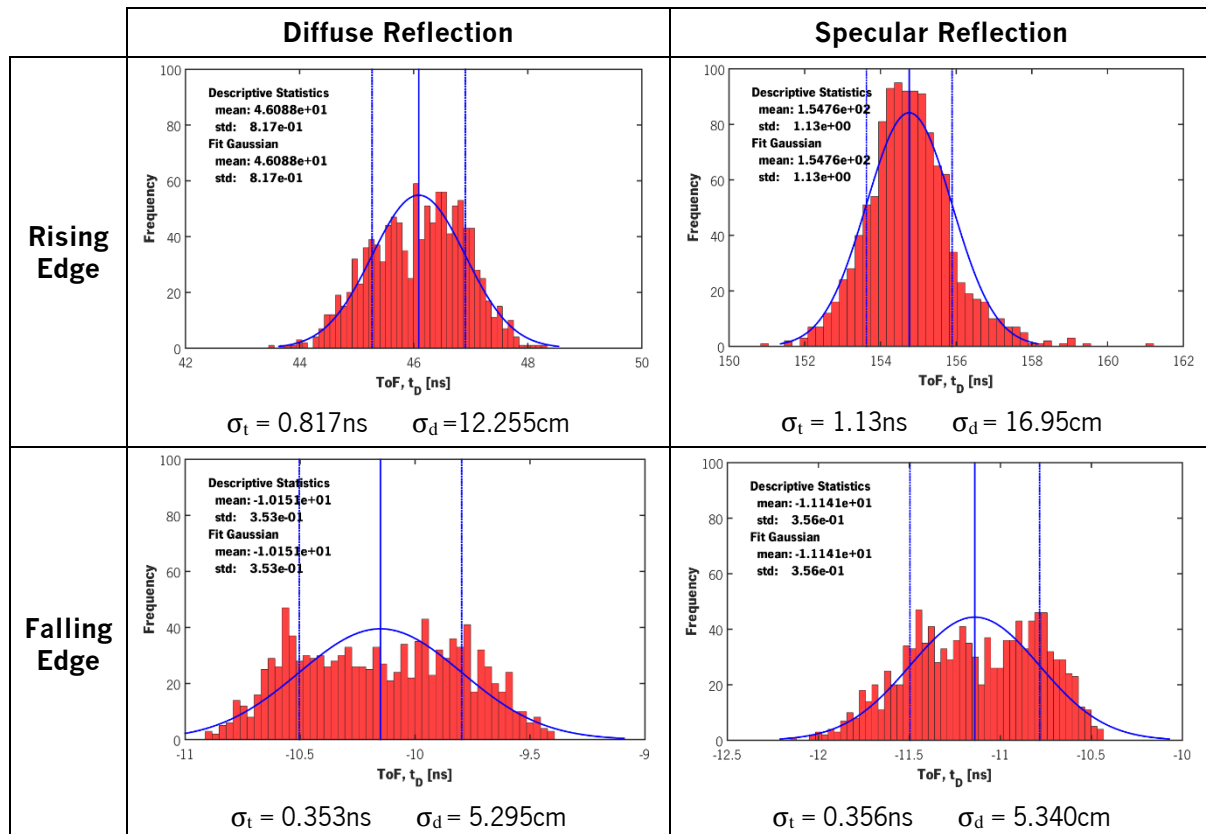
5.1.4.3. Triggering/Timing Edge

The TDCs can be configured to trigger the STOP and START events either on the rising or falling-edges of the pulse received in the respective pins. Besides affecting the measured time-interval, these configurations do also influence the system accuracy. The polarity of the START pulse is not encompassed in this analysis since, in principle, the digital *BP_TRIG* pulse does not have remarkable fluctuations/noise in the fast transitioning edges. To alternate between a STOP stimulation in either one of the transitions, the *CONFIG1* register in TDC1 and TDC2 shall be written according to:

```
uint8_t CONFIG1[] = {0b01000000, 0b10111011}; %STOP on falling-edge
uint8_t CONFIG1[] = {0b01000000, 0b10101011}; %STOP on rising-edge
```

which requires a change in the RX MCU (MSP430FR5969) code. The raw measurements are acquired simultaneously with the extraction for the diffuse and specular discussion in section 5.1.4.1, i.e. under the same conditions, and are also represented in Table 19.

Table 19. Histogram (frequency distributions) for the raw ToF data (2400 points) acquired for diffuse and specular reflection on the *Vauxhall* target at 671mm. In parallel, the results for a STOP trigger in the fall and rise edges of the respective digital pulses. Overlaid with the histograms are the respective gaussian fits.



Straightforwardly from standard deviation estimations, one can deduce that the timing on the leading-edge of the STOP signal is more adequate because it induces a significantly smaller imprecision in the measurements. To understand the reason behind this behavior, one must first consider that, nominally and in practice, the laser pulses have a notably longer fall-time comparing to the rise-time (see return pulses in Table 18). Hence, after photodetection of a return pulse, and since the amplification in the TIA is also accompanied by inversion, the return voltage pulses will cross the threshold at a point with a larger absolute rate-of-change (derivate) if the timing is carried out on the leading-edge (fall) comparing to the trailing-edge (rise). As consequence, the threshold crossing on the falling-edge of the discriminated STOP pulses will be susceptible to less conspicuous noisy fluctuations affecting the timing point (jitter is smaller for faster transitions, in absolute value), contrasting with the comparably long-duration rising edges. This justification is supported by the return pulses visible in Table 18, zoomed-in on the threshold crossing both in the leading and trailing edges, and is also valid for the reference pulses, even though its inversion occurs at the leading-edge discrimination. Moreover, the behavior is also anticipated and confirmed for longer distances since the threshold crossing-time is consistently smaller in the pulse leading-edge. Finally, the conclusions are the same for diffusely and specularly back-reflected light.

5.1.4.4. Return Threshold

The threshold for timing the back-reflected pulses, $V_{th,B}$, is defined analogously to the gain and has a similar effect on the sensor's performance. Ideally, the threshold must be defined the closest as possible to the baseline on the TIA output and just above the noise level to enable a larger dynamic range in the timing discrimination, since smaller amplitudes can be discerned. This threshold is configured directly in the RX MCU and its value is adjustable between approximately 1.2V and 2.3V.

In Figure 109 it is displayed one return pulse acquired in the *Teledyne Lecroy HDO4034* oscilloscope after diffuse reflection on the *Vauxhall* target at 671mm. As the TIA inverts the pulse and introduces an offset in the output signal [165], the threshold voltage shall be maximized to detect the pulses at a smaller fraction of its leading-edges. However, as notorious, the baseline is affected by some oscillations around an estimated mean value of 1.994V. The latter stochastic fluctuations, in the acquisition conditions, are between 2.044V and 1.926V and, therefore, the threshold must be established below 1.9V to avoid false triggerings.

Three thresholds are empirically experimented: 1.8V, 1.7V and 1.6V. For each, the 2400 points are sampled and the standard deviations calculated. The results are, respectively, 5.101cm, 5.295cm and 4.863cm. The differences are unimportant and negligible but, at longer distances and weaker return pulses, the effect starts to be noticeable for the same reason reported for the gain: the timing point shifts gradually to points at a bigger fraction of the amplitude, in which the instantaneous slew rate (voltage rate of change per time unit) is smaller, and, eventually, until the STOP is no longer triggered. Thus, the smaller the threshold (or also, the gain), the smaller the sensor-to-target distance at which the standard deviations starts to deteriorate considerably.

Herewith, the threshold is defined at 1.7V as a precaution to completely ensure no false triggerings disturbing the measurements' accuracy (wrong distance computation). Eventually, this threshold could be increase and settled in the 1.8V to 1.9V interval. To maximize its value, a detailed study would have to be performed to precisely define the limits of the noise level and stablish the threshold accordingly.

Whatever, the sensor's sensitivity does not prove to be the restrictive element in the distance measurements performed in the laboratorial environment, whereby the previous aspect is not critical.

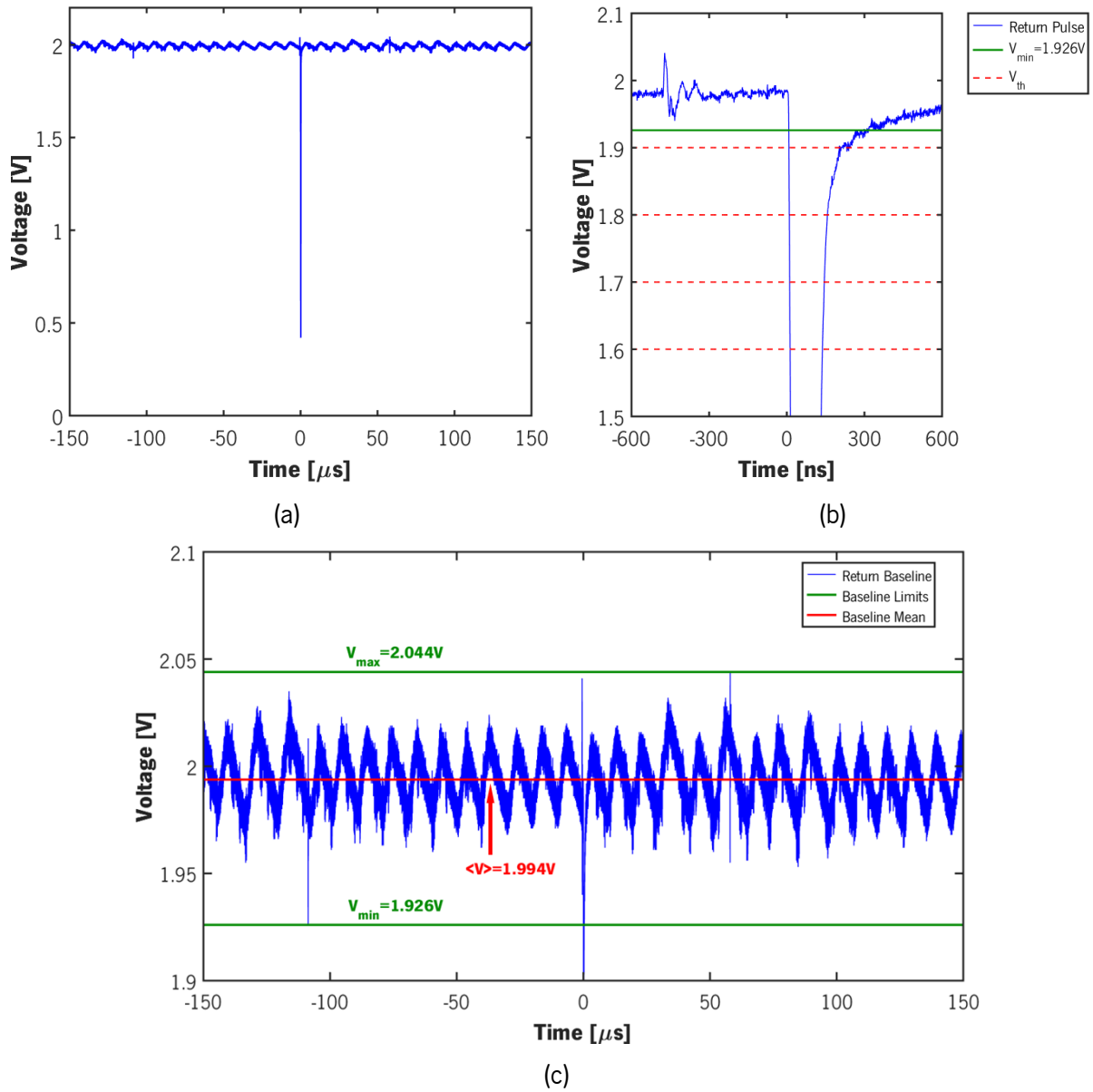


Figure 109. Return pulse acquired with gain 20k for diffuse reflection on *Vauxhall* at 671mm: (a) zoom-out of the pulse to show the oscillations on the baseline, (b) overlaid thresholds and return pulse and (c) zoom-in of the baseline and respective limits and mean value. The back-reflected pulse is detected at $t=0$.

5.1.5. Calibration and Accuracy

With the experimental conditions defined, it is time to start the functional tests on the LiDAR prototype. On this initial phase, the experiments consist of ToF measurements at several distances with the *K-line white* serving as diffusely reflective target. From the previous mensuration, several performance metrics can be scrutinized and interpreted.

Due to the architecture of the system and as in any LiDAR sensor, several inherent delay sources are responsible for a systematic error in the range measurements that restricts the system's accuracy, i.e. the discrepancy from the actual distance to the target. These delays are inevitable and its quantification is non-trivial since diversified independent and correlated sources are present both on the optical paths and, for the most part, on the electrical paths. The delays common to the return and reference paths, such as the one introduced in the Schmitt-trigger (delay block), are automatically cancelled upon subtraction of the measured time in TDC1, ToF1, to the time elapsed in TDC2, ToF2, to yield the effective ToF determination. Nevertheless, the delays exclusive of each path, such as the length of the coaxial cable connecting the reference photodetector to the RX board (91cm), the transamplification and even the axial distance between the RX and TX boards, are accounted in the experimentally sensed range and induce inaccuracy.

Hereupon, and even though the numerical quantification of each individual delay element is not relevant, a calibration must be enforced to eliminate this systematic offset and cancel all the delays. This procedure is indispensable in laser rangefinding to provide reliable measurements and consists on comparing the measured values by the device under test with those of a calibration standard with known accuracy.

To evaluate the accuracy and provide a basis for calibration, it is necessary a methodology to measure and know the actual distance to the target, d_{actual} , and to posteriorly compare it with the prototype measurement results. Thus, to fulfil this need and furnish a reference, a rangemeter is used throughout the results extraction stage. This rangemeter is a *PARKSIDE 20 M PLEM 20 A1* measuring distances from 0.075m to 20m in 1mm increments (resolution) and with 3mm accuracies, by means of a visible class 2 red laser (620-690nm) [183]. The experimental process is schematically condensed in Figure 110 and consists on the following sequence of steps:

- 1) Fix the *K-line white* target at a certain distance
- 2) Align the target and the TX end through slight rotation of the respective optical breadboard to maximize the collection of diffusely reflected light (alignment procedure mentioned in section 5.1.4.1). The point of maximum illumination is ascertained by direct observation of the return pulse on the *Teledyne Lecroy HDO4034* oscilloscope
- 3) Acquire the return pulse after amplification (*return_analog*) at the test point *TP6* directly in the *Teledyne WaveStudio* software
- 4) Measure the actual distance to the target, d_{actual} , using the *PARKSIDE* rangemeter. This distance is evaluated with reference to the front vertex of the LA1401-B receiving lens
- 5) Perform a complete acquisition of a set of 2400 ToF points in the *Java* GUI and under the same exact conditions
- 6) Move the target to modify the distance and repeat from 2)

The data points are collected in a range interval between 0.560m and 4.420m and under the previously stated standard conditions. The distance evaluation attained with the rangemeter serves as the reference for the actual distance to the target, d_{actual} . This instrument has a known accuracy of about 3mm and, since the prototype accuracy is of the order of a few centimeters, it can be partially neglected in the analysis.

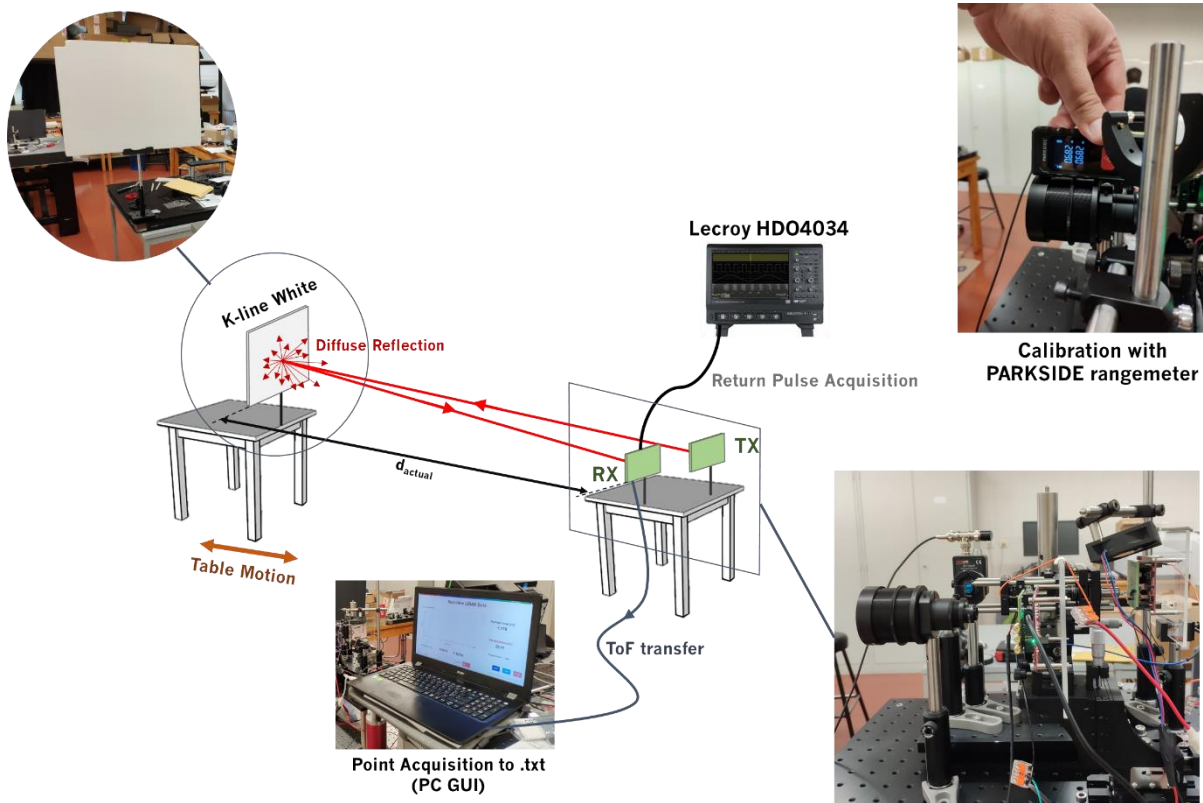


Figure 110. Simplified schematic of the setup for range measurements and characterization of the 1D LiDAR prototype. On the top right, it is shown how the actual distance is measured with the rangemeter: the device is softly landed on top of the RX optics, to ensure a stable and correct measurement without compromising the delicate optical alignment.

For each position, a statistical treatment is applied to the raw data points consisting on the computation of the arithmetic average value and the standard deviation of each set. Although the points are primarily acquired as a ToF in nanoseconds, it is physically more intuitive to undergo this analysis in the spatial domain. Hereby, the transposition between time and spatial domains can be easily accomplished through equation (2.14). The latter calculations are performed using equations (2.9) and (2.10), rewritten herein:

$$\text{Spatial Domain (Range)} \quad \langle d \rangle = \frac{1}{N} \sum_{i=0}^{N-1} d_i \quad (5.4)$$

$$\sigma_d = \sqrt{\frac{\sum_{i=0}^{N-1} (d_i - \langle d \rangle)^2}{N}} \quad (5.5)$$

$$\text{Time Domain (ToF)} \quad \langle t_D \rangle = \frac{1}{N} \sum_{i=0}^{N-1} t_{D,i} \quad (5.6)$$

$$\sigma_t = \sqrt{\frac{\sum_{i=0}^{N-1} (t_{D,i} - \langle t_D \rangle)^2}{N}} \quad (5.7)$$

$$\longleftrightarrow \quad d_i [m] = 0.15 \cdot t_{D,i} [ns] \quad (5.8)$$

where $N=2400$ is the number of points captured in each conditions, $t_{D,i}$ and d_i the i^{th} sampled Time-of-flight and the respective range, and $(\langle d \rangle, \sigma_d)$ and $(\langle t_D \rangle, \sigma_t)$ the average-standard deviation pairs. The

results of the statistical handling of the acquired results are listed in Table 20, both in the spatial and time domains.

Table 20. LiDAR range and ToF measurements after statistical treatment to determine the average and standard deviations. The results are compared with the actual reference values and, on the rightmost column, the calibration constants for each distance are computed. The actual ToF, $t_{D,actual}$, is calculated directly via equation (5.8) using the actual distance, d_{actual} .

Range Data			ToF Data			Calibration	
d_{actual} [m]	$\langle d \rangle$ [m]	σ_d [cm]	$t_{D,actual}$ [ns]	$\langle t_D \rangle$ [ns]	σ_t [ns]	$t_{D,cal}$ [ns]	d_{cal} [m]
0.560	-0.991	3.873	3.733	-6.606	0.258	10.340	1.551
0.659	-0.873	4.017	4.393	-5.817	0.268	10.211	1.532
0.769	-0.769	3.949	5.127	-5.130	0.263	10.257	1.538
0.850	-0.680	4.176	5.667	-4.533	0.278	10.200	1.530
0.944	-0.589	4.260	6.293	-3.926	0.284	10.219	1.533
1.020	-0.515	4.429	6.800	-3.430	0.295	10.230	1.535
1.166	-0.363	4.425	7.773	-2.417	0.295	10.190	1.529
1.264	-0.273	4.490	8.427	-1.817	0.299	10.244	1.537
1.400	-0.124	4.597	9.333	-0.826	0.306	10.159	1.524
1.516	0.004	4.720	10.107	0.026	0.315	10.080	1.512
1.619	0.111	4.560	10.793	0.738	0.304	10.055	1.508
1.745	0.239	4.731	11.633	1.593	0.315	10.040	1.506
1.895	0.403	4.865	12.633	2.683	0.324	9.950	1.492
2.009	0.517	4.856	13.393	3.448	0.324	9.945	1.492
2.091	0.607	4.821	13.940	4.049	0.321	9.891	1.484
2.208	0.734	4.927	14.720	4.891	0.328	9.829	1.474
2.345	0.879	4.980	15.633	5.857	0.332	9.776	1.466
2.450	1.000	5.027	16.333	6.667	0.335	9.666	1.450
2.561	1.110	5.088	17.073	7.397	0.339	9.676	1.451
2.687	1.246	5.566	17.913	8.308	0.371	9.605	1.441
2.794	1.361	5.680	18.627	9.073	0.379	9.554	1.433
2.904	1.490	5.637	19.360	9.933	0.376	9.427	1.414
2.997	1.580	5.664	19.980	10.534	0.378	9.446	1.417
3.123	1.719	6.090	20.820	11.459	0.406	9.361	1.404
3.262	1.874	5.990	21.747	12.493	0.399	9.254	1.388
3.437	2.056	5.837	22.913	13.707	0.389	9.206	1.381
3.560	2.215	6.107	23.733	14.764	0.407	8.969	1.345
3.910	2.579	6.391	26.067	17.195	0.426	8.871	1.331
4.129	2.791	6.737	27.527	18.605	0.449	8.921	1.338
4.420	3.096	7.115	29.467	20.640	0.474	8.826	1.324

Based on the latter calculations, one can notice that, for every evaluated range, the computed mean value is consistently below the expectation. Accordingly, the calibration of the LiDAR prototype consists on adding a constant ToF or range amount to the averaged results, $\langle d \rangle$ and $\langle t_D \rangle$, to correct systematic deviations and enhance the system accuracy. For each distance, the calibration constants d_{cal} and $t_{D,cal}$, are evaluated through:

Spatial Domain (Range)

$$d_{cal} = d_{actual} - \langle d \rangle \quad (5.9)$$

Time Domain (ToF)

$$t_{D,cal} = t_{D,actual} - \langle t_D \rangle \quad (5.10)$$

As a direct deduction from the estimated calibration constants, also present in Table 20, the calibration is not universal nor regular in-between each analyzed range. In fact, d_{cal} declines about 0.227m between the limit ranges of 0.560m and 4.420m, changing from 1.551m to 1.324m. This variation is pictured in Figure 111, where the error bars are an allusive quantification of the standard deviations. This shift is a consequence of a time-walk in the leading-edge discrimination, as it will be discussed down below.

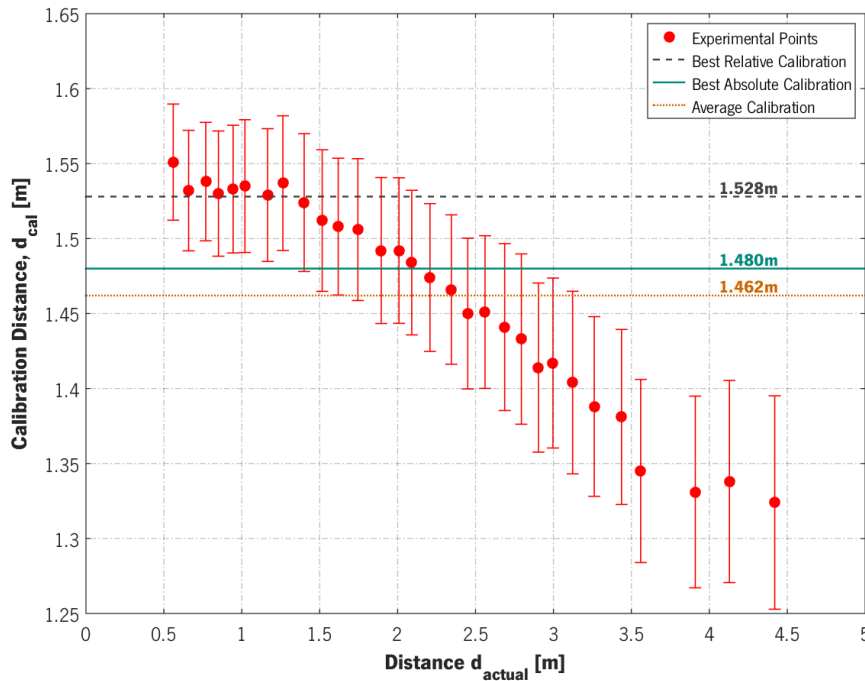


Figure 111. Shift in the calibration distance as a function of the (actual) distance to the *K-line* target. Simultaneously with the experimental points, the error bars are also depicted alongside the three established calibration constants.

From these outcomes, it is possible to declare that the calibration cannot be completely fulfilled by establishing a simple and global calibration constant. Hereafter, the experimental range points need to be traced as a function of the actual distance to better understand the error behavior and the system evolution with the increasing range. The graphical result is given in Figure 112 and reflects a linear trend that can be adjusted through a linear regression with equation:

$$y = 1.0632x - 1.6017 \Leftrightarrow \langle d \rangle = 1.0632 \cdot d_{actual} - 1.6017 \quad (5.11)$$

and a correlation coefficient of $R^2=0.99987$. This response is the commonly denoted calibration curve of the sensor and is an extremely important result since it demonstrates that the average results follow a well-defined and predictable pattern. Therefore, it is possible to validate that a legitimate calibration is conceivable, even though it is non-trivial. The slope superior to 1 indicates that the average distance increases at a rate superior to the increase in the actual distance. This is visible in Figure 111 through the decrease in the calibration distance.

In its most elementary form and ideally, the linear fit to the experimental points should be a straight line with unitary slope and an offset (y intersect) corresponding to the uniform calibration constant and systematic error:

$$y = x \pm b \Leftrightarrow \langle d \rangle = d_{actual} \pm d_{cal} \quad (5.12)$$

By moving the target away or bringing it closer would provoke a shift in the mean measured distance equal to the actual shift in distance. However, there is another factor in this prototype, namely the aforementioned time-walk, that induces an additional dependency beyond the simple time-delays: the intensity of the return signal.

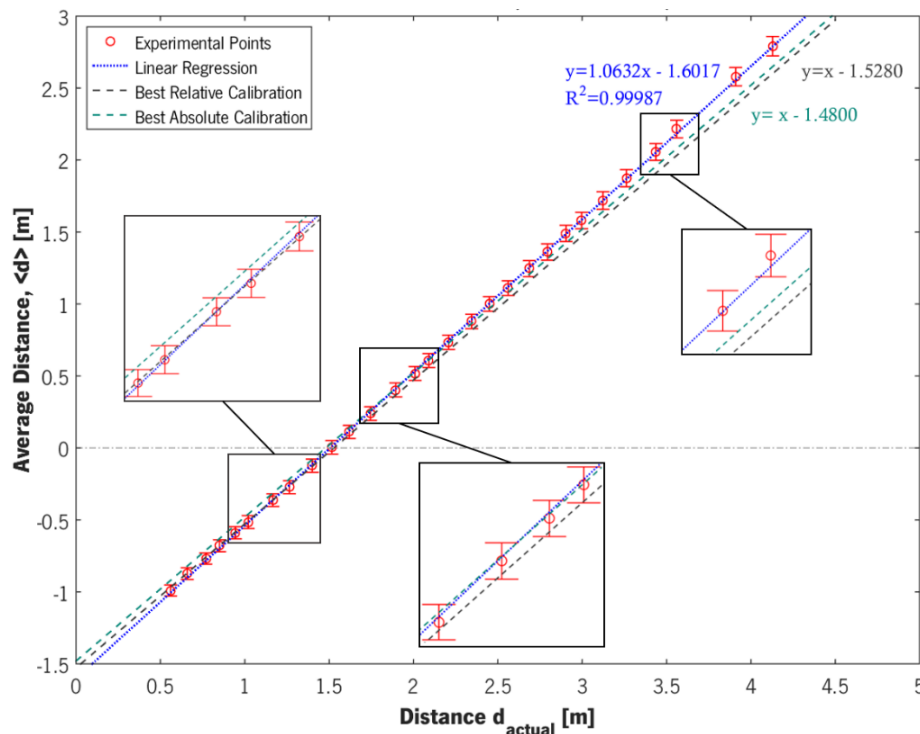


Figure 112. Experimental mean values vs. actual distance measured with the rangemeter. In blue, the calibration line that linearly fits to the experimental points. Simultaneously, the best relative and absolute calibration curves are also traced, with some regions zoomed-in to highlight the misfit from the real response.

From this point, two alternatives for progression arise. If one aims for a simpler and more straightforward calibration, a constant value must be added. On the other hand, if one aspires for higher accuracy within the sensor's working distances, the calibration must be a function of the measured distance. The latter option comes, naturally, at a cost of higher complexity. Yet, as the response is linear, this complexity is substantially lessened. In either circumstance, the FOM to be analyzed is the accuracy.

The range accuracy, δd , is an absolute estimate of the deviation between the sensed distance (in this case, the average) and the real distance measured with the reference rangemeter:

$$\delta d = \left| d_{actual} - \langle d \rangle_{cal} \right| \quad (5.13)$$

Since the finality of calibration is to partially correct systematic errors, it is only meaningful to analyze the accuracy of the calibrated ranges, $\langle d \rangle_{cal}$. Frequently, the accuracy can also be expressed as a percentage/relative value of the actual distance, d_{actual} :

$$\delta d[\%] = \frac{\delta d}{d_{actual}} \quad (5.14)$$

To apply a constant calibration, a compromise must be established. Hence, three values of d_{cal} are studied. The first is the arithmetic average of the systematic deviation at each sampled range, determined to be 1.462m. However, it is possible to attain a better overall accuracy compromise by fine-tuning. Therefore, two alternative values arise. One, denoted as “best absolute calibration” corresponds to the value yielding a minimum average for the overall absolute accuracy. The other, referred to as “best relative calibration” is the configuration accommodating the lowest average error in percentage. The respective values for the former and the latter are 1.480m and 1.528m and the three calibrations are traced in Figure 111. Finally, the calibrated ranges can be determined by simply summing the calibration distance, d_{cal} , to the mean range:

$$\langle d \rangle_{cal} = \langle d \rangle + d_{cal} \quad (5.15)$$

The accuracy results for each one of the simpler calibrations are summarized in Table 21. Regarding the average accuracy in spatial dimensions, $\langle \delta d \rangle$, the configuration yielding a minimum is the “best absolute calibration”, with a result of approximately 5.8cm. On the opposite limit, the “best relative calibration” provokes the maximum average inaccuracy at around 7cm. Notwithstanding, the latter induces the lowest overall accuracy in percentage of around 2.5%. Concerning the average calibration, it is remarkably the least effective among the three possibilities.

Table 21. Accuracy analysis for the three distinct global calibrations studied for the LiDAR prototype. In red and green are highlighted respectively, the best and worst overall results. The values in parenthesis in the last four lines are the actual target distances.

Metric	Average Calibration	Best Absolute Calibration	Best Relative Calibration
d_{cal} [m]	1.462	1.480	1.528
$\langle \delta d \rangle$ [cm]	5.923	5.811	6.997
$\langle \delta d \rangle$ [%]	3.790	3.229	2.506
$(\delta d)_{max}$ [cm]	13.806 (@ 4.420m)	15.606 (@ 4.420m)	20.406 (@ 4.420m)
$(\delta d)_{max}$ [%]	15.889 (@ 0.560m)	12.674 (@ 0.560m)	5.130 (@ 3.437m)
$(\delta d)_{min}$ [cm]	0.441 (@ 2.345m)	0.367 (@ 2.091m)	0.053 (@ 1.166m)
$(\delta d)_{min}$ [%]	0.188 (@ 2.345m)	0.176 (@ 2.091m)	0.046 (@ 1.166m)

To understand the underlying reason beyond the disparities between the best absolute and relative calibrations, the distribution of residues in relation to the ideal calibration lines with unitary slope in Figure 112 shall be checked. These results are no more than the accuracy in the measurements at each range and are displayed in Figure 113 both as absolute values (modulus) and as relative percentages (in relation to the actual distance). While the best relative calibration aims to decrease the error at smaller distances, namely below approximately 1.2m, the best absolute is a rather intermediate calibration and

minimizes the error at a distance of around 2m. As a result, the former calibration provides a lower relative error overall since at smaller distances the absolute error has a larger effect on the percentual deviation. By choosing a middle-term calibration, the absolute distribution within the working ranges is more homogeneous at a cost of increased error at shorter distances, and, therefore, a substantially greater relative error. Anyway, in both cases the inaccuracy tends to escalate above the maximum sensed distance of 4.420m.

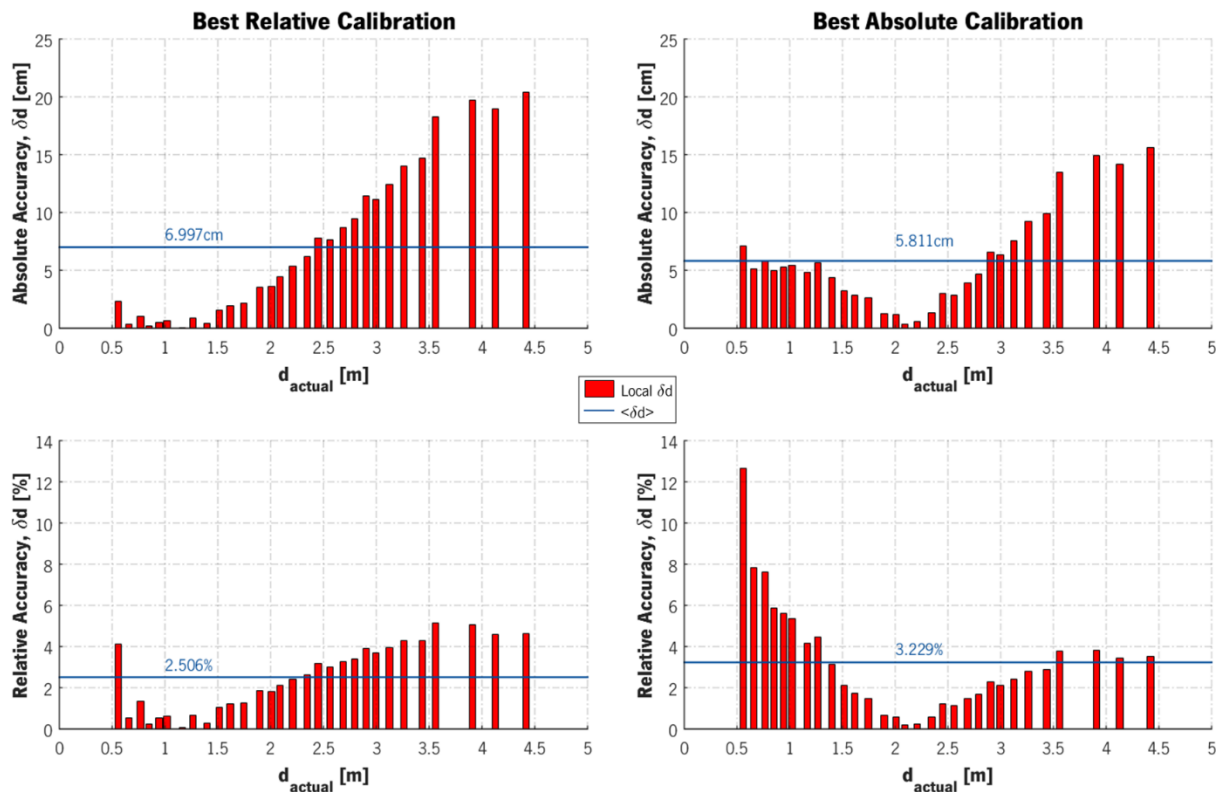


Figure 113. Absolute and relative residues of the ideal linear calibration. On the left, using the “best relative calibration”, applied by summing a constant range of 1.528m to each measured value. On the right, after implementation of the “best absolute calibration” by applying a positive offset of 1.480m to each result.

Exploring the alternative solution, equation (5.11) shall be rewritten to provide the descriptive function of the range-dependent calibration. Rearranging the terms and replacing the actual distance, d_{actual} , by the calibrated average range, $\langle d \rangle_{cal}$, yields:

$$\langle d \rangle_{cal} = \frac{\langle d \rangle + 1.6017}{1.0632} \quad (5.16)$$

where $\langle d \rangle$ is the sensed range, in this specific case, after statistical treatment of the N=2400 points.

The calibrated experimental points are traced as a function of the actual distance in Figure 114, and the linear adjustment reveals a virtually ideal calibration with unitary slope and passing through the referential origin. Whatsoever, the residues are still non-null, reflected by the imperfect correlation coefficient $R^2=0.99987 \neq 1$. Thus, the accuracy is given by the deviation between each point and the linear fit (calibration curve):

$$\text{Mean: } \langle \delta d \rangle = 1.01\text{cm} \quad \langle \delta d \rangle [\%] = 0.71\%$$

$$\text{Maximum: } (\delta d)_{\max} = 2.98\text{cm} \quad @ d = 3.560\text{m}$$

$$(\delta d)_{\max} [\%] = 4.00\% \quad @ d = 0.659\text{m}$$

$$\text{Minimum: } (\delta d)_{\min} = 0.03\text{cm} \quad @ d = 3.123\text{m}$$

$$(\delta d)_{\min} [\%] = 0.01\% \quad @ d = 3.123\text{m}$$

From these results, it is confirmed that, effectively, this is the better-adjusted and most accurate comprehensive calibration and it ensures an adequate correction all over the working distances with an average accuracy of 1.01cm (0.71%). Moreover, the tendency for increased distances beyond 4.420m is for the calibration quality to be preserved.

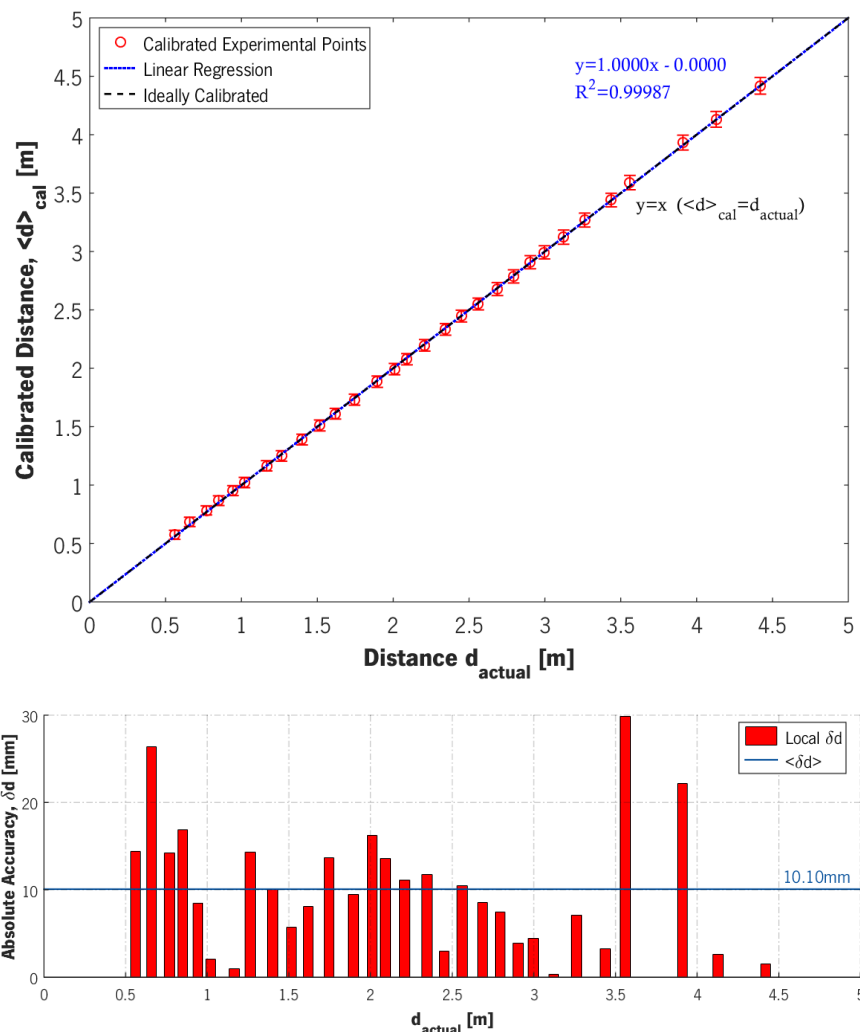


Figure 114. Measured distance vs. actual distance after applying a range-dependent calibration. On top, it is shown the nearly-ideal linear fit with unitary slope and null y intercept. On the bottom, the residues in mm as a function of this distance. The latter are the calculated deviations from the linear regression and represent the inaccuracy at each marked distance.

To close the calibration topic, some concluding notes might be mentioned. First of all, and even though inconsequential, all the results above are susceptible to a supplementary inaccuracy of $\pm 3\text{mm}$

instituted by the uncertainty of the reference *PARKSIDE* rangemeter (d_{actual}). Secondly, the calibration does not amend the fluctuations in the ToF and the standard deviation does not suffer any alteration, as illustrated through the error bars throughout the present sub-section. Furthermore, even with a perfect calibration, and in the absence of further systematic error, the accuracy is limited by the system imprecision. At last, the calibration can be directly performed at the microcontroller level and before sending the data via UART to the PC, by considering it in the ToF (equation (4.14)) or range calculations, or directly on the *Java* program during the real-time treatment of the raw data. In either case, the final result is exactly the same. However, in a real-case automotive scenario, it is preferable to calibrate the measurements at the sensor level to avoid unnecessary calculations and increase parallelism at the central processing unit fusing the data from LiDARs, cameras and radars. In this specific prototype, the calibration is practiced at the GUI because the optimal calibration involves supplementary computations, other than a simple sum, that require extra clock cycles, which may affect the TDCs reading rates and demand slower point rates (below 6kHz).

5.1.5.1. Amplitude Dependence and Time-walk

This sub-section will show up that the fundamental cause of an unsatisfactory calibration is not the procedure itself but the inadequated leading-edge discrimination technique in the LiDAR ToF timing.

To understand the fundamental reasoning behind the decreasing of the calibration values, the acquired pulses shall be inspected. Hereby, and to support the clarification, the scope pulses for five distinct distances are superimposed in Figure 115 alongside the standardly applied threshold of 1.7V. As visible, the crossing instants of the previous threshold are not constant and increase as the distance to the target increases. Since the STOP2 pulse for the TDC2 is generated whenever the previous boundary is crossed in the descendent sense, the latter variance leads to an additional shift in the ToF, called time-walk, besides the one induced by the change in the distance.

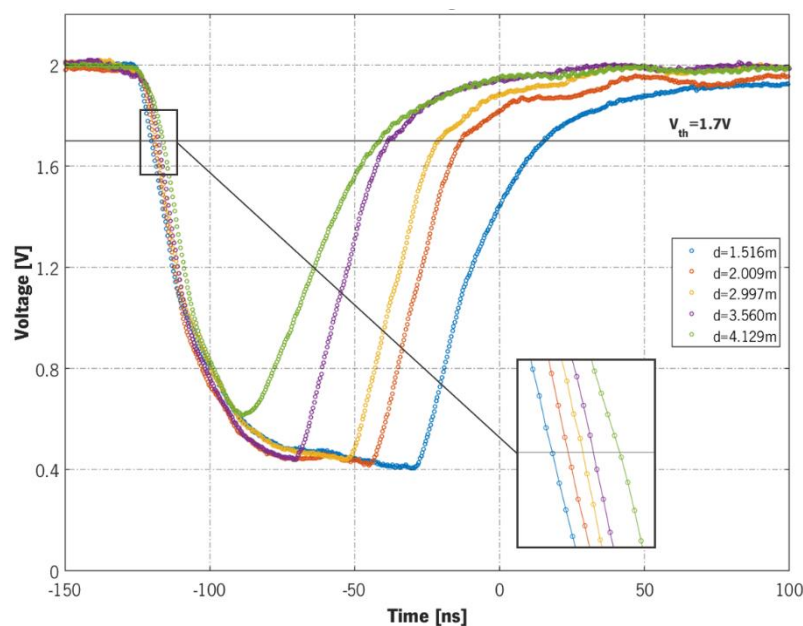


Figure 115. Back-reflected pulses (*return_analog*) on *K-line white* for 5 distinct distances and after transamplification. Inside the highlighted rectangle, a zoom-in on the threshold crossing region.

Bridging the experimental behavior noticed for the calibration constants, described numerically in Table 20 and graphically in Figure 111, with the preceding argumentation, one can recognize the concordance. Until 1.516m, the sum of all delays in the reference path surpasses the delays in the return path plus the effective ToF and, therefore, the overall uncalibrated measure is negative: $t_D = \text{ToF}_2 - \text{ToF}_1$. If the distance is further increased, the ToF2 will also expand due to two factors: the first is the proportional increase due to the shift in distance, estimated through equation (5.8); the other is the added time-walk instituted by the decay in the return optical intensity at the PD. The first determinant is reflected in the unitary slope of the calibration line in the $\langle d \rangle$ vs. d_{actual} graph of Figure 112, while the second is also a function of the actual distance and is responsible for the +0.0632 slope deviation from ideality. The latter effect is verified to be approximately linear since linearity is maintained. As a result, the uncalibrated ToF will move closer to its real value and the calibration constant will continuously diminish within the working distances.

Regarding the reference pulses for TDC1, that also undergo leading-edge discrimination, this problem is considerably less relevant since the detection is performed on a steady optical path and the amplitude suffers minor fluctuations over time due to lasing jitter. Therefore, TDC1 can be considered approximately constant in comparison to TDC2.

Table 22. Numerical evaluation of the time-walk due to the intensity dependence and comparison between the shift in the calibration constants and the shift in the threshold crossing time of *return_analog* pulses. The calibration data is retrieved from Table 20.

d_{actual} [m]	$t_{D,\text{actual}}$ [ns]	$t_{D,\text{cal}}$ [ns]	$V_{\text{th,A}}$ crossing-time [ns]	$\Delta t_{D,\text{cal}}$ [ns]	Δt_{walk} [ns]	$ \Delta t_{D,\text{cal}} - \Delta t_{\text{walk}}$ [ns]	σ_t [ns]
1.516	10.107	10.080	5.86	—	—	—	0.315
2.009	13.393	9.945	5.97	-0.135	+0.11	+0.025	0.324
2.997	19.980	9.446	6.53	-0.499	+0.56	-0.061	0.378
3.560	23.733	8.969	7.02	-0.477	+0.49	-0.013	0.407
4.129	27.527	8.921	7.36	-0.048	+0.34	-0.292	0.449

To substantiate even further the analysis, the shifts in the calibration constant at each studied range can be compared directly in the time-domain with the change in the threshold crossing time. As detailed in Table 22, the reduction in the calibration constant is on the same order of magnitude as the rise in the crossing times, acting both in conformity with the previous discussion. Some slight deviations appear, namely between $d_{\text{actual}}=3.560\text{m}$ and $d_{\text{actual}}=4.129\text{m}$ and are linked to the number of acquisitions and precision. While a single pulse is sampled per measured distance, the calibration constant is computed based on a statistical treatment of a total of 2400 points. Despite, the slight deviations in these estimations are comprehended in the margin established by the standard deviation.

The crossing times are extracted in *Teledyne WaveStudio* software from the analog pulses acquired in the oscilloscope and are referent to the pulse starting/reception instant. The shifts are only determined at the distances depicted in Figure 115, being enough to demonstrate the repercussions. Both the fluctuation in the calibration constant, $\Delta t_{D,\text{cal}}$, and the time-walk, Δt_{walk} , are evaluated in reference to the antecedent point, i.e.:

$$\Delta t_{D,cal} \Big|_{i+1} = (t_{D,cal})_{i+1} - (t_{D,cal})_i \quad (5.17)$$

where $i=1\dots5$ are, respectively, $d_{actual}=1.516\dots4.129m$. The calculation is analogous for the time-walk and is dismissed for $d=1.516m$ due to the lack of a prior reference

Although the calibration measurements reveal a direct effect of the time-walk on slope of the calibration line and a range-dependent correction, other major repercussion is also induced. For a certain distance, if the intensity of the back-reflected signal changes, for e.g. due to reflection on different materials with different reflective properties, then the measured ToF will also vary and different distances will be acquired. This outcome is not perceptible in the previous measurements, but it is relevantly probable in real-case scenarios in automotive LiDARs operation.

To quantify this effect, the *Vauxhall* target is placed at $d_{actual}=1.204m$ and aligned to detect the specular component. The returning pulse is acquired in the *Teledyne Lecroy HDO4034* oscilloscope and 2400 points are sampled. In these conditions, the transamplified voltage pulse is saturated. Posteriorly, the target is rotated slightly until the amplitude of the signal desaturates and decreases. At this point, the prior sampling process is redone. The process is repeated until the amplitude stabilizes at a minimum, corresponding to the competition of the specular-to-diffuse transition. Beyond this point, further rotation of the target does not influence the amplitude of the detected signal with the obvious conclusion that the receiver is only measuring the diffuse component. In total, 5 distinct amplitudes are acquired for the same distance and the analog pulses are represented in Figure 116.

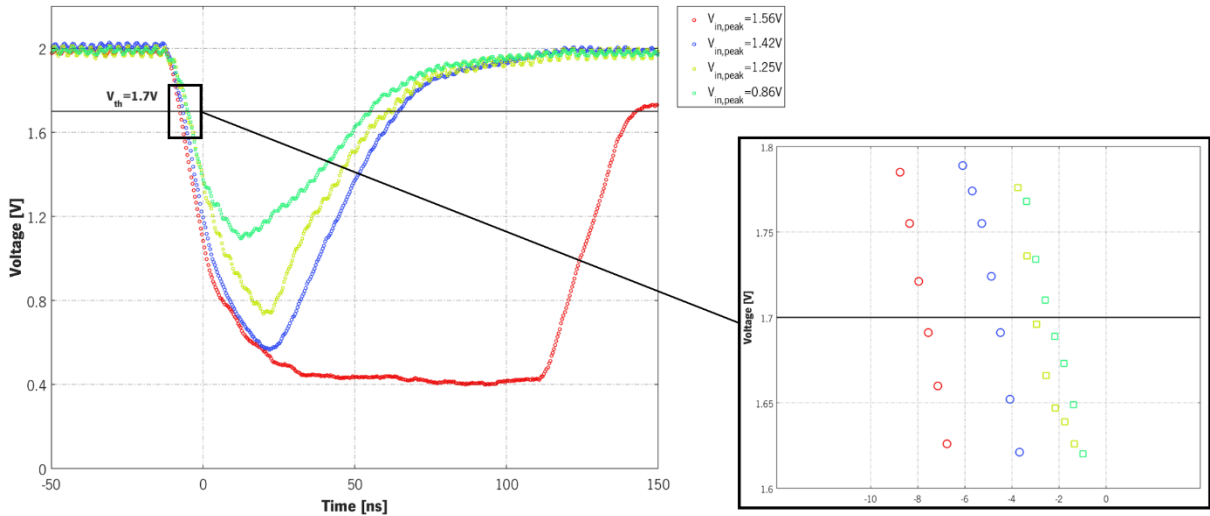


Figure 116. Pulses acquired for the back-reflection on the *Vauxhall* target at $d_{actual}=1.204m$ for different alignments. Zoomed-in, the $V_{th,A}=1.7V$ crossing instant showing that, the greater the amplitude, the faster the crossing instant and, therefore, the shorter the effective ToF.

Subsequently, and after computing the statistical quantities (mean value and standard deviation), the time-walk, Δt_{walk} , is estimated by individually subtracting the average ToF of the specularly reflected pulse, with a peak amplitude of $V_{p,i}=1.56V$, to the ToFs captured in the alternative conditions:

$$\Delta t_{walk} (V_{p,i}) = \left| \langle t_D \rangle \Big|_{V_{p,i}} - \langle t_D \rangle \Big|_{V_{p,i}=1.56V} \right| \quad (5.18)$$

Afterwards, the time-walk variation is graphically represented as a function of the return pulse amplitude. The result, detailed in Figure 117, demonstrate that, the smaller the amplitude, i.e. the weaker the returning pulse intensity, the larger is the walk error because the threshold crossing instant is slower and, therefore, the effective ToF shorter. Naturally, for the specular reflection component, the time-walk is null since the respective ToF is used as reference in the calculations. Furthermore, a variation of 0.7V in the pulse amplitude induces a shift superior to 5ns, i.e. a decay larger than 75cm in the accuracy (62.3% of the actual distance).

In practice, within the working distances of 0.560m and 4.420m, the walk manifests through a variation in the calibration constant between 10.340ns and 8.826ns for reflection on the *K-line white* (Table 20). The absolute difference is about 1.514ns or, equivalently, 22.71cm. However, and even though this experiment overestimates the latter walk-error, it emphasizes more drastically and transparently the importance of this effect in limiting the accuracy.

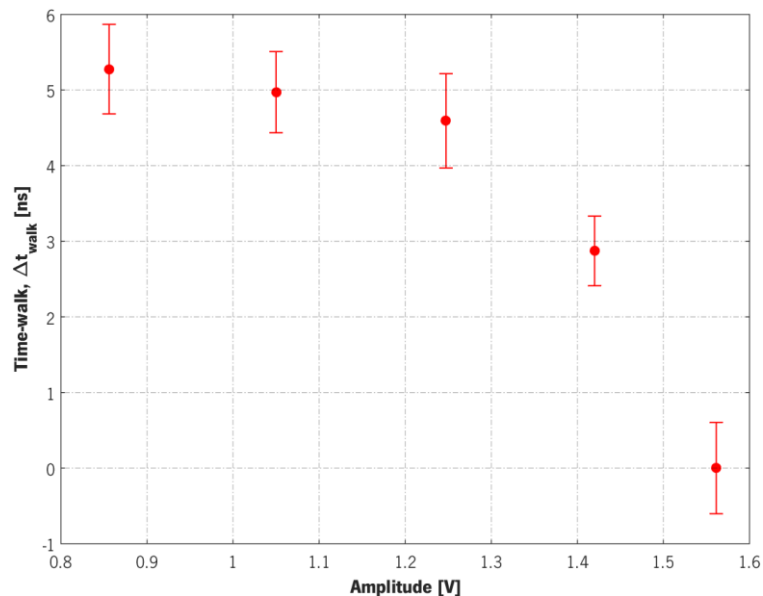


Figure 117. Time-walk vs amplitude of the transampled return pulse after reflection on the *Vauxhall* target at $d_{actual}=1.204m$. The ToF for the specularly reflected component is used as reference and, hence, the time-walk for the respective amplitude (1.56V) is zero. Overlapped with each experimental point are the error bars referent to the standard deviation.

Both Figure 116 and Figure 117 prove that there is a systematic error introduced in the ToF measurements due to the leading-edge discrimination which ultimately influences the calibration and limit the accuracy. Figure 117 additionally shows that the precision is not significantly changed with the back-reflected intensity, since the standard deviations represented through the error bars are comparable and do not have a systematic variation with the signal amplitude.

Conclusively and in summary, the take home message is that the leading-edge discrimination is not an adequate timing technique for LiDAR systems since the Time-of-Flights to measure are of the magnitude order of the evaluated time-walks. The self-consistent explanation is that the timing point at TDC2 (return path) is signal strength dependent due to the fixed threshold and, therefore, it varies with range. As a consequence, the calibration is not constant and is a function of the distance to the target, and the accuracy is strongly deteriorated. Ultimately, the calibration curve prescribed in the previously

($y=1.0632x-1.6017$) is only valid in the tested conditions and will certainly change if another material is measured, due to the walk effect. Therefore, it is of utterly remarkable importance to develop and apply a technique to address this problematic and correct this timing artefact. One possible solution proposed and explored in the next chapter is the Constant Fraction Discriminator (CFD) to trigger the STOP consistently at a uniform fraction of the return signal amplitude.

5.1.6. LiDAR Performance

Besides the calibration intents, the data obtained through the measurement procedures previously completed allows to extract and examine some vital performance metrics of the LiDAR prototype and compare them with four state-of-the-art sensors. Namely, the metrics to be analyzed are the limiting ranges, the sensor's precision and the Signal-to-Noise Ratio (SNR). The preeminent goal is to quantify the reliability of the distance signals acquired and estimate the dynamic spatial range within which the sensor is capable of estimating distances. Further, it will be possible to ascertain if the perceived behavior is qualitatively comparable and in conformity with the experimented for commercial LiDARs.

As reference, one refers to a benchmark of 4 representative state-of-the-art sensors documented in [34]: the *Quanergy M8*, the *Leddar Vu8*, the *Garmin lite v3* and the *Velodyne VLP16*. All these four sensors are reported in chapter 3 and they all implement a ToF technique (although the *Garmin* ToF implementation estimated the ToF by an indirect cross-correlation). The benchmark experiments are performed indoors up to 20m ranges, with 5m increments, and outdoors from 20m to 120m, with steps of 10m (Figure 118). Moreover, and the main motivator for this report article, is the fact that several targets were examined and used, inclusive the *K-line white* with the same properties reported herein.

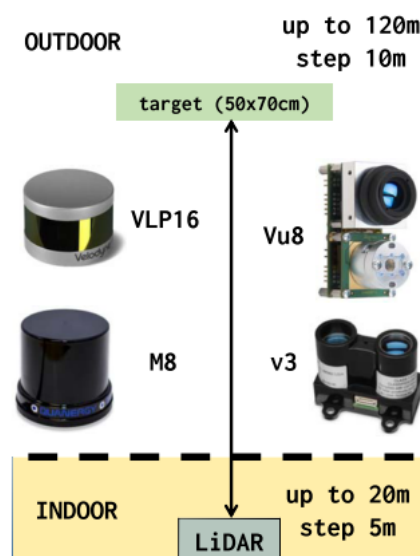


Figure 118. Schematic of the benchmarking experiment [34].

5.1.6.1. Range

One of the most fundamental characteristics of a LiDAR system is the maximum measured range and the sensor shall have the proficiency to detect obstacles at least up to a range of 180m, as required for high levels of autonomous driving.

Specifying in the developed prototype, the upper limit for the experimentally measured range is $d_{\max}=4.420\text{m}$, imposed by empirical restrictions of the test environments. In particular, the length and disposition of the optical laboratory in which the tests are carried out do not allow to dislocate the target farther from the sensor. Additionally, the possibility of transferring the experiments outdoors is eradicated due to eye-safety and reglementary frameworks. Whatsoever, the analog return signal acquired at 4.420m (Figure 119) evidences an amplitude of around 1.2V that heavily surpasses the threshold $V_{\text{th,A}}=1.7\text{V}$ and allows a loose discrimination in this architecture. Hence, one can validate that this distance is not an absolute boundary and it can be expanded.

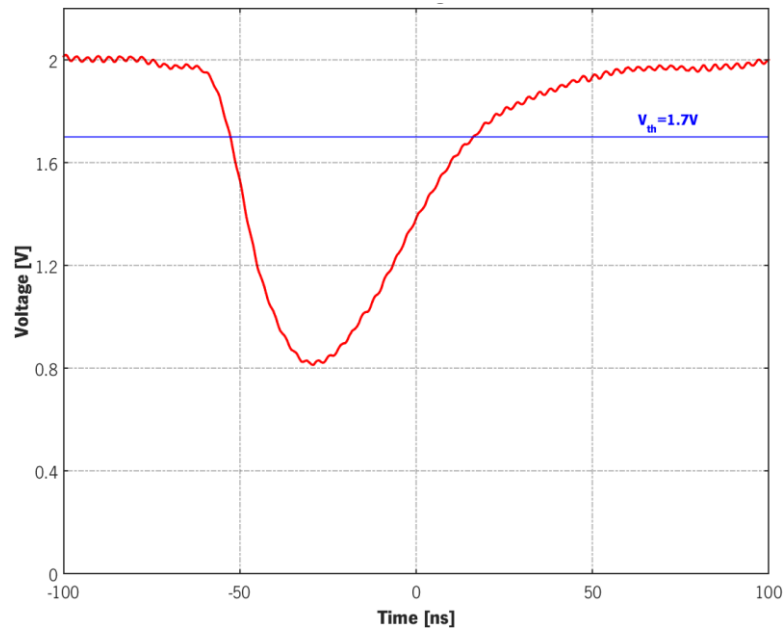


Figure 119. Analog return pulse (*return_analog*) after transamplification and reflected at the *K-line white* target placed at $d=4.420\text{m}$. It is visible that the return optical intensity still triggers a detectable STOP signal do TDC2.

Concerning the minimum distance, the inferior limit is theoretically 0m due to the employment of 2 TDCs to virtually eliminate the blank time blockage. However, experimentally and due to the large footprint of this first prototype, apparent in Figure 101, the minimum measured distance is restricted to around $d_{\min}=0.56\text{m}$. Herein, the fundamental limitation is set by geometrical factors that can be perceived through Figure 120. At short distances, the optics plays a strong role in defining the minimum sensed distance. Consider two targets planes, 1 and 2, placed transversally to the laser beam at distinct distance. For closer ranges (1), the reflected light misses the detector altogether since there is no overlap between the laser spot and the PD FOV. In this situation, no ToF computation is conceivable. Moving the target away from the sensor (2), the laser spot and the detector FOV will eventually overlap. The minimum distance for which there is a minimal overlap between the latter two resembles the inferior limit to the LiDAR's range.

To mitigate this limitation, the footprint ought to be reduced and it is desirable to place the receiver closer to the laser since the larger the lateral separation, the larger the minimum measurable distance. As a side-effect, the alignment TX-target-RX is facilitated. Also, it is verified that, indeed, this restriction is not imposed by hardware since $d_{\text{actual}}=0.56\text{m}$ corresponds to 3.73ns , which is unarguably inferior to the blank time of the TDCs (12ns in Mode 1 and 125ns in Mode 2).

Overall, the experimented operating range for the sensor is, then, from 0.560m to 4.420m, translated by an effective and uncalibrated ToF variation between -6.606ns to 20.640ns.

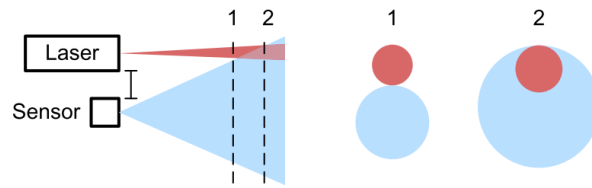


Figure 120. Overlap between laser beam and detector FOV and minimum sensing distance [156].

Naturally and range-wise, this prototype is not comparable to the benchmarked sensors, inasmuch as the most limited sensor, the *Garmin lite v3*, ranges nominally up to 40m. The latter state-of-the-art sensor outputs a mean optical power of about 4mW and the size of the receiving optics is much smaller than in the developed LiDAR prototype. Hereby, through indirect evidence, one can uphold and reinforce that the developed LiDAR can potentially reach and measure distances substantially superior to 4.42m. To expand the maximum distance, the solution is to increase the photosensitivity by replacing the PIN detector by an APD with internal gains that extends to factors of 100. Notwithstanding, this prototype is sufficiently adequate for proving the direct ToF concept, as proposed in the objectives of this dissertation project.

Regarding the minimum distance, there is only information on the *Quanergy M8* starting at 1m and the benchmark does not focus this metric. Even though important, this factor is not critical in the final application in autonomous vehicles due to the sensor fusion and the presence of other supporting sensors to fill the short-range gap.

5.1.6.2. Precision and Fluctuation Sources

Previously, the accuracy of the system was studied. This metric quantifies the reliability of the LiDAR range measurements and is connected to the deviation between the measured and real values, δd . Distinctively, the sensor's precision quantifies its reproducibility and is related to the random fluctuations in the measurement signals relatively to the statistical mean value, independent of any systematic deviation. The distinction between accuracy and precision is made clear in Figure 121, Figure 117 and Figure 111.

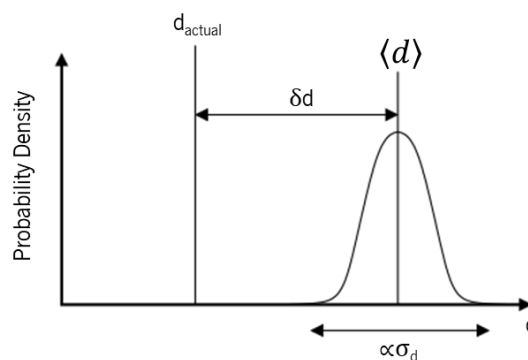


Figure 121. Gaussian probability density distribution and illustration of the difference between accuracy and precision. The accuracy is the deviation between d_{actual} and the mean value $\langle d \rangle$. The precision is linked to the dispersion of the measurements around the mean value, i.e. to the width of the normal distribution in this example.

Ideally on a completely precise system, consecutive range measurements on the exact same conditions should yield the same strict result with no variance. Nonetheless, in real systems there are several stochastic noise sources that add imprecision to the system. Hereby, the precision is usually estimated numerically through the standard deviation, σ , as it describes the dispersion of the measurements around a mean value. The larger the standard deviation, the less precise the system.

With the data from Table 20 one can graphically represent the variation of the system's precision with the calibrated distance to the target. The result is exposed in Figure 122 simultaneously with the histograms of the 2400 points acquired at 0.560m, 2.561m and 4.4420m. In this trace, it is seeable that the standard deviation increases continuously within the working distances starting at 3.87cm and culminating at 7.12cm. Therefore, the precision deteriorates as the target moves away. This effect is a consequence of a wider dispersion of the raw points around the mean value, reflected directly on the histograms. As the noise is completely random, the points distributions do not necessarily tend towards a normal distribution.

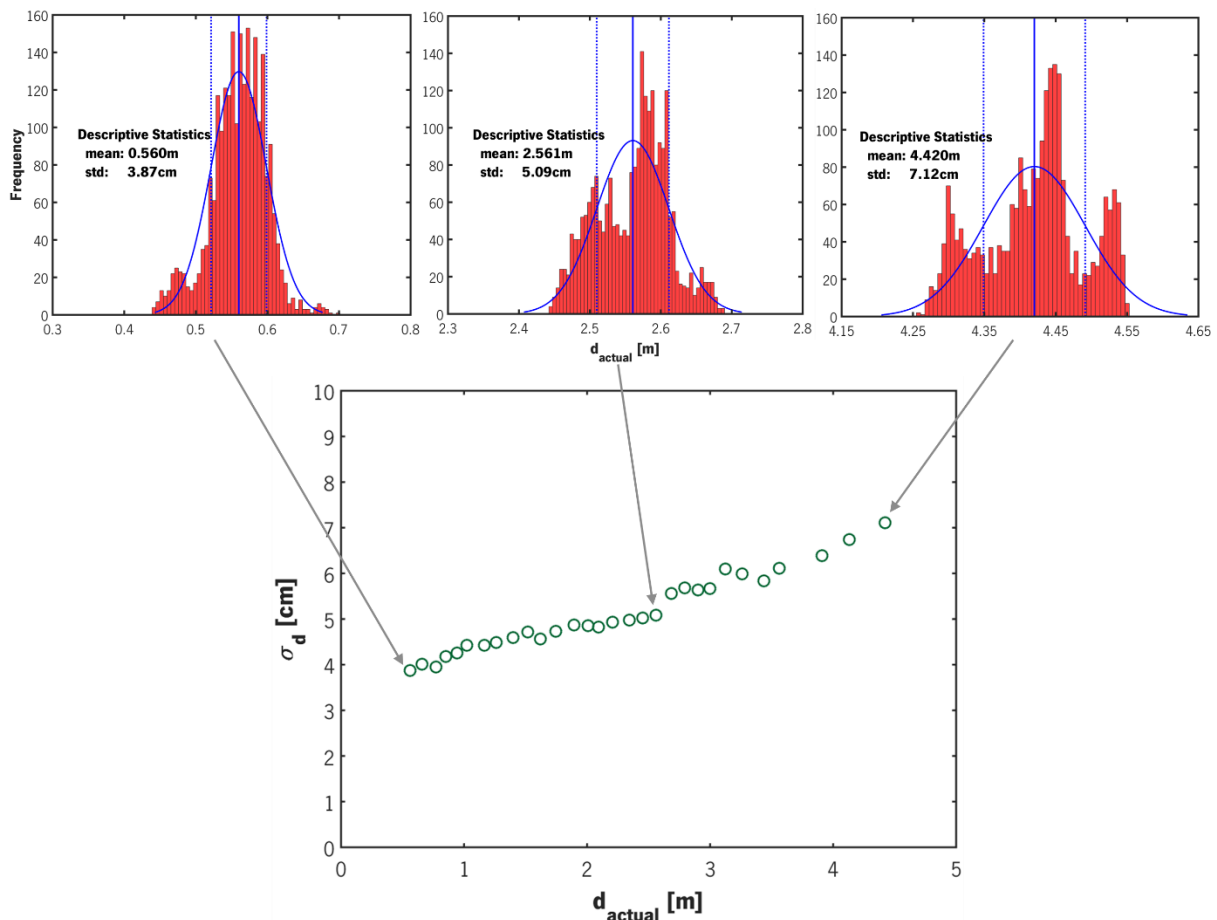


Figure 122. Standard deviation in the range measurements, σ_d , as a function of the calibrated distance to the target. Additionally, for the initial, final and an intermediate distance, the histograms are detailed with the Gaussian fits according to the determined mean and standard deviation.

Several sources of noise are diagnosed as the underlying causes for the stochastic fluctuations in the ToF and are enumerated next:

- Laser Jitter: fluctuations in the rise-time of the transmitted laser pulses due to instability of the laser emitter. Empirically, this effect is translated in a fluctuation of the threshold crossing-time, both in the reference and return paths as the same pulse is detected in the two ends. However, since the effective ToF is calculated by subtracting the time elapsed in TDC1 to the result of TDC2, this effect is nullified, unless the pulses suffer shape's alteration due to non-linear effects on either path. This jitter is quantified in sections 5.3.3 and 5.3.4. In the receiver path, this effect is less noticeable at short distances since the return intensity is superior and, as already exposed, the crossing-time is inferior and the jitter has an inferior absolute effect. As the distance increases, the crossing-time also expands and suffers stronger fluctuations, therefore the precision deteriorates as expressed in the graphical variation.

- Photodetection and Amplification noise: random fluctuations in the electronic signals, mainly induced in photodetection (background, dark-current and shot noise) and amplification (Johnson noise). This source is predominant in the return path due to the transamplification and induces variations in the threshold crossing instants.

- Fluctuations in Power Supply: periodic oscillations (100kHz) in the voltage $V_{cc} \approx 3.5V$ supplied by the RX MCU to the receiver board (Figure 123) that induce changes in the ICs responses. Ideally, this voltage should be constant and uniform over time, what would produce constant thresholds for discrimination. However, these oscillations cause fluctuations on the threshold values that, in turn, change the timing points. In practice, the thresholds are generated in the same IC and this effect shall be noticed in both discriminators and in the same proportion. Therefore, theoretically, this source has an insignificant contribution.

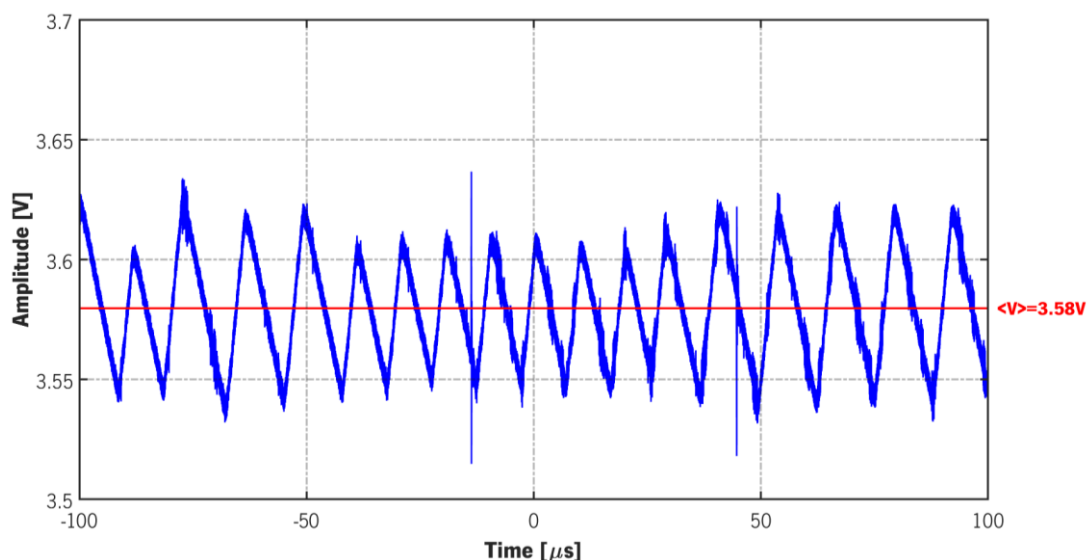


Figure 123. Periodic oscillations in the $BP_{3.3} \equiv V_{cc} \equiv V_S$ signal arising from the RX MCU board around the mean value of 3.58V. The oscillations are periodic with approximately 100kHz frequency.

- Timing Jitter: swinging in the temporal base of both TDCs that causes imprecisions in the time estimations. While the three previous causes lead to fluctuations in the threshold crossing-time of the analog pulses, this source is intrinsic of the underlying time-scale. Each TDC is operated in

Mode 2 and, therefore, relies on two distinct time scales. The first is established by an external clock source of 16MHz (TDC_CLK) generated by the RX MCU. The alternative is an internal integrated oscillator. This way, the temporal jitter can be divided in two sources accordingly. Regarding the external clock, it is expected for the jitter to be canceled because both TDCs share the same signal and the jitter shall affect both equally. However, there are differences in the electrical paths that may induce differences. For the internal scale, the oscillator in each TDC IC is independent and the overall effect is more complex since the jitter in is not correlated and it can either superimpose constructively or destructively. Since the measured ToF varies between -6.606ns and 20.640ns ($\Delta t_D=27.246ns$), the CLOCK_COUNT1 register in TDC2 (TDC1 is always the same since the electrooptical path is fixed) does not suffer a variation larger than 1, correspondent to a complete clock cycle with duration 62.5ns. Hence, the greater variations will be noticed in the TIME2 and TIME1 counters of the internal time-scale. The total jitter is given by the sum of the cycle-to-cycle jitter in the previous base over the accounted cycles. The larger the distance, the larger the counting (after subtraction of both TDCs) and, therefore, the larger the fluctuations in the effective ToF. Since the measured ToF increases linearly with the actual distance (Figure 112), the precision does also vary in a nearly-linear fashion. An estimate for these jitters is performed in section 5.3.6.

Overall, the characterization of the total jitter is a complex and arduous task because it is an added effect of the previous uncorrelated sources and, pragmatically, the message to retain is that the global expression results in a precision on the order of a few centimeters that increases with the range.

The precision cannot be readily improved without major architectural changes since the jitter is usually intrinsic of the hardware components. For that reason, the solution might be the replacement of critical components by more resilient ones such as the leading-edge discriminator by a CFD to reduce the effect of laser jitter and time-walk, the substitution of the PIN by an APD, the use of another microcontroller with a better DC characteristic and more stable CLOCK sources, the implementation of optical and electronic filtering and a better temperature stabilization mechanism for the laser (e.g., thermoelectric cooler, heatsink). Another alternative already adopted is averaging of $N=2400$ ToF signals to attenuate the effect of individual fluctuations with a proportion equal to the square root of the number of measures per distance (equation (5.7)). However, this comes at an expense of lower sensing and, in some real automotive scenarios, the introduction of artefacts due to moving targets.

To conclude, the reported behavior is in conformity with the analogous benchmarked response of commercial LiDAR sensors (Figure 124). Quantitatively, the precision of these sensors is, as expected, superior to the LiDAR prototype. At 100m, the *Quanergy M8* shows a precision of less than 4cm and the *Velodyne VLP16* better than 3cm. At 50m, and in the same order, the former has a precision of 2cm and the second of 1cm. The *Garmin lite v3* underperforms comparatively to the remaining and presents a precision of around 10cm at 40m. At last, the *Leddar Vu8* has an exactly null standard deviation below 20 meters as a practical consequence of the default oversampling and accumulation of the respective software. Beyond these ranges, it increases considerably up to around 3cm at 60m. The superior results are motivated by the more precautious and elaborated designs encompassing thoughtful filtering for noise-reduction, more stable CLOCK sources and more efficient and controlled cooling mechanisms. The qualitative distance-dependence is the same and the precision also correlates with the intensity of the

back-reflected light pulses, i.e. with the distance to the target: lower intensities consistently provide the lower precision (higher standard deviation) distance estimates. [34]

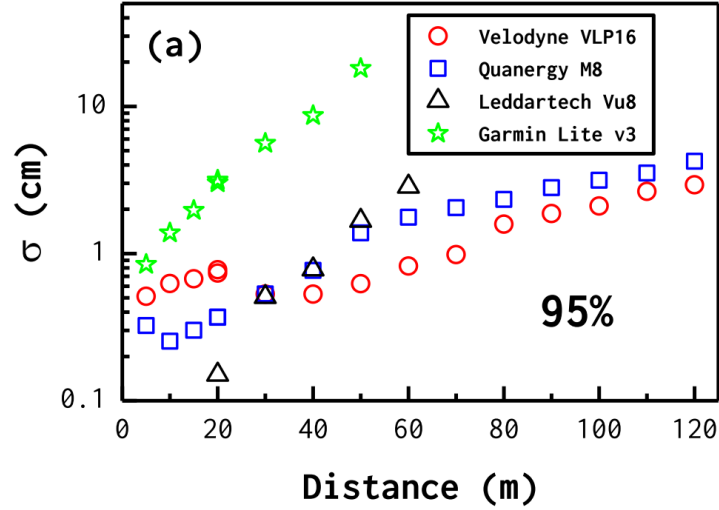


Figure 124. Standard deviation of commercial LiDAR sensors for a 95% diffusely reflective target. The vertical axis is in a logarithmic scale [34].

5.1.6.3. Signal-to-Noise Ratio (SNR)

Similar to the precision, the information about the sensor's Signal-to-Noise Ratio (SNR) may also be straightforwardly extracted from the standard deviation. The SNR is usually one of the preferred FOM to quantify the system reliability since it gives an intuitive estimate of the relative impact of the precision or, stated otherwise, the degree of confidence one can ascribe to the distance estimation [34].

The previous metric compares the level of effective signal with its intrinsic statistical fluctuations, i.e. with the level of noise, and is intrinsically linked to the precision and detection limits. Mathematically, it is defined through the ratio between the mean value of the variable susceptible to fluctuations and its standard deviation. In this context, the variable can either be the distance or the ToF, both yielding the same result [72]:

$$SNR = 10 \log_{10} \left(\frac{\langle d \rangle}{\sigma_d} \right) dB \quad (5.19)$$

where the result is often presented in a logarithmic scale of decibels, dB. Both the average, $\langle d \rangle$, and the standard deviation, σ_d , are obtained from the descriptive statistical treatment for the 2400 points acquired for calibration. The greatest the SNR, the lowest is the relative level of uncertainty. Fundamentally, the lowest SNR from a meaningful measurement is 1, corresponding to an equal amount of uncertainty/noise as the effective signal. However, typical estimates are desired in a much higher SNR level.

The SNR of the LiDAR prototype is portrayed in Figure 125a, parallelly to the reported response for the state-of-the-art sensors. At short distances, the SNR increases quickly from about 12dB and, at around 3m, it starts to level off at around 18dB, corresponding to a signal approximately 63 times larger than the standard deviation. This behavior is not spontaneously deciphered, but the captured physical

information is that the standard deviation increases at a lower rate than the mean value. The SNR vs. distance variation is coherent with the experimented benchmark behavior in which there is an initial high-slope increase that at longer ranges tends to a constant SNR. Additionally, it is also consistent with the applicability of LiDAR since it is targeted for larger ranges and, at close ranges, other automotive sensors perform better [34]. However, both the *Garmin lite v3* and the *Leddar Vu8* at ranges superior to 20m have decreasingly evolving SNRs, as a result of the noise increment and loss in precision.

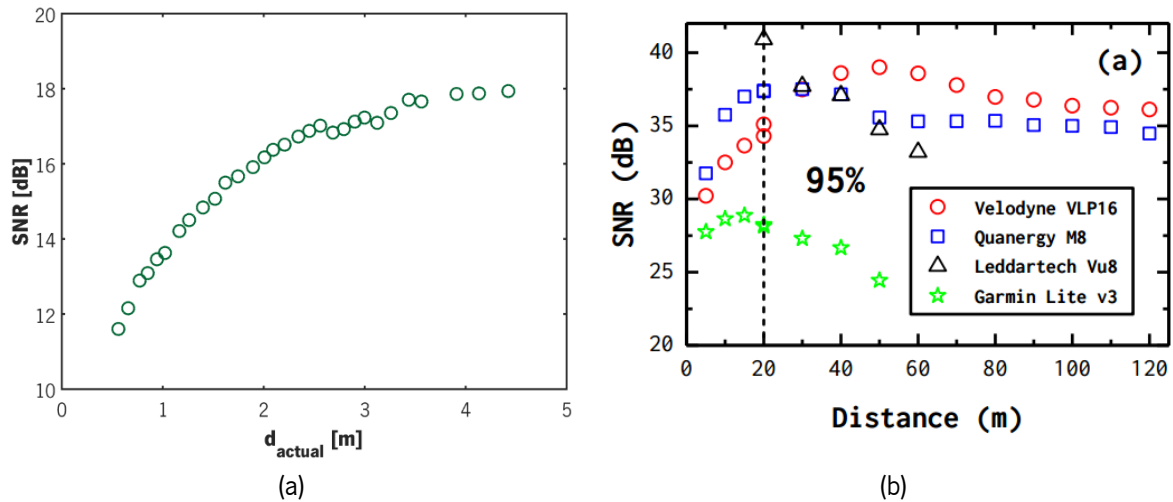


Figure 125. SNR vs. distance for reflection on *K-line white* with 95% overall reflectivity: (a) LiDAR prototype and (b) commercial sensors [156].

Naturally, the quantification is distinct and the developed LiDAR prototype has a smaller SNR in all working distances, as a consequence of the greater imprecision. The benchmarked sensors have a SNR superior to 20 in all the experimented ranges with the *Velodyne VLP16* being the most precise and, therefore, the one with the largest SNR. The SNR increase in this prototype is accomplished by the reduction in the standard deviation described previously. Moreover, it has been verified that, for less reflective targets, the SNR does not suffer significant changes [34].

5.1.6.4. Dynamic Operation

Formerly, the system was characterized at different distances intercalated with the acquisition of 2400 points under the same conditions. Nevertheless, the sensor has the capacity to acquire 6000 points per second and, therefore, to measure a target constantly moving in relation to it. Hereupon, a demonstration of a dynamic measurement of the *K-line white* target is shown in Figure 126 after calibration with the best relative constant (1.528m). The distance is varied between around 4.4m and 2.8m in less than 5 seconds and it is observable the real-time response in the GUI with some latency due to the data sending to the PC and the graphical representation of the experimental points. Dynamically, it is much harder to accomplish a trustworthy analysis and to extract relevant information on the sensor's performance metric. In this scenario, the mean value and standard deviation presented on the lateral are not meaningful since the acquisition conditions are changed.

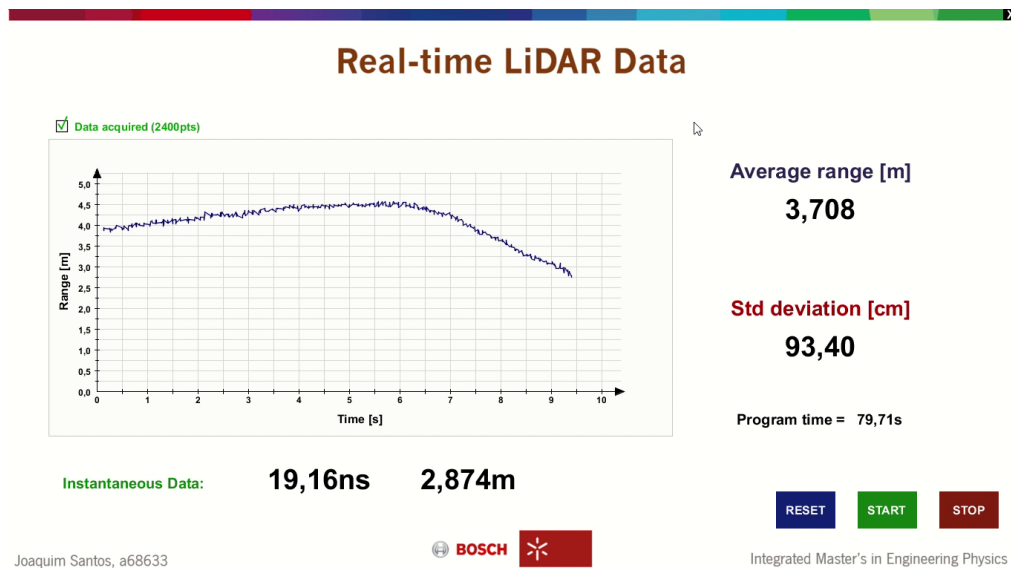


Figure 126. Dynamic response recorded on the GUI for a movement of the *K-line white* target between 4.4m and 2.8m during a total time of less than 5s. The clear fluctuations on the graphical trace are a consequence of the imprecision sources studied.

5.2. Optical Characterization

The LiDAR prototype is composed of two main hardware subsystems: optics and electronics. In this section, the first is studied. The focus is the TX end since the laser optical output and the respective shaping optics play a major function in the system overall performance.

5.2.1. Optical Simulation

With the prime purposes of gaining a more detailed insight on the operation of the optical system and on the sensitivity of the overall sensor's performance on the individual optical elements, and to support the final optimization of the physical sensor by providing information on the critical position of the lenses, some optical simulations are run. Furthermore, these simulations aim to supply numerical reference values for the expected throughput and divergence at the output of the TX shaping optics, to be posteriorly compared with the empirical measurements.

The chosen software is the *ZEMAX OpticStudio v16.5*, a broadly adopted and extremely complete and powerful software for optical design and simulations, as it can solve sequential and non-sequential optical designs encompassing several degrees of complexity [184]. Due to its versatility, *ZEMAX OpticStudio* is adopted by many companies, including *Bosch*, in several projects such as LiDAR.

The system ought to be modulated in non-sequential mode, in which there is no predefined sequence of surfaces the traced rays must hit. Each 3D object is placed globally at an independent (x,y,z) coordinate system with an autonomous orientation. The rays are determined and traced solely by its direction and the object physical position and properties. In contrast, in sequential ray tracing the rays propagate through the same set of surfaces in the same order. [185]

The first step is to define the system objects to be included in the simulation. The *ZEMAX* 3D model for the *SPL LL90_3* laser can be directly retrieved from the *OSRAM* website and loaded with the nominal characteristics. As for the lenses, all the used models are available on the embedded lens database. Next, the elements placement is set in relation to the laser output. This is an extremely complex task because it must be accompanied by a careful examination of the coordinate referential.

In non-sequential mode, the beam cross-section is analyzed in several points by defining “Detector Rectangles” and placing them at the intended positions. These objects do not interfere with the system and are transparent to the light beams. The simulation results are all extracted under the standard conditions exposed in Table 23.

Table 23. Global *ZEMAX* simulation parameters.

Analysis Rays	$1.5 \cdot 10^6$
Detector Pixels	750×750

To set the initial conditions and the reference for the power-transmission efficiency, the laser output is measured directly using a $200 \times 200 \text{ mm}^2$ transversal detector at $z=100 \text{ mm}$. It is noteworthy that *ZEMAX* uses a different referential definition comparing to the one designated in Figure 10, as shown on the bottom-left corner of Figure 127a, and the laser orientation is at 90° comparing to the actual position in the LiDAR setup. As a result, a highly-divergent beam is obtained with a peak power of 69.993 W (Figure 127b) and a nearly-Gaussian cross-sectional profile with larger divergence in the z-y plane (Figure 128). The data drawn in every graph is the Incoherent Irradiance, i.e. the radiant flux received by the detector surface’s per unit area, since the optical simulation is based on incoherent detection. *ZEMAX* automatically calculates the total peak power by integrating the irradiance in each pixel over the whole detector’s area.

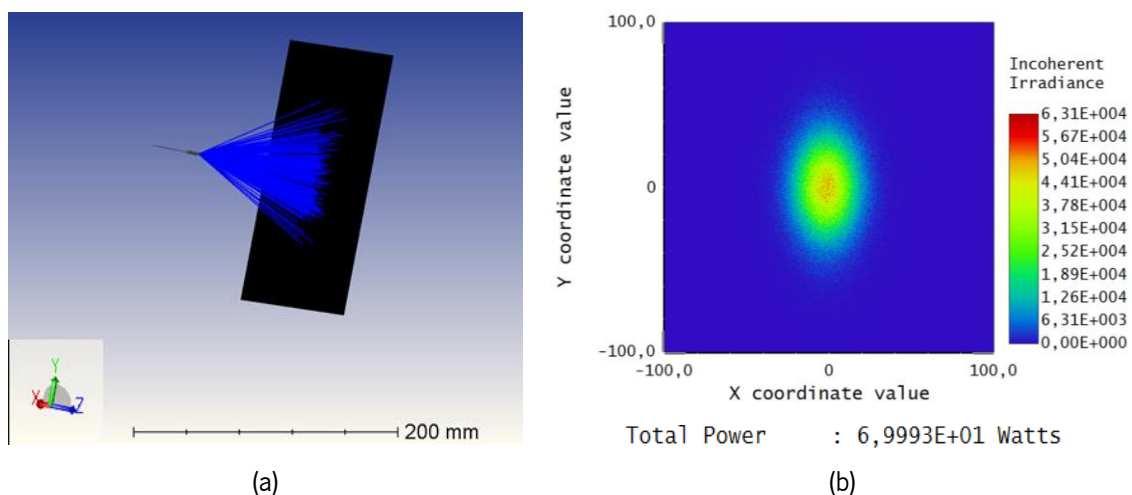


Figure 127. (a) Layout for obtaining the reference conditions and (b) False colormap of the Incoherent Irradiance on the detector plane.

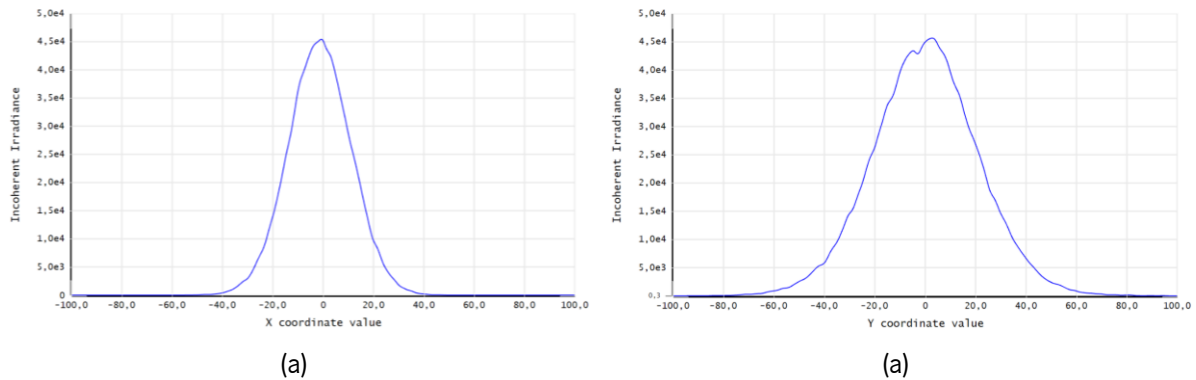


Figure 128. Cross-sectional Incoherent Irradiance profiles along the central detector’s (a) row at $y=0\text{mm}$ (slow-axis) and (b) column at $x=0\text{mm}$ (fast-axis).

The defined object data is displayed in ‘Appendix III – ZEMAX Object Data’ before optimization, according to the layout in Figure 97, and after optimization. The generated merit function is shown in Figure 129 and it encompasses two different target conditions. Firstly, a null setpoint is specified for the RMS (Root Mean Squared) spot radius on an auxiliary $20\times 20\text{mm}^2$ detector placed at 50mm from the Iris output to minimize the beam divergence in both x and y directions and hold the best possible collimation. The auxiliary detector does not represent a physical detector in the LiDAR system and serves only as referral, whilst its position is irrelevant because one is aiming to divergence. For the tangible reference photodetector, a zero target-condition is established for the RMS spot radius to achieve an optimum focusing. The optimization is executed during 31.37min through a Damped Least Squares local algorithm which uses numerically computed derivatives to determine a direction in the solution space yielding a design with a lower merit function. After the elapsed time, the overall Initial Merit Function drops from 5.038 to 0.714.

	Type	Surf	Det#	Pix#	Data	# Ignored	Spatial Freq		Target	Weigh	Value	% Con
1	BLNK											
2	DMFS											
3	NSDD	1	0	0	0	0	0	0,000	0,000	0,000	0,000	
4	BLNK	Non-sequential merit function: Angular Radius (Auxiliary Detector)										
5	NSDD	1	0	0	0	0	0	0,000	0,000	0,000	0,000	
6	NSTR	1	1	1	1	1	0	0,000	1,000	0,000	0,000	
7	NSDD	1	16	0	0	0	0	0,000	0,000	0,000	0,000	
8	OPGT	7						0,100	1,000	0,000	0,000	
9	NSDD	1	16	-9	2	0	0	0,000	1,000	0,000	0,000	
10	BLNK	Non-sequential merit function: Spot Radius (Reference Detector)										
11	NSDD	1	21	0	0	0	0	0,000	0,000	0,000	0,000	
12	OPGT	11						0,100	1,000	0,000	0,000	
13	NSDD	1	21	-9	1	0	0	0,000	1,000	0,000	0,000	
14	BLNK	Non-sequential merit function: Spot Radius (Return Detector)										
15	NSDD	1	27	0	0	0	0	0,000	0,000	0,000	0,000	
16	OPGT	15						0,100	1,000	0,000	0,000	
17	NSDD	1	27	-9	1	0	0	0,000	1,000	0,000	0,000	

Figure 129. Merit Function defined in ZEMAX’s Optimization Wizard.

Throughout the previous process, the lenses’ order is kept as well as its characteristics because they all are off-shelf components. Furthermore, the x and y coordinates are also fixed while only the z-position is set as variable (“V”) since the optical elements must all be aligned along the same optical axis (z-axis). Nonetheless, certain lens’ supports impose some restrictions to changes in the axial distances. Alluding

to Figure 97: $r_2 \geq 41.5\text{mm}$ limited by the aspheric lens housing; r_3 and r_4 are fixed by the pre-mounted housings of the biconvex lenses; $15\text{mm} \leq r_6 \leq 30\text{mm}$, inferiorly limited by the cage supports and superiorly by the cage posts' length, although in practice the Iris position does not have a major influence in the performance; the distance to the glass slide, r_7 is also kept fixed to avoid further changes in the system and because the glass slide reflectivity is constant, removing steadily the same percentage of power from the beam. The Iris aperture diameter is also preserved at 12mm otherwise it would be simply reduced to a minimum (0.8mm) to minimize the merit function.

For the receiver, the simulation is rather qualitative because the performance depends on several factors like the target real characteristics and its actual position and orientation. Herupon, for this side of the system no optimization is performed (all parameters fixed), and no merit function is defined. The distance r_{10} is fixed because the two receiver lenses are screwed together. The distance r_{11} to the detector shall be adjusted manually and experimentally to meet a stable spatial profile (collimation) at the *SFH 2400 FA* with minor fluctuations within the work ranges (minimization of the beam spot radius and angular radius).

The optimized lenses' positions are enumerated in Table 24 alongside the initial state, before optimization. The starting point, detailed in Figure 97, is a set of conditions corresponding to an initial optical setup obtained in the laboratory in the first assembly.

Table 24. Distances between optical elements before and after optimization in ZEMAX.

Distance index	Non-optimized [mm]	Optimized [mm]
r_1	1.76	1.868
r_2	41.5	
r_3	5.1	
r_4	4.5	
r_5	43	41.258
r_6	15	
r_7	37	
r_8	38.5	37.825
r_9	28.9	28.129
r_{10}	82	
r_{11}	41	

For simulation effects, the $18 \times 18\text{mm}^2$ glass slide was defined with a 10% reflectivity on both front and back surfaces and with 90% transmission (no absorption). To simulate the return light collection, a reflective target with 5% overall reflectivity and Lambertian scattering was positioned at 500mm from the Iris and the first receiver lens at a 15° angle with both to receive the specularly reflected component (reflection law). All the optical elements are shifted by $x = -1.4\text{mm}$ to align the optical axis with the beam because the latter is not centered at the origin of the Cartesian Referential [160].

The 3D layout of the complete optical system is exhibited in Figure 130 as a NSC Shaded Model after optimization. The NSC Split Rays and NSC Scattering are enabled, meaning that all the reflected and scattered rays are represented (each color a segment), thus the chaotic appearance. The differences from the original layout are visually subtle.

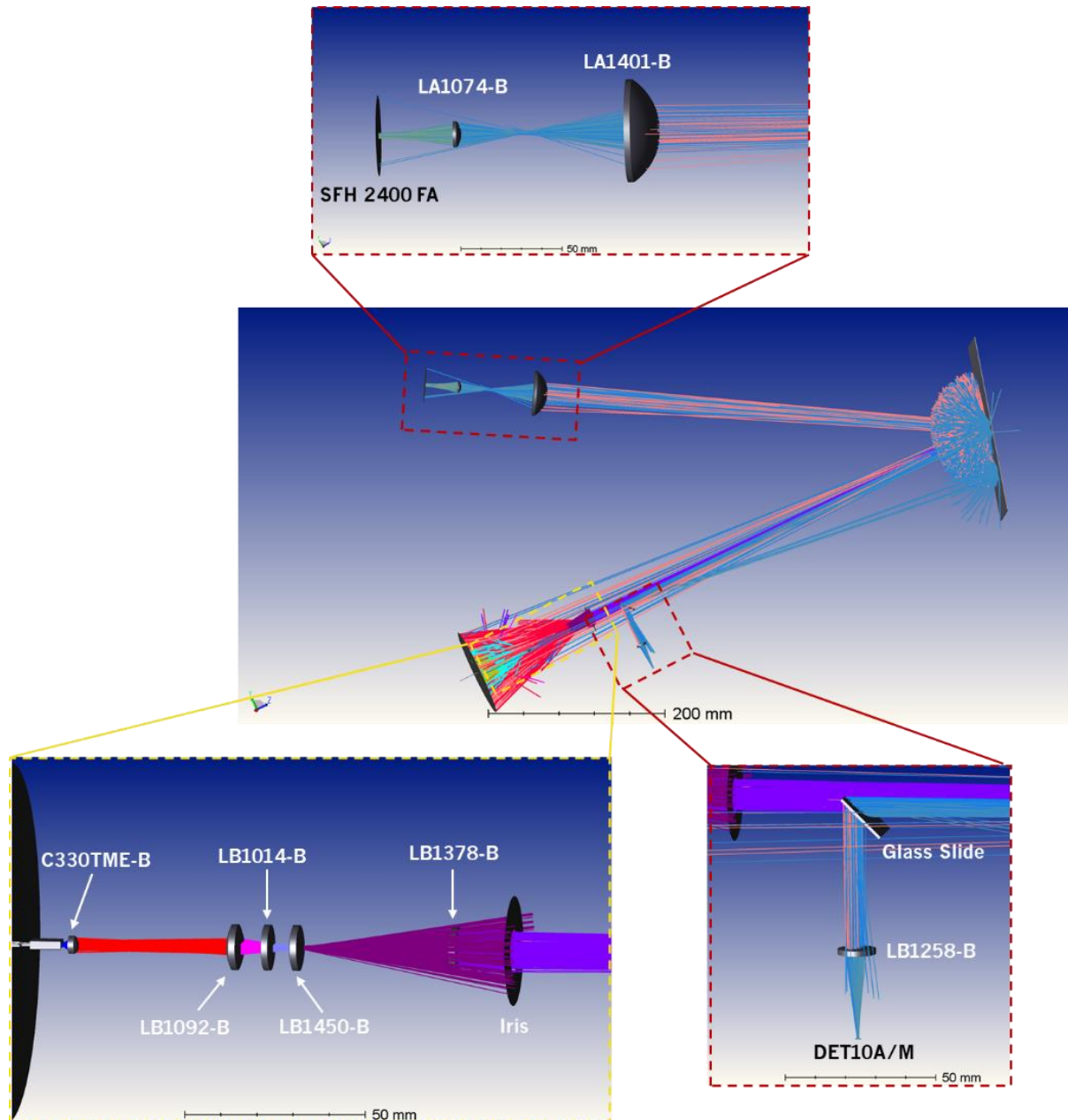


Figure 130. NSC Shaded Model of the LiDAR optics with the most relevant points zoomed-in. The reference number for each optical element are identified.

Next, the results are presented on vital points of the system, either before and after optimization, to provide a quantitative foundation for the improvement in performance. Starting with the TX side, the beam spot profile is shown in Table 25 at different radial distances from the laser output, identified, for simplicity, as relative positions to the optical elements.

Table 25. False color incoherent irradiance at several critical points of the TX optical setup. The size of each detector is not the same and is represented on the 4th column.

	Non-Optimized	Optimized	Detector size (full-width)
Aspheric front vertex			10.0×10.0mm ²
LB1378-B back vertex			12.7×12.7mm ² (LB1378-B diameter)
1mm to Iris			30.5×30.5mm ² (Iris total diameter) Observable the shadowing effect provoked by the lens' edges
50mm from Iris			20.0×20.0mm ²
500mm from Iris			20.0×20.0mm ²
1000mm from Iris			30.0×30.0mm ²

Even though there are no noteworthy differences in the irradiance distribution profile before and after optimization up to the Iris aperture, the preeminent dissimilarities show up after. Besides presenting a seemingly higher energy density around the beam axis, the circular profile induced by the spatial filter is maintained over larger distances and with larger irradiance uniformity between the x and y directions, both resulting from an inferior divergence. Whatsoever, there is still some residual divergence arising from the fact that the laser chip is not a perfect punctual source (cannot be realistically avoided). In either case, the output beam retains the nearly-Gaussian intensity profile as shown in Figure 131 at 500mm from the Iris and after optimization. This result is qualitatively the same for greater distances.

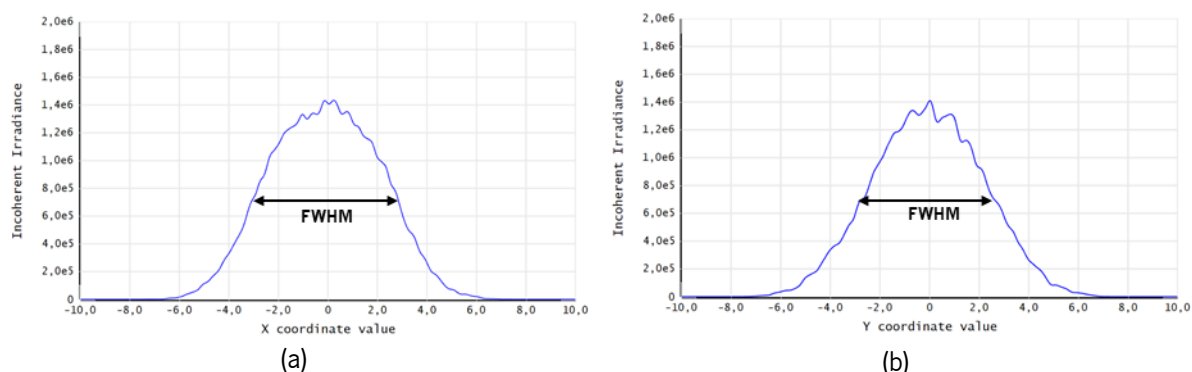


Figure 131. Beam cross-section after optimization along (a) the x-axis for the central pixels' row ($y=0\text{mm}$) and (b) the y-axis for the central pixels' column ($x=0\text{mm}$), both passing through the point of maximum Incoherence Irradiance (central pixel).

In the non-sequential mode, the quantification of the beam divergence is not trivial, and a numerical value cannot be directly obtained. Instead, the divergence is estimated using the cross-sectional data along the x and y axis at two different distances, 500mm and 1000mm. By extracting the beam spatial FWHM from the graphical data and doing a linear interpolation under the assumption of a constant angle in each direction, the full-divergence angle at the output, θ' , and in the z-y and z-x plans can be calculated:

$$\theta' = 2 \arctan \left(\frac{FWHM @ 1000\text{mm} - FWHM @ 500\text{mm}}{2 \cdot 500} \right) \quad (5.20)$$

where the FWHM is in millimeters. The results are exposed in Table 26 and reflect a meaningful correction, i.e. reduction, either comparing with the initial beam divergence of 30° along z-y (perpendicular to p-n junction, θ_{\perp}) and 15° along z-x (θ_{\parallel}) and with the results prior to optimization. Still, the divergence continues to present a disparity between a fast and a slow axis, leading once again to an elliptization after a certain distance (indeed, at 1000mm the beam is already elliptical).

Table 26. Calculations of the output beam divergence before and after optimization.

	Plane	FWHM [mm]		Output FWHM Divergence, θ'	Improvement	
		@ 500mm	@ 1000mm		Absolute	Relative
Before Optimization	z-x	3.52	9.96	0.738°		
	z-y	2.49	12.56	1.154°		
After Optimization	z-x	5.25	5.89	0.073°	-0.665°	-90.11%
	z-y	7.48	11.36	0.445°	-0.709°	-61.44%

Consecutively, in Table 27 the laser peak power results are given for $12.7 \times 12.7 \text{ mm}^2$ detectors (diameter of most of the lenses in the transmitting path) and for the same vital points afore defined. Although the optimization aims uniquely for enhanced collimation, a positive side-effect is the improvement of the power-delivery efficiency of up to approximately 45% at 1000mm and in the defined detectors' area, mainly a consequence of the smaller divergence. Comparing with the laser output power of 69.993W, the optimized power at the latter distance represents a total of 52.28% efficiency. The main losses occur in the segments between the biconvex lenses triplet and the *LB1378-B* back-vertex, due to intermediary divergence before collimation (21.53% relatively to the total laser power and 45.11% of the total power deficit, after optimization), and after the Iris, due to the final residual divergence (14.90% relatively to the total laser power and 31.21% of the total power loss, between 50mm and 1000mm from the aperture and also after optimization). In addition, an extra source of losses are the reflections at the lenses surfaces due to the non-null reflectivity, even with B-coating. Naturally, even with all the losses, the optics remain indispensable. As an example, for the same detector area, the beam power would be 22.664W at 50mm and 0.2964W at 500mm from the laser, without any optical element.

Table 27. Peak powers measured by $12.7 \times 12.7 \text{ mm}^2$ detectors.

	Non-Optimized	Optimized	Relative Improvement (Accumulated / Local)
Aspheric front vertex	66.731W	66.737W	+0.009%
LB1378-B back vertex	48.276W	51.670W	+7.030% / +7.021%
1mm to Iris	43.370W	48.230W	+11.206% / +4.176%
50mm from Iris	42.737W	47.018W	+10.017% / -1.189%
500mm from Iris	42.003W	46.400W	+10.468% / +0.451%
1000mm from Iris	25.252W (For a $20 \times 20 \text{ mm}^2$ Detector: 36.774 W)	36.592W (For a $20 \times 20 \text{ mm}^2$ Detector: 44.726W)	+44.907% / +34.439% (+21.624% accumulated)

With these simulations, the TX optics can now be explained in more detail. Firstly, one must understand geometrically the single-lens collimation process and the dependence on the focal length. The smaller the focal length, the larger is the beam divergence after collimation because it follows a relation similar to equation (5.20) in which the 500mm in the denominator are substituted by the distance to the focusing lens and the numerator by the laser chip aperture. On the other hand, the larger the focal length and for the same input divergence, the larger is the beam spot size at the lens' back-principal plane and the larger the beam diameter after collimation. Hereby, as one wishes to couple the maximum laser power to the TX optics, an aspheric lens is mandatorily chosen as first lens. Due to its short focal length, the power losses due to the high divergence of the beam are minimized since the latter lens can be placed very close to the emitter chip. However, the output divergence is considerable and the beam is posteriorly focused with a smaller angle, comparing to the direct laser output, by the set of 3 biconvex lenses. Subsequently, it is re-collimated by a bigger lens (*LB1378-B*) with a larger focal length to diminish the output divergence.

Finally, although the changes in the axial positions may seem insignificant, the improvements in the TX performance with the optimization are substantial. Experimentally, the fine adjustment is a delicate and complex task because one does not have control on such minor changes. Thereby, the process is executed through small increments in the lenses' positions accompanied by an indirect observation of the beam spot on a NIR-sensitive card or with a camera.

Proceeding to the reference path, the optics is much simpler as is the analysis. The irradiance at the reference photodetector is presented in Figure 132. The detector is defined as a quadrangular area with $1 \times 1 \text{mm}^2$, similar to the photosensitive chip of the *DET10A/M* ($\varnothing 1 \text{mm}$). Since the lens *LB1258-B* is adopted for focusing and the beam divergence is small even after reflection at the glass slide, then its relative position to the reflector is secondary. Indeed, after optimization the latter is barely changed. As for the relative position between the focusing lens and the detector, it should be theoretically the lens' focal length (28.9mm). However, due to spherical aberrations, *ZEMAX* recalculates the best focal plane at 28.129mm. As an overall result of optimizing this segment, the beam spot at the detector is clearly more focused, i.e., the irradiance profile is sharper and more intense. To calculate the focusing efficiency, the power is measured immediately before the lens yielding 4.3212W and 4.9245W with and without optimization respectively. Hence, the outcome is a 90% and 99% efficiency, on the same order.

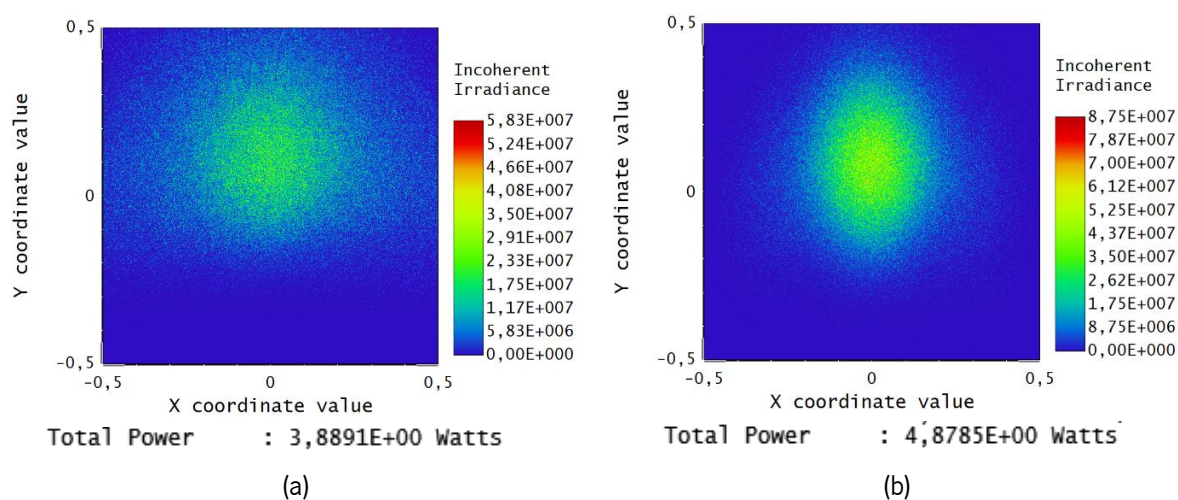


Figure 132. Incoherent irradiance data on the $1 \times 1 \text{mm}^2$ reference detector (a) before and (b) after optimization.

Regarding the reception, the back-reflected power at the LA1450-B lens input vertex is, in the simulated scenario and without optimization, 0.4268W, from which 0.12797W strike the detector, yielding a total of around 30% light-collecting efficiency. The latter result is the same result if considered the RX optimization, with only a difference in the quantitative power.

To complete this sub-section, the previous results and discussion are also valid for smaller optical powers. In case the laser does not operate at the nominal limit of 70W but at rather inferior powers, the only difference shows up at the peak powers that need to be linearly down-scaled to adjust to the actual situation. The relative improvements, efficiencies and divergences remain unchanged because the system performance is independent on the input power.

5.2.2. Optical Alignment and Optimization

The optical alignment and optimization are two critical procedures to ensure a proper optical response of the LiDAR sensor. These processes are performed before the final measurements are taken and using the *ZEMAX* simulations and consequent results as a guideline to support the adjustment direction towards an enhanced response.

From experimental experience, it is extremely important and useful to have both preliminar empirical observations and simulations since they complement mutually. The starting point for the simulation is obtained from experimental work in the laboratory, during which the actual design is started. On the other hand, the simulation gives clear indications to guide the experimental optimization towards an improved overall throughput of laser power.

As the laser is NIR, this process is particularly complex and supplementary instruments are required to support the tasks. Hence, a *ThorLabs IRC3* viewing card is used to convert the laser invisible radiation to a lower and visible wavelength through a fluorescent mechanism (Figure 133a). This card is employed to quickly visualize the beam in different stages of the optics. Moreover, the outputted laser beam is simultaneously projected on the *K-line White* target and the spot profile is imaged in real-time by an *AVT Manta G-917B* 14-bit monochromatic camera connected to a PC and controlled using *Halcon*, a machine vision software. This setup is pictured in Figure 133b and allows to constantly monitor the effect of each modification in the beam spot profile.

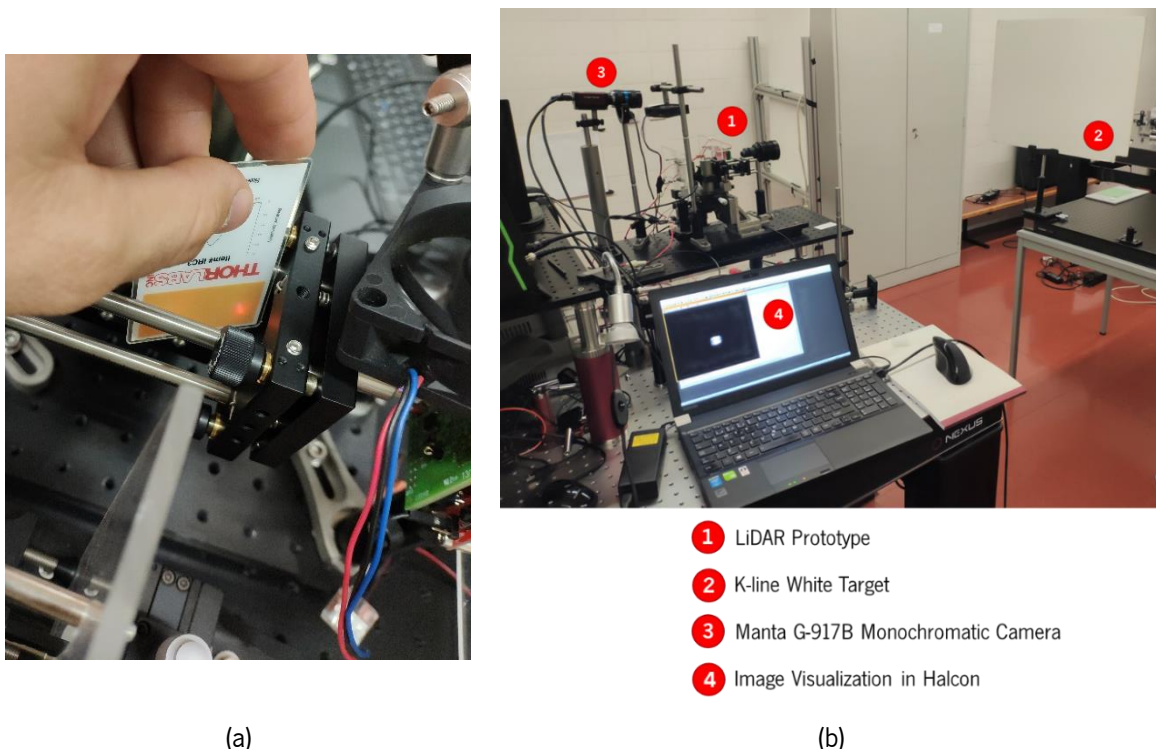


Figure 133. Optical alignment and optimization procedure: (a) beam spot made visible by the NIR-visible converter card and (b) setup for visualizing the beam projection (spot) on the *K-line White* target plane.

The procedure for the TX optics consists on mounting the first aspheric lens on the cage system and adjusting its position in relation to the laser emitter through the 3DOF screws of the support. After aligning

the first element and optimizing the collimation, the other lenses and the iris are mounted on the cage and its axial positions adjusted as identified in the architectural diagram of Figure 97. The cage system ensures that the optical axis of all the elements is correctly aligned. The critical point is the *LB1378-B* lens position as previously identified, that is tuned for a compromise between collimation and output power, despite the latter has not been the simulation spotlight. The optical power is measured between lenses to support the process and, as an outcome, the power is considerably larger than the foreseen in *ZEMAX*, at the expense of a larger divergence.

Regarding the reference and return optics, the process is simpler since both are focusing systems. Here, the spot size enables to simply and straightforwardly compute the focal point of the respective lenses by finding the position along the optical axis yielding a minimum. Thus, using the converter card the focal plane is ascertained and the detectors (*DET10A/M* and *SFH 2400 FA*) are correctly positioned accordingly and, ultimately, by maximizing the pulsed signals' amplitude on the oscilloscope. The results arising from the previous processes are evaluated in the subsequent sub-sections.

5.2.3. Stabilization Time and Laser Spectral Profile

When turned-on and before starting the range measurements, the LiDAR requires a certain amount of time to warm-up and enter a stationary operation regime. This initial interval is imposed by the stabilization time of the pulsed laser emission and it can be empirically estimated using the setup documented in Figure 134.

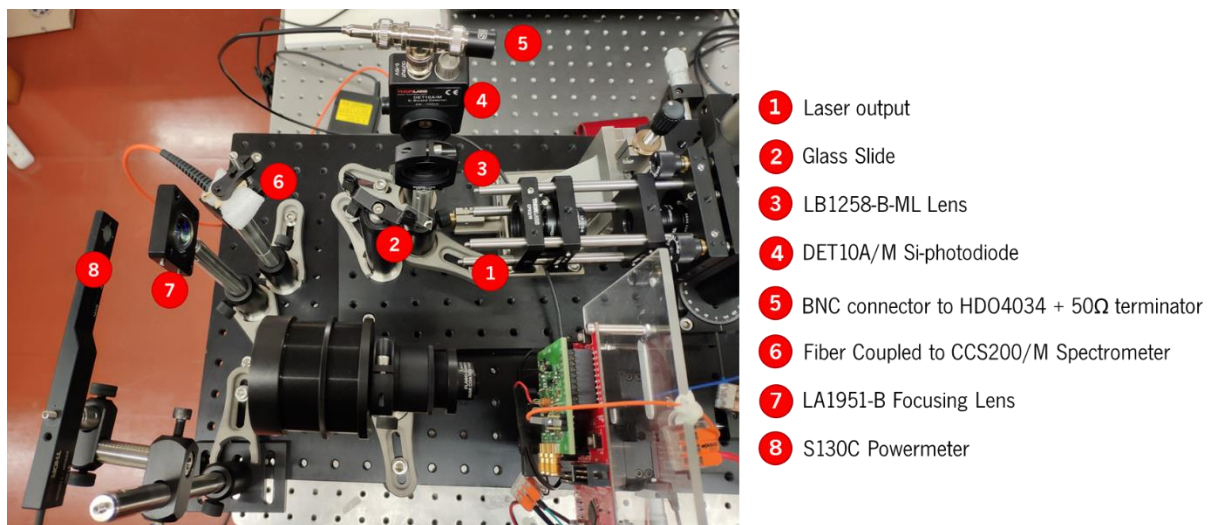


Figure 134. Experimental setup to determine the approximate warm-up time of the LiDAR sensor properly labeled.

Several laser parameters are monitored as function of time until steady-conditions are realized: average power, peak of spectral emission, spectral FWHM, temporal rise-time and FWHM. To acquire all of them simultaneously, the beam output at the TX optical system is split by three sensors: a *DET10A/M* biased Si-photodiode, a *ThorLabs CCS200/M* fiber-coupled compact spectrometer and a *ThorLabs S130C* powermeter. The temporal measurements are performed in the reference path of the prototype. A portion of the beam is reflected at the microscope glass slide (2) and focused on the *DET10A/M* (3 & 4), connected to a *Teledyne Lecroy HDO4034* oscilloscope to capture the laser pulses as post-process

them in the *WaveRunner* software to extract the rise-time and temporal FWHM. The spectral measurements are retrieved directly in the *ThorLabs OSA* software with $<2\text{nm}$ accuracies by connecting the previous spectrometer to the PC. Light is collected by an optical fiber placed in such way that it takes advantage of the laser divergence (5). The light coupling to the fiber is performed using a scattering material that disperses the beam and ensures some photons are collected within the fiber acceptance angle and effectively guided to the measuring unit. Finally, a *LA1951-B* plano-convex lens (6) focuses the remaining light in the powermeter sensitive area (7). This module has a 100pW resolution and measures up to 500mW average powers with 3% accuracy. Herein, the interest is to have a qualitative idea of the laser power behavior rather than an absolute idea of the maximum power. The *SI30C* is connected to a *PM320E* console configured to 920nm for internal wavelength correction/calibration, which, in turn, is linked to the PC to store the data in a *.txt* file.

The variables are acquired every 30 seconds during 30 minutes in the sensor's standard operating conditions (6kHz repetition rate and 65% duty cycle). Throughout these measurements, no external temperature stabilization is applied to the laser (fan OFF) to maximize the variations and provide a genuine idea without external factors.

The most meaningful and clear variations are noticed in the spectral center and average power as shown in Figure 135a. From these results, one can conclude that the peak wavelength increases monotonically starting from around 917.5nm and stabilizes after approximately 10 minutes at around 919.4nm . As for the average power, it decreases initially and also stabilizes after a similar time interval. Hence, every time the device is turned-on, one must ensure that a 10 minutes wait-time elapses before any measurement is taken. The values for the latter parameter are not relevant for this analysis.

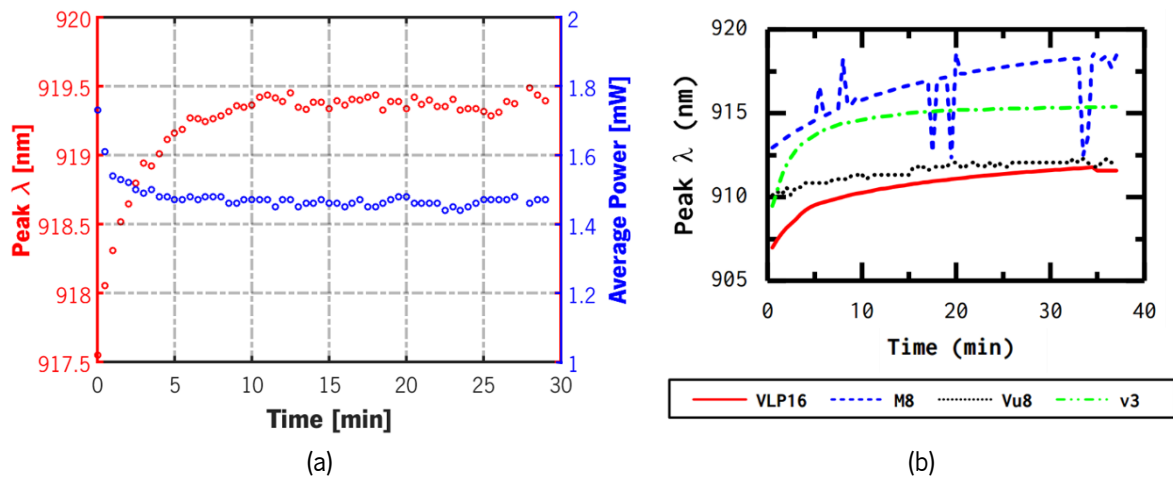


Figure 135. (a) Spectral center and average power variation during warm-up time for the developed LiDAR prototype and (b) peak wavelength for commercial sensors during the stabilization period [34].

Comparing these behaviors with the commercial sensors characterized in [34] (Figure 135b) the response is qualitatively similar with the *Garmin v3* being the faster in warm-up, taking also 10 minutes, and the *Velodyne VLP16* and *Quanergy M8* being the slowest, taking about 40 minutes to stabilize. The *LeddarTech Vu8* takes around 25 minutes. In terms of average power, all the sensors maintain a nearly-constant unremarkable response. The other controlled parameters do not have a well-defined variation pattern and, therefore, are left apart from this discussion.

After a time of approximately 35 minutes since power-up, the steady laser spectrum is acquired in the same standard test conditions ($dc=65\%$, $f_p=6\text{kHz}$, $V_{cc,laser}=15.5\text{VDC}$) and with temperature stabilization to simulate the real case scenario in the operating prototype and avoid shifts in wavelength due to heating. The spectral distribution is exhibited in Figure 136 as directly given by the *CCS200/M* spectrometer with a 30s integration time. In Table 28 the numerical results are presented.

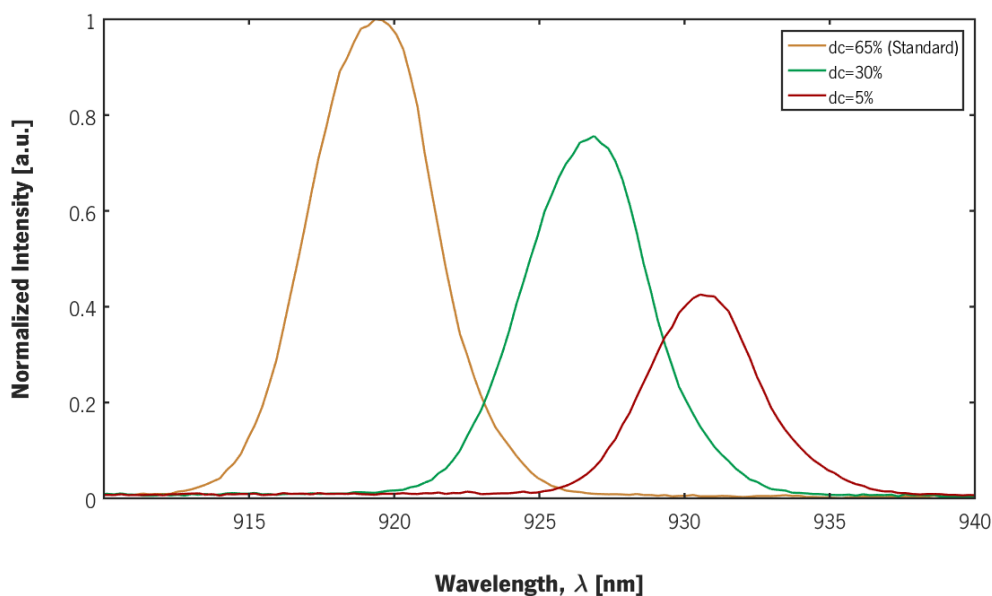


Figure 136. Spectral profile of the developed LiDAR sensor as measured after warm-up with a repetition rate of $f_p=6\text{kHz}$ and for three different duty cycles for the *BP_TRIG* triggering signal: 5%, 30% and 65%.

By looking at the spectrum in the standard test conditions, one can see a clear laser response with a symmetric, well-defined sharp peak with around 5nm FWHM, falling within the nominally stated range in the datasheet [160]. Furthermore, and even though the peak wavelength deviates slightly from the specifications, no significant operational consequences arise. The main, but still unimportant effects are faintly different responsivity of the photodetectors and behavior of the lenses AR coating, both wavelength dependents. This deviation can be explained by the fact that the nominal specifications are defined for a different driver IC (*EL7104C*) and under different conditions: $>50\text{ns}$ pulse width, 1kHz PRR, $V_{cc,laser}=18.5\text{V}$ and at 25°C [160]. Other important factor is the temperature and is not encompassed herein.

Table 28. Comparison between the nominal and experimentally estimated spectral characteristics of the *SPL LL90_3* laser in the standard test conditions of $f_p=6\text{kHz}$ and $dc=65\%$ on *BP_TRIG*.

Spectral Metric	Nominal	Experimental
Peak Wavelength, λ [nm]	895 ... 915	919.214 (+4.214nm)
Spectral FWHM, $\Delta\lambda$ [nm]	7	5.004

Overlaid with the spectrum in Figure 136, two additional spectral responses are shown as acquired in the same PRR conditions but at smaller duty cycles in *BP_TRIG* (30% and 5%). This result aims to substantiate and prove the statement asserted in the previous chapter regarding the off-time required to fully charge the capacitors and consequently maximize the optical response ($44\mu\text{s}$). While for a duty cycle

of 65% the off-time at the driver output is, nominally, $0.65/6000 \approx 108 \mu\text{s}$ (remember that the driver inverts the signal, so the nominal off-time is the on-time in BP_TRIG), for $dc=30\%$ this time decreases to $50 \mu\text{s}$ and for $dc=5\%$ to $8.3 \mu\text{s}$. This drop in the charging time affects the peak current during the laser pulsed emission. Therefore, a shift in the LD optical response (Figure 23) is noticed to lower forward currents (to the left), towards deteriorated stimulated emission, as an upshot of a weaker population inversion, and stronger amplified spontaneous emission. Spectrally, this reflects in a considerable shift to longer peak wavelengths ($\approx 926.6 \text{ nm}$ for $dc=30\%$ and $\approx 930.6 \text{ nm}$ for $dc=5\%$), resulting from lower energy transitions between the conduction and valence bands, and no noteworthy changes in the FWHM. Regarding the optical power, it is also affected as one will validate next. The effect of varying PRR is not studied since in the sensor shall operate at the upper limit, to be explicit in section 5.3.6, as desired to maximize the point acquisition rate.

To complete, as regards with the commercial sensors, the four are nominally established to operate at 905 nm but, alike the prototype, a slight deviation towards longer wavelengths is verified in all, with a maximum of 920 nm peak wavelength for the *Quanergy M8*. FWHM-wise, they range between 3.4 nm (*VLP16*) and 7 nm (*Garmin v3*), which is comparable to the developed sensor [34].

5.2.4. Laser Temporal Profile

Transposing to the time domain, the laser temporal profile is measured in the Reference path (4 in Figure 134) by connecting an oscilloscope probe directly to the *DET10A/M* BNC connector and maintaining the 50Ω terminator for impedance matching. Simultaneously, the driver output signal is monitored through the test point TP2 connected to another scope channel. The pulsed signal is sampled in the *Teledyne Lecroy HDO4034* in the standard conditions and after warm-up. The collected signals are overlaid in Figure 137 and Figure 138 with two different time-scales.

From the signals, it is possible to corroborate that the emission events occur at the rising-edges of the gate driving signal (*GATE_DRV*) and, thence, they are triggered by falling-edges in *BP_TRIG*. Whatsoever, a small delay between the start of a rising-edge in the driving sequence and the detection on the reference path is noticed as an effect of the non-null length of the latter. Notwithstanding, this delay is nullified with calibration.

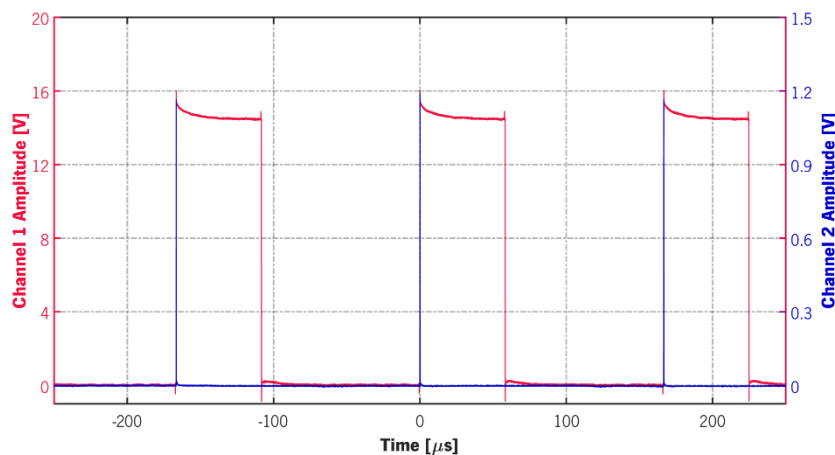


Figure 137. Laser zoomed-out temporal profile for a repetition rate of $f_p=6 \text{ kHz}$ and 65% duty cycle. In red, the laser driving signal and, in blue, the emitted light pulses detected in the reference path.

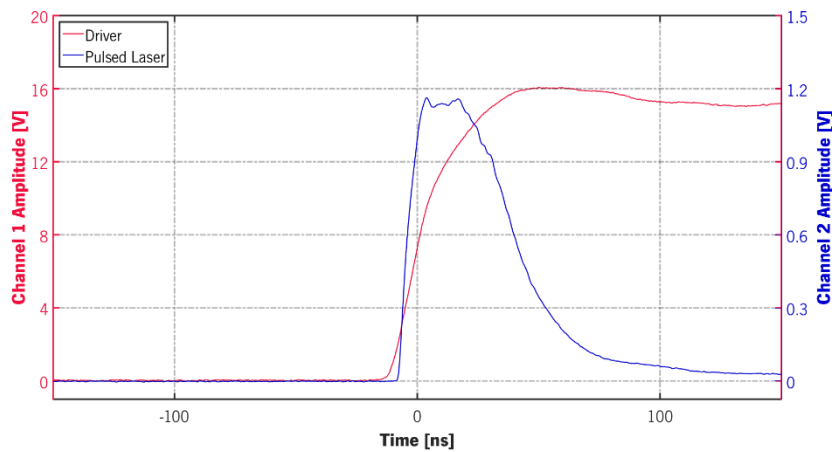
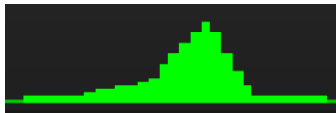
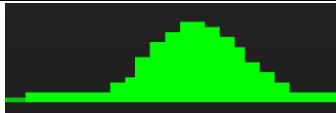
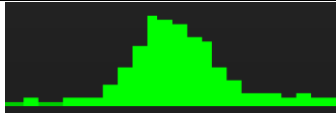


Figure 138. Zoomed-in profile in a rising-edge transition of the driving signal. The overshoot at the abrupt transitions in the driving signal (red) is induced by the long ground wire of the oscilloscope scope used to measure the signals.

Posteriorly, an automatic analysis of individual laser pulses is performed directly on the oscilloscope under the same conditions to statistically study the relevant temporal parameters: FWHM, rise-time and fall-time. A total of 2429 pulses are accumulated for the calculations and the outcomes of the statistical treatment are disclosed in Table 29.

Table 29. Temporal parameters characterizing the laser pulsed emission: experimental vs. nominal. $\langle X \rangle$ is the arithmetic average and σ_x the respective standard deviation of the experimental values, presented as histograms acquired directly from the *Teledyne HDO4034*.

Pulse Temporal Metric	Nominal	Experimental
Pulse FWHM, t_{pulse} [ns]	37 ... 43	 $\langle X \rangle = 45.552$ $\sigma_x = 0.413$
Rise-time, t_r [ns]	7 ... 13	 $\langle X \rangle = 7.077$ $\sigma_x = 0.255$
Fall-time, t_f [ns]	40 ... 45	 $\langle X \rangle = 42.106$ $\sigma_x = 1.120$
Optical Duty cycle (FWHM), dc_{opt} [%]	0.1 (max.)	0.0265

The first aspect to remark is the difference between the optical duty cycle, dc_{opt} , calculated as denoted in equation (2.22), and the *BP_TRIG* duty cycle, dc . As mentioned in the architectural discussion, the width of the optical pulses is limited by hardware to a nominal maximum of 80ns in total, and up to 43ns FWHM. If the width of the triggering pulses is larger than 80ns, then the light output saturates and does not increase beyond this point. Hence, for a PRR of 6kHz and a $dc=65\%$, $dc_{\text{opt}} \approx 0.0265\%$ which is smaller than the limit of 0.1% for the *SPL LL90_3*.

Followingly, the average FWHM is slightly above the specifications, which does not have any influence on the system operation. However, a critical temporal metric is the rise-time since all the events are uniquely triggered by the rising-edge of the optical pulses. The estimated value is inside the expected values with a standard deviation of around 255ps (3.825cm). This indicates that, although the laser pulses are nearly uniformly shaped, there is a small optical jitter in the laser that induces fluctuations in the rise-times and, consequently, fluctuations in the average ToF (imprecision) due to the variation in the timing point.

5.2.5. Optical Power and Eye-safety

To measure the optical powers contemplated in the system, the *ThorLabs S130C* powermeter is employed. The optical power is sensed both directly at the laser emitter output and after the TX optical system (before the glass slide). Contrary to the stabilization time measurement, this time the absolute power is targeted and, therefore, one must ensure the beam spot is completely comprehended inside the photosensitive area of the powermeter. This way, in the first case the powermeter is placed as closer as possible to the *SPL LL90_3* to prevent divergence losses while, in the second scenario, a *LA1951-B* plano-convex lens is applied after the Iris to focus the output beam onto the powermeter. The results are retrieved after the stabilization time and using the standard conditions of $f_p=6\text{kHz}$ repetition rate with 65% duty cycle of BP_TRIG.

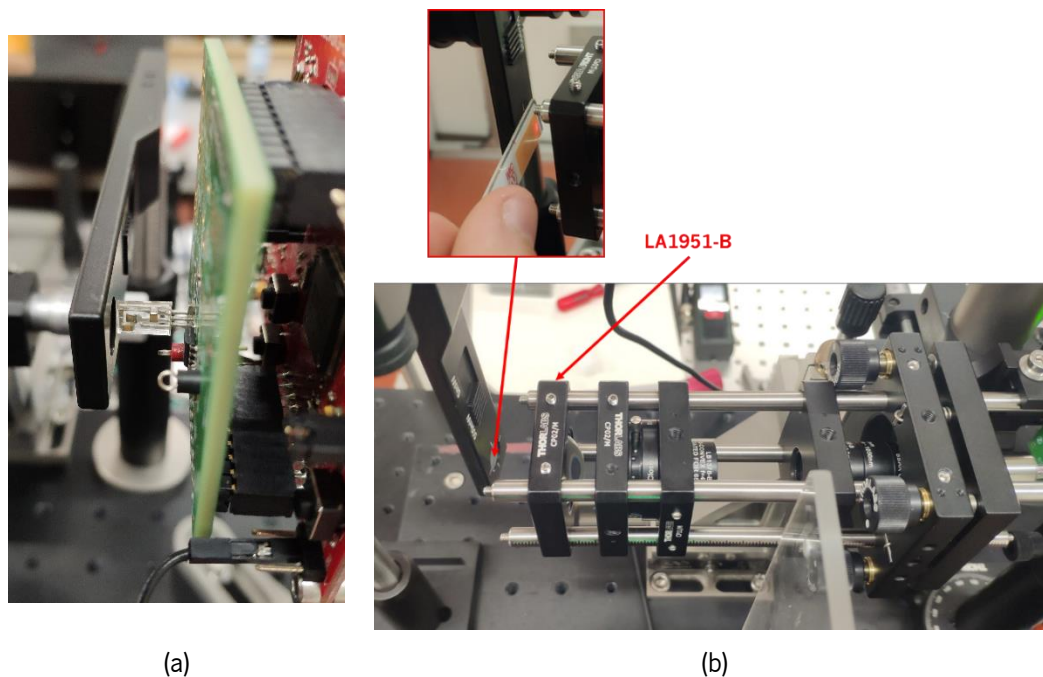


Figure 139. Setup for measuring the transmitted optical power (a) at the laser emitter output and (b) after the TX optics. In the second image, the focusing on the powermeter photosensitive area is verified using the NIR-visible converter card.

The powermeter does only measure the average power of the incident optical beam, P_{avg} . In practice, it is physically more meaningful to quantify the energy carried in each laser pulse and, thereby, the peak

power, P_{peak} , is commonly given. Mathematically, the pulsed power over time, $P(t)$, can be described as the peak power times a normalized time-varying function, f_0 , reflecting the pulses' temporal profile:

$$P(t) = P_{peak} \cdot f_0(t) \quad (5.21)$$

and the average power can be estimated by integrating the latter function over a complete period/cycle of duration T_p (pulses' period):

$$P_{avg} = \frac{1}{T_p} \int_t^{t+T_p} P(t) \cdot dt \quad (5.22)$$

Combining the two equations, the peak power can be written as:

$$P_{peak} = \frac{P_{avg} \cdot T_p}{\int_t^{t+T_p} f_0(t) \cdot dt} \quad (5.23)$$

Frequently, in literature, an approximation is performed considering a squared waveform with a constant amplitude over a time equal to the pulse FWHM, t_{pulse} . In this conjecture, the normalized function is defined as:

$$f_0(t) = \begin{cases} 1 & , \quad t_i < t < t_i + t_{pulse} \\ 0 & , \quad t_i + t_{pulse} < t < t_i + T_p \end{cases} \quad (5.24)$$

and reflects a uniform energy distribution over the pulse FWHM. When introduced in equation (5.23), yields the approximate result of equation (2.21) in which T_p is related to the PRR as:

$$PRR \equiv f_p = \frac{1}{T_p} \quad (5.25)$$

Nevertheless, in this context, is relevant to evaluate the peak power more precisely. To fulfill this, the pulses' normalized waveform must be known. Hereupon, the procedure consists in measuring a single optical pulse in the *DET10A/M* reference path detector and extract the voltage signal, $V_p(t)$, to a *.txt* file directly from the *Teledyne HDO4034* oscilloscope. Subsequently, the pulsed signal is loaded into *MATLAB* and normalized to obtain the waveform $f_0(t)$:

$$f_0(t) = \frac{V_p(t)}{\max\{V_p(t)\}} \quad (5.26)$$

The next step is to integrate the normalized waveform over a complete period and, thus, obtain the denominator in (5.23). Numerically, there are several approaches to perform this integration. Since the mathematical expression to describe the signal is unknown, one opts to apply a cubic interpolation, commonly called cubic spline, to posteriorly apply a numerical integration method. In this method, the waveform is locally interpolated at the point-level by a 3rd degree polynomial with continuity C^2 and, overall, it can be written as [186]:

$$f_0(t) \approx S(t) = \begin{cases} C_1(t), & t_0 \leq t \leq t_1 \\ \dots \\ C_i(t), & t_{i-1} \leq t \leq t_i \\ \dots \\ C_n(t), & t_{n-1} \leq t \leq t_n \end{cases}, \quad C_i(t) = a_i + b_i t + c_i t^2 + d_i t^3 \quad (d_i \neq 0), \quad i = 1, \dots, n \quad (5.27)$$

This method is particularly adequate to perform this calculation considering that the pulse's shape is smooth and does not have abrupt transitions, making it less error-prone and more accurate comparing with other interpolation techniques such as Lagrange and Newton polynomials [186].

Finally, the numerical integration is carried out using the *Gauss-Kronrod* quadrature formula motivated by its superior accuracy. In this numerical approach, a defined integral are approximated by a $2n+1$ point quadrature [187]:

$$\int_a^b f_0(t) dt \approx K_{2n+1} f_0 := \sum_{k=1}^{2n+1} f_0(\tilde{t}_k) \tilde{w}_k, \quad \forall f_0 \in P_{3n+1} \quad (5.28)$$

where \tilde{w}_k and \tilde{t}_k are the weights and points at which the function $f(t)$ is evaluated and P_{3n+1} denotes the set of polynomials with degree at most $3n+1$.

The implemented numerical procedure is valid considering that the photodiode has a large-enough bandwidth to preserve the pulses' shape and that the signal does not saturate. As already specified in the previous chapter, the *DET10A/M* has a 1ns rise-time, which is manifestly inferior to the pulses' rise-time estimated in the prior sub-section. Furthermore, no non-linear effects take place at the optics. The implemented code in *MATLAB* is provided in '*Appendix II – Final Codes*'.

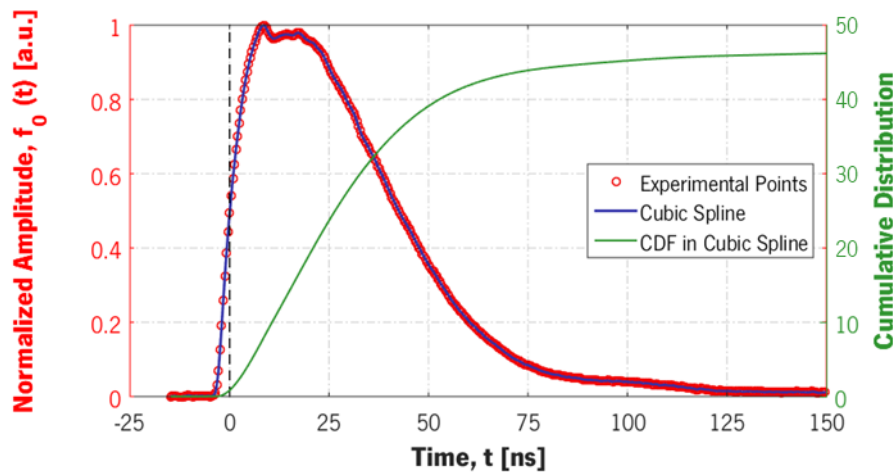


Figure 140. Graphical superposition of the experimental pulsed signal after normalization, the cubically interpolated waveform, $f_0(t)$, and the integral estimation at each point.

In Figure 140 the results of the numerical treatment are shown. In red, the pulse points acquired with the oscilloscope and after amplitude normalization. In blue, the cubic spline interpolation showing a nearly-perfect fit to the experimental points. In green, the Cumulative Distribution Function (CDF) yielding the accumulated result of the integral at each point. The integral is evaluated using $n=5000$ points and

the final area value is given by the CFD at $t=150\text{ns}$. The normalized pulse area has time-units since $f_0(t)$ is adimensional and the computed result is:

$$\int_t^{t+T_p} f_0(t) \cdot dt \approx 46.54\text{ns} \quad (5.29)$$

In Table 30, the average powers measured directly with the powermeter at the two mentioned stages of the TX side are presented as well as the matching peak powers computed through this procedure. The approximated results are calculated using equation (2.21) with a FWHM of 45.6ns , retrieved directly from the cubic splined curve. The first and evident judgment that can be drawn is that there is a significant difference in the results attained considering the pulse's actual waveform or the approximated expression. The disparity rises above 3W which upholds the conclusion that it is essential to use a realistic model of the pulse shape to accurately evaluate the peak power, instead of the commonly employed expression. Followingly, the peak power at the laser output is around 69.95W and meets the typical nominal value specified for the *SPL LL90_3* of 70W [160]. Regarding the effective output, a peak power of approximately 60W is transmitted throughout the TX optics to the circumambient with a total of 13.37% energy loss, or, equivalently, 86.63% transmission efficiency. This high percentage result is a clear indication that the design and the practical alignment is rather efficient power-wise. The dominant losses are induced in the segment between the tripled of biconvex lenses and the *LB1378-B* back-vertex due to beam divergence. This statement is backed by the *ZEMAX* simulations.

Table 30. Average optical power measurements and numerically computed peak-powers directly at the laser emitter output and after the transmitting optical system. The power loss is calculated using the average powers since the peak powers provide a less accurate estimate due to the numerical approximation induced by the employed computational methods.

Pulsed Laser Power		SPL LL90_3 Output	TX Optics Output
Average Power, P_{avg} [mW]		19.45	16.85
Peak Power, P_{peak} [W]	Approx. (FWHM \approx 44ns)	73.67	63.83
	Cubic-spline	69.95	60.34
Power Loss [%]		-13.37%	

Comparing the optical powers for the different duty cycles studied before and to complement the statements, a decrease of 5% in the peak power is determined between 65% and 30% , and 42% between 65% and 5% . This drop can also be graphically seen directly through the normalized amplitudes in Figure 136 since the optical duty cycle and the pulses' shape does not change unless the triggering signal falls below 80ns , which is not the case even for the smallest duty cycle. In addition, the spectrometer integrates over a 30s period, yielding an intensity value proportional to the average power, which, in turn, is proportional to the peak power as per equation (5.23).

Ultimately, to endorse the eye-safety topic, the standards concerning the safe manipulation of laser sources must be conferred and interpreted. Since the interpretation of the IEC 60825 standard is non-trivial and requires an ample technical know-how to retrieve the relevant information, one opts to use an calculator developed by *Kentek*, a certified company providing training, auditing and consulting services

on laser safety [188]. However, the underlying standard employed in this platform is the ANSI Z136.1-2014 American standard for safe use of lasers and not the international regulation. Yet, it still provides an idea on the safety conforms.

The calculation is carried-out considering the worst case scenario of a direct exposure during 10s, as usually considered [61], and a repetitive pulse train with the computed characteristics for the prototype's laser beam. The calculator interface with all the parameters introduced and the result is explicit in Figure 141, considering the average power directly at the laser output. In these conditions, an eyewear with a minimum OD of 1.265 is required to ensure a fully safeguard when operating the laser. If one uses the average power at the TX optics output instead, that is the light outputted to the circumambient in a real case-scenario, the latter value drops to 1.203. In either case, the system is not eye-safe and the safety-glasses (*LG12* with OD 7+) must be continuously worn.

LASER PARAMETERS		
Wavelength (nm)	919.214	
Operating Mode	Repetitive Pulse	
Power (W)	0.01945	Average
Exposure Duration (s)	10	
Pulse Duration (s)	45.552e-9	
Pulse Rate (Hz)	6000	
REPORT		
Ocular MPE (W/cm ²)	2.74e-3	MPE rule = 2
Eyewear (OD)	1.265	worst case

Figure 141. *EASY HAZTM* laser hazard analysis calculator to evaluate the system eye-safety and ascertain the suitable eyewear protection.

5.2.6. Beam Spatial Profile

Up until this point, the LiDAR optical output has been characterized in the spectral and temporal domains and in terms of power. Here, the empirical extraction of two fundamental spatial properties is circumscribed: the cross-sectional intensity distribution and the divergence profile. The setup for evaluating the beam spatial profile is the same presented in Figure 133a and used throughout the optical alignment and optimization processes. The laser beam is projected on a target and the spatial spot profile is directly imaged by the *Manta* camera with the objective configured for a f/5.6 aperture, as recommended in the standard '*ISO12233- Photography. Electronic still picture imaging. Resolution and spatial frequency responses*'. The images are acquired with unitary gain in *Halcon* and the exposition time, T_{exp} , is adjusted to ensure that none of the pixels is saturated (linear regime). The frame resolution is 2710×3384 with each pixel in a 14-bit grayscale intensity. A *Balzers ZWL916* optical BPF is mounted right in front of the objective to reject wavelengths outside the laser spectrum. This filter has a bandpass characteristic with a 916nm central wavelength, 50nm FWHM and a peak transmission of 94.63% @ 913nm for a 0° incidence angle, as characterized in the *Agilent Cary Series 7000 Spectrometer*.

In each set of measurements, the projection in two targets is acquired. To evaluate the beam cross-sectional intensity profile, the *K-line White* is used since a background with uniform reflectivity is needed

for the whole spot to be reflected under the same conditions and in the same proportions and, thus, for the intensity profile to be preserved. To evaluate the divergence, one must have a subjacent length scale to correlate the number of pixels in the image to a well-known spatial dimension. Thereby, a calibration target is used, as it will be described next. For each target, 12 images are acquired at 6 distinct distances to be posteriorly averaged and for the mean image to be pos-processed in *MATLAB*. The distances, d , are evaluated in relation to the iris aperture, similarly to the *ZEMAX* simulation, using the *PARKSIDE* rangemeter with 1mm precision to allow a direct comparison. The procedure to acquire each set of measurements is as follows:

- 1) Define the initial minimum distance, limited by the lens working distance
- 2) Measure the distance with the rangemeter
- 3) Align the beam spot with the center of the calibration target using the NIR-vis card
- 4) Adjust the *Manta* camera objective for maximum aperture
- 5) Zoom-in and focus the camera on to the target plane
- 6) Switch to a f/5.6 aperture as recommended in *ISO12233*
- 7) Configure the exposition time in Halcon to avoid saturation
- 8) Acquire 12 images
- 9) Remove the calibration target to illuminate the *K-line White*
- 10) Readjust the exposition time (different reflective properties)
- 11) Acquire 12 images
- 12) Increment distance and repeat from 2).

Before drawing the profiles and estimating the divergence, the scale calibration shall be performed. This calibration consists on assigning a distance on the target plane to each pixel in the averaged image for the *K-line* projection. The process is divided in the following steps:

- 1) Digitalize the calibration target
- 2) Open the digitalized target sample in *ImageJ* (open-source image processing software)
- 3) Physically measure the width of a feature in the calibration target using a ruler. Preferentially, and to reduce uncertainty, a big feature shall be measured
- 4) Measure the same feature in *ImageJ* to retrieve the corresponding number of pixels
- 5) Calibrate *ImageJ* scale with these measurements (associate the number of image pixels to the real length in mm)
- 6) Zoom-in on the central circular feature and measure its diameter (*ImageJ*). The result yields a diameter of $\varnothing_{\text{mm}}=5.50\text{mm}$. These steps are illustrated in Figure 142.

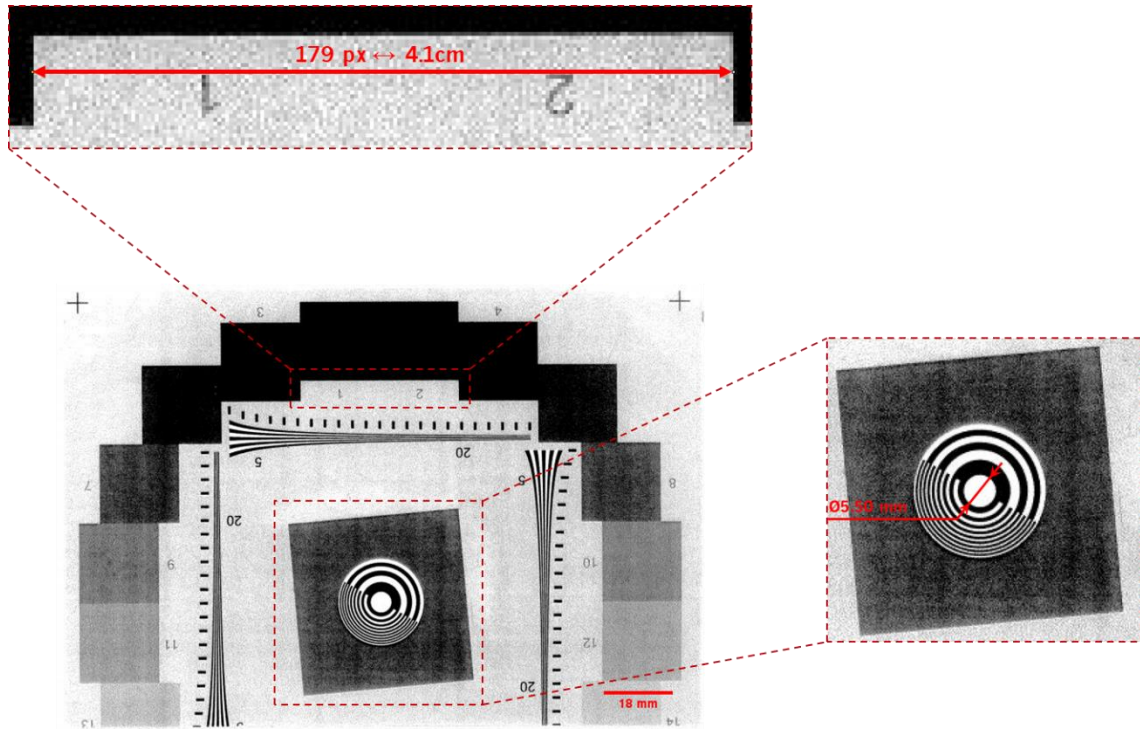


Figure 142. Scale calibration in *ImageJ* and measurement of the central circular feature.

- 7) Load and average the images obtained for the same target in *MATLAB*
- 8) Draw the averaged image and zoom-in to the circular feature of the calibration target measured previously, until the pixels are completely distinguishable. For all measurements at different distance one ensures the beam spot does always illuminate this feature
- 9) Measure the diameter of the circular region in pixels number. In *MATLAB* this is performed using the *Data Cursor* tool and retrieving the index of two pixels on opposite sides of the circumference. To diminish the error in this measurement, the diameter is evaluated in the vertical and horizontal directions and the arithmetic average is performed. The process is illustrated in Figure 143 for the acquisition at a range $d=489\text{mm}$. The calculation yields:

$$\varnothing_{\text{pixels}} = \frac{(1814 - 1708) + (1371 - 1266)}{2} = 105.5 \text{ px} \quad (5.30)$$

- 10) Finally, knowing the actual diameter in mm and the respective number of pixels, the pixels are mapped to a length in the target plane (right-hand result for $d=489\text{mm}$):

$$\text{mm} / \text{px} = \frac{\varnothing_{\text{mm}}}{\varnothing_{\text{pixels}}} = \frac{5.50}{105.5} \quad (5.31)$$

Although the reference target is always the same for distinct ranges, the correspondence in the camera FPA, i.e. the number of pixels encompassed in the circular region, changes with the distance and the objective zoom. Hereupon, the steps 7) to 10) are repeated for each distance to provide a proper adjustment.

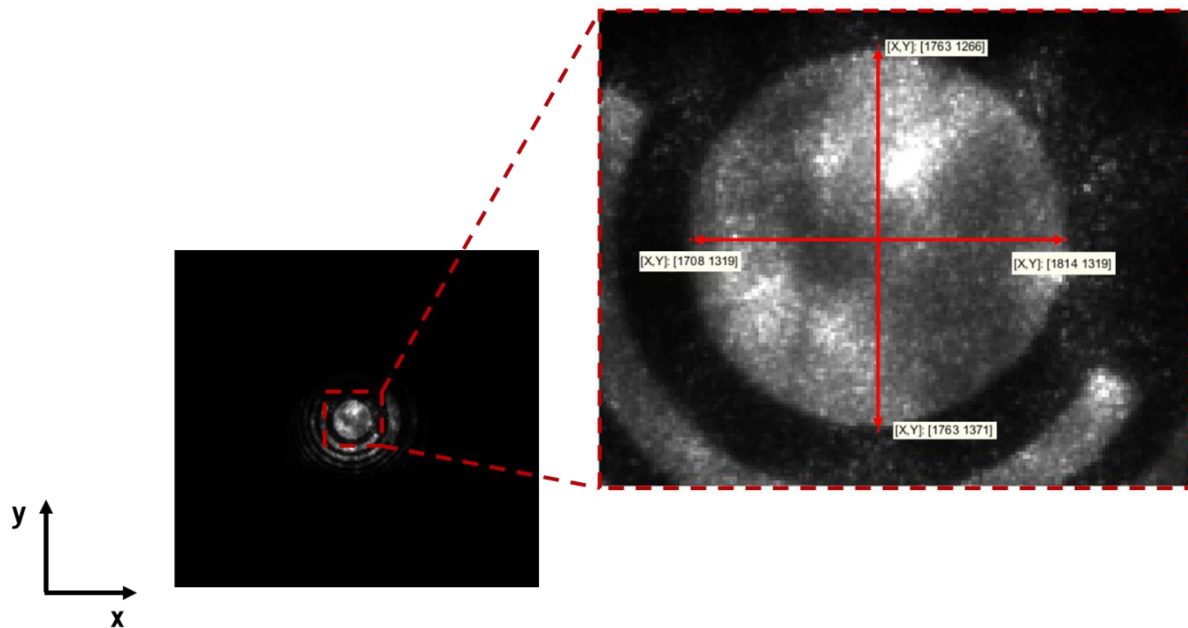


Figure 143. Estimation of the diameter of the central circular feature in the calibration target. As visible, the acquired monochromatic images reflect the underlying projection pattern. On the bottom left corner, the coordinate referential used in the image processing procedures.

The cross-sectional intensity profiles in 14-bits grayscale are drawn along the horizontal and vertical lines with 1-pixel width and passing through the beam centroid, $\{\bar{x}, \bar{y}\}$. The vertical coordinate for the beam spot centroid, \bar{y} , is computed by finding the line for which the sum of all columns is maximum. Similarly, the horizontal coordinate, \bar{x} , is evaluated through the column for which the sum of all lines is maximum.

In what concerns with the beam divergence, it is not a trivially extractable quantity since there is no direct experimental procedure to do so. *ThorLabs* manufactures a beam analyzing equipment, the *M2MS*, to estimate the beam quality (M^2) and its divergence. This device was experimentally tested but the direct output beam diameter was not narrow enough to be examined without using additional shaping optics to diminish the spot size (which changes the beam divergence). Hereby, an alternative methodology to compute a numerical estimate is taken. The latter consists on evaluating the beam spot width through the spatial-domain intensity profiles. As the profiles along the horizontal and vertical lines passing through the centroid have substantial fluctuations, they are not adequate for this estimation. Thence, one opts to separately sum all the image lines and columns to yield, respectively, an integrated horizontal and vertical profile. The profiles are subsequently normalized. Since the noise at FWHM is still meaningful, the widths are computed through the full width at $1/e^2$ from the maximum, as referred in the '*ISO11146:2018 – Lasers and Laser-related equipments*'. At last, the output divergences in the parallel (θ'_{\parallel}) and perpendicular (θ'_{\perp}) planes can be determined via a generalization of equation (5.20):

$$\theta'_{\perp} = 2 \arctan \left(\frac{(\Delta x_{1/e^2})_{i+1} - (\Delta x_{1/e^2})_i}{2 \cdot |d_{i+1} - d_i|} \right)$$

$$\theta'_{\parallel} = 2 \arctan \left(\frac{(\Delta y_{1/e^2})_{i+1} - (\Delta y_{1/e^2})_i}{2 \cdot |d_{i+1} - d_i|} \right)$$
(5.32)

where i and $i+1$ are two measurements at different distances d so that $d_{i+1} > d_i$, $\Delta x_{1/e^2}$ and $\Delta y_{1/e^2}$ are, respectively, the horizontal and vertical widths at $1/e^2$.

Another spot characterizing metric that can be computed based on these measurements is the beam circularity at each distance. This quantity is evaluated through the ratio of the minor and major axis of the elliptical spot, at $1/e^2$:

$$Circularity = \frac{\min \left\{ (\Delta x_{1/e^2})_i, (\Delta y_{1/e^2})_i \right\}}{\max \left\{ (\Delta x_{1/e^2})_i, (\Delta y_{1/e^2})_i \right\}}$$
(5.33)

According to *ISO11146*, the beam profile may be considered to have circular symmetry at the measuring location if the circularity is larger than 0.87. Naturally, a perfectly circular spot has unitary quotient.

The processed results for *K-line* are condensed in Table 31 and Table 32 for 4 of the measured distances, excluding the divergence computation. The beam spot images are zoomed-in in the region of interest and centered on the beam centroid, marked by the intersection of the red and blue straight lines. The images are all in a length scale of millimeters in the target plane, after calibrating and applying equation (5.31). Simultaneously, the intensity profiles along the vertical and horizontal lines passing through the spot centroid are traced parallelly to the respective axis. These profiles are relative because the pixels intensity is not only a function of the beam intensity distribution on the target plane but also of the acquisition conditions, such as the camera gain and exposition time. Hence, the amplitudes are only qualitative, even though the variation is preserved.

Table 31. Beam spatial profiles acquired at d=489mm and d=632mm from the output iris, for the projection in the *K-line White* target.

d [mm]	489	632
T _{exp} [μs]	325	650
Scale [mm/px]	5.50/105.5	5.50/89.5
Intensity profile @ centroid		
Integrated profiles & Width @ 1/e ²		
Circularity [%]	73.87	68.67

Table 32. Beam spatial profiles acquired at d=1103mm and d=1514mm from the output iris, for the projection in the *K-line White* target.

d [mm]	1103	1514
T _{exp} [μs]	850	1650
Scale [mm/px]	5.50/57	5.50/43
Intensity profile @ centroid		
Integrated profiles & Width @ 1/e ²		
Circularity [%]	61.67	56.61

The process for evaluating the divergence is susceptible to a non-negligible uncertainty, for the most part introduced in the stage of assigning the spatial scale to the image and also due to the highly irregular spatial profile. Hereafter, a numerical estimate for the divergence in both planes is determined by adjusting the experimental horizontal, $\Delta x_{1/e^2}$, and vertical, $\Delta y_{1/e^2}$, spatial widths directly depicted in the integrated profiles graphs in Table 31 and Table 32 as a function of the distance to the target, d . The linear fit to the latter points is shown in Figure 144 alongside the 95% confidence interval ($\pm 2\sigma$).

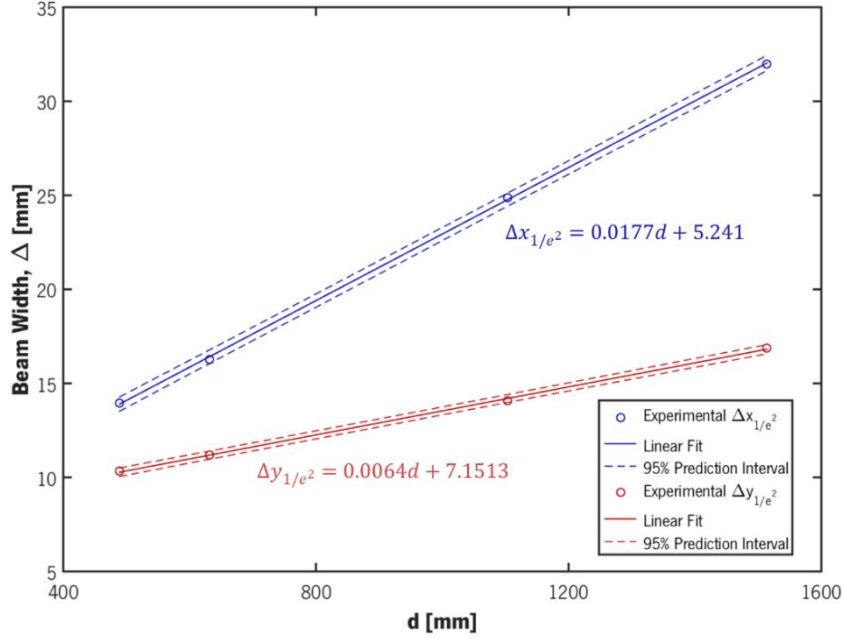


Figure 144. Linear fit to the spatial widths in the horizontal, x , and vertical, y , directions experimentally measured as a function of the distance to the target, d . In dashed lines, the 95% confidence interval is represented ($\pm 2\sigma$).

Based on Figure 6 and specifying equation (1.3) for this LiDAR prototype, one can describe the evolution of the beam spatial widths as a function of the distance in the far-field, d .

$$\begin{aligned}\Delta x_{1/e^2} &= D_x + 2 \tan\left(\frac{\theta'_\perp}{2}\right) d \\ \Delta y_{1/e^2} &= D_y + 2 \tan\left(\frac{\theta'_\parallel}{2}\right) d\end{aligned}\tag{5.34}$$

and, intuitively from the linear fit equations, it is possible to straightforwardly retrieve the output divergence in each direction, θ'_\parallel and θ'_\perp , from the slope, and the spot dimensions at the LiDAR optical aperture, D_x and D_y , from the y -intercept at $d=0$. The latter results are enumerated in Table 33.

Table 33. Estimations of the parallel (θ'_\parallel) and perpendicular (θ'_\perp) divergence angles and the spot size at the TX output aperture.

$\bar{\theta}'_\parallel$ [°]	0.367°
$\bar{\theta}'_\perp$ [°]	1.014°
D_x [mm]	5.241
D_y [mm]	7.151

Starting by discussing the spot circularity, one can notice that, in no occasion, the profile is circular. Indeed, above 489mm the profile is always elliptical, with the circularity factor decreasing continuously within the measured ranges (around 74% at $d=489\text{mm}$ and 57% at $d=1514\text{mm}$). Whatsoever, there is a gap in the measurements between 0mm and 489mm, since the working distance of the camera objective does not allow a focusing in this range. Hence, some pictures are taken with a smartphone camera for the beam projection in the *K-line white* at 115mm, 330mm and 408mm from the iris (Figure 145). As observable, the beam is outputted with an ellipticity inverted comparing to the aforesaid profiles. However, due to the substantial difference in the divergence angles between the parallel (vertical direction in the images) and perpendicular (horizontal) planes, the ellipse axis inverts at around 330mm, distance at which the spot is approximately circular. These results are coherent with the *ZEMAX* simulation (Table 25), in which the inversion occurs at around 500mm. The 170mm difference in the circularity range arises from the fact that the optical optimization did not strictly follow the simulation and a configuration yielding a superior power throughput is adopted. Moreover, since the minimum measurable distance is estimated to be around 560mm (section 5), then in the working ranges of this LiDAR prototype, the beam will always preserve the ellipticity direction. One must take into consideration that the laser in the prototype is rotated by 90° in comparison with the optical simulation and, therefore, so are the spot profiles. This arises from the fact that one performed the optical simulations before realizing the actual laser orientation in the laboratorial reference.

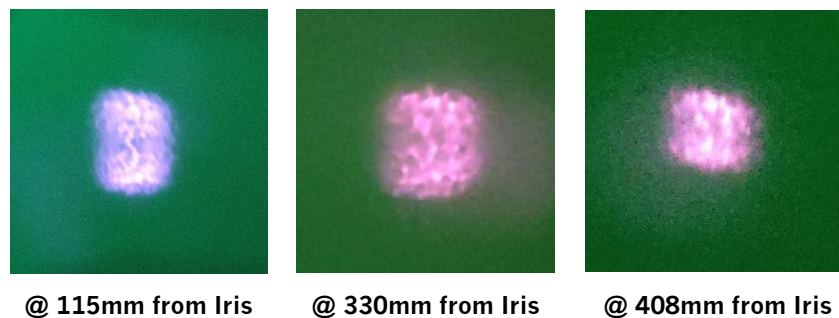


Figure 145. Raw photos of the beam projected in *K-line* at distances below 489mm. It is visible the granularity of the beam spot.

Regarding the intensity profiles through the centroid, a Gaussian-like behavior is not noticed for any distance and, instead, the profiles are marked by multiple distinct intensity peaks, translated in a granular appearance of the beam spot. In the vertical direction, the intensity peaks variations are less pronounced, and the integrated profiles are nearly-Gaussian for 1103mm and above. In this direction and alongside the increase in distance, the profile tends to evolve towards a more gaussian shaped profile with less amplitude variance. As for the horizontal, there is a constant feature noticed for every distance, consisting on an absolute maximum followed by a local intensity minimum. This feature does also appear in the integrated profiles and tends to be suppressed at higher distances. The previous evolutionary statements are supported by the profiles visible in Figure 146a at the 6th measured distance of 3890mm. In either case, these results do not reflect the cross-sectional profiles obtained in *ZEMAX* (Figure 131), in which a well-defined Gaussian shape is perceived, motivated by the ideal simulation conditions.

In addition, while moving away from the LiDAR output, the beam spot progresses to a more distinct intensity distribution, with a peak approximately at the center and a decrease in intensity with the radial

distance to the latter. This progression is accompanied by a shift of the centroid to the central region of the spot, strongly acknowledged by comparing the centroid position at 489mm and 3890mm.

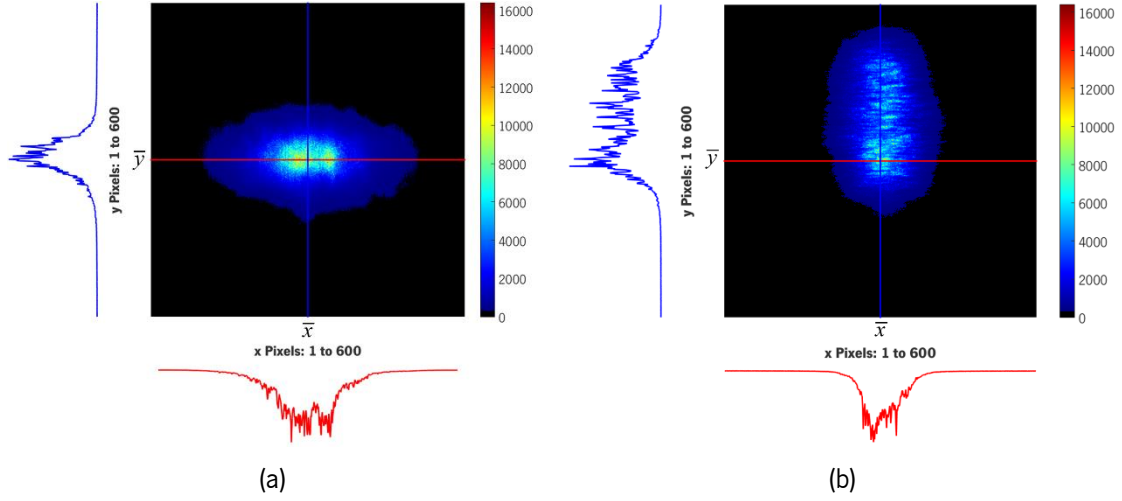


Figure 146. (a) Acquired beam spot image at $d=3890\text{mm}$ and respective intensity profiles over the vertical and horizontal lines passing through the centroid. (b) Beam cross-sectional profiles and appearance at 930mm for the *Garmin lite v3* commercial sensor projected on *K-line White*. In both images, the centroid coordinates are generically marked.

The spatial profiles show, in all cases, an irregular pattern with several intensity peaks and high spatial frequency fluctuations. The rapid oscillations cannot be attributed to the passive beam-shaping optics and must, therefore, arise from the laser itself. The laser is an edge-emitting chip specified with having 3 epitaxially nanostacked emitters and an aperture size of $200 \times 10 \mu\text{m}^2$ [160]. Each resonant cavity can operate in the multimode regime and the 3 emitters overlap to give rise to the single output beam. This is the most likely cause of the irregular spatial patterns. In principle, one must consider both spatial (transversal) and temporal (longitudinal) coherence effects. The temporal coherence is described by the coherence length, coherence length, L_c , which can be estimated considering, in a good approximation, a Gaussian emission spectrum [189]:

$$L_c = \sqrt{\frac{2 \ln(2)}{\pi}} \frac{\lambda^2}{\Delta\lambda} \quad (5.35)$$

where λ is the peak wavelength and $\Delta\lambda$ the spectral width. Replacing the experimental results in Table 28 in the previous equation yields a coherence length of about $110 \mu\text{m}$. The high-frequency spatial variations in intensity can be possibly ascribed to speckle fluctuations arising from the diffuse reflection in the *K-line* target. This effect is understood if the reflectivity function is modelled as an array of scatterers that add coherently. The superposition of the scattered waves can result in constructive (local maximum) and destructive (local minimum) interference, depending on the relative phases of each waveform [190]. Speckle noise results from these interference patterns observed in intensity variations in the acquired images. The speckle is usually evaluated by local intensity contrast in the acquired image and is known as speckle contrast. Besides the source coherence length and the roughness of the scattering surface, the speckle contrast is dependent on the imaging optics (the ratio of the typical size of the imaged single speckle grain to the pixel size) and even if the optics is focused in the scattering surface at infinity (or far-

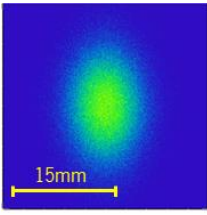
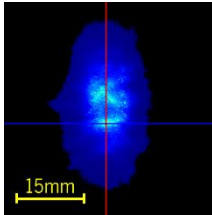
field) [191]. In literature, there are reports on significant speckle contrast for both edge-emitting [191] as well as VCSELs [192] lasers, usually linked to image projection, in which the speckle is an issue since it can degrade image quality. Based on these works, the most likely cause of the high-frequency oscillations is intensity speckle. A simple check for the corroboration is to change the scattering target material: the replacement of the white *K-line* target (smooth surface) with office paper or cardboard should change the speckle pattern, increasing its importance. Nevertheless, a definitive speckle identification can only be done with a detailed and specifically designed study, which is beyond the scope of this work. In any circumstance, the impact of speckle for the practical LiDAR application is null.

The profiles for the developed prototype are compared with the *Garmin lite v3* commercial sensor. Since this is also a 1D LiDAR, it is easier to access the intensity profile and the analogy can be directly performed. The beam spot and the profiles through the centroid are portrayed in Figure 146b. Alike the prototype, the beam spot observed at 930mm is elliptical and the intensity peaks are also observed, which is consistent with the previous explanation since the projection target is the same.

In terms of beam divergence, the spot size increases approximately 6.56mm vertically and 18.01mm horizontally in the range interval between 489mm and 1514mm. This increase is translated angularly into an overall parallel and perpendicular divergence of $\bar{\theta}'_{\parallel} \approx 0.367^{\circ}$ and $\bar{\theta}'_{\perp} \approx 1.014^{\circ}$, respectively.

To finalize the analysis, the correspondence between the optical simulations and these empirical measurements are summarized in Table 34, including the results for the optical peak power. As seen, the beam spot aspect is identical in both situations at comparable distances, both in shape and size (notice that the experimental spot is rotated by 90° to match the simulation referential). Numerically, the peak power can be directly compared since the initial conditions at the direct laser output are practically the same: 69.993W for the simulation and 69.95W experimentally.

Table 34. Comparison between the simulated results and the empirically acquired results.

Pulsed LD Metric		Simulation	Experimental	Difference
Output Peak Power, P_{peak}		47.02W (@ 50mm from Iris)	60.34W (@ 20mm from Iris)	+13.32W / +28.3%
Beam Spot Profile		 @1000mm	 @1103mm	NA
Divergence	Parallel to p-n, θ'_{\parallel}	0.073°	0.367°	+0.294°
	Perpendicular to p-n, θ'_{\perp}	0.445°	1.014°	+0.569°

Overall, and as already mentioned, the critical element for the establishment of the collimation/power balance is the *LB1378-B* lens: bringing this lens closer to the triplet of biconvex lenses increases the power-collection but worsens the collimation and vice-versa. The improvement in one metric comes at a cost of a deterioration in the other. Experimentally, one tries to find a good compromise through an

adjustment of the lens position by hand. Comparing with the *ZEMAX* simulation, the final setup yields a meaningful increase in the output power of around 13.32W, with the drawback of a notoriously expanded divergence by 0.294° and 0.569° in the parallel and perpendicular directions, correspondingly. However, the latter increases cannot be linearly compared in the same percentual proportions because the compromise must take into account the tests environment and the hardware architecture. In the set of ranges experimentally sensed, between 0.56m and 4.420m, and considering that the return photodetector is a low-responsivity PIN PD without gain, it is preferable to have more power to maximize the detected signal. Hence, to complete, as the increase verified in this scenario for the beam spot size is not critical for the sensors' performance, one can conclude that a good agreement is accomplished.

Furthermore, there is a good agreement between the simulation and the actual experimental observations regarding the optical behavior of the LiDAR sensor, even though the final empirical optimization did not follow strictly the simulation results and focused on a better balance between power and divergence.

Once again, the lenses' choice was not judicious and what drove towards this setup was an experimental trial-and-error process by direct observation of the beam profile in conjunction with the lenses' availability at the laboratory. The *ZEMAX* simulation was not intended to design the optical system from ground but rather to validate the setup. Several other options were investigated and tested, including spatial filtering using a pinhole and anamorphic prism pairs (*ThorLabs PS877-B*). However, with the available optical elements, this layout is, overall, the best compromise between high-power and small output divergence.

After proper designing and optimization, the transmission optics can be greatly simplified and optimized (for divergence and power transmission), especially by choosing the most adequate aspheric lens for initial collimation and a convenient circularization technique. In [193], three approaches for circularizing a collimated LD beam are explored and compared under the same initial conditions and measurement setups. The three techniques explored are cylindrical lens pair, anamorphic prism pair and spatial filtering (pinhole), and the FOM are the beam circularity and the optical power throughput. The comparison is summarized in Table 35.

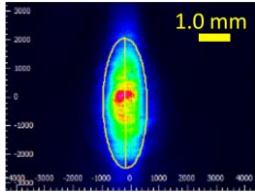
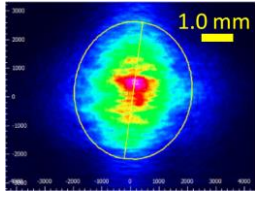
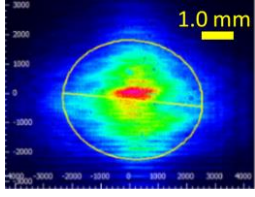
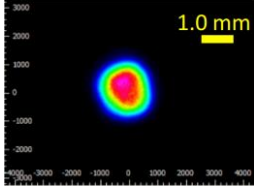
Overall, the cylindrical lens pair is the optimal option and yields a better balance between circularization, power transmission and beam quality [193]. Simultaneously to circularization, this pair also collimates the beam with good divergence control. Besides, due to its axial asymmetry, this alternative corrects astigmatism by precisely tuning the relative powers (focal lengths) of both lenses.

A cylindrical lens pair circularizes the beam by expanding it in one direction (slow diverging axis). Each lens is placed to collimate the beam in one axis (in the lens' plane of curvature) and the ratio of focal lengths of both lenses (f_1 and f_2) is related to the ratio of the beam divergence in both axis [193]:

$$\theta_{\perp} = \theta_{\parallel} \frac{f_2}{f_1} \quad (5.36)$$

Since the focal length ratio depends on the LD divergence angles, the lenses shall be designed specifically for the *SPL LL90_3*.

Table 35. Comparison of three different approaches for beam circularization: cylindrical lens pair, anamorphic prism pair and spatial filtering (adapted from [193]).

Method	Beam Intensity Profile	Circularity (=1 for perfect circle)	Transmitted Power
Collimated Source Output		0.36	NA
Cylindrical Lens Pair		0.84	91%
Anamorphic Prism Pair		0.82	80%
Spatial Filter (Pinhole)		0.93	34%

5.2.7. Reference and Return Paths

Lastly, in regard to the reference and return paths, the optical characterization is not as pivotal and it is also harder to provide a direct characterization due to the low power levels flowing through both. Notwithstanding, some observations are empirically carried-out to verify the optics functioning. In Figure 147, a photo of the beam reflected in the glass slide is shown as seen in the NIR-visible converter card to illustrate that it is exquisitely troublesome to acquire a reliable representation of the beam spot because the camera sensor (in this case, a smartphone) does not reproduce credibly the beam spot.

Starting with the reference path, the microscope glass slide is placed in such manner that the outgoing beam only illuminates a very small part of the slide, i.e., less than $\frac{1}{4}$ in one corner. Besides, the angle is also adjusted to reflect the needed power to the reference PD and thereby generate a pulse (*laser_on*) with an amplitude just enough to trigger the STOP1 pulse to the TDC, since the power is being removed from where it is required the most. In practice, this implies an angle slightly above 50° , as per Fresnel's laws, and a pulse amplitude of around 1.2V in *DET10A/M*. As for the focusing lens, one verifies that the deflected power is almost entirely focused in the photosensitive area.

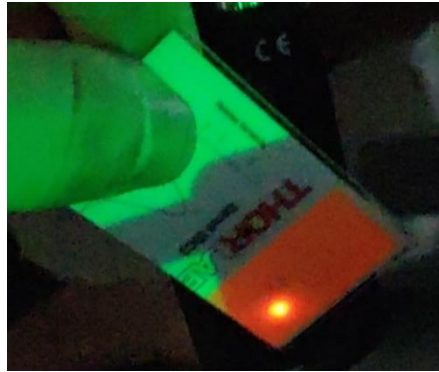


Figure 147. Photography of the beam spot after reflection on the microscope slide. The actual beam spot is imperceptible due to a glare in the surrounding area.

In the return path, the tests are performed in the sense of proving the necessity of the additional lens (*LA1074-B*). By fixing the target distance and varying the detector axial position (RX PCB) using the 3DOF stage, one verifies that, in a total displacement of 2cm, the amplitude of the detected pulses is essentially preserved. This result validates that, although the beam spot area is slightly larger than the photosensitive area of the return PD and the collimation is not absolute, this additional lens ensures a condition of small beam-size variation in the photodetector plane. This can be understood through the schematics in Figure 148. As aforementioned, this effect is particularly relevant for the working distances applied in the laboratorial measurements and, in a real automotive LiDAR ranging beyond 100m, this problem is less influential.

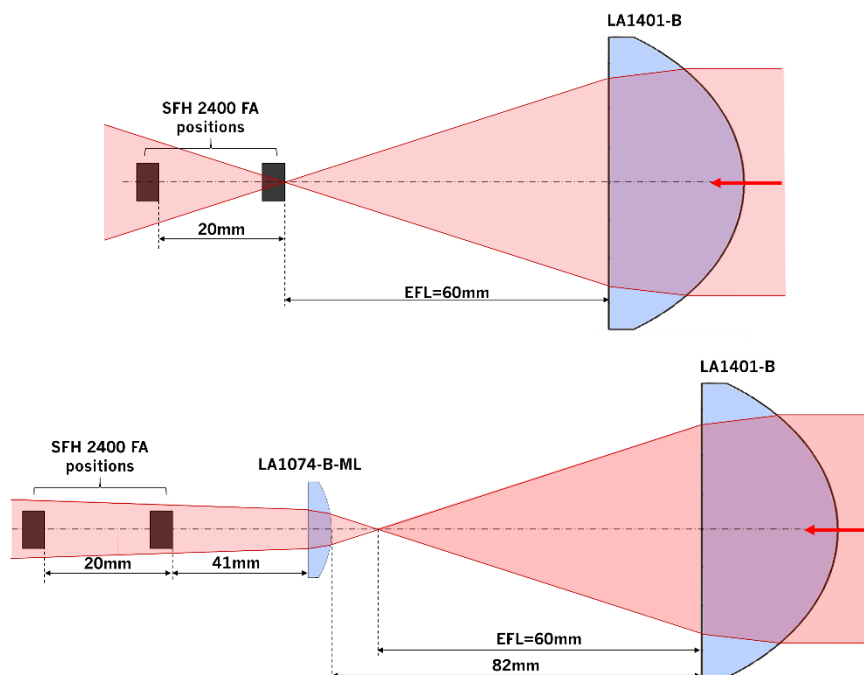


Figure 148. Schematic process showing the process implemented by the additional *LA1074-B-ML* lens in the return path. In the first situation, when the photodetector is translated axially by 2cm, the intensity detected decreases since the received power is dispersed over a larger area. In the second case, the additional lens collimates the beam to yield a more constant intensity on the $1 \times 1 \text{mm}^2$ photosensitive area. Yet, the residual divergence still induces a small variation in intensity.

5.3. Electrical Characterization

Now, the sensor's hardware is characterized from an electrical point of view. This includes the study and measurement of the voltage signals in every step of the way, from the generation of *BP_TRIG* to the sending of the ToF signals to the microcontroller. The study focuses mainly in the role of each component and block in the sensor's operational conditions and, therefore, this is not an exhaustive nor extensive inquiry.

As already pronounced, when possible, the measurements are performed with the short ground lead and using the test points. However, when there is no GND close to the measuring point, the standard ground probe is employed, and when there is no test point at a specific circuit spot, the probe tip is used to establish the conductive contact. To understand the effect of the probe's inductance in the signal acquisitions, one performs a very simple test consisting on sampling a digital signal, in this case, the laser driver output, with the two probes. The results are displayed in Figure 149, and the direct measures in the *Teledyne HDO4034* oscilloscope reveal an overshoot of 2.5% with the short ground lead and 5.3% with the standard post. Moreover, the secondary oscillations are more pronounced in the latter case, as well as the rise-time.

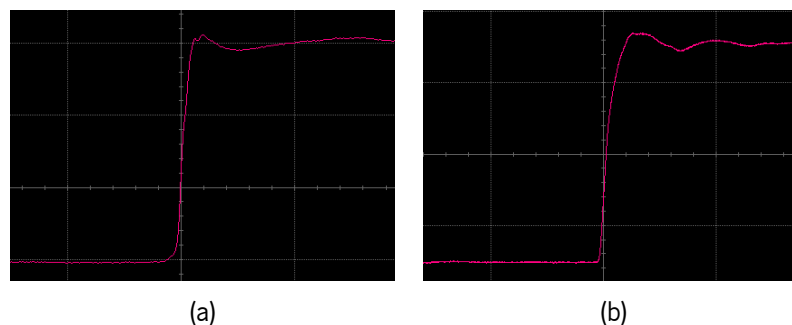


Figure 149. Rising-edge of the laser driving signal: (a) acquired with the short ground lead and with (b) the standard ground probe.

5.3.1. Electrical simulation

Initially, the transmitting-end is simulated using a free-software provided by *Texas Instruments*, the *TINA-TI v9.3*. The software integrates the required SPICE-based (Simulated Program with Integrated Circuit Emphasis) analog simulation to analyze the LiDAR RX. The drawn schematic is depicted in Figure 150.

To simulate the actual circuit and improve the veracity of the results, the SPICE models of each component are directly loaded into the software. The models are made available by the manufacturers and can be found at the respective webpages. However, two models are missing. The first is the *SN74LVC2G14* Schmitt-trigger, and the other the *SPL LL90_3* laser diode. To replace the first, a non-inverting comparator with hysteresis is defined using a *TLV3501* high-speed AmpOp. The thresholds are set to $V_{T+}=1.8V$ and $V_{T-}=1.3V$, inside the nominal limits of the Schmitt-trigger IC. To simulate the laser, the *OSRAM SPL PL90_3* model is used. This is also a 905nm laser with 3 emitters and with 75W peak

power. However, the laser module is not integrated with the NMOS stage and the capacitors. Thereby, the model of the *Infineon's BSP318S* NMOS must be also added and the 47nF capacitors mounted.

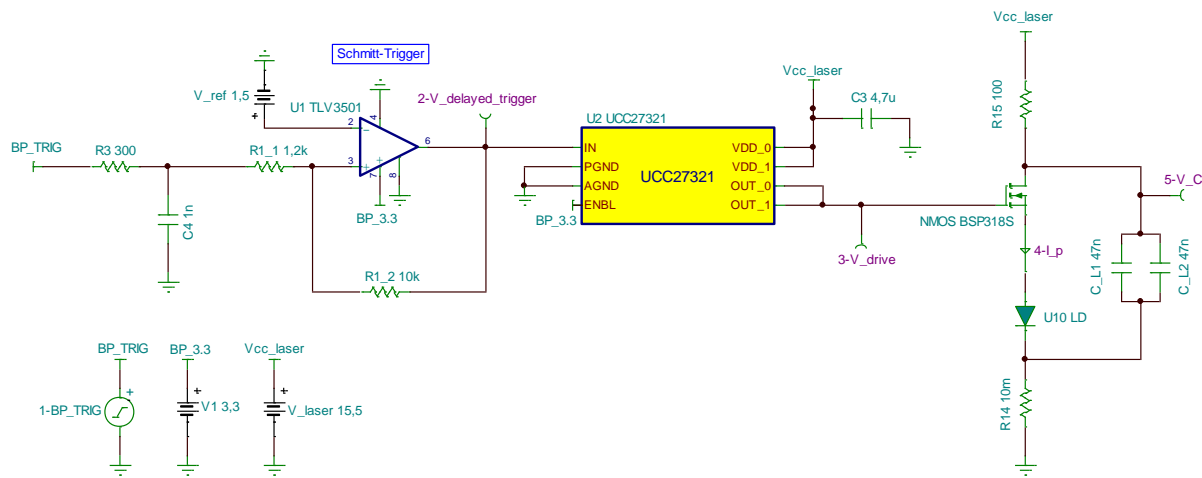


Figure 150. Transmitter schematic as simulated in *TINA*.

The signal BP_TRIG is set with the standard definition of a 6kHz frequency and 65% duty cycle and a transient analysis is run with zero initial conditions. The relevant results are exposed in Table 36. Besides the delays introduced in the Schmitt-trigger in the rising, t_{dr} , and falling, t_{df} , edges, it is also encompassed the charge time of the lasing capacitors, t_{charge} , the propagation delay in the driver and the laser forward bias, $U_{c,th}$. The simulation results are in conformity with the expectations.

The signals obtained are traced in Figure 151 and correspond to the points identified in the implemented electrical schematic. The laser pulse has a 30A peak current, a quite unrealistic value considering the nominal maximum current drive capability of 9A provided by the *UCC27321* laser driver [159], and a FWHM of approximately 40ns.

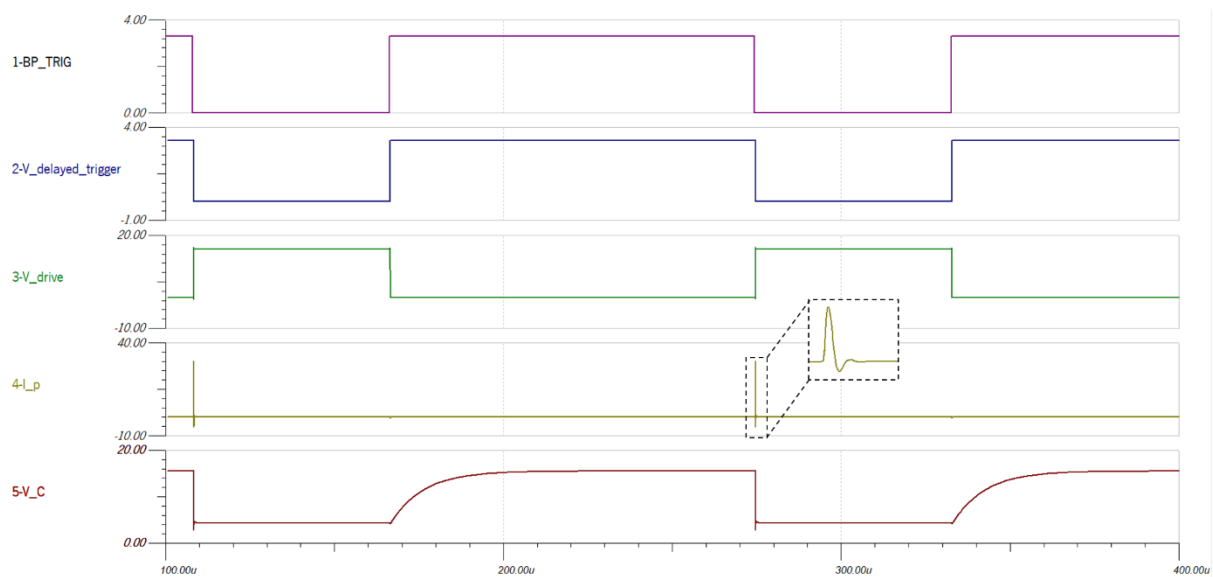


Figure 151. Electrical signals achieved in the simulation and identified in Figure 150.

5.3.2. Transmitter Signals

Starting with the signals involved in the pulsed laser transmission, and to bridge the experimental results with the previous simulations, the fundamental signals within the TX board are acquired in the *Teledyne Lecroy HDO4034* oscilloscope and traced in *MATLAB*. These signals are portrayed in Figure 152, properly identified, and reflect a great similarity comparing with the simulation. Please notice that the peak current on the LD cannot be directly measured in practice and, thereby, is not depicted.

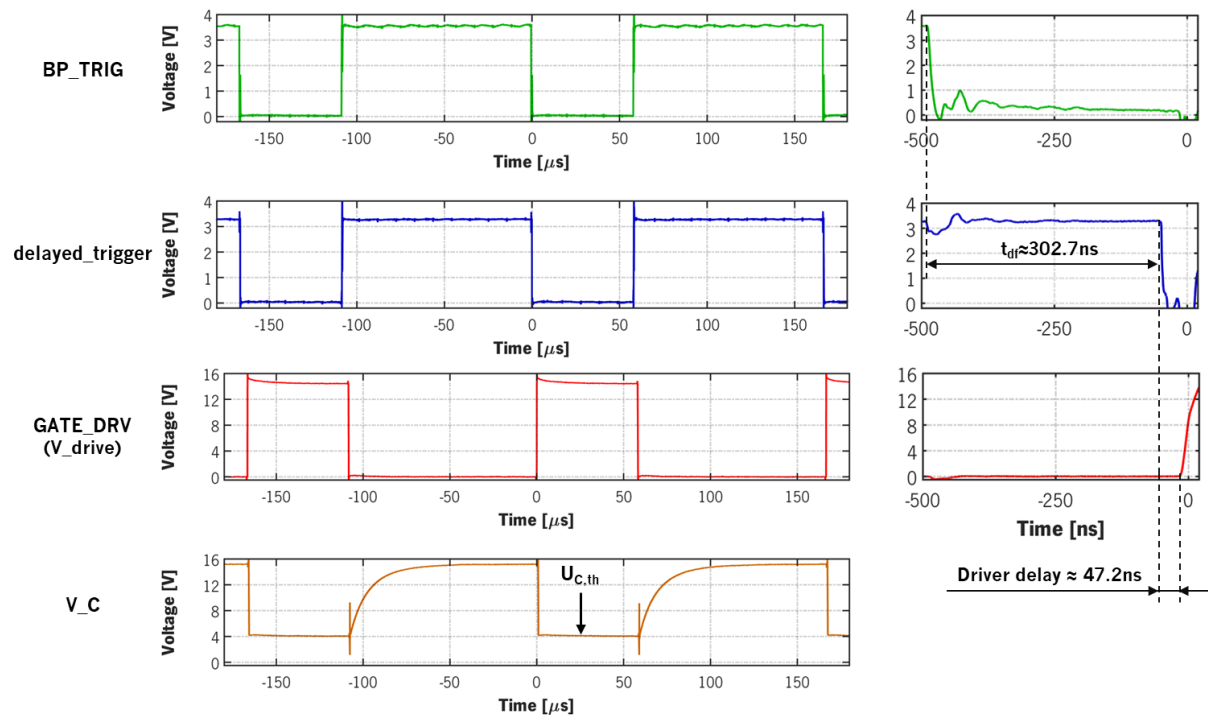


Figure 152. Electrical signals throughout the electronics for the pulsed LD emission. The *BP_TRIG* shown herein is directly measured on the TX board, after the jumper wire. On the right, the zoom-in evidencing the dephasings between the falling-edges of *BP_TRIG*, *delayed_trigger* and the rising edge of *GATE_DRV*.

Firstly, the signal *BP_TRIG* is a PWM digital sequence generated by the RX MCU with an empirical duty cycle of $dc=64.94\%$ and a frequency of around 6.0038kHz , translating into a time-on of around $t_{on} \approx 108.17 \mu\text{s}$ in the standard test conditions. These results validate the configuration employed in the RX board software and the correct reproduction by the hardware. Although, the frequency and dc suffer slight jitter over time in the fourth decimal place, with no physical implication in the sensor's operation since the ToF measures are only started on the falling-edge. After generation, *BP_TRIG* is transferred to the TX board through a 29.5cm long jumper wire that, naturally, introduces a delay of around 0.8ns and degrades the signal, by inducing additional noisy fluctuations in the baseline (Figure 153). Nevertheless, since this is a digital signal, the critical information is on the edges with rise and fall-times of around 2ns, this effect is inconsequential.

The 65% nominal duty cycle is chosen from direct observation of the spectrum as it is the value encompassing a spectral peak closer to the nominal specifications (Figure 136) of 895-915nm (below this dc there is no difference in the peak location), and since it allows for the capacitors to fully charge and to maximize the optical output power.

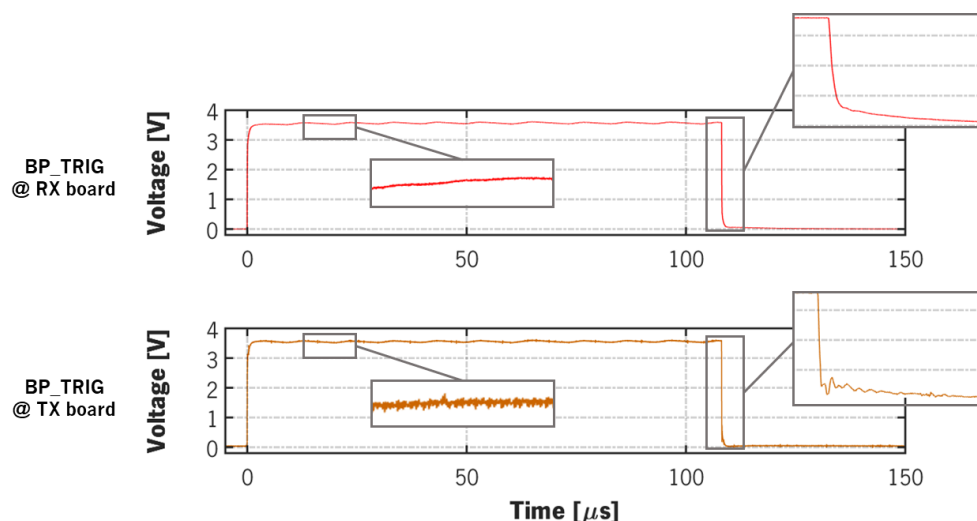


Figure 153. BP_TRIG signal as generated in the RX board (top) and after the jumper wire, on the TX board (bottom). Although the baseline presents more noise, the falling-edge does not suffer visible changes.

After generation, BP_TRIG goes through the delay block, from which a delayed version (*delayed_trigger*) arises. The delay mechanism, presented in the architecture section 4.1.1, is responsible for an empirical retardation between the rising and falling-edges of around $t_{dr} \approx 303\text{ns}$ and $t_{df} \approx 434\text{ns}$ respectively, measured as per Figure 65b. From these, and since the START is triggered on the falling-edge, only the delay t_{df} is accounted in both ToF1 and ToF2. The difference between the 2 latter times yields the increase in the *delayed_trigger* pulses comparably with BP_TRIG ($\approx 131\text{ns}$). Posteriorly, the *UCC27321* laser driver inverts the triggering signal and boosts the voltage-high level to $V_{cc,laser}=15.5\text{V}$, to then be applied to the gate of the MOSFET and generated the pulsed optical response. At this stage, a delay of around 47ns is further introduced between the falling-edge of *delayed_trigger* and the rising-edge of *GATE_DRV*. Ultimately, the charging capacitors in parallel with the LD are charged whenever *GATE_DRV* is at a low state, taking about $46\mu\text{s}$ to charge between $U_{c,th}=4.1\text{V}$ and $V_{cc,laser}$. When the driving signal commutes, the capacitors are quickly discharged through the LD and an optical pulse is outputted.

Table 36. Comparison of the computed, simulated and experimentally measured delays and laser charge voltage.

	t_{dr} [ns]	t_{df} [ns]	t_{charge} [μs]	$U_{c,th}$ [V]	Driver delay (rise) [ns]
Calculation / Nominal	150 ... 330	280 ... 511	44	4.5	70 (max.)
Simulation	217	294	44.3	4.3	46
Experimental	302.7	433.6	46.3	4.1	47.2

The comparison between the simulation results, the experimental measures and the predicted nominal/calculated values is described in Table 36. It is noticeable a good agreement between the three circumstances, with the delays falling inside the anticipated range and the waveforms being in conformity with the electrical simulation. Whatsoever, as the laser direct bias is inferior to the nominal, the capacitors charge-time is superior to the calculated because the starting point for the charging process is accordingly smaller (from 4.1V and not 4.5V).

5.3.3. Reference Path

Simultaneously with every rising-edge transition of the driving signal *GATE_DRV*, the laser emits a train of light pulses that are detected at the reference photodetector to mark the beginning of the effective ToF count. The superposition between the laser driver signal and the *laser_on* in the reference detector was already reported in Figure 138 and properly discussed in section 5.2.4. The glass slide is adjusted so that a peak voltage of around 1.2V is achieved in the reference path. This way, it is attainable a pulsed sequence with high enough amplitude to be discriminated and generate an adequate STOP1 to TDC1, without compromising significantly the optical power outputted at the sensor's TX path.

Antecedently, an estimate for the reference pulses' FWHM, rise-time and fall-time was provided and its fluctuations over time were evaluated based on 2429 sampled pulses. In principle, the referenced laser jitter is on the order of magnitude of the rise-time's standard deviation. However, to grant a better estimate, the laser jitter is computed through the threshold crossing-time in the leading-edge as this is the event marking the timing instant. Experimentally, the threshold is measured with a multimeter (*Amprobe AM-530-EUR*) in DC mode and the acquired value is $V_{th,B}=0.163V$. This evaluation is more accurate because the absolute jitter effect in the rise-time is not uniformly distributed through the 10%-to-90% portion of the rising-edge.

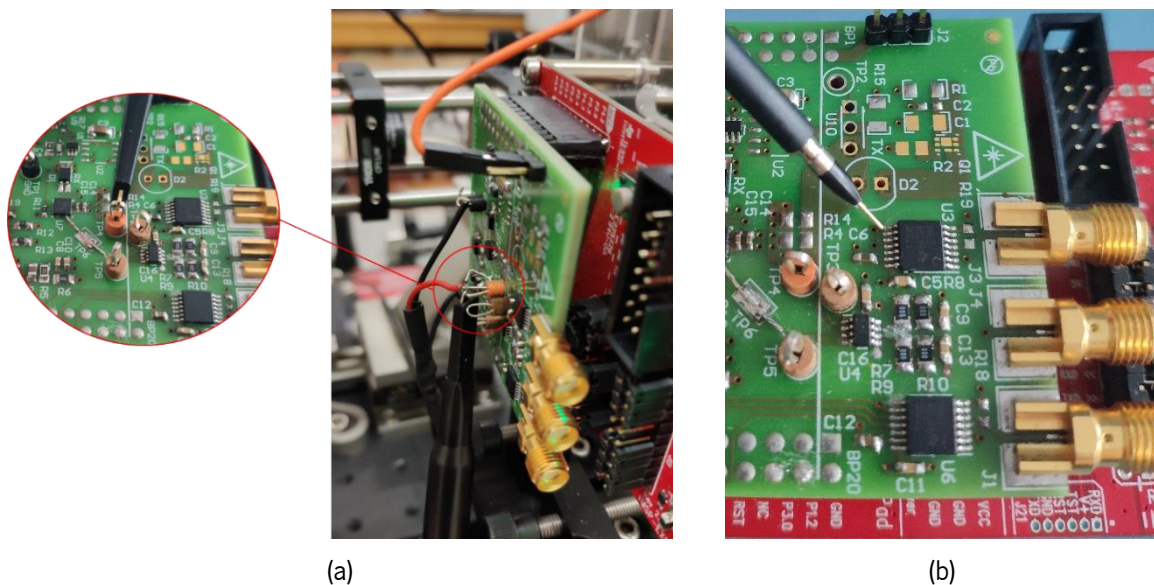
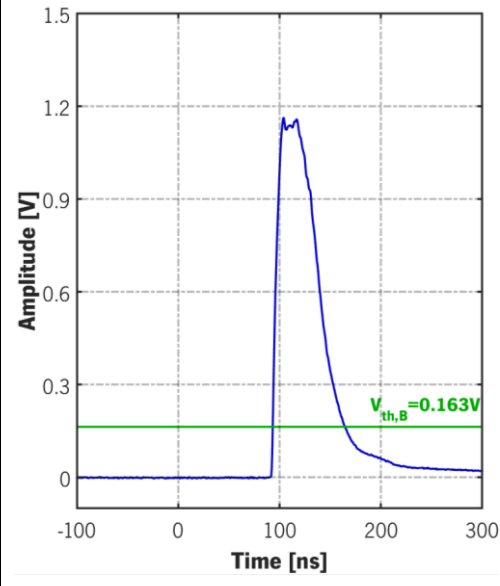
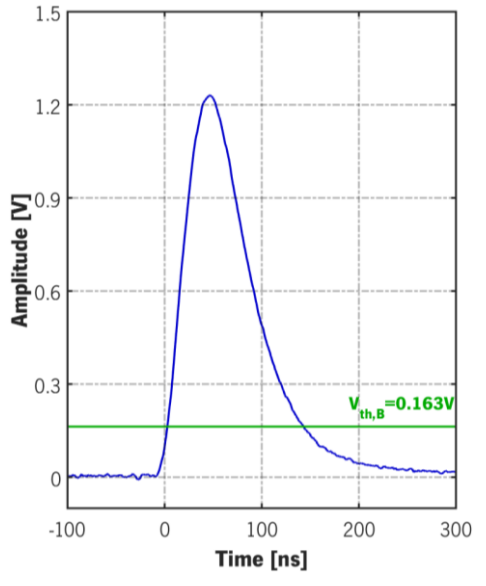












Figure 154. (a) Measurements with the oscilloscope probe directly in the test point TP2 and (b) example of measurement with the tip contacting the measurement point.

The previous procedure is applied to the pulsed signal at the *DET10A/M* BNC output, measured directly in the *Teledyne HDO4034* oscilloscope. Notwithstanding, to have an even more realistic idea, the signal must also be analyzed on the test point TP4, at the extremity of the coaxial cable (Figure 154). Hereby, it is possible to ascertain if the pulse is effectively inputted at the RX board, without major distortions. The previous procedure is, then, replicated in these conditions and the same statistics are retrieved. The overall results are enumerated in Table 37.

Table 37. Comparison of the reference pulse parameters: directly in the *DET10A/M* photodetector, on the left, and at TP4 on the RX board (*laser_on*), on the right. The threshold crossing points are marked by the intersection between the pulses (blue) and the threshold value (green). The statistical quantities are directly retrieved from the *HDO4034* oscilloscope. $\langle X \rangle$ is the arithmetic average and σ_x the respective standard deviation.

	Reference PD Output			laser_on at TP4		
Pulses' Morphology						
#Acquisitions	2429			2420		
	$\langle X \rangle$	σ_x	Histogram	$\langle X \rangle$	σ_x	Histogram
Amplitude [V]	1.271	0.033		1.125	0.022	
FWHM [ns]	45.552	0.413		74.823	0.334	
Rise-time, t_r [ns]	7.077	0.255		31.429	0.572	
Fall-time, t_f [ns]	42.106	1.120		91.995	2.225	
Jitter @ Crossing [ps]	—	30.59		—	407.39	

Analyzing the previous results, the signal amplitude is slightly affected by the transmission throughout the 91cm-long coaxial cable and an average loss of around 150mV is estimated. This loss may be a result of a slight mismatch between the 50 Ω terminator and the cable characteristic impedance. Hence, one must pay no mind to the superior amplitude in the *laser_on* signal exposed in Table 37 because the two pulses were acquired at distinct time instants and the average peak voltage is the result to keep in consideration. Further, comparing both pulses with the electrical simulation in *TINA*, the undershoot seen in Figure 151 is not observable in practice but the shape is consistent.

Proceeding to the temporal pulse parameters, the FWHM and the rise and fall-times increase significantly after propagation in the coaxial cable, as well as the respective absolute standard deviations

(except for the FWHM, in which a slight decrease is verified). As the fluctuations in the rise-time escalate, then the jitter at the threshold crossing level is also considerably affected with an expansion from 30.59ps (0.46cm) to 407.39ps (6.1cm). All these temporal effects are explained by the dispersion phenomenon in the coaxial cable. Due to the latter, the phase velocity of the propagating electromagnetic pulsed signal is a function of the frequency. Hence, the higher-frequency transitions propagate at smaller velocities throughout the cable, inducing a distortion in the output pulses' shape. As the faster-varying edge in the present signal is precisely the rising-edge, then the most significant deformation is noticed in the latter, as demonstrated through the results (much greater percentual discrepancy). This change in the pulses' morphology is compatible with the observations reported in [194] due to a similar effect. Overall, the values to consider are the ones measured at TP4, since this is the actual signal at the RX board.

Subsequently, for the on-board *laser_on* pulse, the jitter in the opposing threshold crossing (trailing-edge) is also studied and the obtained result is about 793.91ps, under the same conditions. This result is concordant with the explanation and histograms provided in sub-section 5.1.4.3, where one stated that the more abrupt-edge (leading) is less propitious to noisy fluctuations.

At last, the reference electroptical pathway is static and, therefore, the previous results are applicable to any distance. Naturally, in a posterior iteration of this prototype, the logical evolution encompasses the inclusion of the reference detector on-board. In this scenario, the 50Ω adapter will no longer be needed because the coaxial cable is dispensed. Whatsoever, in this design the 50Ω impedance is indispensable, otherwise the truly detected pulsed response will not be correctly transmitted to the RX board (Figure 155).

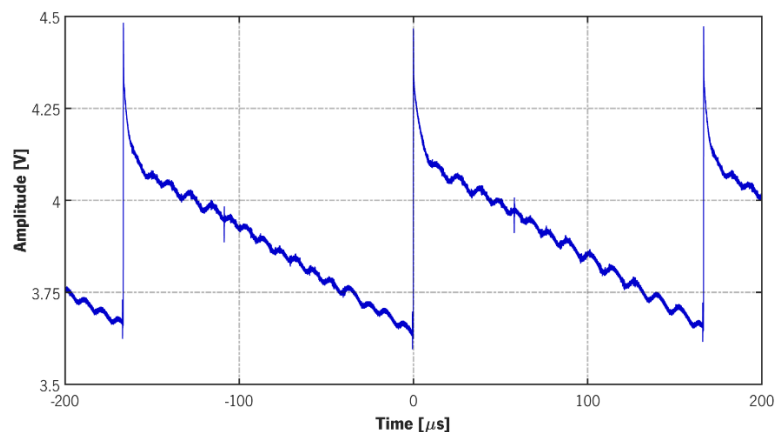


Figure 155. *laser_on* signal without the BNC 50Ω terminator to match the coaxial cable's characteristic impedance to the *DET10A/M* impedance.

5.3.4. Photodetection and Amplification

The procedure to measure the returning light pulses is similar to the aforementioned. The laser is projected on the *K-line* target at two distinct *g* distances: 0.560m and 3.560m. These two ranges are chosen because they both correspond to measured points in section 5.1.5 and to two very disparate situations, allowing for greater variations in the electric signals. For each distance, the back-reflected pulse is detected by the *SFH 2400 FA* PD and the photocurrent pulse is converted with a 20kΩ transimpedance gain into a voltage pulse, *return_analog*. The latter pulse is acquired at the test point

TP6 and a statistical treatment with around 2400 pulses is carried out through direct accumulation in the oscilloscope (same measurement setup). The measured pulse parameters encompass the amplitude, the FWHM, the rise and fall-times and the threshold crossing jitters. The threshold $V_{th,A}$ is nominally defined at 1.7V but, in practice, the real value as measured with a multimeter is $V_{th,A}=1.733V$. The results are summarily expressed in Table 38.

Table 38. Comparison of the return pulses for reflection on the *K-line* target at two distinct ranges: 0.560m and 3.560m. The statistical quantities are directly retrieved from the *HDO4034* oscilloscope. $\langle X \rangle$ is the arithmetic average and σ_x the respective standard deviation.

	D=0.560m			d=3.560m		
Pulses' Morphology						
#Acquisitions	2450			2479		
	$\langle X \rangle$	σ_x	Histogram	$\langle X \rangle$	σ_x	Histogram
Amplitude [V]	1.570	0.003		1.559	0.021	
FWHM [ns]	90.826	1.372		53.163	1.702	
Rise-time, t_r [ns]	45.359	1.062		49.592	3.355	
Fall-time, t_f [ns]	29.418	0.219		27.185	1.003	
Jitter @ Crossing [ps]	—	181.65		—	212.00	

The acquisition results for both distances show that the at 0.560m the return pulses are saturated in the transimpedance amplifier and, at the farther distance, the pulse is already transitioning to a non-saturated distance, revealed by the slight amplitude decrease from 1.570V to 1.559V. The inferior voltage limitation is around 0.4V, lightly below the nominal specification of 0.6V [165], while the mean value of the baseline is around 1.994V. Recalculating the established baseline voltage in section 4.2.4.1, using a

more precise voltage of $+V_S = BP_3.3 \approx 3.58V$, the expected value yields $1.989V (5 \times V_S / 9)$, which is coherent with the empirical result.

Regarding the pulses' shape, the measured response is very clean and practically noise-free (unless in the baseline) and, again, this observation can be attributed to the *SFH 2400 FA* packaging. Comparing the relevant temporal quantities with the reference values from the direct measurement of the laser output (*'Reference PD Output'* in Table 37), and having into consideration that the return pulse is inverted (leading-edge is a falling-edge and, thus, the fall-time in the response pulse corresponds to the rise-time of the direct laser pulse, and vice-versa), one can remark a significant increase in all parameters' mean values and standard deviations. This degradation arises from a pulse distortion at the receiver, relative to its true temporal profile. The underlying phenomenon cannot be explicitly and easily identified through experimental evidences and it cannot also be related to an improper bandwidth in the TIA (100MHz, translated into a response time of 3.5ns [165]. A possible justification is reported in [195]. Theoretically, the nominal 10-90% response time of the PIN PD is determined by its terminal capacitance (11pF) and the reading circuitry resistance and, for a 20V bias, its value is 5ns [164]. Thus, the photodiode presents a fast-enough response time to detect with full amplitude to the laser pulses. However, the response time is not only governed by the RC effects but two additional phenomena: carriers drift and diffusion. The drift component of the photocurrent is determined by a fast movement of nonequilibrium carriers under the electric-field in the depletion region, while the drift component is a slow movement of carriers due to concentration gradients outside the depletion region. Hence, the response time, t_r , is defined as [195]:

$$t_r = \sqrt{(2.2\tau_{RC})^2 + \tau_{diff}^2 + \tau_{drift}^2} \quad (5.37)$$

where τ_{RC} , τ_{drift} and τ_{diff} are the RC, drift and diffusion time constants. The multiplier 2.2 accounts the exponential charging and discharging in the RC circuit. In ideal conditions, the RC time constant dominates the response-time. However, for a constant reverse bias, the larger the illumination, the larger the density of photogenerated carriers and the larger response time due to drift and diffusion of carriers in and outside the depletion region, respectively. This explanation is coherent with the results since, for shorter distances and more intense back-reflections, the FWHM is larger, as well as the fall-time. Nevertheless, and even with this distortion, the initial time-instant for the leading-edge is not altered since this is demarked by the moment in which the pulse returns to the receiver.

Lastly, at both distances the jitter is inferior to the estimation for the reference *laser_on* pulses (407.39ps) but superior to the direct measurement at *DET10A/M* (30.59ps), as a consequence of the increase in the rise-time. Whatsoever, and since the distortion phenomena in the reference and return paths is not the same, then the pulses cannot be straightforwardly compared inter-paths. In between the two distances, the increase in the timing jitter is not significant: from 181.65ps (2.71cm) to 212.00ps (3.18cm). This increase is inferior to the standard deviation growth between these two distances (3.873cm to 6.107cm, directly from Table 20), leading to the conclusion that the jitter in the threshold crossing times is not the dominant imprecision.

5.3.5. Leading-edge Discriminator

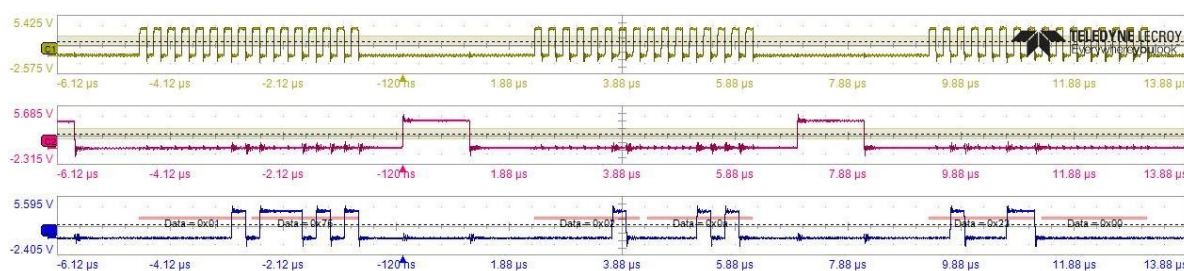
After detecting the reference and the back-reflected light pulses, both are compared with two fixed thresholds in the leading-edge discriminator, in order to establish the timing point and generate a STOP pulse to the TDCs.

5.3.5.1. Thresholds' Configuration

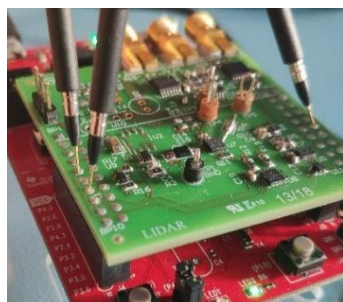
Before progressing to the discrimination process and its outcome, it is relevant to analyze the thresholds' establishment in the *TPL0202-10MRTER* digital potentiometer. The configuration is undertaken via a write-only SPI protocol, by writing directly in the wiper registers that determine the potentiometer position and the voltage division.

The thresholds for discrimination are nominally set to $V_{th,A}=1.7V$ and $V_{th,B}=0.15V$. Referring to equation (4.11), and considering that the RX MCU software encompasses $+V_S=3.5V$, the values to be written to the wiper registers A and B are:

$$\begin{aligned} V_{th,A} &= 117_{10} = 01110101_{10} = 0 \times 75 \\ V_{th,B} &= 10_{10} = 0000110_{10} = 0 \times 0A \end{aligned} \quad (5.38)$$



(a)



(b)

SPI	Time	Data	Bit Rate/Byte
1	-4.655 μs	0x01	4.00655 Mbit/s
2	-2.659 μs	0x75	4.00473 Mbit/s
3	2.336 μs	0x02	4.00981 Mbit/s
4	4.332 μs	0x0a	4.00927 Mbit/s
5	9.320 μs	0x23	4.00450 Mbit/s

(c)

Figure 156. Measurement of the SPI signals for the DPOT configuration: (a) sampled signals (SPI CLK, CS and MOSI, from the top to the bottom), (b) oscilloscope probes contacting the SPI CLK, MOSI and CS pins and (c) real-time decode of the data line.

To validate and visualize the SPI signals involved in the DPOT configuration, the *Teledyne WaveRunner 8254-MS* oscilloscope is used, with a direct measurement setup programmed to decode the data sequence in real-time ('Serial Decode' option). The sampled SPI CLK, MOSI and CS signals and the decoded data packages (MOSI) are displayed in Figure 156. The first data package includes a byte referring to the command for writing on wiper A (0x01), followed by the byte to write on the former register (0x75). Posteriorly, the instruction to write on the wiper B is sent (0x02), as well as the respective

data byte (0x0A). Finally, the command to copy the registers to non-volatile memory is sent (0x23), so that, when the system recovers from shutdown, the previously configuration is restored. The data transfer occurs at 4MHz or 4Mbit/s, as set by the SPI CLK frequency, respecting the maximum specification of 5MHz [166]. In between data packages, the CS pin is written high to disable the communication and the clock interrupted accordingly.

Even though the wiper configurations defined in the RX MCU software are correctly communicated to the DPOT, the reproduced average thresholds are marginally superior to the specification, as ascertained in the already mentioned multimeter measurements: $V_{th,A}=1.733V$ and $V_{th,B}=0.163V$. This difference emerges from the fact that, in the software configuration, $+V_s$ is considered 3.5V but, in practice, the mean value is estimated in Figure 123 to be 3.58V. Further, as $+V_s$ fluctuates at a frequency of about 100kHz, the thresholds also fluctuate in the same manner, as seen in Figure 157 for $V_{th,A}$. These fluctuations constitute an imprecision source because the threshold varies over time and, consequently, so do the pulses' timing point (reference and return).

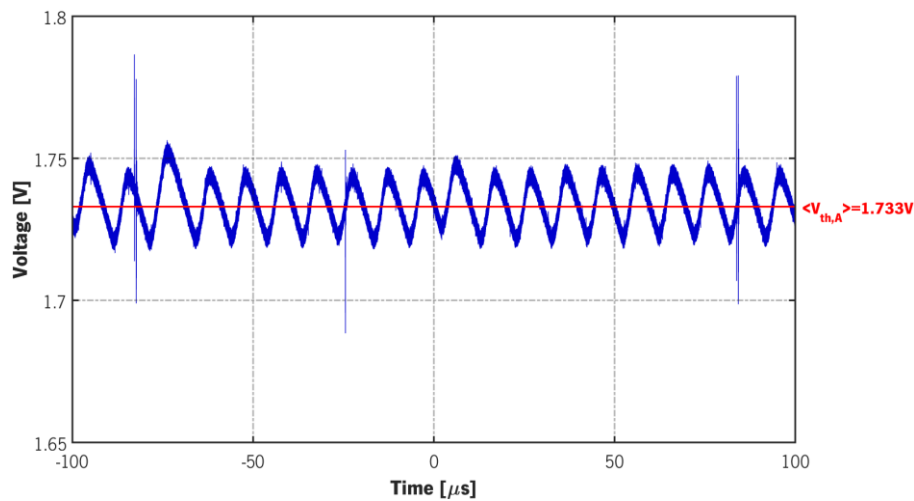


Figure 157. Fluctuations in $V_{th,A}$ around the mean value of 1.733V.

To complete, in the real $+V_s$ conditions, the limiting values in equation (4.10) must be re-evaluated, by writing the wiper registers to the maximum (0xFF) and minimum (0x00) possible values. In addition, the thresholds' resolution (minimum attainable increment), ΔV_{th} , can also be experimentally evaluated by incrementing the wiper register bit-by-bit. Both results are condensed in Table 39.

Table 39. Summary of the empirical values concerning the configuration of the discriminator thresholds.

Potentiometer	V_{th} Setting [V]	V_{th} Min. [V]	V_{th} Max. [V]	ΔV_{th} [mV]
A	1.733	0	2.37	5
B	0.163	1.21	3.533	14.2

5.3.5.2. Timing

In Figure 158, the relevant signals involved in the acquisition of a single ToF point for reflection in *K-line white* at $d_{actual}=3.560m$ are presented, from detection in both the reference and return paths, to the

generation of the STOP events to TDCs and consequent interruption to the RX microcontroller. The signals are sampled with the *Teledyne HDO4034* oscilloscope and, although they are generally self-explanatory, a brief description of the process is provided below. In some of the signals, an oscillating artefact is observable at $t=0$, coincident with BP_TRIG transition and arising from the ground loop induced by the scope probes' common ground. This artefact is not real and is introduced in the measurement activity.

The time-count in each measurement cycle is initiated at the falling-edge of the *BP_TRIG* pulses and the START event is common to both TDCs. After photodetection in the reference path and whenever the *laser_on* pulse surpasses the average threshold level of $V_{th,B}=0.163V$, the output of the leading-edge discriminator commutes to a low-level (STOP1 signal). Analogously, when the transampled return pulse (*return_analog*) falls below $V_{th,A}=0.163V$ in the leading-edge (thus the discrimination technique denotation), the respective discriminator output switches to a low-state (STOP2). The reference threshold is defined presuming that the pulses' amplitude in this arm is approximately constant, apart from the 22mV jitter estimated in Table 37, and to ensure no false triggerings occur. As the pulses' amplitude in TP4 is, on average, 1.125V, then this threshold is sufficient to efficiently induce STOP events. Naturally, the threshold could have been diminished to a value close to the noise level, but this is not critical due to the pulses' stability, contrary to the return path in which the threshold is important to stablish the sensor's dynamic range.

Due to the addition of the C9 and C13 bypass capacitors on the leading-edge comparators' outputs (Figure 76), the STOP2 and STOP1 signals do not switch rapidly. Instead, the capacitors oppose to abrupt voltage changes. Therefore, when the comparators output changes to a low-state the capacitors discharge and, when the output commutes again to a high-state, i.e. when the respective analog pulses cross the thresholds on the trailing-edge, the capacitors initiate the charging process. This way, the capacitors eliminate ringing (abrupt changes in the logical state due to noise) in the discriminator's output, at the expense of increased rise and fall-times in the STOP pulses. Since the capacitor's nominal capacitance is 1000pF, the response time is of the nanosecond order.

Consequently, and consulting the TDCs datasheet [168], the threshold for a low-level input at the START and STOP pins is $V_{IL}=0.3 \times V_S=0.3 \times 3.58=1.074V$. Hence, the STOPs are only effectively recognized by the TDCs whenever the previous value is crossed in the STOP1 and STOP2 pulses, namely in the falling-edge due to the chosen configuration. Similarly, and although the START pulses have a fast fall-time, this is also applicable. The ToF in each TDC is, then, comprehended by the time between the V_{IL} crossing in the *BP_TRIG* signal (START) and in the respective STOP signal.

Afterwards, when the STOP is detected or the CLOCK_COUNT_1 register overflows, an interruption is activated in the INTB pin of the respective TDC, acknowledged through a high-to-low transition in the latter pin. However, and since the calibration of the internal time-base is forced to 2 external clock (*TDC_CLK*) cycles, as specified in Table 14, the previous events are not simultaneous. Hereupon, the temporal delay between the STOP experimentally attained and the interruption is of approximately 125ns. The interruption pins of each TDC is connected to the input of a AND-gate and, therefore, the RX microcontroller is only interrupted when the acquisition is completed in at least one of them. In this specific scenario at $d_{actual}=3.560m$, ToF2 is superior to ToF1 whereby the interruption of TDC1 (*TDC_TX_INT*) occurs earlier and simultaneously with the AND output (*TDC_INT*) commutation to a logic '0'.

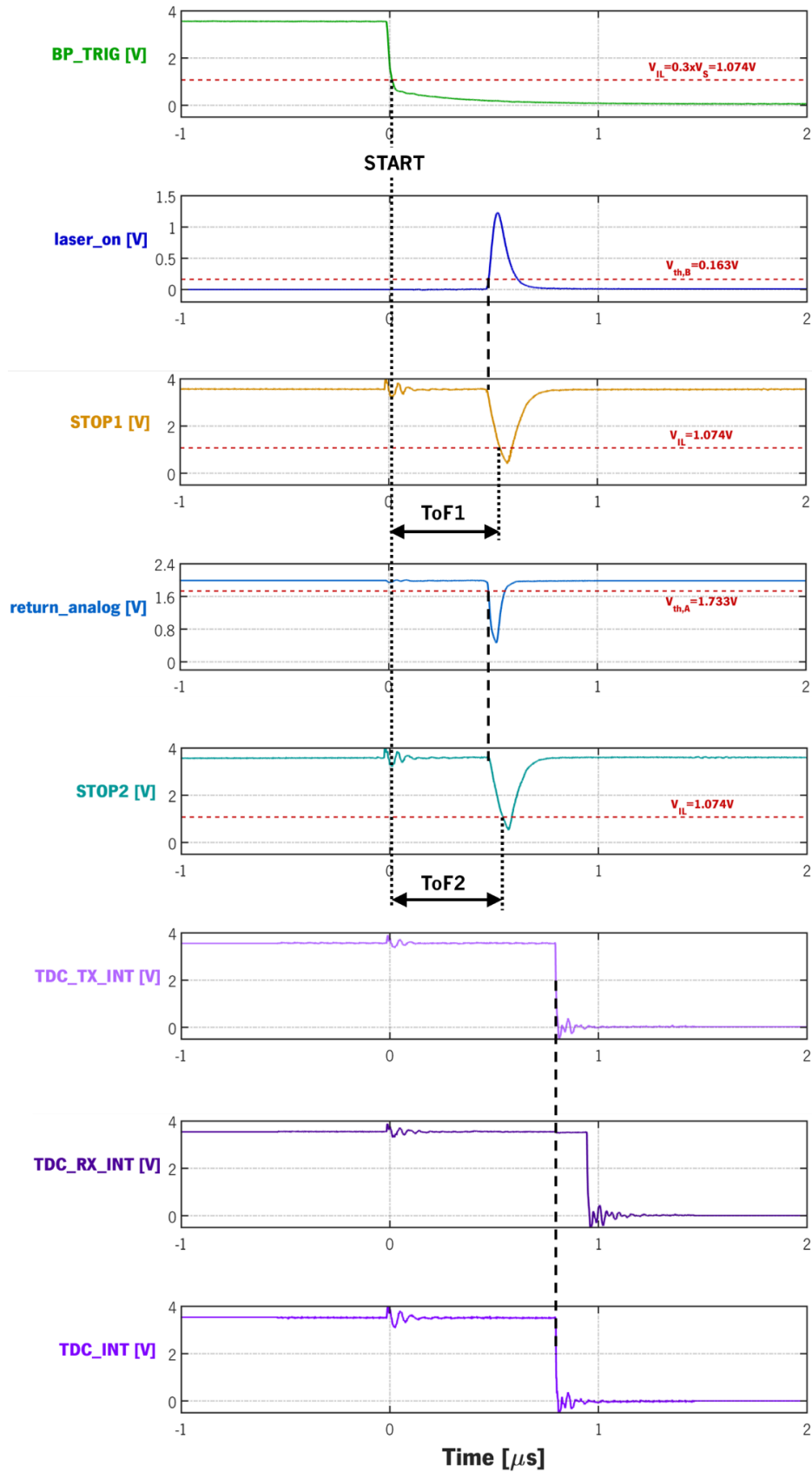


Figure 158. Signals involved in the measure of a single point at 3.560m, from the reception to the STOP events. At alternative distances, the signals appearance is the same unless for the return pulse (as verified in Table 38). Moreover, the timing instants regarding ToF2 also change in accordance with the distance.

The range measurements cease when STOP pulses' amplitude no longer surpasses V_{IL} or when its width recesses below 10ns [168]. In Figure 159, the breadth of STOP1 and STOP2 at 3.560m are evaluated at V_{IL} . In the reference path, the width is around 57.8ns and, in the return path is around 42ns. Hereupon, both pulses respect the minimum specification. However, while in the reference path the width is approximately constant (except for jitter), in the return path it depends on the back-reflected signal intensity. In the latter, the width decreases as the target is moved away from the sensor or, equivalently, as the back-reflected optical intensity peak decreases (for e.g., due to change of the target to a lower reflective material or change from specular to diffuse reflection), because the *return_analog* underdrive relatively to $V_{th,A}$ contracts.

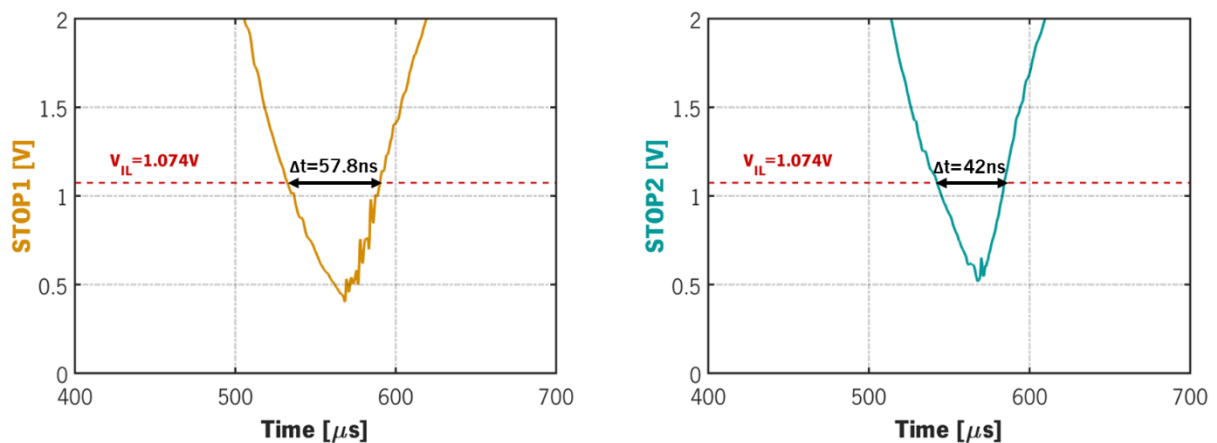


Figure 159. STOP pulses width in the reference and return paths at $d_{actual} = 3.560m$.

5.3.6. Time-to-Digital Converters

Finally, when the interrupt *TDC_INT* is perceived at the RX MCU, the ToF results registers are read and both TDCs are restarted to enter another point-acquisition cycle, by setting the *START_MEAS* bit in the *CONFIG1* register. Herein, the TDCs configuration and the jitter analysis are encompassed.

5.3.6.1. Configuration

The first experiment carried-out in the TDCs is the examination of the established configuration registers, to validate the arrangement theoretically defined in Table 14. Therefore, at the end of each ToF cycle, the *CONFIG1*, *CONFIG2*, *INT_MASK*, *CLOCK_CNTR_OVF_H* and *CLOCK_CNTR_OVF_L* are read in both TDCs and printed in the PC Serial Port Monitor by this order. The printed values are displayed in Figure 160 and are coherent with the data specified in Table 14 after inter-conversion binary \leftrightarrow decimal, unless for *CONFIG1*. The latter disparity arises from the fact that the registers are read at the end of a measurement cycle, in which the *START_MEAS* bit is cleared. However, re-reading the *CONFIG1* after resetting the *START_MEAS* bit, the initial configuration is restored ($187_{10} = 0b10111011$). The remaining registers are kept in the default configuration and there is no point in checking them.

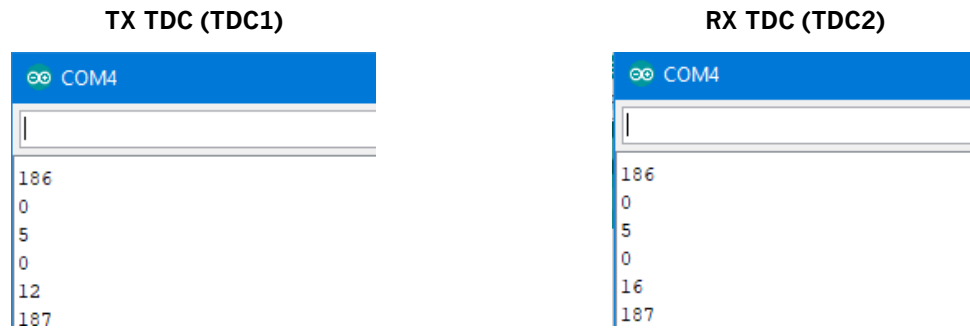


Figure 160. Authentication of the configuration registers in both TDCs. These registers are read and then directly printed on a Serial Monitor.

Further, it is also verified that, after configuration, TDC1 and TDC2 are interrupted after a time of $750\mu\text{s}$ and $1000\mu\text{s}$, respectively, if no valid STOP pulse is received in the defined time window. The electrical signals reflecting this statement are shown in Figure 161, as directly printed from the *Teledyne WaveRunner 8254-MS* oscilloscope.

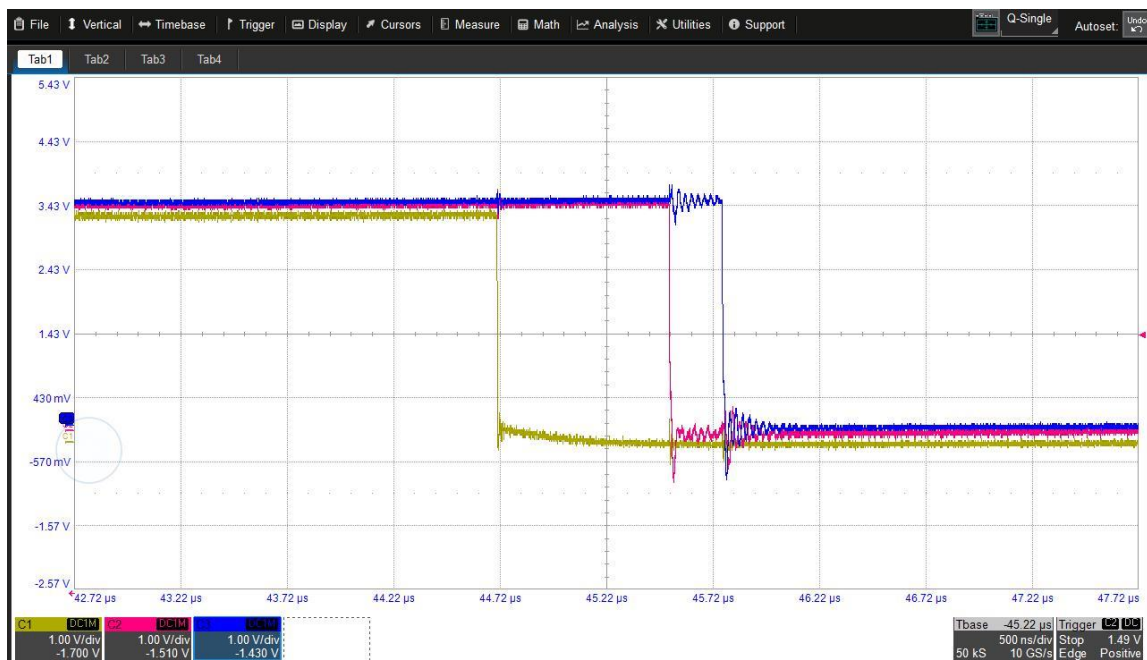


Figure 161. Monitoring of the INTB signals of both TDCs whenever no STOP pulse is detected. In yellow, the falling-edge of the BP_TRIG signal marking the START event. In pink and blue, respectively, the interruption on TDC1 (after $750\mu\text{s}$) and TDC2 (after $1\mu\text{s}$), triggered in the falling-edge.

As already defined and stated, the point acquisition rate of the LiDAR prototype is $f_p=6\text{kHz}$. This value is not randomly defined, and it constitutes an empirical upper limit to be legitimized herein. In theory, the maximum PRR limitation is set by the laser maximum duty cycle and pulses' width to 12.5kHz . Whatsoever, in between STARTs in consecutive falling-edges of BP_TRIG , it is mandatorily to guarantee that all the result registers are read from both TDCs and the $START_MEAS$ bit is reset before the subsequent START. Hereupon, to establish the ultimate f_p , the TDCs' reading process in the previous and final configuration must be investigated. The experiment consists on acquiring (*Teledyne WaveRunner 8254-MS* oscilloscope) a total of six signals at repetition rates of 6kHz , 7kHz and 9kHz :

SPI_CLK, *BP_TRIG*, *TDC_TX_CS*, *TDC_RX_CS*, *TDC_TX_INT* (INT1) and *TDC_RX_INT* (INT2). To encompass the absolute global limitation, the tests are performed without detection in either the return or reference paths. This way, the ToF in each TDC achieves the maximum possible value established in the *CLOCK_CNTR_OVF* register (750ns in TDC1 and 1 μ s in TDC2).

In Figure 162, the acquisitions at $f_p=6$ kHz are displayed in the same order as aforementioned. The SPI communication sequence consists in reading the *TIME1*, *CLOCK_COUNT_1*, *TIME2*, *CALIBRATION1* and *CALIBRATION2* registers alternately from each TDC (1 address byte + 3 data bytes) and, at last, setting the *START_MEAS* bit in both (1 byte). Hence, the low-level in the CS pins alternate in time and, during this interval, the SPI CLK is active. The transactions last a total of approximately 120 μ s and after the *CONFIG1* registers are reconfigured, the *INTB* pins are reset to '1'. Comprehensively, the two interrupt signals are capable of following the *BP_TRIG* frequency and, in between each *START*, the RX MCU is able to timely communicate with both TDCs and get ready to initiate a new cycle.

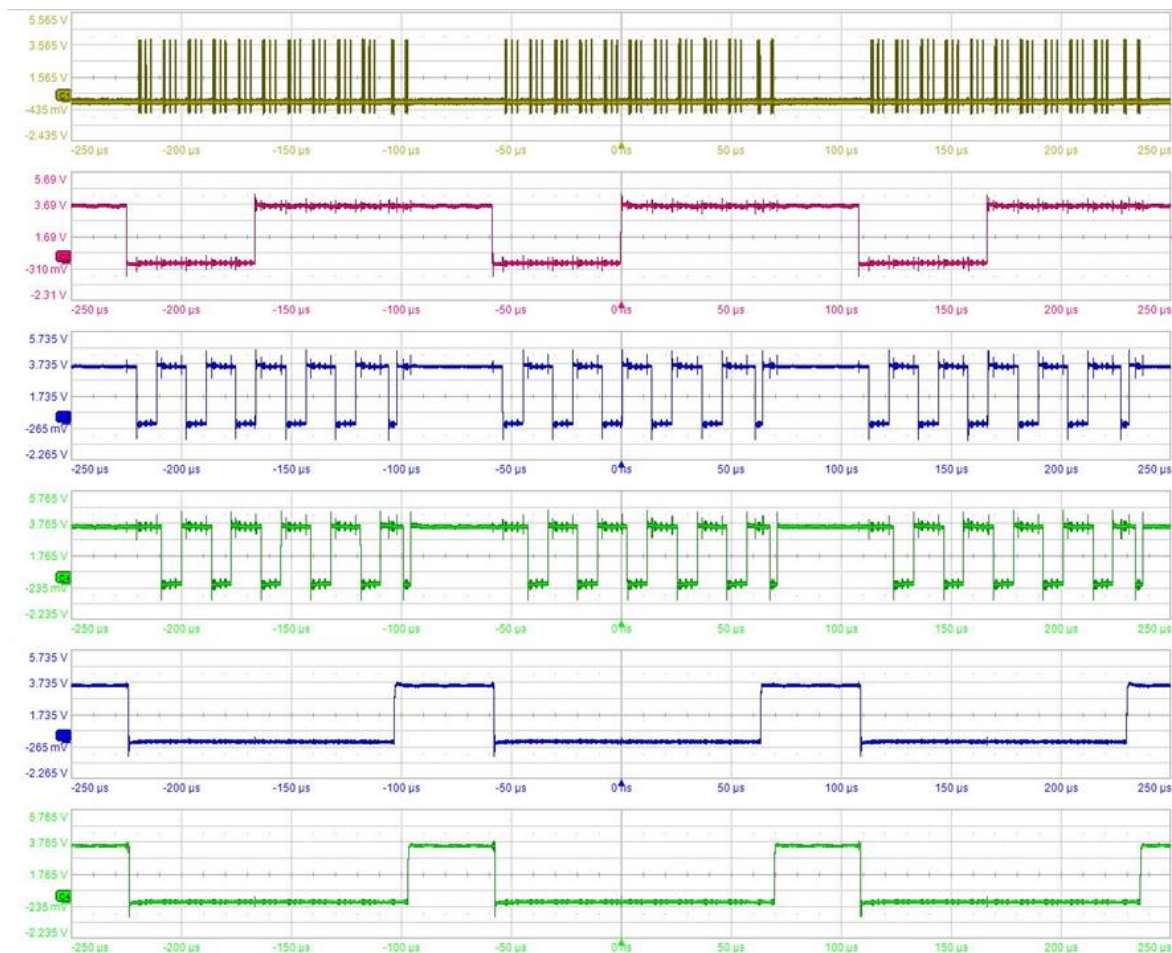


Figure 162. Some signals involved in the ToF acquisitions in each TDC for $f_p=6$ kHz. From the top: *SPI_CLK*, *BP_TRIG*, *TDC_TX_CS*, *TDC_RX_CS*, *TDC_TX_INT* and *TDC_RX_INT*. The horizontal time-scale is 50 μ s/div and the vertical 1V/div. Since the TDCs reading time is inferior to the time between consecutive falling-edges in *BP_TRIG*, the point acquisition frequency replicates the laser pulses frequency f_p , as seen in the last two signals.

Increasing the frequency to 7kHz, it is observable that the reading speeds cannot follow the *START* pulses' repetition rate and, consequently, both interrupts cease and no time-measurements are attained. Increasing f_p further to 9kHz, the ToF estimations are re-established. However, and as seen in Figure

163, the transactions terminate after the falling-edge of the subsequent START pulse. Thus, and in a nutshell, the effective point rate deteriorates to exactly a half of f_p , i.e. 4.5kHz as one in each two consecutive laser/START pulses is disregarded (seen in the TDC_TX_INT and TDC_RX_INT signals comparatively to BP_TRIG).

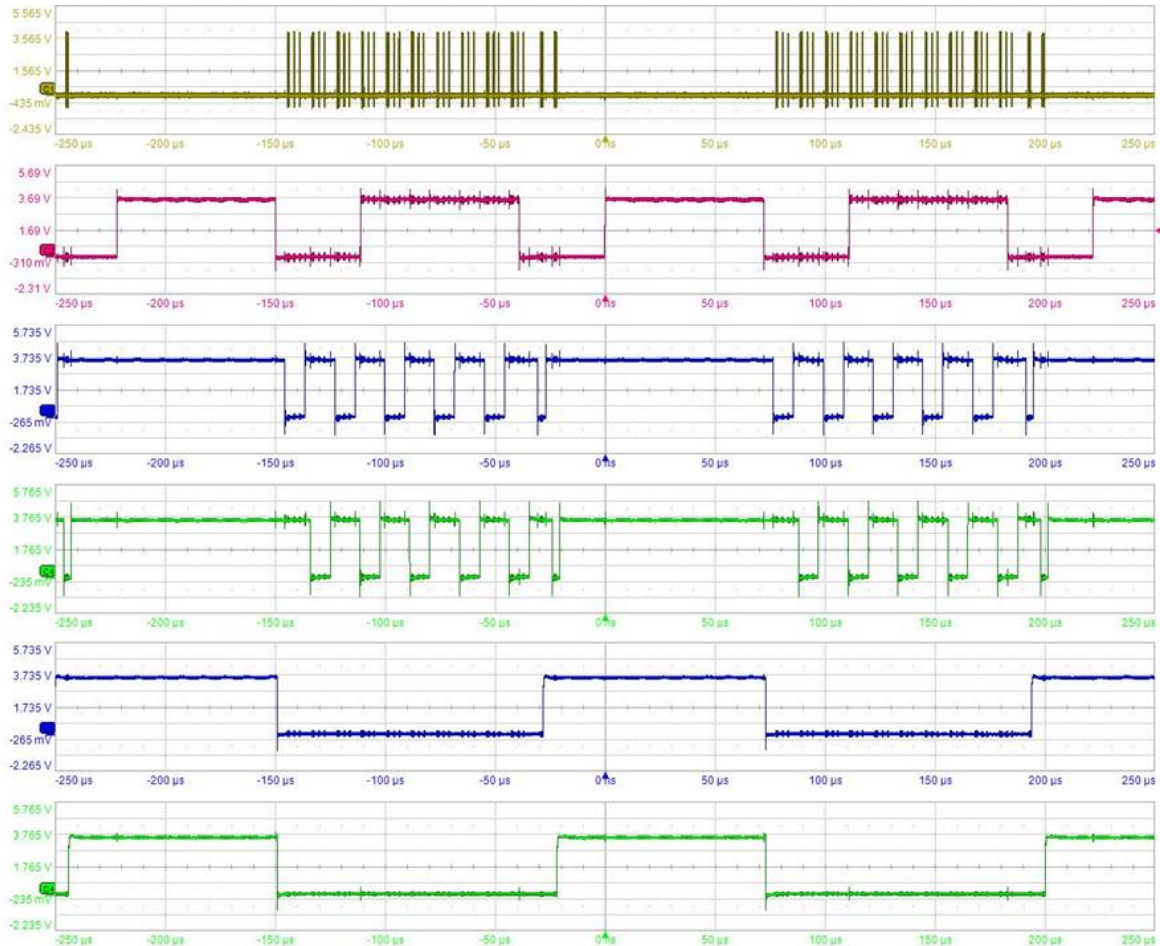


Figure 163. Some signals involved in the ToF acquisitions in each TDC for $f_p=9\text{kHz}$. From the top: SPI_CLK , BP_TRIG , TDC_TX_CS , TDC_RX_CS , TDC_TX_INT and TDC_RX_INT . The horizontal time-scale is $50\mu\text{s}/\text{div}$ and the vertical $1\text{V}/\text{div}$. The frequency of the two interrupt signals on the bottom is exactly 4.5kHz because the TDCs reading-times cannot trail the laser pulses frequency and one in two START/laser pulses are ignored by the sensor.

Conclusively, the fundamental limitation to the maximum PRR in the developed LiDAR sensor is not settled by the laser maximum PRR but by the TDCs reading speeds to $f_p=6\text{kHz}$. For a 1D system, this point acquisition rate is pragmatically plentiful but, for a scanning LiDAR it may be necessary to go further to accomplish the frame resolution and rate. Hereupon, the TDCs reading times must be diminished and the obvious solution is to replace the MSP430FR5969 MCU by a unit with superior clock frequencies.

5.3.6.2. Jitter Analysis

Finally, to complete the electrical characterization, the temporal jitter is globally studied to better understand the preminent precision-limiting sources. The jitter is referred to as the noisy fluctuations either around the true periodicity of the signals (e.g. clock) or around the average timing points (e.g. in the ToF measurements).

As invoked in the TDCs operating principle, these time-measuring units rely on two distinct time-bases to estimate the ToF between a START and STOP pulse in Mode 2. The first is an internal time-base set by a local oscillator and it underlies the TIME1 and TIME2 registers. The second is a time-base externally established by the SMCLK @ 16MHz furnished by the RX MCU (*TDC_CLK*) and is accounted on the CLOCK_COUNT1 register. Both temporal grounds are susceptible to noisy fluctuations affecting the ToF precision and, since they are independent, they ought to be separately scrutinized.

Starting with the external time-base, the fluctuations arise from deviations in the external clock from the absolutely accurate periodicity. Hence, the cycle-to-cycle jitter in the *TDC_CLK* signal frequency is straightforwardly quantified in the *Teledyne HDO4034* oscilloscope by monitoring and accumulating a total of 52247 periods. The raw data is exposed in Figure 164, alongside the sampled SMCLK signal, and the relevant results are summarized in Table 40.

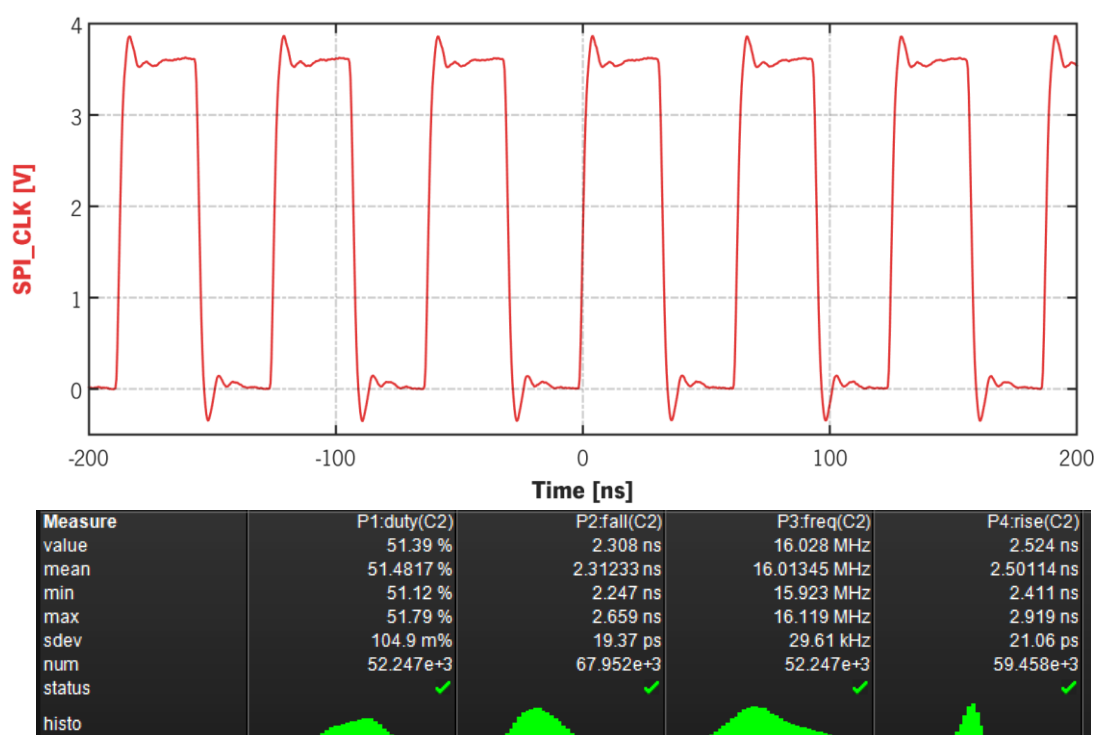


Figure 164. TDCs' external clock signal with 16MHz nominal frequency and cycle-to-cycle jitter quantification as directly provided in the *HDO4034* oscilloscope.

The latter results reveal that the average clock frequency, f_{CLK} , is slightly above the nominal specification and, therefore, the period (T_{CLK}) is approximately 62.45ns, suffering a mean cycle-to-cycle jitter of around 0.12ns. To evaluate the effect on the final ToF1 and ToF2 estimations, the CLOCK_COUNT1 register shall be known in order to propagate the previous jitter over the entire cycle count. For the reference TDC1, the CLOCK_COUNT1 register is almost constantly set to 8 at the end of each punctual measurement. Since the reference path is fixed, this result is kept for varying distances. In the return path, the CLOCK_COUNT1 in TDC2 oscillates between 8, at a distance of 0.560m, and 9 at 3.560m. Hereupon, and considering that the jitter accumulates on each clock cycle, then the associated uncertainty in the timing point is a function of the clock jitter and the number of cycles measured (CLOCK_COUNT1) [156]:

$$\sigma_{t,ext} = \sqrt{CLOCK_COUNT1} \times \sigma_{t,CLK} \quad (5.39)$$

where $\sigma_{t,ext}$ is the overall effect of the external clock jitter in the respective ToF and $\sigma_{t,CLK}$ is the jitter in the external clock source. Substituting the numerically retrieved results in this equation, results in a total imprecision of around 327ps (4.95cm) and 346ps (5.19cm) for a CLOCK_COUNT1 of, respectively, 8 and 9. However, the total ToF is computed by subtracting the two ToF results and, as the external clock source is common and synchronous to both TDCs, one can assume in a good approximation that this jitter cancels overall (disregarding differences in the electrical path). Hence, the SMCLK clock jitter can be discarded as the dominant imprecision source as well as the prevailing basis for the increase with the distance (0.24cm from 0.560m to 3.560m vs the overall increase of 2.23cm reported in Table 20).

Table 40. Summarized results of the jitter analysis on the external clock source for the TDCs.

TDC_CLK Metric	$\langle X \rangle$	σ_x
Frequency, f_{CLK} [MHz]	16.01345	0.02961
Period, T_{CLK} [ns]	62.44751	0.11547

Regarding the internal time-base, the nominal specification in the *TDC7200* datasheet mentions a nominal LSB resolution of 55ps [168]. Whatsoever, at the end of each measurement cycle, each TDC is calibrated to more accurately quantify the actual LSB value for TIME1 and TIME2. Because TDC1 and TDC2 are encompassed in separate ICs, the internal time-bases are unallied. This way, in Figure 165 the statistical distributions of the resolution are described after acquisition of 2400 calibrated LSB point for each TDC. Firstly, and as the calibration is carried-out using the common shared clock source as reference, the jitter in the LSB values is approximately equal for both TDCs (0.146ps for TDC1 versus 0.145ps for TDC2). Nonetheless, since the ICs are distinct, the internal time-base differs from an average of 56.221ps in TDC1 to 57.658ps in TDC2. The almost 1.5ps offset can be attributed to manufacturing tolerances and slight internal discrepancies arising during the fabrication stages. Finally, the calibrated LSBs are both slightly above the nominal specification.

To calculate the jitter propagation in each ToF arising from the internal time-base, equation (5.39) shall be rewritten considering the first term of the ToF calculation in Mode 2 encompassed in equation (4.13):

$$\sigma_{t,int} = \sqrt{TIME1 - TIME2} \times \sigma_{t,LSB} \quad (5.40)$$

where $\sigma_{t,int}$ is the overall effect of the internal temporal jitter in the respective ToF and $\sigma_{t,LSB}$ is the jitter in the LSB value. However, and then again, due to the common jitter source (also the external clock, accounted twice), the subtraction of ToF2 to ToF1 does also partially cancel the resulting jitter, with the excess ToF contributing to the global jitter. The determination of the *TIME1-TIME2* excess is possible directly from the ToF data in Table 20 but it encompasses all the jitter sources and it is impossible to dissociate the single effect of the temporal jitter in the internal time-base.

Overall, as the ToF in each TDC is a sum of the internal and external time-base contributions in equation (4.13), then the two sources shall be summed to give the overall time jitter induced in the TDCs, $\sigma_{t,TDC}$:

$$\sigma_{t,TDC} = \sigma_{t,int} + \sigma_{t,ext} \quad (5.41)$$

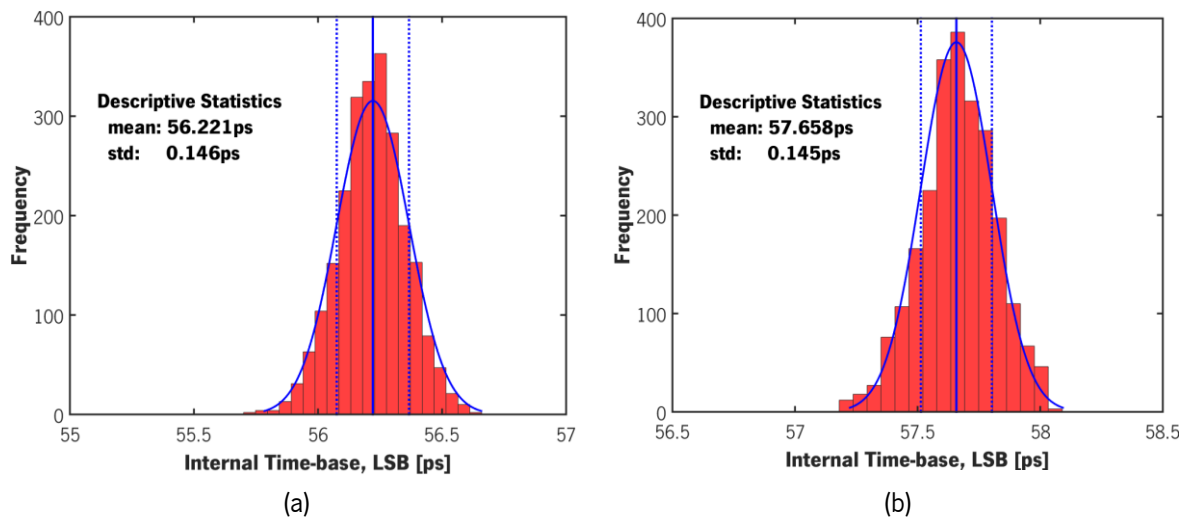


Figure 165. Histograms and respective gaussian fits showing the LSB distributions for the internal time-base in (a) TDC1 (reference) and (b) TDC2 (return). Directly printed on each graph, the average and standard deviation results of the descriptive statistical analysis.

Conclusively and globally, it is a complex and demanding task to superimpose all the fluctuation sources and predict the quantitative effect in the sensor's final precision. The main justification is the presence of both correlated (TDCs time bases) and uncorrelated sources (like the oscillations in the BP_3.3V trigger, common to both TDCs but dependent on the pulse discrimination instants), and the fact that the effective ToF is a result of the subtraction of ToF1 to ToF2. Hereby, the knowledge to ultimately retain is the overall precision discussed in section 5.1.6.2, increasing between 3.873cm and 7.115cm as the target is moved away from 0.560m to 4.420m to the LiDAR sensor. This is the bigger picture in the precision scene and it is extremely relevant to keep track and identify the critical sources to, in a posterior prototype, minimize the fluctuations effect by applying of the options also enumerated earlier.

5.4. Adjustments to TIDA-00663 Design

As already stated, the *Texas Instruments'* reference design presents some negative aspects that had to be overcome to arrive to the final and fully-functioning prototype. These inconveniences were identified and experimentally proven in the first iteration of this work and led to radical modifications in the development approach. Hereby, to close this chapter, these issues are exposed, as well as the solutions used to address them. The positive and negative aspects of the prototype are not encompassed here and are left to the conclusions.

1) Proximity laser-photodetector

The original design was projected to integrate the LiDAR system onto a single PCB. Due to the small dimensions of the board, it implies an impracticable proximity between the laser and the photodetector,

identified as U10 and D1 respectively in Figure 62 or as seen in Figure 90. Consequently, two problems arise. Firstly, it inhibits the placement of optical elements in front of each component. Secondly, some residual emission from the laser lateral edges was directly detected. To deal with the problem, the laser was removed from the board and soldered to it through three jumper wires, as shown in Figure 166a. However, with this solution problem #2 was aggravated.

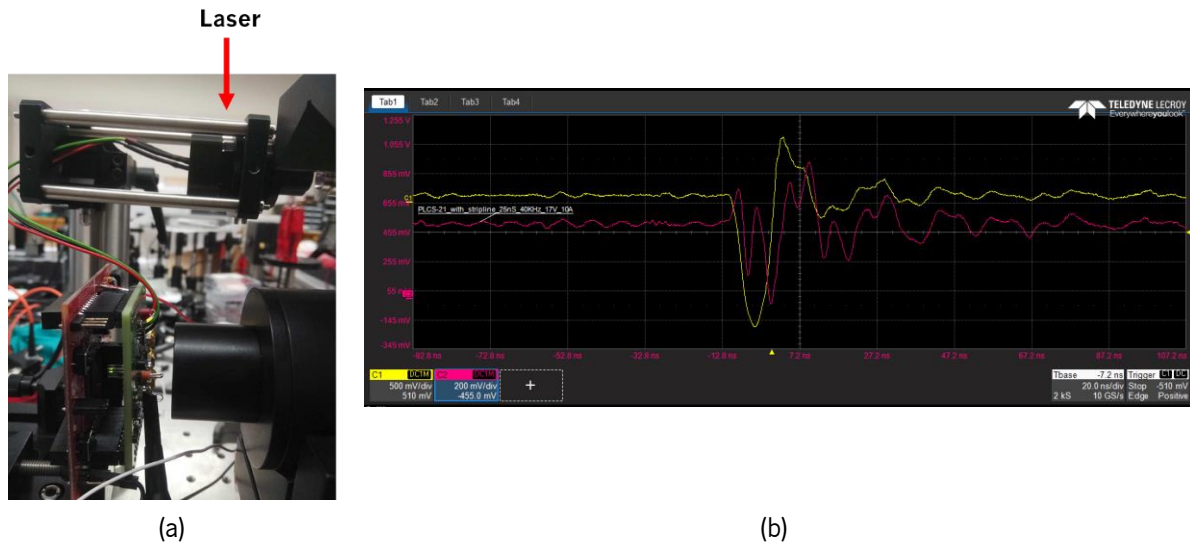


Figure 166. First iteration of the LiDAR prototype: (a) laser connected through jumper wires to the PCB; (b) *laser_on* (yellow) and *laser_on_threshold* (red) signals.

2) Reference pulse for STOP1

Originally, the reference signal *laser_on* used to trigger STOP1 after discrimination, is obtained through the voltage difference across the resistor $R_{14}=10\text{m}\Omega$ in series with the laser. This is unthinkable because, intuitively, the amplitude of the generated signal will be utterly small. To make an overestimation, one supposes a 5A peak current whenever a laser pulse is emitted. In this condition, a 50mV peak voltage would be detected in this resistor. Through equation (4.8) for the respective discriminator, the minimum non-zero threshold voltage is obtained for $W_B=1$, corresponding to a *laser_on_threshold* of 13mV. Although it was still possible to discriminate the signal *laser_on* in this scenario, the width of the resulting STOP pulse was undoubtedly insufficient to be resolved by the respective TDC. To support and even aggravate this conclusion, the simulation in *TINA* showed a peak of around 15mV in *laser_on*.

Adding to the deficient amplitude, the wires connecting the laser to the board introduced a significant stray inductance with an immediate effect in the ringing of *laser_on* (Figure 166b), leading to multiple threshold crossings. Besides, the wires also led to increased rise and fall times and power losses between the board and the laser (increased overheating).

3) Ground-loop

The third problem is identified as a ground loop. This effect is an unintentionally induced feedback loop caused by the shared common ground between the PCB, i.e. the microcontroller connected via USB to the PCB, and the external power source, connected to the main. Ideally, all the grounded points should be at the same potential. However, different ground points on the initial system were at different potentials mainly due to the current transients from the heavy current loads (laser and driver), a current flowed

between them and a current ground loop was created, inducing voltages that lead to unstable referencing. This instability translated in voltage oscillations in the whole system whenever the laser driver switched state (Figure 167) and was strongly aggravated by the laser wires inductance. This cause was identified because one verified that the oscillations in every point of the circuit were strongly correlated, as seen in Figure 166b between the *laser_on* and *laser_on_threshold* signals.

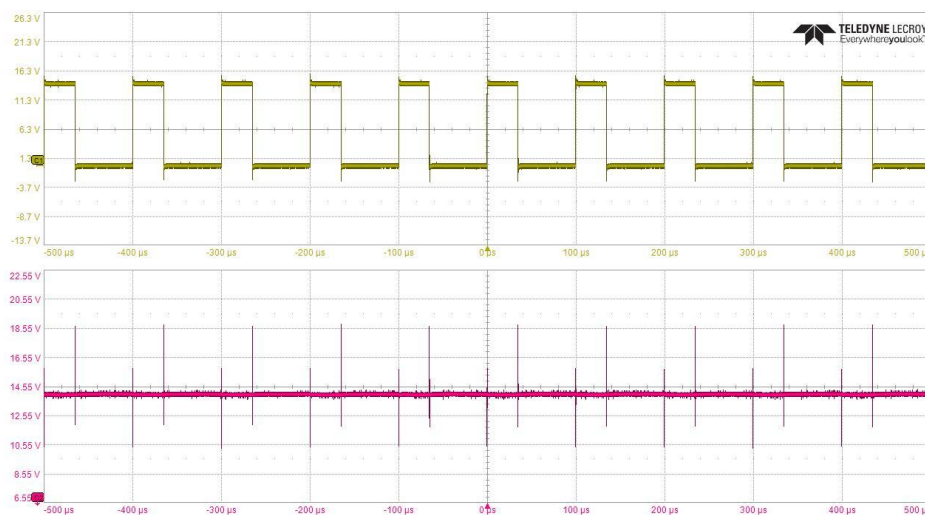


Figure 167. Effect of the ground-loop. In yellow, the laser driver signal, and, below, the direct output of the external power supply $V_{cc,laser}$. Whenever the driver switches, a strong voltage peak is noticed in the latter, with polarity depending on the edge.

To solve the previous three critical factors, the laser was isolated from the receiver by separating the single PCB in RX and TX boards, independently supplied. Also, the referencing to TDC1 was completely altered, and the *DET10A/M* external detector was introduced to instruct the laser firing instants. To solve the inductance issue, the latter was connected to the board via a low-inductance coaxial cable. The ground loop is efficiently corrected because the RX supply is completely isolated from the high-current loads on the TX board. Since the photodiode does not consume current from the external source, a stable supply is guaranteed in the RX board, where the critical components for detection are included. This is validated through the monitorization of the output of both power supplies (Figure 168).

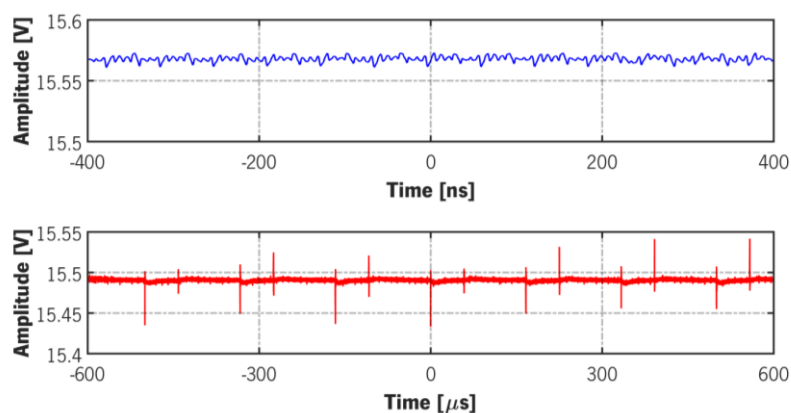


Figure 168. $V_{cc,laser}$ signals supplied to each board. On top, the signal generated by the *Agilent 3630A* to the RX board. On the bottom, the signal generated by the *Agilent 3631A* to the RX board. The voltage peaks in the latter board do not propagate to the former.

4) Narrow dynamic range for *return th*

At first, the resistors R_{12} and R_{13} in series with Potentiometer A of the *TPL0202-10MRTER* had, respectively, $142\text{k}\Omega$ and $178\text{k}\Omega$ resistances. Replacing these values in equation (4.8) and considering the maximum and minimum resistance state of the Wiper A, an adjustable threshold in the interval between 1.89V and 1.99V is attained. These values are unconceivable because they barely underpass the noise level at the TIA output and provide short-adjustability and limited flexibility. Hence, both resistors were replaced by $10\text{k}\Omega$ substitutes.

5) On-board Calibration

The last and less significant aspect is the embedded on-board calibration circuit. The TIDA-00663 takes advantage of the *OPA857* test mode to evaluate the delay introduced in transamplification through the generation of a test pulse in the microcontroller that propagates through the receiving path. However, this feature is fruitless because there are several other delay sources to be accounted. So, one opted to deactivate the circuit and proceed with external calibration.

– This page is intentionally left blank –

6

GUIDELINES TOWARDS ADVANCED FUNCTIONALITIES

Although the developed prototype is a LiDAR for single-point measurements, it is perceptible the level of complexity and the exorbitant number of factors that need to be taken into consideration. The next step is to improve the sensor performance by adding functionalities with valuable relevance within the context of autonomous driving.

Then, in this penultimate chapter, three functionalities are proposed and the guidelines for its integration are drawn. Some results are presented to support the proof-of-concept. The first upgrade is the addition of a scanning technique to expand the FOV to multiple points. The second consists on the detection of the returning light polarization for material classification. The last is an advanced timing technique to replace the leading-edge discriminator and substantially decrease the time-walk. It is noteworthy that, the main goal is only to provide the directions and give a well-established foundation for the evolution of the developed design towards a sensor more adequate to the final goal of an implementation targeting the automotive market.

6.1. Scanning with Micromirror

In order for a LiDAR to be applied in an automotive context, the sensor must be able to perform measurements in a 2D FOV to endow 3D information of the circumambient and support decision making in real-time. As established in the theoretical background, the requisites for L4 and L5 autonomies are a FOV of at least $50^{\circ} \times 9^{\circ}$ with a maximum $0.15^{\circ} \times 0.5^{\circ}$ angular resolution and a minimum frame rate of 10Hz.

The developed LiDAR prototype can only perform single-point measurements so one critical improvement is the addition of a scanning technique to provide a tridimensional perspective. The proposition is to interface the LiDAR system transmitter with the *Maradin MAR1100* scanning micromirror to project the laser pulses onto the FOV.

The choice is motivated by three factors, besides the advantages stated in section 2.4.4. Firstly, it is a compact device that allows the integration in the prototype with minor changes. In fact, it does not require alterations in hardware, although slight modifications must be done to the optics to meet the projection requirements. The second argument is that, spec-wise, this micromirror allows to virtually accomplish the abovementioned requisites. The module can accomplish a maximum FOV of $45^\circ \times 30^\circ$ (H×V) with a frame resolution of up to 1280×600 pixels, translated in a minimum angular resolution of $0.035^\circ \times 0.0625^\circ$, at a fixed frame rate of 30Hz [196]. At last, *Maradin* provides documents with the critical information required for this integration and it also distributes an actual scanning Evaluation Kit for the *MAR1100 (DM003100)* for premature testing. Further relevant characteristics of the *MAR1100* are exposed in Table 41.

Table 41. *MAR1100* optical and mechanical characteristics (typical values). [196]

Oscillation Frequency (H×V)	10.25kHz × 1.8kHz
MEMS Power Consumption	70mW
Effective Mirror Size	1mm × 1.1mm
Laser Maximum Spot Size	0.7mm
Incident Angle (H×V)	$22^\circ \times 0^\circ$

The micromirror is a MEMS device combining electro-static actuation with electro-magnetic actuation to rotate a reflector around two orthogonal axis (Figure 169). Each axis is assigned to a capacitive sensor that measures the angular position and sends it to a controller board to serve as a reference for generating the triggering signals.

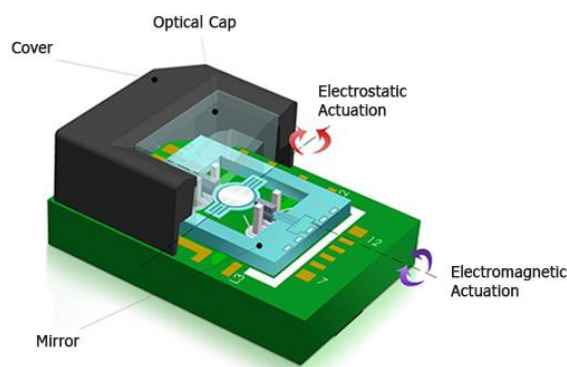


Figure 169. *MAR1100* MEMS micromirror. The mirror is electrostatically and electromagnetically actuated in normal axis and is covered by a package with a transparent optical cover. The module has a total size of $12 \times 6.5 \times 5.9 \text{ mm}^3$ (L×W×H) [197].

The micromirror is integrated in a static housing with a polycarbonate optical window that protects the MEMS and filters undesired wavelengths. By default, this coating is an AR filter tuned for visible wavelengths. However, in this context, a customized module with an AR filter for 905nm is employed. The optical efficiency is influenced by the mirror reflectivity and the cover transparency. The mirror is

coated with aluminum and has a reflectivity above 91% at 905nm. The optical cover has a transparency above 97%. [198]

The *MAR1100* module is connected to a controller board denoted *Gilboa* (Figure 170). This board includes the micromirror control block, more specifically the *MAR2100* ASIC (Application Specific IC), and a FPGA that implements all timing algorithms to synchronize the laser to the mirror position. Additionally, the FPGA also includes a CPU to control all the system parameters and an interface to the PC for GUI. The *Gilboa* board can be interfaced electrically with the external laser diode (*SPL LL90_3*) alongside its standalone driving hardware to synchronize the MEMS deflection with the firing instants. [199]

6.1.1. Optomechanical Guidelines

Even though the integration of this module does not require major adjustments to the developed LiDAR prototype, there are some technicalities and aspects to consider that are not straightforward. These elements are considered and explained herein.

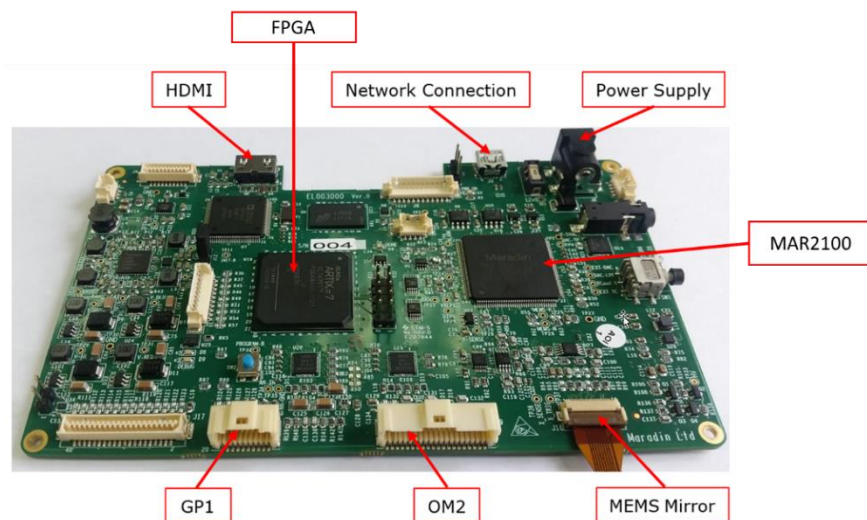


Figure 170. *Gilboa* control board. The FPGA and the *MAR2100* ASIC are indicated, as well as all the connectors to the MEMS micromirror, power supply, external laser circuit, among others (adapted from [199]).

For larger flexibility in the mechanical assembly, the *MAR1100* micromirror shall be detached from the control board and mounted separately from its driving electronics. The module is connected to PCB via a flexible Flat Printed Cable (FPC) extender with a receptacle for the MEMS on one side, and a ZIF (Zero Insertion Force) connector on the other end to link to the *Gilboa* (Figure 171). [199]

However, this configuration requires the definition of an aligned and static setup. The reference for mounting the scanning module with respect to the laser diode shall be the alignment surface of the MEMS housing. The alignment of the *MAR1100* must be performed using the top surface of the housing. This surface is parallel to the mirror with a tolerance of $\pm 1^\circ$ and is at a vertical distance of $2.06 \pm 0.05\text{mm}$ from the latter. The suggested method for a precise assembly between the scanner module and other elements in the LiDAR transmitter is by gluing the mounting surface to a fixed element inside a mechanical housing. [198]

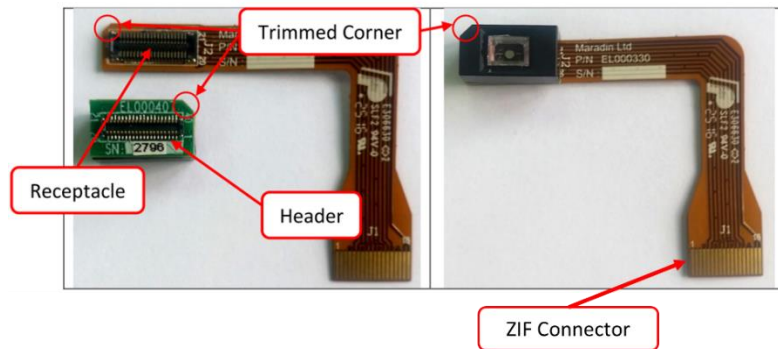


Figure 171. FPC connector to attach the MEMS micromirror to the control board and proper assembly. The trimming is essential due to the symmetry of the electrical connector that theoretically accepts two assembly configurations with a 180° rotation (adapted from [198]).

Regarding the optical side, the laser incidence angle on the micromirror shall be between $15\text{-}22^\circ$ relatively to axis perpendicular to its surface and parallel to the mirror horizontal position, to ensure mutually parallel horizontal lines [198]. The recommended beam diameter at the micromirror is 0.7mm , determined based on the assembly tolerances, laser incident angle, mirror deflection and its effective area (spot must fit completely in the reflective region to avoid energy losses) [198]. Thereby, the length of the optical path between the laser output and the micromirror must be minimized to ensure the previous spot size, which calls for a modification on the prototype optical system. The solution is to keep a small aspheric lens at the laser output, to collimate the beam and avoid the increase in the spot size due to the highly-divergent profile of the *SPL LL90_3*. Furthermore, a fixed mirror shall be added at $15\text{-}22^\circ$ from the normal to the micromirror surface to reflect the light directly to micromirror to posteriorly scan it. Finally, in order to have a rectangular FOV, the Maradin must be placed at 11° tilt (half of the horizontal incidence angle) in relation to the projection plane. The complete transmitter layout is shown in Figure 172.

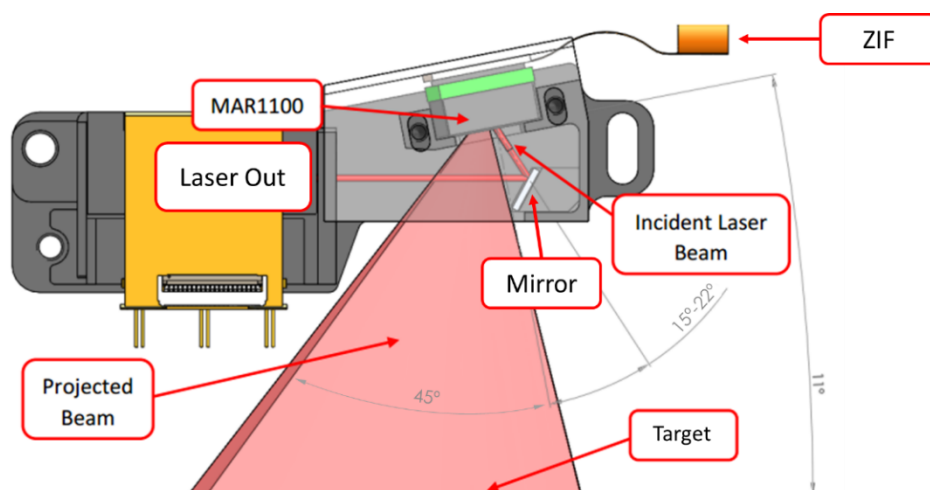


Figure 172. Top view of the mechanical assembly for the proposed LiDAR scanning system, highlighting the angular orientation of the elements. The laser is focused on a fixed mirror at a 22° angle in relation to the axis normal to the micromirror surfaced. The light is directly reflected to the MEMS reflective region that oscillates to scan the beam over a maximum 45° HFOV [198].

6.1.2. Electrical Guidelines

Before introducing the methodology to link the scanning system with the prototype, one must discuss the scanning pattern. The *Maradin* has the flexibility to allow the configuration of a customized pattern. The projection can, thereby, be controlled by two means. First, by connecting the board via the “Network Connection” (micro-USB) to the PC using a USB communication cable. In the PC, a dedicated GUI permits the manual control of some projection parameters. The alternative is to flash the board memory with fixed parameters so that the micromirror can repeatedly and consistently scan the FOV under the same conditions. The latter alternative is the one to be applied in an end-product since it must be independent of the PC connection and the pattern shall be preserved and restore upon power on.

The FOV scanning sequence is performed line by line as evidenced in Figure 173. The lines are numbered from 0 to L-1. The FPGA is implemented with interlaced projection using even an odd field. Each frame is projected in two fields: L/2 lines in the even field (0, 2, 4 ... L-2) and L/2 in the odd field (1, 3, 5 ... L-1). The pattern refresh rate is fixed at 60fields/sec or 30FPS, even though the laser firing instants can be controlled to decrease it to lower values, for instance, to cope with the speed of the signal acquisition and processing. The number of horizontal pixels, P, can be set to an arbitrary number limited to 1280. In every field, the lines are alternatively scanned in the forward direction (from left to right from the micromirror’s point of view) and backwards.

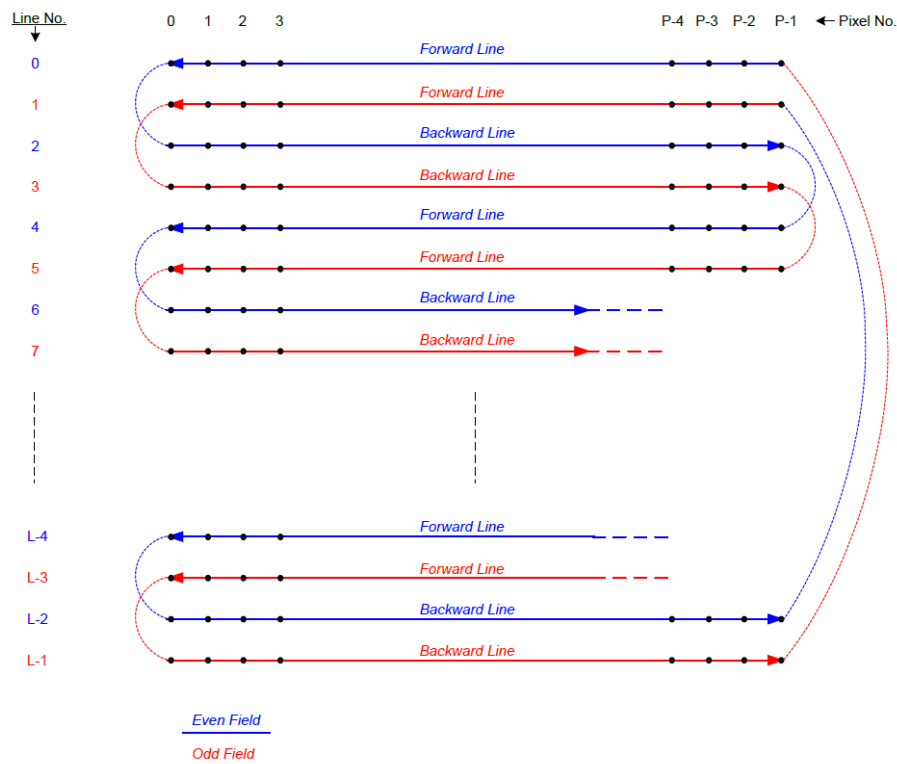


Figure 173. Maradin projection sequence [200].

The micromirror is continuously oscillating horizontally at a frequency of $\approx 10\text{kHz}$ and vertically at 1.8kHz to fulfil the 30Hz frame rate, and its position is monitored by the *Gilboa*. To generate the desired pattern, the pixel activation instants are controlled accordingly. For e.g., if one wants to measure the

limiting points of the FOV, only the pixels 0 and P-1 in lines 0 and L-1 will be activated, i.e., only in these positions a triggering signal will be sent to the external laser driving circuit. [200]

To bridge the pattern generation with the external circuitry, the control board outputs 3 synchronization signals (Figure 174) at an J18 connector marked as GP1 in Figure 170 [200]:

- Vsync: signal that marks the start of an even and odd fields as, respectively, rising and falling-edges. This signal has the same frequency as the frame rate.
- Pixel Out (Active Pixel): signal that provides one pulse for each frame pixel to trigger the laser driver and generate a laser pulse. The breadth of this pulse can be any multiple of 6.25ns (160MHz).
- Active line: signal that is high whenever the scanned line has one or more active pixels.

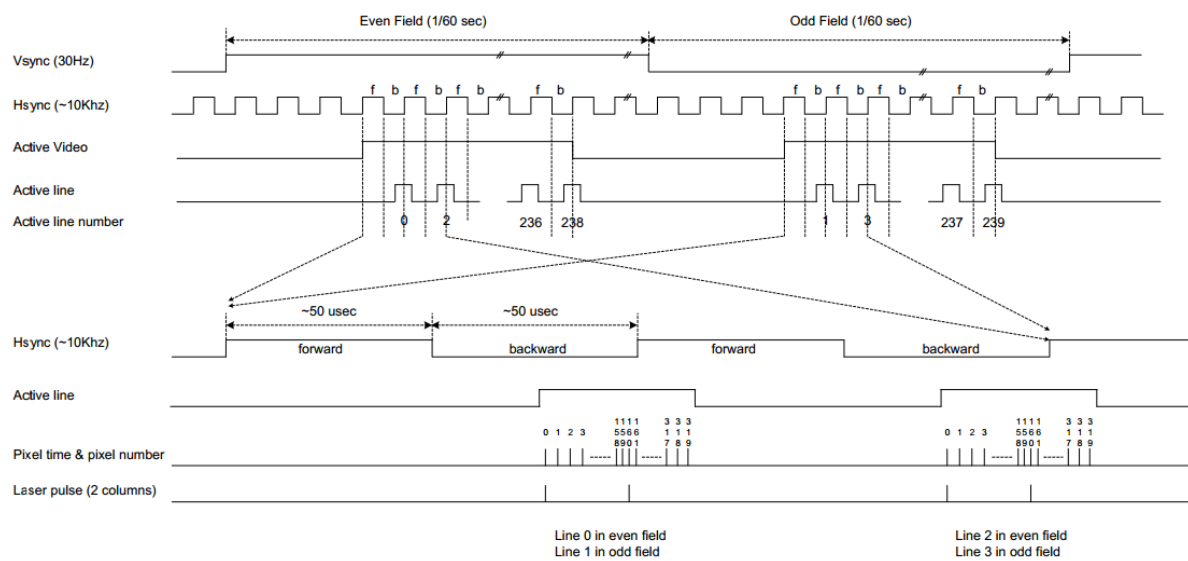


Figure 174. Maradin timing diagram and outputted signals [200].

The implementation of the scanning technique in the LiDAR prototype can be performed as represented schematically in Figure 175. Programming-wise, the initial configuration of the system (TDCs, TIA, DPOT and communication protocols) remains unchanged with the addition of configuring a free pin of the RX MCU as an external interrupt for the pixel activation pulses (*Pixel Out*). Since the triggering instants are now defined by the *Gilboa* board, the PWM for BP_TRIG is deactivated and replaced by an ISR routine that, whenever an interrupt from the *Maradin* is detected, a pulse is sent in BP_TRIG. Posteriorly, the point acquisition cycle initiates. The process to acquire a single point is as follows:

- 1) Reception of *Maradin* pulse (External Interrupt in RX MCU) – Maradin to MSP430FR5969
- 2) Generation of trigger pulse *BP_TRIG* – MSP430FR5969
- 3) Start time counting in TDCs at the falling-edge – MSP430FR5969 to TDC7200
- 4) Add delay and activate laser – UCC27321
- 5) Emission of an optical pulse in the direction set by the micromirror deflection – *SPL LL90_3 & MAR1100*
- 6) Detection of a portion of the sent pulse and conversion to a voltage pulse – DET10A/M;
- 7) Detection of the back-reflected light pulse – SFH 2400 FA;
- 8) Conversion and amplification of the induced current pulse to a voltage pulse – OPA857;

- 9) Leading-edge discrimination of both analog voltage pulses with fixed thresholds to yield the STOP signals – TLV3502;
- 10) Stop the time counting and activate interrupt on INTB – TDC7200;
- 11) Acquisition of the measurement registers from TDCs – MSP430FR5969;
- 12) ToF calculation and storage in the respective position of a matrix – MSP430FR5969
- 13) If the ToF matrix is completed (full frame acquired), send to PC – MSP430FR5969 to PC
- 14) Restart cycle

Rather than storing the results in a matrix at the MSP430FR5969, the measurements can be sent to the PC via UART and organized there. Whatsoever, this implies a superior time-waste in communication. The matrix data can then be represented as a point cloud, where each pixel corresponds to a measured range. The delay induced in hardware does not represent a problem because it is only a time shift that can be considered in the indexation.

The main challenge in this integration process concerns with the indexation of each ToF measurement to the position in the FOV, i.e. the frame matrix. The RX MCU must be capable to identify the beginning of each frame and, from that point, address each result to a micromirror position. A suggestion to overcome this question is to check the signal V_{sync} to detect the beginning of an even field. As each frame starts with an even field, a rising-edge in V_{sync} can be used to initiate a measurement cycle through an additional external interrupt in the microcontroller. Knowing the scan pattern and the frame resolution, and starting from this instant, one can associate each pulse in the *Pixel Out* signal to the respective pixel. During an even field, the ToFs are stored in even lines of the matrix, and during odd fields in odd lines. At the end of each odd field, the interrupt in V_{sync} is re-detected and the process repeats.

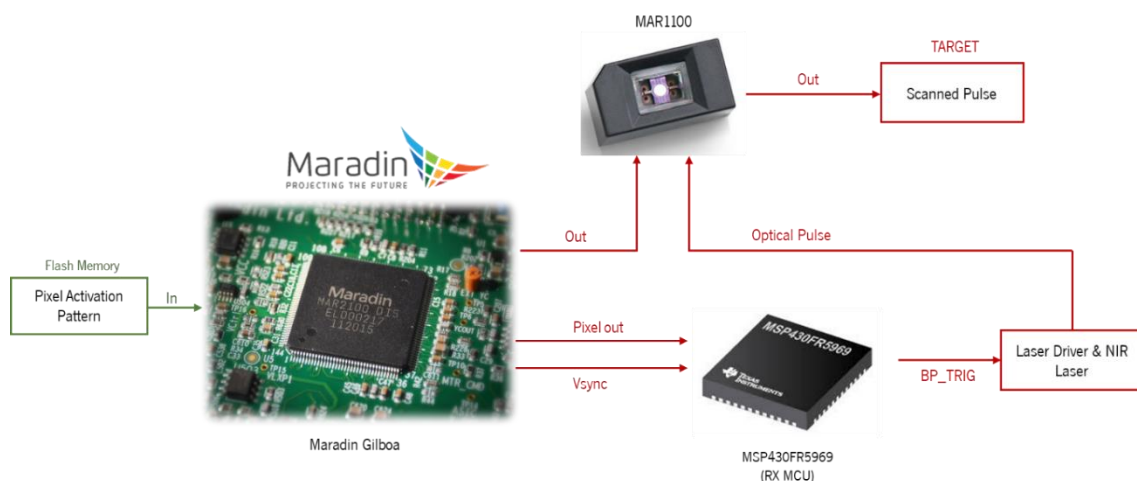


Figure 175. Simplified block diagram of the scanning system integration in the developed sensor. The receiver side remains unaltered.

6.1.3. Projection Testing

The tests to the *Maradin* were not performed directly on the developed prototype since the integration process is lengthy and complex. Additionally, to make the system static, a process of mechanical design and fabrication of holders would be needed to fix and correctly align the optical elements. Rather, the

LiDAR prototype developed during the *INNOVCAR*, a partnership program between University of Minho and Bosch, is used to execute the tests. The referred system also uses a scanning mechanism based on the same module plus the mechanical housing to support the components, designed according to the previously given guidelines (Figure 177a). This prototype was only used to test the projection and the pattern definition.

For these tests, a visible LD was used with a wavelength of 450nm (blue) instead of the NIR LD at 905nm to allow a direct visualization of the projection motif. The two patterns adopted are shown in Figure 176. The first, pattern A, consists of a 900×480 frame where each column of pixels repeats periodically after 6 blank pixels and each horizontal line after 4. Thereby, the total number of active pixels in each frame is 150×120. The second, pattern B, is simply the 900×480 rectangular frame with pixels in contiguous positions, plus two lines passing through the rectangle's center. Both patterns were generated in MATLAB and then flashed one at a time into the *Gilboa* board.

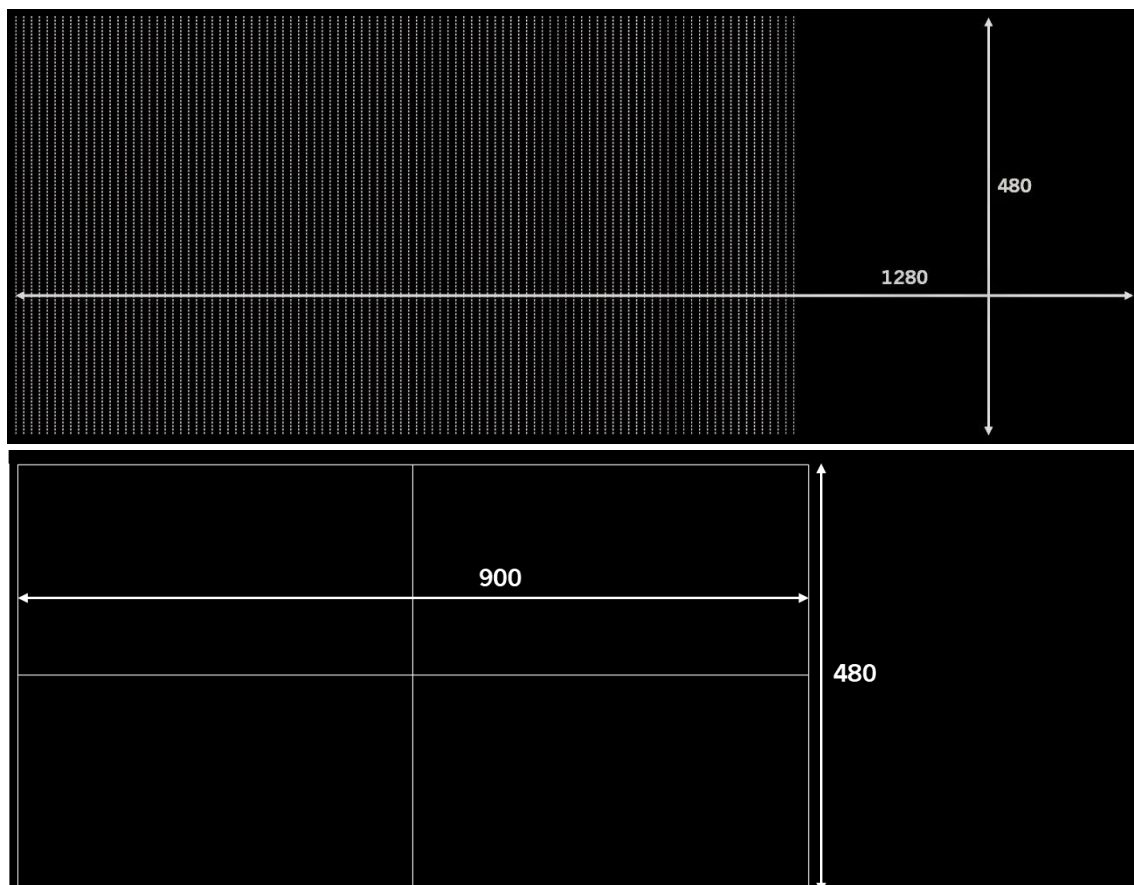


Figure 176. Tested patterns, both with a total used resolution of 900×480 pixels. On top, pattern A, on the bottom, pattern B.

First, the *Gilboa* output signals are tested with pattern A. The *Pixel Out* signal is directly measured from the Pin 1 of the J18 connector (pin number is directly marked on the control board) on the oscilloscope, as shown in Figure 177b before connecting the PCB to the microcontroller unit. The retrieved signal is depicted in Figure 178 during 3 complete scanning cycles.

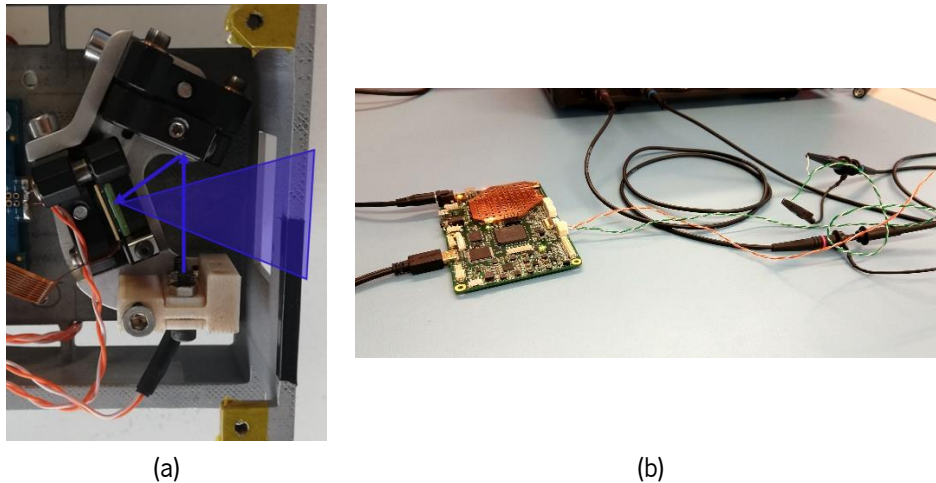


Figure 177. Experimental setup to test the *Maradin* scanning system: (a) emitter of the *INNOVCAR* prototype, designed according to the optomechanical guidelines aforementioned; (b) connection between the *Gilboa* control board and the oscilloscope to measure the *Pixel Out* pin.

The oscilloscope capture shows 6 segments constituted by 152×60 pulses each, corresponding to the activation of individual pixels, even though they cannot be resolved in the used time-scale. Each of this segment is a field (odd or even) and repeats after a cyclic period of 16.67ms, as measured directly on the oscilloscope. This time corresponds to a repetition rate of 59.99Hz. As the fields alternate between odd and even, each pair corresponds to a frame with 152×120 pulses, that repeats at a rate of $1/33.35\text{ms} = 29.98\text{Hz}$. These results validate the nominal specifications of the *Maradin* and never change regardless of the defined pattern.

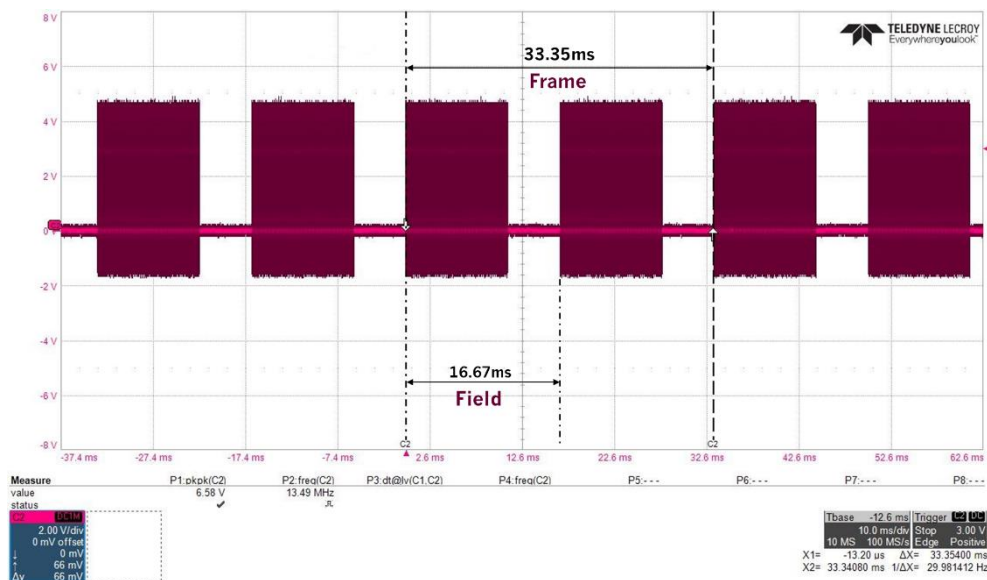


Figure 178. *Pixel Out* signal during 3 complete scanning cycles. Each segment corresponds to a complete field and, therefore, each pair to a complete frame.

Posteriorly, the *Pixel Out* signal is connected directly to the microcontroller of the prototype (*STM32F746ZGT6*, 216MHz clock) and the laser driver (*PLCS-21*) is configured to receive an external trigger generated at the latter. This way, the laser firing instants are synchronized with the *Maradin* pixel activation pulses through an external interrupt. To verify that the MCU recognizes the pulses from the

Gilboa with a width of approximately 20ns, the *Pixel Out* signal (yellow) is monitored simultaneously with the triggering signal to the laser driver (red) – Figure 179. As a result, the pulse can effectively be detected but with a short time delay of around 136.2ns. Furthermore, the microcontroller does not have enough response time to detect all pulses and, approximately 2 in 3 are ignored.

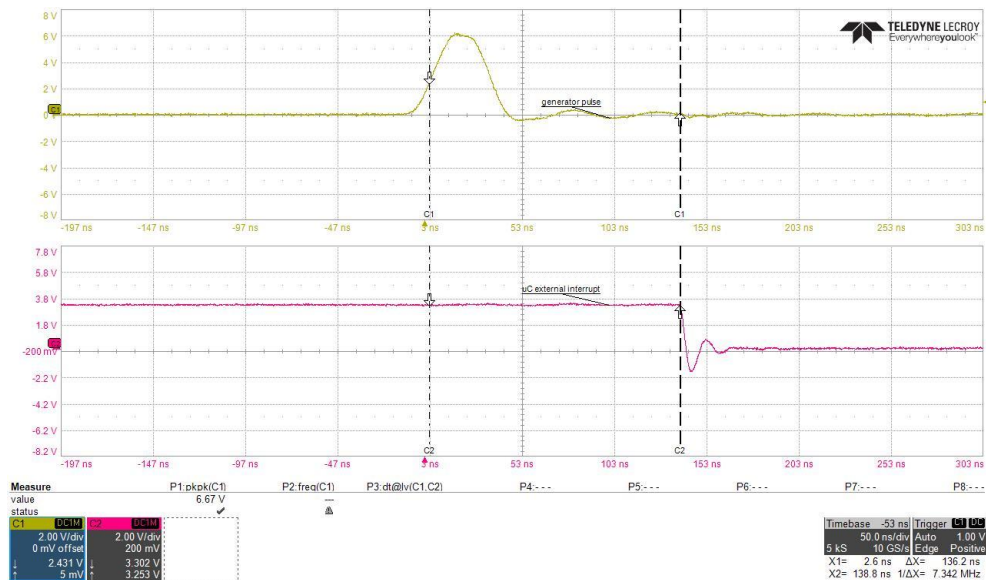


Figure 179. Pixel activation pulse (yellow) versus the MCU external interruption (red). A time delay of 136.2ns is verified between the rising-edge of the first and the falling-edge of the latter.

From these results, one can take several conclusions. First of all, the *Maradin* outputs 5V signals. However, the MSP430FR5969 of the prototype developed herein only accepts inputs up to $V_{cc}+0.3 \approx 3.8V$ [171]. Thus, the signals must be down-converted using, for example, two silicon diodes in series between the *Gilboa* and the RX MCU interrupt pin. When the diodes are forward-biased, the voltage drop across the series will be around $2 \times 0.7 = 1.4V$. Followingly, there are two limitations to the frame rate, the first imposed by the hardware and the second by the LiDAR working principle:

- The MCU CPU frequency: in the prototype, the maximum PRR for the laser is found to be 6kHz, because the MSP430FR5969 needs to read the TDCs before passing to the next point. Hence, and since the micromirror oscillates horizontally at 10kHz, the maximum theoretical horizontal resolution is $0.6 \times 1280 = 768$. To improve this resolution, the MCU clock frequency must be increased to lessen the TDCs reading time and extend the laser PRR (maximum of 12.5kHz). This is only possible if the microcontroller is replaced, since it is already operating at its maximum frequency of 16MHz.
- Unambiguity in measurements: since a single photodetector is used, the system must wait, at each point, for the measurement to be concluded before proceeding to the following. If the maximum range is, for example, 180m, then only after the corresponding ToF of $1.2 \mu s$ the sensor might start a new measurement to guarantee no any other echo will be detected. To better understand this, consider 2 adjacent points, the first at 180m and the other at 0.1m. If a laser pulse is sent to the first and less than $1.2 \mu s$ after to the second, then the second return will be detected first and addressed to the position of the earliest point.

After the electrical authentication, the blue laser beam is projected on a wall at 108cm from the system output. The two patterns are checked and the results are pictured in Figure 180. On the left, the pattern B is shown to verify that the pattern is completely presented through the LiDAR output aperture and centered. On the right, pattern B is illustrated with the width and height marked to determine the FOV. These dimensions are estimated using measuring tape. The horizontal lines cannot be discriminated because the beam is not collimated and, thereby, each pixel is not perfectly punctual. The vertical are discriminated because the spacing between adjacent lines is larger. The FOV can be determined as follows:

$$xFOV = 2 \times \arctan \frac{x}{2d} \quad (6.1)$$

where x is the measured length in the horizontal or vertical dimensions (H or V). Moreover, the angular resolution can also be estimated by simply dividing the respective FOV by the number of points. The results are given in Table 42.

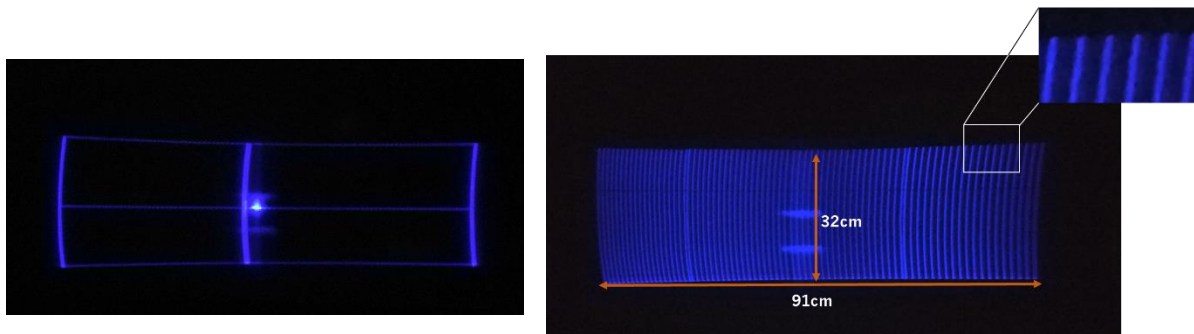


Figure 180. Projected patterns on a wall at 108cm. On the left, pattern A. On the right, pattern B with the width and height marked to calculate the FOV.

With these results, the vertical requirements for L4/L5 vehicles are met. Whatsoever, horizontally the performance is slightly below the specification. The HFOV cannot be increased to the required 50° because it is intrinsically limited by the micromirror morphology. The angular resolutions can be improved by decreasing the spacing between vertical lines. For example, if the latter is decreased from 6 to 3 pixels, the number of horizontal points is extended to 300 and, consequently, the horizontal angular resolution decreased to 0.15° . Withal, this scanning system is still suitable for ADAS to support highway navigation since, in this driving ambience, the FOV requirements are not so strict.

Table 42. Estimated FOV and angular resolutions.

	Horizontal	Vertical
FOV [°]	45.69	16.85
Angular Resolution [°]	0.30	0.14

6.2. Polarization Sensing

Up until this point, the functional system focused solely on the light wavelength and intensity. However, supplementary properties may be examined to extract additional information on the sensor's circumbient, such as polarization. The polarization of light refers to one of the fundamental properties of optical electromagnetic waves and is defined to be the description of the geometrical orientation of the electric field oscillations [201]. Most of the common light sources, such as LEDs and sunlight, produce unpolarized light, meaning that the direction of the electric field fluctuates randomly in time. Whatsoever, the laser sources employed in LiDAR emit polarized light with a well-defined orientation. Depending on the electric field orientation, polarized light can be classified in three types: linearly polarized, in which the electric field is confined to a single plane along the direction of propagation; circularly polarized, in which the electric field rotates in a circle around the propagation direction and consists of two linear components perpendicular to each other with the same amplitude and a phase difference of $\pi/2$; elliptically polarized, in which the electric field describes an ellipse [202]. Additionally, and the most general case to be expected for reflected/scattered light in LiDAR applications, partially polarized light is a mixture of both polarized and unpolarized light.

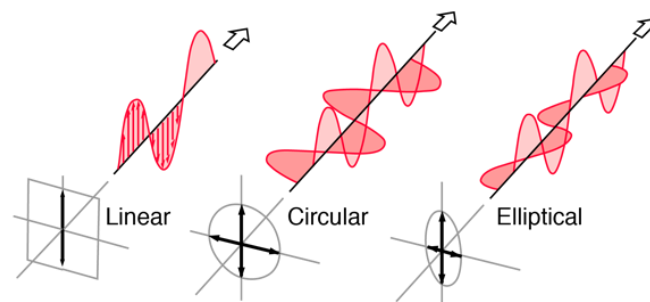


Figure 181. The three states of polarization.

The resolved detection of the return light polarization state in a LiDAR system is sustained by the premise that this property may vary upon light-matter interaction. Considering the initial polarization state of the laser output is roughly fully polarized, as a result of the stimulated emission, the degree of polarization preserved in the back-reflected light will ultimately depend on the hard target (e.g. a car, a wall, a pedestrian) properties, namely the material and surface finishing. Thereby, the clear goal is to complement the ToF measurements with estimations of the polarization state of the returning radiation to subsequently assist material classification in automotive LiDAR systems. This is a topic also explored in the scope of the *INNOVCAR* project and is currently awaiting patenting, whereby no profound reasonings can be given in this document.

The laser output beam is linear vertically polarized (90°) until reflection (initial state), evaluated experimentally by rotating a linear-polarizer until achieving a null output intensity (crossed polarization axis). For this reason, one proposes and validates herein a setup for evaluating the polarization of the returning light in the receiver without any hardware modifications and with minor alterations in the RX optics.

6.2.1. Advanced Polarimetric Imaging

Before establishing the experimental setup, some quantitative polarization measures are executed to demonstrate the alteration of the laser initial polarization state upon reflection on different target materials. Aiming to fulfil this intention, a *Genie Nano M2450* polarimetric camera is utilized to capture images of the beam spot on two targets. The camera sensor consists on a stack of three different arrays (Figure 182a): the superior layer is a micro-lens array to focus the light on the pixels and reduce crosstalk; underneath, a quad-micropolarizer nanowire filter array allows the independent detection of four distinct polarization angles; below, a CMOS sensor converts the received light in an electrical signal to computationally reconstruct the whole frame, in which each pixel is addressed to an individual polarizer element and, thereby, to a specific polarization state. The latter sensor is a *Sony Pregius IMX250MZR* monochrome 8-bits CMOS with a total 2056×2464 resolution (5.1MP). Each pixel intensity ranges from 0 (black) to 255 (white). [155]

The filter array has a 2×2 periodic pattern with four linear polarizers at disparate angles: 0° , 135° (or -45° equivalently), 45° and 90° . Hereupon, the output image is arranged in pixel blocks with the odd lines alternating between 0° and 135° polarization projections and the even between 45° and 90° (Figure 182b). Each 2×2 aggregate constitutes a super-pixel with a total intensity given by the sum of the four individual parts. To obtain an isolated image for an individual polarization state, the 3 remaining pixels shall be rejected, resulting in a resolution loss of three fourths of the original frame (1028×1232). [155]

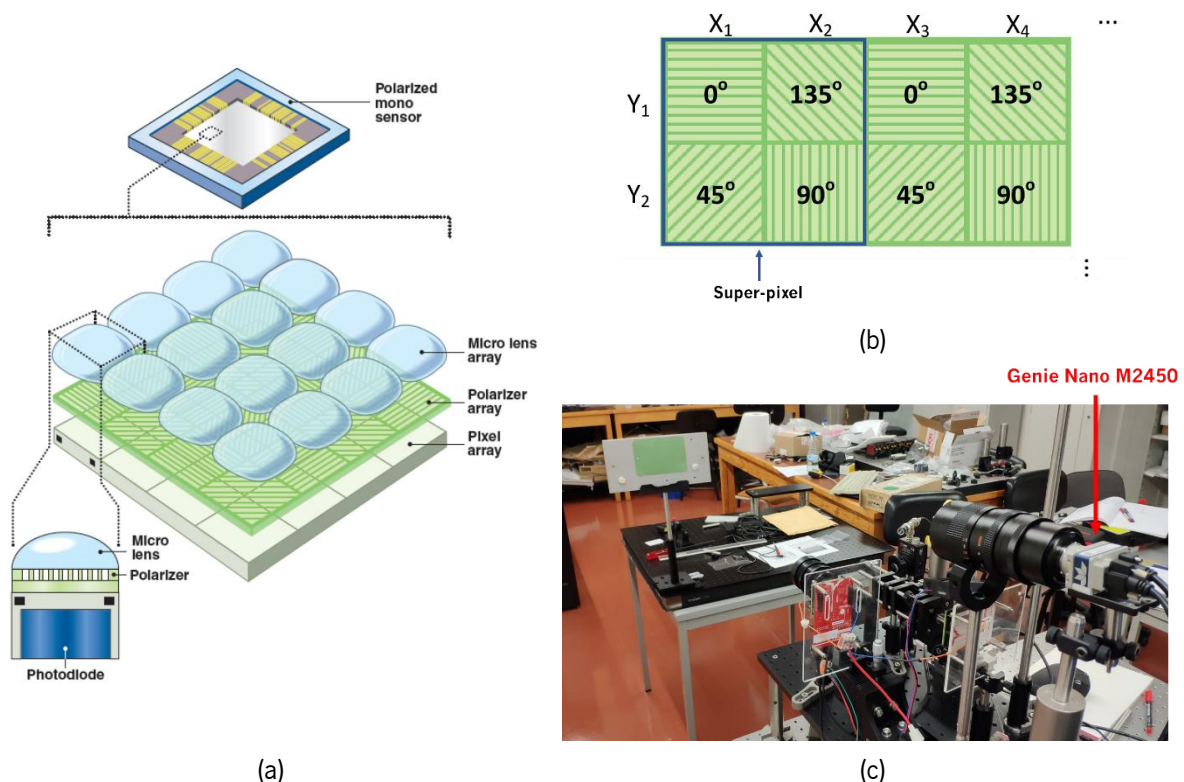


Figure 182. *Genie Nano M2450* polarimetric camera: (a) stack of arrays comprising the sensor, (b) micropolarizers disposal and identification of a super-pixel and (c) setup for polarimetric measurements of the Vauxhall target [155].

Empirically, the camera is mounted on the same optical breadboard as the LiDAR prototype and directed to the target (Figure 182c). The image is constructed on the camera sensor through a C-Mounted zoom-lens (*Goyo GMZ161100MCN*) adjusted to a $f/5.6$ aperture and a 100mm focal length for maximum zoom-in. Since the photosensitive elements are made of silicon, the camera is sensible to wavelengths ranging from visible to NIR. To eliminate spurious components outside the laser spectrum, like unpolarized sunlight, the *Balzers ZWL916* optical BPF is mounted on the lens.

The vertically polarized laser is projected in the targets characterized in the previous chapter: the *K-line white* (diffuse) and the *Vauxhall Green Lemon Grass Metallic*. The targets are placed at 1095mm from the front of the camera lens, evaluated with the rangemeter, to ensure the best compromise between zoom and focus on the beam spot. For the camera to detect solely the diffuse reflection component, the specular reflection on the second target is aligned with the LiDAR receiver. For each target, 12 full-frames with the same exposure time are captured in *Halcon*.

After acquisition, the frames are processed in *MATLAB* to extract relevant polarization parameters. Firstly, the 12 images obtained in similar conditions are averaged to attenuate noise and mitigate possible artefacts. Posteriorly, the resulting images are divided in the distinct polarization states, knowing the pixels disposition within the array. It shall be noted that the camera orientation must be taken into account. For e.g., while taking these measures, the camera is mounted upside down and, thus, the pixels disposal is rotated by 180° . The image processing code is provided in '*Appendix II – Final Codes*'.

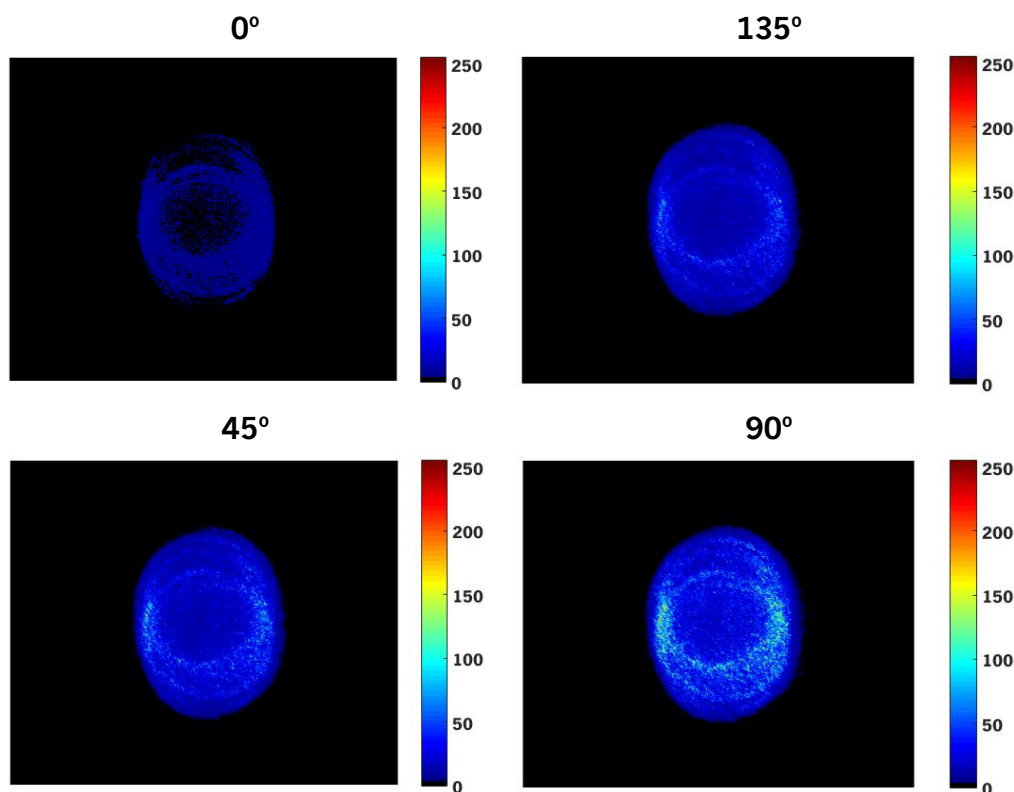


Figure 183. False Color intensity images of the laser polarization states in the region of interest for four angles after reflection on the *Vauxhall Green Lemon Grass Metallic* target.

The resulting 8-bits images are displayed in Figure 183 for reflection in the *Vauxhall Green Lemon Grass Metallic* target. The complete frames were acquired with unitary gain and an exposition time of

6ms, controlled to dismiss intensity saturation and, thus, avoid non-linearity. The peak intensity is found to be 239 for vertical polarization (90°). From these initial outcomes, one may already formulate that the reflected light is for the most part vertically polarized due to the imperceptible spot for 0° , opposing to the high-intensity spot for 90° . Furthermore, the intensities for 135° and 45° are identical owing to the projection of the latter onto these directions.

As for the *K-line White*, the frames were acquired in the same conditions but with a 10ms exposure time, yielding a peak pixel intensity of 200 for a 45° polarization state. The images exhibited in Figure 184 show a uniformity in the intensity for all states and, thereby, one may declare that the reflected light is strongly unpolarized.

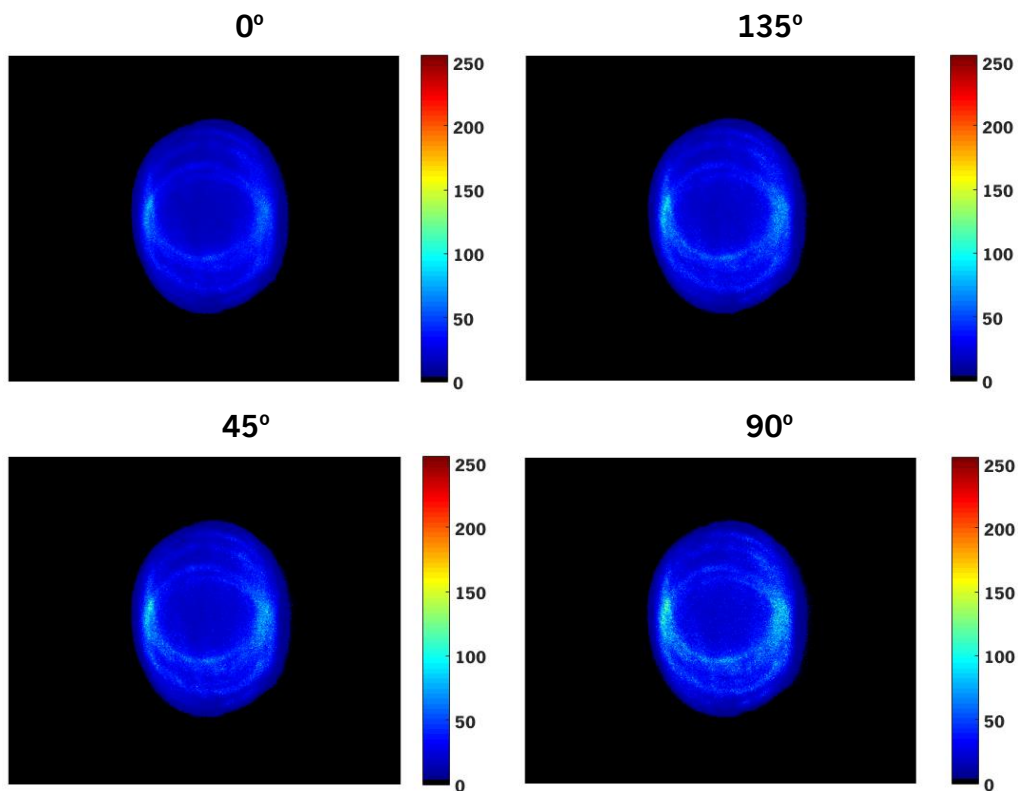


Figure 184. False color intensity images of the laser polarization states in the region of interest for four angles after reflection on the *K-line White* target.

The previous images were taken before optimizing the optical system and show a distorted laser spot profile with two shifted circles, an artefact resulting from a lens misalignment (reflections within the TX optics) combined with the non-zero iris thickness. Nonetheless, this effect does not have a direct influence in these measurements because the qualitative and quantitative changes in polarization do not depend on the laser spatial profile but on its initial polarization state.

6.2.2. Stokes Parameters and Quantitative Analysis

The polarization state of the reflected laser beam can be quantified using the Stokes polarization parameters to support the conclusions drawn in the last sub-section. The Stokes parameters are the appropriate parameters used to describe partially polarized light when the measurement is a sum of

incoherent contributions, as is the case herein. For coherent sums, the physical insight is described by the Jones formalism. For convenience, the four Stokes parameters for a plane wave are arranged in a column vector, where the first element, S_0 , represents the total intensity of light (determined by summing two orthogonal states), S_1 the amount of linear or horizontal polarization, S_2 the amount of linear +45° or -45° polarization and S_3 the amount of right or left circular polarization contained within the beam [201]:

$$S = \begin{pmatrix} S_0 \\ S_1 \\ S_2 \\ S_3 \end{pmatrix} = \begin{pmatrix} E_x E_x^* + E_y E_y^* \\ E_x E_x^* - E_y E_y^* \\ E_x E_y^* + E_y E_x^* \\ i(E_x E_y^* - E_y E_x^*) \end{pmatrix} = \begin{pmatrix} E_{0x}^2 + E_{0y}^2 \\ E_{0x}^2 - E_{0y}^2 \\ 2E_{0x} E_{0y} \cos \delta \\ 2E_{0x} E_{0y} \sin \delta \end{pmatrix} = \begin{pmatrix} I_0 + I_{90} \\ I_0 - I_{90} \\ I_{45} - I_{135} \\ I_{LCP} - I_{RCP} \end{pmatrix} \quad (6.2)$$

In equation (6.2), it is defined that the Stokes parameters are real and measurable quantities that can be directly computed using the intensity data acquired with the micropolarizer camera, for each super-pixel. Whatsoever, to measure the left and right circular components, I_{LCP} and I_{RCP} , a quarter-wave plate would have to be used and, for this reason, it is left aside from the calculations. In fact, S_3 can be neglected because the laser output light is Linear Vertically Polarized (LVP) due to the assembly direction in the prototype. This degenerate polarization state is described by the following Stokes vector, normalized to S_0 :

$$S_{LVP} = S_0 (1 \quad -1 \quad 0 \quad 0)^T \quad (6.3)$$

Besides the calculation of the linear Stokes parameters, the polarimetry measurements in the previous sub-section also allow to calculate an additional parameter called the Degree of Linear Polarization (DoLP) of the back-reflected light. The DoLP can be regarded as the fraction of returning light in a linear polarization state and is quantified by [155]:

$$DoLP = \frac{\sqrt{S_1^2 + S_2^2}}{S_0} \quad (6.4)$$

Furthermore, the Stokes parameters can be shown to be related to the ellipse orientation angle Ψ , also referred to as Angle of Linear Polarization (AoLP) [155]:

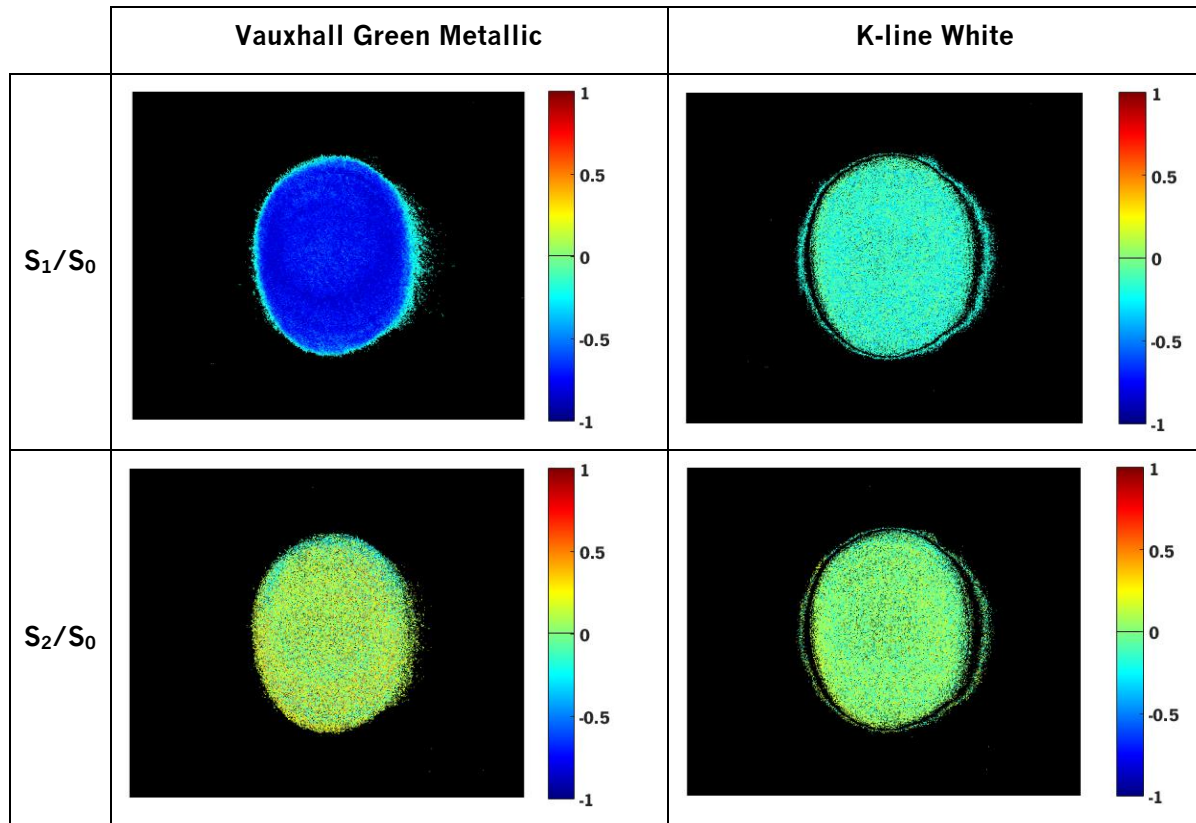
$$\Psi \equiv AoLP = \frac{1}{2} \arctan\left(\frac{S_2}{S_1}\right) \quad , \quad 0 \leq \Psi \leq \pi \quad (6.5)$$

Both parameters can be directly related to the target material properties.

Because the *Genie Nano* camera gives a complete frame, the S_1 and S_2 Stokes parameters are calculated (super)pixel by (super)pixel and represented as a false colormap of the region of interest in Table 43 for both target materials. However, the absolute intensity does not have a physical connotation, and, in fact, the true meaning is encoded in the intensity ratios, whereby both parameters are normalized to the total intensity, S_0 . Since I_{90} surpasses I_0 , the corresponding parameter can take negative values. Similarly, the DoLP and the AoLP are also estimated at pixel-level and represented as a false color image in Figure 185 and Figure 186. Finally, in Table 44, the average values are disposed, as calculated after

data segmentation to extract the area illuminated by the beam spot from background noise. For this segmentation, a mean background noise level of about 2 on the area unexposed to the laser beam is estimated from the raw intensity data. The latter value is then used as an intensity threshold to isolate the effectively illuminated area in both targets (only pixels with intensity >2 are considered in the numerical computations).

Table 43. False color normalized S_1 and S_2 parameters for both analyzed targets in the region of interest.



Starting with the analysis and discussion of the results for the *Vauxhall Green Metallic* target, as expected for reflection on a metallic surface, the polarization state in back-reflection is mostly retained, revealed by the 92% DoLP and the average AoLP of 87.55° . Moreover, these results are coherent with the Stokes parameters. S_1 has negative value on the beam spot because $I_{90} > I_0$, i.e., the back-reflected light is mainly LVP. As for S_2 , its intensity is practically null because the vertically polarized light is equally projected at 45° and 135° angles and because the unpolarized component has the same contribution in orthogonal directions. Ideally for reflection on metals, the returned light should be completely polarized in the same direction as the input. However, slight deviations are observed as there is a non-negligible unpolarized component arising from intrinsic heterogeneities on the target superficial layers. In fact, the metallic behavior in this target is accomplished through small metallic flakes randomly spread across the basecoat, made visible in Figure 104b.

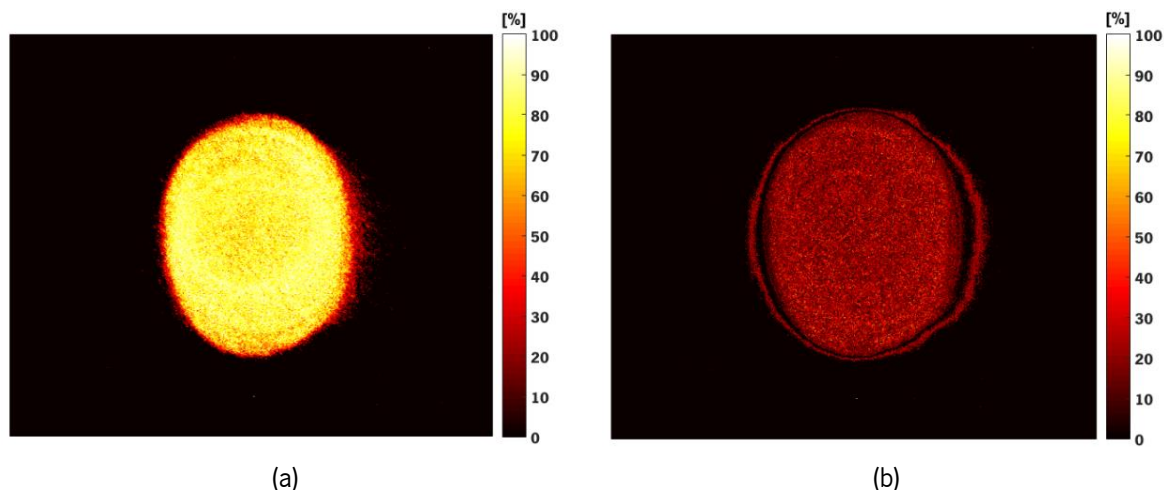


Figure 185. Degree of Linear Polarization in percentage after reflection on the (a) *Vauxhall Green Metallic* and (b) *K-line White* targets.

In what concerns with the *K-line White*, a dominant fraction of the reflected light is unpolarized and cancels itself at normal angles, as demonstrated by the differential intensity S_2 parameter (average of 0). Hence, this material efficiently depolarizes the incident light. Due to the latter reason, the false-color image for the AoLP is not determined owing to the lack of physical connotation. Because unpolarized light implies random oscillations of the electric field, an angle of linear polarization cannot be defined. Nonetheless, the total intensity can be decomposed in the sum of a polarized component, I_{pol} , and an unpolarized component, I_{unpol} :

$$I = I_{pol} + I_{unpol} \quad (6.6)$$

and the AoLP calculated to the former. This calculation is trivial and is not executed at pixel-level. The fraction of approximately 13% of the total intensity still preserve the linear vertical polarization of the initial beam, whereby the calculation for S_7 yields negative results.

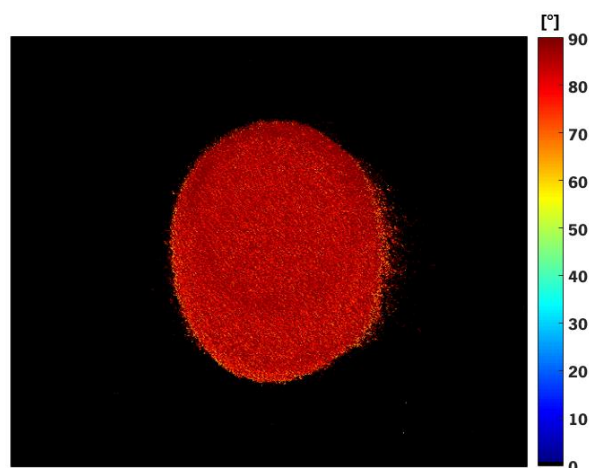


Figure 186. False color image of the calculated Angle of Linear Polarization, Ψ , after reflection on the *Vauxhall Green Metallic* target. Note that the black background region does not represent an AoLP of 0° but the absence of polarization (NaN in *MATLAB*) since it corresponds merely to background noise and not an actually illuminated region.

Table 44. Average values estimated after segmentation. The Stokes parameters are normalized to S_0 .

Polarization Parameter	Vauxhall Green Metallic	K-line White
S_0 (Normalized/Intensity)	1 / 35	1 / 46
S_1/S_0	-0.87	-0.13
S_2/S_0	0.08	0.02
DoLP	92%	13%
AoLP	87.55°	85.27°

Coming to a conclusion, with these results, one demonstrates and confirms that the polarization state of the reflected beam depends on the target material and that this fundamental property of light might be used in LiDAR systems to support classification of target materials. While the *K-line* efficiently depolarizes the incident light, the polarization preserved in the back-reflection in the metallized *Vauxhall* paint reveals an extremely good sensitivity to classify this material (100% theoretical maximum for DoLP).

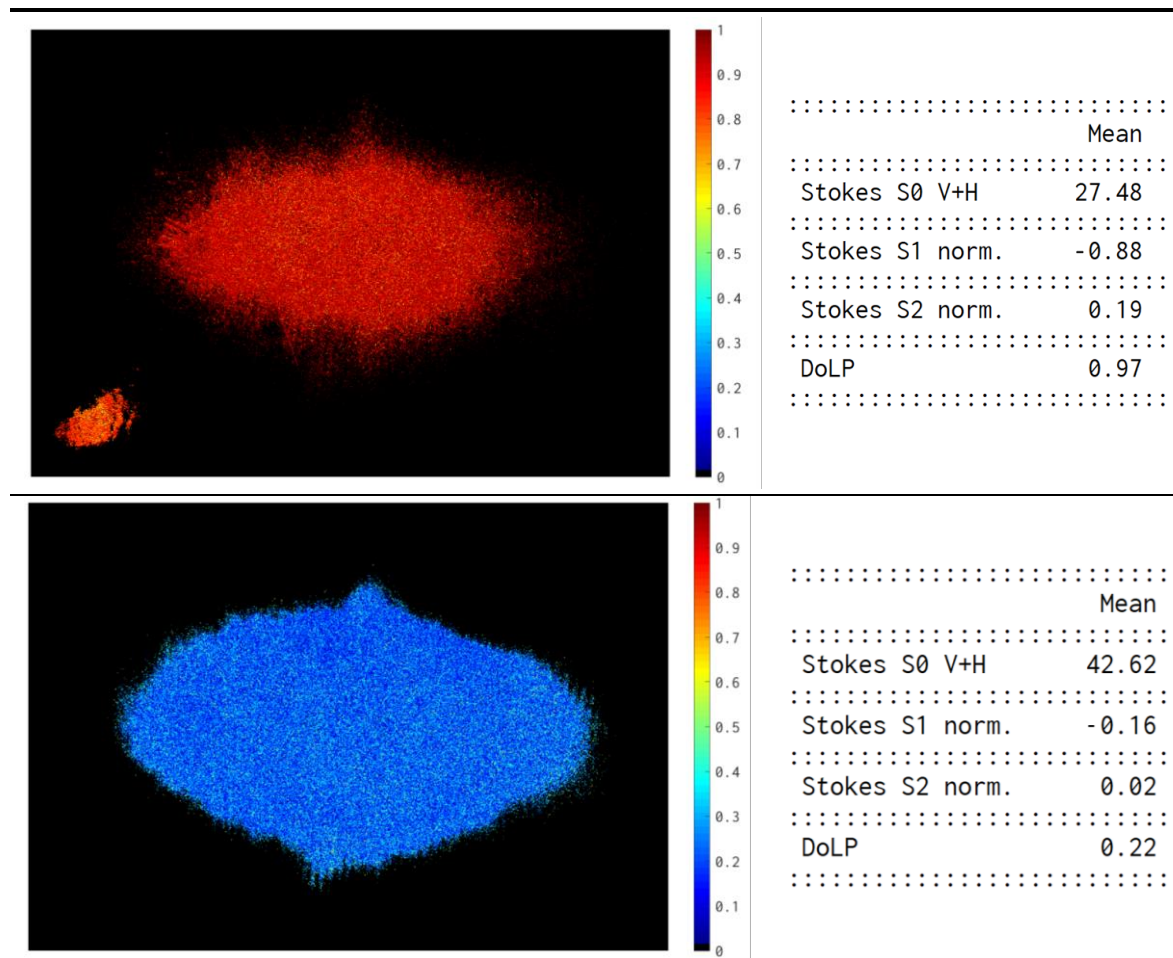


Figure 187. Polarimetric measurements of the DoLP for an optical setup with no internal reflections and no artefacts in the beam spatial profile. On top, for projection on the *Vauxhall* target and on the bottom for the *K-line*. The average results are also presented on the right-side.

The polarimetric camera measurements are replicated with the LiDAR prototype for a comparatively optimized optical configuration to understand the influence of the internal reflections within the TX optical path, between the laser and the output. The results, displayed in Figure 187, demonstrate that the DoLP of the returning light achieves 97% for reflection on the *Vauxhall* metallic target. This computation is in concordance with the independent measurements carried out at University of Minho in September 2017 for another LiDAR prototype, which yielded a DoLP of 98%. Thus, one can deduce that the internal reflections in the optics responsible for the profile distortion affect the polarization throughput and this degradation propagates, reducing the maximum attainable DoLP at the detector. For the *K-line*, the new results yield a 22% DoLP in the back-diffused light.

The previous outcomes reveal that the optical optimization is also important in the definition of the output polarization state. Notwithstanding, the optical setup for these last results is not the final configuration exposed in section 5.2 and the experiments for the newly proposed setup presented followingly are performed with the first non-optimized setup.

6.2.3. Experimental Setups and Results

Although the polarimetric camera allows to efficiently study the polarization characteristics post-reflection, it cannot be conveniently integrated in a LiDAR system. The preeminent goal of the antecedent experiment was just to illustrate in a more tangible manner the proof-of-principle of using the polarization encoded in the back-reflected NIR radiation for material classification.

As explored in section 3.2.5 of the state-of-the-art, several suitable alternatives to detect orthogonal states of linear polarization ought to be adopted. In this situation, the Pockels cell for electro-optical modulation is not needed because the range information is directly encoded on the arrival time of the back-reflected laser pulses and not in the intensity (polarization is only a supplementary measurement).

The simplest solution is using a polarizing beam-splitting element to divide the incoming beam in two orthogonal states and measure them independently with two photodetectors. However, this apparently simple solution comes at an expense of bulkiness and complex calibration and alignment processes. Since the polarization information of interest for material classification is encoded in the ratio of amplitudes in both detectors, it is difficult to warrant that the difference in amplitudes is merely the result of differences in intensities of orthogonal components, and not also a result of misalignments. Moreover, it is also challenging to warrant that both detectors will preserve the alignment during the lifetime of the sensor. On top of this, the PBS duplicates the photodetectors budget, which is critical especially in implementations at 1550nm that require expensive InGaAs detectors. Alternatively, it is possible to use a mechanical apparatus to alternatively place two linear polarizers with crossed transmission axis in front of a single detector. However, this is unconceivable in the targeted context due to mechanical vibrations to which the sensor is susceptible and the mechanism is not fast enough to accompany the LiDAR point rate. Ultimately, and similarly to the polarimetric camera, a photodetector array can be integrated with a micropolarizer grid to directly detect different polarization states using a single FPA and potentiate miniaturization. Whatsoever, this option sacrifices resolution. Although not critical in standard CMOS/CCD sensors with several megapixels, in an FPA with APDs, due to the current

limitation of technology and pixels integration, the decrease in resolution can jeopardize the requirements of the design.

Herein, a third alternative for polarized detection is approached using a liquid crystal (LC) retarder and a linear polarizer to measure the polarization states of the reflected beam in two orthogonal axis straightforwardly with a unique PD. For the polarized detection to be possible with a single photodetector, a combination of a variable wave retarder and a linear polarizer shall be used. The linear polarizer, placed in front of detector, selects the component of the back-reflected light with the same linear polarization as the one prescribed by the orientation of its transmission axis. In the work reported herein, the polarizer is set with a horizontal transmission axis, i.e. at 0° . To measure the amplitude of two orthogonal states of linear polarized light, an element is needed to rotate the plane of polarization of the incoming light by 90° . Thus, a variable Liquid Crystal (LC) retarder oriented with a fast axis at 45° provides a way to neatly alternate between no effective retardation and half-wave retardation (90°) and, ultimately, to intercalate between the measurement of the linear horizontal (LHP) and vertical (LVP) polarization components, respectively.

A photo of the proposed setup is shown in Figure 188 and is composed of a *LCC1223T-A* full-wave LC retarder, an *LPNIR100-MP2* linear polarizer at 0° and an *LA1450-B* focusing lens. These three components are placed between the RX optics of the prototype and an auxiliary *DET10A/M* detector. The latter is used instead of the on-board prototype's photodetector to avoid the inversion and amplitude limitation imposed by the TIA, visible, for instance, in the saturated pulses in Figure 115. The back-reflected light is collected in the RX optics and inputted at the variable LC retarder. Posteriorly, the horizontal polarization component of the arising light field is selected by the linear polarizer and focused on the detector.

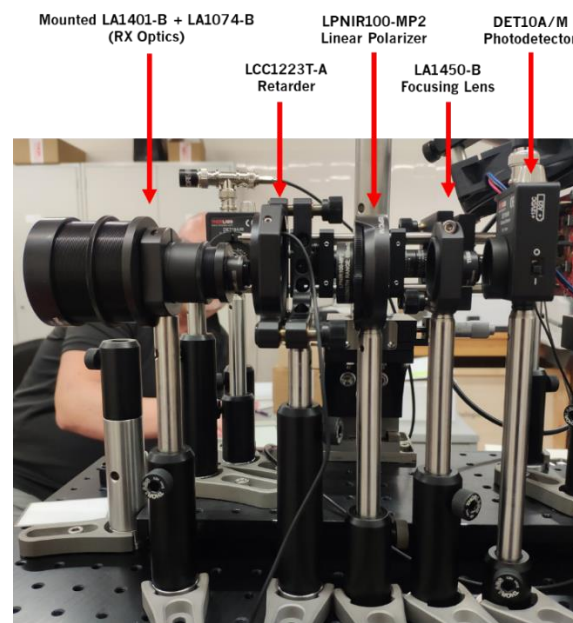


Figure 188. Proposed polarization measurement setup with a single photodetector.

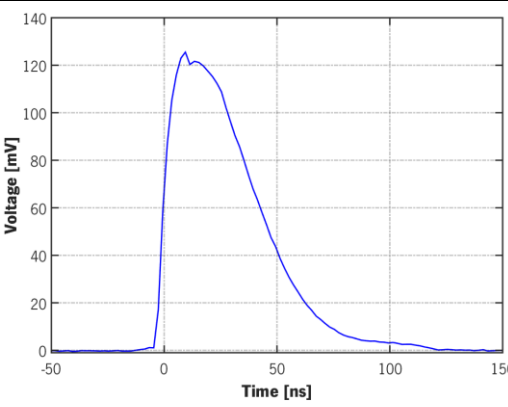
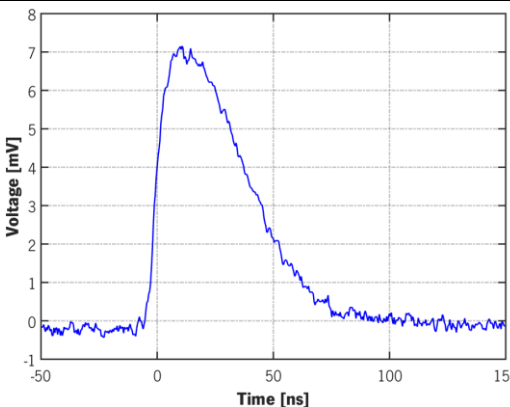
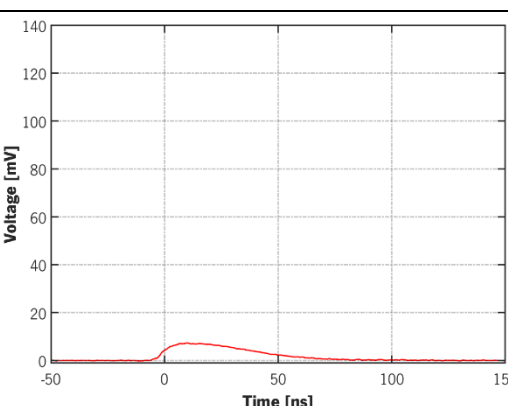
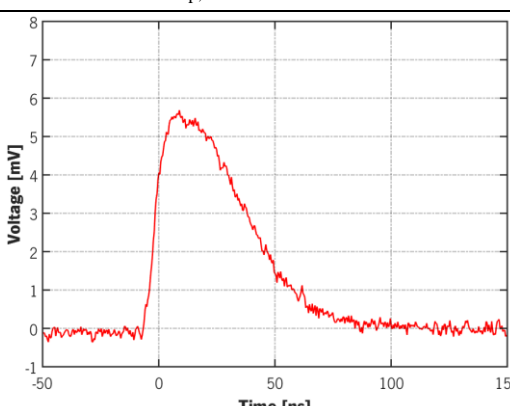
The experiments to validate the optical setup are carried out analogously to the previous encompassing the polarimetric camera. Similarly, the light emitted by the TX board is reflected on the *Vauxhall* and *K-line* targets disposed at a distance $d=1.095\text{m}$ from the sensing unit (front-vertex of RX

optics). The photogenerated voltage pulses respecting each polarization state are acquired on the *Teledyne Lecroy HDO4034* oscilloscope. The pertinent polarization information regarding the raw return light is encrypted on the relative amplitudes of the transduced pulses, proportional to the optical intensity. Eventually, the retained polarization might be roughly computed through the DoLP:

$$DoLP = \frac{\sqrt{S_1^2 + S_2^2}}{S_0} \approx \frac{|I_{90} - I_0|}{I_{90} + I_0} = \frac{|I_{LVP} - I_{LHP}|}{I_{LVP} + I_{LHP}} = \frac{|V_{p,LVP} - V_{p,LHP}|}{V_{p,LVP} + V_{p,LHP}} \quad (6.7)$$

where $I_{90} \equiv I_{LVP}$ is the intensity of the vertically polarized component, $I_0 \equiv I_{LHP}$ the intensity of the horizontally polarized component and $V_{p,LVP}$ and $V_{p,LHP}$ the amplitudes of the acquired pulses. This equation is an approximation of equation (6.4) under the assumption that the reflected optical field partially preserves the initial polarization state (LVP) and, the remaining part is unpolarized with the same projection at 0° and 90° , i.e. S_2 is negligible comparably to S_1 (rough estimation considering the results in Table 44 evidencing a ratio of 1:7). The empirical results achieved with the prospected arrangement are disposed in Table 45.

Table 45. Peak voltage of the back-reflected laser pulses for each target and each selected polarization component. Additionally, the DoLP is also provided. For each material, the pulses are represented at the same scale.

	Vauxhall	K-line
LVP	 <p>$V_{p,LVP} = 125.52\text{mV}$</p>	 <p>$V_{p,LVP} = 7.16\text{mV}$</p>
LHP	 <p>$V_{p,LHP} = 8.42\text{mV}$</p>	 <p>$V_{p,LHP} = 5.69\text{mV}$</p>
DoLP	87.43%	11.44%

To understand more profoundly the operating principle and results, the inner workings and the experimental process shall be detailed. Firstly, the variable retarder consists of a transparent cell filled with a solution of LC molecules and functions as a variable wave-plate. In their nematic phase, the molecules have an ordered orientation, which together with the stretched shape of the molecules creates an optical anisotropy (Figure 189a). When an electric field is applied, the molecules align to the field (Figure 189b) and the level of birefringence is controlled by the tilting of the LC molecules, i.e. by the voltage rms value [203]. The electric field is applied longitudinally to the propagation axis via transparent conductive films and, to minimize effects due to ions in the material, the LC is driven using an AC square voltage generated by the dedicated *LCC25* LC controller [203].

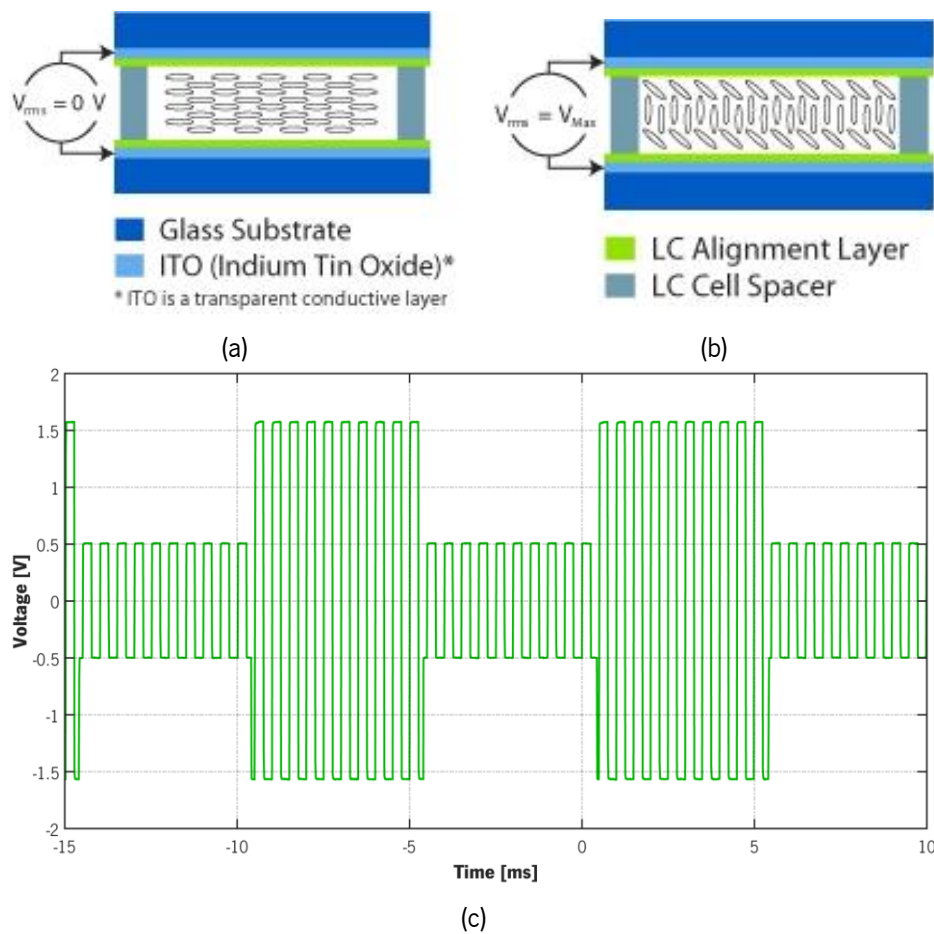


Figure 189. Operation of a Liquid Crystal: (a) when no electric field is applied, the molecules create an optical anisotropy in the media; (b) if an electric field is applied, the molecules tilt according to its intensity, creating birefringence [203]; (c) modulated signal to be applied to allow alternation between horizontal and vertical polarization measurements.

The retardance vs. driver rms voltage transfer curve is directly provided by the manufacturer in [203]. However, this data is only available for 635nm and 405nm. Thus, the adjustment process is executed experimentally using the *Vauxhall* as reflective target, and for an optical alignment corresponding to specular reflection, in order to further minimize the contribution of horizontal polarized light in the detected radiation. The maximum voltage is gradually increased from 0V until a minimum is identified on the oscilloscope directly monitoring the detector's output. For this voltage, found to be 0.516V, the LC does not alter the input polarization state (no retardation). Hence, the linear polarizer blocks the

vertically polarized component to yield a minimum at the detector. Posteriorly, the voltage is further increased until a maximum is detected at 1.556V. In this configuration, the LC acts as a half-wave plate ($\delta=\lambda/4=90^\circ$ rotation), because the LC axis is pre-aligned at 45° , and the beam polarization plane is projected to the horizontal plane (LHP) and transmitted through the polarizer, as portrayed in Figure 190. Hence, alternating between these two voltages, it is possible to consecutively measure two orthogonal polarization components (horizontal and vertical for, respectively, the smaller and higher voltages). The signal to be applied to the LC is then a bipolar square-wave with 2kHz and alternating between $\pm 0.516V$ and $\pm 1.560V$ at a modulation frequency of 100Hz (Figure 189c).

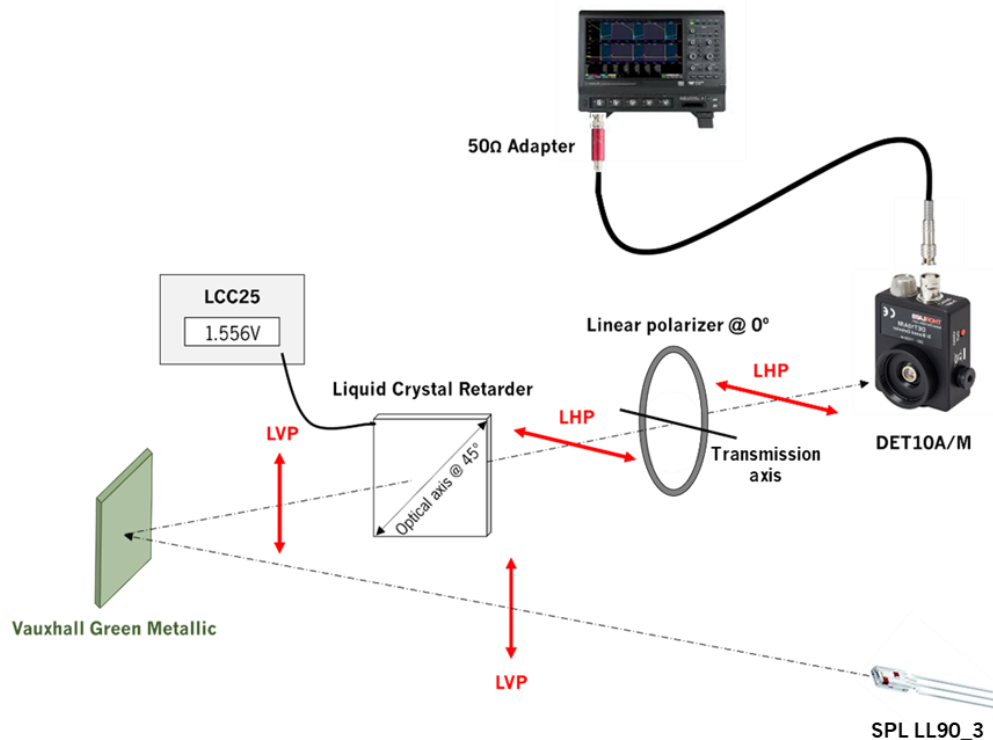


Figure 190. Setup for detection of the vertical polarization component and polarization states on each step of the way for reflection on the *Vauxhall Green Metallic* target. For simplicity, the lenses are not represented because they do not interfere directly in the process. The optical axis of the LC is oriented at 45° to allow the interconversion between linear vertical and horizontal polarization components.

The process for the reflected light on the *Vauxhall* target is elucidated above. The minimum detected voltage is not completely 0V because, as previously seen, the reflected light is not fully polarized and the unpolarized component is still discerned. For the K-line, the incoming light is dominantly unpolarized, whereby an approximately constant intensity passes through the linear polarizer, independently of the LC retardation. Nonetheless, it is still noticeable a small-difference at 1.560V because the small fraction of polarized light is LVP and is rotated 90° to be transmitted to the detector (Figure 191). For the K-line, the amplitudes are considerably smaller only because the total amplitude of the detected signal is smaller.

Numerically, the DoLP evaluated with this setup are self-consistent with the results computed using the polarimetric camera: 87.43% vs 92% for *Vauxhall*; 11.44% vs 13% for *K-line*. These outcomes proclaim the validity of this measuring concept as long as the incoming pulses do not saturate when transamplified. Unfortunately, no further details can be given due to the ongoing patenting process.

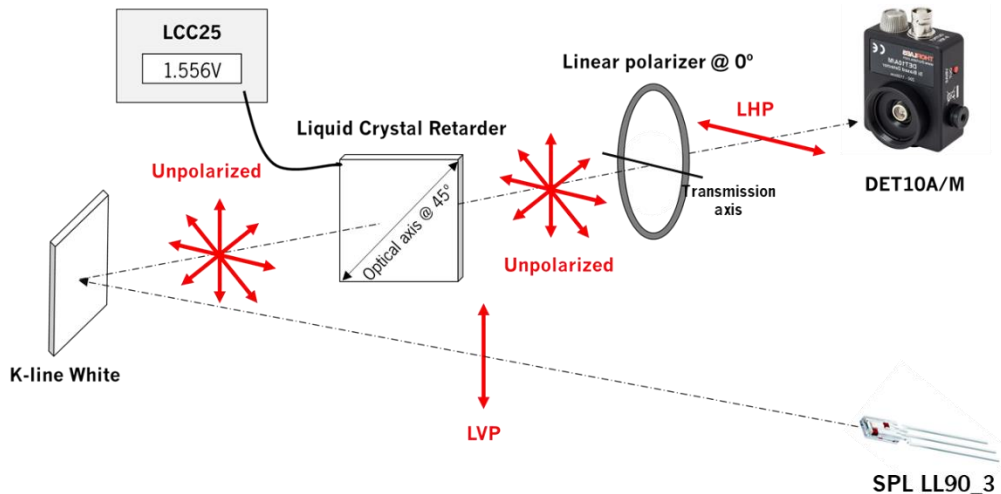


Figure 191. Process for measuring the vertical polarization component for reflection on the *K-line white* target. Since the reflected light is mostly unpolarized, there is always a substantial intensity detected, independently on the LC configuration.

Regarding the hindrances, with the available LC retarder, it is not possible to interface this setup with the prototype receiver because the maximum modulation frequency is 150Hz and, therefore, the alternation between the two voltage, i.e. the two polarization states, cannot be synchronized with the laser PRR. To support that, the LC should have to be commuted with a frequency equal to the laser PRR (6kHz) and completely tuned with the pulses, to yield an effective point rate of 3kHz (biggest disadvantage of this methodology). Moreover, as the LC is AR-coated for visible light from 350 to 700nm, the transmission efficiency is not optimized for the laser wavelength ($T=87.2\%$ @ 905nm) and the amplitude on the detector is deteriorated [203]. Withal, it must be emphasized that this implementation was intentional from the very start and the proof-of-principle is still successfully provided, targeting actual implementations for automotive applications.

6.3. Advanced Timing Discrimination

In the previous chapter, time-walk in the leading-edge discriminator was pointed out as the main source of inaccuracy in the range measurements. This problem precludes the application of a stable and absolute calibration since the timing-point fluctuates with the amplitude of the return signal, i.e., with the intensity of the returning light. As, in principle, the returning pulses are consistent in shape, presenting homogeneous rise and fall-times, the threshold-crossing instant depends exclusively on the signal amplitude. This problem is enhanced in automotive LiDAR, where the dynamic range of the back-reflected pulses can exceed a ratio of 1:1000 and a 1 nanosecond uncertainty reflects in 15cm inaccuracy [73].

Aiming for a highly-accurate detection and for the elimination of the systematic error, an alternative technique is presented and simulated, in which the timing event is insensitive to the level of the optical signal. This technique is denoted Constant Fraction Discrimination (CFD) and consists on triggering a digital STOP pulse at an optimum and constant fraction of the input pulse amplitude to diminish the time-walk. Generally speaking, this linear processing mechanism relies on the conversion of the received

unipolar pulse (only positive voltage values) into a bipolar shape whose zero-crossing instant depends purely on shaping constants. By detecting the zero-crossing point, the timing can be determined accurately. The CFD is electronically implemented and is intended to replace the leading-edge discriminator in the prototype and to interface the transimpedance amplifier with the TDCs.

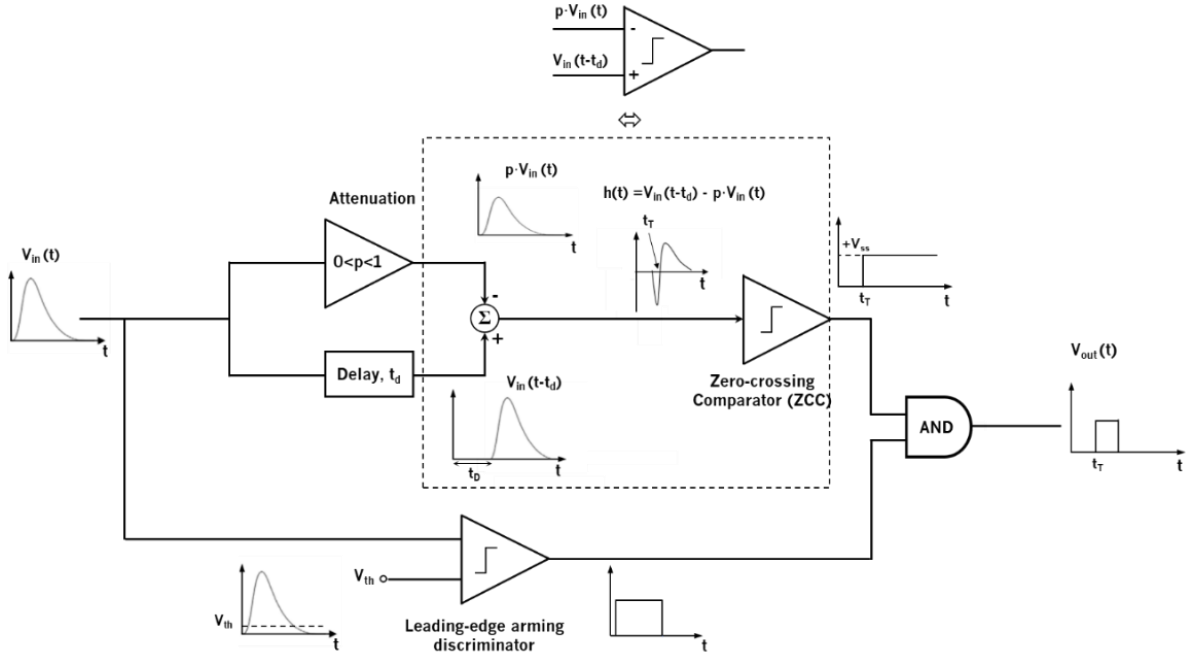


Figure 192. CFD block diagram with a leading-edge arming discriminator. Illustrative pulse shapes are shown on each stage.

The block diagram of the proposed technique is shown in Figure 192 with all the steps needed to carry-out the discrimination. The input is the voltage pulse outputted by the TIA. This signal is initially split equally: one portion is delayed by t_d and the other attenuated by a factor $0 < p < 1$. Then, the latter is subtracted to the former to result into a bipolar waveform expressed in the time domain as: [204]

$$h(t) = V_p(t - t_d) - p \cdot V_p(t) \quad (6.8)$$

where $V_p(t)$ is incoming voltage pulse (*return_analog*). The timing point is ultimately identified by means of a zero-crossing comparator that triggers a digital STOP signal at the same instant the previous signal intersects the zero voltage. Writing the voltage pulses as an amplitude, V_0 , multiplied by a time-varying normalized function, $f_0(t)$ [204]:

$$V_p(t) = V_0 \cdot f_0(t) \quad (6.9)$$

and considering that at the timing instant, t_T , the signal yields:

$$V_p(t_T) = \alpha \cdot V_0 = V_0 \cdot f_0(t_T) \quad (6.10)$$

where α is the constant triggering ratio, one may write [204]:

$$h(t = t_T) = 0 \Leftrightarrow V_0 \cdot f_0(t_T - t_d) = p V_0 \cdot f_0(t_T) \Rightarrow \alpha = \frac{V_p(t = t_T)}{\max(V_p)} = \frac{f_0(t_T - t_d)}{p} \quad (6.11)$$

Thus, the triggering ratio, i.e., the fraction of the amplitude at which the STOP is triggered, is independent on the maximum level of the input, and is only conditioned by the delay and attenuation factors. This relation is only valid when the shape of the input pulses, $f_0(t)$, is uniform and remains unchanged over times, otherwise the timing point fluctuates.

The proposed CFD architecture has an additional arming circuit to limit the resulting digital pulse length and prevent the zero-crossing comparator from triggering on noise inherent to the baseline. Hereupon, input signal is applied to an auxiliary leading-edge discriminator implemented in parallel with the CFD. Then, both the CFD and the auxiliary-arm outputs are fed to the input of a AND-gate. [205]

A possible hardware implementation is presented in Figure 193. The delay line is implemented by a RC circuit that adds a retardation in the order of $\tau=R_I \times C_I$, with a small loss of signal in the resistor. The attenuation is implemented by a voltage divider with a 3-terminal potentiometer (P_1), whose wiper position controls p between 0 and 1. The subtraction of both signals and the zero-crossing detection are performed simultaneously by comparing the attenuated and delayed signals. The previous are inputted, respectively, at the non-inverting and inverting terminals of a comparator IC. Finally, the leading-edge arm is implemented as in the prototype and a 2-input AND Gate compares the discriminated signals.

To physically implement the CFD, the *TLV3502* IC can be used as in the prototype, which includes two high-speed comparators. The potentiometers for adjusting the attenuation and fix the threshold of the arming discriminator can, similarly, be materialized by the *TPL0202-10MRTER*. For the delay to be configurable, the resistor R_I can be replaced by a third potentiometer. The 2-input AND can be, for example, the *SN74LVC1G08* IC. This approach requires minor changes to the current PCBs as one opted to use mostly capacitors and resistors to minimize propagation delays. The $0.1\mu\text{F}$ bypass capacitors are mandatory.

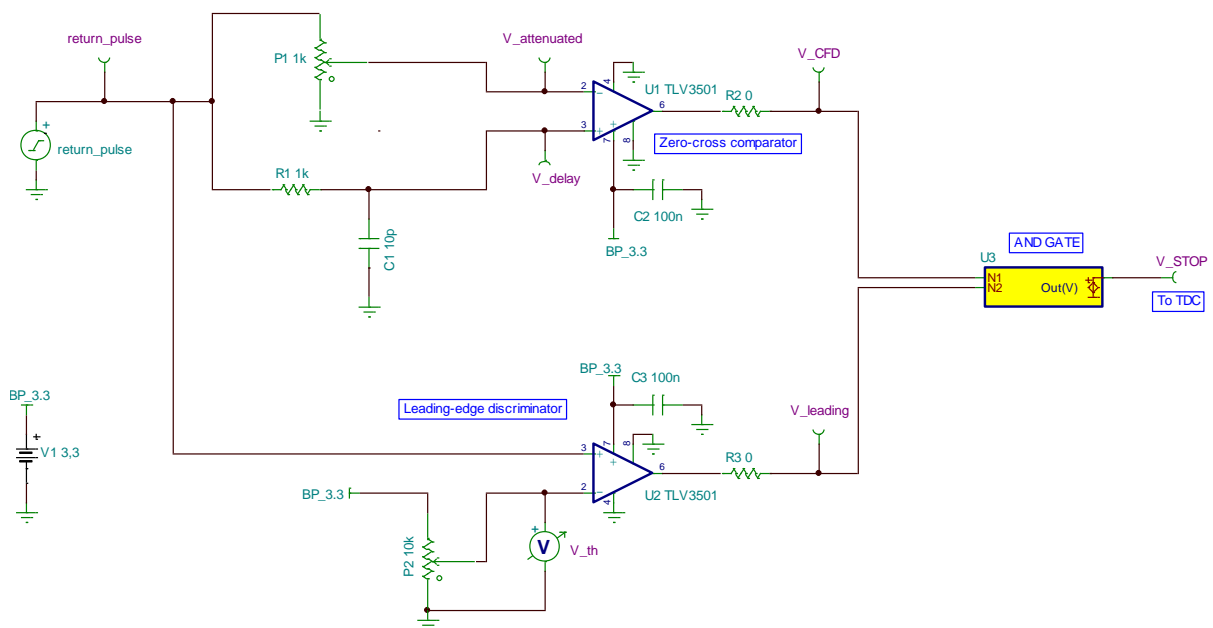


Figure 193. CFD circuit implemented and tested in *TINA-TI*.

To validate the CFD, a transient analysis is carried out in *TINA* with zero initial conditions. As input, a sinusoidal pulse with 80ns duration is generated, since the free-version of this software does not allow to define more complex waveforms. The acquisition contemplated input amplitudes of 0.5V, 0.8V, 1V, 1.2V, 1.5V and 2V to demonstrate the time-walk improvement. Further, different attenuations (0.2, 0.5 and 0.8) and delays (about 10, 20, 30 and 40ns) are also investigated. To alternate between them, R_I is varied between 1k Ω and 4k Ω in 1k Ω increments, and the potentiometer position set to the fraction p . The auxiliary arming discriminator does not interfere with the leading edge of the STOP pulse and serves only as a limiter for the pulse breadth. The threshold voltage, V_{th} , can be defined just above the noise level and it is set to 0.15V. The graph data is transferred to a *.txt* file and processed in *MATLAB*.

In Table 46 and Table 47 are displayed the timing results for each situation aforementioned. The timing point, t_T , is measured from the begin of the pulse at $t=0$. The delay time, t_d , is computed as the difference in temporal instants between the peak in V_{in} and the peak in V_{delay} . The triggering ratio is determined as per equation (6.11). Finally, the maximum time-walk is computed by:

$$\Delta t_{walk,max} = \max_{i=1...4} \{t_T(i)\} - \min_{i=1...4} \{t_T(i)\} \quad (6.12)$$

where $t_T(i)$ are the timing points for each input amplitude.

Table 46. CFD results for three distinct attenuation factors. Highlighted in green, the condition that minimizes the time-walk.

p	V_{in,peak} [V]	t_d [ns]	t_T [ns]	α	$\Delta t_{walk,max}$ [ps]
0.3	0.50	11.00	12.704	0.4784	628.81
	1.00	11.00	12.328	0.4655	
	1.50	11.00	12.075	0.4566	
	2.00	11.00	12.604	0.4751	
0.5	0.50	11.00	21.655	0.7516	282.54
	1.00	11.00	21.750	0.7541	
	1.50	11.00	21.467	0.7470	
	2.00	11.00	21.656	0.7516	
0.8	0.50	10.92	42.404	0.9956	472.31
	1.00	11.15	42.021	0.9969	
	1.50	10.70	41.977	0.9970	
	2.00	11.23	41.931	0.9971	

From the results, one can deduct that, in fact, the timing point occurs at a constant fraction of the input pulse, translating in an utterly small time-walk. The best conditions are found for $p=0.5$ and $t_d=11ns$ and yield a maximum time-walk of 282.54ps for oscillations between 0.5V and 2V amplitudes. Using equation (2.14), this translates in a time inaccuracy of about 4.2cm. Furthermore, the time-delay is increased by increasing R_I . However, it does not increase in the same proportion due to the frequency response of the RC low-pass filter. Generically, its cut-off frequency (-3dB), f_c , is defined as:

$$f_c = \frac{1}{2\pi R_1 C_1} \quad (6.13)$$

The phase shift (equivalent to time delay) introduced in the output signal V_{delay} at this frequency is -45° , where it has a maximum derivate, and varies between 0° for $f < f_c$ and -90° for $f > f_c$. For a constant pulse shape, by increasing the resistance, two effects arise: 1) the cut-off frequency decreases and, therefore, the rate of change of t_d decreases; 2) the signal attenuation increases. For example, between $R_1=1k\Omega$ and $R_1=2k\Omega$, the delay increases approximately 7ns and between $R_1=3k\Omega$ and $R_1=4k\Omega$ increases around 3ns.

Table 47. CFD results for increasing time delays. Highlighted in green, the condition that minimizes the time-walk.

t_d [ns]	$V_{in,peak}$ [V]	t_T [ns]	α	$\Delta t_{walk,max}$ [ps]
11.00	0.50	21.655	0.7516	282.54
11.00	1.00	21.750	0.7541	
11.00	1.50	21.467	0.7470	
11.00	2.00	21.656	0.7516	
17.93	0.50	36.057	0.9881	471.03
18.00	1.00	35.993	0.9877	
17.87	1.50	35.586	0.9851	
18.00	2.00	35.853	0.9868	
22.20	0.50	45.466	0.9772	401.78
21.73	1.00	45.316	0.9783	
21.14	1.50	45.127	0.9799	
21.25	2.00	45.064	0.9803	
24.58	0.50	51.920	0.8925	520.04
24.50	1.00	51.460	0.9005	
24.96	1.50	51.400	0.9015	
24.19	2.00	51.732	0.8976	

In Figure 194, the dependences of the timing point and the triggering ratio on the time delay and attenuation factor are depicted. The effect of an increase in both is practically the same. Primarily, the timing point increases continuously in a linear-fashion because the time during which $V_{attenuated}(t) > V_{delay}(t)$ escalates. As for the triggering ratio, it raises up to 1, corresponding to the timing point at the peak of the sinusoidal pulse, i.e., 40ns. A further increase from this point results in a decrease in α as the timing switches from the leading-edge to the trailing-edge of the pulse. This response is sinusoidal as it follows the pulse's shape, and the inflection point depends on the shaping parameters: $p=0.8$ for $t_d=11ns$ and $t_d=25ns$ for $p=0.5$.

Since the leading-edge of the output STOP pulse is only generated after both the CFD and the leading-edge digital signals have commuted to a high-state, a limitation to the minimum attenuation factor exists. If the CFD crossing occurs sooner than the leading-edge crossing, when $V_{in}(t)=V_{th}$, then the STOP time instant will purely be specified by the latter transition and, therefore, the leading-edge will take over the control as discriminator.

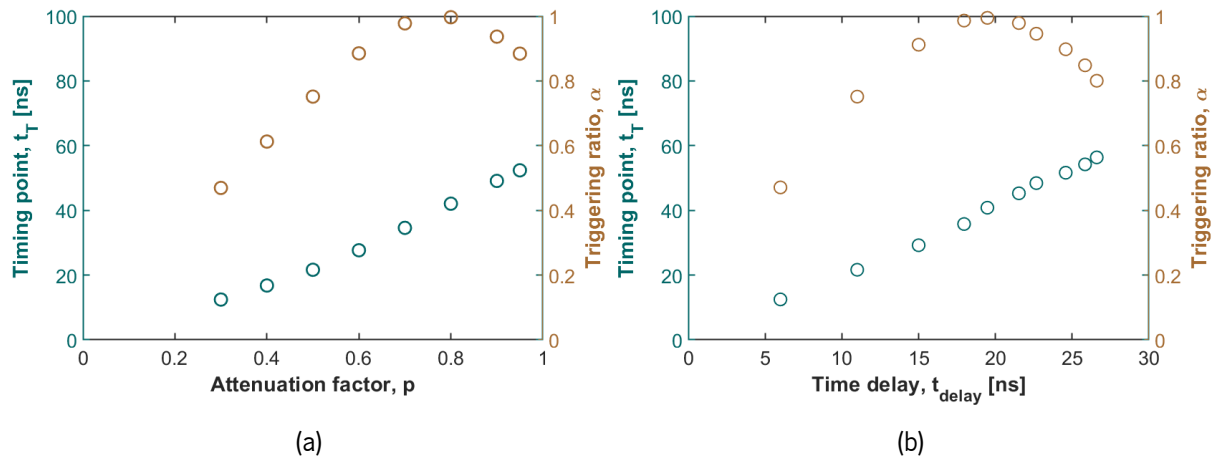


Figure 194. Study of the impact of the shaping parameters on the timing point and triggering ratio: (a) varying p with $t_d=11ns$ and (b) varying t_d with $p=0.5$.

Continuing, Figure 195 features the changes in the input signal with $V_{in,peak}=1.2V$ throughout the whole discrimination in the remarked optimal settings. The CFD output is triggered whenever the delayed version of the input surpasses the attenuated signal. At the same time, the AND output, V_{STOP} , is triggered. The trailing-edge of the STOP pulse occurs when the input drops below V_{th} , thus the complement of the auxiliary arm for temporal limitation of the former. The time-delay between the intersections in the analog signals and the respective digital transitions is around 3ns and is induced by the adopted ICs.

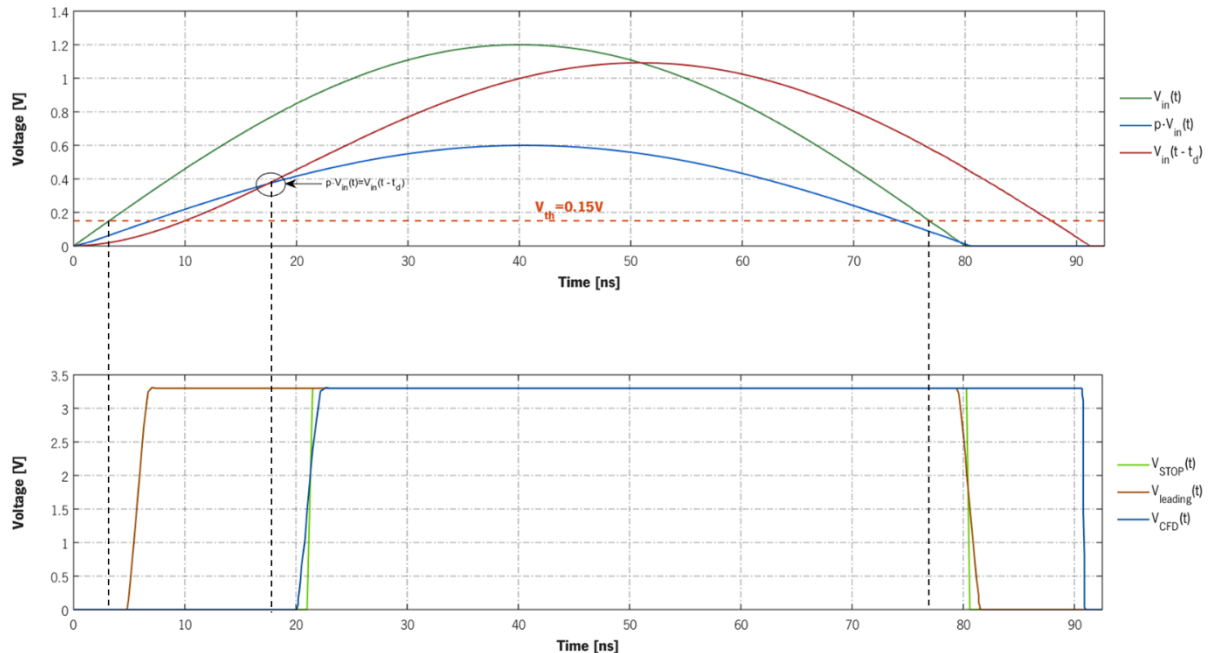


Figure 195. Transient signals for $p=0.5$ and $t_d=11ns$. The input pulse has a 1.2V peak and the graphs are divided in analog (above) and digital (below) signals. The transition points are marked to demonstrate the time delay.

To finalize the proof of appropriateness of this technique, the time-walk is represented graphically in Figure 196. As one can observe, the timing-point does not have a well-defined behavior pattern consonant with the input amplitude. The core fundament arises from the variable resolution adopted by default in

the software, i.e. each simulation is not performed with the same amount of points, inducing a noisy fluctuation/artefact in the results. Nonetheless, it is demonstrated that this technique is a good alternative for discrimination since it essentially removes all the time-walk by detecting the signals at a constant fraction of the peak.

Comparing the leading-edge with the CFD, one uses the pulses with limit amplitudes of 0.5V and 2V. While the first generates a time-walk of approximately 5.85ns for a 0.15V threshold and which expands with an increase in the latter, the CFD results in a 1ps inaccuracy, as calculated using the data in the tables above. Experimentally, the time-walk introduced in the leading-edge discriminator estimated between a return pulse with 1.56V amplitude and 0.86V amplitude is above 5ns, reflecting in a 75cm range difference at an actual distance of 1.204m. Hence, one can conclude that with this discriminator block, one can theoretically achieve submillimetric range accuracies (1ps \rightarrow 0.15mm) arousing a total interest within LiDAR to accomplish a more stable calibration and more accurate measurements. This latter result excels the time-walks reported in [205], [206] and [207], although the average result of 283ps in the best parametric conditions ($p=0.5$ and $t_d=11$ ns), comes closer to the reports.

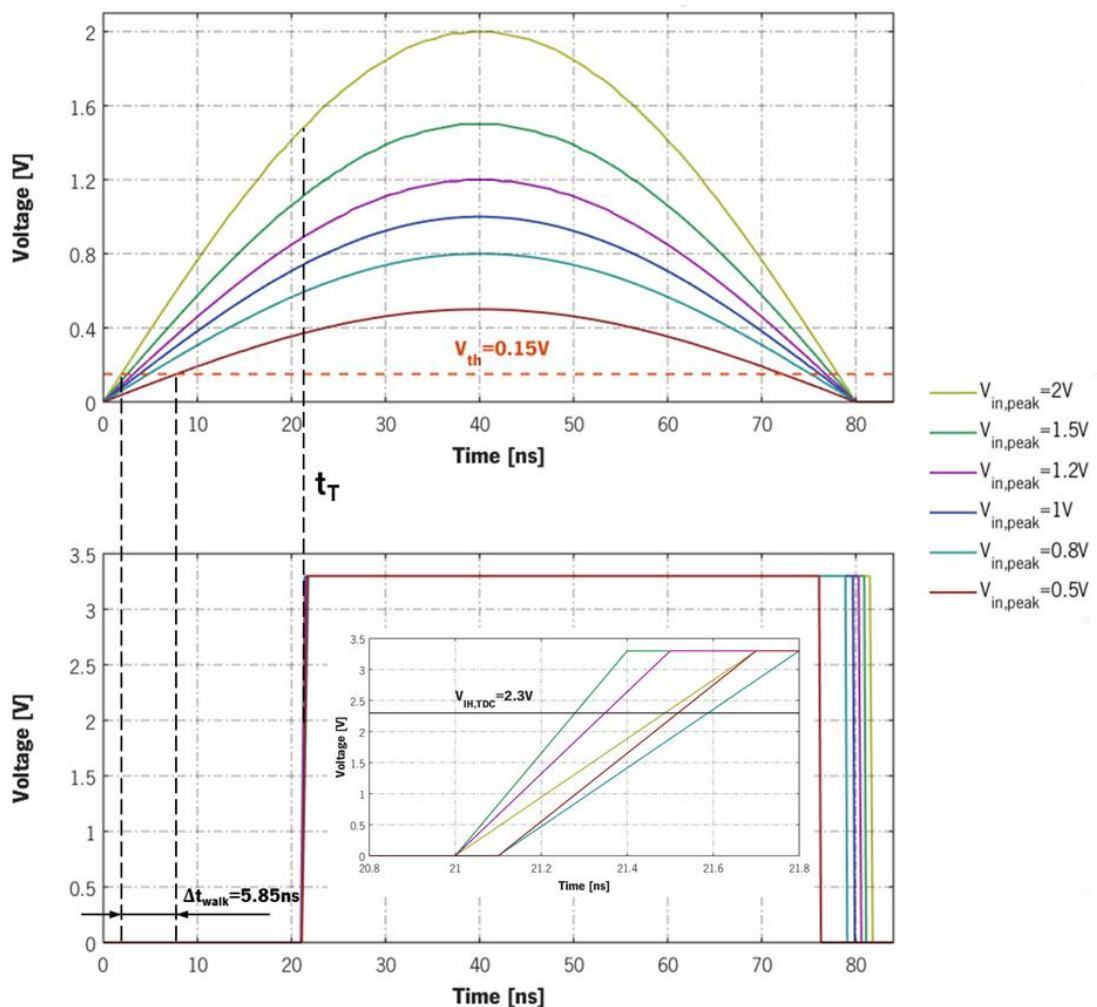


Figure 196. Graphical representation of the time-walk for $p=0.5$ and $t_d=11$ ns. On top, the input sinusoidal pulses with amplitudes from 0.5V to 2V. On the bottom, the corresponding STOP signals, with emphasis on the zoomed-in leading-edge transition. Complementary, the time-walk between the limit amplitudes for a leading-edge discriminator with $V_{th}=0.15V$ is also pictured.

Notwithstanding, the CFD does not eliminate the fluctuations induced by the jitter sources identified in the previous chapter and the statistical fluctuations around the average ToF will persist, even though they do not arise originally from the discriminator. In this scenario, the accuracy might be mainly limited by the system precision and, since the quantification of section 5.1.6.2 depends on the time-walk, it will no longer be valid and must be redone.

Another factor that is patent in Figure 196 is the STOP signal width. Although the timing of the leading-edge is the central concern, since it ceases the time count, the digital pulse width must be enough to meet the *TDC7200* specifications. With this CFD circuit and conditions, the 10ns minimum [168] is safeguarded. In fact, for $V_{in}=0.5$, the STOP width is around 54ns, using as triggering point the crossing point at $V_{in}=V_{IH,TDC}=0.7 \times 3.3 \approx 2.3V$, where $V_{IH,TDC}$ is the voltage input high of the TDC [168].

Three final aspects regarding the CFD application in the developed prototype must be remarked. First, the returning pulse in the current architecture is inverted, i.e., it has a falling-edge as leading-edge. Yet, the previous reasoning and functionality is still applicable. Second, the detection of the sending events in the reference path is performed approximately at a fixed point and, since the emitted laser pulses are uniformly-shaped and with nearly-constant amplitude, the timing with the leading-edge discriminator is consistent. For this reason, this technique needs only to be applied at the receiver. Finally, the CFD is a linear technique and the pulses morphology must be steadily maintained. During the light flight through the atmosphere and at reflection, only linear effects take place. Notwithstanding, the pulses may be distorted at the receiver due to saturation in the TIA. Thus, for the signal to be processed in a strictly linear manner in the abovementioned dynamic range, an Automatic Gain Control (AGC) mechanism is mandatory at the TIA to adjust the amplification gain to the dynamic of the returning pulse and prevent amplitude saturation. At low input currents, the gain must be high to obtain enough voltage and low noise. At high input currents, the gain must be low to prevent saturation. Currently, there are already a few ICs that completely integrate this control and a few of them are exposed in Table 48.

Table 48. Examples of Transimpedance Amplifier ICs with integrated AGC and respective specifications. The electrical current values are peak-to-peak (N/S-Not Specified).

Model	Manufacturer	Gain [Ω]	Bandwidth @ -3dB [Hz]	Dynamic Range In	Power Dissipation	Ref.
TZA3036	<i>Philips Semiconductors</i>	0.10-69k	0-160M	0.18 μ A-1.5mA (\approx 1:8300)	300mW	[208]
S3095	<i>AMCC</i>	100-3.3k	28k-11.5G	60 μ A-2.2mA (\approx 1:360)	900mW	[209]
M02014	<i>Mindspeed Technologies</i>	200-11.1k	28-2.1G	5.3 μ A-8mA (1:1500)	N/S	[210]
ONET8531T	<i>Texas Instruments</i>	Up to 4.5k	30k-10G	Up to 3.5mA (minimum N/S)	100mW	[211]
MAX3797	<i>Maxim Integrated</i>	Up to 5.5k	12.5k-7.7G	Up to 5mA (minimum N/S)	105mW	[212]

Within the given options, the *TZA3036* is spec-wise the most apppellative due to the superior dynamic range that covers the expected pulses' dynamics. Regarding the bandwidth, it is inferior to all the other ICs but, yet, using equation (2.29), it yields a response time, t_r , of 6.25ns. As the laser rise and fall times are, at least, 7ns, with this choice one still guarantees that the TIA can respond with full amplitude to the incoming pulse and no distortion occurs. The AGC block diagram is shown in Figure 197a. It essentially is a feedback loop with a peak detector that spots the amplitude of the output signal and regulates the feedback gain resistance so that the amplifier remains linear [208]. The resistance is implemented using a MOS transistor operating as a voltage-controlled resistor. When the AGC is inactive, the transimpedance is at its maximum [208]. The details and technicalities on how this amplifier should be integrated are not explored herein because it is outside the scope of the project.

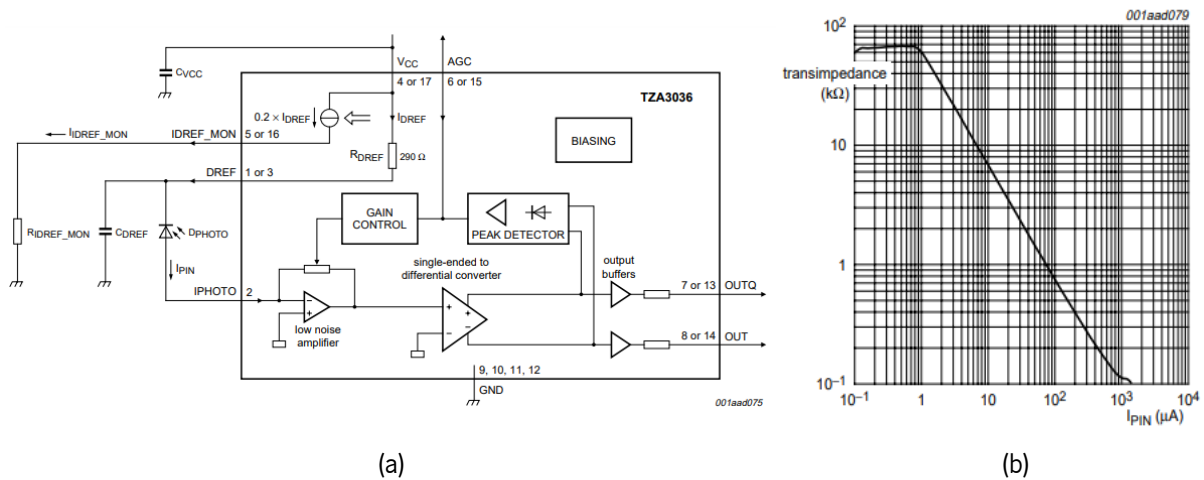


Figure 197. *TZA3036* AGC integrated circuit. In (a) the block diagram. The photodiode is connected directly to the *IPHOTO* (2) pin and is reversely biased by V_{CC} . The output is at the pin *OUT* (8 or 14). In (b), the transimpedance response in $k\Omega$ as a function of the PIN photogenerated current in μA . [208]

To consummate the analysis, it is meaningful to keep in mind that the CFD is a well-known signal processing technique whose application to overcome time-walk artifacts resulting from leading-edge discrimination traces back to the 1960s, during a time in which the electronics to time ionizing radiation in Nuclear Instrumentation Modules (NIMs) were being developed [206]. Posteriorly, after its pioneer adoption in NIMs, the CFD was also transported to the detection of photons by the technique of single photon timing, more commonly known by the earlier term time-correlated photon counting [213]. Nowadays, the enhancement of this technique is still being pursued, with several articles reporting applicability mainly in nuclear and particle physics [214] and medical imaging [205] to determine the arrival time of particles.

– This page is intentionally left blank –

Part III
Epilogue

– This page is intentionally left blank –

You must live in the present, launch yourself in every wave, find your eternity in each moment.

Fools stand on their island of opportunities and look toward another land.

There is no other land, there is no other life but this.

David Thoreau in *Walden*

– This page is intentionally left blank –

7

CONCLUSIONS AND FUTURE WORK

In this culminating chapter, the final considerations regarding the work developed throughout this dissertation project are presented. Supplementary, the main aspects to be improved are identified seeking for its addressment in a future prototype.

7.1. Conclusions

In recent decades, autonomous driving has been ceasing to be a futuristic idealization and has been emerging as the fresher and most auspicious revolution within the automotive industry, aiming to address the problematics arising from the exponential growth in mobility induced by the global development trends in modern society. The increase in vehicle's automation through the gradual introduction of ADAS and, ultimately, fully autonomous driving is expected to extensively lessen road accidents and make driving safer, by gradually removing the human driver from the equation, to reduce atmospheric emissions, by optimizing the traffic flow, and to accompany the population ageing, by broadening the accessibility. On the other front, car-sharing has also been growing day-by-day as a complementary solution to reduce the impact of road transportation.

To handle and standardize the technicalities regarding autonomous vehicles, the J3016 standard was formulated and it stratifies autonomous driving in six levels ranging from no automation (Level 0) to a fully self-driving vehicle (Level 5). To progress to high-automation levels (4 and 5) and remove the onus from the human driver, there is a need to provide the vehicle with the required situational awareness by accurately detect and define the relative positions, dimensions and movement of targets in the vehicle's circumambient (obstacle tracking and detection). This will be made successfully possible through the synergistic implementation of artificial vision cameras, Radars and LiDAR since neither sensor absolutely covers all driving scenarios by itself and each of them plays a leading role within different occasions. These technologies must work in tandem (sensor fusion) to provide robust, reliable, resilient and redundant real-time data, to support safe driving decisions.

In the roadmap towards autonomous vehicles, LiDAR has been pointed out as a key-enabler as it bridges the resolution gap between cameras and Radar, it is resilient to background illumination (efficient either during day and night) and it can furnish a topographic map with distance estimates to objects in the surrounding environment up to several dozens of meters (>200m). Nevertheless, the impact of weather conditions utterly deteriorates the reliability under harsh weather conditions.

Hereafter, and considering the relevance of LiDAR within the aforementioned context, the primary purpose of this dissertation project consisted on the development of a LiDAR sensor to validate the direct ToF measurement concept, obtain empirical know-how concerning test procedures and identify critical points limiting the sensor's performance. Therefore, in the first stage and before projecting the sensor, a bibliographical endeavor was conducted aiming to acquire fundamental knowledge and provide a deep conceptual understanding on the foundations of LiDAR technology.

Generically, the physical principle of LiDAR consists on a laser source emitting optical waves to the circumambient within a determined FOV. Whenever the light interacts with a target, a portion is reflected/scattered at its surface and returns to the receiver, depending on the target's reflective properties. By detecting the changes in the echoed signal, some properties of the object can be inferred in real-time, namely its position relatively to the sensing unit.

Concerning the suitable application in autonomous vehicles, the sensor must obey a strict set of requirements regarding performance metrics and operation. The vital requisites were deduced in the theoretical background from typical driving ambiances. One concluded that, in order to prevent any kind of situation that can jeopardize the occupants' safety and allow timely decision-making, the sensor shall range above 180m, within a FOV of at least $50^{\circ} \times 9^{\circ}$ at ≥ 10 FPS and with a resolution of $0.15^{\circ} \times 0.5^{\circ}$ (H×V). Furthermore, the light source shall be classified as Class 1 under the IEC 60825 standard and must fulfill the imposed eye-safety requisites to avoid damage to biological systems. Other technicalities to contemplate are the hermetically sealed housing with electromagnetic shielding, to prevent interference from external sources and withstand environmental conditions, and a temperature control and stabilization system, to avoid thermal gradients within optical elements and ensure that the components operate inside the limit ratings.

Subsequently, several techniques for range estimation using lasers were detailed, from which Frequency Modulated Continuous Wave (FMCW) and direct Time-of-Flight (ToF) were highlighted as the most auspicious due to the potential to meet the specified requirements. In the former technique, the frequency of a continuous light field is swept across a determined range and the distance to the target is retrieved indirectly from the frequency shift between the transmitted and received fields, measured in an interferometric scheme. In direct ToF, the distance is directly computed through the delay between sending and receiving events of a laser pulse. Comparing both techniques, direct ToF is more straightforward and allows for greater peak powers, potentiating stronger return signals and higher upper distance limits, contrary to FMCW in which the light is continuously emitted to the circumambient and the fundamental distance is imposed by the unambiguous range. On the other hand, FMCW employs coherent detection, yielding the capacity to additionally estimate the target's speed through the Doppler shift, to grant resilience to interference and to theoretically accomplish substantially enhanced accuracies (sub-micrometrical).

At last, the fundamental constituent blocks of a generic system were individually studied, aiming to survey and compare the technological alternatives. Usually, the radiation wavelength is selected in the NIR in a compromise between minimization of background solar irradiance and costs. Two preeminent wavelengths are adopted by automotive LiDAR manufacturers, both corresponding to local minimums in the solar spectrum at the Earth's surface: 905nm and 1550nm. The most commonly employed wavelength is around 905nm, motivated by the larger availability of inexpensive laser sources and silicon photodetectors, in turn, due to the maturity of fabrication technologies for this semiconductor. Nevertheless, the 1550nm spectral range is safer for human-vision and lasers with much more radiant power can be used, although it requires costly InGaAs detectors. As for photodetection, there are several available types of solid-state detectors, namely SPADs and the APDs, with internal gain mechanisms induced by avalanche multiplication, and PIN photodiodes, with no internal gain. Naturally, the latter option restricts the sensor sensibility to shorter ranges. After photodetection, the current signal is converted to a voltage pulse and amplified, to posteriorly be sampled by an ADC or to be discriminated and trigger a STOP event to a time-to-digital converter, allowing the estimation of the effective ToF in a microcontroller unit or FPGA. Additionally, an optical system at the transmitter collimates and shapes the output beam to reduce divergence and maximize the power delivered to the target and, at the receiver, a set of optical lenses collects the back-reflected light and focuses it on the photosensitive element. To minimize the effect of the light component caused by solar radiation and increase the SNR, optical filters are applied on the glass cover to selectively transfer and reject spurious radiation outside the employed spectral band.

Followingly, a survey on the state-of-the-art LiDAR sensors for the automotive industry was undertaken to give the bigger picture on the current panorama, understand common characteristics and verify if the market offer accomplishes the requisites for level 4 and 5 automation. The leading presences and contributors in the market were identified to be *Velodyne*, *Quanergy*, *Innoviz*, *LeddarTech*, *Valeo* and *Continental*.

Among the researched sensors, one identified that, at the moment, the most apppellative solution spec-wise is the *InnovizPro*, ranging up to 150m with 3cm accuracies and scanning the beam with a MEMS micromirror over a $73^{\circ} \times 20^{\circ}$ FOV, at 20FPS and with a $0.15^{\circ} \times 0.3^{\circ}$ resolution. Whatsoever, nowadays none of the manufacturers offers a compact and reliable solution fulfilling thoroughly the requirements for L4 and L5 self-driving vehicles, lacking mostly in cost and maximum range and/or angular resolution. Withal, several solutions can potentially be applied in L3 vehicles, such as the *Valeo SCALA*, currently employed in the commercial *Audi A8*.

Regarding the technological approaches, mechanical macro-scanners with rotating head have dominated the market, with *Velodyne* being highlighted as the pioneer, but there is a keen tendency for this scanning technique to be replaced by solid-state technology to potentiate mass-production and massive cost-reduction, while improving performance. Summarizing, the main problem with scanning LiDARs is the moving parts that can wear out over time and potentially be a source of failure, requiring a lot more adjustment and calibration, making the high-volume manufacturing a costly proposition. Solid-state LiDARs are more robust since no moving parts are present either at macro and microscales, removing one of the most failure-prone elements of the previous class. This assures a highest level of performance, reliability, reproducibility, robustness and cost-efficiency, since everything can be easily

assembled in a high-scale production line. Notwithstanding, the FOV is usually restricted horizontally to 120° and the point cloud resolution is restricted by the resolution of the photodetector arrays, whereas in mechanical macro-scanners a full horizontal coverage is accomplished (360° HFOV) and the multiple laser-detector channels provide highly dense frames. Alternatively, hybrid LiDARs combine distinct scanning techniques in a single device as, for example, the proposition of *LeddarTech* to merge horizontal beam scanning with a micromirror and vertical flash detection. Concerning the employed rangefinding technique, direct ToF is outstandingly dominant.

Conclusively, the deficiency for a suitable LiDAR is undoubtedly delaying and compromising the roll out of driverless vehicles. In general, multiple companies have already identified the gaps and, inclusively, are already working towards the addressment of the shortcomings. Indeed, the pointed manufacturers have proposed systems overperforming the requirements and that are to be launched to the market in short-term (1 to 2 years).

After the bibliographical research, the ToF LiDAR system was implemented. The sensor was divided in two PCBs: the transmitter (TX), encompassing an edge-emitting laser diode and the respective driving electronics responsible for sending short light pulses to the target, and a receiver (RX), comprising a PIN photodiode to detect the back-reflected light, a transimpedance amplifier with $20k\Omega$ gain, two leading-edge discriminators with a fixed threshold, to convert the analog returning pulses into a STOP event, and two Time-to-Digital Converters (TDCs), to estimate the ToF and virtually eliminate the blank time restriction. Additionally, an external PIN photodetector was employed in the reference path to time the laser firing instants. The whole system was controlled by the a *MSP430FR5969* RX microcontroller (16MHz), for which a firmware code was exclusively written in C++ to automate the laser rangefinding system and acquire 6000 pts/sec. This MCU acted as brain, controlling the laser activation instants in real-time (coincident with the START to both TDCs), reading the TDCs result registers and streaming the ToF result at the end of each acquisition cycle to the computer to display the results in a GUI and save a pre-established amount of points in a .csv file for posterior analysis. Lastly, a lens system was mounted with off-shelf components in both the transmitter and receiver ends to optimize the optical performance by, respectively, collimating the highly-divergent laser beam and focusing the back-reflected pulses onto the return photodetector. To provide temperature stabilization, a CPU fan was directed towards the laser emitter. The whole system was mounted on optical breadboards using *ThorLabs* supports, to yield a larger degree of flexibility and mobility in the optical components, and electrically supplied by two external voltage sources ($V_{cc,laser}$ for RX and TX boards) and the computer serial port (USB).

The genesis for the final LiDAR architecture was the TIDA-00663 design proposed by *Texas Instruments*, from each the PCBs layouts and electrical hardware components had been reused. The central motivation and the strengths for this choice were the low-cost, the straightforwardness, the absence of a blank distance imposed by the *TDC7200* blank time between START and STOP events, the simplicity of the laser driver (single IC) and the adaptability to interface the electrical subsystem with an external optical subsystem. Whatsoever, after some experimental testing in an initial iteration, some changes to the original design had to be carried out to achieve a fully-functional prototype, due to the proximity laser-photodetector, the inappropriate generation of a reference pulse for STOP1, the feedback ground-loop inducing oscillations in the external supply voltage $V_{cc,laser}$ and the narrow dynamic range for the return pulse threshold, preventing the back-reflected pulses from being effectively discriminated.

After attaining the functional system, its experimental characterization was executed by running a sequence of test procedures usually applied in benchmarking of LiDAR sensors. Both the overall sensor performance and the individual operation of the electrical and optical subsystems were encompassed in this empirical study. The pertinent characteristics are compiled in Table 49, as acquired under the standard conditions initially established by direct observation and found to yield the best overall precision performance and to be the most representative of practical measurement scenarios within the automotive context: $V_{th,A}=1.7V$ (threshold for returning pulses), $V_{th,B}=0.15V$ (threshold for reference pulses), timing on the falling-edge, $20k\Omega$ transimpedance gain, 65% duty cycle of the triggering signal (*BP_TRIG*) and diffusely reflected component on a *K-line white* target with 95% overall reflectance at 905nm.

Table 49. Summary of the specifications of the developed *LiDAR* prototype.

Overall	Class	1D Fixed-point LiDAR
	#Lasers / #Detectors	1 / 1+1 (reference and return)
	Range	0.560m to 4.420m (maximum limited by test conditions)
	Precision	3.87cm to 7.12cm
	Range Accuracy	± 3 cm (maximum) ± 1 cm (average)
	Data Acquisition Rate (Sampling Rate)	6k px/sec
Electrical	Input Voltage	15.5 VDC ($V_{cc,laser}$)
	Interfaces	RS-232 (Serial)
Laser	Operation Mode	Pulsed
	Wavelength / Spectral Width (FWHM)	$\approx 919\text{nm} / 5\text{nm}$
	Pulse Width / Rise-time	$\approx 46\text{ns} / 7\text{ns}$
	Peak / Average Power	$\approx 60\text{W} / \approx 17\text{mW}$
	Output Beam Divergence	$0.37^\circ \times 1.01^\circ$ ($\parallel \times \perp$)
	Warm-up Time	10min

As regards with one of the most fundamental characteristics of a LiDAR system, the upper distance limit was established to be $d_{max}=4.42\text{m}$, imposed by restrictions in the test environments, in particular, the length of the optical laboratory. The possibility to transfer the experiment to the outdoors was eradicated by eye-safety and reglementary framework. Whatsoever, one ascertained from the acquired return pulse at the latter distance that the threshold for discrimination (1.7V) was still heavily surpassed, what indicated that this range was not an absolute boundary and it can certainly be expanded if the tests are transferred to a larger space. Furthermore, comparing with the state-of-the-art *Garmin lite v3* sensor, which ranges up to 40m with a smaller receiving optics (related to the light-collecting ability) and a mean

output power about 4 times smaller (4mW), one could uphold and reinforce that the developed LiDAR can potentially reach greater distances. The limitation to the minimum distance of $d_{\min}=0.560\text{m}$ was dictated by geometrical factors, due to the large sensor footprint. It was further verified that this restriction was not imposed by the TDCs blank time since this distance corresponds to 3.73ns and the blank time in measurement Mode 2 is around 125ns (for a 16MHz clock). To expand the maximum distance, the identified solution was to increase the photosensitivity by replacing the return PIN photodiode by an APD with internal gains extending to factors of 100. Notwithstanding, the distance was not the primary focus of this prototype and these ranges were adequate enough for proof-of-concept.

With the primary goal of quantifying the reliability of the distance signals, the sensor precision was estimated through the standard deviation of a total of 2400 points acquired under the same conditions. The system precision deteriorated continuously as the target was moved away from the sensor, starting at 3.87cm and culminating at 7.12cm. Several noise sources were diagnosed as the underlying causes for the stochastic fluctuations in the raw measurements: fluctuations in the rise-time of the transmitted laser pulses, denoted as laser jitter, translated in a fluctuation of the threshold crossing-time (other than time-walk); photodetection (dark, shot and background) and amplification (thermal) noise; periodic fluctuations (100kHz) in the MCU power supplies that affected the threshold and induced changes in the ICs responses over time; jitter in the TDCs time-bases (internal and external).

To provide a more realistic idea of the precision impact on the distance measures, the Signal-to-Noise Ratio (SNR) was also computed through the ratio of the distance to the standard deviation. This is the preferred Figure-of-Merit (FOM) to quantify the system reliability because it gives an intuitive estimate of the relative impact of the precision. The SNR increased quickly from about 12dB and it started to level off at approximately 18dB, corresponding to a signal 63 times larger than the standard deviation. This indicated that the imprecision increased at a lower rate than the distance.

Both the precision and the SNR behaviors were qualitatively compared to a benchmark of 4 representative state-of-the-art sensors carried out during the *INNOVCAR* project: the *Quanergy M8*, the *Leddar Vu8*, the *Garmin lite v3* and the *Velodyne VLP16*. It was possible to authenticate the concordance in the experimented responses of commercial sensors. Quantitatively, the precision of these sensors was superior and, therefore, so was the SNR. This was also consistent with the applicability of LiDAR since it is targeted to larger ranges and, at close ranges, other automotive sensors perform better. The precision cannot be readily improved without major architectural changes since the jitter is usually intrinsic of the hardware components.

Accuracy-wise, it was necessary to calibrate the system in order to correct the systematic error in the range measurements, induced by the architecture-inherent differences between the reference and return optoelectronic paths. The calibration procedure consisted on acquiring 2400 raw data points at several distances from the *K-line* target, and then compare the statistically computed mean, $\langle d \rangle$, with the actual distance, d_{actual} , measured with a reference rangemeter (*PARKSIDE 20 M PLEM 20 A1*). After tracing the graph of the experimental points, $\langle d \rangle$, versus the actual distance, one concluded that the calibration could not be completely fulfilled by establishing a trivial and universal calibration constant, as ideal. Whatsoever, the behavior of the experimental points was found to be approximately linear with the actual distance, what led to the conclusion that a legitimate calibration was still conceivable, even though not trivial. The points were adjusted through a linear regression with equation $\langle d \rangle = 1.0632d_{\text{actual}} - 1.6017$

($R^2=0.9987$), which described the ultimately applied and best overall calibration within the measured working distances. After applying the previous calibration, the system accuracy was studied, culminating in a mean value of about 1.01cm, oscillating between 0.03cm @ $d_{\text{actual}}=3.123\text{m}$ and 2.98cm @ $d_{\text{actual}}=3.560\text{m}$.

The fundamental reasoning behind the decreasing calibration values, reflected in the slope above unity in the past linear regression, was found to be the time-walk arising from the discrimination of the returning pulses at a fixed threshold value, independently of the distance. As the target was moved away, the intensity of the back-reflected signal decreased and the threshold-crossing times increased accordingly. Hereby, the ToF expanded with the distance due to two factors: the proportional increase due to the shift in distance and the added time-walk instituted by the decay in the return optical intensity. The first determinant manifested itself in the unitary slope of the linear fit in $\langle d \rangle$ vs. d_{actual} , while the second was also a function of the actual distance and was reflected in the +0.0632 systematic excess in the slope. The latter effect was verified to be approximately linear, since linearity was maintained. One further validated these conclusions by comparing the variation of the calibration constants ($d_{\text{cal}}=d_{\text{actual}}-\langle d \rangle$), due to the time-walk, with the variation of the thresholds crossing-times at several distances, which were, indeed, found to be accurately similar. This problem was neglected in the reference path since the detection was performed on a steady optical path.

The take home message from the latter results was that the leading-edge discrimination with a fixed threshold is not an adequate technique for high-accuracy timing in LiDAR as it introduces an additional dependency on the distance (intensity) and, hence, an alternative technique molding to the dynamics of the returning pulses' intensity should be proposed. To substantiate even further this statement, and because the previous calibration was undertaken using a single material, an additional test was executed at a fixed distance and varying the amplitude of the returning signal, to show, for example, the repercussion of changing the target material, i.e. the reflective properties. It was concluded that a simple change of 0.7V in the amplitude of the transamplified return pulses led to a time-walk error of about 75cm at $d_{\text{actual}}=1.204\text{m}$.

Still referring to the first phase of development and testing of the LiDAR prototype, a separate characterization of the electrical and optical hardware was performed to give a more fundamental insight on the improvement points for future work.

To optimize the optical system in terms of power transmission and collimation, a simulation was run in *ZEMAX OpticStudio*. This simulation provided a detailed understanding on the sensitivity of the overall performance on the individual optical elements and it furnished information on the critical lenses' positioning. Moreover, the simulations granted the reference values for the expected power throughput and divergence, to be posteriorly compared with the empirical measurements. Through simulation and after optimization grounded on an initial experimental configuration, a divergence of $0.073^\circ \times 0.44^\circ$ (parallel vs. perpendicular) and an output peak power of 47W were achieved. Additionally, one concluded that the critical element in setting this performance metrics was the last lens on the transmitting path (*LB1378-B*). The lenses' choice was not judicious and what drove towards this setup was an experimental trial-and-error process by direct observation of the beam profile in conjunction with the lenses' availability at the laboratory. The *ZEMAX* simulation was not intended to design the optical system from ground but rather to validate the setup and provide the target FOM for the actual optimization of the hardware.

In practice, and considering the working distances, one opted by a configuration with larger power efficiency, at an expense of larger divergence. To determine the peak power, the average power was measure with a powermeter at the optical system output (16.85mW). Posteriorly, to accurately determined the peak value, it was demonstrated the need to apply a numerical method to take in consideration the actual temporal profile in the laser. Hence, the pulses' waveform was integrated and, based on the energy distribution, a peak power throughput of 60.34W was achieved in the final configuration. Ultimately, this reflected in a power transmission efficiency of around 86.63%. This high-percentage result was a clear indication that the design and practical alignment were rather effective power-wise. Whatsoever, considering the measured pulse width of 45.5ns (7ns rise-time), one concluded that the safety-glasses with an OD ≥ 2 were required to operate the sensor, under the ANSI Z136.1-2014 American standard. Concerning the beam collimation, a divergence of $0.367^\circ \times 1.014^\circ$ was accomplished and the beam spot profile remained elliptical in all the measured distances, with a continuously decreasing circularity. Regarding the cross-sectional intensity profiles, a grainy non-gaussian profile was identified both vertically and horizontally at several distances. Even though the final empirical optimization did not follow strictly the simulation results and focused on a better balance between power and divergence, a good agreement between simulation and the actual experimental observations regarding the optical behavior of the LiDAR sensor was noticed. To fulfill a better compromise between divergence, power transmission and circularity, several alternatives were examined: cylindrical lens pair, anamorphic prism pair and spatial filter (pinhole). In between these, the better option turned out to be the cylindrical lens pair. Hereupon, in a posterior evolution of this prototype, a pair of these lenses shall be designed specifically and properly for the employed laser. Moreover, by correctly adjusting the relative focal lengths of each lens, it is also possible to correct beam astigmatism.

The laser stabilization time was evaluated, and, after around 10 minutes, the laser response achieved a steady-state. This result proved to be equal to the experimented with the *Garmin lite v3*. After warm-up, one concluded that the wavelength peak was dependent on the duty cycle of the triggering signal, *BP_TRIG*. For a 65% duty cycle and 6kHz repetition rate, the wavelength peak was around 919nm, with a spectral width of 5nm. This result deviated slightly from the nominal specification, justified by the different characterization conditions (PRR, voltage supply, duty cycle and temperature). Decreasing the duty cycle, one detected a shift on the peak wavelength upwards to a point that, at 5%, the peak wavelength was 930.6nm. This behavior was directly associated with the lasing capacitors charging time, which required an on-time of, at least, 44 μ s to fully charge and maximize the optical response.

At the receiver optics, it was demonstrated the need for an additional collimating lens after the big light-collecting and focusing lens, to ensure a condition of smaller spot size variation in the photodetector plane with the distance to the target.

Electrically-wise, the signals were measured at several points of the circuit, the configuration of the ICs (digital potentiometers and TDCs) was validated and a quantification of some jitter sources was provided. In the TX board, the experimented signals were compared with an electrical simulation carried out in *TINA* spice software, which revealed an excellent concordance. In the reference path, the glass slide was positioned to obtain around 1.2V amplitude in the respective photodetector, so that a detectable STOP1 sequence could be generated without compromising significantly the power transmitted to the target.

After, the analysis focused mainly on jitter estimates. In the reference path, one measured around 2400 pulses either directly on the external reference photodiode (*DET10A/M*) output and after the coaxial cable transmitting the signal to the RX board. The voltages pulses were shown to be distorted due to the dispersion effect in the cable and the jitter in the respective threshold crossing (0.15V) was estimated at around 407ps on-board. In the return path, the same procedure was applied. The jitter in the threshold (1.7V) crossing-time was quantified by accumulating approximately 2400 pulses at two distinct distances. At 0.56m, the jitter was around 182ps and at 3.56m it increased to 212ps. This result validated the conclusion regarding the superior susceptibility to absolute noisy fluctuations in pulses with larger crossing-times, i.e. with smaller intensity. Similarly, in the reference path, the pulses were also distorted and a possible cause concerning the effect of drift and diffusion of carries within the photodetector was appointed, adding to the terminal capacitance to increase response time comparatively to the nominal specification. Lastly, the jitter in the internal and external time-bases of the TDCs was evaluated. In the external temporal scale, i.e. the external clock supplied by the RX MCU (16MHz), the cycle-to-cycle jitter was estimated at around 115ps. In the internal time-base settled by a local oscillator, a jitter of around 145ps and 146ps was obtained for each TDC. Although the TDCs are independent ICs with different internal bases (56.2ps vs 57.7ps), the calibration of these was underlined by a common external clock, which lead to a jitter of the same order. As the distance to the target increases, the time accounted also increases as a consequence of counting a larger number of cycles in the time-bases. Therefore, since the jitter is cumulative from cycle-to-cycle, the imprecision increased accordingly in a nearly-linear fashion, with the added effect of the increase in the threshold crossing-time. Withal, the correlation between all the noise-sources to evaluate the total jitter is utterly complex and the pragmatic message to retain was the expression in the overall precision on the order of a few centimeters. The solution to diminish the jitter impact and improve precision might be the substitution of critical components by more resilient ones. Some hypothetical solutions were identified: substitution of the PIN by an APD, the use an alternative microcontroller with better DC characteristics and more stable CLOCK sources, the implementation of optical and electronic filtering and a better temperature stabilization mechanism for the laser. Besides, design changes in the timing are also expected to improve precision (leading-edge discriminator by a constant fraction discriminator).

To close the characterization stage, the TDCs were studied. It was demonstrated the maximum fundamental limitation to the point rate (6kHz), arising from the TDCs reading time: after both STOPs were received, both TDCs should have the time to read the result registers and reset the START_MEAS bit to restart another cycle. For a 1D system, this point acquisition rate is pragmatically plentiful but, for a scanning LiDAR it may be necessary to go further to accomplish the frame resolution and rate. Hereupon, the TDCs reading times must be diminished and the obvious solution is to replace the MSP430FR5969 MCU by a unit with superior clock frequencies.

One relevant test was set aside from this characterization: the study of mutual interference between sensors. This will be a pertinent problem in a possible future in case the LiDARs applicability in autonomous vehicles reaches large scales. In this scenario, the sensors are susceptible to cross-talk whenever its line-of-sight crosses the one from another sensor using the same wavelength, generating an erroneous distance measurement unless the sensor has a unique signature. However, currently, this

is not a question that needs to be deepened due to the exceedingly reduced number of LiDARs in circulation.

As in any embryonic stage of a project, the starting point was to come up with a functional prototype to validate the proposed concept, to acquire critical knowledge and know-how (conceptual and empirical) and, ultimately, to identify the critical aspects to establish the pathway towards a newly improved solution. This first phase was successfully accomplished with this prototype completely adequate for proofing the principle of ToF range measurements, as proposed in the objectives of this dissertation.

Afterwards, in the second and last stage of the present work, the guidelines for the proposed advanced functionalities were given and some tests were performed to support it. The first and, perhaps, the foremost, was the implementation of a 2D scanning system using the *Maradin MAR1100* micromirror to obtain a tridimensional point cloud map. The opto-electromechanical guidelines to interface the scanning mechanism with the prototype were provided. The tests were performed on the *INNOVCAR* LiDAR prototype using the *Gilboa* board to electrically interface the micromirror with a pulse generator and, therefore, synchronize the laser firing instants with the mirror position. A 150×120 pattern was generated in MATLAB and flashed into the *Gilboa* board. The acquisition of the outputted electrical signals validated that each frame was divided into even and odd fields corresponding to, respectively, even and odd lines and proved that the *Gilboa* board efficiently interrupts a microcontroller unit whenever a pixel is activated in order to trigger the emission of a light pulse. After the electrical authentication, the previous pattern was projected on a wall using a visible blue laser within a FOV of $45.69^\circ \times 16.85^\circ$ (H \times V) with a respective resolution of $0.30^\circ \times 0.14^\circ$ at 30FPS. These results meet the FOV and angular resolution requirements for Level 4 and 5 autonomous vehicles, unless for the horizontal resolution that can be increased if the number of active columns in the pattern is extended, for e.g. to 300 (which yields a horizontal resolution of 0.15°).

Aiming to complement object recognition with material classification on LiDAR, the ToF measurements can be combined with polarization sensing, under the premise that the degree of polarization preserved in the back-reflected light depends on the target properties, namely the material and surface finishing. The laser output was measured to be linear vertically polarized (90°) and the Degree of Linear Polarization (DoLP) was assumed to be 100%. In a first approach, to validate the concept and estimate the polarization retained in the returning light, some images were acquired with a *Genie Nano M2450* polarimetric camera for projection in the *K-line white* (scatterer) and in the *Vauxhall Green* (metallic). This camera consists on a CCD array on top of which a micropolarizer grid with a $\times 2$ periodic pattern with four linear polarizers at disparate angles: 0° , 135° , 45° and 90° . Each 2×2 aggregate constitutes a super-pixel whose total intensity is the sum of the four individual parts. With the measured intensities in each target, one calculated the S_0 , S_1 and S_2 Stokes parameters and, subsequently, the DoLP of the back-reflected light. For the *K-line* target, it was verified an efficient depolarization, with a retention of only 13% of the initial polarization state, while in the other target, due to the metallic properties, the polarization state was extensively preserved with an estimated DoLP of 92%. The latter result met the expectations since, ideally for reflection on metals, the returned light should be completely polarized in the same direction as the input. The slight depolarization was attributed to the intrinsic heterogeneities on the target superficial layers (the metallic behavior in this target is accomplished

through small metallic flakes randomly spread across the basecoat). These results led to the conclusion that the polarization properties of the returning light are truly dependent on the reflective material.

After corroboration, an experimental setup was recommended and tested, consisting on a Liquid Crystal (LC) variable wave retarder with fast axis at 45° (variable half-wave plate) and a linear polarizer. By applying a modulated voltage between $\pm 0.516\text{V}$ and $\pm 1.560\text{V}$ to the LC, one alternated between no effective retardation and half-wave retardation (90°). Hence, the light transmitted through the linear polarizer to a single photodetector intercalated between linear vertical and horizontal polarization components. Analogously, the relative intensities of the two orthogonal polarization states were measured for back-reflection in the same targets, which allowed to determine the DoLP. Numerically, the computed DoLP resulted in 11% and 87% respectively for the *K-line* and *Vauxhall* targets, which proved to be self-consistent with the polarimetric camera measurements. Hence, it was proclaimed the legitimacy and sensitivity of this measuring concept, as long as the incoming pulses do not saturate when transampled. This system was a satisfactory alternative to the patented technologies for polarization measurement employing a polarizing beam splitter to divide the incoming beam in two orthogonal states to be measured by independent photodetectors, requiring complex calibration and alignment.

The last contribution of this work for LiDAR is a timing technique to replace the leading-edge discriminator and designated to virtually eliminate the systematic time-walk error arising from the discrimination at a fixed threshold. This technique, denoted Constant Fraction Discrimination (CFD), triggers a STOP pulse at a constant and optimum fraction of the returning pulses, irrespective its amplitude. Hence, this implementation potentially allows for an absolute calibration and, consequently, highly-accurate range measurements. A hardware implementation was proposed, consisting of splitting the returning pulse equally and, then, attenuate a portion by a fraction $0 < p < 1$ and add a delay, t_d , to the other. Posteriorly, the former was subtracted to the latter and the zero-crossing point was recognized, marking the instant at which the input pulse crossed the established fraction by generating the STOP signal. Parallely, to limit the temporal width of the produced STOP pulses, one had to append an additional leading-edge arming circuitry. For the delay and attenuation factor to be configurable, the implementation encompassed two digital potentiometers to adjust the previous setpoints. The electrical circuit was simulated in *TINA* and, for the optimum parameters found by trial-and-error, $p=0.5$ e $t_d=11\text{ns}$, the time-walk error was estimated at about 1ps (0.15mm) between amplitudes of 0.5V and 2V. This way, with this discrimination technique one can potentially reach range accuracies down to millimetric order, which arouses a total interest within the automotive LiDAR technology and represents an impactful contribution. Notwithstanding, the CFD does not amend the noise in ToF measures induced by the jitter sources and the statistical fluctuations around the average ToF will persist. Ultimately, the accuracy shall be limited by the system precision. In the reference path, the discrimination is performed approximately at a fixed point since the emitted laser pulses are uniform, and the CFD implementation is not critical.

To complete, the CFD is a linear technique and its efficiency is guaranteed assuming that the returning pulses' shape is constant and uniform over time. Thus, and because in the automotive context the dynamic range of the back-reflected pulses can exceed a ratio of 1:1000, it is mandatory to replace the transimpedance amplifier with an amplifier with an Automatic Gain Control (AGC) mechanism. This way, one can prevent the pulses from saturating as the gain is adjusted automatically to the dynamic of the returning pulses. Nowadays, there are already integrated devices with an internal feedback loop and

peak detection to regulate the feedback gain resistance. After a market survey, the best offer was the *TA3036* IC manufactured by *Philips Semiconductors*, with a gain adjustable between 0.1Ω and $6.9k\Omega$ to amplify current pulses between $0.18\mu\text{A}$ and 1.5mA ($\approx 1:8300$ dynamic range).

Comprehensively and in overview, all the initially proposed objectives were successfully accomplished, having been bestowed a completely functional LiDAR sensor based on direct ToF estimation and validated a panoply of contributions for added functionalities which may constitute valuable implementations towards a more adequate sensor for the ultimate goal targeting the automotive market.

7.2. Future Work

With all the basis for a LiDAR system developed and tested, the natural evolution is to implement the proposed improvements and find solutions to work around the identified weak points, aiming for a more matured, apt and refined outcome. Forasmuch as the prototype has a wide margin for progression, assorted improvements are recognized.

Primarily, it is vital to integrate the advanced functionalities with the 1D sensor not only to introduce qualitative but also quantitative enhancements. Both the CFD and the scanning with micromirror must be the focus and priority since it will lead to a more powerful impact. In what comes to the former aspect, the receiver PCB layout shall be redesigned to replace the leading-edge discriminator with the amplitude-independent timing and also to substitute the *OPA857* TIA with an amplifier with AGC, for e.g., the *TZA3036*. The leading-edge on the reference path can be maintained as the laser pulses are stable and therefore, the constant threshold does not introduce a significant time-walk. Regarding the micromirror introduction, the *MSP-EXP430FR5969* must be replaced by a faster microcontroller to allow an increase in the frame resolution to meet the required horizontal angular resolution. The suggestion is the *STM32 NUCLEO-F746ZG* development board with a 216MHz CPU frequency and integrated with all the peripherals to ease the programming process and interface with other boards. Furthermore, a fixation mechanism must be conceived to support the optical elements and a point cloud data visualization software must be developed or found to replace the Java GUI interface and show the 3D results in real-time. Some manufacturers, like *Hesai (PandarView)* or *Velodyne (VeloView)*, provide these softwares for free on their websites for Linux, and for their products, but it is necessary to ascertain if they are compatible with other devices.

Although the resolved polarization sensing is a relevant feature for a LiDAR system, it represents a secondary addition because it does not interfere directly with the 3D mapping process. Consequently, this point might have to be left apart, also because the available LC variable retarders cannot fulfil the switching times required to keep up with the laser PRR. Additionally, at low temperatures the nematic phase is destroyed. Yet, other alternatives may be studied and tested.

As concerns with architectural enhancements, the most noteworthy upgrade is to switch the *SFH 2400 FA* PIN photodiode with an APD to increase the receiver's sensibility. This will not only increase heavily the maximum measurable range, since these photodetectors can attain internal gains up to 100,

but also stabilize even further the sensor's calibration. Notwithstanding, as a drawback, the superior sensitivity will also bring additional noise (background, gain, dark-current and gain noise) which may call for electronic filtering for noise reduction and, consequently, enhanced precision. Naturally, this advancement depends strongly on the available budget since APDs are significantly more expensive than PINs. A suggestion is the *Hamamatsu S8890-10* APD with a peak sensitivity for 940nm, a 280MHz bandwidth and an internal gain of 100. In addition, it is pertinent to re-design the TX optics from ground zero, instead of using off-shelf lenses for a greater adaptation. Preferably, cylindrical lens must be adopted to ensure a better compromise between transmitted power, collimation and circularity, as well as astigmatism correction. The dimensioning shall be performed in *ZEMAX* for optimization and a finer tuning.

In terms of testing, the LiDAR sensor must be tested outdoor to study its operation in a real case scenario and understand the effect of different atmospheric conditions. Also, the system shall be tested indoors in a longer space to ascertain the maximum range limitation. Additionally, it must be characterized for different target materials and morphologies. If possible, real targets like traffic signals, cars and persons, shall be tested at different distances. Although in the indoor experiments performed herein the background illumination was not an obstacle, since they were performed in low-light conditions and with the PIN package filter, in this new scenario optical filtering will be mandatory. The recommendation is the *Balzers ZWL916* BPF used in the Polarization measurements. These tests are extremely crucial to diagnose new problematics and understand the evolving direction.

For the previous tests to be possible, two problems must be addressed: eye-safety and compactness. First and foremost, the laser must be in conformity with the restrictions dictated by the IEC 60825-1 regulatory framework to ensure it can be securely handled on the outdoors. Secondly, the global sensor footprint must be strongly reduced to promote mobility. The main limiters are the optical supports for the lenses and the PCB holders. Thereby, the solution consists in the mechanical CAD (Computer Assisted Design) of a housing to accommodate all the optical elements and PCBs, properly aligned. The enclosure must be hermetically sealed with electromagnetic compatibility to prevent electrical interference and withstand harsh environmental conditions. Moreover, to minimize space, the system can be integrated in a single board. This requires, again, the re-design of the TIDA-00663 PCB to remove the unused components and to include the CFD and TIA with AGC. To eliminate the voltage spikes verified in the first iteration when a single board was being used and guarantee more stable DC voltages, a ferrite bead must be applied in every power supply (external or from the microcontroller) to suppress high frequency noise induced by the ground loops. Also, the reference photodetector must be included on-board. The *SFH 2400 FA* can be adopted and it is required to add a TIA to convert the photocurrent into a voltage pulse. The latter can be the *OPA857*. To detect a portion of the emitted beam for reference, the photodiode can be placed very close to the *SPL LL90_3*, since a residual portion of light is emitted from the lateral edges, or parallelly to the output optics, so the residual reflection on the lenses is detected. The laser and the return photodetector must be optically isolated from each other and the input and output optical apertures must be coated, respectively, with an AR and BPF optical filters. Finally, the external power source has to be replaced by a portable supply. The best option is to use an electrical transformer to interface the ~230V power main plug with the PCB ($V_{cc, laser}$). As beneficial side-effects of this miniaturization, the input and output optical apertures can be brought closer to diminish the

geometrical limitation to the minimum measurable distance and the TX MCU can be dispensed (board controlled by a single unit).

Other accessory tasks include the thermal analysis and application of either passive (heatsinks) or active (fan or thermoelectric Peltier) cooling techniques to stabilize the temperature inside the housing (especially critical for the laser response), perform more exhaustive optical simulations in *ZEMAX* with tolerances and thermal examination and, at last, design an f-theta lens for the scanning system. This lens will allow to have a uniform spot distribution on the target plane, i.e. the height of the scanned beam on the target plane will be proportional do the scan angle by a term conditioned by the lens' focal length [215]. A simplified block diagram for a potential evolved version of the first LiDAR prototype is portrayed in Figure 198.

Ultimately, in a farther future, new technological paradigms can be studied, namely solid-state combined with FMCW measurements to answer the interference susceptibility obstacle.

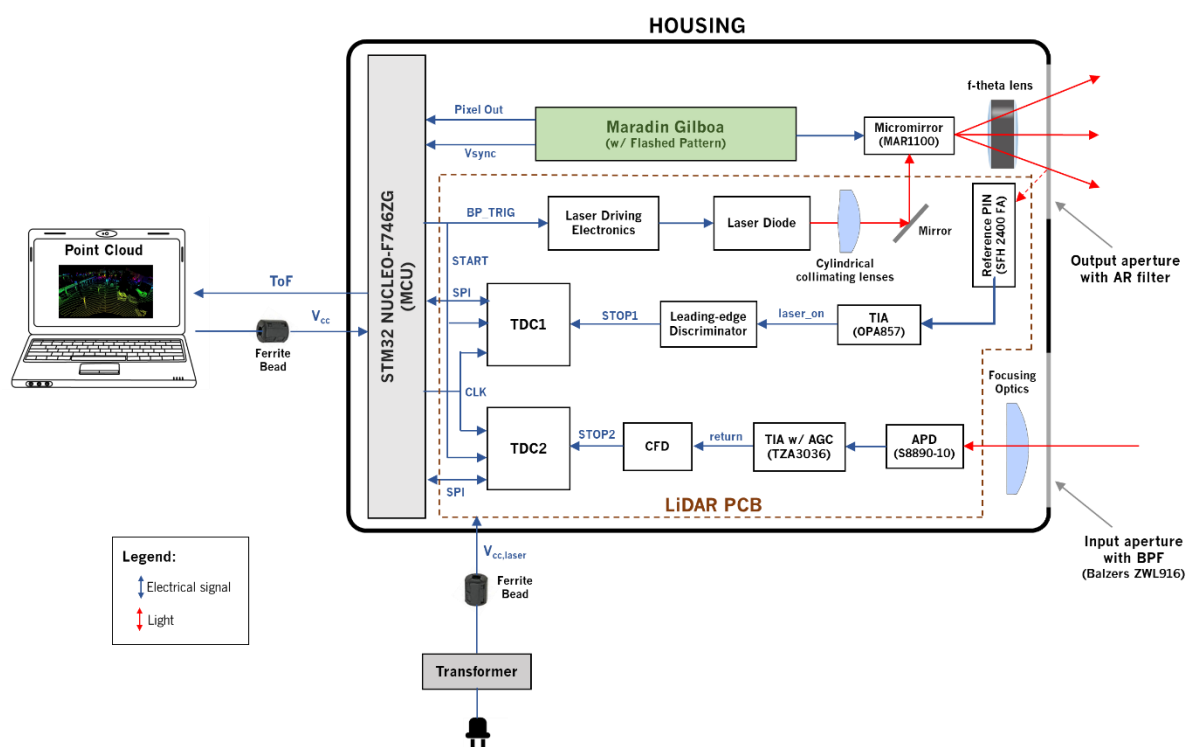


Figure 198. Possible block diagram for the LiDAR system with all the identified improvements. The models for the new hardware components are evidenced, while the remaining do not suffer any changes comparing with the initial prototype. The polarization sensing is not included due to the unavailability of compatible LC retarders. For simplicity the ferrite beads are represented outside the LiDAR PCB although in practice they must be integrated on-board as close as possible from the DC supply inputs.

Bibliography

- [1] E. Louay, "LiDAR and the Autonomous Vehicle Revolution for Truck and Ride Sharing." Quanergy Systems, Automated Vehicles Symposium, 2017.
- [2] "Leddar Optical Time-of-Flight Sensing Technology: A new approach to detection and ranging." LeddarTech, pp. 1–13, 2016.
- [3] "YellowScan Mapper II," *YellowScan*. [Online]. Available: <http://www.yellowscan.fr/products/yellowscan-mapper2>. [Accessed: 25-Mar-2018].
- [4] S. Narnakaje, "TI ' s smart sensors ideal for automated driving applications." Texas Instruments, pp. 1–7, 2017.
- [5] J. Christian Gerdes and M. Maurer, *Autonomous Driving: Technical, Legal and Social Aspects*. Springer, 2018.
- [6] J. Axelsson, "Safety in vehicle platooning: A systematic literature review," *IEEE Trans. Intell. Transp. Syst.*, vol. 18, no. 5, pp. 1033–1045, 2017.
- [7] M. Muratori, J. Holden, M. Lammert, A. Duran, S. Young, and J. Gonder, "Potentials for Platooning in U.S. Highway Freight Transport," *SAE Int. J. Commer. Veh.*, vol. 10, no. 1, pp. 2017-01–0086, 2017.
- [8] A. K. Bhoopalam, N. Agatz, and R. Zuidwijk, "Planning of truck platoons: A literature review and directions for future research," *Transp. Res. Part B Methodol.*, vol. 107, pp. 212–228, 2018.
- [9] "Connected and Automated Parking," *Bosch Mobility Solutions*. [Online]. Available: <https://www.bosch-mobility-solutions.com/en/highlights/connected-mobility/connected-and-automated-parking/>. [Accessed: 28-Aug-2018].
- [10] "ADAS Market Size Worth \$67.43 Billion By 2025 | CAGR: 19.0%," *Grand View Research*, 2018. [Online]. Available: <https://www.grandviewresearch.com/press-release/global-advanced-driver-assistance-systems-ad-as-market>. [Accessed: 25-Mar-2018].
- [11] "Semi-Autonomous and Autonomous vehicles market 2017 - Global Forecasts to 2021 & 2030," *Research and Markets*, 2017. [Online]. Available: <https://www.prnewswire.com/news-releases/semi-autonomous-and-autonomous-vehicles-market-2017-global-forecasts-to-2021-2030-research-and-markets-300466134.html>. [Accessed: 25-Mar-2018].
- [12] "Surface Vehicle Information Report: Taxonomy and Definitions for Terms Related to On-Road Motor Vehicle Automated Driving Systems." SAE International, pp. 1–12, 2014.
- [13] "Adaptive Cruise Control with stop & go function," *Audi Technology*. [Online]. Available: <https://www.audi-technology-portal.de/en/electrics-electronics/driver-assistant-systems/adaptive-cruise-control-with-stop-go-function>. [Accessed: 25-Mar-2018].
- [14] "Parking Assist," *Kia*. [Online]. Available: http://www.kia.com/worldwide/experience_kia/drive_wise/parking_assist.do. [Accessed: 25-Mar-2018].
- [15] R. Thakur, "Optical Sensors : Key Technology for the Autonomous Car." Osram Opto

- Semiconductors, pp. 1–7, 2016.
- [16] J. Hughes, “Car Autonomy Levels Explained,” *The Drive*, 2017. [Online]. Available: <http://www.thedrive.com/sheetmetal/15724/what-are-these-levels-of-autonomy-anyway>. [Accessed: 29-Aug-2018].
- [17] C. De Beaumont, “Renault SYMBIOZ Demo Car: Innovative, People-focused Design,” *Renault*. [Online]. Available: <https://group.renault.com/en/news/blog-renault/renault-symbioz-demo-car-an-innovative-people-focused-design/>. [Accessed: 31-Oct-2018].
- [18] E. Adams, “How long, really, until self-driving cars hit the streets?,” *The Drive*, 2017. [Online]. Available: <http://www.thedrive.com/tech/16768/how-long-really-until-self-driving-cars-hit-the-streets>. [Accessed: 25-Mar-2018].
- [19] R. Lange, “3D Time-of-flight distance measurement with with custom custom solid-state image sensors in CMOS / CCD-technology,” University of Siegen, 2000.
- [20] V. Mitrache, “Delphi Switches Focus to EV and Autonomous Tech, Splits into Two Companies,” *Autoevolution*, 2017. [Online]. Available: <https://www.autoevolution.com/news/delphi-switches-focus-to-ev-and-autonomous-tech-splits-into-two-companies-117474.html%0A>. [Accessed: 30-Mar-2018].
- [21] H. Paul, “Night vision for cars,” *Telegraph*, 2009. [Online]. Available: <https://www.telegraph.co.uk/motoring/road-safety/6582568/Night-vision-for-cars.html>. [Accessed: 27-Mar-2018].
- [22] “E5.1.13 - Protótipo inicial do sistema de detecção e de medição de distância.” Bosch, 2017.
- [23] G. Reina, D. Johnson, and J. Underwood, “Radar sensing for intelligent vehicles in urban environments,” *Sensors (Switzerland)*, vol. 15, no. 6, pp. 14661–14678, 2015.
- [24] B. Gain, “Solid-State LiDAR Emerges as the Flavor of Choice for Self-Driving Cars,” *Wonder How To*, 2017. [Online]. Available: <https://driverless.wonderhowto.com/news/one-lidar-rule-them-all-solid-state-lidar-emerges-as-flavor-choice-for-self-driving-cars-0177707/>. [Accessed: 27-Mar-2018].
- [25] B. Shaffer, “Why are automotive radar systems moving from 24GHz to 77GHz?,” *Texas Instruments*, 2017. [Online]. Available: https://e2e.ti.com/blogs_/b/behind_the_wheel/archive/2017/10/25/why-are-automotive-radar-systems-moving-from-24ghz-to-77ghz. [Accessed: 27-Mar-2018].
- [26] K. Heineke, P. Kampshoff, A. Mkrtchyan, and E. Shao, “Self-driving car technology: When will the robots hit the road?,” *McKinsey & Company*, 2017. [Online]. Available: <https://www.mckinsey.com/industries/automotive-and-assembly/our-insights/self-driving-car-technology-when-will-the-robots-hit-the-road>. [Accessed: 25-Mar-2018].
- [27] “LiDAR : Driving the Future of Autonomous Navigation - Analysis of LiDAR technology for advanced safety.” Frost & Sullivan, pp. 1–30, 2016.
- [28] D. Santo, “Autonomous Cars’ Pick: Camera, Radar, Lidar?,” *EE Times*, 2016. [Online]. Available: https://www.eetimes.com/author.asp?section_id=36&doc_id=1330069. [Accessed: 27-Mar-2018].
- [29] “LiDAR for Automotive Applications.” First Sensor, pp. 1–2, 2012.
- [30] “Flash Lidar key benefits.” Phantom Intelligence, pp. 1–6, 2018.

- [31] R. D. R. and S. C. Cain, *Direct Detection LADAR System*. 2010.
- [32] I. R. Kenyon, *Light Fantastic: A modern Introduction to Classical and Quantum Optics*. Oxford University Press.
- [33] “Mie Scattering,” *HyperPhysics*. [Online]. Available: <http://hyperphysics.phy-astr.gsu.edu/hbase/atmos/blusky.html>. [Accessed: 27-Mar-2018].
- [34] H. Peixoto, J. Teixeira, and E. J. Nunes-Pereira, “Performance of Commercial LiDAR Sensors for Autonomous Driving,” *ISPRS J. Photogramm. Remote Sens.*, 2018.
- [35] D. Ben-Bassat, “Session 5: Science and Entrepreneurship!” INL 2018 Summit, 2018.
- [36] H. Estl, “Advanced safety and driver assistance systems paves the way to autonomous driving,” *Texas Instruments*, 2014. [Online]. Available: https://e2e.ti.com/blogs_/b/behind_the_wheel/archive/2014/02/04/advanced-safety-and-driver-assistance-systems-paves-the-way-to-autonomous-driving. [Accessed: 25-Mar-2018].
- [37] B. Behroozpour, P. A. M. Sandborn, M. C. Wu, and B. E. Boser, “Lidar System Architectures and Circuits,” no. October, pp. 135–142, 2017.
- [38] “Bosch: Our Company,” *Robert Bosch GmbH*. [Online]. Available: <https://www.bosch.com/our-company/>. [Accessed: 03-Jul-2018].
- [39] “Bosch Car Multimedia Portugal S.A.,” 2018.
- [40] “E1.1.2 - Requisitos de deteção e medição de distância.” Bosch, 2016.
- [41] “Velodyne’s HDL-64E: A high definition LiDAR sensor for 3D applications.” Velodyne LiDAR, pp. 1–7, 2007.
- [42] Y. Zeng *et al.*, “An improved calibration method for a rotating 2D LIDAR system,” *Sensors (Switzerland)*, vol. 18, no. 2, pp. 1–12, 2018.
- [43] “Speed limits by country,” *Wikipedia*. [Online]. Available: https://en.wikipedia.org/wiki/Speed_limits_by_country. [Accessed: 28-Mar-2018].
- [44] B. N. J. Persson, U. Tartaglino, O. Albohr, and E. Tosatti, “Rubber friction on wet and dry road surfaces: The sealing effect,” *Phys. Rev.*, pp. 1–8, 2005.
- [45] G. R. Widmann *et al.*, “Comparison of Lidar-Based and Radar-Based Adaptive Cruise Control Systems,” *SAE Technical*, no. 724, 2000.
- [46] M. Pfennigbauer and A. Ullrich, “Multi-Wavelength Airborne Laser Scanning,” *Int. LiDAR Mapp. Forum*, pp. 1–10, 2011.
- [47] S. Piatek and J. Li, “LIDAR: A photonics guide to the autonomous vehicle market,” *Hamamatsu*. [Online]. Available: http://www.hamamatsu.com/jp/en/community/optical_sensors/articles/LiDAR_guide_to_autonomous_vehicle_market/index.html. [Accessed: 03-Apr-2018].
- [48] A. Kilpela, “Pulsed time-of-flight laser range finder techniques for fast, high precision measurement applications,” University of Oulu, 2004.
- [49] E. Sternå, “Development of a low-cost laser range-finder (LIDAR) Peter Kaldén,” Chalmers University of Technology, 2015.
- [50] “Distance-Based Photoelectric Sensors.” Pepperl+Fuchs, pp. 1–32.
- [51] B. Journet and J. C. Lourme, “Laser range finding based on correlation Method.”

- [52] H. Peixoto, J. Teixeira, and E. Pereira, "Status Meeting UMinho: WP1 - Benchmarking." 2018.
- [53] P. Zanuttigh, G. Marin, C. D. Mutto, F. Dominio, L. Minto, and G. Cortelazzo, *Time-of-Flight and Structured Light Depth Cameras: Technology and Applications*. Springer, 2016.
- [54] M. Hansard, S. Lee, O. Choi, and R. Horaud, *Time-of-Flight Cameras: Principles, Methods and Applications*. Springer, 2013.
- [55] T. Bosch, M.-C. Amann, R. Myllylä, and M. Rioux, "Laser ranging: a critical review of usual techniques for distance measurement," *Opt. Eng.*, vol. 40, no. 1, p. 10, 2001.
- [56] S. Jain, "A survey of Laser Range Finding," *Unpubl. Pap. Accessed March*, vol. 30, p. 2007, 2003.
- [57] "Solid-state Lasers," *RP Photonics Encyclopedia*. [Online]. Available: https://www.rp-photonics.com/solid_state_lasers.html. [Accessed: 07-Apr-2018].
- [58] "Laser Diodes," *RP Photonics Encyclopedia*. [Online]. Available: https://www.rp-photonics.com/laser_diodes.html. [Accessed: 07-Apr-2018].
- [59] "TIDA-01187: LIDAR-Pulsed Time-of-Flight Reference Design Using High-Speed Data Converters." Texas Instruments, pp. 1–29, 2017.
- [60] "LASER Safety Manual," no. August. Radiation Safety Office, Washington, 2007.
- [61] International Electrotechnical Commission, "International Standard - IEC 60825-1 - Safety of Laser Products," p. 122, 2001.
- [62] P. F. McManamon and Society of Photo-optical Instrumentation Engineers, *Field guide to lidar*. 2015.
- [63] A. Kilpelä and J. Kostamovaara, "Laser pulser for a time-of-flight laser radar," *Rev. Sci. Instrum.*, vol. 68, no. 6, pp. 2253–2258, 1997.
- [64] A. Kasturi, V. Milanovic, B. H. Atwood, and J. Yang, "UAV-borne lidar with MEMS mirror-based scanning capability," *SPIE Def. Commer. Sens. Conf. 2016*, 2016.
- [65] N. Mokey, "A self-driving car in every driveway? Solid-state lidar is the key," *Digital Trends*, 2018. [Online]. Available: <https://www.digitaltrends.com/cars/solid-state-lidar-for-self-driving-cars/>. [Accessed: 21-Apr-2018].
- [66] "Automotive LiDAR solutions," *LeddarTech*. [Online]. Available: <https://leddartech.com/automotive/>. [Accessed: 19-Apr-2018].
- [67] J. A. Christian and S. Cryan, "A survey of LIDAR technology and its use in spacecraft relative navigation," *AIAA Guidance, Navigation, and Control (GNC) Conference*. pp. 1–7, 2013.
- [68] "Quanergy Technology," *Quanergy Systems*. [Online]. Available: <http://quanergy.com/technology-2/>. [Accessed: 19-Apr-2018].
- [69] "Leddar Technology Fundamentals," *LeddarTech*. [Online]. Available: <https://leddartech.com/technology-fundamentals/>. [Accessed: 19-Apr-2018].
- [70] "LeddarTech Press Room," *LeddarTech*. [Online]. Available: https://leddartech.com/home/press_room/. [Accessed: 23-Apr-2018].
- [71] "DET10A/M Si Biased Detector User Guide," no. Rev. E. ThorLabs, p. 20, 2017.
- [72] B. E. A. Saleh and M. C. Teich, *Fundamentals of Photonics*, 2nd Editio. Wiley, 2007.

- [73] “Range Finding Using Pulse Lasers - Application Note.” OSRAM, pp. 1–7, 2004.
- [74] “Si APD, MPPC,” in *Solid State Photomultipliers*, Hamamatsu, pp. 1–25.
- [75] “Si APD.” Hamamatsu, pp. 1–6, 2011.
- [76] J. Wojtanowski, M. Zygmunt, M. Kaszczuk, Z. Mierczyk, and M. Muzal, “Comparison of 905nm and 1550nm semiconductor laser rangefinders’ performance deterioration due to adverse environmental conditions,” *Opto-Electronics Rev.*, vol. 18, no. 2, pp. 121–136, 2010.
- [77] S. Cova, M. Ghioni, A. Lacaita, C. Samori, and F. Zappa, “Avalanche photodiodes and quenching circuits for single-photon detection,” *Appl. Opt.*, vol. 35, no. 12, p. 1956, 1996.
- [78] S. Bellisai *et al.*, “SPAD Smart Pixel for Time-of-Flight SPAD Smart Pixel for Time-of-Flight,” *IEEE Photonics*, vol. 4, no. 3, 2012.
- [79] S. Hodges, M., Grabher, “Single-Photon Avalanche Diode,” *Laser Components*, pp. 1–4, 2012.
- [80] “Photodetectors for LiDAR,” no. May. Hamamatsu, 2017.
- [81] “Pixel size & sensitivity.” pco.imaging, pp. 1–7.
- [82] B. M. Chevrier, S. Manager, and I. Systems, “How to build a LIDAR system with a time-to-digital converter.” Texas Instruments, pp. 1–6, 2017.
- [83] “Choosing the Right Timing Discriminator for the Application Fast-Timing Discriminators,” *ORTEC*. ORTEC.
- [84] “Laser beam,” *Integrated Optics*. [Online]. Available: <https://integratedoptics.com/laser-beam-collimation>. [Accessed: 24-Apr-2018].
- [85] “LiDAR Market - Segmented by Component, Product, End-user Industry, and Geography - Growth, Trends and Forecasts (2018 - 2023).” Mordor Intelligence, 2018.
- [86] “Top Companies in the Global Automotive LiDAR Sensors Market,” *Technavio*, 2016. [Online]. Available: <https://www.technavio.com/blog/top-companies-global-automotive-lidar-sensors-market>. [Accessed: 29-Jun-2018].
- [87] Yole Développement and W. C. Partners, “The Automotive LiDAR Market,” 2018.
- [88] “Application Note VLP-16: Packet Structure & Timing Definition.” Velodyne LiDAR.
- [89] “Velodyne LiDAR Industry,” *Velodyne LiDAR*. [Online]. Available: <http://velodynelidar.com/industry.html>. [Accessed: 23-May-2018].
- [90] “HDL-64E S3: High definition real-time 3D LiDAR.” Velodyne LiDAR, 2017.
- [91] “Velodyne VLS-128,” *Velodyne LiDAR*. [Online]. Available: <http://velodynelidar.com/vls-128.html>. [Accessed: 25-May-2018].
- [92] “Product Guide.” Velodyne LiDAR.
- [93] “HDL-32E: High resolution real-time 3D LiDAR.” Velodyne LiDAR, p. 2.
- [94] “Puck VLP-16: Real-time 3D LiDAR sensor.” Velodyne LiDAR, 2017.
- [95] “Velodyne LiDAR: Ultra Puck VLP-32C,” *Velodyne LiDAR*. [Online]. Available: <http://velodynelidar.com/vlp-32c.html>. [Accessed: 24-May-2018].
- [96] F. O. R. A. Systems, “ULTRA Puck VLP-32C: High-definition real-time 3D LiDAR for autonomous systems (Preliminary).” Hyper-tech Systems, pp. 1–2.

- [97] "Velodyne LiDAR Announces New 'Velarray' LiDAR Sensor," *Business Wire*, 2017. [Online]. Available: <https://www.businesswire.com/news/home/20170419005516/en/Velodyne-LiDAR-Announces-New-Velarray-LiDAR-Sensor>. [Accessed: 25-May-2018].
- [98] "VelodyneLiDAR Products," *Velodyne LiDAR*. [Online]. Available: <https://velodynelidar.com/products.html>. [Accessed: 23-Apr-2018].
- [99] "Quanergy Markets," *Quanergy Systems*. [Online]. Available: <http://quanergy.com/markets/>. [Accessed: 25-May-2018].
- [100] P. Godsmark, "Quanergy's new \$250 Solid-state LiDAR could bring self-driving to the masses," 2017. [Online]. Available: <https://driverless.wonderhowto.com/news/quanergys-new-250-solid-state-lidar-could-bring-self-driving-masses-0175790/>. [Accessed: 26-May-2018].
- [101] "M8 LiDAR Sensor." Quanergy Systems.
- [102] "S3 Solid State LiDAR Sensor." Quanergy Systems.
- [103] "Patents Assigned to Innoviz Technologies Ltd.," *JUSTIA Patents*. [Online]. Available: <https://patents.justia.com/assignee/innoviz-technologies-ltd>. [Accessed: 25-May-2018].
- [104] "InnovizPro: High-resolution 3D LiDAR sensor." Innoviz Technologies, 2018.
- [105] "InnovizOne Automotive Grade," *Innoviz*. [Online]. Available: <https://innoviz.tech/innovizone/>. [Accessed: 25-May-2018].
- [106] I. Technologies, "Innoviz's Solid-State LiDAR Wins CES 2019 'Best of Innovation' Award," *Cision PR Newswire*, 2018. [Online]. Available: <https://www.prnewswire.com/news-releases/innoviz-solid-state-lidar-wins-ces-2019-best-of-innovation-award-300746904.html>. [Accessed: 05-Dec-2018].
- [107] "About LeddarTech," *LeddarTech*. [Online]. Available: <https://leddartech.com/about-leddartech/>. [Accessed: 28-May-2018].
- [108] "Leddar Technology." LeddarTech.
- [109] "LeddarVu: 8-segment solid-state LiDAR sensor modules." LeddarTech.
- [110] "Automotive Laserscanner SCALA." *AutonomouStuff*, 2016.
- [111] "Valeo SCALA," *Valeo*. [Online]. Available: <https://www.valeo.com/en/valeo-scala/>. [Accessed: 28-May-2018].
- [112] "3D Flash Lidar," *Continental AG*. [Online]. Available: <https://www.continental-automotive.com/en-gb/Landing-Pages/CAD/Automated-Driving/GlobalHighlights/3D-Flash-Lidar>. [Accessed: 28-May-2018].
- [113] I. Sensors, L. Channel, and R. Channel, "SRL 1 + SRL 1C: Infrared Short Range Lidar Sensor." Continental AG, 2017.
- [114] "OS-1 Performance Lidar Sensor." Ouster.
- [115] "OS-2 Performance Lidar Sensor." Ouster.
- [116] "About RoboSense," *RoboSense*. [Online]. Available: <http://www.robosense.ai/company>. [Accessed: 04-Jun-2018].
- [117] "RS-LiDAR-16 Multi-beam real time LiDAR." RoboSense, 2018.
- [118] "RS-LiDAR-32 Multi-beam real time LiDAR." RoboSense, 2018.

-
- [119] “About RS-LiDAR-M1,” *RoboSense*, 2018. [Online]. Available: <http://www.robosense.ai/rslidar/rs-lidar-M1>. [Accessed: 05-Jun-2018].
- [120] “Peregrine 3D Flash LIDAR Vision System,” *Advanced Scientific Concepts*. [Online]. Available: <http://www.advancedscientificconcepts.com/products/peregrine.html>. [Accessed: 29-May-2018].
- [121] “About Ibeo,” *Ibeo Automotive*. [Online]. Available: <https://www.ibeo-as.com/aboutibeo/>. [Accessed: 01-Jun-2018].
- [122] Ibeo Automotive, “The Ibeo LUX sensor family.” *AutonomouStuff*.
- [123] “Pandar40: 40-channel Mechanical Lidar User’s Manual.” Hesai, 2017.
- [124] “LiDAR Market by Type (Mechanical LiDAR and Solid-State LiDAR), Installation (Airborne and Ground-Based), Application (Corridor Mapping, ADAS & Driverless Car, and Engineering), Range, Component, Service, and Geography - Global Forecast to 2023.” *MarketsandMarkets*, 2018.
- [125] “Benewake Home,” *Benewake*. [Online]. Available: <http://www.benewake.com/en/index.html>. [Accessed: 04-Jun-2018].
- [126] “Cepton Vista LiDAR,” *Cepton*. [Online]. Available: <http://www.cepton.com/vista.html>. [Accessed: 04-Jun-2018].
- [127] “Cepton HR80 Series LiDAR,” *Cepton*. [Online]. Available: <http://www.cepton.com/hr80.html>. [Accessed: 04-Jun-2018].
- [128] “DENSO Home,” *DENSO*. [Online]. Available: <https://www.denso.com/global/en/>. [Accessed: 04-Jun-2018].
- [129] “Hella Home,” *HELLA*. [Online]. Available: <https://www.hella.com/hella-us/en/index.html>. [Accessed: 04-Jun-2018].
- [130] “Neptec Technologies Products,” *Neptec Technologies*. [Online]. Available: <http://www.neptectechnologies.com/products/>. [Accessed: 04-Jun-2018].
- [131] “Ocular Robotics 3D LiDAR,” *Ocular Robotics*. [Online]. Available: <http://www.ocularrobotics.com/products/lidar/>. [Accessed: 04-Jun-2018].
- [132] “Phantom Intelligence Products,” *Phantom Intelligence*. [Online]. Available: <http://phantomintelligence.com/en/products/>. [Accessed: 04-Jun-2018].
- [133] S. Ito, S. Hiratsuka, M. Ohta, H. Matsubara, and M. Ogawa, “Small imaging depth LIDAR and DCNN-based localization for automated guided vehicle,” *Sensors*, vol. 18, no. 1, 2018.
- [134] “TriLumina Home,” *TriLumina*. [Online]. Available: <http://www.trilumina.com/>. [Accessed: 04-Jun-2018].
- [135] “Luminar Technology,” *Luminar*. [Online]. Available: <https://www.luminartech.com/technology/index.html>. [Accessed: 13-Jun-2018].
- [136] P. E. Ross, “Luminar’s LiDAR enters mass production,” *IEEE Spectrum*, 2018. [Online]. Available: <https://spectrum.ieee.org/cars-that-think/transportation/sensors/luminars-lidar-enters-mass-production>. [Accessed: 13-Jun-2018].
- [137] A. J. Hawkins, “LiDAR maker Luminar is scaling up and slashing costs in effort to dominate self-driving cars,” *The Verge*, 2018. [Online]. Available:
-

- <https://www.theverge.com/2018/4/12/17224836/luminar-lidar-scale-cost-self-driving-car>. [Accessed: 13-Jun-2018].
- [138] S. R. Campbell, R. W. Cleye, J. M. Eichenholz, L. A. Martin, and M. D. Weed, "Scan Patterns for LIDAR systems," US9869754 B1, 2018.
- [139] J. M. Eichenholz *et al.*, "LiDAR System," US9874635 B1, 2018.
- [140] "Aeva Homepage," *Aeva*. [Online]. Available: <http://www.aeva.ai/>. [Accessed: 14-Jun-2018].
- [141] "Oryx Vision Homepage," *Oryx Vision*. [Online]. Available: <http://oryxvision.com/>. [Accessed: 14-Jun-2018].
- [142] "Blackmore LiDAR," *Blackmore INC*. [Online]. Available: <https://blackmoreinc.com/>. [Accessed: 21-Nov-2018].
- [143] "LiDAR Lite v3 Operation Manual and Technical Specifications." Garmin, pp. 1–14, 2016.
- [144] C. V. Poulton and M. R. Watts, "MIT and DARPA Pack Lidar Sensor Onto Single Chip," *IEEE Spectrum*, 2016. [Online]. Available: <https://spectrum.ieee.org/tech-talk/semiconductors/optoelectronics/mit-lidar-on-a-chip>. [Accessed: 14-Jun-2018].
- [145] C. V. Poulton, "Integrated LIDAR with Optical Phased Arrays in Silicon Photonics," Massachusetts Institute of Technology, 2016.
- [146] "LASiris VR - 3D Reality Capture Camera," *NCTech*. [Online]. Available: <https://www.nctechimaging.com/lasiris/>. [Accessed: 15-Jun-2018].
- [147] "iDAR - The new, intelligent LiDAR," *AEye*. [Online]. Available: <https://aeye.ai/idar/>. [Accessed: 15-Jun-2018].
- [148] "A long-range high definition 4D Camera," *TetraVue*. [Online]. Available: <https://www.tetravue.com/technology>. [Accessed: 15-Jun-2018].
- [149] P. S. Banks, B. Schmidt, S. Tuvey, and L. N. Venneri, "3D Imaging System and Method," US20170248796A1, 2017.
- [150] J. Taboada and L. A. Tamburino, "Laser Imaging and Ranging System Using Two Cameras," US005157451A, 1992.
- [151] P. S. Banks, "Systems and Methods of High Resolution Three-Dimensional Imaging," US20100128109A1, 2010.
- [152] S. Jo, H. J. Kong, H. Bang, J.-W. Kim, J. Kim, and S. Choi, "High resolution three-dimensional flash LIDAR system using a polarization modulating Pockels cell and a micro-polarizer CCD camera," *Opt. Express*, vol. 24, no. 26, p. A1580, 2016.
- [153] S. L. Chuang, *Physics of Photonic Devices*, 2nd ed. Wiley Series in Pure and Applied Optics, 2009.
- [154] K. W. Ayer, W. C. Martin, J. M. Jacobs, and R. H. Fetner, "Laser IMaging And Ranging System (LIMARS): A proof of concept experiment," vol. 1633, pp. 54–62, 1992.
- [155] "G3-AN0006 Genie Nano-Polarized Demo Application Note." Teledyne Dalsa, pp. 1–9, 2018.
- [156] Texas Instruments, "TIDA-00663: LIDAR-Pulsed Time of Flight Reference Design," no. December, pp. 1–24, 2016.
- [157] "SN74LVC2G14 Dual Schmitt-Trigger Inverter." Texas Instruments, 2015.

- [158] “Fundamentals of MOSFET and IGBT Gate Driver Circuits,” no. April 2002. Texas Instruments, pp. 1–48, 2017.
- [159] “UCC2732x / UCC3732x - Single 9-A High-Speed Low-Side Mosfet Driver With Enable.” Texas Instruments, pp. 1–22, 2016.
- [160] “SPL LL90_3 Radial Smart Laser.” Osram Opto Semiconductors, pp. 1–11, 2018.
- [161] “Operating the Pulsed Laser Diode SPL PLxx - Application Note.” OSRAM, pp. 1–5, 2004.
- [162] “BSP318S Small-signal Transistor.” Infineon.
- [163] W. Reeb, “Drive Electronics for Pulsed Laser Diodes: Power where it Matters.” Laser Components GmbH.
- [164] “SFH 2400 FA Silicon PIN Photodiode.” Osram Opto Semiconductors, 2018.
- [165] “OPA857: Ultralow-Noise, Wideband, Selectable-Feedback Resistance Transimpedance Amplifier.” Texas Instruments, 2014.
- [166] “TPL0202: 256-Taps Dual Channel Digital Potentiometer With SPI and Non-Volatile Memory.” Texas Instruments, 2017.
- [167] “TLV350x: 4.5-ns , Rail-to-Rail , High-Speed Comparator in Microsize Packages.” Texas Instruments, 2016.
- [168] “TDC7200: Time-to-Digital Converter for Time-of-Flight Applications in LIDAR, Magnetostrictive and Flow Meters,” no. 1. Texas Instruments, p. 50, 2016.
- [169] Texas Instruments, “MSP430FR5969 LaunchPad™ Development kit,” vol. 5969, no. February 2014. Texas Instruments, pp. 1–43, 2014.
- [170] J. H. Davies, *MSP430 Microcontroller Basics*, 1st ed. Newnes, 2008.
- [171] “MSP430FR59xx Mixed-Signal Microcontrollers.” Texas Instruments, 2017.
- [172] Texas Instruments, “MSP430F5529 LaunchPad™ Development Kit.” Texas Instruments, 2015.
- [173] “C330TME-B Mounted Geltech Aspheric Lens,” *ThorLabs*. [Online]. Available: <https://www.thorlabs.com/thorProduct.cfm?partnumber=C330TME-B>. [Accessed: 02-Oct-2018].
- [174] “N-BK7 Bi-Convex Lenses (AR Coating: 650-1050nm),” *ThorLabs*. [Online]. Available: https://www.thorlabs.com/newgrouppage9.cfm?objectgroup_id=4849&pn=LB1092-B#4858. [Accessed: 02-Oct-2018].
- [175] “LA1401-B N-BK7 Plano-Convex Lens,” *ThorLabs*. [Online]. Available: <https://www.thorlabs.com/thorproduct.cfm?partnumber=LA1401-B>. [Accessed: 02-Oct-2018].
- [176] “Mounted N-BK7 Plano-Convex Lenses (AR Coating: 650 - 1050 nm),” *ThorLabs*. [Online]. Available: https://www.thorlabs.com/newgrouppage9.cfm?objectgroup_id=6278&pn=LA1074-B-ML#6290. [Accessed: 02-Oct-2018].
- [177] “Optical Coatings,” *ThorLabs*. [Online]. Available: https://www.thorlabs.com/newgrouppage9.cfm?objectgroup_id=5840. [Accessed: 02-Oct-2018].
- [178] “Certified Laser Safety Glasses,” *ThorLabs*. [Online]. Available: https://www.thorlabs.com/newgrouppage9.cfm?objectgroup_id=762&pn=LG12. [Accessed: 16-Oct-2018].

- [179] J. C. Stover, *Optical Scattering: Measurement and Analysis*, 3rd ed. SPIE, 2012.
- [180] “Agilent Cary Universal Measurement Accessory (UMA).” Agilent Technologies.
- [181] R. Smetana, “Overview of Reflectance Models Focused on Car Paint Simulation,” Comenius University, 2008.
- [182] “Technical Guide: Reflectance Materials and Coatings.” Labsphere.
- [183] “Laser Distance Measurer 20 M PLEM 20 A1.” PARKSIDE.
- [184] “Virtual prototypes speed time to market for solid-state lidar.” ZEMAX.
- [185] “Exploring Non-Sequential Mode in OpticStudio,” ZEMAX. [Online]. Available: <https://customers.zemax.com/os/resources/learn/knowledgebase/exploring-non-sequential-mode-in-zemax>. [Accessed: 02-Oct-2018].
- [186] “Cubic Spline Interpolation,” Wikiversity. [Online]. Available: https://en.wikiversity.org/wiki/Cubic_Spline_Interpolation. [Accessed: 01-Nov-2018].
- [187] D. Calvetti, G. Golub, and W. Gragg, “Computation of Gauss-Kronrod quadrature rules,” *Math. Comput.*, vol. 69, no. 231, pp. 1035–1052, 2000.
- [188] “EASY HAZ™ Basic Web Version,” Kentek. [Online]. Available: <https://lasersafetyu.kentek.com/easy-haz-laser-hazard-software-basic-web-version/>. [Accessed: 02-Nov-2018].
- [189] Y. Deng and D. Chu, “Coherence properties of different light sources and their effect on the image sharpness and speckle of holographic displays,” *Sci. Rep.*, vol. 7, no. 1, pp. 1–12, 2017.
- [190] M. Forouzanfar and H. A. Moghaddam, “Ultrasound Speckle Reduction in the Complex Wavelet Domain,” in *Principles of Waveform Diversity and Design*, no. January, M. Wicks, E. Mokole, S. Blunt, R. Schneible, and V. Amuso, Eds. SciTech Publishing, 2010, pp. 558–577.
- [191] M. Xu, W. Gao, Y. Shi, J. Liu, and X. Chen, “Experimental speckle evaluation of broad-area edge-emitting lasers,” *Optik (Stuttg.)*, vol. 127, no. 3, pp. 1043–1048, 2016.
- [192] F. Riechert, G. Verschaffelt, M. Peeters, G. Bastian, U. Lemmer, and I. Fischer, “Speckle characteristics of a broad-area VCSEL in the incoherent emission regime,” *Opt. Commun.*, vol. 281, no. 17, pp. 4424–4431, 2008.
- [193] “Importance of Beam Circularization.” ThorLabs, pp. 1–18.
- [194] A. Stolow, “Gigahertz bandwidth ultrahigh vacuum 50 Ω coaxial high-voltage coupling capacitor for photoelectron spectroscopy,” *Rev. Sci. Instrum.*, vol. 67, pp. 1777–1780, 1996.
- [195] A. O. Goushcha and B. Tabbert, “On response time of semiconductor photodiodes,” *Opt. Eng.*, vol. 56, no. 9, p. 1, 2017.
- [196] “MAR1100 | 2D MEMS LASER SCANNING MIRROR The MAR1100 is a dual-axis MEMS based,” no. October. Maradin, 2017.
- [197] “Maradin - MEMS Based Scanning Solution for Displays and Sensors,” Maradin. [Online]. Available: <http://www.maradin.co.il/>. [Accessed: 23-Oct-2018].
- [198] M. Yehiel and G. Cahana, “Mechanical and Optical Guidelines - Maradin Optical Setup.” Maradin, 2016.
- [199] “DM003100 - Maradin Evaluation Kit User Guide.” Maradin, 2016.

-
- [200] G. Yearim and M. Yehiel, “Maradin EVK system Interface for External Laser.” Maradin, 2016.
- [201] D. H. Goldstein, “Polarized Light.” CRC Press, p. 746, 2010.
- [202] “Introduction to Polarization,” *Edmund Optics*. [Online]. Available: <https://www.edmundoptics.com/resources/application-notes/optics/introduction-to-polarization/>. [Accessed: 11-Oct-2018].
- [203] “Full-Wave Liquid Crystal Retarder with Temperature Control,” *ThorLabs*. [Online]. Available: https://www.thorlabs.com/newgrouppage9.cfm?objectgroup_id=8983&pn=LCC1223T-A. [Accessed: 15-Oct-2018].
- [204] R. Zheng and G. Wu, “Constant fraction discriminator in pulsed time-of-flight laser rangefinding,” *Front. Optoelectron.*, vol. 5, no. 2, pp. 182–186, 2012.
- [205] A. Garbolino, S. ; Martoiu, S. ; Rivetti, “Implementation of Constant-Fraction-Discriminators (CFD) in Sub-micron CMOS Technologies,” *IEEE Nucl. Sci. Symp. Conf. Rec.*, pp. 1530–1535, 2011.
- [206] D. A. Gedcke and W. J. McDonald, “A Constant Fraction of Pulse Height Trigger for Optimum Time Resolution,” *Nucl. Instruments Methods*, vol. 55, pp. 377–380, 1967.
- [207] H. Lim, “Constant fraction discriminator involving automatic gain control to reduce time walk,” *IEEE Trans. Nucl. Sci.*, vol. 61, no. 4, pp. 2351–2356, 2014.
- [208] “TZA3036 SDH/SONET STM1/OC3 transimpedance amplifier,” no. March. Philips Semiconductors, 2006.
- [209] “S3095: 10.7 Gbps Transimpedance Amplifier with Automatic Gain Control.” Applied Micro Circuits Corporation, pp. 1–14, 2002.
- [210] T. Agc, “M02014: CMOS Transimpedance Amplifier with AGC for Fiber Optic Networks up to 2.5 Gbps,” no. August. Mindspeed Technologies, 2007.
- [211] I. Current and L. Operation, “ONET85831T: 11.3 Gbps Linear Transimpedance Amplifier With AGC and RSSI,” no. March. Texas Instruments, 2008.
- [212] “MAX3797: 10.3Gbps, Low-power Transimpedance Amplifier for 10GBASE-SR Applications.” Maxim Integrated, pp. 1–12.
- [213] D. V. O’Connor and D. Phillips, *Time-Correlated Single Photon Counting*. Academic Press, 1984.
- [214] F. Loddo and T. Maerschalk, “Design of a constant fraction discriminator for the VFAT3 front-end ASIC of the CMS GEM detector,” 2015.
- [215] X. Lee and C. Wang, “Optical design for uniform scanning in MEMS-based 3D imaging lidar,” *Appl. Opt.*, vol. 54, no. 9, pp. 2219–2223, 2015.

– This page is intentionally left blank –

Appendix I – Bill of Materials

Designator	Quantity	Description	Part Number	Manufacturer	Package
R3	1	SMD Resistor, 300 Ω , 150V, Thick Film, 125mW, $\pm 5\%$	ERJ-6GEYJ301V	Panasonic	0805
C4	1	SMD Multilayer Ceramic Capacitor, 1000pF, 50V, $\pm 1\%$, COG/NP0	GRM1885C1H102FA01J	MuRata	0603
U1	1	Dual Schmitt-Trigger Inverter	SN74LVCG14DCKR	Texas Instruments	DCK006A
C3	2	SMD Multilayer Ceramic Capacitor, 4.7 μ F, 50V, $\pm 10\%$, X5R	GRM319R61H475KA12D	MuRata	1206
U2	1	Single 9A High-speed low-side MOSFET Driver with ENABLE	UCC27321DR	Texas Instruments	D0008A
TP2	1	PCB Test Point, Compact, Red, Through hole	5005	Keystone	-
R15	1	SMD Resistor, 100 Ω , Thin film. $\pm 0.1\%$, 0.25W	TNPW1206100RBEEA	Vishay-Dale	1206
U10	1	Hybrid Pulsed Laser Diode with Integrated Driver State, 905nm, 70W peak	SPL LL90_3	OSRAM	-
R14	1	SMD Resistor, 0.01 Ω , 0.25W, $\pm 1\%$	WSL0805R0100FEA18	Vishay-Dale	0805
TP3, TP5	2	PCB Test Point, Multi-purpose, Purple, Through hole	5129	Keystone	-
TP4	1	PCB Test Point, Orange, Through hole	5013	Keystone	-
TP6	1	PCB Test Point, Miniature, SMT	5015	Keystone	-
U4	1	Rail-to-rail Analogue Comparator, High-speed, Dual, 4.5ns	TLV3502AIDCNR	Texas Instruments	DCN0006A
C5, C11, C16, C19	4	SMD Multilayer Ceramic Capacitor, 0.1 μ F, 16V, $\pm 5\%$. X7R	0603YC104JAT2A	AVX	0603
R7, R8, R9, R10	4	SMD Resistor, 0 Ω , 150V, Thick Film, 125mW, $\pm 1\%$	CRCW08050000Z0EA	Vishay-Dale	0805
C9, C13	2	SMD Multilayer Ceramic Capacitor, 1000pF, 50V, $\pm 10\%$, X7R	C0603X102K5RACTU	KEMET	0603
U8	1	256-Taps Dual Channel Digital Potentiometer with SPI, 10k Ω	TPL0202-10MRTER	Texas Instruments	RTE0016D
R12, R13, R16, R17	4	SMD Resistor, 10k Ω , 75V, Thick Film, 100mW, $\pm 1\%$	CRCW060310K0FKEA	Vishay-Dale	0603

D1	1	Silicon PIN Photodiode, 60°, 1nA, 900nm, SMD-3	SFH 2400 FA-Z	OSRAM	-
R11	1	SMD Resistor, 1kΩ, 75V, Thick Film, 100mW, ±1%	CRCW06031K00FKEAC	Vishay-Dale	0603
C14, C15	2	SMD Multilayers Ceramic Capacitor, 0.1μF, 10V, ±10%, X5R	GRM155R61A104KA01D	MuRata	0402
U7	1	Ultra-low-noise, Wideband, Selectable Feedback Resistor TIA	OPA857IRGTT	Texas Instruments	RGT0016A
U3, U6	2	Time-to-Digital Converter	TDC7200	Texas Instruments	PW0014A
C6, C12	2	SMD Multilayer Ceramic Capacitor, 1μF, 16V, ±10%, X7R	EMK107B7105KA-T	Taiyo Yuden	0603
U9	1	Singe 2-Input Positive AND Gate	SN74LVC1G08QDCKRQ1	Texas Instruments	DCK005A
J7, J8	4	Connector, Receptacle, 10×2, Gold plated, Right angle, 100" pitch	SSW-110-23-F-D	Samtec	-
J2	2	Connector, Vertical, 2.54mm pitch, 3×1, Header, Gold, Through hole	61300311121	Würth Elektronik	-
TP1	2	PCB Test Point, Compact, Black, Through Hole	5006	Keystone	-
-	1	Evaluation Kit, USB Launchpad MCU, 25MHz, 128KB Flash, 8KB RAM	MSP-EXP430F5529	Texas Instruments	-
-	1	Evaluation Kit, USB Launchpad MCU, 16MHz, 64KB FRAM, 2KB SRAM	MSP-EXP430FR5969	Texas Instruments	-
-	1	Si Detector, 200 - 1100 nm, 1 ns Rise Time, 0.8 mm ²	DET10A/M	ThorLabs	-
-	1	50Ω Fixed Stub-style BNC Terminator	FT500	ThorLabs	-
-	1	Mounted Geltech Aspheric Lens, AR: 600-1050nm, f=3.1mm, NA=0.68	C330TME-B	ThorLabs	-
-	1	Mounted Bi-convex lens, AR: 600-1050nm, f=15mm, Ø1/2", N-BK7	LB1092-B-ML	ThorLabs	-
-	1	Mounted Bi-convex lens, AR: 600-1050nm, f=25mm, Ø1/2", N-BK7	LB1014-B-ML	ThorLabs	-
-	1	Mounted Bi-convex lens, AR: 600-1050nm, f=20mm, Ø1/2", N-BK7	LB1450-B-ML	ThorLabs	-
-	1	Mounted Bi-convex lens, AR: 600-1050nm, f=40mm, Ø1/2", N-BK7	LB1378-B-ML	ThorLabs	-
-	1	Mounted Bi-convex lens, AR: 600-1050nm, f=30mm, Ø1/2", N-BK7	LB1258-B-ML	ThorLabs	-
-	1	SM1 Lever-Actuated Iris Diaphragm, Ø0.8- Ø12mm	SM1D12	ThorLabs	-
-	1	Plano-convex lens, AR: 600-1050nm, f=60mm, Ø2", N-BK7	LA1401-B	ThorLabs	-
-	1	Mounted dPlano-convex lens, AR: 600-1050nm, f=20mm, Ø1/2", N-BK7	LA1074-B-ML	ThorLabs	-

Appendix II – Final Codes

RX MCU Code (C language)

```
/*
  Code developed by: Joaquim Santos
  Course: Integrated Master's in Engineering Physics
*/

#include <msp430fr5969.h>
#define nop __asm__ __volatile__("nop\n\t"); //No operation (62.5ns)
/*----- Variables Definition -----*/
int TIA_gain=20; // TIA gain (20k or 5k)
float f_p=6, duty_cycle=0.65; // PWM settings for BP_TRIG
float V_th_A=1.7, V_th_B=0.15; // Discriminator Thresholds
uint8_t TIME1_1[3]={}, CLOCK_COUNT_1_1[3]={}, TIME2_1[3]={},
CALIBRATION1_1[3]={}, CALIBRATION2_1[3]={}; // Buffers for TDC1
uint8_t TIME1_2[3]={}, CLOCK_COUNT_1_2[3]={}, TIME2_2[3]={},
CALIBRATION1_2[3]={}, CALIBRATION2_2[3]={}; // Buffers for TDC2
uint8_t restart[2]={0b01000000, 0b10111011}; // Restart sequence to TDCs
int restart_len=sizeof(restart)/sizeof(restart[0]);
float ToF, ToF_1, ToF_2, calCount_1, calCount_2, normLSB_1, normLSB_2;
float ToF_cal = 0; // Calibration constant [ns]
/*----- Functions Statement -----*/
void setup_DPOT(float , float);
void setup_PWM(float , float);
void setup_TDC();
void SPI_send(uint8_t * , int , int);
void SPI_receive(uint8_t * , uint8_t , int);
void ToF_read();
/*----- Initialization -----*/
void setup() { // Setup system
  PM5CTL0 &= ~LOCKLPM5; // Disable GPIO default impedance mode to
activate previously configured port settings
  Serial.begin(9600); // Initialize UART
  P1DIR |= 0x01; // Turn-on GREEN_LED (LiDAR in operation)
  P1OUT |= 0x01;

  P2DIR &= ~0x10; // External Interrupt in P2.4 (TDC_INT)
  P2REN |= 0x10; // Pull-up interrupt
  P2IES |= 0x10; // High-to-low transition (INTB active low)
  P2IFG &= ~0x10; // Clear Interrupt flag
  P2IE |= 0x10; // Enable Interrupt

  P3DIR |= 0x10; // Output SMCLK @ 16MHz on P3.4 (TDC_CLK)
  P3SEL1 |= 0x10;

  P3DIR |= 0b01100000; // Setup TIA gain (P3.5) and Test_mode (P3.6)
(TIA_gain == 20 ? P3OUT |= 0x20 : P3OUT &= ~0x20);
  P3OUT &=~ 0x40; // Disable Test_mode (writting to 0)

  setup_DPOT(V_th_A,V_th_B); // Configure DPOT

  delay(2); // Settling time for TDCs (~1.9ms)
```

```

setup_TDC(); // Setup TDCs

setup_PWM(f_p,duty_cycle); // Setup PWM for BP_TRIG
}
/*----- Code to run cyclically -----*/
void loop(){
  nop;
  Serial.println(ToF); // Send ToF via UART to PC
  nop;
}

#pragma vector=PORT2_VECTOR
__interrupt void PORT2_ISR_HOOK(void){ // ISR for P2.4
  ToF_read(); // Read and Restart TDCs
  P2IFG &= ~0x10; // Clear Interrupt flag
  P2IE |= 0x10; // Re-enable Interrupt
}
/*----- Sub-routines -----*/
void setup_PWM(float f_pwm, float dc_pwm) { // Set the PWM
  P1DIR |= 0x04; // Output on P1.2
  P1SEL0 |= 0x04; // Activate PWM output

  TA1CTL |= TASSEL_2 | ID_1 | MC_1 | TACLK; // Timer clocked by SMCLK
(16MHz) | Prescaler 1 | Up Mode | Clear clock divider and count direction
  TA1CCTL1 = OUTMOD_7; // Reset Mode
  int T_0 = int(16000 / f_pwm); // Timer count limit
  int T_1 = int(dc_pwm * T_0); // Set ON-time
  TA1CCR0 = T_0; // Sets frequency
  TA1CCR1 = T_1; // Set ON-time (duty_cycle)
}

void setup_DPOT(float V_A , float V_B){
  // Determine decimal Wiper registers
  float R_A = (V_A*30/3.5)-10, R_B = (V_B*10/3.5);
  int W_A = int(R_A*256/10), W_B = int(R_B*256/10);
  W_A = (W_A < 0 ? 0 : W_A); // Limit Wiper between 0 and 255 (1byte)
  W_A = (W_A > 255 ? 255 : W_A);
  W_B = (W_B < 0 ? 0 : W_B);
  W_B = (W_B > 255 ? 255 : W_B);

  uint8_t stream_DPOT[] = {0b00000001, W_A, // Data stream to DPOT
                           0b00000010, W_B,
                           0b00100011, 0b00000000};

  // Configure SPI (USCIB0);
  P4DIR |= 0x08; // CS Output in P4.3
  P4OUT |= 0x08; // CS set high to disable communication (active-low)
  UCB0CTLW0 = UCSWRST | UCSSEL_2; // USCI in reset mode (to write on
USCIB0 registers) | SMCLK as SPI_CLK source
  UCB0CTLW0 |= UCCKPH | UCMSB | UCSYNC | UCMST; // CPHA=~UCCKPH=0 | MSB
first | Synchronous
  UCB0CTLW0 &= ~UCCKPL; // CPOL=0
  P1DIR |= 0b01000000;
  P1SEL1 |= 0b01000000; // Enable MOSI in P1.6
  P1SEL0 &= ~0b01000000;
  P2DIR |= 0b00000100;
  P2SEL1 |= 0b00000100; // Enable SPI_CLK in P2.2
  P2SEL0 &= ~0b00000100;
  UCB0BR0 = 4; // SPI_CLK @ 4MHz
  UCB0BR1 = 0;
  UCB0CTLW0 &= ~UCSWRST; // Activate USCI

```

```

SPI_send(stream_DPOT, sizeof(stream_DPOT)/sizeof(stream_DPOT[0]), 1);
// Transfer data to DPOT
}

void setup_TDC(){
    P3DIR |= 0x01;      // CS Output in P3.0 for TDC1
    P3OUT |= 0x01;      // Active-low
    P1DIR |= 0x10;      // CS Output in P1.4 for TDC2
    P1OUT |= 0x10;      // Active-low
    UCB0CTLW0 = UCSWRST | UCSSEL_2; // Reconfigure SPI communication
    UCB0CTLW0 |= UCCKPH | UCMSB | UCSYNC | UCMST;
    // Same configuration as previously for DPOT
    UCB0CTLW0 &= ~UCCKPL;
    P1DIR &= ~0b10000000;
    P1DIR |= 0b01000000;
    P1SEL1 |= 0b11000000; // This time MISO in P1.7 ENABLED
    P1SEL0 &= ~0b11000000;
    P2DIR |= 0b00000100;
    P2SEL1 |= 0b00000100;
    P2SEL0 &= ~0b00000100;
    UCB0BR0 = 1;        // SPI Clock @ 16MHz (maximum 20MHz for TDCs)
    UCB0BR1 = 0;
    UCB0CTLW0 &= ~UCSWRST;
    // Configure TDCs registers, other left to default values
    uint8_t CONFIG1[] = {0b01000000, 0b10111011};
    uint8_t CONFIG2[] = {0b01000001, 0b00000000};
    uint8_t INT_MASK[] = {0b01000011, 0b00000101};
    uint8_t CLOCK_CNTR_OVF_H[] = {0b01000110, 0b00000000};
    // Overflow condition for TDC1
    uint8_t CLOCK_CNTR_OVF_L_1[] = {0b01000111, 0b00001100};
    // Overflow condition for TDC2
    uint8_t CLOCK_CNTR_OVF_L_2[] = {0b01000111, 0b00010000};
    int config_len = sizeof(CONFIG1)/sizeof(CONFIG1[0]);

    SPI_send(CONFIG2, config_len, 2); // Configure registers one by one
    SPI_send(INT_MASK, config_len, 2);
    SPI_send(CLOCK_CNTR_OVF_H, config_len, 2);
    SPI_send(CLOCK_CNTR_OVF_L_1, config_len, 2);

    SPI_send(CONFIG2, config_len, 3);
    SPI_send(INT_MASK, config_len, 3);
    SPI_send(CLOCK_CNTR_OVF_H, config_len, 3);
    SPI_send(CLOCK_CNTR_OVF_L_2, config_len, 3);

    SPI_send(CONFIG1, config_len, 2);
    SPI_send(CONFIG1, config_len, 3);
}

void ToF_read(){
    // Read data from TDCs whenever MCU is interrupted
    SPI_receive(TIME1_1, 0x10, 2);
    SPI_receive(TIME1_2, 0x10, 3);
    SPI_receive(CLOCK_COUNT_1_1, 0x11, 2);
    SPI_receive(CLOCK_COUNT_1_2, 0x11, 3);
    SPI_receive(TIME2_1, 0x12, 2);
    SPI_receive(TIME2_2, 0x12, 3);
    SPI_receive(CALIBRATION1_1, 0x1B, 2);
    SPI_receive(CALIBRATION1_2, 0x1B, 3);
    SPI_receive(CALIBRATION2_1, 0x1C, 2);
    SPI_receive(CALIBRATION2_2, 0x1C, 3);
}

```

```

if(CLOCK_COUNT_1_1[2] == 0 || CLOCK_COUNT_1_2[2] == 0) ToF = 1000;
//If one TDC overflows => ToF=1us (d=150m)
else{
    calCount_1=
    int) (CALIBRATION2_1[0]*65536+CALIBRATION2_1[1]*256+CALIBRATION2_1[2])-
    (CALIBRATION1_1[0]*65536+CALIBRATION1_1[1]*256+CALIBRATION1_1[2]);
    normLSB_1 = (float) (62500/calCount_1); // LSB in picoseconds
    ToF_1 = (float)normLSB_1*(TIME1_1[0]*65536+TIME1_1[1]*256+TIME1_1[2]-
    TIME2_1[0]*65536-TIME2_1[1]*256-
    TIME2_1[2])*0.001+(CLOCK_COUNT_1_1[1]*256+CLOCK_COUNT_1_1[2])*62.5;
    // ToF calculation in nanoseconds

    calCount_2 =
    (float) (CALIBRATION2_2[0]*65536+CALIBRATION2_2[1]*256+CALIBRATION2_2[2])-
    (CALIBRATION1_2[0]*65536+CALIBRATION1_2[1]*256+CALIBRATION1_2[2]);
    normLSB_2 = (float) (62500/calCount_2);
    ToF_2 = (float)normLSB_2*(TIME1_2[0]*65536+TIME1_2[1]*256+TIME1_2[2]-
    TIME2_2[0]*65536-TIME2_2[1]*256-
    TIME2_2[2])*0.001+(CLOCK_COUNT_1_2[1]*256+CLOCK_COUNT_1_2[2])*62.5;

    ToF = ToF_2 - ToF_1 + ToF_cal;
}

SPI_send(restart,restart_len,2); // Set the START_MEAS bit in CONFIG1
SPI_send(restart,restart_len,3); // and start new measurement cycle
}

void SPI_send(uint8_t *data, int len, int sel) {
    // Send data (sel=2 =>TDC1 sel=3 =>TDC2 sel=1 =>DPOT)
    while (len){ // Go through all the bytes
        (sel==1 ? P4OUT &= ~0x08 : (sel==2 ? P3OUT &= ~0x01 : P1OUT &=
        ~0x10)); // Enable communication (CS active low)
        while(!(UCB0IFG & UCTXIFG)); // Wait for TX buffer to be free
        UCB0TXBUF = *(data++); // Send and increment pointer
        while(!(UCB0IFG & UCTXIFG));
        UCB0TXBUF = *(data++); // Send 2nd byte
        while (UCB0STAT & UCBUSY); // Ensure last byte was sent
        (sel==1 ? P4OUT |= 0x08 : (sel==2 ? P3OUT |= 0x01 : P1OUT |= 0x10));
        // Idle communication
        len-=2; // Next data byte pair
    }
}

void SPI_receive(uint8_t *buffer, uint8_t addr, int sel){
    // Receive data from TDCs
    (sel==2 ? P3OUT &= ~0x01 : P1OUT &= ~0x10);
    while(!(UCB0IFG & UCTXIFG));
    UCB0TXBUF = addr; // Address to read
    for(int w=0;w<3;w++){ // Result registers with 3 bytes
        while(!(UCB0IFG & UCTXIFG));
        UCB0TXBUF = 0x00; // Dummy byte to activate SPI_CLK
        while (UCB0STAT & UCBUSY);
        buffer[w] = UCB0RXBUF; // Receive and store byte
    }
    while (UCB0STAT & UCBUSY);
    (sel==2 ? P3OUT |= 0x01 : P1OUT |= 0x10);
}

```

TX MCU Code (C language)

```
/*
  Code developed by: Joaquim Santos
  Course: Integrated Master's in Engineering Physics
*/

#include <msp430f5529.h>
#define nop __asm__ __volatile__("nop\n\t"); // No Operation(62.5ns)

void setup(){
  WDTCTL = WDTPW | WDTHOLD; // Stop watchdog timer
  P7DIR |= 0x10; // GPIO_EN to the driver (P7.4)
  P7OUT |= 0x10; // HIGH => ENABLE

  P1DIR |= 0x01; // Set RED_LED as output
  P1OUT &= ~0x01; // LED OFF
  P4DIR |= 0x80; // Set GREEN_LED (LiDAR ON)
  P4OUT |= 0x80; // GREEN LED ON

  // Set button to STOP the Laser whenever it is pressed
  P1REN |= 0x02; // Enable P1.1 internal interrupt
  P1OUT |= 0x02; // Set P1.1 as pull-Up
  P1IES &= ~0x02; // Low-to-high transition
  P1IFG &= ~0x02; // Clear Interrupt Flag
  P1IE |= 0x02; // Interrupt enabled
}

void loop(){
  nop;
  nop;
}

#pragma vector=PORT1_VECTOR
__interrupt void PORT1_ISR_HOOK(void){ // ISR for P1.1
  P1OUT |= 0x01; // Turn-on RED_LED
  P4OUT &= ~0x80; // Turn-off GREEN_LED
  P7OUT &= ~0x10; // Disable Driver
  while(true); // Infinite cycle; Press reset button to Restart
}
```

GUI Interface Code (Java)

```
/*
  Code developed by: Joaquim Santos
  Course: Integrated Master's in Engineering Physics
*/

import processing.serial.*;
import controlP5.*;

ControlP5 LiDAR_GUI;
Serial serial_port;

PrintWriter range_out;
PrintWriter ToF_out;
PImage bg;
PFont font;
int lf=10, buffer_length=100000, i=0;
int j=0, nr_acq=2400;
boolean START=false, RESET= false, STOP=false;
String ToF_stream = null;
float[] ToF=new float[buffer_length];
float[] range=new float[buffer_length];
float rng_sum=0, square=0;
float rng_mean=0, rng_std=0;
float time_1=0, time_2=0, time_3=0, time=0;
int t=0, q=0;
float[] aux_rng=new float[buffer_length];
float[] aux_time=new float[buffer_length];
float range_max_init = 5, range_max = range_max_init;

void setup(){
  fullScreen();
  bg = loadImage("background_GUI.png");
  frameRate(20); // Refresh Rate (20Hz)
  background(255);

  ToF_out = createWriter("ToF_data.csv"); // Create .csv files
  range_out = createWriter("range_data.csv");
  ToF_out.println("ToF [ns]");
  range_out.println("range [m]");

  LiDAR_GUI = new ControlP5(this); // Create control object
  font = createFont("arial bold",16);

  LiDAR_GUI.addButton("START") // Create buttons
  .setPosition(1150,650)
  .setColorActive(0xff11aa11)
  .setColorBackground(0xff117811)
  .setSize(80,50)
  .setFont(font);

  LiDAR_GUI.addButton("STOP")
  .setPosition(1260,650)
  .setColorActive(0xffcc1111)
  .setColorBackground(0xff852211)
  .setSize(80,50)
  .setFont(font);
}
```



```

LiDAR_GUI.addButton("RESET")
    .setPosition(1040,650)
    .setColorActive(0xff1111cc)
    .setColorBackground(0xff112275)
    .setSize(80,50)
    .setFont(font);

LiDAR_GUI.addButton("X")
    .setPosition(1346,0)
    .setColorActive(0xff000000)
    .setColorBackground(0xff000000)
    .setSize(20,15)
    .setFont(font);

serial_port = new Serial(this,Serial.list()[0],9600); // Serial Port
serial_port.clear();
}

void draw(){
    if(START){
        while(serial_port.available() > 0){
            set_background();
            textSize(20);
            textAlign(CENTER,CENTER);
            time_1 = millis() - time; // Time counting
            text(nf(time_1/1000,0,2)+"s",1180,550);
            ToF_stream = serial_port.readStringUntil(lf); // Read ToF
            if(ToF_stream != null){
                ToF[i] = float(ToF_stream); // Convert to float
                if(!Float.isNaN(ToF[i])){ // Discard if NaN
                    range[i] = ToF[i]*0.15;
                    aux_rng[t] = range[i];
                    aux_time[t] = time_1 % 10000; // Graph 10s refresh rate
                    graph_layout(); // Draw graph
                    textAlign(CENTER,BOTTOM);
                    textSize(38);
                    text(nf(ToF[i],0,2)+"ns",425,655);
                    text(nf(range[i],0,3)+"m",625,655);
                    if(q>100 && j<nr_acq){ // Dismiss first 500 points
                        range_out.println(nf(range[i],0,3));
                        ToF_out.println(nf(ToF[i],0,2));
                        j++;
                        if(j==nr_acq) finish_acquisition();
                    }
                    rng_sum += range[i]; // Sum ranges
                    i++;
                    t++;
                    q++;
                    rng_mean = rng_sum/i; // Mean range
                    square += (range[i-1]-rng_mean)*(range[i-1]-rng_mean);
                    rng_std = sqrt(square/i)*100; // Standard deviation [cm]
                    textAlign(CENTER,CENTER);
                    text(nf(rng_mean,0,3),1100,265);
                    text(nf(rng_std,0,2),1100,450);
                }
            }
        }
    }
}
}
}
}
}

```

```

void set_background(){
    background(bg);
    fill(43,38,78);
    textSize(28);
    text("Average range [m]",1100,215);
    fill(170,0,0);
    text("Std deviation [cm]",1100,400);
    fill(39,102,28);
    textSize(24);
    textSize(20);
    fill(0,0,0);
    text("Program time =",1060,550);
    textAlign(CENTER,BOTTOM);
    fill(10,125,10);
    text("Instantaneous Data:",175,650);
    fill(255);
    stroke(0);
    rect(70,150,15,15);
    if(j==nr_acq){
        stroke(0,150,0);
        strokeWeight(2);
        line(77.5,161,73,155);
        line(77.5,161,84,145);
        fill(0,150,0);
    }
    else fill(150,0,0);
    textSize(15);
    text("Data acquired (" +nr_acq+"pts)",180,167);
    fill(0,0,0);
}

void graph_layout(){ // Draw graph
    fill(252);
    stroke(140);
    strokeWeight(0.5);
    rect(60,175,840,400);
    stroke(0);
    strokeWeight(1);
    line(125,515,835,515); // Draw x axis
    line(125,515,125,215); // Draw y axis
    fill(0);
    triangle(125,215,130,227,120,227);
    triangle(835,515,823,510,823,520);
    textSize(16);
    text("Time [s]",480,550); // Add label to x-axis
    pushMatrix();
    translate(116,68);
    rotate(-HALF_PI);
    text("Range [m]",-300,-38); // Add rotated label to y-axis
    popMatrix();
    fill(0);
    textSize(12);
    int sec = 0;
    // Adjust vertical scale
    if(aux_rng[t] >5 && aux_rng[t] <10) range_max = 10;
    else if(aux_rng[t] >10 && aux_rng[t] <20) range_max = 20;
    else if(aux_rng[t] >20 && aux_rng[t] <30) range_max = 30;
    float inc = range_max / 10;
    for(int k=125;k<810;k+=720/21){
        if(k!=125){ // Add vertical grid

```

```

        stroke(215);
        line(k,220,k,518);
        stroke(0);
        line(k,512,k,518);
    }
    text(sec++,k,525);           // Add x scale
    k+=720/21;
    if(k<810){
        stroke(215);
        line(k,220,k,518);
        stroke(0);
        line(k,512,k,518);
    }
}
float range = 0;
for(int k=515;k>230;k-=300/21){
    if(k!=515){                // Add horizontal grid
        stroke(215);
        line(122,k,830,k);
        stroke(0);
        line(122,k,128,k);
    }
    text(nf(range,0,1),108,k); // Add y scale
    range = range+inc;
    k-=300/21;
    stroke(215);
    line(122,k,830,k);
    stroke(0);
    line(123,k,127,k);
}
if(t!=0){
    if(aux_time[t]<aux_time[t-1]){ // Refresh graph every 10 seconds
        t=0;
        range_max = range_max_init;
    }
    // Map values within the graph window
    aux_rng[t] = 515 - aux_rng[t]*(600/21)*(10/range_max);
    aux_time[t] = 125 + (aux_time[t]/1000)*(700*2/21);
    stroke(0,0,100);
    strokeWeight(1.2);
    for(int w=1;w<t;w++) // Draw graph
        if(aux_rng[w-1]<=515 && aux_rng[w-1]>=230 && aux_rng[w]<=515 &&
aux_rng[w]>=230)
            line(aux_time[w-1],aux_rng[w-1],aux_time[w],aux_rng[w]);
}
}

void START(){
    START = true;
    if(j==0)
        time = millis();
    if(STOP && !RESET){
        time_3 = millis();
        time = time + time_3 - time_2 ;
        STOP = false;
    }
    else if(RESET){
        time = millis();
        RESET = false;
        STOP = false;
    }
}

```

```

}

void STOP(){
    START = false;
    STOP = true;
    RESET = false;
    serial_port.stop();
    serial_port = new Serial(this,Serial.list()[0],9600);
    serial_port.clear();
    time_2 = millis();
}

void RESET(){
    i = 0;
    t = 0;
    range_max = range_max_init;
    rng_sum = 0;
    square = 0;
    set_background();
    textAlign(CENTER,CENTER);
    graph_layout();
    textSize(20);
    text(nf(0,0,2)+"s",1180,550);
    textAlign(CENTER,BOTTOM);
    textSize(38);
    text(nf(0,0,2)+"ns",425,655);
    text(nf(0,0,2)+"m",625,655);
    textAlign(CENTER,CENTER);
    text(nf(0,0,3),1100,265);
    text(nf(0,0,2),1100,450);
    if(START && !STOP){
        time = millis();
        RESET = false;
    }
    else RESET = true;
}

void X(){ // Terminate serial port and close program
    serial_port.stop();
    exit();
}

void finish_acquisition(){ // Print nr_acq points to .csv files
    range_out.flush();
    range_out.close();
    ToF_out.flush();
    ToF_out.close();
}

```

Cubic Spline and Peak Power Evaluation (MATLAB)

```

% Clear Workspace, Command window and Figures
clc; clear all; close all;

% Average Powers measured in S130C [mW]
Laser_P_avg = 19.45;
Optics_P_avg = 16.85;
f_p = 6000;

```

```

% Load pulse voltage waveform
filename = 'C:\Users\Joaquim\Desktop\Engenharia Física\5º
Ano\Dissertação_II\TIDA_Final_Results\Measurements\26_10\Power\Laser_Puls
e_Scope.txt';
delimiter = ' ';
formatSpec = '%f%f%[\n\r]';
fileID = fopen(filename,'r');
dataArray = textscan(fileID, formatSpec, 'Delimiter', delimiter,
'MultipleDelimsAsOne', true, 'ReturnOnError', false);
fclose(fileID);
Time_ = dataArray(:, 1);
Voltage_ = dataArray(:, 2);
f_0_ = Voltage_./max(Voltage_); % Normalize function (f_0)
clearvars filename delimiter formatSpec fileID dataArray ans;

scope_time_ns =Time *1e9; % Time to ns
scope_traces_mean_ =f_0_;

% Determine Pulse FWHM [ns]
halfMax = (min(scope_traces_mean_) + max(scope_traces_mean_)) / 2;
index1 = find(scope_traces_mean_ >= halfMax, 1, 'first');
index2 = find(scope_traces_mean_ >= halfMax, 1, 'last');
FWHM_ = scope_time_ns_(index2) - scope_time_ns_(index1);

% Cubic spline
pp_spline_ =spline(scope_time_ns_,scope_traces_mean_);

% Cubic spline evaluation and integration
nbins_ =1000; % number of bins for integration
time_ns_spline_ =linspace(scope_time_ns_min_,scope_time_ns_max_,nbins_+1)';
;
trace_spline_ =ppval(pp_spline_,time_ns_spline_);
cdf_splined_ =nan(size(time_ns_spline_));

% Function handle for quadrature
fh_splined_quad_ =@(u_)splined_quad(u_,pp_spline_);
% quadrature in function handle :: always starts quadrature in highest
value of the function

cdf_splined_(1)=0;
RELTOL_ =1.0e-9;
ABSTOL_ =1.0e-12;
MAXINTERVALCOUNT_ =5000;
for n =2:1:nbins_+1
% Numerically evaluate integral, adaptive Gauss-Kronrod quadrature
sum_ =ZERO_;
sum_ =quadgk(fh_splined_quad_,time_ns_spline_(n),time_ns_spline_(1),
...
'RelTol',RELTOL_,'AbsTol',ABSTOL_,'MaxIntervalCount',MAXINTERVALCOUNT_);
cdf_splined_(n) =-sum_;
end
n_ =max(size(cdf_splined_)); % Integral result

% Estimate Peak Powers
duty_cycle_ =((FWHM_*10^(-9))/(1/f_p_));
Peak_Laser_approx_ =(Laser_P_avg_*10^(-3))/duty_cycle_;
Peak_Optics_approx_ =(Optics_P_avg_*10^(-3))/duty_cycle_;
Peak_Laser_actual_ =Laser_P_avg_*10^(-3)*(1/f_p_)/(cdf_splined_(n_)*10^(-
9));

```

```

Peak_Optics_actual_ = Optics_P_avg * 10^(-
3) * (1/f_p_) / (cdf_splined_(n_) * 10^(-9));

% Print results
fprintf('\n');
fprintf('\n');
fprintf('::::::::::::::::::::::::::::::::::::::::::::::::::::::::::::::::::
::::::::::::\n');
fprintf('  Approximated Peak Power Laser (W):
%.2f\n', Peak_Laser_approx_);
fprintf('  Approximated Peak Power Optics (W):
%.2f\n', Peak_Optics_approx_);
fprintf('  Duty cycle (FWHM):    %.3e\n', duty_cycle_);
fprintf('::::::::::::::::::::::::::::::::::::::::::::::::::::::::::::::::::
::::::::::::\n');

fprintf('\n');
fprintf('\n');
fprintf('::::::::::::::::::::::::::::::::::::::::::::::::::::::::::::::::::
::::::::::::\n');
fprintf('  Real Peak Power Laser (W):    %.2f\n', Peak_Laser_real_);
fprintf('  Real Peak Power Optics (W):    %.2f\n', Peak_Optics_real_);
fprintf('::::::::::::::::::::::::::::::::::::::::::::::::::::::::::::::::::
::::::::::::\n');

function f_ = splined_quad_ (u_, pp_spline_)
    y_ = ppval(pp_spline_, u_);
    y_ = max(y_, 0.0);
    f_ = y_;
    return
end

```

Polarimetric Images Processing (MATLAB)

```

% Clear Workspace, Command window and Figures
clc; close all; clear;

% Number of images loaded for each target and acquisition conditions
n_file_end_ = 12;
file_ext_ = '.tif';

% Images size
m_pixels_ = [1 2056];
n_pixels_ = [1 2464];

% Directories
Vauxhall_file_root_ = 'C:\Users\Joaquim\Desktop\Engenharia Física\5°
Ano\Dissertação_II\TIDA_Final_Results\Measurements\08_10_Polarization\LAB
\Input Images\Vauxhall\Exposure=6000\';
Kline_file_root_ = 'C:\Users\Joaquim\Desktop\Engenharia Física\5°
Ano\Dissertação_II\TIDA_Final_Results\Measurements\08_10_Polarization\LAB
\Input Images\K-line\Exposure=10000\';

% Load Images to 3D matrix
Vauxhall_ = zeros(m_pixels_(2), n_pixels_(2), n_file_end_);
Kline_ = zeros(m_pixels_(2), n_pixels_(2), n_file_end_);

for i_ = 1:n_file_end_

```

```

Vauxhall_file_name_ =strcat(Vauxhall_file_root_,num2str(i_),file_ext_);
Kline_file_name_ =strcat(Kline_file_root_,num2str(i_),file_ext_);
Vauxhall_(:, :, i_)=(imread(Vauxhall_file_name_,'tiff'));
Kline_(:, :, i_)=(imread(Kline_file_name_,'tiff'));
end

% Average Images
Vauxhall_avg_ =zeros(m_pixels_(2),n_pixels_(2));
Kline_avg_ =zeros(m_pixels_(2),n_pixels_(2));

for i_ =m_pixels_(1):m_pixels_(2)
    for j_ =n_pixels_(1):n_pixels_(2)

Vauxhall_avg_(i_,j_)=(sum(Vauxhall_(i_,j_,1:n_file_end_))/n_file_end_);
Kline_avg_(i_,j_)=(sum(Kline_(i_,j_,1:n_file_end_))/n_file_end_);
        end
    end

% Convert to uint8 (round by default)
Vauxhall_avg_ =uint8(Vauxhall_avg_);
Kline_avg_ =uint8(Kline_avg_);

% Resulting images dimensions
m_pixels_ =[1 2056/2];
n_pixels_ =[1 2464/2];

% Separate 4 Polarization States
I0_Vauxhall_ =zeros(m_pixels_(2),n_pixels_(2));
I45_Vauxhall_ =I0_Vauxhall_;
I90_Vauxhall_ =I0_Vauxhall_;
I135_Vauxhall_ =I0_Vauxhall_;
I0_Kline_ =I0_Vauxhall_;
I45_Kline_ =I0_Kline_;
I90_Kline_ =I0_Kline_;
I135_Kline_ =I0_Kline_;

r_aux_ =1; % Auxiliary Variables to write on new images
c_aux_ =1;

% Since the camera was upside down, the pixels order is reverted, thus
from
% the first (1,1) pixel corresponds to 90°, and then, from the top left
% corner clockwise: I90, I45, I0, I135
for i_ =m_pixels_(1):m_pixels_(2)
    m_odd_ =mod(i_,2);
    for j_ =n_pixels_(1):n_pixels_(2)
        n_odd_ =mod(j_,2);
        if(m_odd_ && n_odd_)
            I90_Vauxhall_(r_aux_,c_aux_) =Vauxhall_avg_(i_,j_);
            I90_Kline_(r_aux_,c_aux_) =Kline_avg_(i_,j_);
        elseif(m_odd_)
            I45_Vauxhall_(r_aux_,c_aux_) =Vauxhall_avg_(i_,j_);
            I45_Kline_(r_aux_,c_aux_) =Kline_avg_(i_,j_);
            c_aux_ =c_aux_ +1;
        elseif(n_odd_)
            I135_Vauxhall_(r_aux_,c_aux_) =Vauxhall_avg_(i_,j_);
            I135_Kline_(r_aux_,c_aux_) =Kline_avg_(i_,j_);
        else
            I0_Vauxhall_(r_aux_,c_aux_) =Vauxhall_avg_(i_,j_);
            I0_Kline_(r_aux_,c_aux_) =Kline_avg_(i_,j_);
        end
    end
end

```

```

        c_aux_=c_aux_+1;
    end
end
    if(~m_odd_) r_aux_=r_aux_+1; end
    c_aux_=1;
end

% Calculate Stokes Parameters

% S0 (Total Intensity); if each individual pixel I90/I0 does not
saturate,
% there is no problem if S0 overcomes 255 (linearity is still mantained)
S0_Vauxhall_=I0_Vauxhall_+I90_Vauxhall_;
S0_Kline_=I0_Kline_+I90_Kline_;

S1_Vauxhall_=(I0_Vauxhall_-I90_Vauxhall_)./S0_Vauxhall_;
S2_Vauxhall_=(I45_Vauxhall_-I135_Vauxhall_)./S0_Vauxhall_;

S1_Kline_=(I0_Kline_-I90_Kline_)./S0_Kline_;
S2_Kline_=(I45_Kline_-I135_Kline_)./S0_Kline_;

% Calculate AoP and DoPL
AoP_Vauxhall_=0.5*atan2d(S2_Vauxhall_,S1_Vauxhall_);
AoP_Kline_=0.5*atan2d(S2_Kline_,S1_Kline_);

DoLP_Vauxhall_=(sqrt(S1_Vauxhall_.^2+S2_Vauxhall_.^2)).*100;
DoLP_Kline_=(sqrt(S1_Kline_.^2+S2_Kline_.^2)).*100;

% Map Angle to Interval [0,180°]
for i_=m_pixels_(1):m_pixels_(2)
    for j_=n_pixels_(1):n_pixels_(2)
        if(AoP_Vauxhall_(i_,j_)<0)
AoP_Vauxhall_(i_,j_)=180+AoP_Vauxhall_(i_,j_); end
        if(AoP_Kline_(i_,j_)<0) AoP_Kline_(i_,j_)=180+AoP_Kline_(i_,j_);
    end
end
end

% Estimate Average Results in Beam Spot Area (Segmentation; unpolarized
% background neglected (Intensity Threshold >3)

I0_Vaux_average_=average_segment(I0_Vauxhall_,2,m_pixels_(2),n_pixels_(2)
);
I135_Vaux_average_=average_segment(I135_Vauxhall_,2,m_pixels_(2),n_pixels
_(2));
I45_Vaux_average_=average_segment(I45_Vauxhall_,2,m_pixels_(2),n_pixels_(
2));
I90_Vaux_average_=average_segment(I90_Vauxhall_,2,m_pixels_(2),n_pixels_(
2));

S0_Vaux_average_=double(I0_Vaux_average_)+double(I90_Vaux_average_);
S1_Vaux_average_=(double(I0_Vaux_average_)-double(I90_Vaux_average_))/
S0_Vaux_average_;
S2_Vaux_average_=(double(I45_Vaux_average_)-double(I135_Vaux_average_))/
S0_Vaux_average_;

DoLP_Vaux_average_=(sqrt(double(S1_Vaux_average_^2+S2_Vaux_average_^2)))*
100
AoP_Vaux_average_=0.5*atan2d(double(S2_Vaux_average_),double(S1_Vaux_aver
age_))

```



```

if(AoP_Vauxhall_average_<0)
AoP_Vauxhall_average_ =AoP_Vauxhall_average_+180; end

I0_K_average_ =average_segment(I0_Kline_,2,m_pixels_(2),n_pixels_(2));
I135_K_average_ =average_segment(I135_Kline_,2,m_pixels_(2),n_pixels_(2));
I45_K_average_ =average_segment(I45_Kline_,2,m_pixels_(2),n_pixels_(2));
I90_K_average_ =average_segment(I90_Kline_,2,m_pixels_(2),n_pixels_(2));

S0_K_average_ =double(I0_K_average_)+double(I90_K_average_);
S1_K_average_ =(double(I0_K_average_)-double(I90_K_average_))/
S0_K_average_;
S2_K_average_ =(double(I45_K_average_)-double(I135_K_average_))/
S0_K_average_;

DoLP_K_average_ =sqrt(double(S1_K_average_^2+S2_K_average_^2))*100
AoLP_K_average_ =0.5*atan2d(double(S2_K_average_),double(S1_K_average_))

function I_avg_ = average_segment(I_,th_,m_,n_)
count_Vaux_ =0;
sum_Vaux_ =0;
for i_ =1:m_
    for j_ =1:n_
        if(I_(i_,j_)>th_)
            count_Vaux_ =count_Vaux_+1;
            sum_Vaux_ =sum_Vaux_+I_(i_,j_);
        end
    end
end
I_avg_ =sum_Vaux_/count_Vaux_;
I_avg_ =uint8(I_avg_);
end

```

– This page is intentionally left blank –

Appendix III – ZEMAX Object Data

Before Optimization

Object Type	Comment	Ref Object	Inside Of	X Position	Y Position	Z Position	Tilt About X	Tilt About Y	Tilt About Z	Material	Par 1 (unused)	Par 2 (unused)	Par 3 (unused)	Par 4 (unused)
Source File	rayfile_SPL_LL90_3_SM_0104...	0	0	0.000	0.000	0.000	0.000	0.000	0.000	-	200	1500000	70.000	0
CAD Part: STEP/IGES/SAT	SPL_LL90_3_020909_GEO.ME...	0	0	0.000	0.000	0.000	0.000	0.000	0.000	-	1.000	1	5	5
Annulus	Stop Iris (TX PCB)	0	0	0.000	0.000	-15.000	0.000	0.000	0.000	ABSORB	50.000	50.000 P	0.000	0.000
Null Object	Laser beam center	1	0	-1.400	0.000	0.000	0.000	0.000	0.000	-				
Even Asphere Lens	C330TMD-B.1	4	0	0.000	0.000	5.014 V	0.000	180.000	0.000	D-ZK3M	2.500	3.214		
Null Object	Referential Rotation	5	0	0.000	0.000	0.000	0.000	180.000	0.000	-				
Standard Lens	LB1092-B.1	6	0	0.000	0.000	41.500 V	0.000	0.000	0.000	N-BK7	14.600	0.000	6.350	6.350
Null Object	LB1092-B Thickness	7	0	0.000	0.000	4.700	0.000	0.000	0.000	-				
Standard Lens	LB1014-B.1	8	0	0.000	0.000	5.100	0.000	0.000	0.000	N-BK7	25.150	0.000	6.350	6.350
Null Object	LB1014-B Thickness	9	0	0.000	0.000	3.400	0.000	0.000	0.000	-				
Standard Lens	LB1450-B.1	10	0	0.000	0.000	4.500	0.000	0.000	0.000	N-BK7	19.920	0.000	6.350	6.350
Null Object	LB1450-B1 Thickness	11	0	0.000	0.000	3.900	0.000	0.000	0.000	-				
Standard Lens	LB1378-B.1	12	0	0.000	0.000	43.000 V	0.000	0.000	0.000	N-BK7	40.720	0.000	6.350	6.350
Null Object	LB1378-B Thickness	13	0	0.000	0.000	2.800	0.000	0.000	0.000	-				
Annulus	SM1D12	14	0	0.000	0.000	15.000 V	0.000	0.000	0.000	ABSORB	15.250	15.250 P	6.000	6.000 P
Null Object	Referential translation	15	0	0.000	-6.365	6.365	0.000	0.000	0.000	-				
Rectangular Volume	Glass Slide (10% reflectivity)	16	0	0.000	0.000	37.000	-45.000	0.000	0.000	-	9.000	9.000 P	1.000	9.000 P
Null Object	Referential rotation	17	0	0.000	0.000	0.000	315.000	0.000	0.000	-				
Standard Lens	LB1258-B.1	18	0	0.000	3.183	-48.000 V	0.000	0.000	0.000	N-BK7	30.360	0.000	6.350	6.350
Detector Rectangle	DET10A/M	19	0	0.000	0.000	-28.900 V	0.000	0.000	0.000	-	0.500	0.500 P	750	750 P
Annulus	Absorber behind detector	20	0	0.000	0.000	-1.000E+...	0.000	0.000	0.000	ABSORB	1.000	1.000 P	0.000	0.000
Rectangular Volume	Target ("K" Line)	15	0	0.000	0.000	500.000	15.000	0.000	0.000	-	75.000	100.000	1.000	75.000
Null Object	Referential rotation	22	0	0.000	0.000	0.000	15.000	180.000	0.000	-				
Standard Lens	LA1401-B.1	23	0	0.000	0.000	500.000	0.000	0.000	0.000	N-BK7	30.900	0.000	25.400	25.400
Standard Lens	LA1074-B.1	24	0	0.000	0.000	98.300	0.000	0.000	0.000	N-BK7	10.300	0.000	6.350	6.350
Detector Rectangle	SFH 2400 FA	25	0	0.000	0.000	45.000	0.000	0.000	0.000	-	0.500	0.500 P	750	750 P
Annulus	SFH 2400 FA positon	26	0	0.000	0.000	1.000	0.000	0.000	0.000	ABSORB	20.000	20.000 P	0.000	0.000

After Optimization

Object Type	Comment	Ref Object	Inside Of	X Position	Y Position	Z Position	Tilt About X	Tilt About Y	Tilt About Z	Material	Par 1 (unu)	Par 2 (unu)	Par 3 (unus)	Par 4 (unus)
Source File	rayfile_SPL_LL90_3_SM_0104...	0	0	0.000	0.000	0.000	0.000	0.000	0.000	-	200	15000...	70.000	0
CAD Part: STEP/IGES/SAT	SPL_LL90_3_020909_GEO.ME...	0	0	0.000	0.000	0.000	0.000	0.000	0.000	-	1.000	1	5	5
Annulus	Stop Iris (TX PCB)	0	0	0.000	0.000	-15.000	0.000	0.000	0.000	ABSORB	50.000	50.000 P	0.000	0.000
Null Object	Laser beam center	1	0	-1.400	0.000	0.000	0.000	0.000	0.000	-				
Even Asphere Lens	C330TMD-B.1	4	0	0.000	0.000	5.122 V	0.000	180.000	0.000	D-ZK3M	2.500	3.214		
Null Object	Referential Rotation	5	0	0.000	0.000	0.000	0.000	180.000	0.000	-				
Standard Lens	LB1092-B.1	6	0	0.000	0.000	41.500 V	0.000	0.000	0.000	N-BK7	14.600	0.000	6.350	6.350
Null Object	LB1092-B Thickness	7	0	0.000	0.000	4.700	0.000	0.000	0.000	-				
Standard Lens	LB1014-B.1	8	0	0.000	0.000	5.100	0.000	0.000	0.000	N-BK7	25.150	0.000	6.350	6.350
Null Object	LB1014-B Thickness	9	0	0.000	0.000	3.400	0.000	0.000	0.000	-				
Standard Lens	LB1450-B.1	10	0	0.000	0.000	4.500	0.000	0.000	0.000	N-BK7	19.920	0.000	6.350	6.350
Null Object	LB1450-B1 Thickness	11	0	0.000	0.000	3.900	0.000	0.000	0.000	-				
Standard Lens	LB1378-B.1	12	0	0.000	0.000	41.258 V	0.000	0.000	0.000	N-BK7	40.720	0.000	6.350	6.350
Null Object	LB1378-B Thickness	13	0	0.000	0.000	2.800	0.000	0.000	0.000	-				
Annulus	SM1D12	14	0	0.000	0.000	30.000 V	0.000	0.000	0.000	ABSORB	15.250	15.250 P	6.000	6.000 P
Null Object	Referential translation	15	0	0.000	-6.365	6.365	0.000	0.000	0.000	-				
Rectangular Volume	Glass Slide (10% Reflec)	16	0	0.000	0.000	37.000	-45.000	0.000	0.000	-	9.000	9.000	1.000	9.000
Null Object	Referential Rotation	17	0	0.000	0.000	0.000	315.000	0.000	0.000	-				
Standard Lens	LB1258-B.1	18	0	0.000	3.183	-47.325 V	0.000	0.000	0.000	N-BK7	30.360	0.000	6.350	6.350
Detector Rectangle	DET10A/M	19	0	0.000	0.000	-28.129	0.000	0.000	0.000	-	0.500	0.500 P	750	750 P
Annulus	Detector Absorbs Light	20	0	0.000	0.000	-1.000E+...	0.000	0.000	0.000	ABSORB	1.000	1.000	0.000	0.000
Rectangular Volume	Target ("K" Line)	15	0	0.000	0.000	500.000	15.000	0.000	0.000	-	75.000	100.000	1.000	75.000
Null Object	Referential Rotation	22	0	0.000	0.000	0.000	15.000	180.000	0.000	-				
Standard Lens	LA1401-B.1	23	0	0.000	0.000	500.000	0.000	0.000	0.000	N-BK7	30.900	0.000	25.400	25.400
Standard Lens	LA1074-B.1	24	0	0.000	0.000	98.300	0.000	0.000	0.000	N-BK7	10.300	0.000	6.350	6.350
Detector Rectangle	SFH 2400 FA	25	0	0.000	0.000	45.000 V	0.000	0.000	0.000	-	0.500	0.500 P	750	750 P
Annulus	SFH 2400 FA positon	26	0	0.000	0.000	1.000	0.000	0.000	0.000	ABSORB	20.000	20.000 P	0.000	0.000